International Journal of Photoenergy

Environmental Photocatalysis 2013

Guest Editors: Jiaguo Yu, Christos Trapalis, Pengyi Zhang, Guisheng Li, and Huogen Yu

Environmental Photocatalysis 2013

International Journal of Photoenergy

Environmental Photocatalysis 2013

Guest Editors: Jiaguo Yu, Christos Trapalis, Pengyi Zhang, Guisheng Li, and Huogen Yu

Editorial Board

Contents

Hindawi Publishing Corporation
International Journal of Photoenergy
Volume 2013, Article ID 786806, 3 pages
http://dx.doi.org/10.1155/2013/786806

Editorial

Environmental Photocatalysis 2013

Jiaguo Yu,[1] Christos Trapalis,[2] Pengyi Zhang,[3] Guisheng Li,[4] and Huogen Yu[5]

[1] *State Key Laboratory of Advanced Technology for Material Synthesis and Processing, Wuhan University of Technology, Luoshi Road No. 122, Wuhan 430070, China*
[2] *Institute of Materials Science, National Centre for Scientific Research "Demokritos," Ag. Paraskevi, Attikis, Greece*
[3] *State Key Joint Laboratory of Environment Simulation and Pollution Control, School of Environment, Tsinghua University, Beijing, China*
[4] *Department of Chemistry, Key Laboratory of Resource Chemistry of Ministry of Education, Shanghai Normal University, Shanghai 200234, China*
[5] *Department of Chemistry, School of Science, Wuhan University of Technology, Wuhan 430070, China*

Correspondence should be addressed to Jiaguo Yu; jiaguoyu@yahoo.com

Received 16 December 2013; Accepted 16 December 2013

Semiconductor photocatalysis has caused enormous attention in recent year and has been demonstrated to be one of the "green" and effective methods for water and air purification, water disinfection, hazardous waste remediation, antibacterial, and self-cleaning. However, owing to low photocatalytic efficiency, the environmental applications of various photocatalytic materials and technologies are still very limited. Thus, more improvement and investigations are highly required from the viewpoint of practical use.

This special issue contains 20 papers, which are mainly related to pollutant degradation and environmental purification. Among them, 10 papers are related to composite of two semiconductors including TiO_2 and other semiconductors, 4 papers deal with fabrication of new photocatalytic materials, 2 papers are about doping of TiO_2, and 4 papers are devoted to immobilization of TiO_2. Furthermore, there are 13 papers devoting degradation of pollutant in water, 4 papers on air purification including decomposition of formaldehyde, NO and benzene, 2 papers related to hydrogen production, and 1 paper dealing with bactericidal activity of TiO_2. We would like to express our sincere thanks to all the authors for submitting their interesting works to this special issue. A brief summary of all 20 accepted papers is provided as follows.

In "A cost-effective solid-state approach to synthesize g-C_3N_4 coated TiO_2 nanocomposites with enhanced visible light photocatalytic activity," the authors describe the fabrication and photocatalytic performance of g-C_3N_4/TiO_2 nanocomposites by a facile solid-state method using urea and commercial TiO_2 as precursors. The prepared nanocomposites exhibited enhanced absorption and photocatalytic performance for degradation of aqueous MB in visible light region.

The paper "Synthesis and characterization of pyrochlore $Bi_2Sn_2O_7$ doping with praseodymium by hydrothermal method and its photocatalytic activity study" reports preparation of Pr-doped $Bi_2Sn_2O_7$ (BSO) by a hydrothermal method. The photocatalytic activity of the prepared samples was evaluated by the degradation of rhodamine Bextra (RhB) and 2,4-dichlorophenol (2,4-DCP) in aqueous solution under visible light. Pr-doped BSO samples exhibited enhanced visible-light photocatalytic activity and the optimal dopant amount of Pr was determined to be 1.0 mol%.

The paper "Single step formation of C-TiO_2 nanotubes: influence of applied voltage and their photocatalytic activity under solar illumination" presents fabrication of self-aligned and high-uniformity carbon (C)-titania (TiO_2) nanotube arrays by single step anodization of titanium (Ti) foil at 30 V for 1 h. The photocatalytic activity evaluation of C-TiO_2 samples was performed by degradation of methyl orange (MO) solution. The results revealed that controlled nanoarchitecture C-TiO_2 photocatalyst led to a significant enhancement in photocatalytic activity.

The paper "Removal of formaldehyde using highly active Pt/TiO_2 catalysts without irradiation" describes preparation of TiO_2 supported Pt catalysts by sol-gel method and their application for eliminating formaldehyde (HCHO) at room temperature without irradiation. More than 96% of the conversion of HCHO was obtained over 0.5 wt% Pt/TiO_2-H_2 sample, on which highly dispersed metallic Pt nanoparticles with ~2 nm were identified.

The paper "CTAB-assisted hydrothermal synthesis of $Bi_2Sn_2O_7$ photocatalyst and its highly efficient degradation of organic dye under visible-light irradiation" reported preparation of Pyrochlore-type $Bi_2Sn_2O_7$ (BSO) nanoparticles by a hydrothermal method assisted with cetyltrimethylammonium bromide (CTAB). The photocatalytic activity of the BSO assisted with CTAB was two times that of the reference BSO.

The paper "H_2 fuels from photocatalytic splitting of seawater affected by nano-TiO_2 promoted with CuO and NiO" described preparation and photocatalytic performance of nanostructured TiO_2 loaded with NiO (2.5%) and CuO (2.5%). The accumulated H_2 yielded from the photocatalytic splitting of seawater containing oxalic acid (50 mM) as the sacrificial reagents on CuO/nano-TiO_2 was 8.53 μmol/g_{cat} after the 5 h radiation. On the NiO/nano-TiO_2 photocatalyst, the H_2 yield was relatively low (i.e., 1.46 μmol/g_{cat}).

In "Dynamic hydrogen production from methanol/water photo-splitting using Core@Shell-structured CuS@TiO_2 catalyst wrapped by high concentrated TiO_2 particles," core@shell-structured CuS@TiO_2 catalysts were prepared and the prepared samples exhibited a wide absorption range above 700 nm comparing with pure TiO_2. Hydrogen evolution rate from methanol/water photo-splitting over the core@shell-structured CuS@TiO_2 photocatalyst was about 10-fold higher than pure CuS.

In "Enhanced visible light photocatalytic activity for TiO_2 nanotube array films by codoping with tungsten and nitrogen," a series of W, N codoped TiO_2 nanotube arrays (TNAs) with different dopant contents, were fabricated by anodizing, followed with hydrothermal treatment. W and N codoping successfully extended the absorption of TNAs into the whole visible light region and resulted in remarkably enhanced photocatalytic activity under visible light irradiation.

The paper "Kinetics study of photocatalytic activity of flame-made unloaded and Fe-loaded CeO_2 nanoparticles" reported preparation and enhanced photocatalytic activity of Fe-doped and undoped CeO_2 by flame spray pyrolysis method. Photocatalytic studies showed that Fe-doped CeO_2 sample exhibited higher activity than un-doped CeO_2 sample, with optimal 2.00 mol% of iron loading concentration.

The paper "Solar photocatalytic degradation of bisphenol A on immobilized ZnO or TiO_2" reported the removal of bisphenol A (BPA) under simulated solar irradiation in the presence of either TiO_2 or ZnO catalysts immobilized onto glass plates. BPA degradation followed first-order reaction kinetics.

In "Supported zinc oxide photocatalyst for decolorization and mineralization of orange G dye wastewater under UV365 irradiation," a photocatalytic system by utilizing both cold cathode fluorescent light (CCFL) UV irradiation and steel mesh supported ZnO nanoparticles in a closed reactor for the degradation of azo dye C.I. Orange G (OG) was reported. The ZnO-coated steel mesh can be repeatedly used over 10 cycles without significant loss of catalyst mass.

In "The multiple effects of precursors on the properties of polymeric carbon nitride," polymeric graphitic carbon nitride (g-C_3N_4) materials were prepared by direct pyrolysis of thiourea, dicyandiamide, melamine, and urea under the same conditions, respectively. The photocatalytic activity of the samples was evaluated by the removal of NO in gas phase under visible light irradiation. Considering the cost, toxicity, and yield of the precursors and the properties of g-C_3N_4, the best precursor for preparation of g-C_3N_4 was melamine.

In "One-step synthesis of TiO_2/perlite composites by flame spray pyrolysis and their photocatalytic behavior," TiO_2/perlite composites were prepared by facile one-step flame spray pyrolysis (FSP) route using titanium alkoxide (TIPO) and expanded perlite as Ti source and substrate, respectively. The porosity and the light absorbance of the TiO_2/perlite composites were examined and their photocatalytic activity in NO oxidation was evaluated. The best photocatalytic activity of the composites was connected to almost equal anatase-rutile ratio and possible synergetic effect of the two TiO_2 phases.

The paper "Au/TiO_2 reusable photocatalysts for dye degradation" reported preparation of Nanogold-doped TiO_2 catalysts and their application in the photodegradation of dye pollutants. Au-doped systems showed very good photoactivity in the degradation of dye pollutants under UV irradiation as well as in sunlight.

The paper "Fabrication, modification, and emerging applications of TiO_2 nanotube arrays (TNAs) by electrochemical synthesis: a review" reviewed the recent progress of the new research achievements of TNAs on the preparation processes, forming mechanism, and modification. In addition, the authors also reviewed potential and significant applications in the photocatalytic degradation of pollutants, solar cells, water splitting, and other aspects. Finally, the existing problems and further prospects of this renascent and rapidly developing field were also briefly addressed and discussed.

In "Photocatalytic degradation of organic dyes by $H_4SiW_6Mo_6O_{40}/SiO_2$ sensitized by H_2O_2," $H_4SiW_6Mo_6O_{40}/SiO_2$ was sensitized by H_2O_2 solution that significantly improved its catalytic activity under simulated natural light. The photodegradation of malachite green, methyl orange, methylene blue, and Rhodamine B were also tested, and the degradation rate of dyes reached 90%–98%.

In "Enhancement of photocatalytic activity on TiO_2-nitrogen-doped carbon nanotubes nanocomposites," TiO_2-nitrogen-doped carbon nanotubes (TiO_2-CNx) nanocomposites were successfully synthesized by a facile hydrothermal method. TiO_2-CNx nanocomposites exhibited much higher photocatalytic activity than neat TiO_2 and TiO_2-CNTs mechanical nanocomposites. The improved photodegradation performances were attributed to the suppressed recombination of electrons and holes caused by the effective transfer of photogenerated electrons from TiO_2 to CNx.

In "Effect of different calcination temperatures on the structural and photocatalytic performance of Bi-TiO_2/SBA-15," the Bi-TiO_2/SBA-15 composite was synthesized by an easy wet impregnation method. It was found that SBA-15 retained the ordered hexagonal mesostructure after incorporation of TiO_2 and Bi. The Bi-TiO_2/SBA-15 composite exhibited higher photocatalytic activities than pure TiO_2 and Bi_2O_3.

The paper "Photocatalytic oxidation of gaseous benzene under 185 nm UV irradiation" reported that benzene removal efficiency of Photocatalytic oxidation (PCO) with 254 nm UV irradiation (denoted as 254-PCO) was only 2.1%, while it was greatly increased to 51.5% in 185-PCO. 185-PCO exhibited superior capacity for benzene oxidation. In the 185-PCO process, much ozone was left in case of TiO_2 as photocatalysts while it could be nearly eliminated by 1% Co-TiO_2.

The paper "Bactericidal activity of TiO_2 on cells of pseudomonas aeruginosa ATCC 27853" presented the antibacterial effects of TiO_2 and light exposure (at 365 nm) on Pseudomonas aeruginosa ATCC 27853. Following 90 minutes exposure to TiO_2 and UV light, logarithm of cell density was reduced from 6 to 3.

Jiaguo Yu
Christos Trapalis
Pengyi Zhang
Guisheng Li
Huogen Yu

Hindawi Publishing Corporation
International Journal of Photoenergy
Volume 2013, Article ID 752605, 10 pages
http://dx.doi.org/10.1155/2013/752605

Research Article

Au/TiO_2 Reusable Photocatalysts for Dye Degradation

Silija Padikkaparambil,[1] Binitha Narayanan,[2] Zahira Yaakob,[1] Suraja Viswanathan,[1] and Siti Masrinda Tasirin[1]

[1] *Department of Chemical and Process Engineering, Faculty of Engineering and Built Environment, Universiti Kebangsaan Malaysia (UKM), 43600 Bangi, Selangore, Malaysia*
[2] *Department of Chemistry, Sree Neelakanta Government Sanskrit College, Pattambi, Kerala 679306, India*

Correspondence should be addressed to Zahira Yaakob; zahira65@yahoo.com

Received 1 July 2013; Revised 11 September 2013; Accepted 13 September 2013

Academic Editor: Jiaguo Yu

Nanogold doped TiO_2 catalysts are synthesized, and their application in the photodegradation of dye pollutants is studied. The materials are characterized using different analytical techniques such as X-ray diffraction, transmission electron microscopy, UV-visible diffuse reflectance spectroscopy, and X-ray photoelectron spectroscopy. The results revealed the strong interaction between the metallic gold nanoparticles and the anatase TiO_2 support. Au doped systems showed very good photoactivity in the degradation of dye pollutants under UV irradiation as well as in sunlight. A simple mechanism is proposed for explaining the excellent photoactivity of the systems. The reusability studies of the photocatalysts exhibited more than 98% degradation of the dye even after 10 repeated cycles.

1. Introduction

Even though dyes are classified as pollutants, they are widely applied in the textile manufacturing industries. The discharge of dyes causes soil as well as water pollution depending on its mode of disposal. In addition, since the dye stuffs are intentionally designed to resist aerobic oxidation by microorganisms, only partial degradation of dye molecules are possible with aerobes, and it results in the formation of volatile carcinogenic compounds. So the treatment of these dye effluents is highly desired for the preservation of clean air, soil, and water.

TiO_2, in the anatase form, is one of the best photocatalysts for pollutant degradation [1]. However, because of the relatively high intrinsic band gap of anatase TiO_2 (3.2 eV), ultraviolet (UV) irradiation is required for its photoactivity [2, 3], and thus only 4% of the sunlight (UV fraction of solar spectrum) can be utilized effectively [4]. Thus, pure TiO_2 based systems have been found to be inactive under sunlight. Application of UV lamps has serious disadvantages including high energy consumption and handling problems. Keeping this in mind, researchers focused to develop TiO_2 based systems having decreased band gap so as to show photocatalytic activity in the visible region. This will enable the use of sunlight for photocatalysis [5]. Several modification methods are available to shift the wavelength of absorption of TiO_2 from UV to visible region, among which anion doping succeed in this matter [6–11]. Nitrogen is the widely studied anion dopant where the photoactivity of the N doped TiO_2 even arises by the presence of molecularly adsorbed N_2 [12]. Thus, the activity may decrease by storing the catalyst for long time.

The second main drawback associated with the photocatalytic activity of TiO_2 is that most of the activated charge carriers will undergo recombination before reaching the surface, preventing interaction with adsorbed molecules. In fact, 90% of the charge carriers may be lost within a nanosecond of their generation leading to low photoactivity of TiO_2 [13]. The high recombination rate of photogenerated electron-hole pairs, which controls the photocatalytic efficiency of semiconductors, can be reduced by trapping the electrons with noble metals [14]. The noble metals such as Pt, Ag, and

Au, when deposited over TiO_2, can act as electron traps, since they have the high Schottky barriers among the metals [15–19].

Our aim is to develop highly competent catalysts, which can prevent the recombination of charge carriers effectively, so that the photocatalysts can act well even by utilizing the UV light from the sun. In the present work, the surface doping of sol gel TiO_2 has been done with gold nanoparticles (AuNPs), with an aim to trap the electrons to prevent recombination. The selection of AuNPs as dopant was also based on its property of UV light absorption, causing the transition of 5d electrons to the 6sp band (interband transition) [20, 21]. It is also reported that due to the high photon energy, UV light is able to drive chemical reactions on AuNPs [22]. AuNP supported over zeolite, ZrO_2, and SiO_2, were found to be effective for the degradation of dye pollutant sulforhodamine-B [22]. The incorporation of nanogold over supports other than TiO_2 required high percentage loading of gold for its effective photocatalytic activity [22]. Thus, a combination of AuNP and TiO_2 can lead to the formation of a cost effective photocatalyst.

In the present study, nanogold particles were doped over TiO_2 catalysts, using chloroauric acid as the gold precursor, by deposition-precipitation method. TiO_2 was prepared by sol-gel method. Highly dispersed gold nanoparticles with diameter less than 5 nm were found to be deposited over TiO_2. All the TiO_2 based catalysts of the present study were found to exist in the anatase phase. The reaction parameters were varied in the degradation of methylorange (MO) for attaining best conditions for photocatalysis.

2. Experimental

2.1. Preparation of Titania Support. Titania photocatalysts using titanium (IV) isopropoxide (Sigma Aldrich) as titanium precursor were prepared by sol-gel method with slight modifications from the reported procedure [23]. 0.0628 mol titanium (IV) isopropoxide and 0.8563 mol ethyl alcohol (Hamberg Chemicals), were mixed first. Then a mixture of 0.8563 mol ethyl alcohol, 0.2186 mol glacial acetic acid (R &M Chemicals) and 6.25 mL distilled water was added to the above solution. The resultant solution was stirred to get transparent titania sol. It was then aged for 2 days and dried in an air oven at 80°C. Ground into fine powder and calcination was done at 400°C for 5 h to obtain TiO_2 powder.

2.2. Preparation of Nanogold Doped Titania. For the preparation of nanogold, 2.1×10^{-3} M chloroauric acid (Sigma Aldrich) solution was used as the gold precursor, and NaOH (R&M Chemicals) was added to it under stirring so as to adjust the pH of the solution to 8. For nanogold doping over TiO_2, required amount of TiO_2 powder was added to the freshly prepared nanogold solution where the pH of 8 was kept constant at 70°C, and the solution was stirred well for 2 hours. The mixture was filtered, and the residue was washed with distilled water to remove chloride ions. The nanogold incorporated TiO_2 was dried at 80°C and calcined at 200°C for 5 h. The doped systems were designated as n%Au/TiO_2, where n indicates the weight percentage of gold taken for doping over TiO_2.

2.3. Catalyst Characterization. XRD patterns of the samples were recorded for 2θ between 3 and 80° on a Bruker AXS D8 Advance diffractometer employing a scanning rate of 0.02°/S with Cu Kα radiation (λ = 1.5418 Å). Transmission electron microscopic (TEM) analyses were conducted using ZEISS LIBRA 200 electron microscope. XPS of 1.5%Au/TiO_2 sample was recorded with a SPECS spectrometer using nonmonochromatic AlKα source (1486.6 eV) run at 150 W (12 kV and 12.5 mA). Survey scan was obtained with 70 eV pass energy and high resolution scan of Ti 2p, O 1s and Au 4f with 40 eV pass energy. The binding energies reported here were calculated with reference to C 1 s peak at 284.6 eV. Au 4f core level was curve fitted into several components with Gaussian-Lorentzian peaks after subtracting Shirley background. Diffuse reflectance Ultraviolet-visible spectroscopy (UV-vis DRS) of powder catalyst samples was carried out at room temperature using a Varian, Cary 5000 spectrophotometer in the range of 200 to 800 nm. Elemental composition of the prepared samples was determined by using Thermo Electron IRIS INTREPID II XSP DUO Inductively Coupled Plasma Atomic Emission Spectrometer (ICP-AES).

2.4. Photoactivity Measurements. The efficiency of the nanogold doped TiO_2 photocatalysts was examined by the photodegradation of dye pollutants in a Rayonet type Photoreactor (Associate Technica, India) having 16 UV tubes of 8W (HITACHI F8T5 8 WATT Hittach, Ltd., Tokyo, Japan) capacity. In a typical experiment, 50 mL of 10 mg/L of MO was placed in a quartz tube containing 3 g/L of catalyst and was irradiated with UV light under continuous stirring by air flow for 1 h. The above mentioned conditions were used in all experiments unless otherwise mentioned. The MO concentration was analyzed using a Varian, Cary spectrophotometer by absorbance measurements at the wavelength of maximum absorption of MO (464 nm) before and after degradation. The reaction conditions such as catalyst weight (1 to 5 g/L), dye concentration (5 to 20 mg/L), irradiation time (30 to 120 min under sunlight and 15 to 90 min under UV light irradiation), weight percentage of gold over TiO_2, and so forth were varied to find out the best condition for maximum photodegradation. The degradation studies were also conducted under different pH. Performance of 2%Au/TiO_2 in degrading different dyes in the selected conditions was also evaluated. Activity studies under sunlight were investigated using 1.5%Au/TiO_2.

3. Results and Discussion

3.1. Catalyst Characterization. XRD patterns of the undoped and AuNP doped samples in Figure 1 showed anatase as the only phase (major peak at $2\theta = 25.5°$), which is reported as the most photocatalytically active crystalline state of TiO_2 [24]. No peaks for gold are found to be present, indicating efficient dispersion of the inserted metal with dimensions lower than 5 nm [25]. TEM images shown in Figure 2 supported the

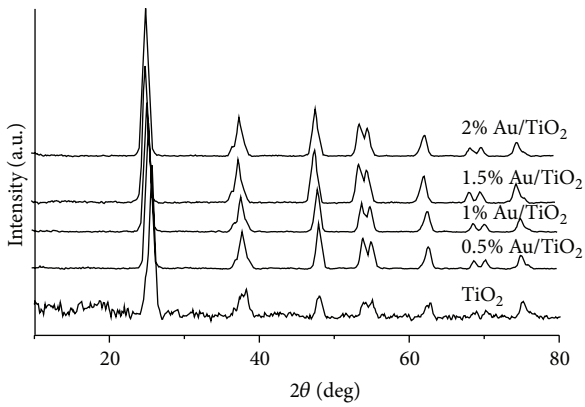

Figure 1: XRD patterns of the prepared photocatalysts.

above supposition. Well-dispersed gold nanoparticles, in the range of 2-3 nm diameters, appeared as black spots over the gray-coloured spherical particles of TiO_2. Since AuNP over TiO_2 is having diameter less than 5 nm, it lies in the size range required for effective use of nanogold in catalysis [26]. The spherical shaped titania particles have diameters in the range of 15–25 nm. Anatase lattice fringes are visible, and the micrograms demonstrate that the particles are connected to each other to form a mesoporous crystalline framework [27].

The XPS spectrum of the representative sample, 1.5%Au/TiO_2, was measured to elucidate the chemical state of Au and other species in the prepared samples. Figure 3 shows the wide scan spectra of the sample, and the spectra corresponding to Ti 2p, O 1s and Au 4f. From the high resolution spectra, it can be seen that the Ti 2p peaks appeared at binding energies (B.E.) of 458.7 ($2p_{3/2}$) and 464.4 ($2p_{1/2}$). The peak at 458.7 corresponds to titanium in pure anatase. Here, the energy splitting between Ti $2p_{1/2}$ and Ti $2p_{3/2}$ is 5.7 eV, which confirms the existence of titanium as Ti^{4+} [28]. It is also reported that the position of the Ti $2p_{3/2}$ component at 458.7 eV corresponds to the oxidation state of +4 of Ti in titanium dioxide [29, 30]. The O 1s B.E. of the sample is located at 530.0 eV, which is assigned to bulk oxide (O^{2-}) in the TiO_2 lattice. Therefore, it can be concluded that no obvious changes on the chemical state of Ti and O were caused by doped and deposited Au.

Au 4f XPS spectrum of 1.5%Au/TiO_2 sample exhibited peaks at the B.E. values of 83.6 and 87.1 eV for $4f_{7/2}$ and $4f_{5/2}$ electrons, corresponding to Au in the metallic state [31]. In addition, peaks arising from Au^{+1} are observed at 84.8 eV ($4f_{7/2}$) and 88.6 ($4f_{5/2}$). It is depicted that 92% of Au exists in Au^0 state and 8% exists in its ionic state, Au^+. This confirms the formation of nanogold, Au^0 on the TiO_2 surface. As per the reported data [32, 33], the doublet of Au^0 was centered at 84.0 and 87.7 eV. The decrease in the binding energies of Au 4f peaks in the present Au doped TiO_2 system may be due to the negative charge of the Au nanoparticles as a result of the charge transfer from the TiO_2 substrate as already reported [34]. The formation of negative charge of the Au nanoparticles may be due to the large difference in the work function of Au and TiO_2 which facilitates the electron transfer from TiO_2 to Au [34]. The negative shift in comparison with bulk gold thus suggests the formation of a strong metal-support interaction [35] over the present catalyst. XPS analysis also confirmed the absence of any contamination from sodium and chlorine species (NaOH and $HAuCl_4$), which were used during the doping process.

Two bands are observed in the UV-visible diffuse reflectance spectra of Au doped TiO_2 samples (Figure 4). The intense band with absorption maxima around 320 to 350 nm is associated to the O^{2-}-Ti^{4+} charge-transfer, corresponding to the electronic excitation from the valence band to the conduction band [36]. In the case of undoped TiO_2, this band is found to be highly intense, which may be a result of the presence of greater number of Ti^{4+} ions and consequently a greater number of Ti^{4+}-O^{2-} bonds [37]. Gold doping decreases the intensity of this band, which can be due to the interaction between Au nanoparticles with the TiO_2 support [38]. The metal-support interaction is already suggested from the interpretation of XPS results. A slight red shift of the above band is observed upon gold doping. The shift may be due to the insertion of metal ions into the TiO_2 at substitutional sites [39]. XPS analysis revealed the presence of a minor percentage of Au^+ in the representative sample, 1.5%Au/TiO_2, supporting this possibility. Nanogold doped samples show the presence of a comparatively less intense band with λ_{max} in the region of 540–570 nm. This band can be attributed to the surface plasmon resonance of Au, which arises from the collective oscillations of the free conduction band electrons that are induced by the incident electromagnetic radiation [40, 41].

The elemental analysis results of representative samples, 1%Au/TiO_2, 1.5%Au/TiO_2, and 2%Au/TiO_2, reveals the inserted Au contents as 0.074 wt%, 0.182 wt%, and 0.225 wt%, respectively. Increase in the amount of gold precursor in the preparation showed an increase in the amount of metal incorporated over TiO_2. The incorporated amount was less than the amount of gold taken, which may be due to the loss of unbound nanogold while washing the catalysts with distilled water during the preparation.

3.2. Photocatalytic Activity. The activity of the different systems under visible light was investigated, and it was found that the photocatalysts were not active under visible light. But the experiments under UV irradiation were satisfactory in the degradation of MO. The reaction parameters were varied to get best results.

Figure 5 describes the effect of reaction conditions on the performance of the catalyst. Initial steep rise in photodegradation capacity is observed with increase in the amount of catalyst weight, which then attains saturation at a catalyst dosage of 3 g/L. Thus a catalyst weight of 3 g/L (0.15 g) was selected for further studies. The dye concentration is varied, and from the results, it is observed that the catalyst showed 100% degradation of the dye pollutant at low concentrations. The activity decreased from an increased dye concentration of 15 mg/L onwards as seen from the data shown in Figure 5(b). We also varied the pH of the solution, since the dye pollutant effluent from the industry may be of different pH. The

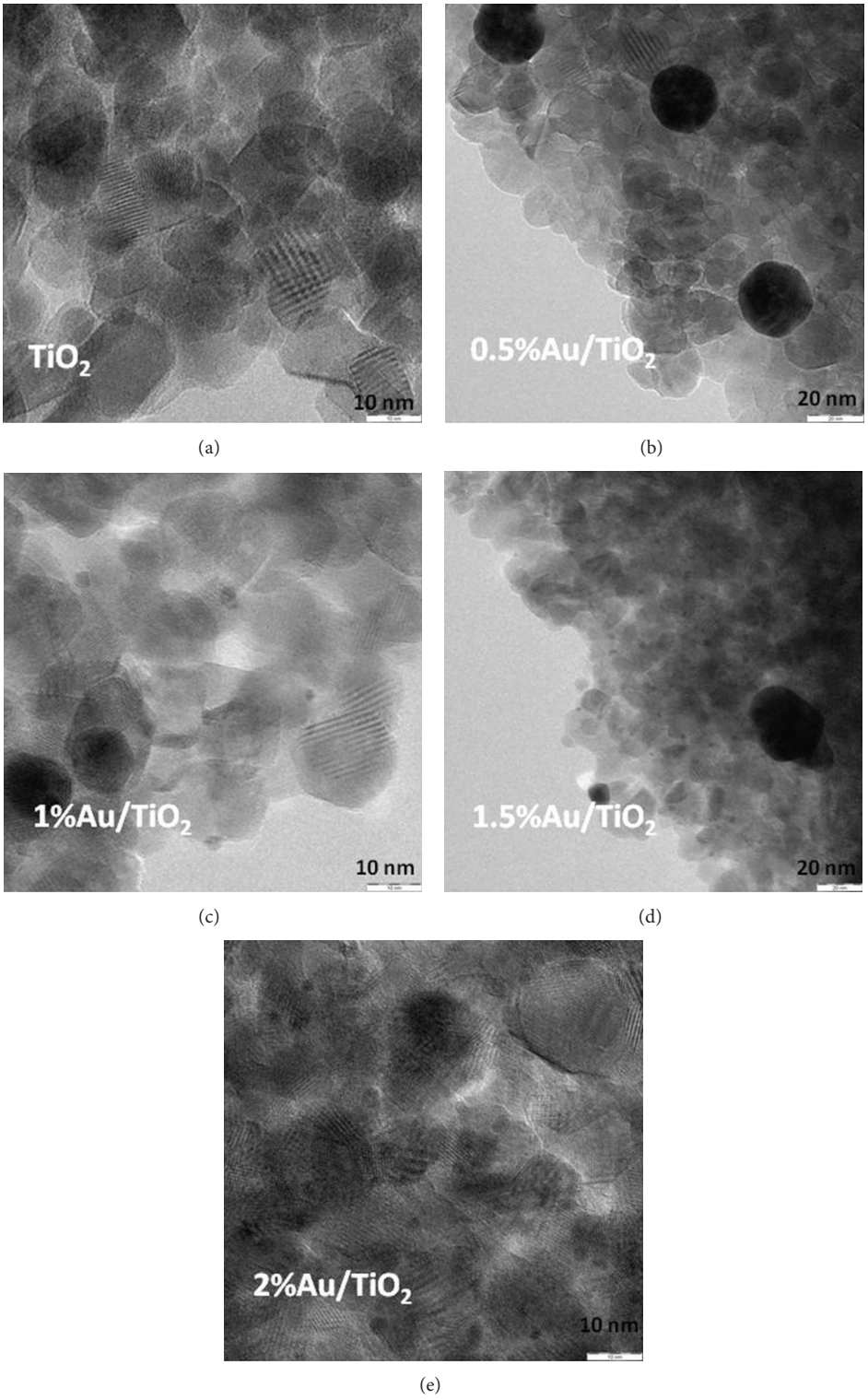

Figure 2: TEM image of TiO_2 and AuNP loaded TiO_2 photocatalysts.

catalysts worked well in lower pH values till the natural pH of the solution. Under basic pH, activity is reduced and the percentage dye degradation decreased to 84.9% at a high pH value of 11. Still, the activity is better since the percentage dye degradation is more than 80% as observed in the results shown in Figure 5(c).

The percentage of gold doping over TiO_2 is varied to attain maximum photoactivity, and the dye degradation is

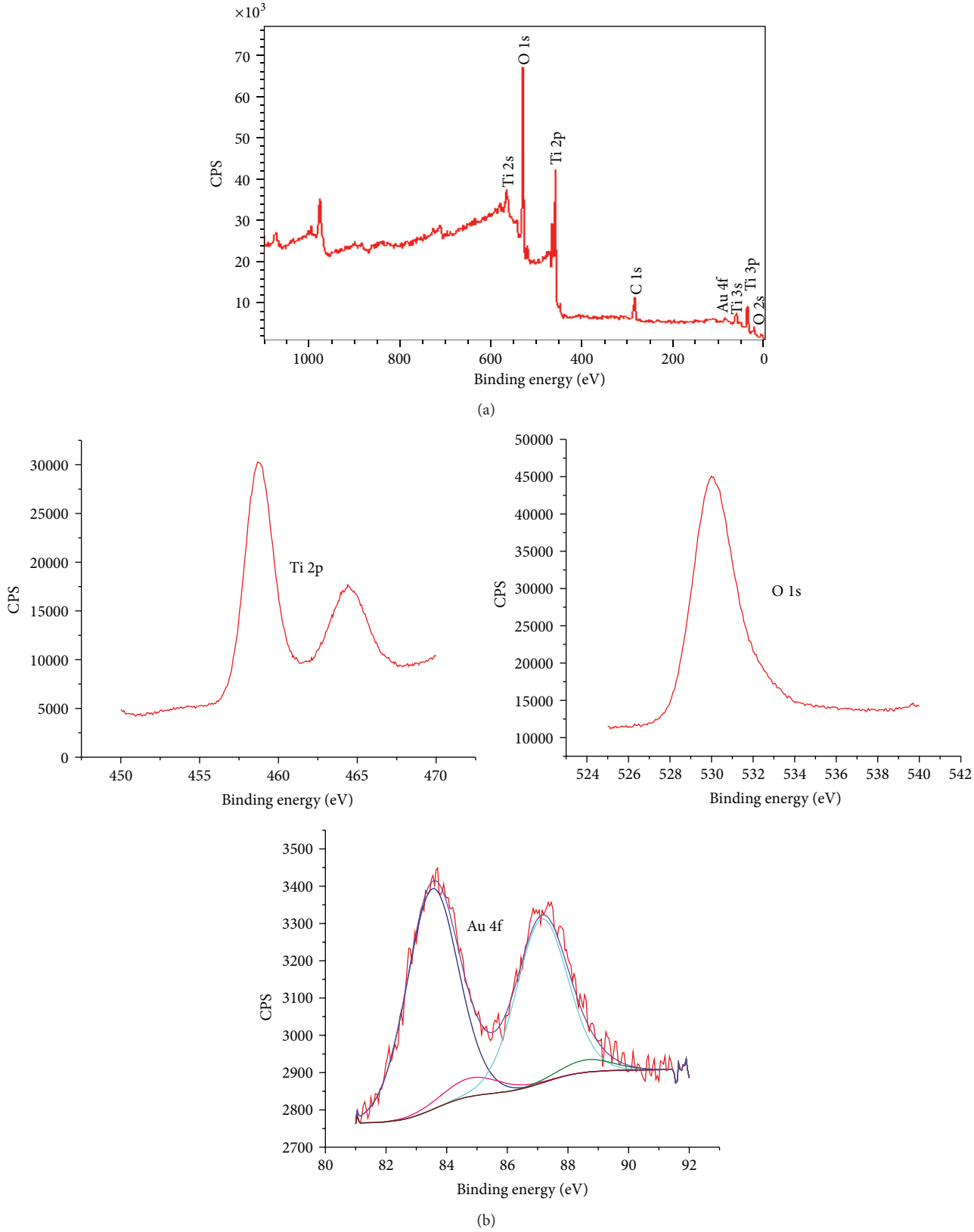

Figure 3: XPS spectra of 1.5%Au/TiO_2: (a) wide scan spectra, (b) high resolution spectra corresponding to Ti 2p, O 1s, and Au 4f.

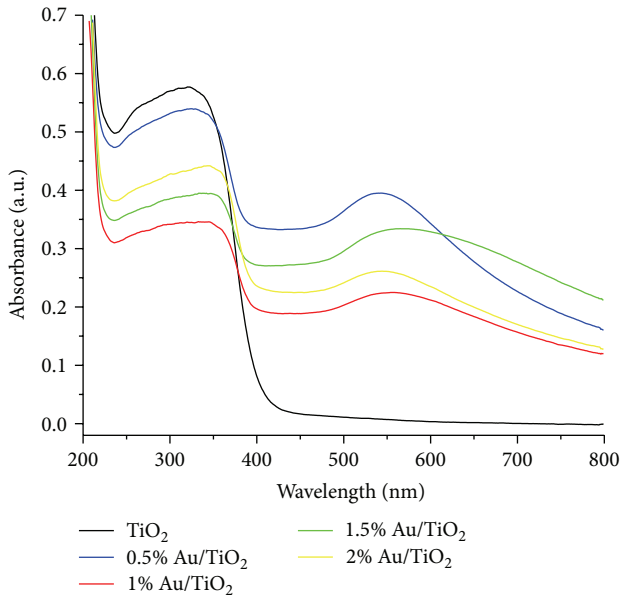

Figure 4: UV-visible diffuse reflectance spectra of Au doped TiO_2 samples.

monitored. Incorporation of gold increases the activity of TiO_2 drastically, which again moves up with increase in the amount of gold. Both 1.5% and 2 wt% AuNP doped systems gave 100% degradation of 50 mL, 10 mg/L MO dye over 3 g/L catalyst for 2 h exposure to UV light. In order to recognize the best Au doping, the time of UV irradiation was changed to 1 h, where 2%Au/TiO_2 provided the complete dye degradation. The results given in Figure 5(d) suggest 2%Au/TiO_2 as the best photocatalyst of the present investigation.

Reusability of the catalyst is one of the most projected attractions of any heterogeneous catalyzed reaction, but only limited experiments are there on the reusability studies of powder photocatalysts [42, 43]. This may be due to the difficulties in separation of the catalyst powder after pollutant degradation and may also be due to the low reusability of the catalysts. Present catalysts are easily separable from the solution and also well dispersible under stirring. It is simple to detach the catalyst from the cleaned solution either by filtration or by centrifugation. There was no permanent adsorption of dye over the catalyst, and the cleaning merely arises from photodegradation. Regeneration of the best catalyst, 2%Au/TiO_2, was done after each reaction, by centrifugation, washing with water, and further treatment at the calcination temperature of the catalyst, that is, at 200°C, for 1 h. The photocatalytic activity of the nanogold doped titania remains intact even up to ten consecutive experiments under the selected reaction conditions (Figure 6). The performance of the 2% Au/TiO_2 in the degradation of a number of dye pollutants was also tested where the activity is found to be admirable. The results are given in Table 1.

The excellent activity of the present nanogold loaded TiO_2 photocatalysts under UV light pinched us to test its ability to harvest the UV present in the sunlight. The photoactivity was also evaluated by the direct use of sunlight that may immediately turn the attention of industries for pollutant treatment. Akbarzadeh et al. had reported vanadium doped TiO_2 systems that are effective under sunlight where the catalyst used both UV and visible spectra of the sunlight for photoactivity [44]. The 0.5% vanadium doped TiO_2 showed 53.99% degradation of methyleneblue after 1 h irradiation. Present AuNP doped TiO_2 displayed very good activity under sunlight where more than 80% of the methylorange dye is degraded within 1 h and degradation reached around 93% by 2 h exposure to sunlight over 1.5%Au/TiO_2. The use of UV radiation of sunlight for the photocatalytic degradation is investigated in our experiments. When the reaction is conducted under sunlight using glass tubes instead of quartz tubes, the activity dropped drastically. Glass is opaque to UV light and that may be the reason for decreased activity which suggests the use of UV light for degradation. The degradation data of MO under sunlight over 1.5%Au/TiO_2 with time is presented in Figure 7(a). The degradation results under UV lamps are also offered for comparison in Figure 7(b).

Table 1: Photodegradation of aquatic dye pollutants over Au NP doped TiO_2.

Dyes	% Degradation
Methylorange	100.00
Crystal violet	98.63
Methylene blue	95.30
Malachite green	100.00
Orange II	99.05
Acid blue	94.69

Reaction conditions: 50 mL of 10 mg/L dye solution, 0.15 g catalyst, 1 h, 2% Au/TiO_2.

3.3. Proposed Mechanism of Photodegradation. The plausible reaction mechanism for the photodegradation of dyes over nanogold doped TiO_2 under UV irradiation is suggested here. Upon UV irradiation, the electrons present in the valance band (VB) get promoted to the conduction band (CB) since the band gap of TiO_2 lies in the UV region [45–47]. In the CB, the electrons can be further transferred to the adsorbed O_2 on the surface of TiO_2 to form the superoxide radical anions, $O_2^{\bullet-}$ [48, 49]. In addition, in the case of metal nanoparticle doped TiO_2, the metal nanoparticles can be considered as an electron sink, where the electrons in the conduction band can migrate to the noble metal surface, thereby preventing the recombination of electron-hole (e^--h^+) pairs [40, 45]. Thus the migration of electrons from the interior of the photocatalyst to the metal surface results in increased photoquantum efficiency, which can be the reason for the excellent photoactivity for the present nanogold doped systems even by using low intensity UV present in the sunlight. The transferred electrons in the metal surface facilitate the formation of oxygen superoxide radical anion. In the VB, the holes interact with water molecules, resulting in the formation of hydroxyl radical ($^{\bullet}OH$) and proton. Protonation of the superoxide anion, $O_2^{\bullet-}$, creates $^{\bullet}OOH$ radicals which leads to the formation of H_2O_2 and

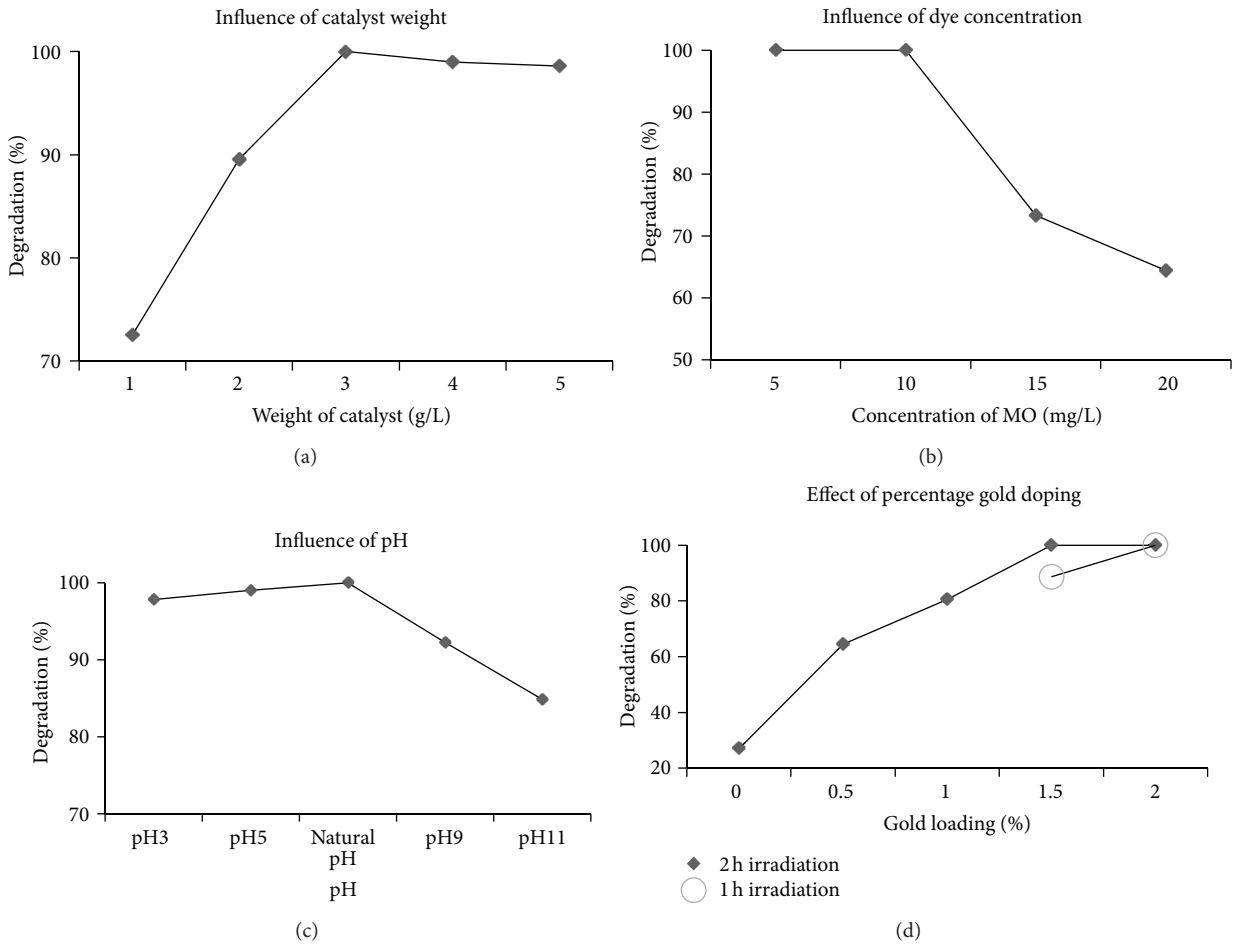

Figure 5: Influence of reaction conditions on photodegradation of methylorange over different photocatalysts.

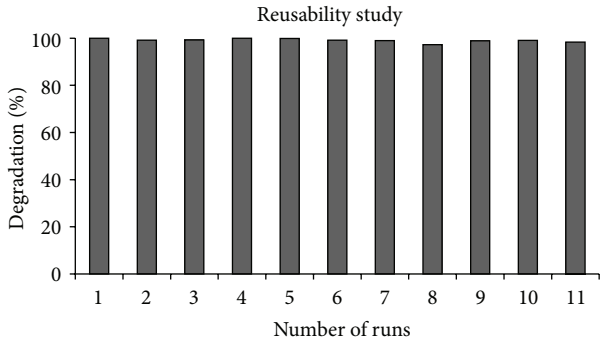

Figure 6: Reusability data over 2%Au/TiO_2 in the degradation of 50 mL of 10 mg/L MO, over 3 g/L catalyst, for 1 h irradiation under UV.

finally $^{\bullet}$OH radical [50]. These $^{\bullet}$OH radicals are responsible for the degradation of dye molecules. The presence of $^{\bullet}$OH radicals for photoactivity is already confirmed in previous reports [50–53]. Thus it can be understood that insertion of AuNP as well as increase in the amount of inserted nanogold particles can increase the photoactivity of TiO_2 significantly. Increase in the number of AuNPs over the support can lead to the enhanced migration of electrons from the CB of TiO_2 to the Au surfaces which promotes the electron transfer to the adsorbed O_2 molecules [54, 55]. This will facilitate the formation of more number of $O_2^{\bullet-}$ and finally can lead to the formation of more number of $^{\bullet}$OH which is responsible for dye degradation. This explains the observed increase in the dye degradation over the present photocatalysts with an increase in the percentage gold doping. The mechanism of photodegradation is schematically represented in Figure 8.

4. Conclusions

Highly efficient photocatalysts were prepared by nanogold doping over sol-gel TiO_2. XRD patterns show the exclusive existence of anatase crystalline phase of TiO_2. Majority of the incorporated gold exists in its metallic state, where the particles have diameters less than 5 nm. The strong interaction between the Au and the support, as evident from the characterization of the materials, leads to enhanced photocatalytic activity. The gold nanoparticles act as effective trapping centres to prevent recombination of electron-hole pairs, making the catalysts even active under sunlight for the efficient degradation of pollutants. Another attractiveness of

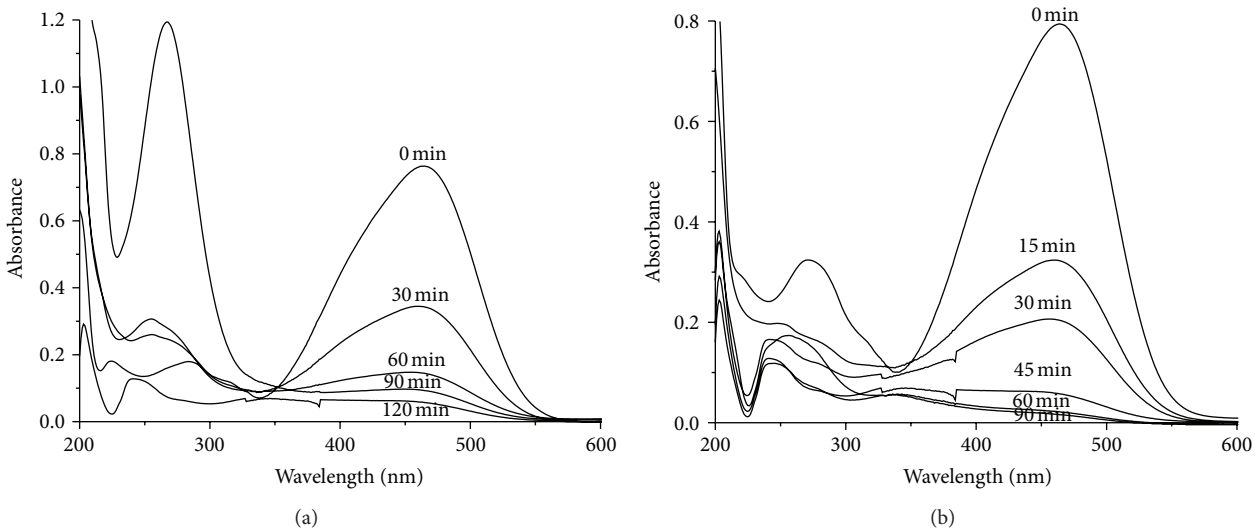

Figure 7: (a) Degradation of 10 mg/L MO under sunlight over 3 g/L of 1.5%Au/TiO_2. (b) Degradation of 10 mg/L MO under UV irradiation over 3 g/L of 2%Au/TiO_2.

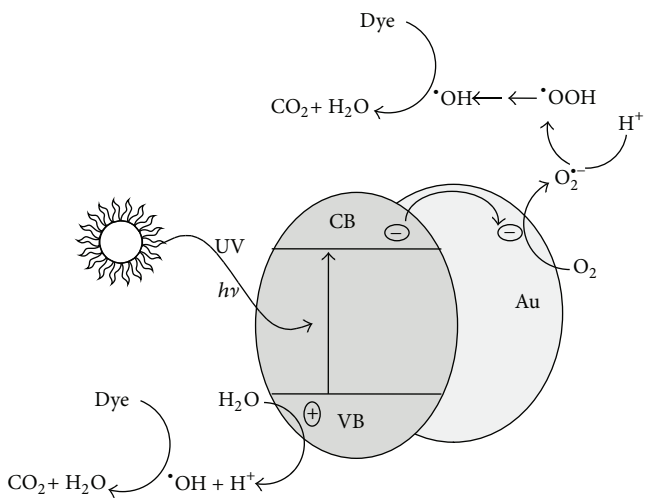

Figure 8: Plausible mechanism of photodegradation of dyes over AuNP doped TiO_2.

the present photocatalysts lies in their easy separation from the cleaned solution and reusability.

Acknowledgments

The authors acknowledge UKM, Grant number UKM-GUP-NBT-08-26-091, for financial support. SAIF KOCHI, CUSAT, India, is acknowledged for XRD, UV-vis DRS, and ICP-AES measurements. The authors would like to thank Dr. C. Anandan from SED, National Aerospace Laboratories, Bangalore, India, for XPS analysis. Binitha Narayanan thanks University Grants Commission, New Delhi, India, for UGC Research Award.

References

[1] R. I. Bickley, T. Gonzalez-Carreno, J. S. Lees, L. Palmisano, and R. J. D. Tilley, "A structural investigation of titanium dioxide photocatalysts," *Journal of Solid State Chemistry*, vol. 92, no. 1, pp. 178–190, 1991.

[2] K. Nakata and A. Fujishima, "TiO_2 photocatalysis: design and applications," *Journal of Photochemistry and Photobiology C*, vol. 13, no. 3, pp. 169–189, 2012.

[3] A. Fujishima, T. N. Rao, and D. A. Tryk, "Titanium dioxide photocatalysis," *Journal of Photochemistry and Photobiology C*, vol. 1, no. 1, pp. 1–21, 2000.

[4] H. L. Qin, G.-B. Gu, and S. Liu, "Preparation of nitrogen-doped titania using sol-gel technique and its photocatalytic activity,"

Materials Chemistry and Physics, vol. 112, no. 2, pp. 346–352, 2008.

[5] A. R. Gandhe and J. B. Fernandes, "A simple method to synthesize N-doped rutile titania with enhanced photocatalytic activity in sunlight," *Journal of Solid State Chemistry*, vol. 178, no. 9, pp. 2953–2957, 2005.

[6] K. Zhang and W. C. Oh, "Kinetic study of the visible light-induced sonophotocatalytic degradation of MB solution in the presence of Fe/TiO_2-MWCNT catalyst," *Bulletin of the Korean Chemical Society*, vol. 31, no. 6, pp. 1589–1595, 2010.

[7] A. Hattori, M. Yamamoto, H. Tada, and S. Ito, "A promoting effect of NH_4F addition on the photocatalytic activity of sol-gel TiO_2 films," *Chemistry Letters*, no. 8, pp. 707–708, 1998.

[8] T. Umebayashi, T. Yamaki, H. Itoh, and K. Asai, "Band gap narrowing of titanium dioxide by sulfur doping," *Applied Physics Letters*, vol. 81, no. 3, pp. 454–456, 2002.

[9] S. U. M. Khan, M. Al-Shahry, and W. B. Ingler Jr., "Efficient photochemical water splitting by a chemically modified n-TiO_2," *Science*, vol. 297, no. 5590, pp. 2243–2245, 2002.

[10] S. Sato, "Photocatalytic activity of NO_x-doped TiO_2 in the visible light region," *Chemical Physics Letters*, vol. 123, no. 1-2, pp. 126–128, 1986.

[11] P. Zhou, J. Yu, and Y. Wang, "The new understanding on photocatalytic mechanism of visible-lightresponse N–S codoped anatase TiO_2 by first-principles," *Applied Catalysis B*, vol. 142-143, pp. 45–53, 2013.

[12] T. Horikawa, M. Katoh, and T. Tomida, "Preparation and characterization of nitrogen-doped mesoporous titania with high specific surface area," *Microporous and Mesoporous Materials*, vol. 110, no. 2-3, pp. 397–404, 2008.

[13] N. N. Binitha, Z. Yaakob, and R. Resmi, "Influence of synthesis methods on zirconium doped titania photocatalysts," *Central European Journal of Chemistry*, vol. 8, no. 1, pp. 182–187, 2010.

[14] M. Zhou, J. Zhang, B. Cheng, and H. Yu, "Enhancement of visible-light photocatalytic activity of mesoporous Au–TiO_2 nanocomposites by surface plasmon resonance," *International Journal of Photoenergy*, vol. 2012, Article ID 532843, 10 pages, 2012.

[15] P. V. Kamat, "Photochemistry on nonreactive and reactive (semiconductor) surfaces," *Chemical Reviews*, vol. 93, no. 1, pp. 267–300, 1993.

[16] C. Y. Wang, C. Y. Liu, X. Zheng, J. Chen, and T. Shen, "The surface chemistry of hybrid nanometer-sized particles. I. photochemical deposition of gold on ultrafine TiO_2 particles," *Colloids and Surfaces A*, vol. 131, no. 1–3, pp. 271–280, 1998.

[17] A. Sclafani and J. M. Herrmann, "Influence of metallic silver and of platinum-silver bimetallic deposits on the photocatalytic activity of titania (anatase and rutile) in organic and aqueous media," *Journal of Photochemistry and Photobiology A*, vol. 113, no. 2, pp. 181–188, 1998.

[18] A. Wold, "Photocatalytic properties of TiO_2," *Chemistry of Materials*, vol. 5, no. 3, pp. 280–283, 1993.

[19] J. Yu, J. Xiong, B. Cheng, and S. Liu, "Fabrication and characterization of Ag–TiO_2 multiphase nanocomposite thin films with enhanced photocatalytic activity," *Applied Catalysis B*, vol. 60, no. 3-4, pp. 211–221, 2005.

[20] S. Link, C. Burda, Z. L. Wang, and M. A. El-Sayed, "Electron dynamics in gold and gold-silver alloy nanoparticles: the influence of a nonequilibrium electron distribution and the size dependence of the electron-phonon relaxation," *Journal of Chemical Physics*, vol. 111, no. 3, pp. 1255–1264, 1999.

[21] C. Voisin, N. D. Fatti, D. Christofilos, and F. Vallee, "Ultrafast electron dynamics and optical nonlinearities in metal nanoparticles," *Journal of Physical Chemistry B*, vol. 105, no. 12, pp. 2264–2280, 2001.

[22] H. Zhu, X. Chen, Z. Zheng et al., "Mechanism of supported gold nanoparticles as photocatalysts under ultraviolet and visible light irradiation," *Chemical Communications*, no. 48, pp. 7524–7526, 2009.

[23] H. Qin, G. Gu, and S. Liu, "Preparation of nitrogen-doped titania and its photocatalytic activity," *Rare Metals*, vol. 26, no. 3, pp. 254–262, 2007.

[24] N. N. Binitha, Z. Yaakob, M. R. Reshmi, S. Sugunan, V. K. Ambili, and A. A. Zetty, "Preparation and characterization of nano silver-doped mesoporous titania photocatalysts for dye degradation," *Catalysis Today*, vol. 147, pp. S76–S80, 2009.

[25] M. Riad, L. Saad, and S. Mikhail, "Influence of support type on the pore structure and the catalytic activity of Pt–Sn/ aluminosilicate catalysts," *Australian Journal of Basic and Applied Sciences*, vol. 2, no. 2, pp. 262–271, 2008.

[26] M. Haruta, S. Tsubota, T. Kobayashi, H. Kageyama, M. J. Genet, and B. Delmon, "Low-temperature oxidation of CO over gold supported on TiO_2, α-Fe_2O_3, and Co_3O_4," *Journal of Catalysis*, vol. 144, no. 1, pp. 175–192, 1993.

[27] V. Belova, T. Borodina, H. Möhwald, and D. G. Shchukin, "The effect of high intensity ultrasound on the loading of Au nanoparticles into titanium dioxide," *Ultrasonics Sonochemistry*, vol. 18, no. 1, pp. 310–317, 2011.

[28] L. Luo, A. T. Cooper, and M. Fan, "Preparation and application of nanoglued binary titania-silica aerogel," *Journal of Hazardous Materials*, vol. 161, no. 1, pp. 175–182, 2009.

[29] László Kőrösi, Szilvia Papp, Judit Ménesi et al., "Photocatalytic activity of silver-modified titanium dioxide at solid-liquid and solid-gas interfaces," *Colloids and Surfaces A*, vol. 319, no. 1–3, pp. 136–142, 2008.

[30] F. Zhang, G. K. Wolf, X. Wang, and X. Liu, "Surface properties of silver doped titanium oxide films," *Surface and Coatings Technology*, vol. 148, no. 1, pp. 65–70, 2001.

[31] Y. Wu, J. Zhang, L. Xiao, and F. Chen, "Preparation and characterization of TiO_2 photocatalysts by Fe^{3+} doping together with Au deposition for the degradation of organic pollutants," *Applied Catalysis B*, vol. 88, no. 3-4, pp. 525–532, 2009.

[32] Y.-C. Liu and L. C. Juang, "Electrochemical methods for the preparation of gold-coated TiO_2 nanoparticles with variable coverages," *Langmuir*, vol. 20, no. 16, pp. 6951–6955, 2004.

[33] M. C. Henry, C. C. Hsueh, B. P. Timko, and M. S. Freund, "Reaction of pyrrole and chlorauric acid: a new route to composite colloids," *Journal of the Electrochemical Society*, vol. 148, no. 11, pp. D155–D162, 2001.

[34] T. Ioannides and X. E. Verykios, "Charge transfer in metal catalysts supported on doped TiO_2: a theoretical approach based on metal-semiconductor contact theory," *Journal of Catalysis*, vol. 161, no. 2, pp. 560–569, 1996.

[35] J. Huang, W. L. Dai, H. Li, and K. Fan, "Au/TiO_2 as high efficient catalyst for the selective oxidative cyclization of 1,4-butanediol to γ-butyrolactone," *Journal of Catalysis*, vol. 252, no. 1, pp. 69–76, 2007.

[36] P. Silija, Z. Yaakob, M. A. Yarmo, S. Sugunan, and N. N. Binitha, "Visible light active anion codoped sol gel titania photocatalyst for pollutant degradation," *Journal of Sol-Gel Science and Technology*, vol. 59, no. 2, pp. 252–259, 2011.

[37] T. Barakat, V. Idakiev, R. Cousin et al., "Total oxidation of toluene over noble metal based Ce, Fe and Ni dopedtitanium oxides," *Applied Catalysis B*, vol. 146, pp. 138–146, 2014.

[38] A. C. Gluhoi, N. Bogdanchikova, and B. E. Nieuwenhuys, "Alkali (earth)-doped Au/Al_2O_3 catalysts for the total oxidation of propene," *Journal of Catalysis*, vol. 232, no. 1, pp. 96–101, 2005.

[39] O. Carp, C. L. Huisman, and A. Reller, "Photoinduced reactivity of titanium dioxide," *Progress in Solid State Chemistry*, vol. 32, no. 1-2, pp. 33–177, 2004.

[40] P. V. Kamat, "Photophysical, photochemical and photocatalytic aspects of metal nanoparticles," *Journal of Physical Chemistry B*, vol. 106, no. 32, pp. 7729–7744, 2002.

[41] Y. C. Liu and L. C. Juang, "Electrochemical methods for the preparation of gold-coated TiO_2 nanoparticles with variable coverages," *Langmuir*, vol. 20, no. 16, pp. 6951–6955, 2004.

[42] N. Sridewi, L. T. Tan, and K. Sudesh, "Solar photocatalytic decolorization and detoxification of industrial batik dye wastewater using P(3HB)-TiO_2 nanocomposite films," *Clean—Soil, Air, Water*, vol. 39, no. 3, pp. 265–273, 2011.

[43] D. Marković, B. Jokić, Z. Šaponjić, B. Potkonjak, P. Jovančić, and M. Radetić, "Photocatalytic degradation of dye C.I. direct blue 78 using TiO_2 nanoparticles immobilized on recycled wool-based nonwoven material," *Clean—Soil, Air, Water* , vol. 41, no. 10, pp. 1002–1009, 2013.

[44] R. Akbarzadeh, S. B. Umbarkar, R. S. Sonawane, S. Takle, and M. K. Dongare, "Vanadia-titania thin films for photocatalytic degradation of formaldehyde in sunlight," *Applied Catalysis A*, vol. 374, no. 1-2, pp. 103–109, 2010.

[45] D. Jose, C. M. Sorensen, S. S. Rayalu, K. M. Shrestha, and K. J. Klabunde, "Au-TiO_2 nanocomposites and efficient photocatalytic hydrogen production under UV-visible and visible light illuminations: a comparison of different crystalline forms of TiO_2," *International Journal of Photoenergy*, vol. 2013, Article ID 685614, 10 pages, 2013.

[46] A. Fujishima, K. Hashimoto, and T. Watanabe, *TiO_2 Photocatalysis: Fundamentals and Applications*, Tokyo BKC, Tokyo, Japan, 1st edition, 1999.

[47] K. Ikeda, H. Sakai, R. Baba, K. Hashimoto, and A. Fujishima, "Photocatalytic reactions involving radical chain reactions using microelectrodes," *Journal of Physical Chemistry B*, vol. 101, no. 14, pp. 2617–2620, 1997.

[48] A. L. Linsebigler, G. Lu, and J. T. Yates Jr., "Photocatalysis on TiO_2 surfaces: principles, mechanisms, and selected results," *Chemical Reviews*, vol. 95, no. 3, pp. 735–758, 1995.

[49] B. G. Kwon and J. Yoon, "Experimental evidence of the mobility of hydroperoxyl/superoxide anion radicals from the illuminated TiO_2 interface into the aqueous phase," *Bulletin of the Korean Chemical Society*, vol. 30, no. 3, pp. 667–670, 2009.

[50] J. Yu, G. Dai, Q. Xiang, and M. Jaroniec, "Fabrication and enhanced visible-light photocatalytic activity of carbon self-doped TiO_2 sheets with exposed {001} facets," *Journal of Materials Chemistry*, vol. 21, no. 4, pp. 1049–1057, 2011.

[51] Q. Xiang, J. Yu, and P. K. Wong, "Quantitative characterization of hydroxyl radicals produced by various photocatalysts," *Journal of Colloid and Interface Science*, vol. 357, no. 1, pp. 163–167, 2011.

[52] J. Yu and J. Ran, "Facile preparation and enhanced photocatalytic H_2-production activity of $Cu(OH)_2$ cluster modified TiO_2," *Energy and Environmental Science*, vol. 4, no. 4, pp. 1364–1371, 2011.

[53] J. Yu, G. Dai, and B. Cheng, "Effect of crystallization methods on morphology and photocatalytic activity of anodized TiO_2 nanotube array films," *Journal of Physical Chemistry C*, vol. 114, no. 45, pp. 19378–19385, 2010.

[54] J. Yu, L. Yue, S. Liu, B. Huang, and X. Zhang, "Hydrothermal preparation and photocatalytic activity of mesoporous Au–TiO_2 nanocomposite microspheres," *Journal of Colloid and Interface Science*, vol. 334, no. 1, pp. 58–64, 2009.

[55] Q. Xiang, J. Yu, B. Cheng, and H. C. Ong, "Microwave-hydrothermal preparation and visible-light photoactivity of plasmonic photocatalyst Ag–TiO_2 nanocomposite hollow spheres," *Chemistry*, vol. 5, no. 6, pp. 1466–1474, 2010.

Hindawi Publishing Corporation
International Journal of Photoenergy
Volume 2013, Article ID 729460, 8 pages
http://dx.doi.org/10.1155/2013/729460

Research Article

One-Step Synthesis of TiO_2/Perlite Composites by Flame Spray Pyrolysis and Their Photocatalytic Behavior

M. Giannouri,[1] Th. Kalampaliki,[1] N. Todorova,[1] T. Giannakopoulou,[1] N. Boukos,[1] D. Petrakis,[2] T. Vaimakis,[2] and C. Trapalis[1]

[1] *Institute of Advanced Materials, Physicochemical Processes, Nanotechnology and Microsystems, NCSR Demokritos, Agia Paraskevi, Attikis, 153 10 Athens, Greece*
[2] *Department of Chemistry, University of Ioannina, 451 10 Ioannina, Greece*

Correspondence should be addressed to C. Trapalis; trapalis@ims.demokritos.gr

Received 16 September 2013; Accepted 17 October 2013

Academic Editor: Jiaguo Yu

TiO_2/perlite composites were prepared via facile one-step flame spray pyrolysis (FSP) route. Titanium alkoxide (TIPO) and expanded perlite were used as Ti source and substrate, respectively. Precursor TIPO-ethanol solutions containing homogeneously dispersed perlite particles were processed through FSP setup at different experimental conditions regarding the gas flow and precursor supply rates. The structure, morphology, and the composition of the obtained powders were investigated. The porosity and the light absorbance of the TiO_2/perlite composites were examined and their photocatalytic activity in NO oxidation was evaluated. Commercial titania powder P25 was also FSP processed and investigated for comparison. The XRD analysis revealed that biphased titania with different anatase-rutile ratio and particles size 20–40 nm was synthesized onto the perlite which according to microscopy results was covered by neck-connected TiO_2 nanoparticles. The anatase-rutile interplay was also demonstrated by the Raman spectra where presence of Si-O-Ti vibrational modes was observed for some samples. The UV-Vis diffuse reflectance spectra of the TiO_2/perlite composites revealed up to 70% reflection that was connected to the presence of the gray perlite and superficial carbon. The best photocatalytic activity of the composites was connected to almost equal anatase-rutile ratio and possible synergetic effect of the two TiO_2 phases.

1. Introduction

The TiO_2 semiconductor is one of the most investigated materials during the last years. TiO_2 nanoparticles are used nowadays in an enormous spectrum of applications such as solar cells [1], gas sensors [2], photochromic devices [3], superhydrophilic surfaces [4] and photocatalysts [5]. The above applications are related to the three different crystalline phases of TiO_2, anatase, rutile, and brookite [6]. Both anatase and rutile crystal structures are commonly used as photocatalysts with anatase showing a greater activity for most photocatalytic processes. This is attributed to anatase's slightly higher Fermi level, its lower capacity to adsorb oxygen, and its higher degree of hydroxylation [7, 8]. There are also studies which claim that a synergetic effect occurs and a mixture of anatase and rutile is more active than pure anatase [9]. The enhanced activity arises from the increased efficiency of the electron-hole separation due to the multiphase nature of the photocatalyst [10].

Various procedures are established for producing photocatalyst particles such as chemical vapour deposition [11], precipitation [12, 13], sol-gel methods [14], and hydrothermal synthesis [15–18].

The last one is a fast, profitable, and flexible process for the production of a wide variety of different nanoparticles [19]. In this process, flame is being used to drive chemical reactions of precursor compounds [20–26], resulting in the formation of clusters, which grow to nanometer-sized products by coagulation and sintering. In particular, TiO_2 or TiO_2-containing composite systems were studied by flame spray pyrolysis such as $(TiO_2)_x(Al_2O_3)_{1-x}$ [20], Au/TiO_2 [21],

Pt/TiO_2, Fe/TiO_2 [22], V_2O_5/TiO_2 [23], Cr/TiO_2 [24], Ag/TiO_2 [25], and $SiO_2/V_2O_5/WO_3/TiO_2$ systems [26].

There are several works investigating deposition of TiO_2 nanoparticles on various surfaces such as polymeric matrices [27], graphene oxide [28], carbon fibers [29], clays [30], and layered double hydroxide LDH [31–33]. Systems of nanosized TiO_2 with highly adsorptive supports enhance the performance of the photocatalysts due to larger specific area, porosity, and higher adsorption capacity in comparison to the bare TiO_2. Support limits the aggregation of TiO_2 nanoparticles, induces the microporosity into the materials [31], and contributes to the efficient spatial separation between the photogenerated electrons and holes. Glassy substrates were also used for deposition of TiO_2 photocatalysts [34–37]. Such a glassy substrate is the perlite which is a natural amorphous material widely used in construction and industry. The use of natural perlite in blended cement production was investigated and the results revealed that perlite possesses sufficient pozzolanic characteristics [38]. Its average chemical composition is approximately 75% SiO_2 with oxides of Al (14.8%), K (4.8%), Na (2.9%), Ca (0.9%), Mg (0.1%), Fe_2O_3 (1.5%), and water (4.0%) [39]. Crude perlite particles expand after heating to 870°C due to the presence of water and form innumerable sealed glassy cells in a manner similar to popcorn. These account for the excellent insulating properties and light weight of the expanded perlite. Being highly porous and chemically inert media, perlite granules can act as a good adsorbent. Therefore, expanded perlite can be selected as substrate for TiO_2 particles.

TiO_2/perlite composites prepared by various experimental methods were investigated aiming at enhanced photocatalytic activity in water and air decontamination. Thus, the TiO_2-coated perlite granules were prepared using sol-gel method and tested for photocatalytic purification of furfural polluted waste water [40]. Also, TiO_2 (Evonik-Degussa P25) immobilized on different supports (perlite granules, glass plates, and steel fiber) by sol-gel and investigated their photocatalytic oxidation of phenol [41]. The preceding works on TiO_2/perlite composite materials used mainly wet chemistry to immobilize the photocatalyst onto the substrate. To the best of our knowledge, there is only one report on preparation of Ag-coated perlite by the spray pyrolysis method in order to obtain a catalyst for ozone decomposition using a cheap natural glass as substrate [42].

In this paper we present for the first time the one-step synthesis of the TiO_2/perlite composites by flame spray pyrolysis (FSP) processing. The structural and the morphological properties of the prepared materials as well as their photocatalytic performance in air pollutants oxidation are examined.

2. Experimental

2.1. Precursor Materials. The expanded perlite was provided by S&B Industrial Minerals S.A. to be used as a support for deposition of TiO_2 nanoparticles. Perlite was ground in a planetary mill for 2 h in order for fine granules to be obtained.

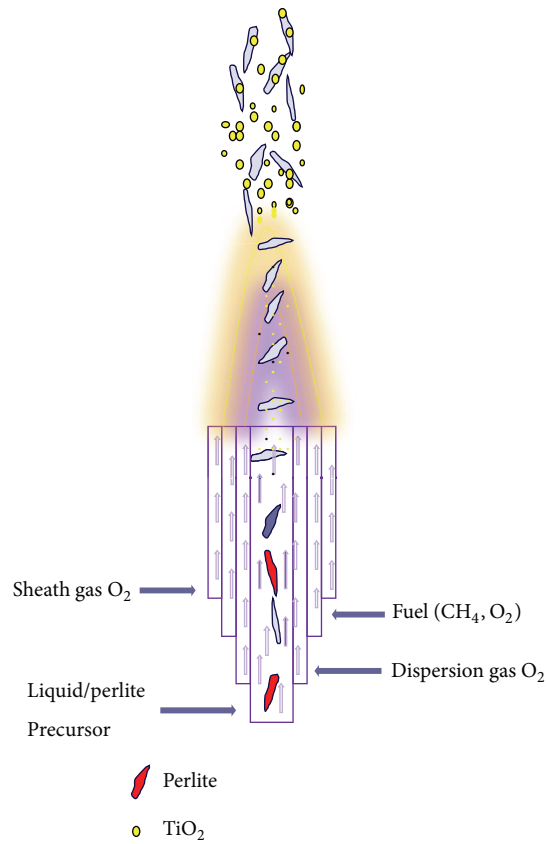

Figure 1: Schematic of the flame spray pyrolysis device. During spray procedure and after evaporation and combustion of precursor, TiO_2 nanoparticles are formed on perlite substrate.

The TiO_2/perlite composite materials were prepared as follows. Initially, 5 mL titanium isopropoxide (TIPO), Aldrich 97%, was dissolved in 40 mL ethanol, Carlo Erba, and stirred for 30 min. Then, 5 g perlite was added and the dispersion was stirred for 60 min. The mixture was further homogenized using an ultrasound tip sonicator (Hielscher UIP 1000 hd). Total energy input of 1 Wh was applied for sonication time for 2 min. Finally, the slurry was diluted with ethanol to receive 100 mL suspension and the liquid obtained was nominated as precursor solution (PS). The prepared PS was ready to be processed through the flame spray pyrolysis system. It should be noted that water was not used in order to avoid hydrolysis.

2.2. Flame Spray Pyrolysis Device. A homemade FSP setup was used to synthesize TiO_2/perlite composites. In Figure 1 the schematic of the experimental set-up is shown. The FSP reactor consisted of four stainless steel concentric tubes. The PS was fed by a syringe pump (Inotec, IER-560) through the innest capillary tube (i.d. 0.8 mm). Oxygen was used as dispersion gas fed through the surrounding annulus (i.d. 2.5 mm, o.d. 3.0 mm) with a pressure drop of 1.5 bar and a rate in the range of 10–20 L min^{-1}.

The resulting spray was ignited by a circular premixed flame (i.d. 17.0 mm, o.d. 19.7 mm) of CH_4 (1.5 L min^{-1}) and O_2 (3.2 L min^{-1}). An additional O_2 sheath flow (20–40 L min^{-1})

Table 1: Anatase (W_A%) and rutile (W_R%) compositions, crystallite sizes (d_A and d_R) under different sheath, dispersion oxygen fractions, and syringe pump flow rates.

Samples	Dispersion flow rates L min^{-1}	Sheath flow rates L min^{-1}	Syringe pump rates mL min^{-1}	d_A nm	d_R nm	W_A (%)	W_R (%)
P25				20	27	85	15
FSPA	14.0	20.0	12.0	24	30	48	52
FSPB	19.0	28.9	10.0	29	42	72	28
FSPC	17.3	38.8	12.0	27	31	70	30
FSPD	10.9	55.0	10.0	30	28	55	45

for complete combustion of the precursor was supplied through a sinter metal ring (i.d. 30 mm, o.d. 38 mm). In this paper, the total O_2 flow rate represents the sum of dispersion and sheath O_2 supply. The gas flow rates were regulated by calibrated mass flow controllers (Bronkhorst EL-Flow). The PS was processed through the FSP and the resulting powders were collected on glass microfiber filters (Whatman GF/D, 257 mm diameter) with the aid of a vacuum pump. Different TiO_2/perlite samples were prepared by variation of the experimental conditions, namely, the gas flow rates (dispersion and sheath) and the syringe pump rate for the PS supply. Table 1 summarizes the above parameters used during the FSP process as well as the fraction of anatase and rutile phases of the flame made samples.

2.3. Characterization of TiO_2/Perlite Composites. The XRD patterns of the samples were obtained by X-ray diffractometer (SIEMENS D500) with secondary graphite monochromator and CuKa radiation operating in Bragg-Brentano geometry. The measured 2θ range between 10° and 90° was scanned in steps of 0.03°/2 s. The accelerating voltage and applied current were 40 kV and 35 mA, correspondingly. The crystalline phases were identified with reference to the PDF cards of the International Centre for Diffraction Data. The average crystallite sizes of the anatase and rutile phases were determined from the intensities of the primary peaks of anatase (101) reflection at $2\theta_B = 25.3°$ and rutile (110) reflection $2\theta_B = 27.5°$ using the Scherrer relation [43] as follows:

$$d\,(\text{nm}) = \frac{0.89 \times \lambda}{B\,(\text{rad})\cos\theta_B}, \tag{1}$$

where $\lambda = 0.15418$ nm is the X-ray wavelength, B (rad) is the full width at the half maximum of the diffraction peak, and θ_B is the Bragg angle.

Since only the anatase and rutile phases are present in the examined TiO_2/perlite composites, the weight content of these phases was derived from the area of the corresponding peak after the background substraction using (2) [44] as follows:

$$W_R\,(\%) = \frac{S_R}{0.886 \times S_A + S_R}, \qquad W_A\,(\%) = 100 - W_R\,(\%), \tag{2}$$

where S_R and S_A are the surfaces of the primary rutile (110) and anatase (101) peaks, correspondingly.

Table 2: Measured BET SSA of the TiO_2/perlite composites and calculated SSA of their TiO_2 component with respect to the total oxygen flow rate.

Samples	SSA_{COMP} m^2/gr	SSA_{TiO_2} m^2/gr	O_2 flow rate L min^{-1}
FSPA	20.0	55.6	34.0
FSPB	20.2	48.4	47.9
FSPC	19.4	53.4	56.1
FSPD	12.8	51.1	66.0

The specific surface areas (SSA) of the powders were determined via Brunauer-Emmett-Teller (BET) method. Standard device Sorptomatic 1990 FISONS was used for the nitrogen adsorption/desorption measurements at 77°K. All the samples were degassed at 453°K for 12 h. Assuming spherical and unagglomerated particles, the SSA of the TiO_2 nanoparticles (SSA_{TiO_2}) was calculated from the average particle diameter estimated by XRD spectra, $d^{XRD}{}_{A(R)}$, and the weighted density of the particles $\rho_{A(R)}$ (anatase: $\rho_A = 3.84$ gr/cm^3, rutile: $\rho_R = 4.26$ gr/cm^3) by (3) as follows:

$$SSA_{A(R)} = \frac{6}{\left(\rho_{A(R)} \times d^{XRD}{}_{A(R)}\right)}. \tag{3}$$

The SSA_{TiO_2} was calculated taking into account the mass fraction of anatase and rutile phases. The BET measured SSA of TiO_2/perlite composites (SSA_{COMP}) and the calculated SSA_{TiO_2} are presented in Table 2.

The structural properties of the prepared composite materials were examined by Raman spectroscopy. The Raman spectra were measured with an inVia Raman microscope (Renishaw) using the 514.5 nm line of Ar+ laser emission with a resolution of 1.1 cm^{-1}. The laser power was 50 mW as an output and Raman emission signal at each measurement point was accumulated for 20 s for all samples.

UV-Vis diffuse reflectance of the powders in the wavelength range 350–800 nm as obtained using UV-2100 Shimadzu instrument. The measurements were performed using $BaSO_4$ etalon as a baseline.

The morphology of the powders was observed using scanning electron microscopy (SEM). An FEI Inspect microscope with tungsten filament operating at 25 kV was employed. In order to improve the surface conductivity of the samples standard gold deposition was applied through vacuum evaporation.

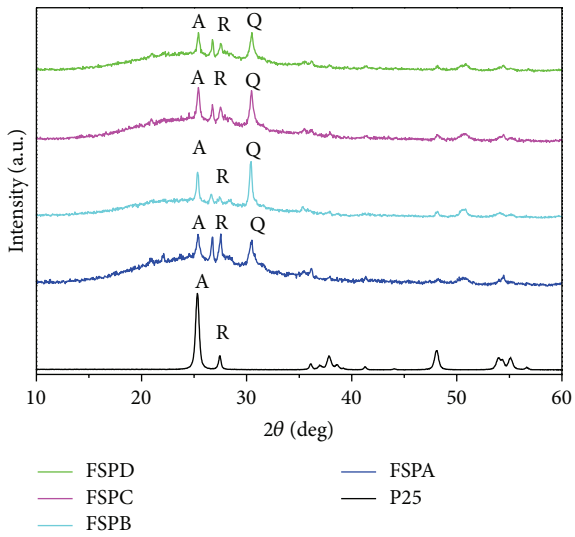

Figure 2: XRD patterns of TiO_2/perlite correspond to the (101) reflection of the anatase and to the (110) of the rutile. For comparison, the XRD pattern of Degussa P25 is presented.

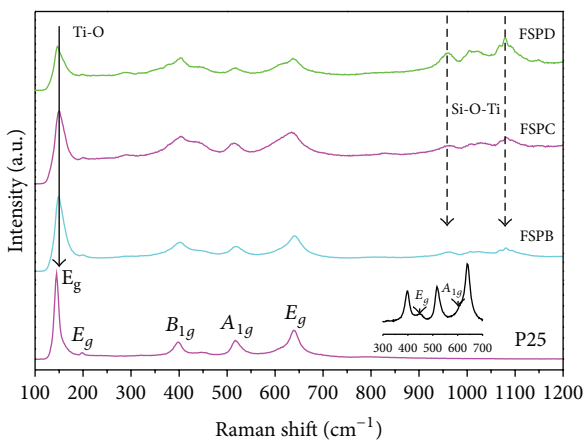

Figure 3: Raman spectra of samples P25, FSPB, FSPC, and FSPD.

The samples were also investigated using transmission electron microscopy (TEM). An FEI CM20 microscope operated at 200 kV was used. The samples for TEM observation were prepared as follows. Small amounts of the studied photocatalysts were dispersed in ethanol and the suspensions were treated in ultrasonic bath for 10 min. Then, a drop of the dilute suspension was placed on a carbon-coated grid and was allowed to dry by evaporation at ambient temperature.

Nitric oxide (NO) was chosen as representative airborne pollutant due to its potential health risks and ability to generate photochemical smog. The photocatalytic oxidation of NO by the prepared TiO_2/perlite composite materials was investigated employing standard procedure based on ISO/DIS 22197-1 [45]. The experimental set-up, the procedures of specimens' preparation, and photocatalytic activity measurement are described elsewhere [46–49]. Briefly, the samples were placed in a flow-type photoreactor where model air containing 1 ppm NO was issued. Flow rate of 3 L/min

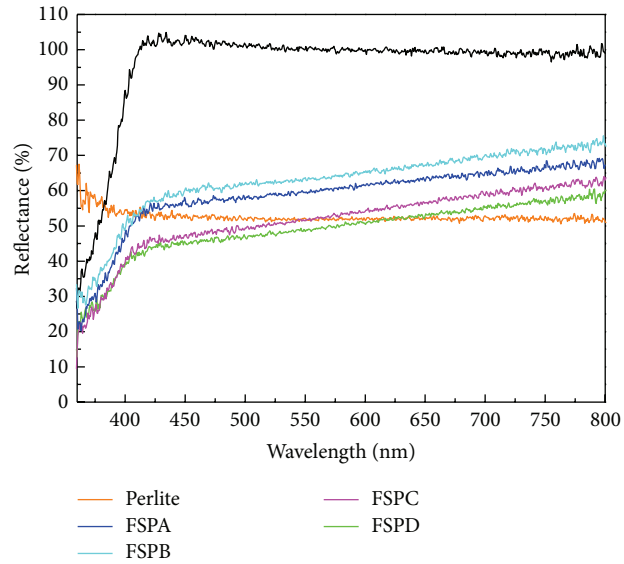

Figure 4: Diffuse reflectance spectra of TiO_2/perlite samples.

and relative humidity of 50% were retained during the experiment. UV-A light illumination with intensity 10 W/m^2 for 90 min was applied. The concentrations of the NO, NO_2, and NO_x (NO_x = NO − NO_2) were monitored in dark and under illumination. The photocatalytic activity of the samples was expressed by the calculated photonic efficiency ζ (mole/einstein) in NO and NO_2 oxidation as well as in NO_x removal for the entire illumination period.

3. Results and Discussion

The measured XRD patterns of the prepared materials are shown in Figure 2. It can be observed that the samples were crystallized in the form of anatase and rutile. The position and the relative intensities of the peaks are consistent with the anatase TiO_2 JCPDS card number 21-1272 and rutile TiO_2 JCPDS card number 21-1276. The average crystallite size obtained from the most intensive diffraction peaks (101) and (110) at $2\theta = 25.28^\circ$ and $2\theta = 27.45^\circ$ ranged between 20 and 30 nm for anatase phase and 27 and42 nm for rutile phase, respectively (Table 1). Also, a broadened bump in the 2θ range from 20° to 35° was observed originating from the amorphous nature of perlite. In the same time, the diffraction peaks (100), (101) and (110) were attributed to evident partial crystallization of the perlite during the flame processing procedure. The broadened part and quartz peaks are absent in the sample FSPA, which consist of P25 Degussa only. Finally, the interplay between the anatase and rutile phases in the composites (Table 1) is influenced by the PS and total O_2 flow rates [50], but the clear tendency in its behavior cannot be determined from our experiments.

In previous papers, it was demonstrated that the SSA of the particles decreased with the increase of the precursor flow rate [51, 52] as well as with the increase of the oxygen flow rate [23]. Higher precursor flow rate provokes higher frequency of the particle collision and sintering due to higher

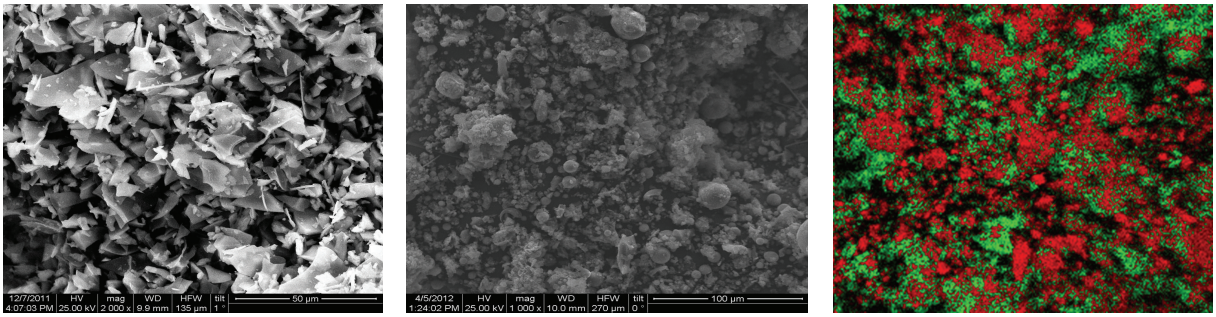

(a) (b) (c)

Figure 5: Scanning electron microscopy (SEM) micrographs of pure perlite (a), composite TiO_2/perlite (b), and elemental mapping for the FSPD sample using energy dispersive spectroscopy (c). Red colour corresponds to Si and green to Ti.

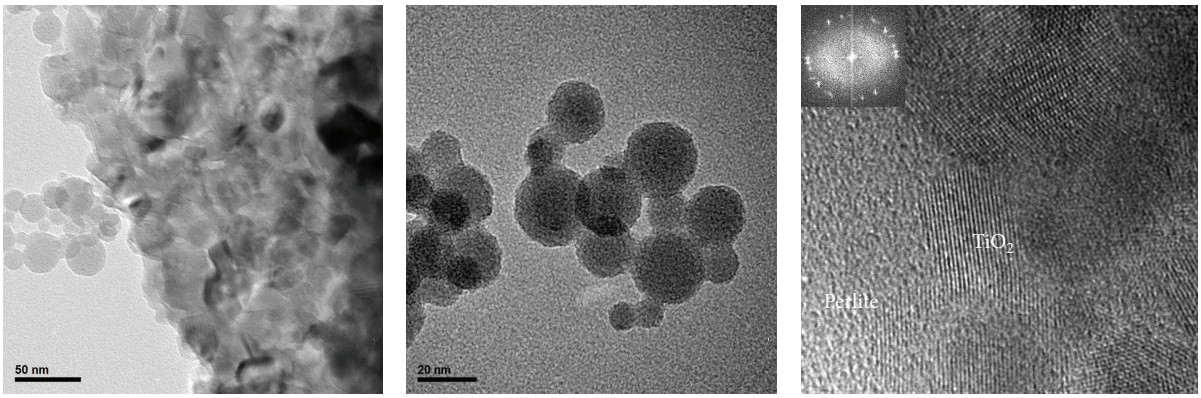

(a) (b) (c)

Figure 6: TEM micrographs of the composite TiO_2/Perlite (a), TiO_2 nanoparticles (b), and HRTEM image of TiO_2/Perlite (c).

concentration of the forming powder in the flame. Also, higher oxygen flow rate leads to higher flame temperature encountered by the particles. As a result, the enlargement of particle size and reduction of their SSA were observed in both cases.

The BET measured SSA of the composites (SSA_{COMP}) and the calculated SSA of TiO_2 particles (SSA_{TiO_2}) as well as total oxygen flow rate used in our experiments are given in Table 2. It can be perceived that the SSA_{COMP} is lower than SSA_{TiO_2}. This can be explained by mixing of photocatalytically active TiO_2 component with porous but lower SSA perlite substrate. In addition, given that the precursor flow rate does not vary considerably, it seems that both SSA values decrease with the increase of the oxygen flow rate. This correlates with the literature results mentioned above.

The Raman spectra of the investigated composites as well as of the reference P25 sample are given in Figure 3.

The presence of the two anatase and rutile phases demonstrated by the XRD results above and their alteration can be observed also for the prepared composites. Thus, the Raman lines of the anatase phase [53] at 144 cm^{-1} (E_g mode), 197 cm^{-1} (E_g mode), 399 cm^{-1} (B_{1g} mode), 515 cm^{-1} (A_{1g} mode), and 639 cm^{-1} (E_g mode) can be observed in all the samples. Additionally, a weak peak at 450 cm^{-1} and a small shoulder around at 610 cm^{-1} were also found in the reference sample (Figure 3-inset). Both peaks correspond to the E_g and A_{1g} modes of the rutile phase, respectively [54]. These rutile peaks were changed in the spectra of the TiO_2/perlite composites (samples FSPA, FSPB, and FSPD). More specifically, the shoulder at 610 cm^{-1} disappeared and the weak peak at 450 cm^{-1} caused a broadening of the anatase peak around 399 cm^{-1}.

It can be also observed that the lowest E_g anatase mode near 144 cm^{-1} is shifted to higher wavenumbers in the binary TiO_2/perlite systems (samples FSPB, FSPC, and FSPD) in comparison to the bare TiO_2 nanoparticles (reference P25). The blue shift can be attributed to compressive stresses appeared in the samples during the flame processing procedure [55]. This procedure is very abrupt and can evoke stresses in the flame-made nanoparticles produced using alkoxide precursor in comparison to the sample P25.

In addition, the peaks at 950 cm^{-1} and 1080 cm^{-1} related to the vibrational modes of Si-O-Ti [56] were observed for the samples FSPB, FSPC, and FSPD. This is an indication of the bond formation between TiO_2 photocatalysts and perlite substrate during the FSP processing.

The UV-Vis diffuse reflectance spectra for the prepared photocatalysts are given in Figure 4. It can be observed that

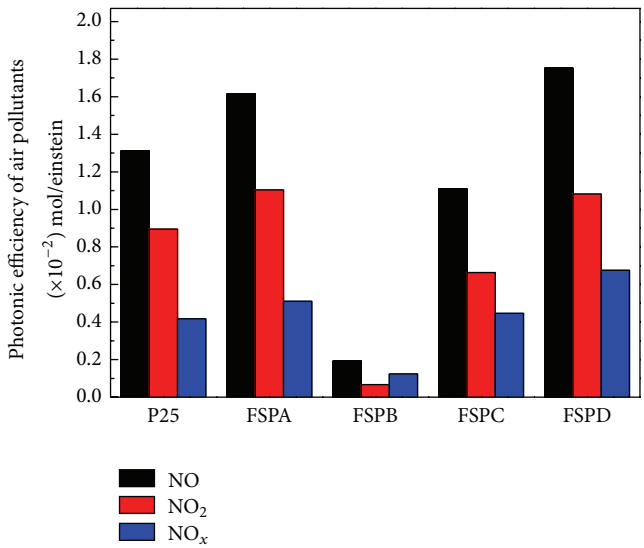

Figure 7: Photonic efficiencies in NO oxidation, NO_2 formation, and overall NO_x removal of the TiO_2/perlite composites.

the reflectance was high only for the reference sample P25. The bare perlite and all the TiO_2/perlite composites had a reflectance not higher than 70%. It was attributed to the presence of gray colored perlite in the prepared composites and probably to a large amount of residual carbon from the precursor and gas combustion.

The SEM images of the pure perlite and the perlite with immobilized titania nanoparticles are shown in Figures 5(a) and 5(b), respectively. It can be seen that bare perlite has a flake-like form. In the FSP composites, the flakes become rounded and are covered with TiO_2 agglomerates. This change in the perlite morphology is attributed to the high temperature FSP processing. The elemental mapping analysis presented in Figures 5(b) and 5(c) reveals that titania (Ti green colour) is homogenously dispersed on the surface of perlite (Si red colour).

Further morphological and structural characterization of the samples was carried out using TEM. As can be seen in Figure 6(a) the perlite flakes are almost entirely covered by TiO_2 nanoparticles that appear as an aggregation of small spherical neck-connected particles. It is suggested that these particle aggregations were created from large precursor solution droplets originated from 800 μm nozzle diameter. The precursor rapid hydrolysis accompanied with droplets' abrupt shrinkage, during their passage through the flame zone, results in the formation of neck-connected spherical TiO_2 nanoparticles, as shown in Figure 6(b). Their mean size is about 20 nm in agreement with XRD results.

A typical HRTEM image of the TiO_2 nanocrystals on the perlite substrate is presented in Figure 6(c). It is evident that each nanoparticle is single crystalline. The lattice fringes shown in the HRTEM image correspond to the rutile and anatase crystal structure with d-spacing $d = 0.325$ nm and $d = 0.352$ nm, respectively. This result is further confirmed by the fast Fourier transform of the HRTEM image shown as inset in Figure 6(c).

The calculated photonic efficiencies of the investigated samples are presented in Figure 7. The calculated values for the commercial Evonik-Degussa P25 are also given for comparison. It can be seen that the FSPA and FSPD TiO_2/perlite composite samples exhibited improved photocatalytic activity in comparison to P25. In these samples, the anatase and rutile phase as well as TiO_2 are almost equal according to the XRD results.

Although the anatase is considered a more superior photocatalyst than rutile, the better photocatalytic performance of these composites can be related to possible synergistic effect between the two titania phases. Below is given a simple interpretation of this effect. Because of the higher position of the anatase's conduction band edge relative to that of rutile, transfer of the photogenerated electrons from the anatase to rutile takes place. This leads to reduction of the electron-hole recombination rate and as a result to enhancement of the photocatalytic activity of the composite material. Furthermore, the observed enhanced photoactivity of the TiO_2/perlite system can be also attributed to the presence of semitransparent porous perlite substrate that facilitates the dispersion of the TiO_2 particles as well as the penetration of UV-irradiation into the depth of the material [52, 57].

4. Conclusions

TiO_2/perlite composites were synthesized with the help of a homemade FSP reactor and using milled perlite flakes dispersed in TIPO and ethanol as precursor solution. The obtained TiO_2 consisted of interconnected spherical nanoparticles homogenously distributed on perlite flakes. The XRD analysis showed that titania crystallized in the form of anatase and rutile with nanoparticles' size ranging from 20 to 40 nm. Raman microscopy revealed attachment of titania nanoparticles onto perlite substrate via formation of the Si-O-Ti bond. The SSA of the TiO_2/perlite composites decrease with the increase of the oxygen flow rate. Although the SSA of the TiO_2/perlite composites was lower than that of P25 sample, their photocatalytic activity in NO oxidation was comparable and even higher for some of them. This result was attributed to the presence of perlite glassy substrate that facilitates photocatalyst dispersion as well as to the synergistic effect between two crystalline phases.

Acknowledgment

This work was partially supported by the General Secretariat for Research and Technology of Greece under the projects 09SYN-42-925-ARISTON and 12SLO ET36 62.

References

[1] B. O'Regan and M. Grätzel, "A low-cost, high-efficiency solar cell based on dye-sensitized colloidal TiO_2 films," *Nature*, vol. 353, no. 6346, pp. 737–740, 1991.

[2] M. J. Madou and S. R. Morrison, *Chemical Sensing with Solid State Devices*, Academic Press, Harcourt Brace Jovanovich Publisher, Boston, Mass, USA, 1987.

[3] M. Biancardo, R. Argazzi, and C. A. Bignozzi, "Solid-state photochromic device based on nanocrystalline TiO_2 functionalized with electron donor-acceptor species," *Inorganic Chemistry*, vol. 44, no. 26, pp. 9619–9621, 2005.

[4] R. Wang, K. Hashimoto, A. Fujishima et al., "Light-induced amphiphilic surfaces," *Nature*, vol. 388, no. 6641, pp. 431–432, 1997.

[5] M. R. Hoffmann, S. T. Martin, W. Choi, and D. W. Bahnemann, "Environmental applications of semiconductor photocatalysis," *Chemical Reviews*, vol. 95, no. 1, pp. 69–96, 1995.

[6] J. F. Banfield and H. Zhang, "Nanoparticles in the environment," *Reviews in Mineralogy and Geochemistry*, vol. 44, pp. 1–58, 2001.

[7] A. L. Linsebigler, G. Lu, and J. T. Yates Jr., "Photocatalysis on TiO_2 surfaces: principles, mechanisms, and selected results," *Chemical Reviews*, vol. 95, no. 3, pp. 735–758, 1995.

[8] K. Tanaka, M. F. V. Capule, and T. Hisanaga, "Effect of crystallinity of TiO_2 on its photocatalytic action," *Chemical Physics Letters*, vol. 187, no. 1-2, pp. 73–76, 1991.

[9] R. I. Bickley, T. Gonzalez-Carreno, J. S. Lees, L. Palmisano, and R. J. D. Tilley, "A structural investigation of titanium dioxide photocatalysts," *Journal of Solid State Chemistry*, vol. 92, no. 1, pp. 178–190, 1991.

[10] H. Gerischer and A. Heller, "Photocatalytic oxidation of organic molecules at TiO_2 particles by sunlight in aerated water," *Journal of the Electrochemical Society*, vol. 139, no. 1, pp. 113–118, 1992.

[11] K. Okuyama, Y. Kousaka, N. Tohge et al., "Production of ultrafine metal oxide aerosol particles by thermal decomposition of metalalkoxide vapors," *AIChE Journal*, vol. 32, no. 12, pp. 2010–2019, 1986.

[12] K. Palmisano, V. Augugliaro, A. Sclafani, and M. Schiavello, "Activity of chromium-ion-doped titania for the dinitrogen photoreduction to ammonia and for the phenol photodegradation," *Journal of physical chemistry*, vol. 92, no. 23, pp. 6710–6713, 1988.

[13] W. Choi, A. Termin, and M. R. Hoffmann, "The role of metal ion dopants in quantum-sized TiO_2: correlation between photoreactivity and charge carrier recombination dynamics," *Journal of Physical Chemistry*, vol. 98, no. 51, pp. 13669–13679, 1994.

[14] G. P. Fotou, S. Vemury, and S. E. Pratsinis, "Synthesis and evaluation of titania powders for photodestruction of phenol," *Chemical Engineering Science*, vol. 49, no. 24, pp. 4939–4948, 1994.

[15] S. Liu, J. Yu, and M. Jaroniec, "Tunable photocatalytic selectivity of hollow TiO_2 microspheres composed of anatase polyhedra with exposed 001 facets," *Journal of the American Chemical Society*, vol. 132, no. 34, pp. 11914–11916, 2010.

[16] J. Yu, W. Liu, and H. Yu, "A one-pot approach to hierarchically nanoporous titania hollow microspheres with high photocatalytic activity," *Crystal Growth and Design*, vol. 8, no. 3, pp. 930–934, 2008.

[17] K. Cheng, W. Sun, H. Y. Ying Jiang, J. Liu, and J. Lin, "Sonochemical deposition of Au nanoparticles on different facets-dominated anatase TiO_2 single crystals and resulting photocatalytic performance," *Journal of Physical Chemistry C*, vol. 117, no. 28, pp. 14600–146007, 2013.

[18] M. V. Sofianou, V. Psycharis, N. Boukos et al., "Tuning the photocatalytic selectivity of TiO_2 anatase nanoplates by altering the exposed crystal facets content," *Applied Catalysis B*, vol. 142, pp. 761–768, 2013.

[19] S. E. Pratsinis, "Flame aerosol synthesis of ceramic powders," *Progress in Energy and Combustion Science*, vol. 24, no. 3, pp. 197–219, 1998.

[20] S. Kim, J. J. Gislason, R. W. Morton, X. Q. Pan, H. P. Sun, and R. M. Laine, "Liquid-feed flame spray pyrolysis of nanopowders in the alumina-titania system," *Chemistry of Materials*, vol. 16, no. 12, pp. 2336–2343, 2004.

[21] G. L. Chiarello, E. Selli, and L. Forni, "Photocatalytic hydrogen production over flame spray pyrolysis-synthesised TiO_2 and Au/TiO_2," *Applied Catalysis B*, vol. 84, no. 1-2, pp. 332–339, 2008.

[22] W. Y. Teoh, L. Mädler, D. Beydoun, S. E. Pratsinis, and R. Amal, "Direct (one-step) synthesis of TiO_2 and Pt/TiO_2 nanoparticles for photocatalytic mineralisation of sucrose," *Chemical Engineering Science*, vol. 60, no. 21, pp. 5852–5861, 2005.

[23] S. Y. Dhumal, T. L. Daulton, J. Jiang, B. Khomami, and P. Biswas, "Synthesis of visible light-active nanostructured TiO_x ($x < 2$) photocatalysts in a flame aerosol reactor," *Applied Catalysis B*, vol. 86, no. 3-4, pp. 145–151, 2009.

[24] K. A. Michalow, E. H. Otal, D. Burnat et al., "Flame-made visible light active TiO_2:Cr photocatalysts: correlation between structural, optical and photocatalytic properties," *Catalysis Today*, vol. 209, pp. 47–53, 2013.

[25] C. Gunawan, W. Y. Teoh, C. P. Marquis, J. Lifia, and R. Amal, "Reversible antimicrobial photoswitching in nanosilver," *Small*, vol. 5, no. 3, pp. 341–344, 2009.

[26] R. Jossen, M. C. Heine, S. E. Pratsinis, S. M. Augustine, and M. K. Akhtar, "Thermal stability and catalytic activity of flame-made silica-vanadia-tungsten oxide-titania," *Applied Catalysis B*, vol. 69, no. 3-4, pp. 181–188, 2007.

[27] B. Sánchez, J. M. Coronado, R. Candal et al., "Preparation of TiO_2 coatings on PET monoliths for the photocatalytic elimination of trichloroethylene in the gas phase," *Applied Catalysis B*, vol. 66, no. 3-4, pp. 295–301, 2006.

[28] L.-W. Zhang, H.-B. Fu, and Y.-F. Zhu, "Efficient TiO_2 photocatalysts from surface hybridization of TiO_2 particles with graphite-like carbon," *Advanced Functional Materials*, vol. 18, no. 15, pp. 2180–2189, 2008.

[29] N. Keller, G. Rebmann, E. Barraud, O. Zahraa, and V. Keller, "Macroscopic carbon nanofibers for use as photocatalyst support," *Catalysis Today*, vol. 101, no. 3-4, pp. 323–329, 2005.

[30] P. Aranda, R. Kun, M. A. Martín-Luengo, S. Letaïef, I. Dékány, and E. Ruiz-Hitzky, "Titania-sepiolite nanocomposites prepared by a surfactant templating colloidal route," *Chemistry of Materials*, vol. 20, no. 1, pp. 84–91, 2008.

[31] Y. Lee, J. H. Choi, H. J. Jeon, K. M. Choi, J. W. Lee, and J. K. Kang, "Titanium-embedded layered double hydroxides as highly efficient water oxidation photocatalysts under visible light," *Energy and Environmental Science*, vol. 4, no. 3, pp. 914–920, 2011.

[32] S. Pausova, J. Krysa, J. Jirkovsky, G. Mailhot, and V. Prevot, "Photocatalytic behavior of nanosized TiO_2 immobilized on layered double hydroxides by delamination/restacking process," *Environmental Science and Pollution Research*, vol. 19, pp. 3709–3718, 2012.

[33] R. Lu, X. Xu, J. Chang, Y. Zhu, S. Xu, and F. Zhang, "Improvement of photocatalytic activity of TiO_2 nanoparticles on selectively reconstructed layered double hydroxide," *Applied Catalysis B*, vol. 111-112, pp. 389–396, 2012.

[34] M. H. Habibi and M. Zendehdel, "Synthesis and characterization of titania nanoparticles on the surface of microporous perlite using sol-gel method: influence of titania precursor

on characteristics," *Journal of Inorganic and Organometallic Polymers and Materials*, vol. 21, no. 3, pp. 634–639, 2011.

[35] J. Matos, J. Laine, J.-M. Herrmann, D. Uzcategui, and J. L. Brito, "Influence of activated carbon upon titania on aqueous photocatalytic consecutive runs of phenol photodegradation," *Applied Catalysis B*, vol. 70, no. 1–4, pp. 461–469, 2007.

[36] J. Matos, J. Laine, and J.-M. Herrmann, "Effect of the type of activated carbons on the photocatalytic degradation of aqueous organic pollutants by UV-irradiated titania," *Journal of Catalysis*, vol. 200, no. 1, pp. 10–20, 2001.

[37] A. Fernandez, G. Lassaletta, V. M. Jimenez et al., "Preparation and characterization of TiO_2 photocatalysts supported on various rigid supports (glass, quartz and stainless steel). Comparative studies of photocatalytic activity in water purification," *Applied Catalysis B*, vol. 7, no. 1-2, pp. 49–63, 1995.

[38] T. K. Erdem, Ç. Meral, M. Tokyay, and T. Y. Erdoğan, "Use of perlite as a pozzolanic addition in producing blended cements," *Cement and Concrete Composites*, vol. 29, no. 1, pp. 13–21, 2007.

[39] M. Singh and M. Garg, "Perlite-based building materials—a review of current applications," *Construction and Building Materials*, vol. 5, no. 2, pp. 75–81, 1991.

[40] M. Faramarzpour, M. Vossoughi, and M. Borghei, "Photocatalytic degradation of furfural by titania nanoparticles in a floating-bed photoreactor," *Chemical Engineering Journal*, vol. 146, no. 1, pp. 79–85, 2009.

[41] S. N. Hosseini, S. M. Borghei, M. Vossoughi, and N. Taghavinia, "Immobilization of TiO_2 on perlite granules for photocatalytic degradation of phenol," *Applied Catalysis B*, vol. 74, no. 1-2, pp. 53–62, 2007.

[42] K. Genov, I. Stambolova, M. Shipochka, I. Boevski, S. Vassilev, and V. Blaskov, "Ag coated bulgarian natural glass perlite via spray pyrolysis for decomposition of ozone," *Journal of the University of Chemical Technology & Metallurgy*, vol. 46, no. 4, pp. 363–368, 2011.

[43] Y.-H. Tseng, C.-S. Kuo, C.-H. Huang et al., "Visible-light-responsive nano-TiO_2 with mixed crystal lattice and its photocatalytic activity," *Nanotechnology*, vol. 17, no. 10, pp. 2490–2497, 2006.

[44] J. Yu, J. C. Yu, M. K.-P. Leung et al., "Effects of acidic and basic hydrolysis catalysts on the photocatalytic activity and microstructures of bimodal mesoporous titania," *Journal of Catalysis*, vol. 217, no. 1, pp. 69–78, 2003.

[45] "Fine ceramics (advanced ceramics, advanced technical ceramics)—test method for air-purification performance of semiconducting photocatalytic materials. Part 1: removal of nitric oxide," ISO/DIS 22197-1, 2007.

[46] V. Kalousek, J. Tschirch, D. Bahnemann, and J. Rathouský, "Mesoporous layers of TiO_2 as highly efficient photocatalysts for the purification of air," *Superlattices and Microstructures*, vol. 44, no. 4-5, pp. 506–513, 2008.

[47] Y. Ohko, Y. Nakamura, N. Negishi, S. Matsuzawa, and K. Takeuchi, "Photocatalytic oxidation of nitrogen monoxide using TiO_2 thin films under continuous UV light illumination," *Journal of Photochemistry and Photobiology A*, vol. 205, no. 1, pp. 28–33, 2009.

[48] A. Mitsionis, T. Vaimakis, C. Trapalis, N. Todorova, D. Bahnemann, and R. Dillert, "Hydroxyapatite/titanium dioxide nanocomposites for controlled photocatalytic NO oxidation," *Applied Catalysis B*, vol. 106, no. 3-4, pp. 398–404, 2011.

[49] T. Giannakopoulou, N. Todorova, G. Romanos et al., "Composite hydroxyapatite/TiO_2 materials for photocatalytic oxidation of NO_x," *Materials Science and Engineering B*, vol. 177, pp. 1046–1052, 2012.

[50] Y. K. Kho, W. Y. Teoh, L. Mädler, and R. Amal, "Dopant-free, polymorphic design of TiO_2 nanocrystals by flame aerosol synthesis," *Chemical Engineering Science*, vol. 66, no. 11, pp. 2409–2416, 2011.

[51] G. L. Chiarello, I. Rossetti, and L. Forni, "Flame-spray pyrolysis preparation of perovskites for methane catalytic combustion," *Journal of Catalysis*, vol. 236, no. 2, pp. 251–261, 2005.

[52] R. Strobel and S. E. Pratsinis, "Direct synthesis of maghemite, magnetite and wustite nanoparticles by flame spray pyrolysis," *Advanced Powder Technology*, vol. 20, no. 2, pp. 190–194, 2009.

[53] T. Ohsaka, F. Izumi, and Y. Fujiki, "Raman spectrum of anatase, TiO_2," *Journal of Raman Spectroscopy*, vol. 7, pp. 321–324, 1978.

[54] S. P. S. Porto, P. A. Fleury, and T. C. Damen, "Raman spectra of TiO_2, MgF_2, ZnF_2, FeF_2, and MnF_2," *Physical Review*, vol. 154, no. 2, pp. 522–526, 1967.

[55] F. Cerdeira, C. J. Buchenauer, F. H. Pollak, and M. Cardona, "Stress-induced shifts of first-order Raman frequencies of diamond- and zinc-blende-type semiconductors," *Physical Review B*, vol. 5, no. 2, pp. 580–593, 1972.

[56] B. G. Varshal, V. N. Denisov, B. N. Mavrin, G. A. Pavlova, V. B. Podobedov, and E. Kh. Sterin, "Spectra of combination and hypercombination scattering of light by glasses of the TiO_2-SiO_2 system," *Optics and Spectroscopy*, vol. 47, pp. 344–362, 1979.

[57] O. Carp, C. L. Huisman, and A. Reller, "Photoinduced reactivity of titanium dioxide," *Progress in Solid State Chemistry*, vol. 32, no. 1-2, pp. 33–177, 2004.

Hindawi Publishing Corporation
International Journal of Photoenergy
Volume 2013, Article ID 276504, 8 pages
http://dx.doi.org/10.1155/2013/276504

Research Article

Single Step Formation of C-TiO_2 Nanotubes: Influence of Applied Voltage and Their Photocatalytic Activity under Solar Illumination

Chin Wei Lai[1] and Srimala Sreekantan[2]

[1] *Nanotechnology & Catalysis Research Centre (NANOCAT), Institute of Postgraduate Studies (IPS), Universiti Malaya, 3rd Floor, Block A, 50603 Kuala Lumpur, Malaysia*
[2] *School of Materials and Mineral Resources Engineering, Universiti Sains Malaysia Engineering Campus, Seberang Perai Selatan, Pulau Pinang, 14300 Nibong Tebal, Malaysia*

Correspondence should be addressed to Chin Wei Lai; cwlai@um.edu.my

Received 25 June 2013; Revised 29 September 2013; Accepted 7 October 2013

Academic Editor: Huogen Yu

Self-aligned and high-uniformity carbon (C)- titania (TiO_2) nanotube arrays were successfully formed via single step anodization of titanium (Ti) foil at 30 V for 1 h in a bath composed of ethylene glycol (EG), ammonium fluoride (NH_4F), and hydrogen peroxide (H_2O_2). It was well established that applied voltage played an important role in controlling field-assisted oxidation and field-assisted dissolution during electrochemical anodization process. Therefore, the influences of applied voltage on the formation of C-TiO_2 nanotube arrays were discussed. It was found that a minimal applied voltage of 30 V was required to form the self-aligned and high-uniformity C-TiO_2 nanotube arrays with diameter of ~75 nm and length of ~2 μm. The samples synthesized using different applied voltages were then subjected to heat treatment for the conversion of amorphous phase to crystalline phase. The photocatalytic activity evaluation of C-TiO_2 samples was made under degradation of organic dye (methyl orange (MO) solution). The results revealed that controlled nanoarchitecture C-TiO_2 photocatalyst led to a significant enhancement in photocatalytic activity due to the creation of more specific active surface areas for incident photons absorption from the solar illumination.

1. Introduction

Nowadays, various kinds of environmental contaminants are around all of us, especially organic and inorganic pollutants from industrial wastewaters [1–3]. Thus, the treatments of such wastewater have become a major concern and it is urgent to develop a sustainable and cost-effective treatment technology to solve global environmental problems [3, 4]. In recent years, the photocatalyst system has attracted much attention from science community as one of the most promising ways to solve the environmental problems [4–6]. This system is considered to be an ideal and green environmental solution for our green economy future.

In this case, TiO_2 based nanomaterials have been broadly studied as the most promising photocatalyst for environmental remediation such as air purification, water purification, heavy metals degradation, and hazardous waste remediation [6–10]. The reasons are mainly attributed to the non-toxicity, cost-effectiveness, long-term stability, widespread availability, and high stability against photocorrosion with great capacity for oxidation and high photocatalytic property. To date, development of nanoarchitecture of TiO_2 assemblies with precisely controllable nanoscale features has gained significant scientific interest [11, 12]. Among different nanoarchitectures of TiO_2, one-dimensional (1D) TiO_2 is considered as a promising candidate in environmental and industrial pollutants degradation due to the well controllable dimensional features such as pore diameter, length, and wall thickness [6–9, 11–15]. However, its practical application was limited by poor absorption of photons from the solar illumination and high recombination losses of photoinduced electron-hole pairs [1, 4, 10, 16–18].

Recently, numerous research studies have been paid for the rational design of high efficiency heterostructure C-TiO_2 based nanomaterial for remarkable solar absorption and higher separation efficiency of photo-induced charge carriers [4, 19–22]. In particular, C-TiO_2 based nanomaterials can exert a substantial influence on modifying electronic structure and the construction of heterotomic surface structure that allow higher efficiency photocatalysis reaction under solar irradiation [19, 21, 23]. Several literatures have reported that incorporation of anion C-dopants into TiO_2 crystalline could shift its photoresponse into visible region, which accounts for 40–45% irradiation from the solar light. The main reason was attributed to the narrowing of the band gap energy, which resulted from an increase in the width of the valence band. The reduction of band gap energy was believed to be from the mixing of the p-state of C dopants with O $2p$ and Ti $3d$ orbital constituting valence band [21, 23, 24].

In the present study, a detailed study on the C-doped TiO_2 nanotubes via single step of electrochemical anodization technique was performed. An organic electrolyte of ethylene glycol was selected as C source to dope into TiO_2 nanotubes during electrochemical anodization. This study aims to determine the minimal applied voltage to grow the self-aligned and high-uniformity C-TiO_2 nanotubes for better photocatalytic performance. The novelty of this work is to synthesize a potential photocatalyzer, which shows strong absorption range in UV-visible region, strong oxidation ability, cost-effective and time saving process.

2. Experimental Procedure

2.1. Preparation of Anodic C-TiO_2 Nanotubes. 99.6% purity of Ti foils (Strem Chemical, USA) with dimension of 50 mm × 10 mm × 0.127 mm was used in this experimental study. The electrochemical anodization process was performed in an organic electrolyte of EG ($C_2H_6O_2$, >99.5%, Merck, USA), 5 wt% of NH_4F (98%, Merck, USA), and 5 wt% of H_2O_2 (30% H_2O_2 : 70% H_2O, J.T. Baker, USA). This composition was selected because it favors the formation of well-aligned and highly ordered nanotubular structure based on our previous studies [25]. Electrochemical anodization process was conducted for 1 h with three different applied voltages (e.g., 10 V, 20 V, and 30 V). Anodization was performed in a two-electrode configuration bath with Ti foil as the anode and a platinum rod as the cathode. Subsequently, these samples were annealed at 400°C for 4 h in an argon atmosphere.

2.2. Characterization of Anodic C-TiO_2 Nanotubes. The Field Emission Scanning Electron Microscopy (FESEM) and Energy Dispersive X-Ray (EDX) were conducted (FEI Quanta 200 FESEM model, USA). The cross-sectional measurements were carried out on mechanically bent samples, where a partial lift-off of the anodic layer occurred to obtain the thickness of the anodic oxide formed on Ti foil. The crystalline phase of the synthesized samples was identified by power X-ray Diffraction (XRD), using a Bruker X-ray Diffraction Model D-8, USA, equipped with a Cu Kα monochromatized radiation source (λ = 1.5406 Å). The sample with dimension (10 mm × 10 mm) was placed onto a specimen holder and then placed in the rotating unit stage of diffractometer system. The data was collected within 2θ of 10° to 70° with a step size of 0.034° at scan time 71.6 sec. Photoluminescence (PL) spectra were obtained at room temperature using an LS 55 luminescence spectrometer (Jobin-Yvon HR 800UV). The photoelectron spectra were obtained through X-ray photoelectron spectroscopy (XPS; JEOL JPS-1000SX) with a dual X-ray source, in which an Al-Kα (30 kV) anode and a hemispherical energy analyzer were used. The background pressure during data acquisition was maintained at 7.0×10^{-9} Torr. All binding energies were calibrated using contaminant carbon (C1s = 284.8 eV) as a charge reference.

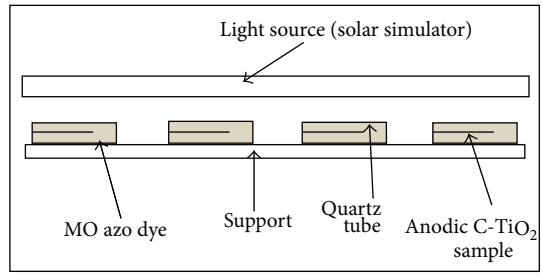

Figure 1: Schematic diagram of the experimental setup for quartz glass tube custom-made photoreactor used in photocatalytic degradation MO dye studies.

2.3. Photocatalytic Degradation of MO Dye Study. Photocatalytic degradation MO dye was conducted by dipping 4 cm^2 of anodic C-TiO_2 nanotubes samples into a 100 mL of quartz glass tube containing 30 ppm of MO dye. The quartz glass tube was then placed in a custom-made photorecator for photocatalytic degradation studies. A schematic diagram of quartz glass tube custom-made photo-reactor used in photocatalytic degradation MO dye is exhibited in Figure 1. In this study, a blank sample (without anodic sample) was prepared in order to eliminate the effect of light towards the degradation of MO dye solution. All anodic samples were left in a custom-made photo-reactor for 30 min in dark environment to achieve adsorption and desorption equilibrium. Then, samples were photoirradiated using a 150 W Xenon solar simulator (Zolix LSP-X150, China) with intensity of 800 W/m^2. Three mL of MO dye solution was withdrawn from the quartz glass tube every 1 h to investigate the degradation of MO dye solution under solar irradiation. The concentration of the degraded MO dye solution assisted by the anodic sample was determined using UV-Vis spectrometer (PerkinElmer Lambda 35, USA).

3. Results and Discussion

3.1. Surface Morphology of Anodic C-TiO_2 Nanotubes. The effect of applied voltage in an organic electrolyte of EG solution containing 5 wt% of NH_4F and 5 wt% of H_2O_2 on the morphology of the self-organized TiO_2 nanotubes

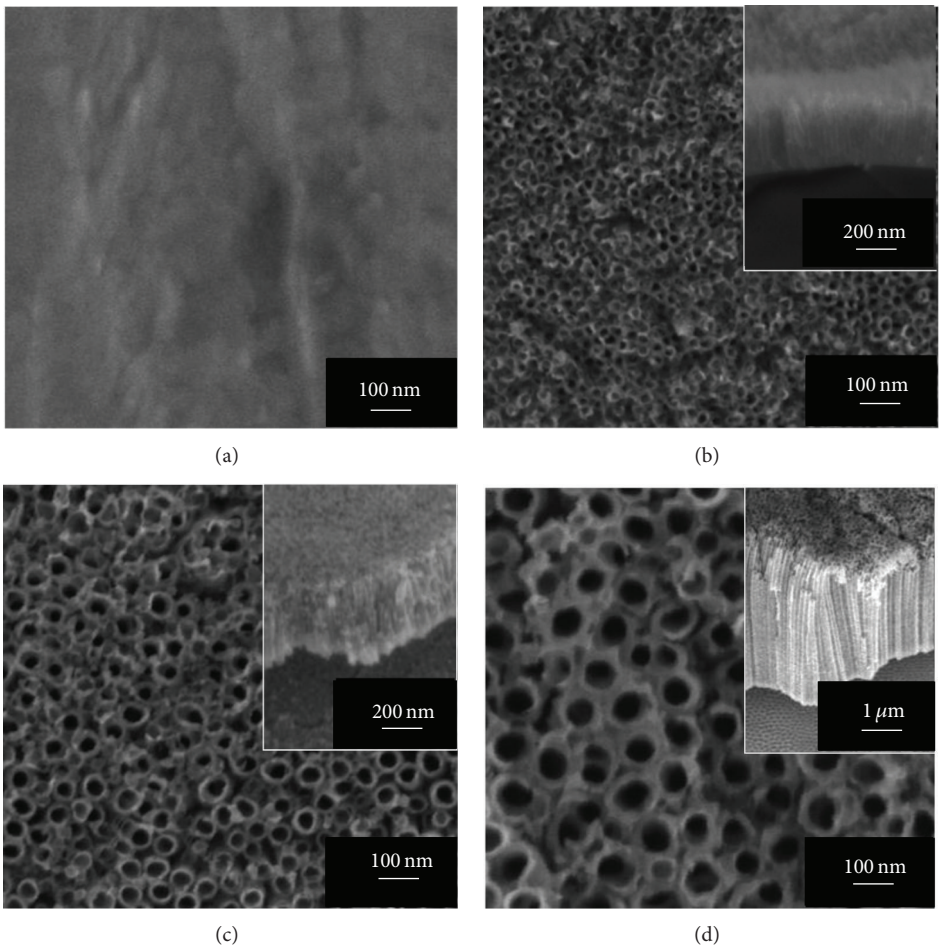

Figure 2: FEESEM images of (a) pure Ti foil and C-TiO_2 nanotube arrays fabricated at different applied voltage in an EG electrolyte containing 5 wt% of NH_4F and 5 wt% of H_2O_2 for 1 h at (b) 10 V, (c) 20 V, and (d) 30 V (inset: cross-sectional view).

is discussed. Based on our preliminary study, an optimum content of 5 wt% H_2O_2 played an important role in increasing the oxidation rate of Ti to form TiO_2, while 5 wt% of NH_4F was sufficient to trigger the chemical dissolution reaction to form nanotubular structure during electrochemical anodization [25–27]. The morphology of the Ti foil before conducting electrochemical anodization was characterized by FESEM (Figure 2(a)). It is clearly shown that Ti foil was flat without any pits or pores on its surface. The oxide layer has not yet been formed. The FESEM micrographs of the synthesized nanostructures of anodic C-TiO_2 samples after electrochemical anodization varied from 10 V to 30 V are shown in Figure 2(b) to Figure 2(d). The inset micrographs show the cross-sectional morphology of oxide layer on the anodized Ti foil. These FESEM micrographs clearly show that the applied voltage affects the geometric features are the appearance of the nanotubular structure on the Ti foils. It could be observed that anodized samples exhibited uniform growth of nanotube arrays throughout the surface of Ti foil. The surface and inset of cross-sectional morphology of the Ti foil anodized at a lower applied voltage of 10 V are shown in Figure 2(b). It was found that an average of 25 nm diameters and an average thickness of 550 nm of nanotube arrays were produced. Upon increasing the applied voltage to 20 V, the average diameter for the nanotubular structure was increased to 45 nm with thickness of 750 nm (Figure 2(c)). It is noteworthy to mention that uniform circular nanotube arrays were successfully formed when minimum voltage of 30 V was applied during electrochemical anodization. The average diameter of 80 nm and thickness of 2 μm nanotubes were produced (Figure 2(d)). Therefore, uniform growth of anodic nanotube arrays at lower 30 V of applied voltage was selected and duplicated for the investigation studies.

3.2. Chemical Compositions of Anodic C-TiO_2 Nanotubes. EDX analysis was employed to investigate the chemical stoichiometry of the anodic C-TiO_2 nanotubes after heating treatment at 400°C in argon atmosphere. As determined through EDX analysis, the anodic C-TiO_2 nanotubes synthesized at 30 V consisted of 60.14 at% of Ti element, 33.68 at% of O element and 6.18 at% of C element (Figure 3). An additional spectrum of C was observed at about 0.2 keV from the EDX spectra. This result showed the presence of C species in anodic TiO_2 nanotubes. The main reason is favorable to the oxidation of organic EG electrolyte to carbonate type

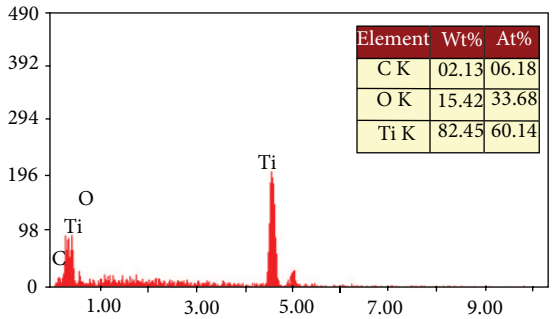

Figure 3: EDX spectra of self-aligned and high-uniformity C-TiO_2 nanotube arrays formed in an EG electrolyte containing 5 wt% of NH_4F and 5 wt% of H_2O_2 for 1 h at 30 V.

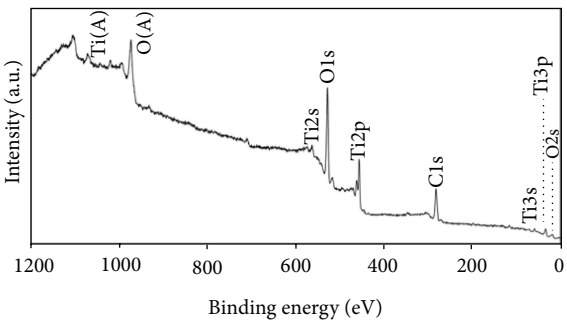

Figure 4: XPS survey spectra of self-aligned and high-uniformity C-TiO_2 nanotube arrays formed in an EG electrolyte containing 5 wt% of NH_4F and 5 wt% of H_2O_2 for 1 h at 30 V.

species which gets absorbed on the wall of nanotubes during the electrochemical anodization [19, 24, 28]. These resultant carbonate type species were reduced to C species during heat treatment process and diffused into the TiO_2 lattice [29]. In this manner, the single step incorporation of C species to TiO_2 nanotubes could be achieved.

Next, XPS measurements were carried out to further investigate the chemical composition and oxidation state of C-TiO_2 nanotubes. XPS survey spectra for the sample synthesized at 30 V are presented in Figure 4. The elements of Ti, O, and C were detected from the XPS survey spectra, which indicated that the carbon species were successfully loaded into the lattice of TiO_2. It was found that the peak of Ti2p (binding energy of about 460 eV) is attributed to Ti^{4+}. Besides, it could be observed that the peak of O1s (binding energy of about 530 eV) showed the presence of oxygen atoms in the TiO_2 structure. Meanwhile, the detection of the peak C1s at about 285 eV can be ascribed to the Ti–C–O bonds of the carbonate species originating from the residual carbon of the organic ethylene glycol electrolyte.

3.3. Crystalline Structure of Anodic C-TiO_2 Nanotubes. In the present study, XRD measurements were conducted to reveal the crystal phase transition of the as-anodized and annealed samples. The results are presented in Figure 5. Based on preliminary study, 400°C was sufficient to convert TiO_2 amorphous structure to high crystallinity of anatase

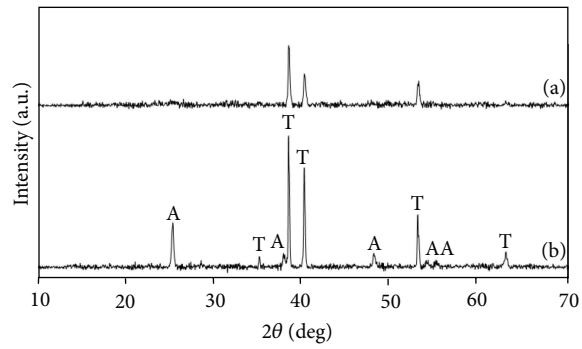

Figure 5: XRD pattern of self-aligned and high-uniformity C-TiO_2 nanotube arrays formed in an EG electrolyte containing 5 wt% of NH_4F and 5 wt% of H_2O_2 for 1 h at 30 V, (a) as-anodized and (b) annealed at 400°C under argon atmosphere for 4 h (Ti: titanium; A: anatase).

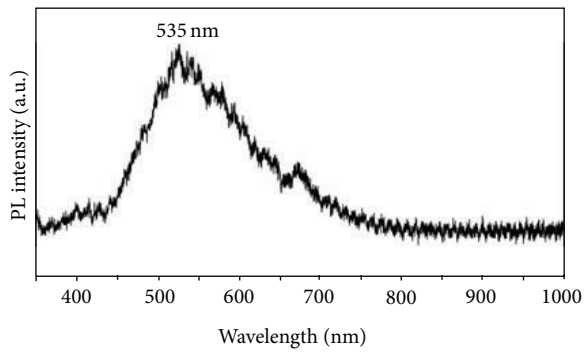

Figure 6: The PL emission spectra of self-aligned and high-uniformity C-TiO_2 nanotube arrays formed in an EG electrolyte containing 5 wt% of NH_4F and 5 wt% of H_2O_2 for 1 h at 30 V.

phase, which exhibited thermodynamically stable and higher surface stability [30–33]. It was found that the presence of Ti phase only was detected from the XRD pattern for the as-anodized sample, which represents the amorphous phase of TiO_2 (Figure 5(a)). However, high crystallinity of anatase phase was detected for the sample subjected to annealing at 400°C in argon atmosphere (Figure 5(b)). It can be seen that the diffraction peaks of the entire samples are ascribed to the TiO_2 with anatase phase (JCPDS no. 21–1272). The diffraction peaks allocated at 25.37°, 38.67°, 48.21°, 54.10°, and 55.26° are corresponding to (101), (112), (200), (105), and (211) crystal planes for the anatase phase, respectively.

3.4. Optical Property of Anodic C-TiO_2 Nanotubes. PL emission spectra were broadly used to investigate the competency of charge carrier trapping, migration, and transfer behaviors of anodic C-TiO_2 nanotubes. The information from PL emission spectra is important to understand the state of electron-hole pairs in C-TiO_2 nanotubes photocatalyst since the emission mainly resulted from recombination dynamics of these free carriers. The PL measurement was conducted at room temperatures in the wavelength range of 350 nm to 1000 nm as presented in Figure 6. The dominant PL emission

spectrum of the samples prepared at 30 V is clearly observed at 535 nm, implying the visible-light characteristics of the sample. The dominant PL spectrum of anatase phase TiO_2 was closely related to the recombination of self-trapped excitons localized on the TiO_6 octahedral, which results from the interaction of the negative electrons located in the Ti $3d$ states with the positive holes in the O $2p$ state [7, 16, 19]. In this case, the peak position at 535 nm might be attributed to the radioactive recombination of self-trapped excitons localized on TiO_6 octahedron. On the other hand, the PL emissions above 535 nm might be attributed to the presence of surface state and intrinsic defects such as oxygen vacancies, which give rise to donor states located below conduction band. Several literatures have reported that the resultant PL emission spectra were attributed to the oxygen-related defects within the sample lattice [34, 35]. Zhao and co-workers have been reported that the carbon species doping into the lattice of TiO_2 nanotubes favored the formation of oxygen vacancies [36]. They proposed that the electrons were easily trapped by those oxygen vacancies, while the holes were trapped by carbon species. This condition could decrease the PL intensity significantly. Hence, the presence of carbon species could improve the separation extent and restrain the recombination losses of the photo-induced charge carriers. Besides, PL technique has been widely used to investigate the energy levels of samples [23, 37]. The energy level (E_b) of the samples was calculated using the equation $E_b = hc/\lambda$, where E_b is the band gap energy, h is Planck's constant (4.135667×10^{-15} eV s), c is the velocity of light (2.997924×108 m/s), and λ is the wavelength (nm) of PL emission. The E_b was found at around 2.3 eV, which is relatively low as compared to the E_b of pure TiO_2 (3.2 eV for anatase phase) [7, 10]. The result clearly demonstrates that visible emission is likely facilitated by the interstitial C species within the lattice of TiO_2.

3.5. Formation Mechanism of Anodic C-TiO_2 Nanotubes. In the present study, applied voltage played an important role in controlling the field-assisted oxidation of Ti metal to form TiO_2 and field-assisted dissolution of Ti metal ions into electrolyte [38, 39]. A simple schematic illustration about the formation mechanism of anodic C-TiO_2 nanotube arrays was presented in Figure 7. The compact oxide layer was formed through the hydrolysis of Ti foil (stage A) which was oxidized to TiO_2 forming a barrier type layer under applied voltage. This layer grew predominantly by the inward migration of oxygen ions (O^{2-}) through this layer toward Ti/TiO_2 interface with further growth of barrier layer (stage B). The high electric field across the oxide layer subsequently induced the polarization of Ti–O bonding. In this manner, Ti^{4+} ions from the barrier layer of TiO_2 will dissolve into the electrolyte and form pits randomly on the surface of oxide layer. The pits will act as nucleation sites for the porosification (stage C). The titanium-fluoro complexes $(TiF_6)^{2-}$ will induce the chemical dissolution and continuous dissolve the pits, which will further enlarge and deepenly the pits into nanotubular structure. The rate of migration of the Ti^{4+}, O_{2-}, and F^- ions was higher during the higher voltage electrochemical anodization. The higher electron flow promoted increased

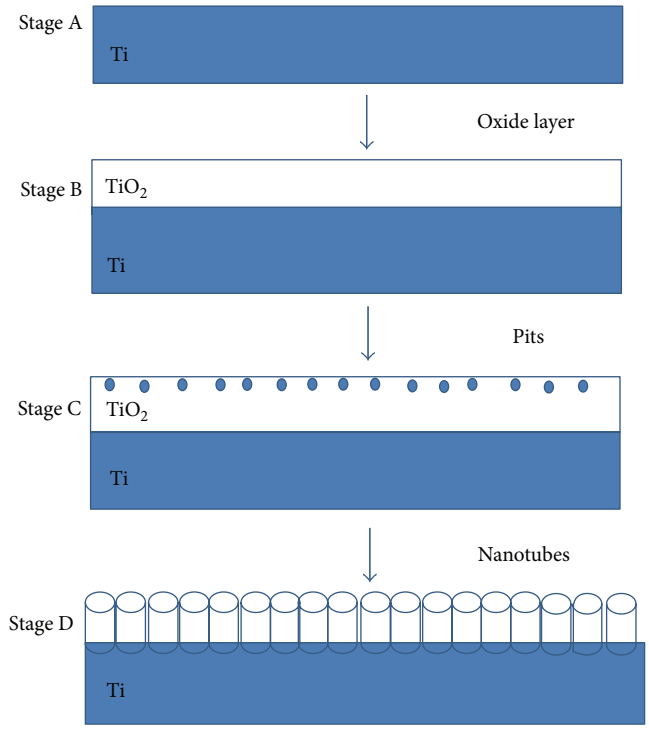

Figure 7: Schematic illustration for the formation mechanism of anodic C-TiO_2 nanotube arrays via electrochemical anodization technique.

field-assisted oxidation and field-assisted dissolution, which leads to an increase in nanotube length and pore size (stage D). The porosity will reach a steady-state, resulting in the formation of uniform of TiO_2 nanotubes [9, 11, 26].

In this manner, organic EG electrolyte was oxidized to carbonate-species under applied voltage, which get absorbed on the wall of nanotubes. Then, these carbonate-species were reduced to C species during annealing treatment process, which might diffuse into the lattice of TiO_2 [29]. Thus, the presence of the C species was found within TiO_2 nanotubes. Valentin and coworkers have proposed that the possible causes for the presence of C atoms in the anatase TiO_2 are due to the substitution of the oxygen lattice with a C atom, the replacement of Ti atoms with a C atom; and stabilization of a C atom at interstitial position of TiO_2 lattice [21]. As a matter of fact, the interstitial C atom arises from the pyrogeneration of EG electrolyte, which reduces the band gap marginally or to introduce mid-gap level to increase the light absorption into visible region. In this case, the band gap level reduction was believed to result from an increase in the width of the valence band due to the mixing of the delocalized p-state of carbon dopants with O $2p$. The mixing p-state of the C dopants with $2p$ of O will shift the valence band edge upwards (~0.8 eV above the valence band) to narrow down the band gap of TiO_2 to ~2.3 eV [11, 19]. A comparison between the pure TiO_2 and C-TiO_2 under solar irradiation for the photo-induced electrons transfer pathways was exhibited in Figure 8. Thus, electronic coupling of these states with electronic

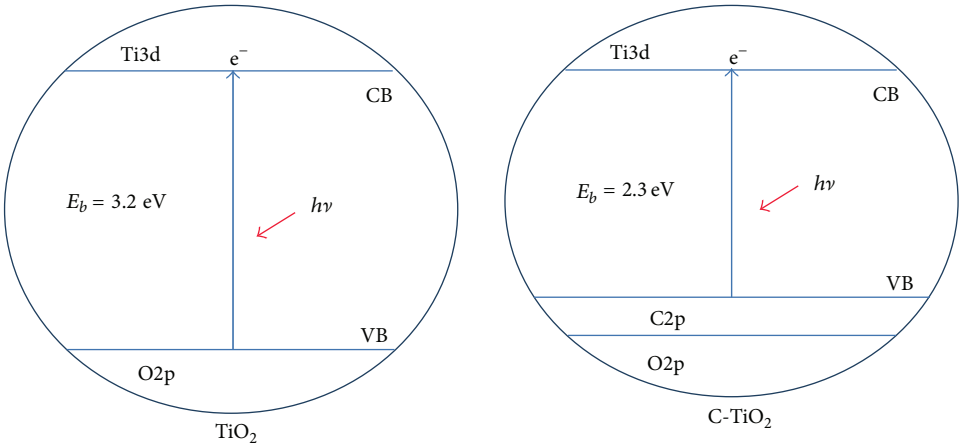

Figure 8: The comparison of the photo-induced electrons transfers pathways for pure TiO_2 and C-TiO_2 under solar irradiation.

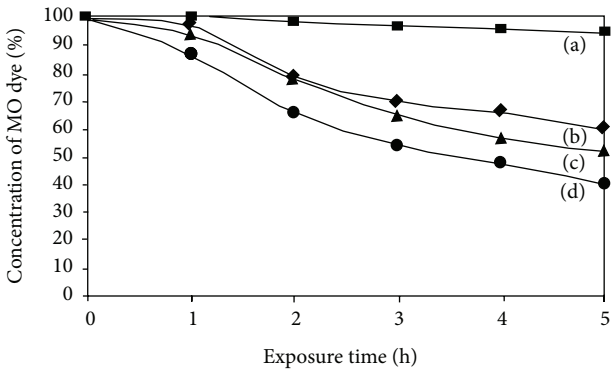

Figure 9: Photodegradation of MO dye solution under solar illumination. (a) Blank sample (without anodic sample); samples of C-TiO_2 nanotube arrays produced at (b) 10 V, (c) 20 V, and (d) 30 V.

continuum of TiO_2 valence band state yields a band of surface state at where the electrons could be generated in conduction band by low energy of visible light irradiation [23].

3.6. Photocatalytic Decolorization of MO Dye Evaluation. The significance of C-TiO_2 nanotubes from different applied voltages (10 V–30 V) was applied as the photocatalytic performance evaluation by decolorization of MO dye under visible light irradiation. Figure 9 clearly shows the continuous decrease in the concentration of MO dyes with increasing exposure time. It was found that the decolorization of MO dye follows an apparent first-order kinetic reaction. The decolorization rate order was C-TiO_2-30 V > C-TiO_2-20 V > C-TiO_2-10 V. It could be observed that the C-TiO_2-30 V exhibited the highest photocatalytic performance of ~60% after exposure to solar irradiation for 5 h. The dominating factor in decolorization of MO dye is attributed to the active surface area of the catalyst to absorb more photons from the solar irradiation [40, 41]. In addition, higher active surface area will allow more organic MO molecules to absorb onto the C-TiO_2 surface. Furthermore, higher uniformity of nanotube arrays will result in more rapid diffusion of the organic MO molecules into the inner of nanotubes for photocatalytic reaction [41, 42]. In this case, C content within the nanotubes could play an important role in reducing the band gap energy of TiO_2 nanotubes (from 3.2 eV to 2.3 eV based on the anatase phase). The visible emission is likely facilitated by the interstitial C species within the lattice of TiO_2. Thus, the photo-induced charge carriers could be generated effectively under solar illumination. Besides, the photo-induced electrons were easily trapped by this C content and led to higher transportation of charge carriers from bulk to surface of TiO_2, which retards the recombination losses. It is a well-known fact that MO molecule has one $-SO_3^-$ group and two alkyl groups ($-CH_3$), which can improve the adsorption of the H_2O or OH^-ions on C-TiO_2 surface [43]. In this manner, C-TiO_2 nanotubes play an essential role in promoting the adsorption of OH species on the inner and outer wall surface of nanotubes and consequently promoting the photocatalytic reaction.

In the present study, photocatalytic reaction in decolorization of MO dye strongly depends on the ability of catalyst to create photo-induced charge carriers, which generate free radicals (hydroxyl radicals of $^{\bullet}OH$) able to undergo secondary reactions [6, 8, 9]. Theoretically, the exposure of a photocatalyst to irradiation ($h\nu$) higher than its E_b will result in the transition of photo-induced electrons (e^-) from the O $2p$ state to the Ti $3d$ state and leave behind photo-induced holes (h^+). Nevertheless, photo-induced e^- and h^+ recombine quickly in ordinary substances. This recombination process can occur either in bulk or on the surface of catalyst by releasing energy in the form of unproductive heat or photons [44]. The photo-induced h^+ escaping from the pair recombination preferentially moves to the photocatalyst/electrolyte interface. The photo-induced h^+ plays an important role in generation of $^{\bullet}OH$ radicals by the trapping of adsorbed H_2O or OH^- ions from the MO dye, which has strong oxidative decomposing power in decolorization of MO dye. Meanwhile, photo-induced e^- escaping from recombination will be trapped on the surface of photocatalyst by reaction with adsorbed oxygen species to generate superoxide anion radicals ($O_2^{\bullet}$), which then will contribute to the formation of

$^{\bullet}$OH radicals by reactions with H_2O [45]. In this case, more $^{\bullet}$OH radicals will react with organic MO dye to decompose them into harmless substance.

4. Conclusion

The formation of C-TiO_2 nanotubes via single step electrochemical anodization technique successfully formed self-aligned and high-uniformity C-TiO_2 nanotube arrays with diameter of ~75 nm and length of ~2 μm with a minimal applied voltage of 30 V. The applied voltage played an important role in enhancing the field-assisted oxidation rate and field-assisted dissolution rate. The reduction of band gap energy level of C-TiO_2 nanotube arrays (3.2 eV to 2.3 eV) was due to the mixing states of the delocalized C $2p$ and O $2p$. In photocatalytic evaluation, it was found that C-TiO_2 synthesized at 30 V exhibited the highest decolorization rate under solar irradiation among samples. The reason was mainly attributed to higher active surface area and higher uniformity of nanotube arrays has better photons absorption from solar illumination to trigger more photo-induced charge carriers for decolorization of MO dye.

Acknowledgment

The authors would like to thank Universiti Malaya for sponsoring this work under UMRG Grant (RP022-2012D).

References

[1] M. Kitano, M. Matsuoka, M. Ueshima, and M. Anpo, "Recent developments in titanium oxide-based photocatalysts," *Applied Catalysis A*, vol. 325, no. 1, pp. 1–14, 2007.

[2] H. J. Oh, J. H. Lee, Y. J. Kim, S. J. Suh, J. H. Lee, and C. S. Chi, "Synthesis of effective titania nanotubes for wastewater purification," *Applied Catalysis B*, vol. 84, no. 1-2, pp. 142–147, 2008.

[3] D. Mohan and C. U. Pittman Jr., "Arsenic removal from water/wastewater using adsorbents-A critical review," *Journal of Hazardous Materials*, vol. 142, no. 1-2, pp. 1–53, 2007.

[4] Y. C. Nah, I. Paramasivam, and P. Schmuki, "Doped TiO_2 and TiO_2 nanotubes: synthesis and applications," *ChemPhysChem*, vol. 11, no. 13, pp. 2698–2713, 2010.

[5] D. A. Tryk, A. Fujishima, and K. Honda, "Recent topics in photoelectrochemistry: achievements and future prospects," *Electrochimica Acta*, vol. 45, no. 15-16, pp. 2363–2376, 2000.

[6] A. Fujishima, X. Zhang, and D. A. Tryk, "TiO_2 photocatalysis and related surface phenomena," *Surface Science Reports*, vol. 63, no. 12, pp. 515–582, 2008.

[7] C. W. Lai and S. Sreekantan, "Preparation of hybrid WO_3-TiO_2 nanotube photoelectrodes using anodization and wet impregnation: improved water-splitting hydrogen generation performance," *International Journal of Hydrogen Energy*, vol. 38, no. 5, pp. 2156–2166, 2013.

[8] A. Kubacka, M. Fernández-García, and G. Colón, "Advanced nanoarchitectures for solar photocatalytic applications," *Chemical Reviews*, vol. 112, no. 3, pp. 1555–1614, 2012.

[9] C. A. Grimes, "Synthesis and application of highly ordered arrays of TiO_2 nanotubes," *Journal of Materials Chemistry*, vol. 17, no. 15, pp. 1451–1457, 2007.

[10] C. W. Lai and S. Sreekantan, "Incorporation of WO_3 species into TiO_2 nanotubes via wet impregnation and their water-splitting performance," *Electrochimica Acta*, vol. 87, pp. 294–302, 2013.

[11] Z. Su and W. Zhou, "Formation, morphology control and applications of anodic TiO_2 nanotube arrays," *Journal of Materials Chemistry*, vol. 21, no. 25, pp. 8955–8970, 2011.

[12] L. M. Sikhwivhilu, S. Mpelane, B. W. Mwakikunga, and S. S. Ray, "Photoluminescence and hydrogen gas-sensing properties of titanium dioxide nanostructures synthesized by hydrothermal treatments," *ACS Applied Materials and Interfaces*, vol. 4, no. 3, pp. 1656–1665, 2012.

[13] S. Sreekantan and L. C. Wei, "Study on the formation and photocatalytic activity of titanate nanotubes synthesized via hydrothermal method," *Journal of Alloys and Compounds*, vol. 490, no. 1-2, pp. 436–442, 2010.

[14] X. Chen and S. S. Mao, "Titanium dioxide nanomaterials: synthesis, properties, modifications and applications," *Chemical Reviews*, vol. 107, no. 7, pp. 2891–2959, 2007.

[15] S. Li, G. Zhang, D. Guo, L. Yu, and W. Zhang, "Anodization fabrication of highly ordered TiO_2 nanotubes," *Journal of Physical Chemistry C*, vol. 113, no. 29, pp. 12759–12765, 2009.

[16] C. W. Lai and S. Sreekantan, "Study of WO_3 incorporated C–TiO_2 nanotubes for efficient visible light driven water splitting performance," *Journal of Alloys and Compounds*, vol. 547, pp. 43–50, 2013.

[17] H. Y. Chang, W. J. Tzeng, and S. Y. Cheng, "Modification of TiO_2 nanotube arrays by solution coating," *Solid State Ionics*, vol. 180, no. 11–13, pp. 817–821, 2009.

[18] A. V. Rupa, D. Manikandan, D. Divakar, and T. Sivakumar, "Effect of deposition of Ag on TiO_2 nanoparticles on the photodegradation of Reactive Yellow-17," *Journal of Hazardous Materials*, vol. 147, no. 3, pp. 906–913, 2007.

[19] R. Taziwa, E. L. Meyer, E. Sideras-Haddad, R. M. Erasmus, E. Manikandan, and B. W. Mwakikunga, "Effect of carbon modification on the electrical, structural, and optical properties of TiO_2 electrodes and their performance in labscale dye-sensitized Solar Cells," *International Journal of Photoenergy*, vol. 2012, Article ID 904323, 9 pages, 2012.

[20] M. Paulose, H. E. Prakasam, O. K. Varghese et al., "TiO_2 nanotube arrays of 1000 μm length by anodization of titanium foil: phenol red diffusion," *Journal of Physical Chemistry C*, vol. 111, no. 41, pp. 14992–14997, 2007.

[21] C. Di Valentin, G. Pacchioni, and A. Selloni, "Theory of carbon doping of titanium dioxide," *Chemistry of Materials*, vol. 17, no. 26, pp. 6656–6665, 2005.

[22] K. Shankar, G. K. Mor, H. E. Prakasam et al., "Highly-ordered TiO_2 nanotube arrays up to 220 μm in length: use in water photoelectrolysis and dye-sensitized solar cells," *Nanotechnology*, vol. 18, no. 6, Article ID 065707, 2007.

[23] C. W. Lai and S. Sreekantan, "Optimized sputtering power to incorporate WO_3 into C–TiO_2 nanotubes for highly visible photoresponse performance," *NANO*, vol. 7, no. 6, Article ID 1250051, 8 pages, 2012.

[24] X. Yang, C. Cao, L. Erickson, K. Hohn, R. Maghirang, and K. Klabunde, "Synthesis of visible-light-active TiO_2-based photocatalysts by carbon and nitrogen doping," *Journal of Catalysis*, vol. 260, no. 1, pp. 128–133, 2008.

[25] S. Sreekantan, L. C. Wei, and Z. Lockman, "Extremely fast growth rate of TiO_2 nanotube arrays in electrochemical bath containing H_2O_2," *Journal of the Electrochemical Society*, vol. 158, no. 12, pp. C397–C402, 2011.

[26] C. W. Lai, S. Sreekantan, and Z. Lockman, "Photoelectrochemical behaviour of uniform growth TiO_2 nanotubes via bubble blowing synthesised in ethylene glycol with hydrogen peroxide," *Journal of Nanoscience and Nanotechnology*, vol. 12, no. 5, pp. 4057–4066, 2012.

[27] C. W. Lai and S. Sreekantan, "Photoelectrochemical performance of smooth TiO_2 nanotube arrays: effect of anodization temperature and cleaning methods," *International Journal of Photoenergy*, vol. 2012, Article ID 356943, 11 pages, 2012.

[28] S. K. Mohapatra, M. Misra, V. K. Mahajan, and K. S. Raja, "Design of a highly efficient photoelectrolytic cell for hydrogen generation by water splitting: application of $TiO_{2-x}C_x$ nanotubes as a photoanode and Pt/TiO_2 nanotubes as a cathode," *Journal of Physical Chemistry C*, vol. 111, no. 24, pp. 8677–8685, 2007.

[29] N. K. Allam, K. Shankar, and C. A. Grimes, "Photoelectrochemical and water photoelectrolysis properties of ordered TiO_2 nanotubes fabricated by Ti anodization in fluoride-free HCl electrolytes," *Journal of Materials Chemistry*, vol. 18, no. 20, pp. 2341–2348, 2008.

[30] C. W. Lai and S. Sreekantan, "Higher water splitting hydrogen generation rate for single crystalline anatase phase of TiO_2 nanotube arrays," *European Physical Journal*, vol. 59, no. 2, Article ID 20403, 8 pages, 2012.

[31] D. Regonini, A. Jaroenworaluck, R. Stevens, and C. R. Bowen, "Effect of heat treatment on the properties and structure of TiO_2 nanotubes: phase composition and chemical composition," *Surface and Interface Analysis*, vol. 42, no. 3, pp. 139–144, 2010.

[32] G. K. Mor, O. K. Varghese, M. Paulose, K. Shankar, and C. A. Grimes, "A review on highly ordered, vertically oriented TiO_2 nanotube arrays: fabrication, material properties, and solar energy applications," *Solar Energy Materials and Solar Cells*, vol. 90, no. 14, pp. 2011–2075, 2006.

[33] C. W. Lai and S. Sreekantan, "Heat treatment effects of WO_3-loaded TiO_2 nanotubes with enhanced water splitting hydrogen generation," *Materials Science in Semiconductor Processing*, vol. 16, pp. 947–954, 2013.

[34] B. Liu, L. Wen, and X. Zhao, "The photoluminescence spectroscopic study of anatase TiO_2 prepared by magnetron sputtering," *Materials Chemistry and Physics*, vol. 106, no. 2-3, pp. 350–353, 2007.

[35] D. Kim, J. Hong, Y. R. Park, and K. J. Kim, "The origin of oxygen vacancy induced ferromagnetism in undoped TiO_2," *Journal of Physics*, vol. 21, no. 19, Article ID 195405, 2009.

[36] Y. Zhao, Y. Li, C. W. Wang et al., "Carbon-doped anatase TiO_2 nanotube array/glass and its enhanced photocatalytic activity under solar light," *Solid State Sciences*, vol. 15, pp. 53–59, 2013.

[37] A. K. L. Sajjad, S. Shamaila, B. Tian, F. Chen, and J. Zhang, "One step activation of WO_x/TiO_2 nanocomposites with enhanced photocatalytic activity," *Applied Catalysis B*, vol. 91, no. 1-2, pp. 397–405, 2009.

[38] C. W. Lai and S. Sreekantan, "Effect of applied potential on the formation of self-organized TiO_2 nanotube arrays and its photoelectrochemical response," *Journal of Nanomaterials*, vol. 2011, Article ID 142463, 7 pages, 2011.

[39] S. Bauer, S. Kleber, and P. Schmuki, "TiO_2 nanotubes: tailoring the geometry in H_3PO_4/HF electrolytes," *Electrochemistry Communications*, vol. 8, no. 8, pp. 1321–1325, 2006.

[40] H.-C. Liang and X.-Z. Li, "Effects of structure of anodic TiO_2 nanotube arrays on photocatalytic activity for the degradation of 2,3-dichlorophenol in aqueous solution," *Journal of Hazardous Materials*, vol. 162, no. 2-3, pp. 1415–1422, 2009.

[41] Y. K. Lai, J. Y. Huang, H. F. Zhang et al., "Nitrogen-doped TiO_2 nanotube array films with enhanced photocatalytic activity under various light sources," *Journal of Hazardous Materials*, vol. 184, no. 1–3, pp. 855–863, 2010.

[42] J. M. Macak, H. Tsuchiya, A. Ghicov et al., "TiO_2 nanotubes: self-organized electrochemical formation, properties and applications," *Current Opinion in Solid State and Materials Science*, vol. 11, no. 1-2, pp. 3–18, 2007.

[43] S. Ahmed, M. G. Rasul, W. N. Martens, R. Brown, and M. A. Hashib, "Heterogeneous photocatalytic degradation of phenols in wastewater: a review on current status and developments," *Desalination*, vol. 261, no. 1-2, pp. 3–18, 2010.

[44] M. Ni, M. K. H. Leung, D. Y. C. Leung, and K. Sumathy, "A review and recent developments in photocatalytic water-splitting using TiO_2 for hydrogen production," *Renewable and Sustainable Energy Reviews*, vol. 11, no. 3, pp. 401–425, 2007.

[45] P. Roy, S. Berger, and P. Schmuki, "TiO_2 nanotubes: synthesis and applications," *Angewandte Chemie International Edition*, vol. 50, no. 13, pp. 2904–2939, 2011.

Hindawi Publishing Corporation
International Journal of Photoenergy
Volume 2013, Article ID 484831, 9 pages
http://dx.doi.org/10.1155/2013/484831

Research Article

Kinetics Study of Photocatalytic Activity of Flame-Made Unloaded and Fe-Loaded CeO_2 Nanoparticles

D. Channei,[1] B. Inceesungvorn,[1] N. Wetchakun,[2] and S. Phanichphant[3]

[1] *Department of Chemistry, Faculty of Science, Chiang Mai University, Chiang Mai 50200, Thailand*
[2] *Department of Physics and Materials Science, Faculty of Science, Chiang Mai University, Chiang Mai 50200, Thailand*
[3] *Materials Science Research Center, Faculty of Science, Chiang Mai University, Chiang Mai 50200, Thailand*

Correspondence should be addressed to S. Phanichphant; sphanichphant@yahoo.com

Received 8 June 2013; Accepted 4 October 2013

Academic Editor: Jiaguo Yu

Unloaded CeO_2 and nominal 0.50, 1.00, 1.50, 2.00, 5.00, and 10.00 mol% Fe-loaded CeO_2 nanoparticles were synthesized by flame spray pyrolysis (FSP). The samples were characterized to obtain structure-activity relation by X-ray diffraction (XRD), high-resolution transmission electron microscopy (HRTEM), Brunauer, Emmett, and Teller (BET) nitrogen adsorption, X-ray photoelectron spectroscopy (XPS), and UV-visible diffuse reflectance spectrophotometry (UV-vis DRS). XRD results indicated that phase structures of Fe-loaded CeO_2 nanoparticles were the mixture of CeO_2 and Fe_2O_3 phases at high iron loading concentrations. HRTEM images showed the significant change in morphology from cubic to almost-spherical shape observed at high iron loading concentration. Increased specific surface area with increasing iron content was also observed. The results from UV-visible reflectance spectra clearly showed the shift of absorption edge towards longer visible region upon loading CeO_2 with iron. Photocatalytic studies showed that Fe-loaded CeO_2 sample exhibited higher activity than unloaded CeO_2, with optimal 2.00 mol% of iron loading concentration being the most active catalyst. Results from XPS analysis suggested that iron in the Fe^{3+} state might be an active species responsible for enhanced photocatalytic activities observed in this study.

1. Introduction

Organic compounds from industries are one of the major causes of water pollution [1]. Various strategies have been employed to remove these toxic compounds [2, 3]. One of the most interesting approaches is heterogeneous photocatalysis because the process is based on the use of solar energy, which is clean and abundant in nature [4, 5]. In the recent years, cerium dioxide (CeO_2 or ceria) has received considerable attention because this material shows promising applications in solid oxide fuel cells [6], environmental catalysis [7, 8], redox catalysis [9], and wet catalytic oxidation of organic pollutants [10]. However, the band gap of CeO_2 (3.22 eV) has limited the activation of solar energy; only UV light can be applied to generate electron-hole pairs at the beginning of photocatalytic processes. Thus, it is necessary to extend the absorbance of CeO_2 into visible region and reduce the electron-hole pairs recombination [11, 12]. There are many methods to modify light absorption properties of CeO_2, such as metal doping [13, 14], surface sensitization [15], and coupling with semiconductor that has smaller band gap [16]. Recently, transition metal doping/loading has been widely used to enhance the light absorption of CeO_2 [17, 18]. It has been reported in many works of literature that the metal ions of Pt [19], Ag [20], Fe [21], Mn [22], Co [23], Ni [24], and Zn [25] in CeO_2 could improve CeO_2 photocatalytic activity towards the visible-light region. Among these metals, Fe has been considered as a candidate owing to its special Fenton reaction of iron. The Fenton process can improve the photocatalytic activity by producing the hydroxyl radicals ($OH^{\bullet}$) which are very powerful oxidizer in photocatalytic process [26]. There are many methods to prepare unloaded CeO_2 and Fe-doped/-loaded CeO_2 nanoparticles such as sol-gel [27], sonochemical [28], homogeneous precipitation [29], hydrothermal [30], microemulsions [31], surfactant-assisted precipitation [32], and flame spray pyrolysis (FSP) methods [33].

Among them, the latter one is a promising approach because FSP can produce the nanoparticle products with particle size in the range of 1–200 nm at high production rates up to 250 g/h in one step [34]. Other advantages are the ability to dissolve the precursor directly in the fuel and the simplicity of introduction of the precursor into the hot flame zone. In addition, the process of loading/doping metal oxide with metals can easily be done by adding dopant in the precursor solution [35, 36]. In the present work, unloaded CeO_2 and Fe-loaded CeO_2 nanoparticles were directly synthesized by FSP method. The formic acid and oxalic acid were chosen as model organic pollutants for photocatalytic study under visible-light irradiation.

2. Experimental

2.1. Preparation of Powders. The precursor solutions for FSP consisted of cerium nitrate hexahydrate (Sigma-Aldrich, 99.99 wt%) and iron acetyl acetonate (Sigma-Aldrich, 97 wt%). The cerium precursor was dissolved in absolute ethanol (Scharlau, 98%) to obtain a 0.50 M concentration. Amounts of Fe loading concentration were varied as 0.50, 1.00, 1.50, 2.00, 5.00, and 10.00 mol% in order to prepare Fe-loaded CeO_2 samples. The precursor mixtures were fed into the center of flame by syringe pump with a rate of 5 mL/min and dispersed by 5 L/min oxygen according to the previous report [37]. Then, the liquid precursor was dispersed quickly in an upward direction by gas stream and ignited by premixed oxygen/methane flame. The gas flow rates of oxygen and methane-supporting flame were set as constant rates of 1.19 and 2.46 L/min, respectively. After evaporation and combustion of liquid precursor droplet, nanoparticle products were collected on a glass microfiber filter papers (Whatmann GF/A, 25.7 cm in diameter) with a vacuum pump controller.

2.2. Characterization of Nanoparticles. The phase and crystallinity of the synthesized samples were analyzed by X-ray powder diffraction (XRD; Philips X'Pert MPD; CuKα radiation). The most intense peak corresponding to (111) plane was chosen to calculate the crystallite sizes (D) using Scherrer equation as follow:

$$D = \frac{k\lambda}{\beta \cos\theta}, \quad (1)$$

where k is a constant equal to 0.89, λ is the X-ray wavelength equal to 0.154 nm, β is the full width at half-maximum (FWHM), and θ is the half-diffraction angle [38]. The chemical composition and oxidation state of material were studied by X-ray photoelectron spectroscopy (XPS) using Mg X-ray source (MgKα, Kratos Axis Ultra DLD). The binding energy of the adventitious carbon (C 1s) line at 285 eV was used for calibration, and the position of other peaks was corrected according to the position of the C 1s signal. High-resolution transmission electron microscopy (HRTEM, JEOL JEM-2010) was employed to determine the morphology of prepared samples. The mean particle size and specific surface area (SSA) were investigated using the Brunauer, Emmett, and Teller (BET) nitrogen adsorption method (QuantachromeAutosorp 1 MP). The reflectance spectra of the nanoparticle powders were obtained by using UV-visible diffuse reflectance spectrophotometry (UV-vis DRS) equipped with integrating sphere detector (Shimadzu, UV-3101PC).

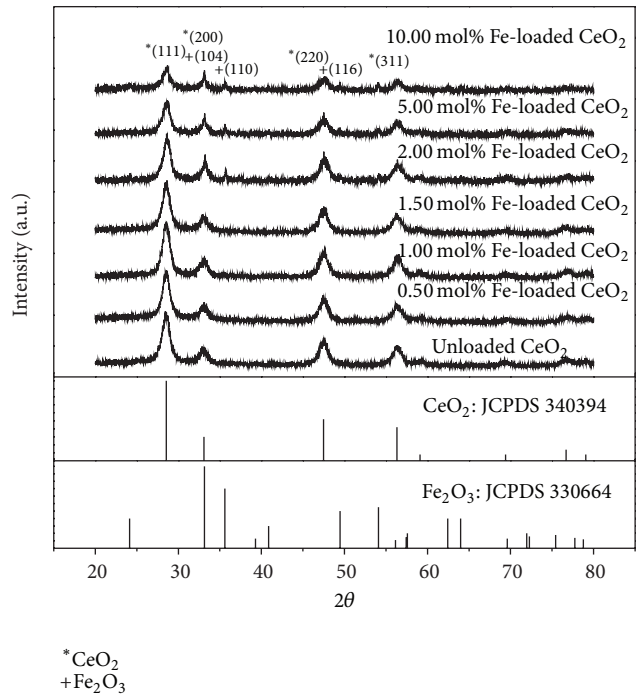

Figure 1: X-ray diffraction patterns of CeO_2 with different iron content.

2.3. Photocatalytic Activity. 1.00 g /L of photocatalyst suspensions was prepared in deionized water and circulated in closed system spiral photoreactor. In a typical run, carbon burn-off step was firstly carried out by illuminating the photocatalyst suspension with a UV-A lamp (Sylvania Blacklight Blue, 18 W) in order to remove any organic impurities from the photocatalyst. The photocatalytic activities were evaluated through formic acid (Sigma-Aldrich, 98 wt%) and oxalic acid (Sigma-Aldrich, 99.99 wt%) degradations under the visible irradiation for 120 min. Finally, the generated carbon dioxide (CO_2) was measured using the conductivity meter (Eutech Instruments Cyberscan PC5500, μS/cm^2 precision). At the end of each photocatalytic experiment, the recorded data presented the increase in conductivity value. In order to calculate amounts of generated CO_2, the values were converted from conductivity at that time to the amount of carbon by the interpolated from calibration curve.

3. Results and Discussion

3.1. X-Ray Powder Diffraction (XRD). In Figure 1, the X-ray diffraction pattern has been used in order to study the structure and phase composition of the prepared samples. It can be seen that all samples had similar diffraction patterns of cubic fluorite structure of ceria (JCPDS 340394) [39]. However,

Table 1: The calculated d-spacing, lattice parameters, unit cell volume, and crystalline size.

Iron loading concentration (mol%)	111 plane				
	2θ (degree)	d-spacing (nm)	Lattice parameter (nm)	Unit cell volume (nm^3)	Crystalline size (nm)
0.00	28.4601	0.3132	0.5426	0.1597	8.3586
0.50	28.5479	0.3123	0.5409	0.1583	7.8555
1.00	28.5699	0.3121	0.5405	0.1579	7.4111
1.50	28.5772	0.3120	0.5404	0.1578	7.4081
2.00	28.6284	0.3114	0.5394	0.1570	6.9682
5.00	28.6490	0.3112	0.5390	0.1566	6.2226
10.00	28.7098	0.3106	0.5380	0.1557	5.7476

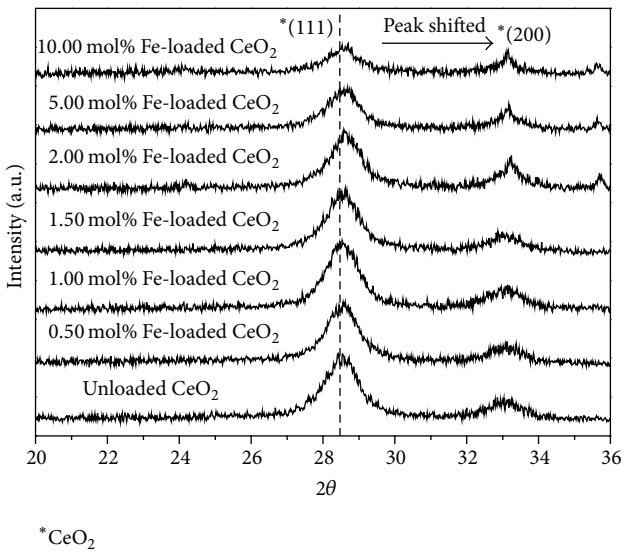

Figure 2: The shift of 2θ of samples.

the sample with high amount of iron loading (2.00, 5.00, and 10.00 mol%) exhibited the mixed phase of CeO_2 and Fe_2O_3 (JCPDS 330664) [40]. The XRD peaks of all samples were magnified as shown in Figure 2. It was found that CeO_2 peaks shifted towards higher 2θ upon increasing iron content. The calculated d-spacing, lattice parameter, unit cell volume, and average crystallite size were also decreased as shown in Table 1. These observations could be ascribed to partial substitution of Ce^{4+} ions (0.101 nm) by Fe^{3+} ions (0.064 nm) [41]. A decrease of unit cell parameters due to the substitution of larger ion by the smaller one was also found in previous reports [42, 43].

3.2. High-Resolution Transmission Electron Microscopy (HRTEM). As seen from Figure 3(a), the unloaded CeO_2 clearly showed the cubic morphology of cubic fluorite CeO_2 structure. In Figure 3(b), the particles became more spherical upon loading CeO_2 with iron. This change in CeO_2 morphology might be due to the incorporation of iron ions in CeO_2 lattice, thus affecting the particle growth and causing lattice deformation [44]. This assumption was supported by the shift of XRD peak and the changes of lattice parameters as reported in Table 1. The average particle sizes as seen from HRTEM image were about 6–8 nm. This was in good agreement with the calculated sizes obtained by using the Scherrer equation. Figure 3(c) shows the lattice fringes of 2.00 mol% Fe-loaded CeO_2. The lattice planes with d-spacing of 0.16 and 0.20 nm were attributed to the (311) and (220) planes of cubic fluorite CeO_2, respectively, whereas the plane with d-spacing of 0.24 was assigned to the (110) plane of Fe_2O_3. These results confirmed the presence of mixed phase between CeO_2 and Fe_2O_3 in the nominal 2.00 mol% Fe-loaded CeO_2 as found previously in the XRD patterns (Figure 1).

Table 2: Summary of analytical data.

Iron loading concentration (mol%)	SSA (m^2/g)	E_g (eV)	BET diameter (nm)
0	130.00	3.21	6.39
0.50	134.00	2.95	6.20
1.00	137.97	2.70	6.02
1.50	137.99	2.65	6.02
2.00	139.00	2.55	5.98
5.00	140.82	2.45	5.57
10.00	148.76	2.35	5.27

3.3. Nitrogen Adsorption-Desorption Isotherms. The specific surface areas (SSA) of different samples were analyzed by Brunauer-Emmett-Teller (BET) method based on the nitrogen adsorption/desorption isotherm. The mean BET diameter (D) was also calculated by using the following equation [45]:

$$D = \frac{6000}{(S_{\mathrm{BET}} \times \rho)}, \tag{2}$$

where S_{BET} is the BET-specific surface area and ρ is the density of the CeO_2 (7.32 g/mL). As shown in Table 2, an increase of surface area accompanied with a decrease of BET diameter was clearly observed upon increasing iron content. This increased surface area would be beneficial to the efficient photocatalytic performance due to high surface adsorption of organic pollutants. The calculated BET diameter was in

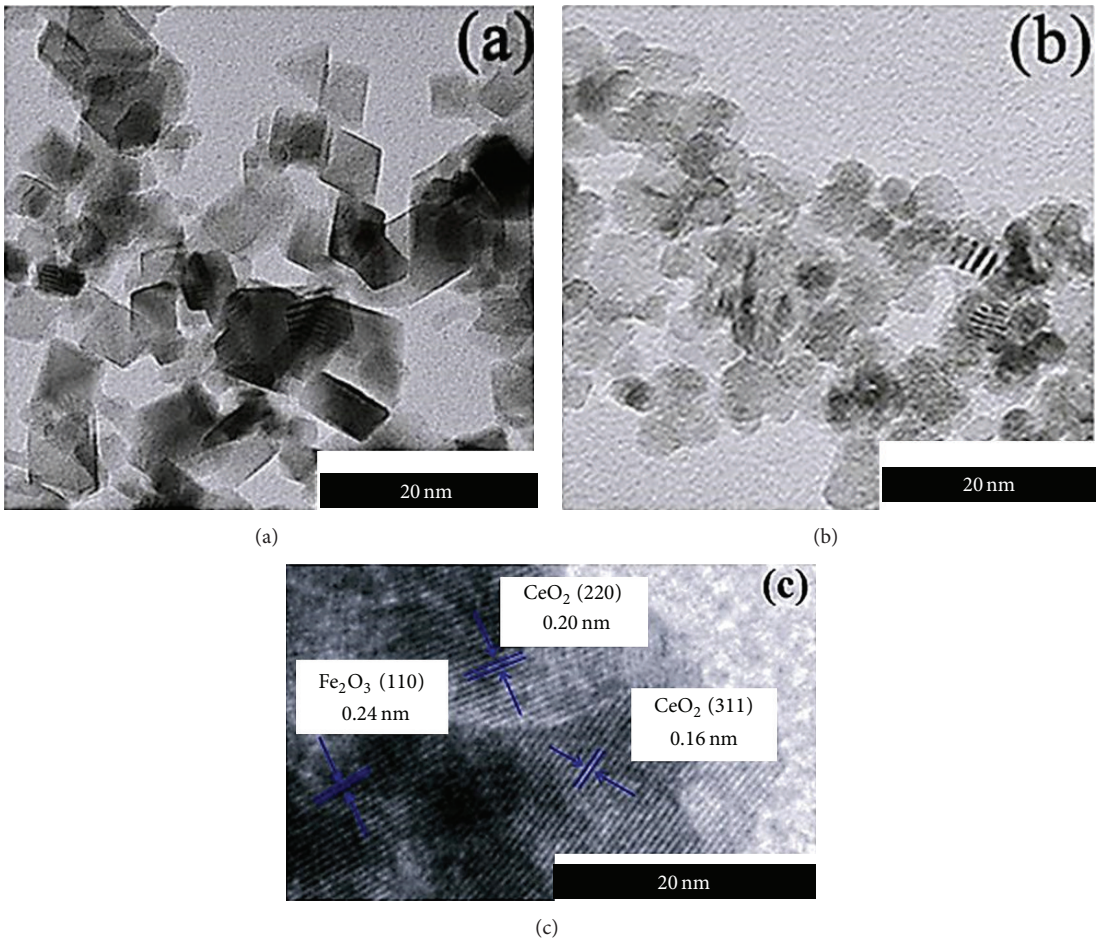

Figure 3: HRTEM images of (a) unloaded CeO_2, (b) 2.00 mol% Fe-loaded CeO_2, and (c) lattice fringe of 2.00 mol% Fe-loaded CeO_2.

the range of 5–7 nm which was very well in agreement with those obtained by using the Scherrer equation (Table 1).

3.4. UV-Visible Spectroscopy. UV-vis reflectance analysis was performed by converting the obtained reflectance spectra (Figure 4(a)) to the Kubelka-Munk absorbance spectra using the Kubelka-Munk equation as follows [46]:

$$F(R_\infty) = \frac{(1 - R_\infty)^2}{2R_\infty}, \quad (3)$$

where $F(R_\infty)$ and R_∞ are the Schuster-Kubelka-Munk absorbance and the absolute reflectance of the sample, respectively. The plot of absorbance against wavelength for the CeO_2 nanoparticle powders is shown in Figure 4(b).

The spectra showed that the absorption edge shifted to longer wavelength upon increasing the iron loading concentration. Band gap energies of the obtained samples can then be determined by using the intercept of the tangent to the graph plotting between the Kubelka-Munk absorption function and photon energy ($h\nu$) as shown in Figure 4(c) [47, 48]. The obtained band gap energies (E_g) as reported in Table 2 decreased with increasing iron loading concentration.

3.5. Photocatalytic Activity. The photocatalytic activity of unloaded and Fe-loaded CeO_2 was evaluated by degradation of formic and oxalic acids. The effects of different iron loading concentrations on the photocatalytic efficiency of CeO_2 nanoparticles were evaluated under visible-light irradiation for 120 min, and the results are presented in Figure 5. According to the results, the photocatalytic activities of Fe-loaded CeO_2 nanoparticles were significantly higher than those of unloaded CeO_2 nanoparticles. This improved photoactivity could be partially ascribed to the enhanced light absorption in visible-light region as observed from the UV-vis study in Figure 4. However, the activity was clearly dependent on the amount of iron loading. The results demonstrated that the nominal 2.00 mol% was an optimal iron concentration for photocatalytic activity of CeO_2 nanoparticles in this research. On the other hand, 5.00% and 10.00 mol% iron concentrations showed poor photocatalytic activity, probably because high iron concentration tended to cover CeO_2 surface, thus preventing light from contacting the CeO_2 surface [49].

Another possible reason was that too high iron loading can act as the electron-hole recombination centers instead of the trapping level, resulting in a decreased photocatalytic activity [47, 50]. The kinetic data for formic and oxalic acids degradations under visible-light illumination were found to

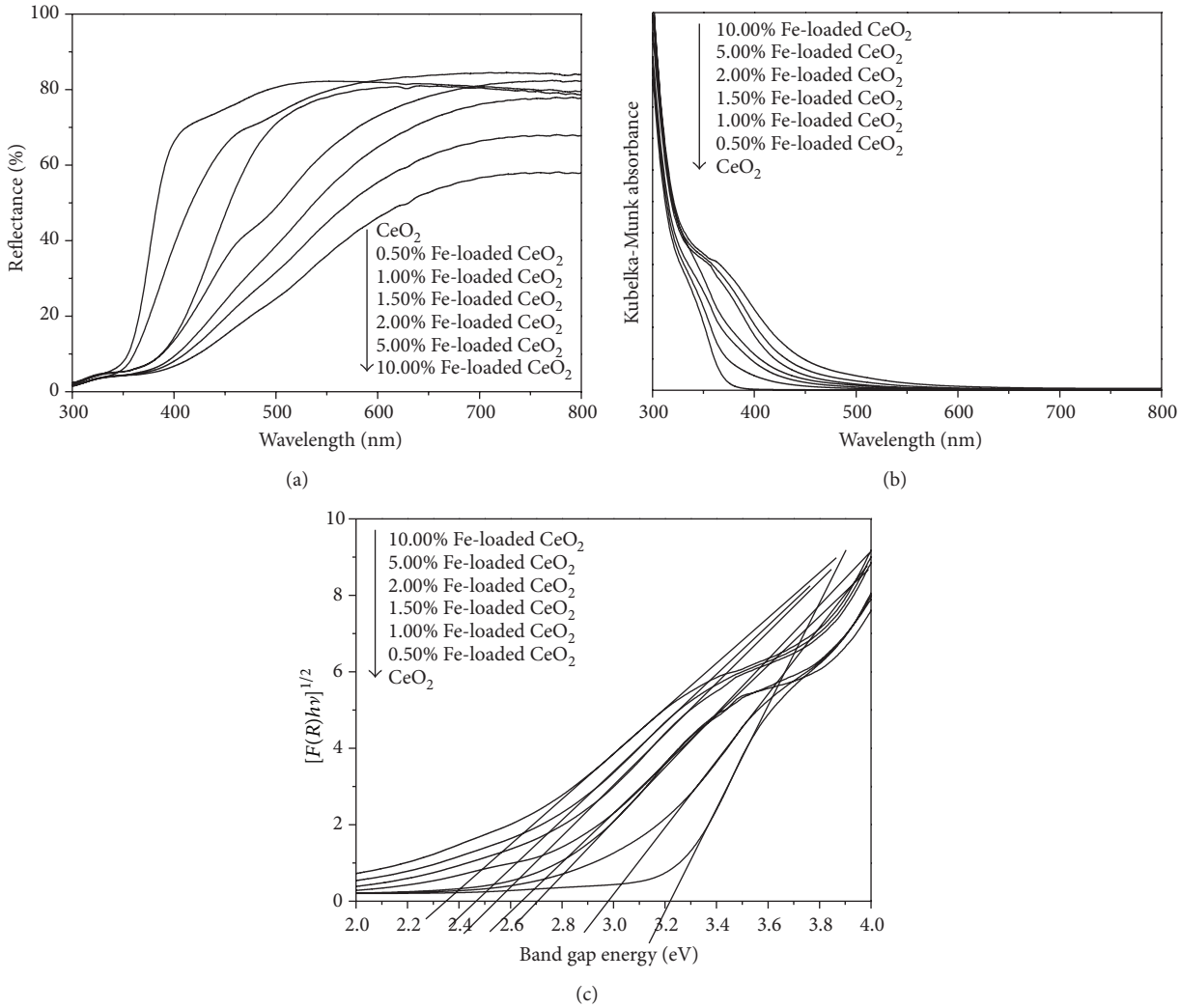

Figure 4: UV-vis (a) reflection spectra, (b) Kubelka-Munk absorbance, and (c) relation between band gap energy and $[F(R)h\nu]^{1/2}$ of CeO_2 with different iron content.

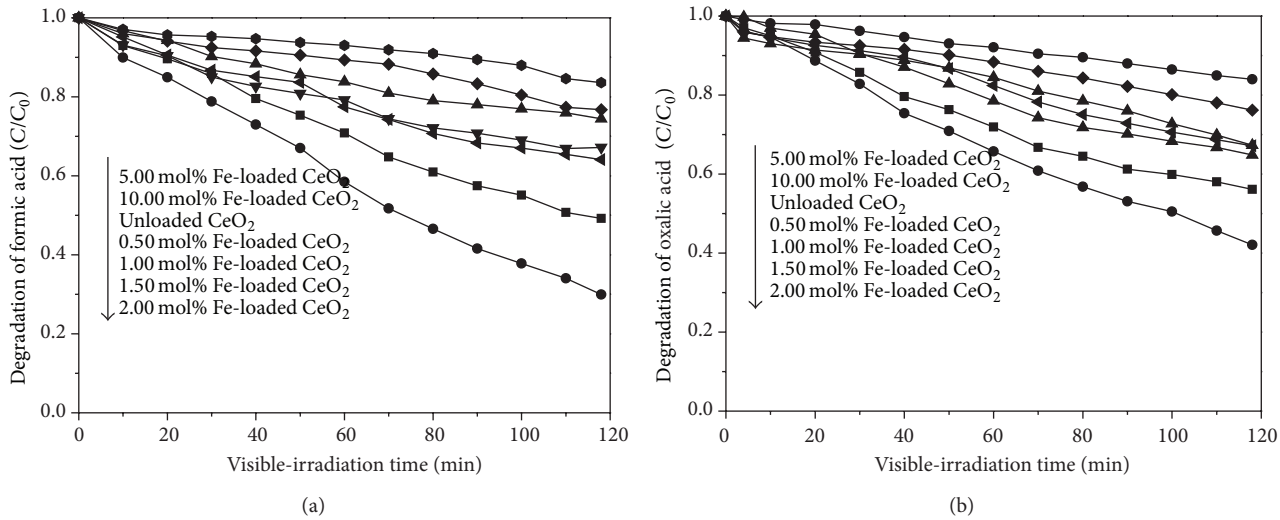

Figure 5: Photocatalytic degradation of (a) formic acid and (b) oxalic acid by CeO_2 with different iron content as a function of visible-light irradiation time.

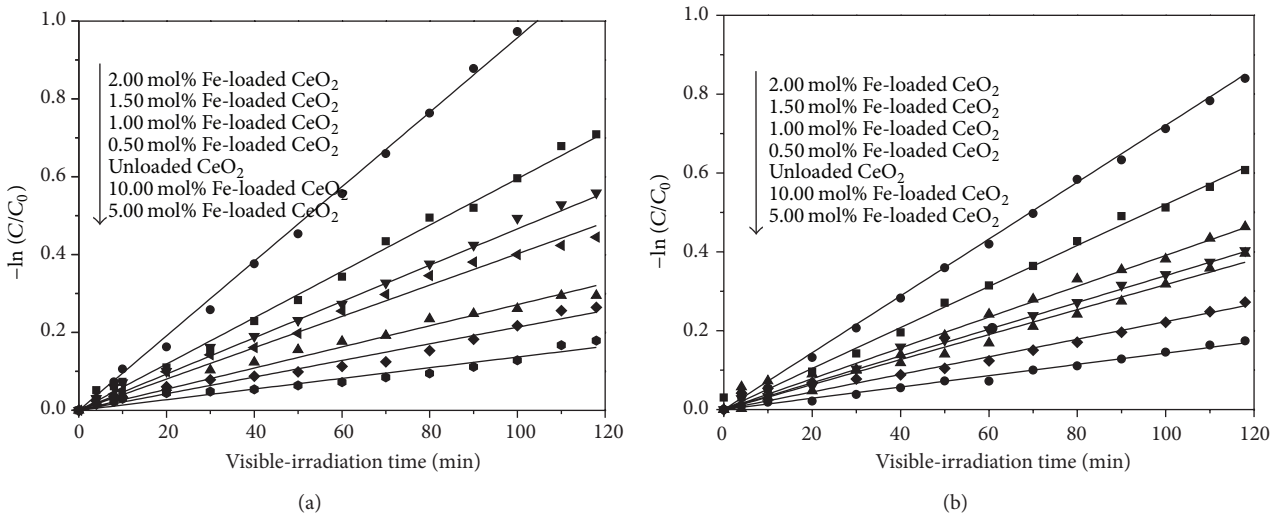

Figure 6: Kinetics plots for linear fitting of data obtained from pseudo first-order reaction for (a) formic acid and (b) oxalic acid degradation under visible-light irradiation.

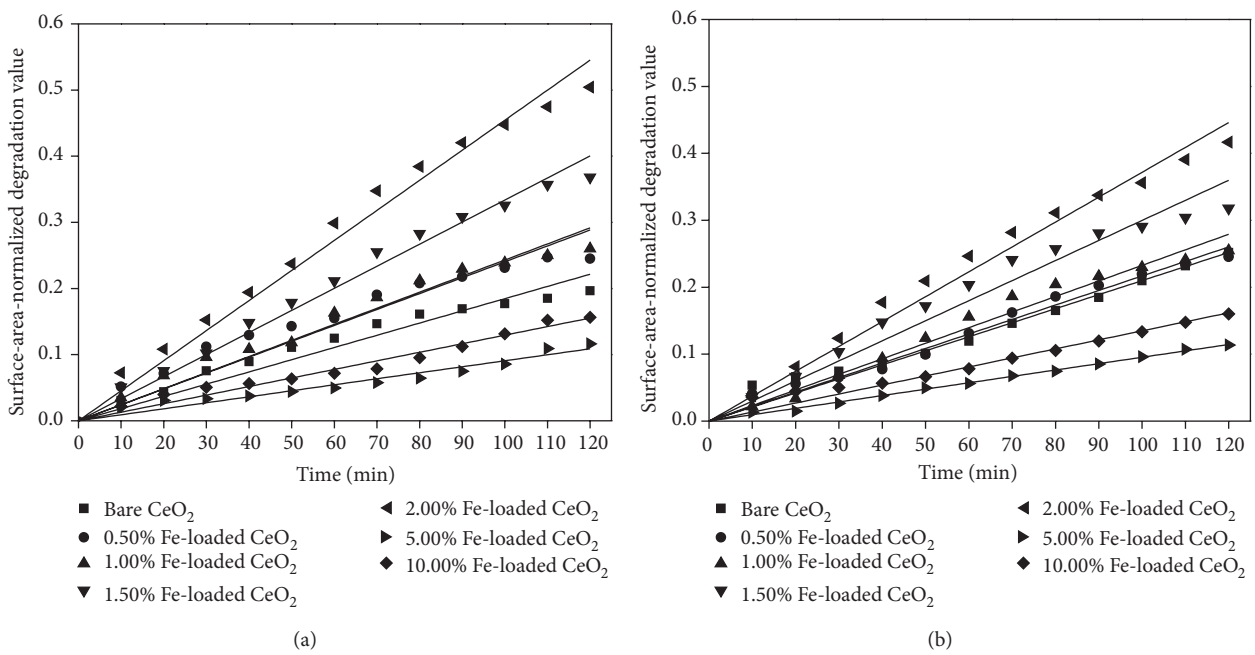

Figure 7: Kinetics plots of the surface-area-normalized degradation values against visible-light irradiation time for (a) formic acid and (b) oxalic acid.

follow pseudo first-order reaction [51] as shown in Figure 6. The pseudo first-order model is explained by

$$-\ln\left(\frac{C}{C_0}\right) = kt, \tag{4}$$

where k is the apparent rate constant (min^{-1}), C_0 means the initial concentration of acid, and C refers to the concentration of acid at various reaction times (t). The determined pseudo first-order rate constants (k, min^{-1}) are presented in Table 3. It can be seen that the loading of 2.00 mol% iron in CeO_2 nanoparticles could remarkably improve the apparent rate constant up to 5 times for formic acid and 3 times for oxalic acid compared with the unloaded one.

In order to investigate the effect of surface area on the degradation activity, the surface-area-normalized degradation values against visible-light irradiation time were plotted as shown in Figure 7, and the calculated surface-area-normalized rate constants are presented in Table 3. The results clearly suggested that surface-area of the catalyst has a crucial impact on the activity of acid degradation in this study because the surface area-normalized rate constants are significantly decreased from the original values. However, other factors such as band gap energy, amount of Fe loading,

Table 3: Apparent rate constants and surface-area-normalized rate constants.

Samples	Rate constant (k, min^{-1})		Surface-area-normalized rate constants (min^{-1} m^{-2} g)	
	Formic acid	Oxalic acid	Formic acid	Oxalic acid
5.00 mol% Fe-loaded CeO_2	0.0014	0.0014	0.0009	0.0010
10.00 mol% Fe-loaded CeO_2	0.0017	0.0020	0.0013	0.0014
Unloaded CeO_2	0.0021	0.0022	0.0019	0.0021
0.50 mol% Fe-loaded CeO_2	0.0040	0.0034	0.0024	0.0022
1.00 mol% Fe-loaded CeO_2	0.0054	0.0039	0.0024	0.0023
1.50 mol% Fe-loaded CeO_2	0.0060	0.0052	0.0033	0.0030
2.00 mol% Fe-loaded CeO_2	0.0096	0.0072	0.0045	0.0037

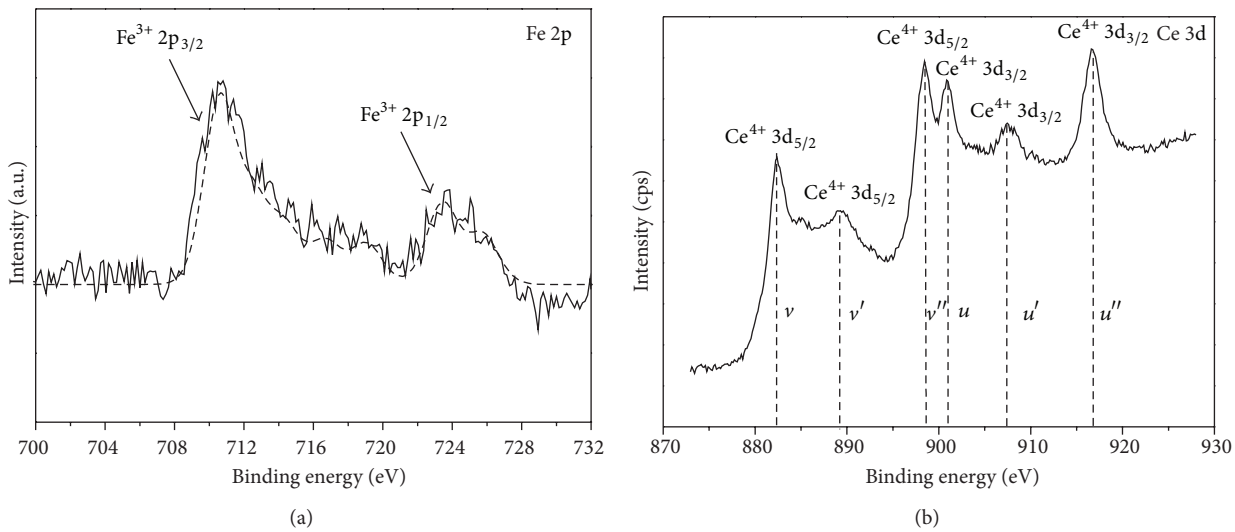

Figure 8: The XPS spectra of Fe-loaded CeO_2 nanoparticles: (a) Fe 2p and (b) Ce 3d.

sample crystallinity, and phase composition [52] could not be neglected as these could also contribute to the difference in photocatalytic activity of the catalysts being studied.

3.6. X-Ray Photoelectron Spectroscopy (XPS). In order to characterize the valence state of cerium and iron in 2.00 mol% Fe-loaded CeO_2, X-ray photoelectron spectroscopy (XPS) was carried out as shown in Figure 8.

According to Figure 8(a), the peaks at 710.6 and 723.4 eV assignable to the core level of $2p_{3/2}$ and $2p_{1/2}$, respectively, corresponded to Fe^{3+} species in Fe_2O_3 [53, 54]. No other peaks due to Fe^0 and Fe^{2+} were found in the XPS results. From the Ce 3d XPS spectrum, the binding energies of all peaks are shown in Figure 8(b). These peaks corresponded to the three pairs of spin-orbit doublets assignable to Ce^{4+} valence state which were very well in agreement with the previous reports [55, 56].

4. Conclusions

Fe-loaded CeO_2 nanoparticles with different iron loading concentrations have successfully been synthesized by flame spray pyrolysis (FSP). Loading CeO_2 with Fe^{3+} resulted in a decrease of d-spacing, lattice parameter, unit cell volume, and crystallite size but an increase of BET surface area. The UV-vis absorption spectra displayed a red shift in the band edge transition upon increasing of iron loading concentration. XPS analysis showed the presence of Fe^{3+} species on the surface of CeO_2. This could be attributed to the presence of Fe_2O_3 as observed from the XRD and HRTEM analyses. Increased photocatalytic activity compared with unloaded CeO_2 was clearly obtained from the Fe-loading sample. It was found from this study that the nominal 2.00 mol% was an optimum iron loading concentration, giving the highest photocatalytic activity. Band gap energy and surface of the catalyst were found to be important factors affecting the photocatalytic activity observed in this study. However, other factors such as amount of Fe loading, sample crystallinity, and phase composition could not be neglected.

Acknowledgments

This work has been supported by Thailand Research Fund (TRF) through the Royal Golden Jubilee (RGJ) Ph.D. Program. The National Research University Project under Thailand's Office of Higher Education Commission; the Materials Science Research Center, Department of Chemistry, Faculty of Science; and the Graduate School, Chiang Mai University, are greatly acknowledged.

References

[1] J. Nowotny, C. C. Sorrell, L. R. Sheppard, and T. Bak, "Solar-hydrogen: environmentally safe fuel for the future," *International Journal of Hydrogen Energy*, vol. 30, no. 5, pp. 521–544, 2005.

[2] T. L. Thompson and J. T. Yates Jr., "Surface science studies of the photoactivation of TiO_2-new photochemical processes," *Chemical Reviews*, vol. 106, no. 10, pp. 4428–4453, 2006.

[3] J. Zhao, C. Chen, and W. Ma, "Photocatalytic degradation of organic pollutants under visible light irradiation," *Topics in Catalysis*, vol. 35, no. 3-4, pp. 269–278, 2005.

[4] I. N. Martyanov, S. Uma, S. Rodrigues, and K. J. Klabunde, "Structural defects cause TiO_2-based photocatalysts to be active in visible light," *Chemical Communications*, vol. 10, no. 21, pp. 2476–2477, 2004.

[5] I. N. Martyanov, T. Berger, O. Diwald, S. Rodrigues, and K. J. Klabunde, "Enhancement of TiO_2 visible light photoactivity through accumulation of defects during reduction-oxidation treatment," *Journal of Photochemistry and Photobiology A*, vol. 212, no. 2-3, pp. 135–141, 2010.

[6] W. Liu and M. Flytzani-Stephanopoulos, "Transition metal-promoted oxidation catalysis by fluorite oxides: a study of CO oxidation over Cu-CeO_2," *Chemical Engineering Journal and the Biochemical Engineering Journal*, vol. 64, no. 2, pp. 283–294, 1996.

[7] G. R. Rao, J. Kašpar, S. Meriani, R. di Monte, and M. Graziani, "NO decomposition over partially reduced metallized CeO_2-ZrO_2 solid solutions," *Catalysis Letters*, vol. 24, no. 1-2, pp. 107–112, 1994.

[8] J. Kašpar, P. Fornasiero, and N. Hickey, "Automotive catalytic converters: current status and some perspectives," *Catalysis Today*, vol. 77, no. 4, pp. 419–449, 2003.

[9] Y. Li, Q. Fu, and M. Flytzani-Stephanopoulos, "Low-temperature water-gas shift reaction over Cu- and Ni-loaded cerium oxide catalysts," *Applied Catalysis B*, vol. 27, no. 3, pp. 179–191, 2000.

[10] G. Neri, A. Pistone, C. Milone, and S. Galvagno, "Wet air oxidation of p-coumaric acid over promoted ceria catalysts," *Applied Catalysis B*, vol. 38, no. 4, pp. 321–329, 2002.

[11] C. Ho, J. C. Yu, T. Kwong, A. C. Mak, and S. Lai, "Morphology-controllable synthesis of mesoporous CeO_2 nano- and micro-structures," *Chemistry of Materials*, vol. 17, no. 17, pp. 4514–4522, 2005.

[12] M. I. Litter, "Heterogeneous photocatalysis: transition metal ions in photocatalytic systems," *Applied Catalysis B*, vol. 23, no. 2-3, pp. 89–114, 1999.

[13] S. Tuprakay and W. Liengcharernsit, "Lifetime and regeneration of immobilized titania for photocatalytic removal of aqueous hexavalent chromium," *Journal of Hazardous Materials*, vol. 124, no. 1–3, pp. 53–58, 2005.

[14] W. Choi, A. Termin, and M. R. Hoffmann, "The role of metal ion dopants in quantum-sized TiO_2: correlation between photoreactivity and charge carrier recombination dynamics," *Journal of Physical Chemistry*, vol. 98, no. 51, pp. 13669–13679, 1994.

[15] S. Kaur and V. Singh, "Visible light induced sonophotocatalytic degradation of reactive red dye 198 using dye sensitized TiO_2," *Ultrasonics Sonochemistry*, vol. 14, no. 5, pp. 531–537, 2007.

[16] M. Grätzel, "Photoelectrochemical cells," *Nature*, vol. 414, no. 6861, pp. 338–344, 2001.

[17] H. J. Avila-Paredes, P. Jain, S. Sen, and S. Kim, "Oxygen transport in Sc-doped CeO_2: cation (45Sc) NMR as a probe of anionic conductivity," *Chemistry of Materials*, vol. 22, no. 3, pp. 893–897, 2010.

[18] Z. Hong, H. Yoshida, and T. Sakuma, "High temperature creep strength of Si_3N_4-$Y_2Si_2O_7$ ceramics by stress relaxation based on a new interpretation model," *Key Engineering Materials*, vol. 336-338, pp. 1420–1423, 2007.

[19] P. Panagiotopoulou, J. Papavasiliou, G. Avgouropoulos, T. Ioannides, and D. I. Kondarides, "Water-gas shift activity of doped Pt/CeO_2 catalysts," *Chemical Engineering Journal*, vol. 134, no. 1–3, pp. 16–22, 2007.

[20] C. Kitiwiang and S. Phanichphant, "Synthesis of silver-doped cerium dioxide nanoparticles by the homogeneous precipitation," *Journal of Microscopy Society of Thailand*, vol. 23, no. 1, pp. 83–86, 2009.

[21] S. Maensiri, S. Phokha, P. Laokul, and S. Seraphin, "Room temperature ferromagnetism in Fe-doped CeO_2 nanoparticles," *Journal of Nanoscience and Nanotechnology*, vol. 9, no. 11, pp. 6415–6420, 2009.

[22] C. Xia, C. Hu, P. Chen, B. Wan, X. He, and Y. Tian, "Magnetic properties and photoabsorption of the Mn-doped CeO_2 nanorods," *Materials Research Bulletin*, vol. 45, no. 7, pp. 794–798, 2010.

[23] J. Sacanell, M. A. Paulin, V. Ferrari, G. Garbarino, and A. G. Leyva, "Surface photoluminescence and magnetism in hydrothermally grown undoped ZnO nanorod arrays," *Applied Physics Letters*, vol. 100, no. 11, pp. 172401–172405, 2012.

[24] S. Kumar, Y. J. Kim, B. H. Koo, and C. G. Lee, "Structural and magnetic properties of Ni doped CeO_2 nanoparticles," *Journal of Nanoscience and Nanotechnology*, vol. 10, no. 11, pp. 7204–7207, 2010.

[25] T. S. Santos, W. S. D. Folly, and M. A. Macêdo, "Ferromagnetism in diluted magnetic Zn-Co-doped $CeO_{2-\delta}$," *Physica B: Condensed Matter*, vol. 407, no. 16, pp. 3233–3235, 2012.

[26] J. Araña, O. González Díaz, M. Miranda Saracho, J. M. Doa Rodríguez, J. A. Herrera Melián, and J. Pérez Pea, "Photocatalytic degradation of formic acid using Fe/TiO_2 catalysts: the role of Fe^{3+}/Fe^{2+} ions in the degradation mechanism," *Applied Catalysis B*, vol. 32, no. 1-2, pp. 49–61, 2001.

[27] Q.-Z. Yan, X.-T. Su, Z.-Y. Huang, and C.-C. Ge, "Sol-gel auto-igniting synthesis and structural property of cerium-doped titanium dioxide nanosized powders," *Journal of the European Ceramic Society*, vol. 26, no. 6, pp. 915–921, 2006.

[28] L. Yin, Y. Wang, G. Pang, Y. Koltypin, and A. Gedanken, "Sonochemical synthesis of cerium oxide nanoparticles—effect of additives and quantum size effect," *Journal of Colloid and Interface Science*, vol. 246, no. 1, pp. 78–84, 2002.

[29] L. Truffault, Q. W. Yao, D. Wexler et al., "Synthesis and characterization of Fe doped CeO_2 nanoparticles for pigmented ultraviolet filter applications," *Journal of Nanoscience and Nanotechnology*, vol. 11, no. 5, pp. 4019–4028, 2011.

[30] M. Hirano and M. Inagaki, "Preparation of monodispersed cerium(IV) oxide particles by thermal hydrolysis: influence of the presence of urea and Gd doping on their morphology and growth," *Journal of Materials Chemistry*, vol. 10, no. 2, pp. 473–477, 2000.

[31] A. Bumajdad, M. I. Zaki, J. Eastoe, and L. Pasupulety, "Microemulsion-based synthesis of CeO_2 powders with high surface area and high-temperature stabilities," *Langmuir*, vol. 20, no. 25, pp. 11223–11233, 2004.

[32] D. Terribile, A. Trovarelli, J. Llorca, C. De Leitenburg, and G. Dolcetti, "The synthesis and characterization of mesoporous

high-surface area ceria prepared using a hybrid organic/inorganic route," *Journal of Catalysis*, vol. 178, no. 1, pp. 299–308, 1998.

[33] L. Mädler, W. J. Stark, and S. E. Pratsinis, "Flame-made ceria nanoparticles," *Journal of Materials Research*, vol. 17, no. 6, pp. 1356–1362, 2002.

[34] R. Mueller, L. Mädler, and S. E. Pratsinis, "Nanoparticle synthesis at high production rates by flame spray pyrolysis," *Chemical Engineering Science*, vol. 58, no. 10, pp. 1969–1976, 2003.

[35] L. Mädler, T. Sahm, A. Gurlo et al., "Sensing low concentrations of CO using flame-spray-made Pt/SnO_2 nanoparticles," *Journal of Nanoparticle Research*, vol. 8, no. 6, pp. 783–796, 2006.

[36] T. Samerjai, N. Tamaekonga, K. Wetchakun et al., "Flame-spray-made metal-loaded semiconducting metal oxides thick films for flammable gas sensing," *Sensors and Actuators B*, vol. 171-172, pp. 43–61, 2012.

[37] C. Liewhiran and S. Phanichphant, "Effects of palladium loading on the response of a thick film flame-made ZnO gas sensor for detection of ethanol vapor," *Sensors*, vol. 7, no. 7, pp. 1159–1184, 2007.

[38] B. Li, X. Wang, M. Yan, and L. Li, "Preparation and characterization of nano-TiO_2 powder," *Materials Chemistry and Physics*, vol. 78, no. 1, pp. 184–188, 2003.

[39] A. Gupta, M. S. Hegde, K. R. Priolkar, U. V. Waghmare, P. R. Sarode, and S. Emura, "Structural investigation of activated lattice oxygen in $Ce_{1-x}Sn_xO_2$ and $Ce_{1-x-y}Sn_xPdyO_{2-\delta}$ by EXAFS and DFT calculation," *Chemistry of Materials*, vol. 21, no. 24, pp. 5836–5847, 2009.

[40] T. Nishimura, H. Katayama, K. Noda, and T. Kodama, "Electrochemical behavior of rust formed on carbon steel in a wet/dry environment containing chloride ions," *Corrosion*, vol. 56, no. 9, pp. 935–941, 2000.

[41] R. D. Shannon, "Revised effective ionic radii and systematic studies of interatomie distances in halides and chaleogenides," *Acta Crystallographica Section A*, vol. 32, no. 5, pp. 751–767, 1976.

[42] G. L. Beausoleil, A. Thurber, S. S. Rao, G. Alanko, C. B. Hanna, and A. Punnoose, "Concentration dependence of magnetic moment in $Ce_{1-x}Fe_xO_2$," *Journal of Applied Physics*, vol. 111, no. 7, pp. 1–9, 2012.

[43] N. Wu, L. Chen, Y. Jiao, G. Chen, and J. Li, "Preparation and characterization of Fe^{3+}, La^{3+} Co-doped TiO_2 nanofibers and its photocatalytic activity," *Journal of Engineered Fibers and Fabrics*, vol. 7, no. 3, pp. 16–20, 2012.

[44] L. Wen, B. Liu, X. Zhao, K. Nakata, T. Murakami, and A. Fujishima, "Synthesis, characterization, and photocatalysis of Fe-doped TiO_2: a combined experimental and theoretical study," *International Journal of Photoenergy*, vol. 2012, Article ID 368750, 10 pages, 2012.

[45] S. Agarwala, M. Kevin, A. S. W. Wong, C. K. N. Peh, V. Thavasi, and G. W. Ho, "Mesophase ordering of TiO_2 film with high surface area and strong light harvesting for dye-sensitized solar cell," *ACS Applied Materials and Interfaces*, vol. 2, no. 7, pp. 1844–1850, 2010.

[46] J. Sirita, S. Phanichphant, and F. C. Meunier, "Quantitative analysis of adsorbate concentrations by diffuse reflectance FT-IR," *Analytical Chemistry*, vol. 79, no. 10, pp. 3912–3918, 2007.

[47] G. Wang, L. Xu, J. Zhang, T. Yin, and D. Han, "Enhanced photocatalytic activity of TiO_2 powders (P25) via calcination treatment," *International Journal of Photoenergy*, vol. 2012, Article ID 265760, 9 pages, 2012.

[48] P. R. Mishra and O. N. Srivastava, "On the synthesis, characterization and photocatalytic applications of nanostructured TiO_2," *Bulletin of Materials Science*, vol. 31, no. 3, pp. 545–550, 2008.

[49] M. K. Seery, R. George, P. Floris, and S. C. Pillai, "Silver doped titanium dioxide nanomaterials for enhanced visible light photocatalysis," *Journal of Photochemistry and Photobiology A*, vol. 189, no. 2-3, pp. 258–263, 2007.

[50] Z. Zhang, C.-C. Wang, R. Zakaria, and J. Y. Ying, "Role of particle size in nanocrystalline TiO_2-based photocatalysts," *Journal of Physical Chemistry B*, vol. 102, no. 52, pp. 10871–10878, 1998.

[51] A. Olad, S. Behboudi, and A. A. Entezami, "Preparation, characterization and photocatalytic activity of TiO_2/polyaniline core-shell nanocomposite," *Bulletin of Materials Science*, vol. 35, no. 5, pp. 801–809, 2012.

[52] Y. Mizukoshi and N. Masahashi, "Photocatalytic activities and crystal structures of titanium dioxide by anodization: their dependence upon current density," *Materials Transactions*, vol. 51, no. 8, pp. 1443–1448, 2010.

[53] T. Yamashita and P. Hayes, "Analysis of XPS spectra of Fe^{2+} and Fe^{3+} ions in oxide materials," *Applied Surface Science*, vol. 254, no. 8, pp. 2441–2449, 2008.

[54] A. P. Grosvenor, B. A. Kobe, M. C. Biesinger, and N. S. McIntyre, "Investigation of multiplet splitting of Fe 2p XPS spectra and bonding in iron compounds," *Surface and Interface Analysis*, vol. 36, no. 12, pp. 1564–1574, 2004.

[55] G. K. Pradhan and K. M. Parida, "Fabrication of iron-cerium mixed oxide: an efficient photocatalyst for dye degradation," *International Journal of Engineering Science and Technology*, vol. 2, no. 9, pp. 53–65, 2010.

[56] A. Khare, R. J. Choudhary, K. Bapna, D. M. Phase, and S. P. Sanyal, "Resonance photoemission studies of (111) oriented CeO_2 thin film grown on Si (100) substrate by pulsed laser deposition," *Journal of Applied Physics*, vol. 108, no. 10, Article ID 103712, 2010.

Hindawi Publishing Corporation
International Journal of Photoenergy
Volume 2013, Article ID 595031, 12 pages
http://dx.doi.org/10.1155/2013/595031

Research Article

Supported Zinc Oxide Photocatalyst for Decolorization and Mineralization of Orange G Dye Wastewater under UV365 Irradiation

Ming-Chin Chang, Hung-Yee Shu, Tien-Hsin Tseng, and Hsin-Wen Hsu

Institute of Environmental Engineering, Hungkuang University, No. 34 Chung-Chie Road, Shalu, Taichung 433, Taiwan

Correspondence should be addressed to Hung-Yee Shu; hyshu@sunrise.hk.edu.tw

Received 18 August 2013; Revised 24 September 2013; Accepted 25 September 2013

Academic Editor: Jiaguo Yu

To solve the environmental challenge of textile wastewater, a UV/ZnO photocatalytic system was proposed. The objective of this study was to prepare a photocatalytic system by utilizing both cold cathode fluorescent light (CCFL) UV irradiation and steel mesh supported ZnO nanoparticles in a closed reactor for the degradation of azo dye C.I. Orange G (OG). Various operating parameters such as reaction time, preparation temperature, mixing speed, ZnO dosage, UV intensity, pH, initial dye concentration, and service duration were studied. Results presented efficient color and total organic carbon (TOC) removal of the OG azo dye by the designed photocatalytic system. The optimal ZnO dosage for color removal was 60 g m^{-2}. An alkaline pH of 11.0 was sufficient for photocatalytic decolorization and mineralization. The rate of color removal decreased with the increase in the initial dye concentration. However, the rate of color removal increased with the increase in the UV intensity. The steel mesh supported ZnO can be used repeatedly over 10 times without losing the color removal efficiency for 120 min reaction time. Results of Fourier transform infrared (FTIR) and ion chromatography (IC) indicated the breakage of N=N bonds and formation of sulfate, nitrate, and nitrite as the major and minor products. The observation indicated degradation of dye molecules.

1. Introduction

In the last few decades, the textile industry is one of the most important industries, which make contribution toward Taiwan's economic development. Wastewater effluents from textile and dye manufacturing industries receive much attention from public and governmental enforcements, because this type of wastewater can hardly meet the national discharge standards. In Taiwan, the national effluent standard (NES) has enforced the criteria of textile dyeing industries that chemical oxygen demand (COD) meets <100 to 160 mg/L and American Dye Manufacturers Institute (ADMI) color index meets <550 unit by the year 2003. On the other hand, most dyestuffs from the effluent of textile dyeing and finishing industry are complicated organic compounds with high color intensity, are recalcitrant to conventional biological wastewater treatment, and cause major environmental concerns [1–4]. To resolve the wastewater treatment problem, textile industrial treatment plants usually employ chemical coagulation integrated with activated sludge process. Unfortunately, these traditional treatment processes cannot meet the increasingly stringent criteria of color in dye wastewater treatment in Taiwan [5]. Under this situation, textile dyeing industries should pursue a more efficient technique to be the pretreatment or polishing processes to decolorize the highly colored wastewater. In this category of wastewater, azo dyes with nitrogen double bond (–N=N–) are the largest class of commercial dyestuffs used in the textile industries. Thus, many studies focused on decolorizing azo dye compounds by various techniques [6–8].

Advanced oxidation processes (AOPs), such as ozonation, UV/H_2O_2, UV/O_3, Fe^{2+}/H_2O_2, and $UV/O_3/H_2O_2$, are widely used to decompose organic products in industrial wastewater and groundwater. The extensive literatures of these technologies have been reviewed by Venkatadri and Peters [9]. These processes have the potential ability to mineralize most of the organic contaminants into carbon dioxide and water. There were reports of successful color removal with final

mineralization from azo dye wastewater using advanced oxidation processes (AOPs) such as UV/H_2O_2 [10–12], UV/O_3 [13, 14], or the Fenton reaction [15, 16]. Additionally, it has been reported that photocatalytic processes such as UV/ZnO system can also be effective in treating dye wastewaters [17–19]. The preparation of ZnO catalyst can be demonstrated by hydrothermal synthesis [20] and the doping of carbon on ZnO can improve its visible light application [21]. Much research focused on slurry type reactor. However, the limitation on the need of further separation of ZnO particles made the process more complicate and expensive. Therefore, fixing the ZnO particles onto supported materials such as glass plate, silica plate can avoid the particle separation step and can enable the easy operation of heterogeneous ZnO photocatalysis [22–24]. The aim of this work was to study the degradation of azo dye C.I. Orange G (OG) using a batch photocatalytic reactor in which the photocatalytic ZnO particles were supported on steel mesh and six cold cathode fluorescent lamps (CCFL) were used (wavelength of 365 nm) to provide UV irradiation. Operating parameters such as preparation temperature, mixing speed, ZnO dosage, UV intensity, pH, initial dye concentration, and reaction time that may affect the degree of the dye degradation were studied. Changes in color intensity, total organic carbon (TOC), pH, oxidation reduction potential (ORP) were monitored in addition to the analysis of reaction products by Fourier transform infrared (FTIR) and ion chromatography (IC).

2. Materials and Methods

2.1. Materials and Apparatus. A mono-azo dye, C.I. Orange G (OG), was selected as target compound for this photocatalytic decolorization study. OG ($C_{16}H_{10}N_2Na_2O_7S_2$, 60% purity) with a characteristic wavelength (λ_{max}) of 479 nm and a molecular weight of 452.38 g mole^{-1} was purchased from Sigma-Aldrich, Inc. and used as received without further purification. The chemical structure of OG can be obtained from our previous study [25]. The commercial available nanosized zinc oxide (ZnO), with a specific surface area of 25.68 m^2 g^{-1} from Aldrich, was used as the photocatalyst. The steel mesh (mesh size no.140, 0.106 mm) was purchased from a local hardware store and trimmed into pieces with a gross area of 252 cm^2 (36 × 7 cm). A dip coating technique was used to prepare ZnO-coated steel meshes. The trimmed steel mesh was washed, dried, and weighted first, then dipped into a designed concentration of ZnO mixed liquid for 30 minutes, and then dried in a 105°C oven for 30 minutes. The coating process was repeated three times. After all, the ZnO-coated steel mesh was weighted to measure the amount of ZnO on steel mesh. The detailed preparation procedure was reported in our previous work with the replacement of TiO_2 with ZnO nanoparticles [25]. Table 1 shows the steel mesh with specific surface. ZnO concentration of 8–67 g m^{-2} can be obtained by dip coating 0.20–1.67 g of ZnO nanoparticles on the given steel mesh with gross area of 252 cm^2. Based on images obtained with the field emission scanning electron microscope (FESEM), model JEOL 6330CF, the bare steel mesh showed smooth surface with no particles attached as shown in Figures 1(a) and 1(b). As for ZnO-coated steel mesh, it is seen that ZnO particles were uniformly coated on the steel mesh surface and the particles were of cylindrical shape as shown in Figures 1(c) and 1(d). The crystallinity of ZnO particles was provided by Aldrich as wurtzite structure. The photocatalytic reactor setup was also presented in our previous work [25]. The reactor was a 36 cm (L) × 7 cm (W) × 7.8 cm (H) black acrylics container fixed on a horizontal shaker with 75 rpm mixing speed. At the upper cover of the reactor, six cold cathode fluorescent lamps (CCFL), each of which has a diameter of 0.25 cm, length of 30 cm, light intensity of 4 W, and irradiation wavelength of 365 nm, were equipped which yielded a total light energy of 2.1 mW cm^{-2} measured at the surface of the solution. In each experimental run, 200 mL dye solution was introduced to the photocatalytic reactor. At the bottom of the reactor, there was ZnO-coated steel mesh with total gross surface area 252 cm^2 placed.

Table 1: The ZnO-coated weight on the steel meshes.

ZnO weight (g) (W_1)	ZnO solution concentration (g L^{-1}) (W_1/V)	ZnO weight on the coated steel meshes (g) (W_2)	ZnO weight per unit area (g m^{-2}) (W_2/A)
15	30	0.20	8
25	50	0.37	15
37.5	75	0.75	30
50	100	1.51	60
62.5	125	1.67	67

V: the ZnO solution of 500 mL, A: the steel net area of 252 cm^2.

2.2. Experimental Procedure and Analysis. OG azo dye solution at various concentrations was prepared with deionized water. The experimental variables studied included reaction time, preparation temperature, mixing speed, ZnO dosage, UV intensity, pH, initial dye concentration, and application duration of ZnO. At a predetermined reaction time, an aliquot of the solution was withdrawn and analyzed for residual dye concentration, TOC, and color.

Dye concentration was determined by measuring the absorbance at a wavelength of 479 nm using Hitachi U-2000 spectrophotometer. Color intensity was determined based on the American Dye Manufacturers Institute (ADMI) standard color measurement by applying the Adams-Nickerson color difference formula following method 2120E of the standard methods. The pH and redox potential (ORP) were monitored by a Eutech PH5500 dual channel pH/ion meter with specific probes. TOC was obtained with a total organic carbon analyzer from O.I. Analytical Aurora, model 1030. Besides, the degradation products were identified using Perkin Elmer FTIR spectrophotometer model, Spectrum One. Ions such as sulfate, nitrate, and nitrite were identified with ion chromatography (IC), Dionex ICS-1000.

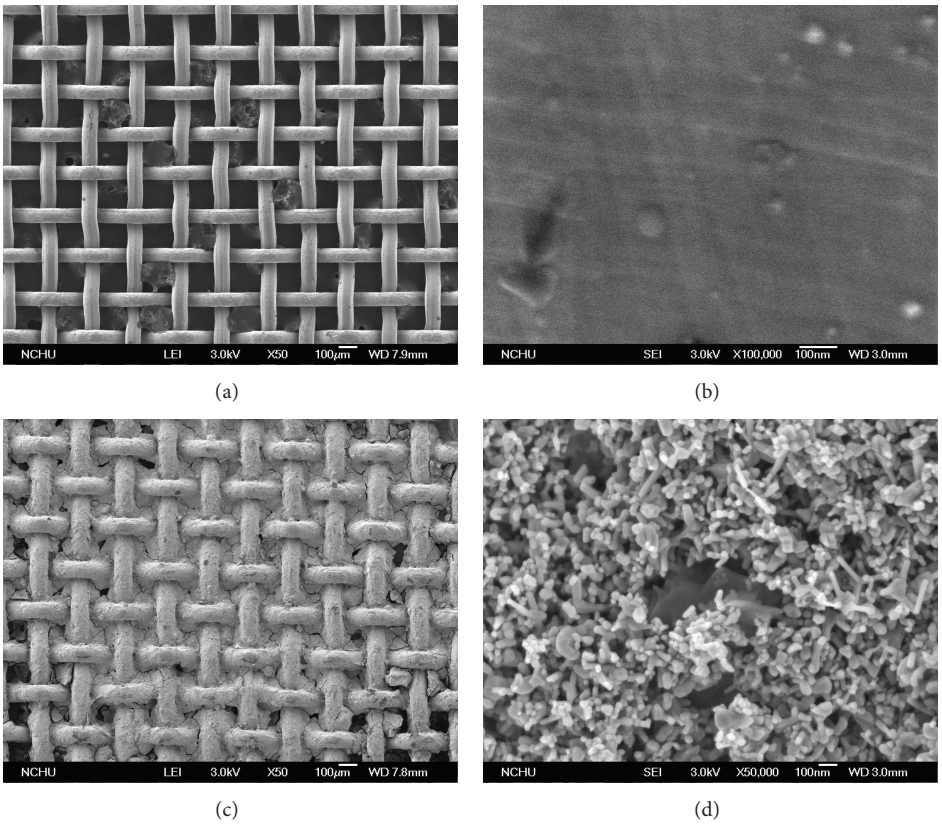

Figure 1: The morphology of ZnO powder coated on steel mesh at 150°C was identified by a JEOL 6330CF field emission scanning electron microscope (FESEM). (a) Bare steel mesh, 50 times enlargement. (b) Bare steel mesh, 100,000 times enlargement. (c) ZnO-coated steel mesh, 50 times enlargement. (d) ZnO-coated steel mesh, 50,000 times enlargement.

3. Results and Discussion

3.1. Synergic Effect of Combining CCFL UV 365 Irradiation and ZnO Catalyst. The color removal was first compared for various systems, that is, UV/ZnO, UV alone, and ZnO alone, at the initial OG concentration of 50 mg L^{-1}, ZnO dosage of 60 g m^{-2}, and 6 CCFL lamps with total light intensity of 24 W and at wavelength of 365 nm in 120 min of reaction in the closed reactor. Figure 2(a) shows results of color removal by various systems. Results indicated that the system of UV alone and ZnO alone could not remove color at any significant level. The UV/ZnO system removed color effectively with 100% removal, in 120 min. It was also observed that the pH remained relatively constant from 5.5 to 5.0 with time. This was expected as ZnO is a known photocatalyst that, upon radiation with light whose wavelength is shorter than that of its bandgap, can generate electron-hole pair and hydroxyl radicals, strong oxidation agents that can oxidize a wide group of organic compounds nonspecifically. Figure 2(b) shows the UV spectra of OG at different reaction time periods. There were three major absorption peaks for OG dye, that is, 248, 330, and 479 nm. During the photocatalytic reaction, all three major absorption peaks were diminished. For example, at the wavelengths of 479, 330, and 248 nm, the original absorbance was 1.8514, 1.1891, and 2.4417, respectively. After 120 min of reaction, the absorbance of 479, 330, and 248 nm changed to 0, 0, and 0.0145, respectively. The figure illustrates the total removal of color by UV/ZnO system.

3.2. Effect of Preparation Temperature and Mixing Speed. The effect of steel mesh supported ZnO preparation temperature on color removal was studied at the initial OG concentration of 50 mg L^{-1}, ZnO load dosage of 60 g m^{-2}, and 6 CCFL lamps in 120 min in the closed reactor. Figure 3(a) shows insignificant color removal differences in the range of 100–300°C. It was noted that pH remained unchanged at around 5 to 6. The reaction kinetics of UV/ZnO photocatalytic system was suggested to follow the Langmuir-Hinshelwood (L-H) reaction kinetics. And, in most of the designed reaction conditions, the L-H kinetic model of the UV/ZnO system can be further simplified into pseudo-first-order reaction kinetics. Therefore, the color removal of this study was treated using pseudo-first-order reaction as follows:

$$C_{\text{dye}} = C_{\text{dye},0} \times e^{-kt}, \tag{1}$$

where k denotes the pseudo-first-order reaction rate constant (min^{-1}), t is the reaction time (min), $C_{\text{dye},0}$ designates the initial concentration (mg L^{-1}) of OG, and $C_{\text{dye},t}$ is the concentration (mg L^{-1}) of OG at time t. The curve fitting of experimental results by (1) was shown in the figures as solid lines to demonstrate the consistence of kinetic model and

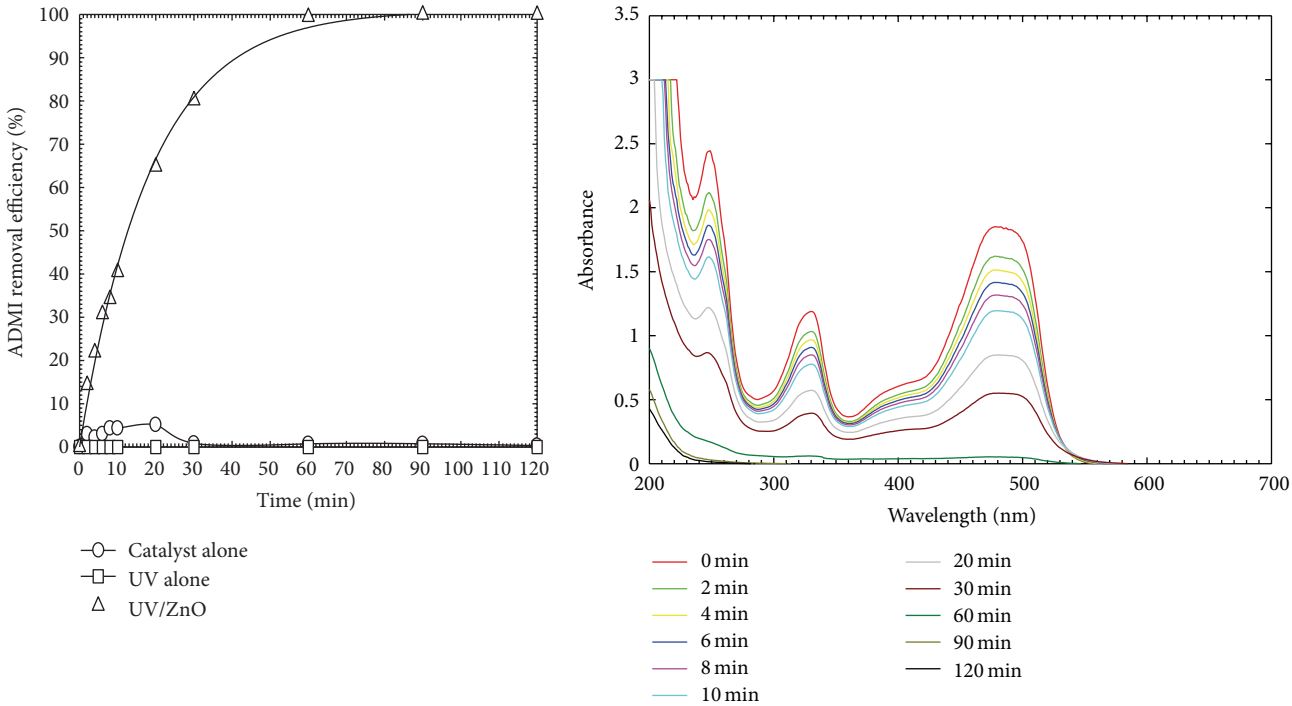

(a) (b)

Figure 2: (a) Synergic effect of UV and ZnO on UV/ZnO photocatalytic system. (b) UV spectra of OG under UV/ZnO decolorization. The conditions were initial dye concentration of 50 mg L^{-1}, ZnO loading of 60 g m^{-2}, light intensity of 2.1 mW cm^{-2}, and reaction time during 120 min.

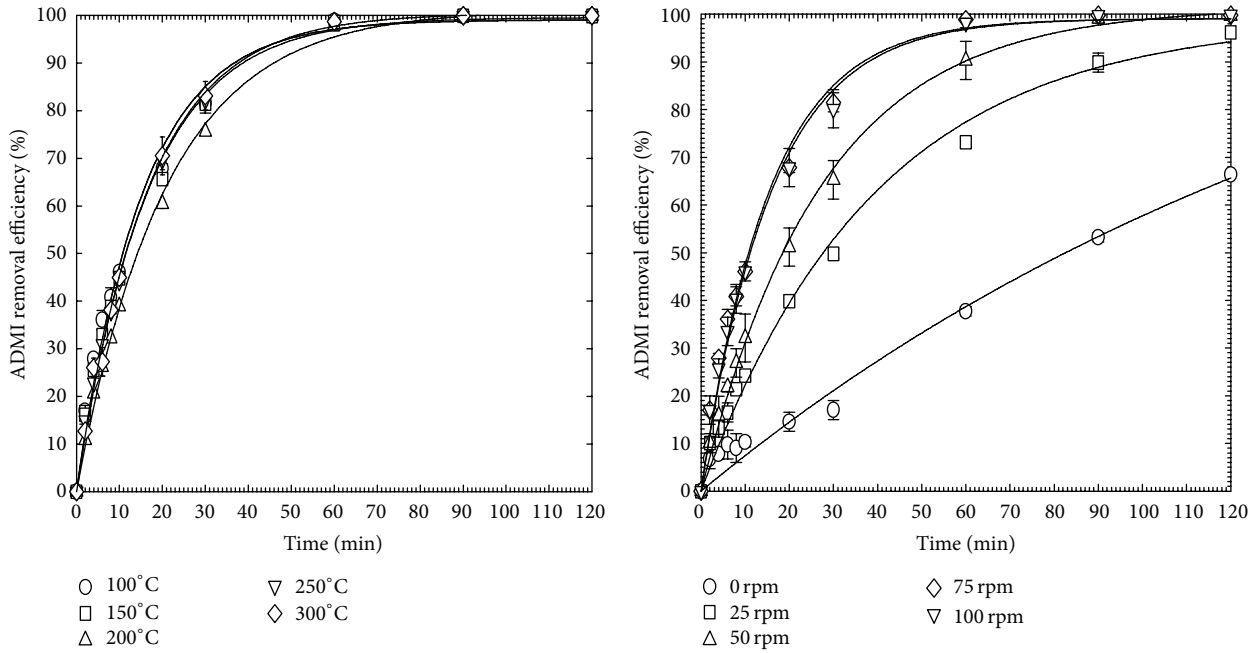

(a) (b)

Figure 3: Effect of (a) preparation temperature and (b) mixing speed. The conditions were initial dye concentration of 50 mg L^{-1}, ZnO loading of 60 g m^{-2}, light intensity of 2.1 mW cm^{-2}, and reaction time during 120 min.

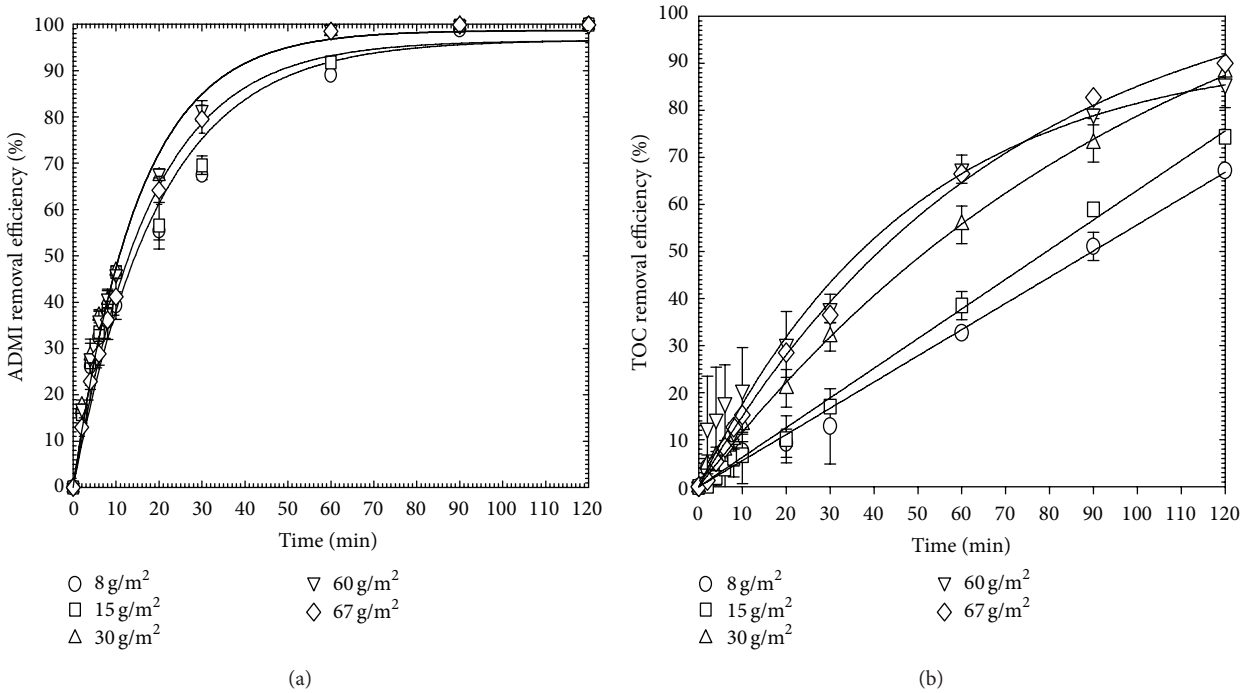

Figure 4: Effect of surface loading of ZnO. The conditions were initial dye concentration of 50 mg L^{-1}, light intensity of 1.05 mW cm^{-2}, and reaction time during 120 min.

experimental data. The calculated rate constants (from curve fitting) were 4.44, 4.37, 3.68, 4.32, and 4.57 (10^{-2}) (min^{-1}) at 100, 150, 200, 250, and 300°C, respectively. The preparation temperature shows neglected effect on OG color removal. Preparation temperature of 150°C was chosen as the working condition for its low energy consumption and fast dyeing speed. Figure 3(b) shows the effect of mixing speed on color removal under UV/ZnO photocatalytic system. Mixing speed is definitely an important factor that affects the color removal efficiency. From the results, the higher the mixing speed is, the faster the decolorizing reaction can be obtained. The calculated rate constants (from curve fitting) were 0.60, 2.78, 4.44, and 4.32 (10^{-2}) (min^{-1}) at 0, 50, 75, and 100 rpm, respectively. Therefore, the mixing speed was fixed at 75 rpm for further experimental runs. Since the photocatalytic degradation of OG happened on the surface of ZnO catalyst, the mass transfer of OG molecules from aqueous solution to the surface of ZnO catalyst was rather important to affect the reaction rate. The higher mixing speed caused better contact of OG molecules and ZnO catalyst and presented higher degradation rate of OG. However, when the mixing speed increased to higher than 75 rpm, the limited surface of ZnO cannot provide enough active sites for OG molecules. Therefore, the degradation rate of OG under UV/ZnO system hardly increased while the mixing speed was adjusted to higher than 75 rpm.

3.3. Effect of ZnO Load Dosage. Figure 4(a) shows the removal of color as a function of load dosage of ZnO under 1.05 mW cm^{-2} of UV irradiation. Results indicated that the color removal increased from 89 to 98.5% in 60 min when the surface loading of ZnO particles increased from 8 to 60 g m^{-2}. The color removal then decreased from 98.9 to 98.5% when the surface loading of ZnO increased from 60 to 67 g m^{-2}. An optimal ZnO loading for color removal occurred at 60 gm^{-2}. However, the differences of color removal rate between various ZnO loads were not significant. The rate constants followed similar trend to percent color removal; the observed rate constants were 0.66, 0.67, 1.25, 2.94, and 2.98 (10^{-2} min^{-1}) at surface ZnO loading dosages of 8, 15, 30, 60, and 67 g m^{-2}, respectively. From Figure 4(b), the TOC removal was 67.2% for ZnO loading of 8 g m^{-2} and increased up to 88.3% for ZnO loading of 60 g m^{-2}. Results indicated that the TOC removal was highly affected by various ZnO loading dosages. On the other hand, ZnO dosage presented insignificant effect on color removal. To decolorize and mineralize simultaneously, one should choose higher ZnO loading to both color and TOC removal requirements.

3.4. Effect of UV Light Intensity. Theoretically, the higher the UV light intensity applied to a photocatalytic system, the faster the electron-hole pairs and OH• free radical form to obtain the higher dye decolorization and mineralization rate. Thus, the rate constant increases by UV intensity increase, while the same ZnO catalyst surface is loading. Since the photolysis of ZnO catalyst is enhanced to produce abundant electron-hole pairs and OH• in the dye solution to be used for decolorization, it is obvious that the more UV intensity employed to the system is, the faster the dye is decolorized.

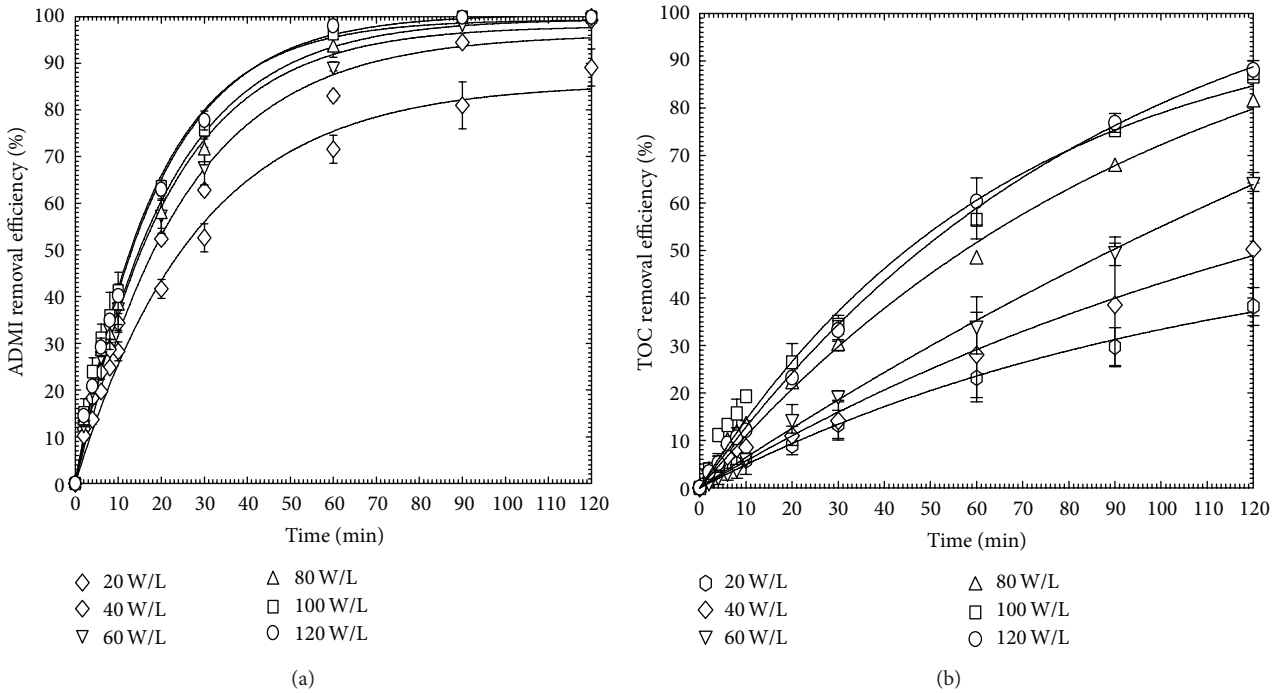

Figure 5: Effect of UV light intensity on OG (a) decolorization and (b) mineralization by UV/ZnO photocatalytic system. The conditions were initial dye concentration of 50 mg L^{-1}, ZnO-coated amounts of 60 g m^{-2}, and UV light intensity of 20 to 120 W L^{-1} (120 W L^{-1} measured as 2.1 mW cm^{-2}).

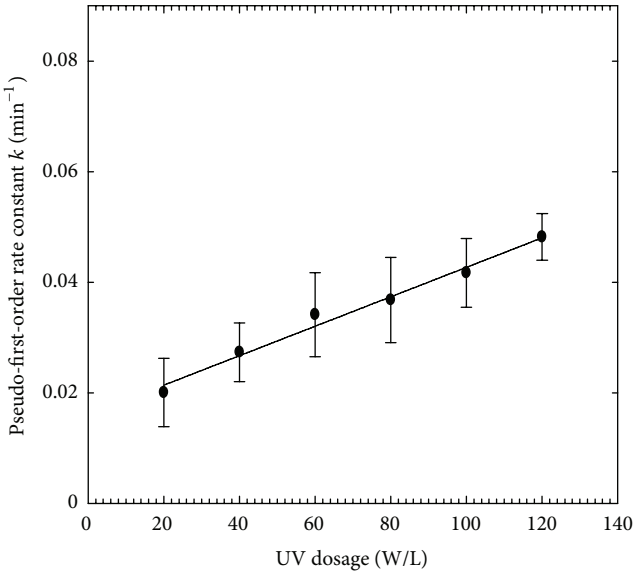

Figure 6: Effect of UV light intensity on pseudo-first-order rate constant of OG decolorization by UV/ZnO photocatalytic system. The conditions were the same as in Figure 5.

Figure 5(a) shows the removal of color as a function of UV intensity. Results indicated that the color removal increased from 71.6 to 98.8% in 60 min when the UV intensity increased from 20 to 120 W L^{-1}. The rate constants followed similar trend to percent color removal; the observed rate constants were 2.01, 3.42, and 4.82 (10^{-2} min^{-1}) at UV intensity which increased from 20, 60, and 120 W L^{-1}, respectively, as shown in Table 2. Figure 5(b) presents the mineralization of OG in solution as a function of UV intensity. Results denote that the TOC removal increased from 38.2 to 88.3% in 120 min when the UV intensity increased from 20 to 120 W L^{-1}. Therefore, applying sufficient UV intensity with ZnO photocatalyst can fairly mineralize portion of TOC to reach almost total mineralization.

Table 2: The first-order reaction rate constant k (10^2 min^{-1}) for operating parameter of UV intensity and initial concentration.

Effect of UV intensity		Effect of initial concentration	
UV intensity, W L^{-1}	k	Concentration, mg L^{-1}	k
20	2.00	12.5	20.14
40	2.74	18.8	16.26
60	3.42	25	17.55
80	3.68	50	5.95
100	4.17	75	5.88
120	4.82		

Figure 6 shows the relationship between pseudo-first-order rate constants and UV light intensity that a linear relationship can be obtained. This presents that the UV light intensity is an important operating parameter which linearly affects the decolorization of OG under UV/ZnO photocatalytic system. In this work, the maximum UV light intensity was 120 W L^{-1}, which can be transferred into photo

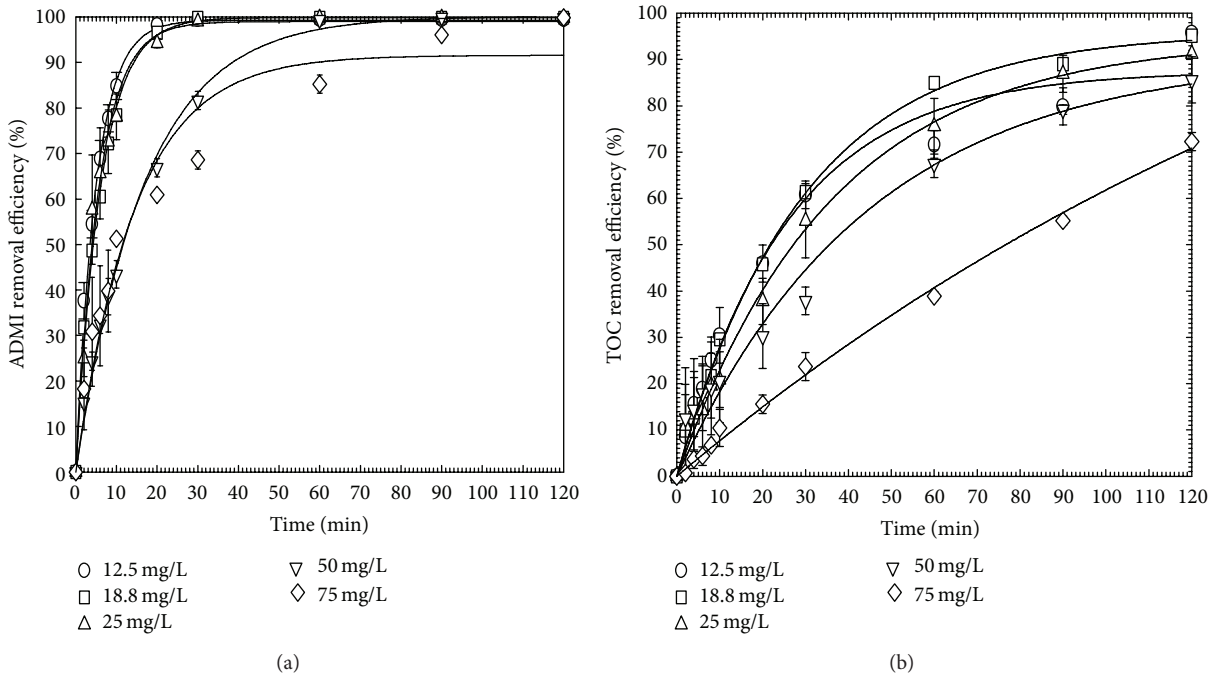

Figure 7: Effect of initial concentration on (a) ADMI color and (b) TOC removal. The conditions were ZnO-coated amounts of 60 gm^{-2}, light intensity of 2.1 mW cm^{-2}, and reaction time during 0–120 min.

flux density as 2.1 mW cm^{-2}. From previous studies, photocatalytic reaction rate constant is linearly increased with UV intensity while operating in low region of UV intensity, that is, between 0 and 20 mW cm^{-2} [17, 20]. The degradation of OG under UV/ZnO system was major caused by formation of OH• free radicals. From a previous study by Xiang et al., ZnO had the third highest formation rate of OH• free radicals following P25 and anatase TiO_2 [26]. Under higher UV irradiation intensity, the formation rate of OH• free radicals was higher. This caused faster degradation reaction of OG under UV/ZnO system.

3.5. Effect of Dye Initial Concentration. To present the validity of L-H model on our CCFL/ZnO system, the effect of initial dye concentrations on the photodegradation of azo OG dye was studied at initial concentrations of 12.5–75 mg L^{-1}, ZnO dosage of 60 gm^{-2}, and 6 CCFL lamps for a period of 120 min in the closed reactor. Figure 7 shows results of dye photodegradation as a function of reaction time at various initial dye concentrations. Results indicated that the rate of dye removal decreased from 20.1 to 5.95 (10^{-2} min^{-1}) when the initial dye concentration was increased from 12.5 to 50 mg L^{-1}, as shown in Table 2. The rate constant then remained constant and independent of the dye concentration as the initial dye concentration increased to greater than 50 mg L^{-1}. This is typical Langmuir-Hinshelwood (L-H) reaction kinetics which is generally capable of modeling UV/ZnO photocatalytic oxidation process [27–30]. According to the L-H reaction kinetics, the rate of dye degradation can be described by the following equation:

$$r = \frac{dC}{dt} = \frac{kK_A C}{1 + K_A C}, \tag{2}$$

where r is the degradation rate of dye (mg L^{-1} min^{-1}) and k, K_A, and C are the rate constant (mg L^{-1} min^{-1}), equilibrium adsorption constant (L mg^{-1}), and residual dye concentration (mg L^{-1}), respectively. According to the above equation, at high dye concentration, that is, $1 \ll KC$, the rate equation is

$$r = k. \tag{3}$$

Likewise, at low dye concentration, that is, $1 \gg KC$, the above equation (2) becomes

$$r = kK_A C. \tag{4}$$

That is, as the initial concentration increases, the reaction no longer follows the first-order expression; it rather becomes independent of the dye concentration as shown in (3). By rearranging (2), one has

$$\frac{1}{r_0} = \frac{1}{kK_A} \times \frac{1}{C_0} + \frac{1}{k}, \tag{5}$$

where r_0 and C_0 are the initial rate (mg L^{-1} min^{-1}) and initial dye concentration (mg L^{-1}), respectively. A plot of the reciprocals of initial rate and initial concentration yields the rate

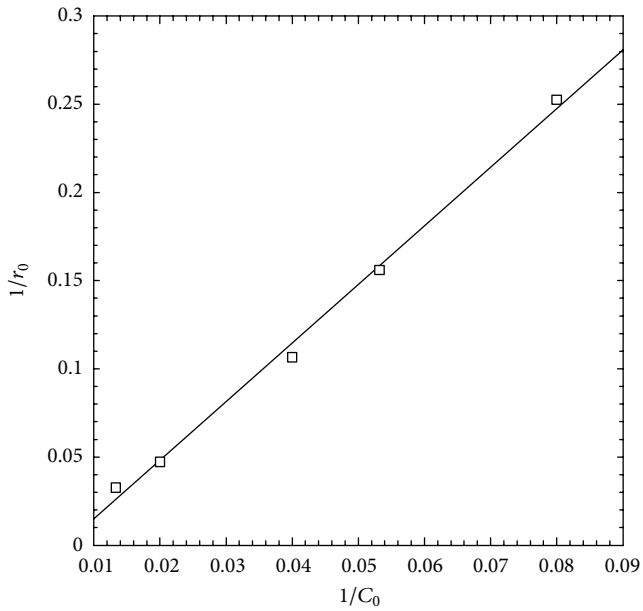

Figure 8: Langmuir-Hinshelwood kinetic model (ZnO loading dosage of 60 g m^{-2} with light intensity of 2.1 mW cm^{-2}).

constant, k, and the adsorption constant, K (Figure 8). The initial rate r_0 was calculated by the first 2 min of Figure 7 with ZnO loading dosage of 60 g m^{-2}. From the slope ($1/kK_A$) and the intercept ($1/k$) of Figure 8, the calculated $k$and K_A were 54.35 mg L^{-1} min^{-1} and 0.0055 mg^{-1} for ZnO loading dosage of 60 g m^{-2}. The rate constants (k) obtained in this work of 54.35 mg L^{-1} min^{-1} were higher than that of previous works [27–30] such as 1.66, 1.67, 0.95, and 0.17 mg L^{-1} min^{-1} for various dyes such as direct red 16, Remazol Black 5, Procion Red MX-5B, and indigo carmine, respectively. Similarly, the equilibrium adsorption constants (K_A) of 0.0055 L mg^{-1} from this work were in the range of previous studies, such as 0.0093, 0.072, 0.071, and 0.78 L mg^{-1}, for various dyes as above. The results indicate that the photocatalytic degradation of Orange G by CCFL/ZnO process followed the Langmuir-Hinshelwood kinetic model with fairly good prediction of $r^2 = 0.996$.

3.6. Effect of pH. The effect of pH on the degradation of azo dye was conducted by adjusting the initial pH value of 5.0 to the range of 2 to 11 using HCl and/or NaOH with initial OG dye concentration of 50 mg L^{-1} and 60 g m^{-2} of ZnO dosage. Figure 9(a) shows OG dye removal as a function of time at various pH values. Results indicated that, at original pH, the color removal reached 78.5% in 30 min of photocatalytic reaction. At acidic pH of 2 and 3, the color removal rates of 76.7 and 76.1% were obtained, respectively. This implies that acidic pH provides no benefit for OG decolorization under UV/ZnO system. On the other hand, at alkaline pH of 11, the color removal rate sharply increased up to 95.6%. Figure 9(b) shows the TOC removal as a function of time at various pH values. Results indicated that, at original pH, the TOC removal reached 88.3% in 120 min of photocatalytic reaction. At acidic pH of 2 and 3, the color removal rates of 70.1 and 82.8% were obtained, respectively. At alkaline pH of 11, TOC removal rate was 87.8%. This implies that the TOC removal rate is rather stable in the range of 82.8–88.3 for pH range 3–11. And for pH 2, an extremely acidic condition, the TOC removal dropped from 12–18% to 70.1%. Extremely acidic pH has disadvantage for TOC removal under UV/ZnO system for OG solution, since 0.1 N HCl solution was used to adjust solution pH value to 2-3. At this operating condition, there were abundant amounts of high concentration chloride ions in the solution to play the role of free radical scavenger. Chloride ions competed with OG molecules to consume free radicals. Therefore, the decolorization and mineralization rate of OG by UV/ZnO system decreased. The observed rate constants for various pH values were summarized in Table 3.

Table 3: The first-order reaction rate constant k (10^2 min^{-1}) for operating parameter of pH and duration.

Effect of initial pH		Duration test	
pH	k	Cycle	k
2	3.74	1	4.41
3	3.74	2	3.95
5	4.18	3	3.44
9	3.69	4	3.33
11	9.15	5	3.24
		6	3.11
		7	2.84
		8	2.35
		9	2.31
		10	2.31

3.7. The Product Analysis by FTIR and IC. The change of functional groups of azo dye after photocatalytic treatment was surveyed. The initial dye concentration was 50 mg L^{-1} and was treated with a ZnO dosage of 60 g m^{-2} and reaction time of 120 min. The scan spectra (Figure 10(a)) for the functional groups are SO_3Na of 1150~1250 cm^{-1}, N=N of 1426, 1462 and 1495 cm^{-1}, C=O of 1690~1760 cm^{-1}, and C–H and N–H of 3300~3500 cm^{-1}. After the photocatalytic oxidation (Figure 10(b)), a new double bond C=O at 1637 cm^{-1} was produced. Meanwhile, the N=N from dye at 1426, 1463, and 1496 cm^{-1} disappeared due to attack by the hydroxyl radicals that cleaved the double bond N=N. Accordingly, the dye molecule was degraded and decolorized. The ions such as sulfate, chloride, nitrite, and nitrate were determined. Figure 11(a) shows that the major ion concentration of sulfate significantly increased to 16 mg L^{-1} over time. The chloride ion produced due to the impurity of OG dye was as low as 1.5 mg L^{-1}. The nitrate ion concentration was about from 1.0 to 4.5 mg L^{-1}, and nitrite concentration was less than 0.5 mg L^{-1} as shown in Figure 11(b).

3.8. Application Duration. The steel mesh supported ZnO catalyst was used repeatedly to treat the OG solution.

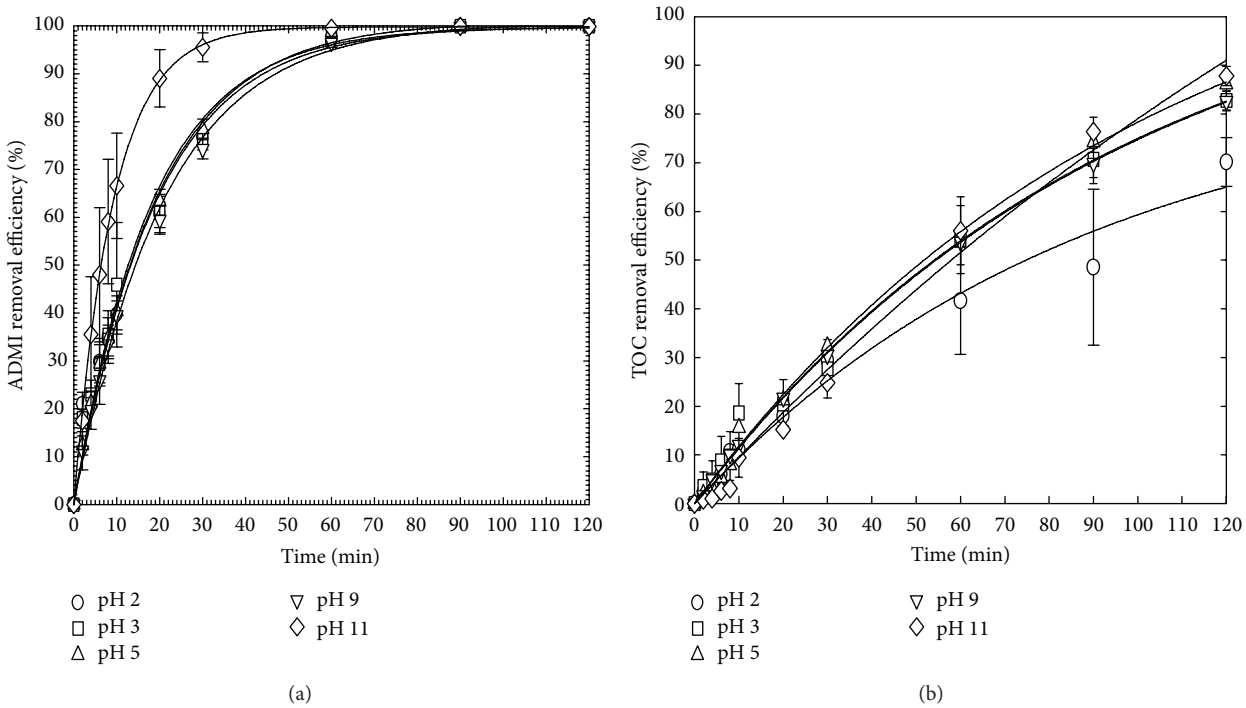

Figure 9: Effect of initial pH on (a) decolorization and (b) mineralization of OG under UV/ZnO system. The conditions were initial dye concentration of 50 mg L^{-1}, ZnO-coated amounts of 60 g m^{-2}, light intensity of 2.1 mW cm^{-2}, and reaction time during 120 min.

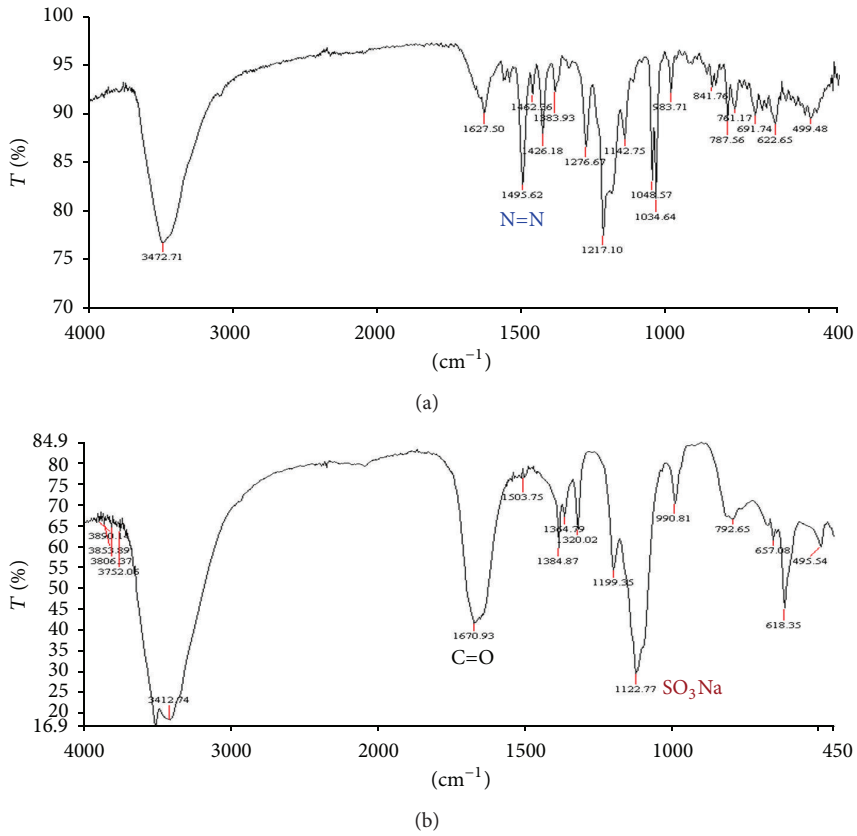

Figure 10: FTIR spectra for OG decolorization and demineralization (a) before and (b) after UV/ZnO photocatalytic degradation. The operating conditions were the same as in Figure 2.

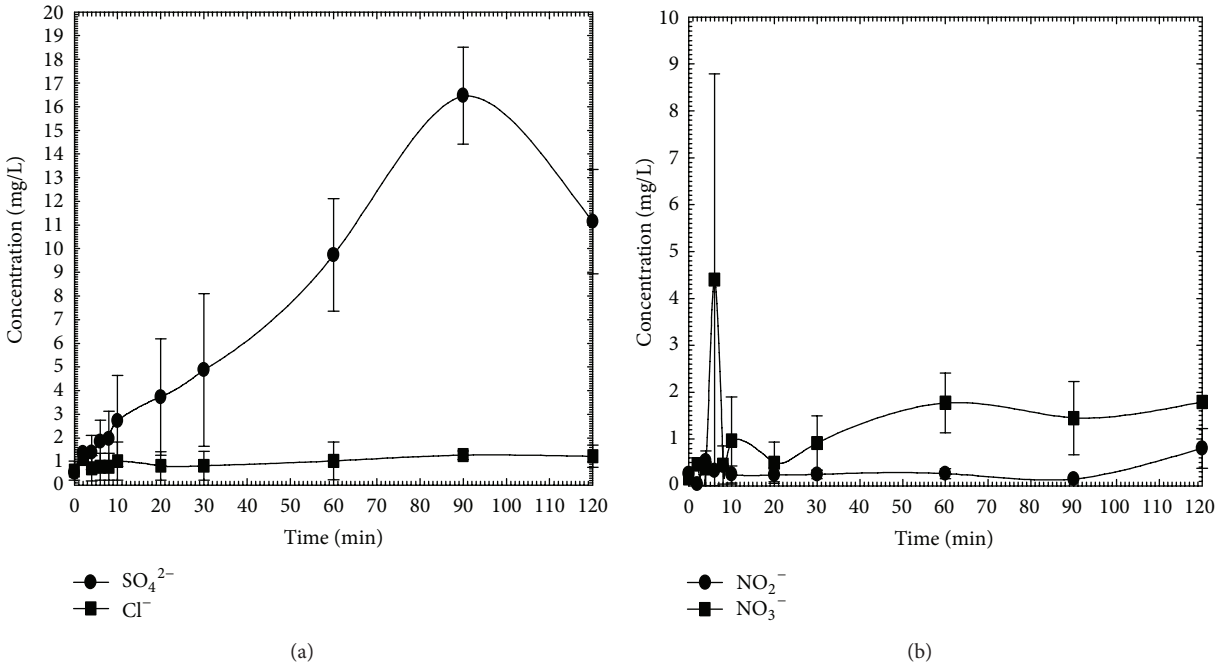

Figure 11: The product analysis by IC, (a) SO_4^{2-} and Cl^-, and (b) NO_3^- and NO_2^-. The conditions were initial dye concentration of 50 mg L^{-1}, ZnO-coated amounts of 60 g m^{-2}, and light intensity of 2.1 mW cm^{-2} at 120 min.

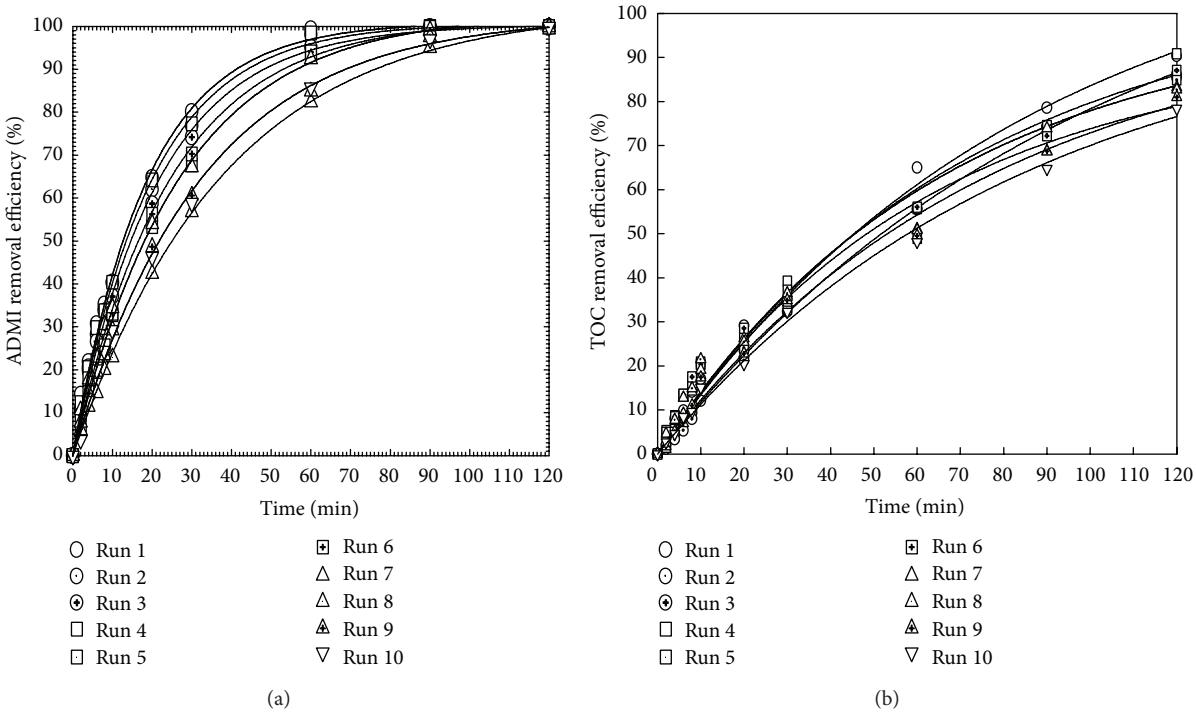

Figure 12: Duration test on (a) color and (b) TOC removal. The conditions were initial dye concentration of 50 mg L^{-1}, ZnO-coated amounts of 60 gm^{-2}, light intensity of 2.1 mW cm^{-2}, and reaction time during 120 min.

Figure 12 shows the system performance over 10 cycles. Results indicated that, although the rate of OG degradation decreased as the reuse cycle of catalyst increased, the total amount of dye removal remained relatively unchanged at 100% in the treatment time range of 100–120 min, however. Instead of ADMI color, the TOC removal decreased from 90 to 78% after ten experimental runs. In the meantime, there was nearly neglected loss (0.04%) of ZnO in each operation even after 10 cycles according to the solution Zn concentration analysis by atomic absorption. The observed

rate constants declined with more reuse cycles as shown in Table 3 from 0.0441 to 0.0231 min^{-1}, however. This can be attributed to potential surface poisoning of the photocatalyst, ZnO, due to adsorption of reaction products.

4. Conclusions

Steel mesh supported ZnO catalyst illuminated with cold cathode fluorescent light (CCFL) UV was effective in the removal of ADMI color and TOC from the OG azo dye solution. Preparation temperature showed insignificant effect on color and TOC removal. An optimal ZnO surface loading or dosage of 60 g m^{-2} exhibited the highest color removal as well as the fastest rate; further increase in surface ZnO loading had no benefit in increasing the color removal, however. An alkaline pH of 11 had the best photocatalytic oxidation rate; the rate of color removal was stable in the range from pH 3 to 9. At pH 2, the TOC removal rate was the lowest among all pH range. The rate of color removal decreased with initial dye concentration as was expected by the Langmuir-Hinshelwood kinetics. The rate of color removal increased with UV intensity linearly. The ZnO-coated steel mesh can be repeatedly used over 10 cycles without significant loss of catalyst mass; the percent dye removal remained close to 100% in 10 cycles except for about 50% decrease in reaction rate constants apparently due to possible surface poisoning. Based on FTIR analysis, there was decrease of N=N bonding which indicated chemical transformation of the dye OG compound. Results of analyzing the inorganic byproducts revealed that sulfate production was predominant; nitrite and nitrate were produced at minor quantities.

Acknowledgments

The authors appreciate the research funding granted by the Taiwan National Science Foundation (NSC 98-2221-E-241-006-MY3) as well as the analysis by NSC Instrumental Center of the National Chung Hsing University and the National Tsing Hua University.

References

[1] N. H. Ince and D. T. Gönenç, "Treatability of a textile azo dye by UV/H_2O_2 ," *Environmental Technology*, vol. 18, no. 2, pp. 179–185, 1997.

[2] U. Pagga and D. Brown, "The degradation of dyestuffs: part II. Behaviour of dyestuffs in aerobic biodegradation tests," *Chemosphere*, vol. 15, no. 4, pp. 479–491, 1986.

[3] M. A. Brown and S. C. DeVito, "Predicting azo dye toxicity," *Critical Reviews in Environmental Science and Technology*, vol. 23, no. 3, pp. 249–324, 1993.

[4] H.-Y. Shu, C.-R. Huang, and M.-C. Chang, "Decolorization of mono-azo dyes in wastewater by advanced oxidation process: a case study of acid red 1 and acid yellow 23," *Chemosphere*, vol. 29, no. 12, pp. 2597–2607, 1994.

[5] C. M. Kao, M. S. Chou, W. L. Fang, B. W. Liu, and B. R. Huang, "Regulating colored textile wastewater by 3/31 wavelength admi methods in Taiwan," *Chemosphere*, vol. 44, no. 5, pp. 1055–1063, 2001.

[6] H.-Y. Shu and C.-R. Huang, "Degradation of commercial azo dyes in water using ozonation and UV enhanced ozonation process," *Chemosphere*, vol. 31, no. 8, pp. 3813–3825, 1995.

[7] C. Galindo and A. Kalt, "UV-H_2O_2 oxidation of monoazo dyes in aqueous media: a kinetic study," *Dyes and Pigments*, vol. 40, no. 1, pp. 27–35, 1999.

[8] M. Neamtu, I. Siminiceanu, A. Yediler, and A. Kettrup, "Kinetics of decolorization and mineralization of reactive azo dyes in aqueous solution by the UV/H_2O_2 oxidation," *Dyes and Pigments*, vol. 53, pp. 93–99, 2002.

[9] R. Venkatadri and R. W. Peters, "Chemical oxidation technologies: ultraviolet light/hydrogen peroxide, Fenton's reagent, and titanium dioxide-assisted photocatalysis," *Hazardous Waste and Hazardous Materials*, vol. 10, no. 2, pp. 107–149, 1993.

[10] H.-Y. Shu, M.-C. Chang, and H.-J. Fan, "Decolorization of azo dye acid black 1 by the UV/H_2O_2 process and optimization of operating parameters," *Journal of Hazardous Materials*, vol. 113, no. 1–3, pp. 201–208, 2004.

[11] H.-Y. Shu, M.-C. Chang, and H.-J. Fan, "Effects of gap size and UV dosage on decolorization of C.I. Acid Blue 113 wastewater in the UV/H_2O_2 process," *Journal of Hazardous Materials*, vol. 118, no. 1–3, pp. 205–211, 2005.

[12] E. Rodríguez, R. Peche, J. M. Merino, and L. M. Camarero, "Decoloring of aqueous solutions of indigocarmine dye in an acid medium by H_2O_2/UV advanced oxidation," *Environmental Engineering Science*, vol. 24, no. 3, pp. 363–371, 2007.

[13] H.-Y. Shu and M.-C. Chang, "Decolorization effects of six azo dyes by O_3, UV/O_3 and UV/H_2O_2 processes," *Dyes and Pigments*, vol. 65, no. 1, pp. 25–31, 2005.

[14] C.-H. Wu and H.-Y. Ng, "Degradation of C.I. Reactive Red 2 (RR2) using ozone-based systems: comparisons of decolorization efficiency and power consumption," *Journal of Hazardous Materials*, vol. 152, no. 1, pp. 120–127, 2008.

[15] T.-H. Kim, C. Park, J. Yang, and S. Kim, "Comparison of disperse and reactive dye removals by chemical coagulation and Fenton oxidation," *Journal of Hazardous Materials*, vol. 112, no. 1-2, pp. 95–103, 2004.

[16] F. Ay, E. C. Catalkaya, and F. Kargi, "Advanced oxidation of direct red (DR 28) by fenton treatment," *Environmental Engineering Science*, vol. 25, no. 10, pp. 1455–1462, 2008.

[17] M. A. Behnajady, N. Modirshahla, and R. Hamzavi, "Kinetic study on photocatalytic degradation of C.I. Acid Yellow 23 by ZnO photocatalyst," *Journal of Hazardous Materials*, vol. 133, no. 1–3, pp. 226–232, 2006.

[18] S. Chakrabarti and B. K. Dutta, "Photocatalytic degradation of model textile dyes in wastewater using ZnO as semiconductor catalyst," *Journal of Hazardous Materials*, vol. 112, no. 3, pp. 269–278, 2004.

[19] N. Daneshvar, M. H. Rasoulifard, A. R. Khataee, and F. Hosseinzadeh, "Removal of C.I. Acid Orange 7 from aqueous solution by UV irradiation in the presence of ZnO nanopowder," *Journal of Hazardous Materials*, vol. 143, no. 1-2, pp. 95–101, 2007.

[20] J. Yu and X. Yu, "Hydrothermal synthesis and photocatalytic activity of zinc oxide hollow spheres," *Environmental Science and Technology*, vol. 42, no. 13, pp. 4902–4907, 2008.

[21] S. Liu, C. Li, J. Yu, and Q. Xiang, "Improved visible-light photocatalytic activity of porous carbon self-doped ZnO nanosheet-assembled flowers," *CrystEngComm*, vol. 13, no. 7, pp. 2533–2541, 2011.

[22] M. A. Behnajady, N. Modirshahla, N. Daneshvar, and M. Rabbani, "Photocatalytic degradation of C.I. Acid Red 27 by

immobilized ZnO on glass plates in continuous-mode," *Journal of Hazardous Materials*, vol. 140, no. 1-2, pp. 257–263, 2007.

[23] V. Koutantou, M. Kostadima, and E. Chatzisymeon, "Solar photocatalytic decomposition of estrogens over immobilized zinc oxide," *Catalysis Today*, vol. 209, pp. 66–73, 2013.

[24] A. Zacharakis, E. Chatzisymeon, V. Binas, Z. Frontistis, D. Venieri, and D. Mantzavinos, "Solar photocatalytica degradation of bisphenol A on immobilized ZnO or TiO_2 ," *International Journal of Photoenergy*, vol. 2013, Article ID 570587, 9 pages, 2013.

[25] M. C. Chang, C. P. Huang, H. Y. Shu, and Y. C. Chang, "A new photocatalytic system using steel mesh and cold cathode fluorescent light for the decolorization of azo dye orange G," *International Journal of Photoenergy*, vol. 2012, Article ID 303961, 9 pages, 2012.

[26] Q. Xiang, J. Yu, and P. K. Wong, "Quantitative characterization of hydroxyl radicals produced by various photocatalysts," *Journal of Colloid and Interface Science*, vol. 357, no. 1, pp. 163–167, 2011.

[27] T. Aarthi, P. Narahari, and G. Madras, "Photocatalytic degradation of Azure and Sudan dyes using nano TiO_2 ," *Journal of Hazardous Materials*, vol. 149, no. 3, pp. 725–734, 2007.

[28] K. Sahel, N. Perol, H. Chermette, C. Bordes, Z. Derriche, and C. Guillard, "Photocatalytic decolorization of Remazol Black 5 (RB5) and Procion Red MX-5B-Isotherm of adsorption, kinetic of decolorization and mineralization," *Applied Catalysis B*, vol. 77, no. 1-2, pp. 100–109, 2007.

[29] N. Barka, A. Assabbane, A. Nounah, and Y. A. Ichou, "Photocatalytic degradation of indigo carmine in aqueous solution by TiO_2-coated non-woven fibres," *Journal of Hazardous Materials*, vol. 152, no. 3, pp. 1054–1059, 2008.

[30] J. Saien, M. Asgari, A. R. Soleymani, and N. Taghavinia, "Photocatalytic decomposition of direct red 16 and kinetics analysis in a conic body packed bed reactor with nanostructure titania coated Raschig rings," *Chemical Engineering Journal*, vol. 151, no. 1–3, pp. 295–301, 2009.

Hindawi Publishing Corporation
International Journal of Photoenergy
Volume 2013, Article ID 761971, 19 pages
http://dx.doi.org/10.1155/2013/761971

Review Article

Fabrication, Modification, and Emerging Applications of TiO_2 Nanotube Arrays by Electrochemical Synthesis: A Review

Jian-Ying Huang,[1] Ke-Qin Zhang,[1] and Yue-Kun Lai[1,2]

[1] *National Engineering Laboratory of Modern Silk, College of Textile and Clothing Engineering, Soochow University, Suzhou 215123, China*
[2] *Physikalisches Institute and Center for Nanotechnology (CeNTech), Westfälische Wilhelms-Universität Münster, 48149 Münster, Germany*

Correspondence should be addressed to Yue-Kun Lai; yklai@suda.edu.cn

Received 9 July 2013; Accepted 30 July 2013

Academic Editor: Jiaguo Yu

Titania nanotube arrays (TNAs) as a hot nanomaterial have a unique highly ordered array structure and good mechanical and chemical stability, as well as excellent anticorrosion, biocompatible, and photocatalytic performance. It has been fabricated by a facile electrochemical anodization in electrolytes containing small amounts of fluoric ions. In combination with our research work, we review the recent progress of the new research achievements of TNAs on the preparation processes, forming mechanism, and modification. In addition, we will review the potential and significant applications in the photocatalytic degradation of pollutants, solar cells, water splitting, and other aspects. Finally, the existing problems and further prospects of this renascent and rapidly developing field are also briefly addressed and discussed.

1. Introduction

Nanostructured materials with peculiar properties are not expected in bulk phase and have already led to a breakthrough in various fields of science and technology. Moreover, much of the current interest in one-dimensional nanostructures, such as nanotube, nanowire, nanorod, and nanobelts, was initiated by the discovery of carbon nanotubes by Iijima et al. in 1991 [1]. Within these nanostructure materials, TiO_2-based nanotubes attracted engrossing interest and intensive researches due to their merits of high specific surface area, ion-changeable ability, and photocatalytic ability. Over the past decades, nanostructured materials derived from TiO_2 have extensively been investigated for many promising applications, including solar cells/batteries, self-cleaning coatings, electroluminescent hybrid devices, and photocatalysis, owing to their peculiar chemical and physical behaviors. Currently, developed methods of fabricating TiO_2-based nanotubes comprise the assisted-template method [2, 3], hydrothermal treatment [4–6], and electrochemical anodic oxidation [7–10]. Each fabrication method has unique advantages and functional features and comparisons among these approaches. Regarding the template-assisted method, anodic aluminum oxide (AAO) nanoporous membrane, which consists of an array of parallel straight nanopores with controllable diameter and length, is usually used as template. However, the template-assisted method often encounters difficulties of prefabrication and postremoval of the previous templates and usually results in impurities. Concerning hydrothermal treatment, the self-assembled TiO_2 nanotubes are based on the treatment of Ti foils or TiO_2 powders in a tightly closed vessel containing highly concentrated NaOH solution (5–10 M) to obtain TiO_2 nanotube layer or TiO_2-based powder [6, 11]. These methods, other than the electrochemical anodic oxidation, are either not suitable for rapid production or notable to yield uniform TiO_2 nanotubes with vertical alignment. The demonstrated architecture of TiO_2 nanotube arrays (TNAs) by a facile electrochemical anodizing process is capable of an ordered alignment with high aspect ratio and establishment of pure-phase TiO_2 structure in one step under ambient environment. More importantly, the electrochemical anodization technique allows the growth

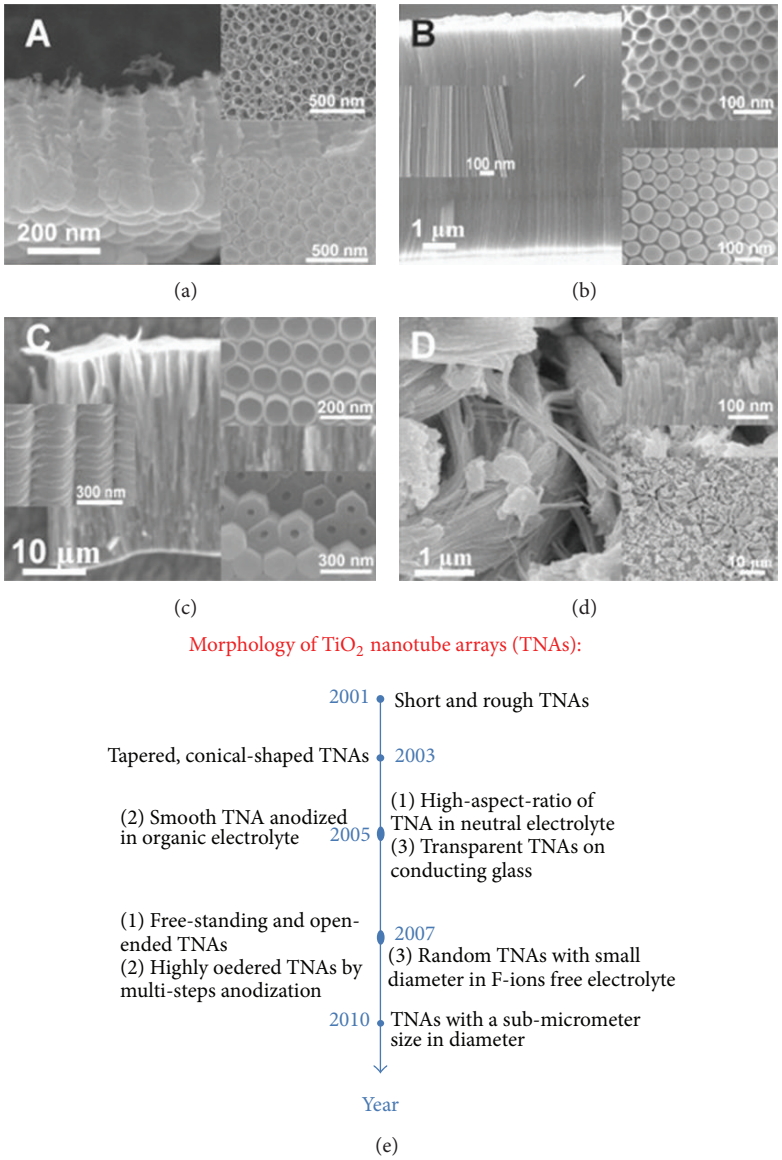

Figure 1: SEM images of TNA layers grown with different electrolytes. (a) Typical morphology obtained in acidic fluoride or HF electrolytes, (b) glycerol/fluoride electrolytes, and (c) ethylene glycol/fluoride electrolytes containing small amount of water. The insets show top views, bottom views, and side walls in detail. (d) Fluoride ions free electrolyte; these tubes grow in disordered bundles within seconds at comparably high anodic potentials. (e) Morphology of new type TNAs with time.

of other oxides with self-ordering nanostructures for several transitional and valve metals, such as Al, Zr, Hf, Nb, Ta, W, and Fe and their alloys TiAl, TiZr, TiNb, Ti_6Al_4V, and so on [8, 10].

In 1999, Zwilling et al. firstly reported the self-ordered TiO_2 nanostructures by a simple electrochemical anodizing process in a fluoride electrolyte [12]. Since then, several anodizing approaches, mainly focused on finding the optimal electrolyte and experimental parameters, have been explored to efficiently achieve high quality self-organized TNAs (Figure 1) [13–18], such as short and rough TNAs [13], tapered and conical-shaped TNAs [18], smooth and high-aspect-ratio TNAs [16, 17], transparent TNAs [19, 20], free-standing and open-ended TNAs [21, 22], highly ordered TNAs by multistep anodization [23, 24], and TNAs with a submicrometer size in diameter [25, 26]. These results demonstrated that structure and morphology of TNAs, including tube diameter, length, wall thickness, and crystallinity, can be controlled by adjusting key parameters such as composition/shape of Ti substrate, electrolyte, pH, temperature, anodization voltage, current, and anodization time. It is, therefore, essential to understand the various factors influencing the characterizations of as-prepared amorphous TNAs. Also, it should be noted that either the annealing posttreatment or the modification of TiO_2-based nanotubes would dominate the corresponding features and the performance of TiO_2-based devices. The aim

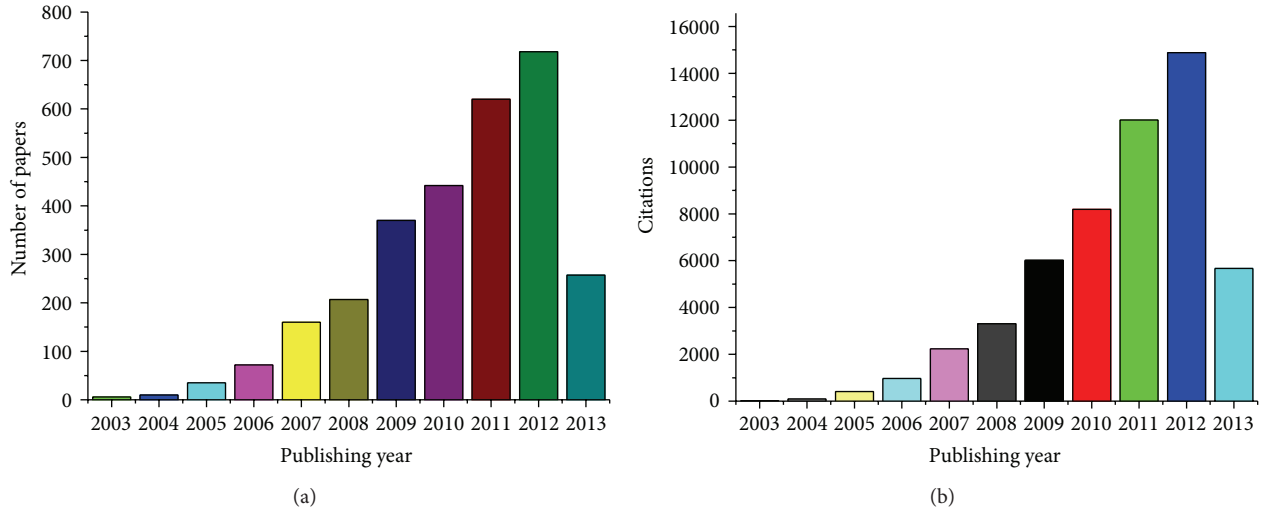

Figure 2: The number of articles (a) published on TNAs formed by electrochemical anodization and corresponding aggregated citations (b). (Statistics analysis was obtained from web of science database on May 30, 2013). Topic: TiO_2 nanotube, with the exclusion of nanotube formed by hydrothermal, sol-gel, and template or carbon nanotube.

is to make the material more suitable for various applications that rely on specific electrical, optical, or chemical properties. In view of electronic properties, annealing to a crystalline structure mainly changes the conductivity and lifetime of charge carriers, while modification with active doping or band gap engineering by introducing other elements targets for the decreasing of the optical band gap, thus enabling a visible-light photoresponse [27].

Based on extensive literatures with regard to self-ordered TNAs, the authors have categorized three broad groups, preparation and formation mechanism, modifications, and applications, which are further subdivided according to their pertinent studies. First, the formation mechanisms and phenomenon of the electrochemical formation of nanopores and nanotubes by a self-ordering process are explained. Among the aforementioned experimental parameters, both electrolyte and anodizing voltage will be focused on and discussed. Then properties and modification of the TNA materials are addressed briefly, including technique examples of doping, noble metal decoration, and semiconductor composite which are to be discussed. Finally, the current stage of knowledge and recent studies on their potential applications, such as photocatalysis, solar cell, water splitting, and other aspects are introduced. Analysis of the physicochemical properties and recent advances in their modification and applications allow the identification of gaps in our knowledge and highlight the need for critical studies in the area of TNAs.

2. Electrochemical Anodization of TNAs

This section presents recent developments on preparation of self-ordered TiO_2 nanoporous and nanotubular, focused primarily on TNAs by electrochemical synthesis. First, the related statistics of the paper about TNAs and phenomenon of the electrochemical formation of nanoporous TiO_2 materials by a self-organization process is introduced. Then some experimental parameters of synthesis, which are responsible for regulation of the morphology of TiO_2 nanostructures, are considered. Finally, the formation mechanisms of TNA materials fabricated by electrochemical anodization are presented.

The progressively increasing research interest in the TNA layers formed by electrochemical oxidation can be easily seen from publication statistics (see Figure 2). Publication number and corresponding aggregated citations increased several times from the first work by Zwilling et al. [12], where only a tube length of a few hundred nanometers with a rough and high degree of disorder morphology could be obtained, to nowadays, where smooth and almost ideally hexagonally ordered arrays can be produced with individual nanotube lengths of hundreds of micrometers [22]. In other words, by controlling the electrochemical anodization parameters of Ti (temperature, potential ramping speed, applied potential, electrolyte species, electrolyte pH, viscosity, aqueous or organic electrolyte, etc.), one can obtain different titanium oxide structures such as a flat compact oxide, a disordered porous layer, a highly self-organized porous layer, or finally a highly self-organized nanotube layer (schematically shown in Figure 3(a)).

2.1. Effects of Fabrication Factors on TNAs

2.1.1. Electrolyte. Hydrofluoric acid (HF) is the firstly and most widely studied electrolyte in titanium anodization to produce TiO_2 nanostructures. Since then, several optimized electrolytes of diverse acid/HF mixed electrolytes are put forward to successful fabrication of TiO_2 nanostructures [14]. A brief summary of various synthesis generations of TNAs is given in Table 1. However, the nanotube length in this first synthesis generation is limited to a few hundred nanometers. This second generation of TNAs was obtained with a remarkably high aspect ratio, in a neutral

Table 1: Brief summary of various synthesis generations of TNAs.

Generation	Electrolyte type	Potential	Anodized time	Morphology	Main Factor	Reference
First generation: inorganic aqueous electrolytes (HF-based electrolyte)	0.5 wt% HF	10–23 V	≥20 min	Short nanotubes Length: 200–500 nm Diameter: 10–100 nm Wall thickness: 13–27 nm	Potential, electrolyte	[13]
	0.3–0.5 wt% HF + 1 M H_3PO_4	1–25 V	2 h	Length: 20–1000 nm Diameter: 15–120 nm Wall thickness: 20 nm		[32]
Second generation: buffered electrolytes (F^--based electrolytes)	1 M Na_2SO_4 + 0.1–1.0 wt% NaF	20 V	10 min–6 h	Roughwall with rings Length: 0.5–2.4 μm Diameter: 100 nm Wall thickness: 12 ± 2 nm	Potential, pH, time	[28]
	1 M $(NH_4)_2SO_4$ + 0.5 wt% NH_4F	20 V	15–30 min	Length: 0.5–1.0 μm Diameter: 90–110 nm		[33]
Third generation: organic electrolyte containing F^- ions	0.5 wt% NH_4F + 0–5 wt% H_2O in glycerol	20 V	13 h	Smooth tube Length: 7.0 μm Diameter: ≈40 nm Wall thickness: 12 ± 2 nm	Potential, water content, time	[17]
	0.1–0.7 wt% NH_4F + 2–3.5 wt% H_2O in ethylene glycol	60 V	216 h	Ultra-long tube Length: 1000 μm Diameter: 120 ± 10 nm		[22]
Fourth generation: fluoride-free electrolytes	0.01–3 M $HClO_4$	1 min	15–60 V	Disordered tubes Length: 30 μm Diameter: 20–40 nm Wall thickness: 10 nm	Electrolyte, time	[30]

type of electrolyte containing fluoride ions, for example, Na_2SO_4/NaF, $(NH_4)_2SO_4$/NH_4F [28, 29]. The reason for the tube-length increase is the limited dissolution on the top of nanotubes in the neutral electrolyte. The nanotubes by the above inorganic electrolyte were always accompanied with a rough external structure, that is, "rings" or "ripples", due to current oscillations along the anodization process. The third-generation electrolyte, organic electrolytes with additions of fluoride salts, allows the construction of smooth and much taller TNAs to the regime of hundreds of micrometers. To date, the highest tube lengths can be up to 1000 μm in organic viscous electrolytes [22]. The pH of the electrolyte and the amount of water greatly influence the morphology, structure, and growth rate of the as-formed TiO_2 nanotube. Recent synthesis development of TNAs by using fluoride-free electrolytes is commonly considered as the fourth generation. The results of this rapid breakdown anodization (RBA) are also bundles of disordered nanotubes that grow within very short times (several minutes) [30, 31]. Depending on electrolyte nature, each electrolyte provides a unique geometrical feature of the nanotubes and consequently varying surface properties; thereby, a selection of electrolyte medium for the TNA fabrication is a primary concern.

2.1.2. Voltage. The anodization voltage influences the morphology of formed nanostructures [34]: pores instead of tubes grow at low voltages of 5 V (Figure 3(b1)), while, at voltages higher than 8 V, the diameter of the TiO_2 nanotubes is also influenced linearly by the applied voltage (Figure 3(b2)). However, at high anodization voltages (>50 V), breakdown events can be observed inside the nanotube resulting in formation of sponge-like structures (Figure 3(b3)). At even higher anodization voltages (>80 V), electropolishing of the samples would take place at a high current density (>100 mA cm^{-2}) in this electrolyte. Therefore, the retardation of breakdown events taking place is vital for the creation of a larger tube diameter. Yin et al. reported that TNAs with larger diameter about 600 nm can be obtained in ethylene glycol electrolytes containing 0.09 M ammonium fluoride and 10 vol% water [35]. Albu and Schmuki further increase the tube diameter to reach 800 nm. However, these tubes are not highly organized and seem loosely assembled in a mesoporous matrix rather than in a neatly defined nanotube array [36]. Recently, Ni et al. successfully demonstrated well-defined, large diameter (680–750 nm) TNAs, with the most uniform and clean morphology by using a higher voltage regime of up to 225 V [25].

2.1.3. Other Factors. In addition to the vital factor of the electrolyte and voltage to the high aspect ratio of the as-prepared nanotube, anodizing time and step, fluoride concentration, and pH and temperature also have a great synergistic effect on the morphology, structure, growth rate, crystallization, and even photoelectrochemical properties of the as-prepared TNAs [8, 37–42]. For example, the transition from porous TiO_2 to a nanotubular structure is not only dependent on water content [43, 44] but also depends on the anodization voltage. The applied voltage directly determines the tube

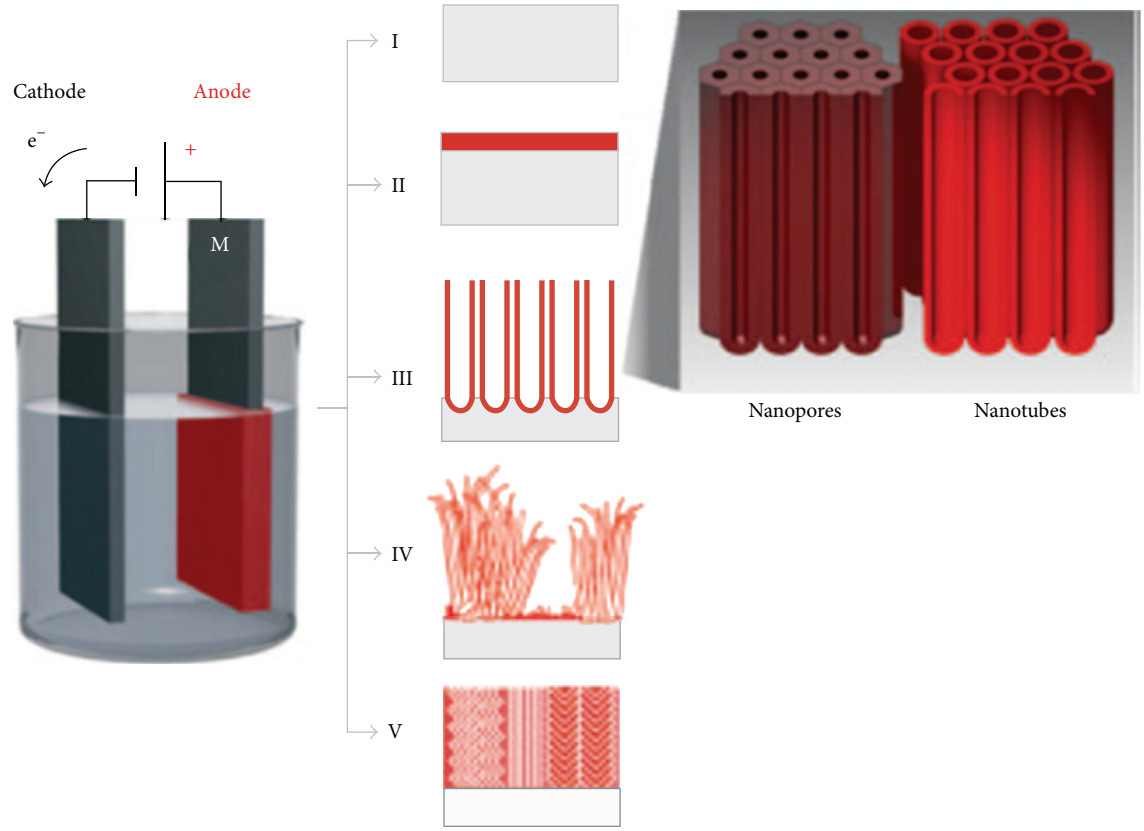

(a) Set-up and mophology

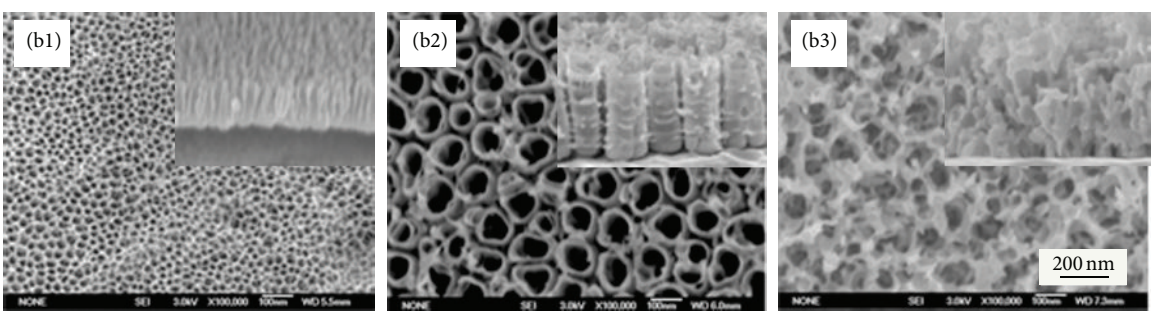

(b) F^- ions electrolyte

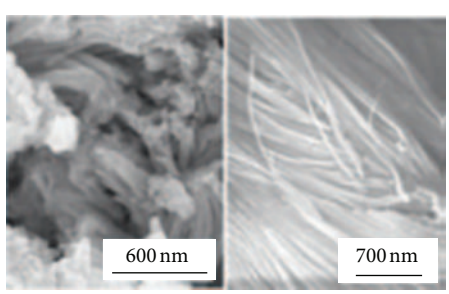

(c) F^- ions free electrolyte

Figure 3: The electrochemical anodization process and typical morphologies: (a) (I) metal electropolishing, (II) formation of compact anodic oxides, (III) self-ordered oxides (nanotubes or nanopores), (IV) ordered nanoporous layers, and (V) rapid (disorganized) oxide nanotube formation. Examples of morphologies of obtained structures: (b) classical ordered TiO_2 nanopores (b1), nanotubes (b2), sponge-like nanoporous structures (b3) anodized in F^- ions containing electrolyte, and (c) disordered TiO_2 nanotubes growing in bundles anodized in F^- ions free electrolyte.

diameters but also strongly influences the rate of TNAs growth, length, and crystallization.

2.2. Growth Mechanism of Anodized TNAs. Self-organized oxide tube arrays or pore arrays can be obtained by an anodization process of a suitable metal, such as transition-metal and valve metal. When metals are exposed to a sufficiently anodic voltage in an electrochemical configuration, an oxidation process will be initiated. Depending mainly on the electrolyte and the particular anodization parameters, essentially three possibilities for reactions exist (see illustration of Figure 3(a)): (I) the metal is continuously dissolved (metal corrosion, or electropolishing), (II) the metal titanium ions (M^{n+}) formed react with O^{2-} (provided by H_2O in the electrolyte) and forma compact oxide layer, and (III) under some electrochemical conditions, competition between dissolution and oxide formation is established leading to porous structures. Under even more specific experimental conditions, a situation is established where self-organized growth of TNAs, formation of thick self-organized mesoporous layers ((IV) in Figure 3(a)), or disordered rapid-breakdown anodization (RBA) of nanotube bundles ((V) in Figures 3(a) and 3(c)) can be observed [10].

In general, it can be concluded that all investigated organized oxide structures grown by anodization in fluoride-containing electrolytes on different metals or alloys seem to follow the same growth mechanism and influence by key factors [7, 8, 10]. Ti was firstly oxidized to form a thin barrier oxide layer of TiO_2 due to interaction of the metal with O^{2-} or OH^- ions. Then, the presence of electric field and fluoride ion led to the creation of random pits and small pores. Finally, self-ordered TNAs formed resulted from the allowance of optimal pores to grow continuously and thicker wall to split by chemical dissolution. The tube diameter is determined by the anodization voltage, etching of the tubes (and thus the achievable length of the tubes) depends on the chemical resistance of the oxide against fluoride etching (in a particular electrolyte), and water plays the key role for providing the oxygen source for tube growth, splits pores into tubes, and is responsible for sidewall rings formation. Obviously, anodization techniques in fluoride-containing electrolytes allow the fabrication of nanostructured oxide layers on an extremely wide range of valve metals and alloys that enable the controllable fabrication of mixed nanostructured oxides with virtually endless possibilities to create enhanced properties and therefore have also a very high and widely unexplored technological potential.

3. Modification of TNA

TiO_2 semiconductor material plays the most important role owing to its excellent chemical and physical properties. However, the higher band gap of the annealed TiO_2 between the valence band (VB) and conduction band (CB) makes them inactive under visible irradiation (Figure 4(a)). In this regard, great efforts have been made to extend the absorption of the wavelength range into the visible light range via the modification of its electronic and optical properties. Over the past decade, considerable effort has gone into the modification of TiO_2 to exploit the solar spectrum much better. For example, dye sensitization and doping TiO_2 using either nonmetal anions or metal cations is one of the typical approaches that have been largely applied (Figure 4(b)). Coupling TiO_2 with a narrow band gap semiconductor represents another approach (Figure 4(c)). Decoration of noble metal particles with surface plasmon effects allows for more efficient charge transfer (Figure 4(d)). In all of these cases, essentially three beneficial effects are expected: (1) to promote the photogenerated separation between the electron hole (e^-/h^+) and to prevent their recombination, (2) surface plasmon effects, leading to field enhancement in the vicinity of noble metal particles and thus allowing more efficient charge transfer and effective visible light absorption, and (3) heterojunction formation that either changes the band bending (metal clusters on semiconductor) or provides suitable energy levels for synergic absorption and charge separation for enhanced utilization of solar energy.

3.1. Doping. Doping or sensitizing pure TiO_2 by introducing a secondary electronically active species into the lattice for sensitizing TiO_2 to visible light, which promotes the harness of the main range of the solar spectrum and also can ensure the charge trapping for effective photogenerated carries separation (Figure 4(b)). Asahi et al. firstly reported that the nitrogen doping on TiO_2 by sputtering in nitrogen containing gas mixture improves the photoelectrochemical reactivity under visible light irradiation [45]. In the following years, other doping species, such as a number of nonmetals like carbon [46], fluorine [47], sulphur [48], and boron [49], have been introduced into TiO_2 by using various techniques. The results indicated that the visible light absorption and photoelectrochemical activities of these doped crystallized TNAs were not only influenced by the energy gaps and the distributions of impurity states but were also affected by the locations of Femi levels and the energies of band gap edges [50, 51]. Among all these anions, the doping of TNAs with nitrogen or carbon has been found to receive significant attention [52–59]. Highly promising N-doping approach for TNAs includes one-step direct electrochemical anodization of a TiN alloy or growing TNAs in a solution containing doping species [59]. High-energy ion implantation or sputtering in an atmosphere of doping species following an annealing process has been verified to be an effective doping method [60, 61]. However, these methods require special high energy accelerators be operated in a high vacuum environment and the doping depth be limited to several micrometers. Thermal treatment of TNAs in gas atmospheres of the doping species is regarded as a facile one-step doping technique [62, 63]. Moreover, such surface-modified nanotubes shows a significant photoresponse in the visible range compared to nonmodified nanotubes.

At the same time, TiO_2 doped with transition metal cations (e.g., Fe, V, Cr, and Mn) [64–66] have also been reported to widen visible light absorption range, increase the redox potential of the photogenerated radicals, and enhance the conversion efficiency by extending the life of photogenerated electrons and holes. Although the metal cation doping of

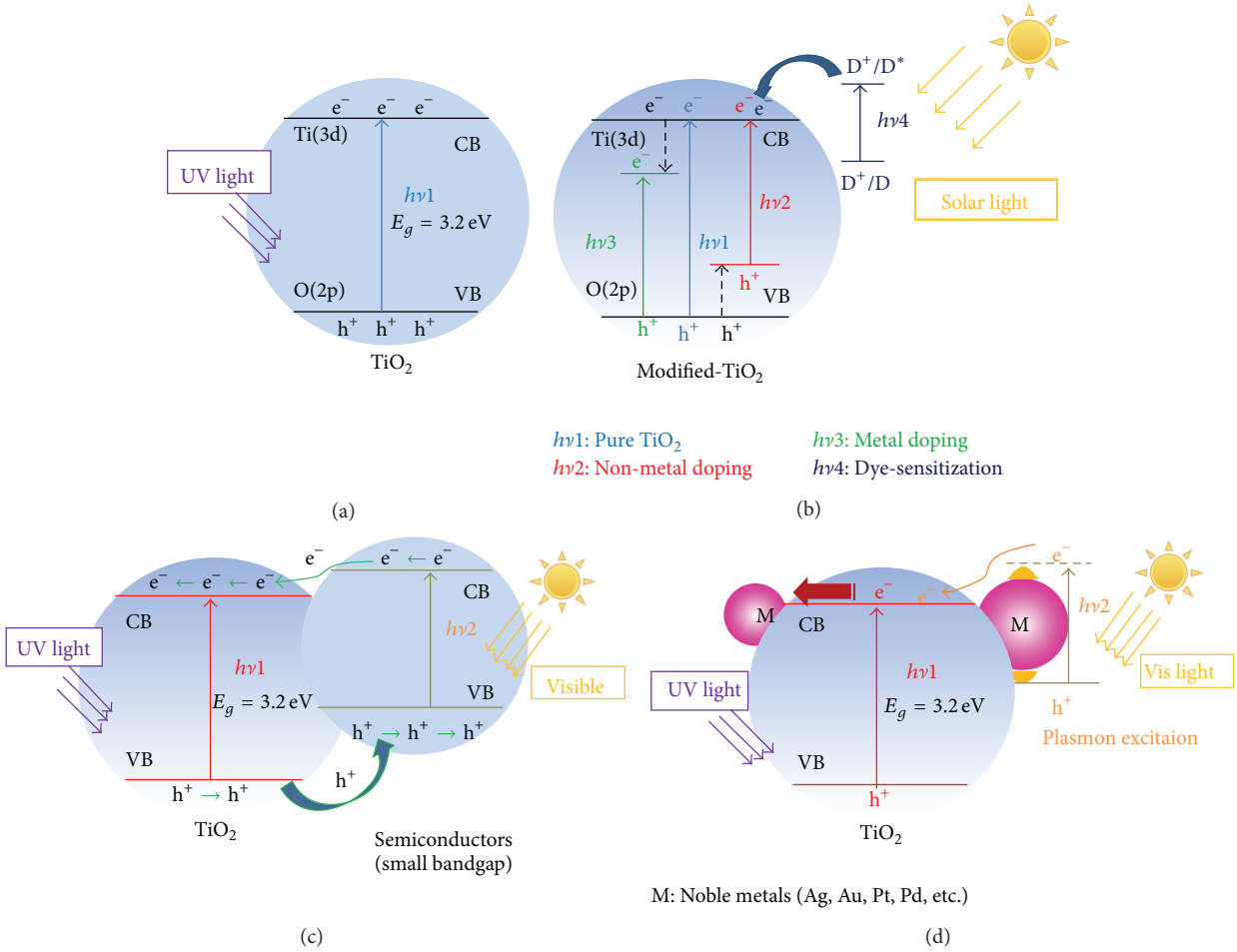

Figure 4: Schematic of energy level of pure TiO_2 (a) and corresponding modification ((b)–(d)). (b) Doping or dye-sensitization, semiconductors (c), and noble metals (d) coupling.

TiO_2 improves the visible light absorption of the host material to increase photocatalytic activity, a large amount of research also concluded that, when the doping content is excessively high, extra defects can also act as recombination centers to decrease the photocatalytic activity. This adverse effect could be avoided by a suitable doping amount or annealing the doped TiO_2.

3.2. Semiconductor Composites. In the past decade, many efforts have been devoted to extend the light absorption range of TNAs and to alleviate the charge carrier recombination, such as formation of semiconductor heterostructures with visible light excited narrow band gap semiconductors (Figure 4(c)), for example, CdS, CdSe, and so forth [67–69]. However, it must be expected that the stability of many applied narrow band gap semiconductors fails quickly, not only due to corrosion or photocorrosion, but also due to instability of some of the materials under applied voltage [70].

TNAs essentially provide a very versatile tool to fill or decorate other semiconductors to form composite electrode [71–73]. One of the most followed-up schemes to establishing p-n heterojunctions for high efficient photoelectrocatalytic devices is the direct deposition of p-type semiconductor onto TNAs [74, 75]. For example, Wang et al. prepared Cu_2O/TiO_2 p-n heterojunction photoelectrodes by depositing p-type Cu_2O nanoparticles on n-type TiO_2 nanotube arrays via an ultrasonication-assisted sequential chemical bath deposition (Figures 5(A)–5(D)) [76]. The largely improved separation of photogenerated electrons and holes was revealed by photocurrent measurements. Consequently, p-n Cu_2O/TiO_2 heterojunction photoelectrodes exhibited a more effective photoconversion capability than single TiO_2 nanotubes (Figure 5(E)). Furthermore, Cu_2O/TiO_2 composite photoelectrodes also possessed superior photoelectrocatalytic activity and stability in rhodamine B degradation with a synergistic effect between electricity and visible light irradiation (Figures 5(F)–5(H)).

TiO_2 nanoparticle decoration on TNAs can be obtained by slow hydrolysis of $TiCl_4$ precursors [20]. In DSSCs, the TNAs decorated with TiO_2 nanoparticles show higher solar cell efficiency in comparison to pure TNAs. The TiO_2 nanoparticles can be deposited inside as well as outside of the tube wall by hydrolysis of a $TiCl_4$ solution, which significantly increases the surface area and thereby improves the solar-cell efficiency [77].

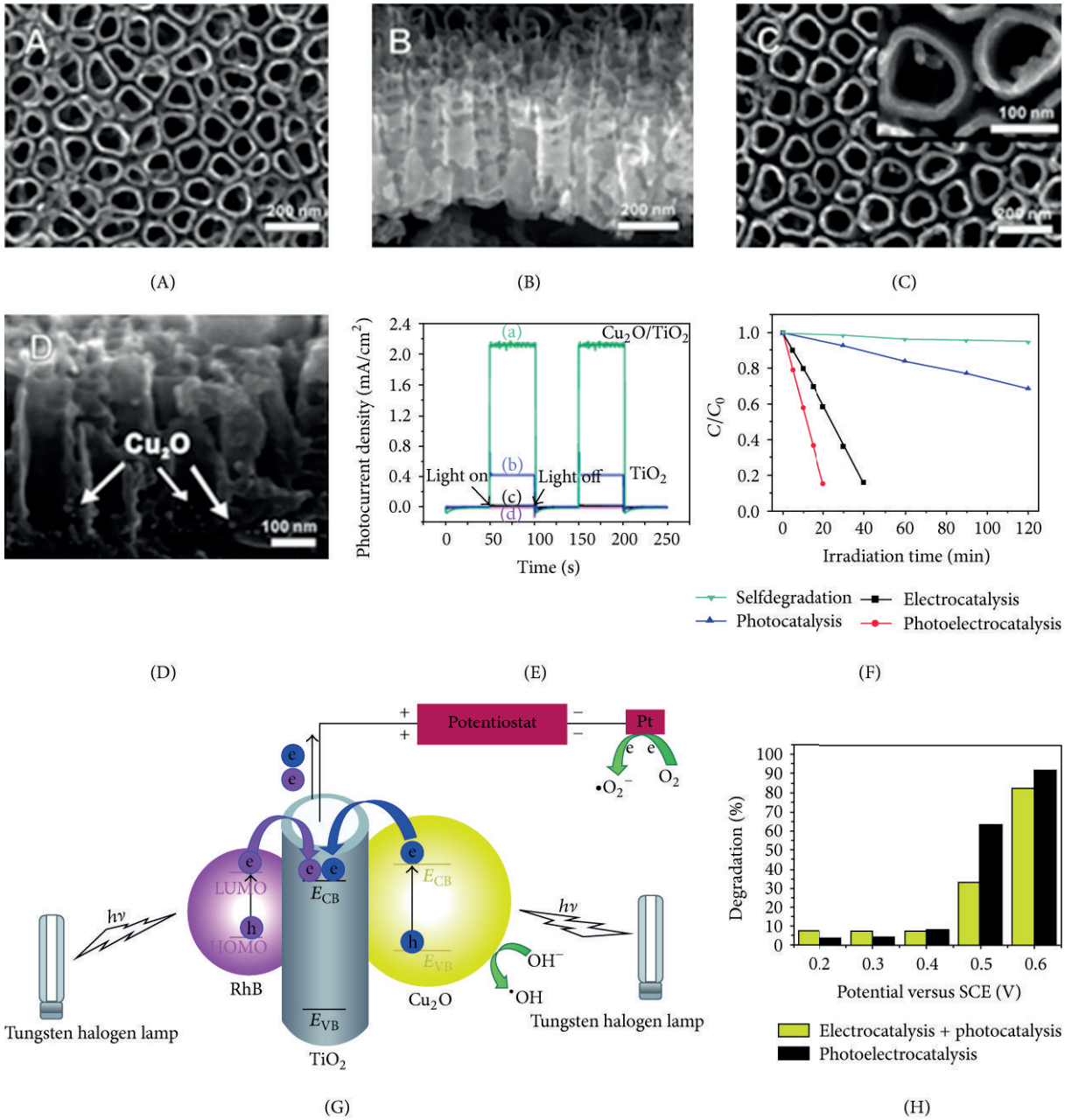

Figure 5: SEM image of TNAs (A, B) and Cu_2O/TiO_2 NTAs (C). TEM image of Cu_2O/TiO_2 NTAs (D). (E) Photoresponse of Cu_2O/TiO_2 NTAs (a, c) and TNAs (b, d) with (a, b) or without (c, d) a bias potential of 0.5 V (versus SCE) under one sun visible light irradiation. (F) Comparison of photocatalytic, electrocatalytic, and photoelectrcatalytic degradation of RhB under visible light irradiation for Cu_2O/TiO_2 NTAs. (G) Schematic illustration of photoelectrocatalytic degradation of RhB under visible light irradiation. (H) Comparison of RhB degradation efficiency using Cu_2O/TiO_2 NTAs in the process of photoelectrocatalysis (right) with the sum of photocatalysis and electrolysis (left).

3.3. Noble Metal Nanoparticles Decoration. Another approach related to TiO_2 modification is the decoration of TiO_2 surfaces with noble metal nanoparticles (such as, Ag, Au, Pt, Pd, or alloys). Noble metal loading is proved to be an effective way to restrain the recombination of photogenerated electron/hole pairs resulting in photoelectrocatalytic activity enhancement (Figure 4(d)) [78–83]. Moreover, recent study reveals that noble metal nanoparticles can improve the photoresponse ability of TiO_2 in the visible region based on the surface plasmon resonance (SPR) [84, 85]. It is known that the free electrons of metal can collectively oscillate induced by light irradiation; when the oscillation frequency of light electromagnetic field is in accordance with the free electrons, the SPR effect is generated and light energy is coupled to the metal nanoparticles in the meantime. For example, Ag nanoparticles can be deposited on the tube wall by a photocatalytically reducing process on a TiO_2 surface with UV illumination [86]. Other metal nanoparticles

are preferably deposited by UHV evaporation, sputtering, or chemical/electrochemical deposition techniques [78, 87]. Pt/TiO_2 or Pd/TiO_2 nanotubes also shows a significantly higher photocatalytic activity and water splitting performance compared with plain nanotubes [79, 80].

3.4. Other Aspects. More recent work deals with decoration with grapheme [88, 89], Ag/AgCl [85], or AgBr [90] onto TiO_2 to enhance their photocatalytic activity. Amorphous nanotubes synthesized by room-temperature electrochemical anodization are also reported to be annealed in oxygen-rich (O_2), oxygen-deficient (Ar, N), and reducing (H_2) environments, to modify TiO_2 crystal structure, morphology, and electronic properties.

4. Applications of TNA Materials

Porous and tubular titanium dioxide nanostructures have attracted great interest because of their applications in photocatalysis, photovoltaic cells (solar cell), water splitting, biomedical scaffold, wetting template, and other aspects. This porous TiO_2 material is desirable for these applications because of its multifunctional semiconductor properties that are based on its excellent physical and chemical behavior, along with its specific nanostructured architecture that owns it high surface area, high surface activity and fast carries transfer path.

4.1. Photocatalyst. One of the most practical applications of TiO_2 today is in photocatalytic toxic pollutant decomposing. After Fujishima and Honda reported for the first time on light-induced water electrochemical photolysis on TiO_2 surfaces, this functional semiconductor material has been intensively investigated for applications in heterogeneous catalysis [91]. Since then, TiO_2 has shown to be an excellent photocatalyst due to the fact that the material has a set of good properties of long-term stability, low-cost preparation, and a strong enough oxidizing power to be useful for the decomposition of unwanted organic compounds [92–96].

The basic principles involved in the photocatalytic mechanism are shown in Figure 6. UV light promotes electrons excited from the valence band to the conduction band, and then separated holes and electrons will be transported to the semiconductor-environment interface and react with adsorbed molecules. In aqueous solution, highly reactive $^{\bullet}OH$ radicals are generated by charge exchange at the valence band ($H_2O + h^+ \rightarrow {}^{\bullet}OH$), whereas excited electrons at the conduction band mainly reduce dissolved molecular oxygen to super-oxide anions ($O_2 + e^- \rightarrow O_2^-$). These $^{\bullet}OH$ radicals and O_2^- ions are able to virtually oxidize all organic materials to CO_2 and H_2O.

Among many TiO_2 nanotubes preparation strategies, the electrochemical anodization process as a simple, cheap, and rapid growth method has been widely utilized to large-scaled preparation of TiO_2 nanotubes with controllable size and morphology [13, 15, 28]. However, smooth surface, relative low surface area, and the amorphous structure of the obtained anodic TiO_2 nanotubes result in low light utilization efficiency and photogenerated charges separation efficiency, thus leading to the poor photocatalytic activity [92]. Many efforts have been made to enhance the photocatalytic activity of the anodic TiO_2 nanotubes. For example, annealing of anodic TiO_2 nanotubes in conventional air environment contributes to converting the amorphous TiO_2 into anatase, which can efficiently enhance the photocatalytic performance [93]. In order to achieve maximal decomposition efficiency, in addition to crystallized TNAs with adequate band edge positions, rapid charge separation, and high quantum yield, a large area of the catalyst is desired. Crystallized TNAs with suitable posttreatment processes fit these requirements comparably well [92–94, 97]. In previous work, we used anatase TNAs as the photoanode and verified that such novel TNAs showed higher efficiencies than common TiO_2 nanoparticle photocatalysts (Figures 6(b)–6(d)) [93]. Moreover, the annealing temperature has also greatly influenced the crystal structure and photocatalytic activity of TNAs [96, 98, 99].

Up to today, many posttreatment methods for the construction of high efficient TNAs photocatalyst, such as annealing in specific gas atmosphere [100, 101], hydrothermal treatment [102, 103], and vapor-thermal treatment [104], have been generally used to synthesize special crystallized TNAs with high devices performance. Annealing the anodic TNAs through a derivative annealing method in a sealed container with specific environments, such as oxygen-rich (O_2), oxygen-deficient (Ar, N), and other reducing (H_2) gas, can modify the TNAs crystal structure, morphology, and electronic properties and influence the photocatalytic performance [105–107]. However, this method is expensive and has high energy consumption. Recently, considerable efforts have been shifted to the construction of hierarchical architectures based on the 1D TNA nanostructure templates. For example, a simple hydrothermal treatment was adopted to reduce the heat treatment temperature for the construction of anatase TiO_2 nanostructure due to a dissolution-recrystallization transformation of amorphous anodic TNAs, and the resultant hierarchical TiO_2 structures decorated with TiO_2 nanoparticles possess a higher surface area than that of smooth TNAs, which showed enhanced photocatalytic performance [103]. Compared to the heteroelement doping (e.g., N, F, and C) of TNAs, very recently, in situ self-doping with homospecies (e.g., Ti^{3+}, and H^+) by an electrochemical reduction treatment has been emerging as a rational solution to enhance TiO_2 photoactivity within both UV and visible light regions [105]. Despite the great efforts contributed by many groups, well-designed posttreatment strategies for constructing desired crystalline structures with high surface area and anatase phase for highly efficient pollutant degradation have still been an attractive ongoing task.

In addition to many posttreatment methods of the anodic TNAs, the direct decoration of noble metal or semiconductor nanoparticles on crystallized TNAs is also verified to be beneficial for photocatalytic activity enhancement [78, 86, 97, 108, 109]. For example, we reported that a pulse current deposition of Ag nanoparticles modified TNAs was used as the photoanode for photoelectrocatalytic decomposition of methyl orange (MO) pollutant [108]. In this case, we found

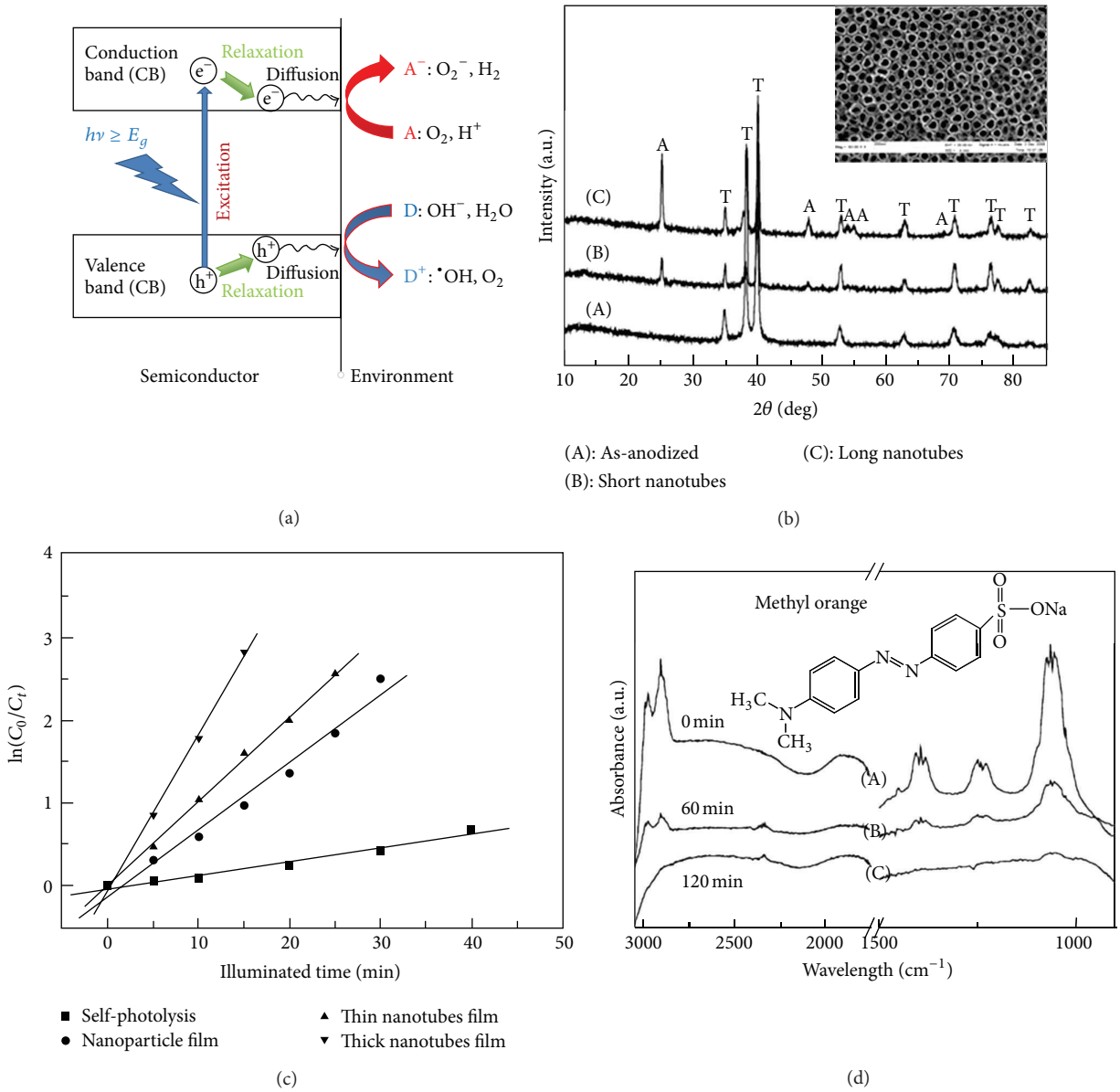

Figure 6: (a) Scheme of photo-induced processes at a TiO_2 semiconductor/electrolyte interface. Light ($h\nu$) excites valence band electron to conduction band. Electrons and holes react with environment acceptor (A) and/or donor (D). (b) XRD patterns of TNAs film. (c) Comparison of photocatalytic degradation rates of MO for nanoparticle film and two different thicknesses of nanotubes films (A) under the high-pressure mercury lamp illumination. (d) ATR–IR spectra of MO before and after photocatalytic degradation.

that photocatalytic activity of titania nanotube layers can be significantly increased by applying an external bias [108]. Xie et al. performed photocatalytic decomposition of a model organic pollutant (methylene blue) in self-organized TNAs decorated with Ag and CdS nanoparticles. The CdS-Ag-TiO_2 three-component nanotube arrays system exhibited superior synergy effect on both photoelectrochemical and photocatalytic activities compared to those of the pure TiO_2 and Ag or CdS modified TiO_2 systems [109].

4.2. Solar Cells. One of the most promising applications of TiO_2 today is in dye-sensitized solar cells (DSSCs), a concept introduced by O'Regan and Grötzel in 1991 [110]. The classical DSSCs operate with sintered or compressed nanoparticulate TiO_2 layers as electron harvesting material. Compared to agglomerate TiO_2 nanoparticle layer containing a high number of grain boundaries that can act as recombination sites, the new architecture of TNAs by electrochemical anodization has been verified to be an ideal photoanode in photoelectrocatalytic devices due to its improved charge-collection efficiency and short pathway for the photogenerated excitons along the vertically aligned tubes to the conducting substrate. As such, it may be expected that optimized TNAs can significantly increase the solar energy conversion efficiency.

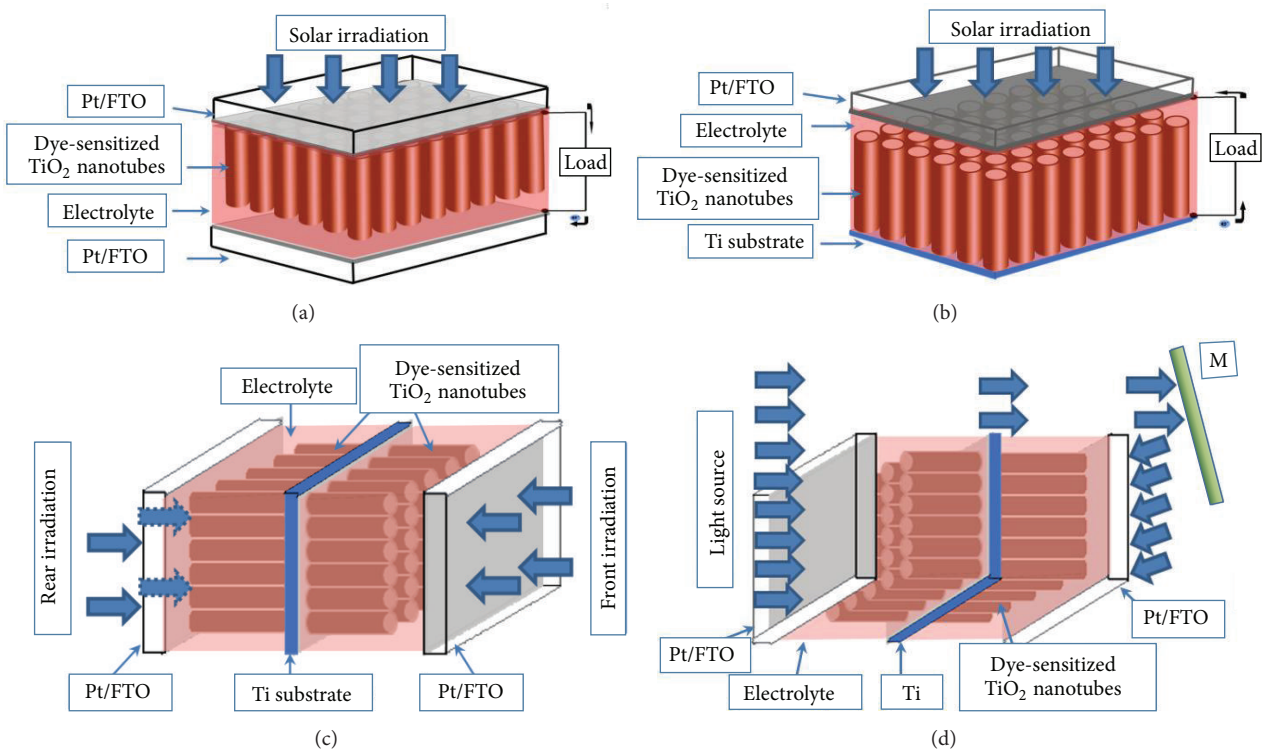

Figure 7: Schematic illustration of front-side illuminated DSSC based on transparent TNAs on FTO substrate (a), backside illuminated DSSC based on TNAs on Ti substrate (b), two light sources illuminated DSSC based on both sides of TNAs on Ti substrate (c), and parallel configuration DSSC with one light source irradiation on double-sided TNAs by using a dielectric mirror (d).

4.2.1. Dye-Sensitized Solar Cells (DSSCs). Owing to well-defined structural parameters and enhanced electronic properties, highly ordered TNAs have been employed to substitute TiO_2 nanoparticles for use in DSSCs [111]. Mor et al. reported the integration of TiO_2 nanoparticles modified transparent nanotube array (360 nm in length) architecture in fluorine-doped tin oxide (FTO) glass for front-side illuminated dye solar cell and displayed a photoconversion efficiency (PCE) of 2.9% (Figure 7(a)) [20]. They also observed that solar cells constructed by longer nanotubes formed from titanium foils (backside illumination) have superior charge transfer efficiency and more dyes absorption in comparison with solar cells fabricated with transparent short nanotubes formed on FTO glass. However, the overall power conversion efficiency of dye-sensitized TNA solar cells remained relatively low as a result of incomplete coverage of dye molecules on the TNAs and insufficient infiltration of electrolyte into nanotubes. For example, backside illuminated N719 DSSC based on 6 μm long TNAs film on titanium substrate shows a PCE of 4.24% under AM 1.5 sunlight source (Figure 7(b)) [112]. To further improve the performance of dye-sensitized TNA solar cells, efforts have been directed toward the improvement of dye loading, charge transport, light absorption, and optimization of TiO_2 nanostructures [77, 111, 113–115]. Recently, Liu and Misra applied double-sided TNAs for bifacial dye-sensitized solar cells and reported that a photocurrent density of such bifacial DSSCs was almost twice that of one-sided illumination (Figure 7(c)) [115]. Sun et al. demonstrated a new parallel configuration of DSSCs using double-sided TNAs as the photoanode and a dielectric mirror for sunlight to be irradiated on both sides of TNA photoanode (Figure 7(d)) [116]. An average 70% increment in photocurrent and 30% enhancement in PCE were obtained relative to those of the single cells. Zheng et al. constructed a layer-by-layer hierarchical photoanode consisting of TiO_2 particles and free-standing TNAs for DSSCs with a PCE of 8.80%, which exhibited increased light-harvesting efficiency, longer electron lifetimes, and more efficient electron extraction than those in single particle film or nanotube array based devices [117].

4.2.2. Quantum Dots Sensitized Solar Cells (QDSSCs). Typically, CdX (X = S, Se, and Te) QDs with size-dependent band gaps provide new opportunities for harvesting light energy yin the visible and infrared regions of solar light [118]. In addition, through the impact ionization effect, it is possible to generate multiple excitons from single-photon absorption in QDs [119]. In the case of the QDSSCs, excited electrons of CdX nanocrystals are injected into a large band gap semiconductor (e.g., TiO_2 and ZnO), and holes reacted with a redox couple. Recently, Sudhagar et al. prepared the CdS/CdSe coupled TiO_2 nanofibrous electrode with a maximum PCE of 2.69% [120], while Shen et al. fabricated a CdSe QDs-sensitized TNAs photoelectrode with an optimal photovoltaic conversion efficiency of 1.80% [121]. Recently, we report that a PCE of 2.74% is achieved on novel QDSSCs

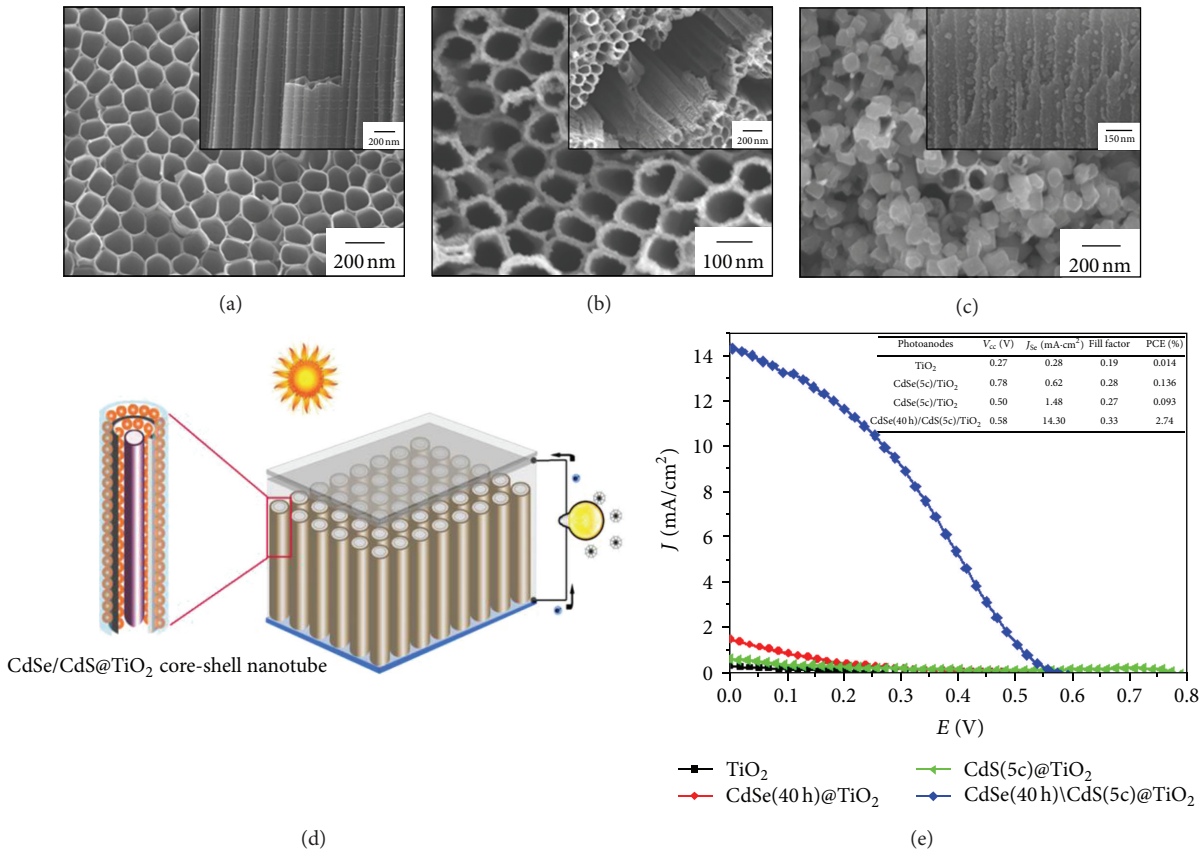

Figure 8: Top view and cross-sectional SEM images of TNAs (a), CdS@TNAs (b), and CdSe/CdS@TNAs (c). (d) Schematic of CdSe/CdS@TNAs for QDSSC. (e) J-V characteristics of corresponding QDSSCs.

based on the CdS/CdSe QDs cosensitized TiO_2 nanocrystal arrays by a sealed annealing process (Figure 8) [67]. We found that such coupled CdS/CdSe QDSSC exhibited a greatly enhanced short-circuit current density (Figure 8(e)) as compared to pure TNAs and single CdS or CdSe QDSSC because the combination of CdS and CdSe QDs has a complementary effect in light harvest and surface area increment, and a stepwise band edge level structure of CdSe/CdS@TNAs beneficiated for electron injection into TNAs. Sun et al. reported a novel CdS QDs sensitized TNA photoelectrodes by a sequential chemical bath deposition technique and found that the CdS QDs among the TNAs significantly increased the QDSSC efficiency up to 4.15% [122]. These results clearly demonstrate that the unique nanotube structure can facilitate the propagation and kinetic separation of photogenerated charges, suggesting potentially important applications of the inorganic TNA QDSSCs in solar cell applications. However, compared to DSSCs with PCE up to 12%, QDSSCs have not been demonstrated as an efficient inorganic dye than expected. Therefore, great efforts are still needed to inhibit charge recombination at the semiconductor surface for the efficiency improvement of QDSSCs [123].

4.3. Water Splitting. Considering that the principle of photoelectrolysis for water splitting is the same with photocatalysis, TNAs are considered as good candidates for high efficient water splitting (see Table 2). The photoelectrolysis process using TiO_2 nanotube cells as a photoanode is as follows: when the photoanode is immersed in water and exposed to light irradiation, it absorbs photonic energy over its band gap energy; then, electron-hole pairs are generated in it. The generated holes oxidize O^{2-} ions from absorbed water and produce oxygen gas and an electric current that moves through the external circuit to the conducting cathode in which it reduces H^+ ions to produce hydrogen gas. Recently, TNAs prepared by anodization of titanium have attracted extensive interest in photocatalytic water splitting. Mor et al. find a hydrogen generation rate of 96 μmol/h/cm^2 for the utilization of nanotube array (224 nm in length) for water splitting under a constant voltage bias of −0.4 V (versus Ag/AgCl) [124]. Recently, we reported an enhanced hydrogen generation rate of 150 μmol/h/cm^2 by a three-step electrochemical anodized TNAs with a regular porous top layer (Figures 9(a) and 9(b)) [125]. Moreover, we found that palladium quantum dots sensitized TNAs exhibited highly efficient photocatalytic hydrogen production rate of 592 μmol/h/cm^2 under 320 mW/cm^2 irradiation (Figures 9(c)–9(h)) [79]. In general, the hydrogen production rate is greatly depending on the electrolyte, external bias, light intensity, and TiO_2 morphology and structure. Therefore, it is important to

Table 2: Summary of TNAs based materials in water splitting.

Photoanode	Light intensity (mW/cm^2)	Electrolyte	Photocurrent (mA/cm^2)	Water splitting ($\mu mol/h/cm^2$)	Reference
C-TNAs	N/A; 500 W Xe lamp	0.1 M Na_2S + 0.02 M Na_2SO_3	N/A	1.6 (0.040 $mL/h/cm^2$)	[126]
TNAs	70; 300 W Xe lamp	1 M KOH	0.58@0.6 V versus NHE	7.1 (0.178 $mL/h/cm^2$)	[127]
C-TNAs (C-containing TiO_2 based nanotube arrays)	12.7, 300 W Xe Lamp	1 M KOH	1.96@0 V versus Ag/AgCl	11.28 (0.282 $mL/h/cm^2$)	[128]
TNAs with etching pretreatment	87, 300 W AM 1.5	1 M KOH	1.78@1.23 V RHE	34.8 (0.87 $mL/h/cm^2$)	[129]
Ru/TNAs@0.05 at% Ru	100	1 M KOH	1.78@0.4 V versus Ag/AgCl	45 (1.08 $mL/h/cm^2$)	[130]
TNAs (224 nm length, 34 nm wall thickness)	100	1 M KOH	13.0@0 V versus Ag/AgCl	96 (2.30 $mL/h/cm^2$)	[124]
TNAs	110	1 M KOH + 0.5 M H_2SO_4	4.95	97 (2.32 $mL/h/cm^2$)	[131]
TNAs	74	1 M KOH	N/A	140 (3.28 $mL/h/cm^2$)	[132]
Leaf-like TiO_2/TNAs	320	2 M Na_2CO_3 + 0.5 M EG	16.3@0.9 V versus SCE	150	[125]
Pyrococcus furiosus/TNAs	74	1 M KOH	N/A	234.88	[133]
TNAs	74	1 M KOH	32.8@1.5 V versus Ag/AgCl	250	[134]
TNAs (three-step anodization)	320	2 M Na_2CO_3 + 0.5 M EG	24@−0.3 V versus SCE	420	[135]
Pt@TNAs	320	2 M Na_2CO_3 + 0.5 M EG	24.2@−0.3 V versus SCE	495	[80]
Pd@TNAs	320	2 M Na_2CO_3 + 0.5 M EG	26.8@0.9 V versus SCE	592	[79]

optimize these parameters and fundamentally understand their possible correlations to clarify the approaches toward to construct high efficient cell for hydrogen generation.

4.4. Other Applications. As mentioned above, another special electrochemical feature of TNAs or some other TiO_2 nanotube based materials is its ability to serve as a host for small ions insertion, typically hydrogen ion or lithium ion, into the lattice, leading to the drastic change of electronic and optical properties for potential applications in lithium-battery [4, 136, 137], electrochromic devices [138, 139], and supercapacitor [140, 141]. The kinetics, magnitude, and reversibility of the ion insertion and electrochromic reaction strongly depend on the ion diffusion length and therefore on geometry of the electrode surface. Due to the specific vertical alignment of the TNAs, a very high contrast can be obtained using vertically oriented nanotubes. By deposition of Ag nanoparticles on the TNAs, a material can be created that shows considerable photochromic contrast [142]. Furthermore, the TNA has also been proved to be good support for Pt or Pt/Ru catalysts for enhanced methanol electrooxidation [143, 144].

Other applications of the TNAs for biomedical implant are wetting template, target hydrogen sensing, electrochemical detection, and photogenerated cathode anticorrosion [145–147]. For instance, the combination of organic modification with a controllable photocatalytic reaction of TiO_2 was used to create microscale patterning surfaces with any desired wettability value. Wetting micropatterns with different physical or chemical properties have frequently acted as templates for fabricating various functional materials in a large scale [148]. Moreover, wetting patterns with tailored and reversible adhesion for microfluidic devices and microdroplet manipulation have also been reported [149]. For example, Ag@TNA micropatterns show not only the high-throughput molecular sensing feature with high sensitive, reproducible performance but also show promising targeted antibacterials properties [148]. For gas sensing, Varghese et al. have shown instant resistance response in order of several magnitudes for the TNA layer upon exposure to 1000 ppm H_2 containing nitrogen atmospheres at room temperature [145].

The applications of TNAs can significantly be expanded if secondary material can successfully be deposited into the tubes. The TNAs can also be converted to other titanates $MTiO_3$ (M = Sr, Pd, Zr) with specific bioactive, piezoelectric or ferroelectric properties and keep with its original tube structure by a simple hydrothermal process in the corresponding precursor solution or a direct anodizing process in appropriate alloy substrates [150–153].

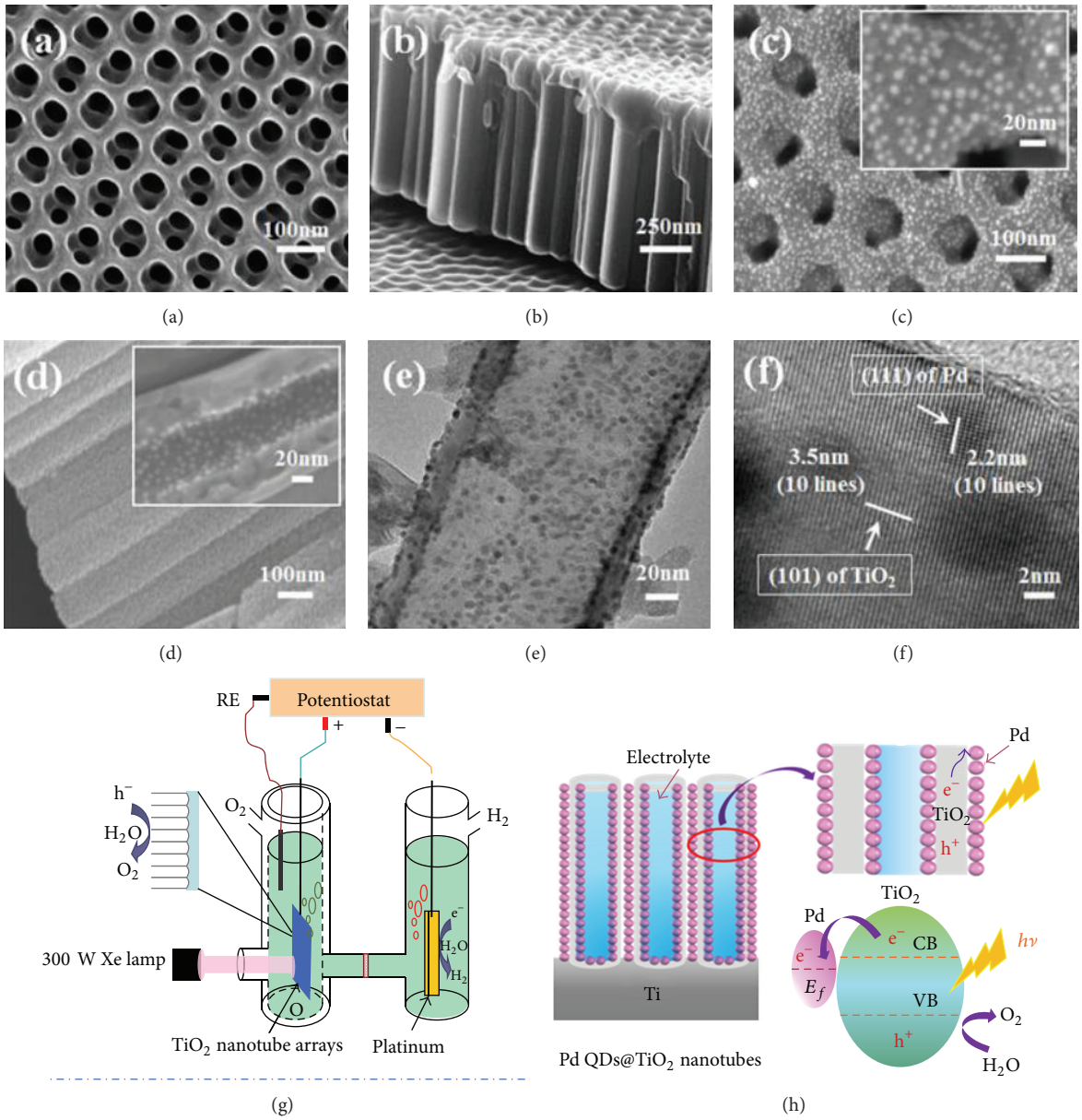

Figure 9: Top and cross-sectional SEM images of pure TNAs ((a), (b)) and Pd QDs@TNAs ((c), (d)). The insets show the corresponding magnified images. TEM images of TNAs coated with Pd QDs. (g) Schematic of TNAs on photoelectrolytic water splitting for hydrogen production. (h) Schematic illustration of TNAs deposited with Pd QDs and the charge transfer process from TiO_2 to Pd (lower right panel).

5. Conclusion

Till now, a large number of fundamental studies and application-oriented researches and developments are extensively carried out by many researchers for this low-dimensional nanomaterial due to the expected various properties of TiO_2 (high surface area and controllable nanotube dimensions, geometries, and surface chemistry). This work has presented the recent progress of preparation and modification on the electrochemically anodized TNA materials. These unique low dimensional nanostructure materials have been shown to have many favourable properties for potential applications, including pollutant photocatalytic decomposition, photovoltaic cells, biomedical scaffold, and wetting template. On the other hand, extensive challenges to fabricate high quality TNAs and develop various oxide nanotubes have been continued. For instance, rapid and high-efficient synthesis of anatase TNAs and other multicomponent nanotubes under ambient low-temperature conditions have recently been reported [154]. Some other aspects aim to encompass the new progress of TiO_2 for an efficient utilization in photocatalytic or photovoltaic applications under visible light, emphasize the future trends of TiO_2 in the environment and/or energy related fields, and suggest new research directions, including preparation aspects for the development of this promising material [155].

Acknowledgments

The authors thank the Alexander von Humboldt (AvH) Foundation of Germany, the EU Microcare project (FP7-PEOPLE-2009-IRSES/247641), and the Natural Science Foundation of Jiangsu Province of China (Grant no. BK20130313) for the financial support of this work. We also acknowledge support from the Priority Academic Program Development of Jiangsu Higher Education Institutions (PAPD).

References

[1] S. Iijima, "Helical microtubules of graphitic carbon," *Nature*, vol. 354, no. 6348, pp. 56–58, 1991.

[2] J. C. Hulteen and C. R. Martin, "A general template-based method for the preparation of nanomaterials," *Journal of Materials Chemistry*, vol. 7, no. 7, pp. 1075–1087, 1997.

[3] M. S. Sander, M. J. Côté, W. Gu, B. M. Kile, and C. P. Tripp, "Template-assisted fabrication of dense, aligned arrays of titania nanotubes with well-controlled dimensions on substrates," *Advanced Materials*, vol. 16, no. 22, pp. 2052–2057, 2004.

[4] D. V. Bavykin, J. M. Friedrich, and F. C. Walsh, "Protonated titanates and TiO_2 nanostructured materials: synthesis, properties, and applications," *Advanced Materials*, vol. 18, no. 21, pp. 2807–2824, 2006.

[5] X. M. Sun and Y. D. Li, "Synthesis and characterization of ion-exchangeable titanate nanotubes," *Chemistry A: European Journal*, vol. 9, no. 10, pp. 2229–2238, 2003.

[6] T. Kasuga, M. Hiramatsu, A. Hoson, T. Sekino, and K. Niihara, "Formation of titanium oxide nanotube," *Langmuir*, vol. 14, no. 12, pp. 3160–3163, 1998.

[7] G. K. Mor, O. K. Varghese, M. Paulose, K. Shankar, and C. A. Grimes, "A review on highly ordered, vertically oriented TiO_2 nanotube arrays: fabrication, material properties, and solar energy applications," *Solar Energy Materials and Solar Cells*, vol. 90, no. 14, pp. 2011–2075, 2006.

[8] J. M. Macak, H. Tsuchiya, A. Ghicov et al., "TiO_2 nanotubes: self-organized electrochemical formation, properties and applications," *Current Opinion in Solid State and Materials Science*, vol. 11, no. 1-2, pp. 3–18, 2007.

[9] C. A. Grimes, "Synthesis and application of highly ordered arrays of TiO_2 nanotubes," *Journal of Materials Chemistry*, vol. 17, no. 15, pp. 1451–1457, 2007.

[10] P. Roy, S. Berger, and P. Schmuki, "TiO_2 nanotubes: synthesis and applications," *Angewandte Chemie—International Edition*, vol. 50, no. 13, pp. 2904–2939, 2011.

[11] Z. R. Tian, J. A. Voigt, J. Liu, B. McKenzie, and H. Xu, "Large oriented arrays and continuous films of TiO_2-based nanotubes," *Journal of the American Chemical Society*, vol. 125, no. 41, pp. 12384–12385, 2003.

[12] V. Zwilling, E. Darque-Ceretti, A. Boutry-Forveille, D. David, M. Y. Perrin, and M. Aucouturier, "Structure and physicochemistry of anodic oxide films on titanium and TA6V alloy," *Surface and Interface Analysis*, vol. 27, no. 7, pp. 629–637, 1999.

[13] D. Gong, C. A. Grimes, O. K. Varghese et al., "Titanium oxide nanotube arrays prepared by anodic oxidation," *Journal of Materials Research*, vol. 16, no. 12, pp. 3331–3334, 2001.

[14] R. Beranek, H. Hildebrand, and P. Schmuki, "Self-organized porous titanium oxide prepared in H_2SO_4/HF electrolytes," *Electrochemical and Solid-State Letters*, vol. 6, no. 3, pp. B12–B14, 2003.

[15] Y.-K. Lai, L. Sun, J. Zuo, and C.-J. Lin, "Electrochemical fabrication and formation mechanism of TiO_2 nanotube arrays on metallic titanium surface," *Acta Physico Chimica Sinica*, vol. 20, no. 9, pp. 1063–1066, 2004.

[16] J. M. Macák, H. Tsuchiya, and P. Schmuki, "High-aspect-ratio TiO_2 nanotubes by anodization of titanium," *Angewandte Chemie—International Edition*, vol. 44, no. 14, pp. 2100–2102, 2005.

[17] J. M. Macak, H. Tsuchiya, L. Taveira, S. Aldabergerova, and P. Schmuki, "Smooth anodic TiO_2 nanotubes," *Angewandte Chemie—International Edition*, vol. 44, no. 45, pp. 7463–7465, 2005.

[18] G. K. Mor, O. K. Varghese, M. Paulose, N. Mukherjee, and C. A. Grimes, "Fabrication of tapered, conical-shaped titania nanotubes," *Journal of Materials Research*, vol. 18, no. 11, pp. 2588–2593, 2003.

[19] G. K. Mor, O. K. Varghese, M. Paulose, and C. A. Grimes, "Transparent highly ordered TiO_2 nanotube arrays via anodization of titanium thin films," *Advanced Functional Materials*, vol. 15, no. 8, pp. 1291–1296, 2005.

[20] G. K. Mor, K. Shankar, M. Paulose, O. K. Varghese, and C. A. Grimes, "Use of highly-ordered TiO_2 nanotube arrays in dye-sensitized solar cells," *Nano Letters*, vol. 6, no. 2, pp. 215–218, 2006.

[21] S. P. Albu, A. Ghicov, J. M. Macak, R. Hahn, and P. Schmuki, "Self-organized, free-standing TiO_2 nanotube membrane for flow-through photocatalytic applications," *Nano Letters*, vol. 7, no. 5, pp. 1286–1289, 2007.

[22] M. Paulose, H. E. Prakasam, O. K. Varghese et al., "TiO_2 nanotube arrays of 1000 μm length by anodization of titanium foil: phenol red diffusion," *Journal of Physical Chemistry C*, vol. 111, no. 41, pp. 14992–14997, 2007.

[23] J. M. Macak, S. P. Albu, and P. Schmuki, "Towards ideal hexagonal self-ordering of TiO_2 nanotubes," *Physica Status Solidi*, vol. 1, no. 5, pp. 181–183, 2007.

[24] G. Zhang, H. Huang, Y. Zhang, H. L. W. Chan, and L. Zhou, "Highly ordered nanoporous TiO_2 and its photocatalytic properties," *Electrochemistry Communications*, vol. 9, no. 12, pp. 2854–2858, 2007.

[25] J. H. Ni, K. Noh, C. J. Frandsen et al., "Preparation of near micrometer-sized TiO_2 nanotube arrays by high voltage anodization," *Materials Science & Engineering C*, vol. 33, no. 1, pp. 259–264, 2013.

[26] S. P. Albu and P. Schmuki, "TiO_2 nanotubes grown in different organic electrolytes: two-size self-organization, single vs. double-walled tubes, and giant diameters," *Physica Status Solidi*, vol. 4, no. 8-9, pp. 215–217, 2010.

[27] A. El Ruby Mohamed and S. Rohani, "Modified TiO_2 nanotube arrays (TNTAs): progressive strategies towards visible light responsive photoanode, a review," *Energy & Environmental Science*, vol. 4, no. 4, pp. 1065–1086, 2011.

[28] J. M. MacAk, K. Sirotna, and P. Schmuki, "Self-organized porous titanium oxide prepared in Na_2SO_4/NaF electrolytes," *Electrochimica Acta*, vol. 50, no. 18, pp. 3679–3684, 2005.

[29] Q. Cai, M. Paulose, O. K. Varghese, and C. A. Grimes, "The effect of electrolyte composition on the fabrication of self-organized titanium oxide nanotube arrays by anodic oxidation," *Journal of Materials Research*, vol. 20, no. 1, pp. 230–236, 2005.

[30] R. Hahn, J. M. Macak, and P. Schmuki, "Rapid anodic growth of TiO_2 and WO_3 nanotubes in fluoride free electrolytes," *Electrochemistry Communications*, vol. 9, no. 5, pp. 947–952, 2007.

[31] K.-I. Ishibashi, R.-T. Yamaguchi, Y. Kimura, and M. Niwano, "Fabrication of titanium oxide nanotubes by rapid and homogeneous anodization in perchloric acid/ethanol mixture," *Journal of the Electrochemical Society*, vol. 155, no. 1, pp. K10–K14, 2008.

[32] S. Bauer, S. Kleber, and P. Schmuki, "TiO_2 nanotubes: tailoring the geometry in H_3PO_4/HF electrolytes," *Electrochemistry Communications*, vol. 8, no. 8, pp. 1321–1325, 2006.

[33] L. V. Taveira, J. M. Macák, H. Tsuchiya, L. F. P. Dick, and P. Schmuki, "Initiation and growth of self-organized TiO_2 nanotubes anodically formed in $NH_4F/(NH_4)_2SO_4$ electrolytes," *Journal of the Electrochemical Society*, vol. 152, no. 10, pp. B405–B410, 2005.

[34] Y. Lai, X. Gao, H. Zhuang, J. Huang, C. Lin, and L. Jiang, "Designing superhydrophobic porous nanostructures with tunable water adhesion," *Advanced Materials*, vol. 21, no. 37, pp. 3799–3803, 2009.

[35] H. Yin, H. Liu, and W. Z. Shen, "The large diameter and fast growth of self-organized TiO_2 nanotube arrays achieved via electrochemical anodization," *Nanotechnology*, vol. 21, no. 3, Article ID 035601, 2010.

[36] S. P. Albu and P. Schmuki, "TiO_2 nanotubes grown in different organic electrolytes: two-size self-organization, single vs. double-walled tubes, and giant diameters," *Physica Status Solidi*, vol. 4, no. 8-9, pp. 215–217, 2010.

[37] S. P. Albu, P. Roy, S. Virtanen, and P. Schmuki, "Self-organized TiO_2 nanotube arrays: critical effects on morphology and growth," *Israel Journal of Chemistry*, vol. 50, no. 4, pp. 453–467, 2010.

[38] Y. Wang, Y. Wu, Y. Qin et al., "Rapid anodic oxidation of highly ordered TiO_2 nanotube arrays," *Journal of Alloys and Compounds*, vol. 509, no. 14, pp. L157–L160, 2011.

[39] A. Ghicov and P. Schmuki, "Self-ordering electrochemistry: a review on growth and functionality of TiO_2 nanotubes and other self-aligned MOx structures," *Chemical Communications*, no. 20, pp. 2791–2808, 2009.

[40] C. W. Lai and S. Sreekantan, "Photoelectrochemical performance of smooth TiO_2 nanotube arrays: effect of anodization temperature and cleaning methods," *International Journal of Photoenergy*, vol. 2012, Article ID 356943, 11 pages, 2012.

[41] Y.-C. Lim, Z. Zainal, W.-T. Tan, and M. Z. Hussein, "Anodization parameters influencing the growth of titania nanotubes and their photoelectrochemical response," *International Journal of Photoenergy*, vol. 2012, Article ID 638017, 2012.

[42] J. Wang and Z. Q. Lin, "Anodic formation of ordered TiO_2 nanotube arrays: effects of electrolyte temperature and anodization potential," *Journal of Physical Chemistry C*, vol. 113, no. 10, pp. 4026–4030, 2009.

[43] Y. Lai, H. Zhuang, L. Sun, Z. Chen, and C. Lin, "Self-organized TiO_2 nanotubes in mixed organic-inorganic electrolytes and their photoelectrochemical performance," *Electrochimica Acta*, vol. 54, no. 26, pp. 6536–6542, 2009.

[44] Y.-Y. Song and P. Schmuki, "Modulated TiO_2 nanotube stacks and their use in interference sensors," *Electrochemistry Communications*, vol. 12, no. 4, pp. 579–582, 2010.

[45] R. Asahi, T. Morikawa, T. Ohwaki, K. Aoki, and Y. Taga, "Visible-light photocatalysis in nitrogen-doped titanium oxides," *Science*, vol. 293, no. 5528, pp. 269–271, 2001.

[46] J. H. Park, S. Kim, and A. J. Bard, "Novel carbon-doped TiO_2 nanotube arrays with high aspect ratios for efficient solar water splitting," *Nano Letters*, vol. 6, no. 1, pp. 24–28, 2006.

[47] D. Li, H. Haneda, N. K. Labhsetwar, S. Hishita, and N. Ohashi, "Visible-light-driven photocatalysis on fluorine-doped TiO_2 powders by the creation of surface oxygen vacancies," *Chemical Physics Letters*, vol. 401, no. 4-6, pp. 579–584, 2005.

[48] T. Umebayashi, T. Yamaki, H. Itoh, and K. Asai, "Band gap narrowing of titanium dioxide by sulfur doping," *Applied Physics Letters*, vol. 81, no. 3, pp. 454–456, 2002.

[49] N. Lu, X. Quan, J. Li, S. Chen, H. Yu, and G. Chen, "Fabrication of boron-doped TiO_2 nanotube array electrode and investigation of its photoelectrochemical capability," *Journal of Physical Chemistry C*, vol. 111, no. 32, pp. 11836–11842, 2007.

[50] P. Zhou, J. G. Yu, and Y. X. Wang, "The new understanding on photocatalytic mechanism of visible-lightresponse N-S codoped anatase TiO_2 by first-principles," *Applied Catalysis B*, vol. 142-143, pp. 45–53, 2013.

[51] J. G. Yu, P. Zhou, and Q. Li, "New insight into the enhanced visible-light photocatalytic activities of B-, C- and B/C-doped anatase TiO_2 by first-principles," *Physical Chemistry Chemical Physics*, vol. 15, no. 29, pp. 12040–12047, 2013.

[52] R. P. Antony, T. Mathews, K. Panda, B. Sundaravel, S. Dash, and A. K. Tyagi, "Enhanced field emission properties of electrochemically synthesized self-aligned nitrogen-doped TiO_2 nanotube array thin films," *Journal of Physical Chemistry C*, vol. 116, no. 31, pp. 16740–16746, 2012.

[53] H.-Y. Wang, X.-J. Xu, J.-H. Wei, R. Xiong, and J. Shi, "Structure and raman investigations of nitrogen-doped TiO_2 nanotube arrays," *Solid State Phenomena*, vol. 181-182, pp. 422–425, 2012.

[54] S. P. Li, S. W. Lin, J. J. Liao, N. Q. Pan, D. H. Li, and J. B. Li, "Nitrogen-doped TiO_2 nanotube arrays with enhanced photoelectrochemical property," *International Journal of Photoenergy*, vol. 2012, Article ID 794207, 7 pages, 2012.

[55] Y.-K. Lai, J.-Y. Huang, H.-F. Zhang et al., "Nitrogen-doped TiO_2 nanotube array films with enhanced photocatalytic activity under various light sources," *Journal of Hazardous Materials*, vol. 184, no. 1–3, pp. 855–863, 2010.

[56] Q. Xue, Y. J. Guan, Z. B. Wang, and S. L. Bai, "Preparation of nitrogen doped TiO_2 nanotube arrays and its visible light responsive photocatalytic properties," *Acta Chimica Sinica*, vol. 68, no. 16, pp. 1603–1608, 2010.

[57] G. Liu, F. Li, D.-W. Wang et al., "Electron field emission of a nitrogen-doped TiO_2 nanotube array," *Nanotechnology*, vol. 19, no. 2, Article ID 025606, 2008.

[58] D. Kim, H. Tsuchiya, S. Fujimoto, F. Schmidt-Stein, and P. Schmuki, "Nitrogen-doped TiO_2 mesosponge layers formed by anodization of nitrogen-containing Ti alloys," *Journal of Solid State Electrochemistry*, vol. 16, no. 1, pp. 89–92, 2012.

[59] D. Kim, S. Fujimoto, P. Schmuki, and H. Tsuchiya, "Nitrogen doped anodic TiO_2 nanotubes grown from nitrogen-containing Ti alloys," *Electrochemistry Communications*, vol. 10, no. 6, pp. 910–913, 2008.

[60] A. Ghicov, J. M. Macak, H. Tsuchiya et al., "TiO_2 nanotube layers: dose effects during nitrogen doping by ion implantation," *Chemical Physics Letters*, vol. 419, no. 4–6, pp. 426–429, 2006.

[61] A. Ghicov, J. M. Macak, H. Tsuchiya et al., "Ion implantation and annealing for an efficient N-doping of TiO_2 nanotubes," *Nano Letters*, vol. 6, no. 5, pp. 1080–1082, 2006.

[62] R. P. Vitiello, J. M. Macak, A. Ghicov, H. Tsuchiya, L. F. P. Dick, and P. Schmuki, "N-Doping of anodic TiO_2 nanotubes using heat treatment in ammonia," *Electrochemistry Communications*, vol. 8, no. 4, pp. 544–548, 2006.

[63] R. Hahn, A. Ghicov, J. Salonen, V.-P. Lehto, and P. Schmuki, "Carbon doping of self-organized TiO_2 nanotube layers by thermal acetylene treatment," *Nanotechnology*, vol. 18, no. 10, Article ID 105604, 2007.

[64] Y.-F. Tu, S.-Y. Huang, J.-P. Sang, and X.-W. Zou, "Preparation of Fe-doped TiO_2 nanotube arrays and their photocatalytic activities under visible light," *Materials Research Bulletin*, vol. 45, no. 2, pp. 224–229, 2010.

[65] A. Ghicov, B. Schmidt, J. Kunze, and P. Schmuki, "Photoresponse in the visible range from Cr doped TiO_2 nanotubes," *Chemical Physics Letters*, vol. 433, no. 4–6, pp. 323–326, 2007.

[66] Z. Xu and J. Yu, "Visible-light-induced photoelectrochemical behaviors of Fe-modified TiO_2 nanotube arrays," *Nanoscale*, vol. 3, no. 8, pp. 3138–3144, 2011.

[67] Y. K. Lai, Z. Q. Lin, D. J. Zheng, L. F. Chi, R. G. Du, and C. J. Lin, "CdSe/CdS quantum dots co-sensitized TiO_2 nanotube array photoelectrode for highly efficient solar cells," *Electrochimica Acta*, vol. 79, pp. 175–181, 2012.

[68] G. S. Li, L. Wu, F. Li, P. P. Xu, D. Q. Zhang, and H. X. Li, "Photoelectrocatalytic degradation of organic pollutants via a CdS quantum dots enhanced TiO_2 nanotube array electrode under visible light irradiation," *Nanoscale*, vol. 5, no. 5, pp. 2118–2125, 2013.

[69] D. H. Li, N. Q. Pan, J. J. Liao, X. K. Cao, and S. W. Lin, "Effects of surface modification of TiO_2 nanotube arrays on the performance of CdS quantum-dot-sensitized solar cells," *International Journal of Photoenergy*, vol. 2013, Article ID 129621, 10 pages, 2013.

[70] Z.-Q. Lin, Y.-K. Lai, R.-G. Hu, J. Li, R.-G. Du, and C.-J. Lin, "A highly efficient ZnS/CdS@TiO_2 photoelectrode for photogenerated cathodic protection of metals," *Electrochimica Acta*, vol. 55, no. 28, pp. 8717–8723, 2010.

[71] J. M. Macak, B. G. Gong, M. Hueppe, and P. Schmuki, "Filling of TiO_2 nanotubes by self-doping and electrodeposition," *Advanced Materials*, vol. 19, no. 19, pp. 3027–3031, 2007.

[72] C. W. Lai and S. Sreekantan, "Preparation of hybrid WO_3-TiO_2 nanotube photoelectrodes using anodization and wet impregnation: improved water-splitting hydrogen generation performance," *International Journal of Hydrogen Energy*, vol. 38, no. 5, pp. 2156–2166, 2013.

[73] C. W. Lai and S. Sreekantan, "Incorporation of WO_3 species into TiO_2 nanotubes via wet impregnation and their water-splitting performance," *Electrochimica Acta*, vol. 87, pp. 294–302, 2013.

[74] Y. Hou, X. Li, X. Zou, X. Quan, and G. Chen, "Photoeletrocatalytic activity of a Cu_2O-loaded self-organized highly oriented TiO_2 nanotube array electrode for 4-chlorophenol degradation," *Environmental Science & Technology*, vol. 43, no. 3, pp. 858–863, 2009.

[75] G. Dai, J. Yu, and G. Liu, "Synthesis and enhanced visible-light photoelectrocatalytic activity of P-N junction BiOI/TiO_2 nanotube arrays," *Journal of Physical Chemistry C*, vol. 115, no. 15, pp. 7339–7346, 2011.

[76] M. Y. Wang, L. Sun, Z. Q. Lin, J. H. Cai, K. P. Xie, and C. J. Lin, "p-n Heterojunction photoelectrodes composed of Cu_2O-loaded TiO_2 nanotube arrays with enhanced photoelectrochemical and photoelectrocatalytic activities," *Energy & Environmental Science*, vol. 6, no. 4, pp. 1211–1220, 2013.

[77] M. Ye, X. Xin, C. Lin, and Z. Lin, "High efficiency dye-sensitized solar cells based on hierarchically structured nanotubes," *Nano Letters*, vol. 11, no. 8, pp. 3214–3220, 2011.

[78] I. Paramasivam, J. M. Macak, and P. Schmuki, "Photocatalytic activity of TiO_2 nanotube layers loaded with Ag and Au nanoparticles," *Electrochemistry Communications*, vol. 10, no. 1, pp. 71–75, 2008.

[79] M. D. Ye, J. J. Gong, Y. K. Lai, C. J. Lin, and Z. Q. Lin, "High-efficiency photoelectrocatalytic hydrogen generation enabled by palladium quantum dots-sensitized TiO_2 nanotube arrays," *Journal of the American Chemical Society*, vol. 134, no. 38, pp. 15720–15723, 2012.

[80] Y. Lai, J. Gong, and C. Lin, "Self-organized TiO_2 nanotube arrays with uniform platinum nanoparticles for highly efficient water splitting," *International Journal of Hydrogen Energy*, vol. 37, no. 8, pp. 6438–6446, 2012.

[81] L. Yang, D. He, Q. Cai, and C. A. Grimes, "Fabrication and catalytic properties of Co-Ag-Pt nanoparticle-decorated titania nanotube arrays," *Journal of Physical Chemistry C*, vol. 111, no. 23, pp. 8214–8217, 2007.

[82] P. F. Fu, P. Y. Zhang, and J. Li, "Simultaneous elimination of formaldehyde and ozone byproduct using noble metal modified TiO_2 films in the gaseous VUV photocatalysis," *International Journal of Photoenergy*, vol. 2012, Article ID 174862, 8 pages, 2012.

[83] Y. Tang, P. Wee, Y. Lai et al., "Hierarchical TiO_2 nanoflakes and nanoparticles hybrid structure for improved photocatalytic activity," *Journal of Physical Chemistry C*, vol. 116, no. 4, pp. 2772–2780, 2012.

[84] Z. Xu, J. Yu, and G. Liu, "Enhancement of ethanol electrooxidation on plasmonic Au/TiO_2 nanotube arrays," *Electrochemistry Communications*, vol. 13, no. 11, pp. 1260–1263, 2011.

[85] J. Yu, G. Dai, and B. Huang, "Fabrication and characterization of visible-light-driven plasmonic photocatalyst Ag/AgCl/TiO_2 nanotube arrays," *Journal of Physical Chemistry C*, vol. 113, no. 37, pp. 16394–16401, 2009.

[86] L. Sun, J. Li, C. Wang et al., "Ultrasound aided photochemical synthesis of Ag loaded TiO_2 nanotube arrays to enhance photocatalytic activity," *Journal of Hazardous Materials*, vol. 171, no. 1–3, pp. 1045–1050, 2009.

[87] Y. Lai, H. Zhuang, K. Xie et al., "Fabrication of uniform Ag/TiO_2 nanotube array structures with enhanced photoelectrochemical performance," *New Journal of Chemistry*, vol. 34, no. 7, pp. 1335–1340, 2010.

[88] C. Liu, Y. Teng, R. Liu et al., "Fabrication of graphene films on TiO_2 nanotube arrays for photocatalytic application," *Carbon*, vol. 49, no. 15, pp. 5312–5320, 2011.

[89] P. Wang, J. Wang, X. F. Wang et al., "One-step synthesis of easy-recycling TiO_2-rGO nanocomposite photocatalysts with enhanced photocatalytic activity," *Applied Catalysis B*, vol. 132, pp. 452–459, 2013.

[90] Y. Hou, X. Li, Q. Zhao, G. Chen, and C. L. Raston, "Role of hydroxyl radicals and mechanism of escherichia coli inactivation on Ag/AgBr/TiO_2 nanotube array electrode under visible light irradiation," *Environmental Science & Technology*, vol. 46, no. 7, pp. 4042–4050, 2012.

[91] A. Fujishima and K. Honda, "Electrochemical photolysis of water at a semiconductor electrode," *Nature*, vol. 238, no. 5358, pp. 37–38, 1972.

[92] Y. Lai, L. Sun, Y. Chen, H. Zhuang, C. Lin, and J. W. Chin, "Effects of the structure of TiO_2 nanotube array on Ti substrate on its photocatalytic activity," *Journal of the Electrochemical Society*, vol. 153, no. 7, pp. D123–D127, 2006.

[93] H.-F. Zhuang, C.-J. Lin, Y.-K. Lai, L. Sun, and J. Li, "Some critical structure factors of titanium oxide nanotube array in its photocatalytic activity," *Environmental Science & Technology*, vol. 41, no. 13, pp. 4735–4740, 2007.

[94] I. Paramasivam, H. Jha, N. Liu, and P. Schmuki, "A Review of photocatalysis using self-organized TiO_2 nanotubes and other ordered oxide nanostructures," *Small*, vol. 8, no. 20, pp. 3073–3103, 2012.

[95] K. Nakata and A. Fujishima, "TiO_2 photocatalysis: design and applications," *Journal of Photochemistry and Photobiology C*, vol. 13, no. 3, pp. 169–189, 2012.

[96] J. Yu and B. Wang, "Effect of calcination temperature on morphology and photoelectrochemical properties of anodized titanium dioxide nanotube arrays," *Applied Catalysis B*, vol. 94, no. 3-4, pp. 295–302, 2010.

[97] J. M. Macak, M. Zlamal, J. Krysa, and P. Schmuki, "Self-organized TiO_2 nanotube layers as highly efficient photocatalysts," *Small*, vol. 3, no. 2, pp. 300–304, 2007.

[98] Y. J. Xin, H. L. Liu, J. J. Li, Q. H. Chen, and D. Ma, "Influence of post-treatment temperature of TNTa photoelectrodes on photoelectrochemical properties and photocatalytic degradation of 4-nonylphenol," *Journal of Solid State Chemistry*, vol. 199, pp. 49–55, 2013.

[99] O. K. Varghese, D. Gong, M. Paulose, C. A. Grimes, and E. C. Dickey, "Crystallization and high-temperature structural stability of titanium oxide nanotube arrays," *Journal of Materials Research*, vol. 18, no. 1, pp. 156–165, 2003.

[100] P. M. Hosseinpour, E. Panaitescu, D. Heiman, L. Menon, and L. H. Lewis, "Toward tailored functionality of titania nanotube arrays: interpretation of the magnetic-structural correlations," *Journal of Materials Research*, vol. 28, no. 10, pp. 1304–1310, 2013.

[101] S. J. Liu, Q. Ma, F. Gao, S. H. Song, and S. Gao, "Relationship between N-doping induced point defects by annealing in ammonia and enhanced thermal stability for anodized titania nanotube arrays," *Journal of Alloys and Compounds*, vol. 543, pp. 71–78, 2012.

[102] Q. Wang, X. Yang, X. Wang, M. Huang, and J. Hou, "Synthesis of N-doped TiO_2 mesosponge by solvothermal transformation of anodic TiO_2 nanotubes and enhanced photoelectrochemical performance," *Electrochimica Acta*, vol. 62, pp. 158–162, 2012.

[103] W. Krengvirat, S. Sreekantan, A. F. M. Noor et al., "Low-temperature crystallization of TiO_2 nanotube arrays via hot water treatment and their photocatalytic properties under visible-light irradiation," *Materials Chemistry and Physics*, vol. 137, no. 3, pp. 991–998, 2013.

[104] J. Yu, G. Dai, and B. Cheng, "Effect of crystallization methods on morphology and photocatalytic activity of anodized TiO_2 nanotube array films," *Journal of Physical Chemistry C*, vol. 114, no. 45, pp. 19378–19385, 2010.

[105] X. Lu, G. Wang, T. Zhai et al., "Hydrogenated TiO_2 nanotube arrays for supercapacitors," *Nano Letters*, vol. 12, no. 3, pp. 1690–1696, 2012.

[106] X. Zhang, Y. Ling, L. Liao, Z. Niu, S. Chen, and C. Zhao, "Effect of heat treatment on the photoelectrocatalytic performance of TiO_2 nanotube array film," *Chinese Journal of Catalysis*, vol. 31, no. 10, pp. 1300–1304, 2010.

[107] P. Xiao, D. Liu, B. B. Garcia, S. Sepehri, Y. Zhang, and G. Cao, "Electrochemical and photoelectrical properties of titania nanotube arrays annealed in different gases," *Sensors and Actuators B*, vol. 134, no. 2, pp. 367–372, 2008.

[108] K. Xie, L. Sun, C. Wang et al., "Photoelectrocatalytic properties of Ag nanoparticles loaded TiO_2 nanotube arrays prepared by pulse current deposition," *Electrochimica Acta*, vol. 55, no. 24, pp. 7211–7218, 2010.

[109] K. Xie, Q. Wu, Y. Wang et al., "Electrochemical construction of Z-scheme type CdS-Ag-TiO_2 nanotube arrays with enhanced photocatalytic activity," *Electrochemistry Communications*, vol. 13, no. 12, pp. 1469–1472, 2011.

[110] B. O'Regan and M. Grätzel, "A low-cost, high-efficiency solar cell based on dye-sensitized colloidal TiO_2 films," *Nature*, vol. 353, no. 6346, pp. 737–740, 1991.

[111] K. Zhu, N. R. Neale, A. Miedaner, and A. J. Frank, "Enhanced charge-collection efficiencies and light scattering in dye-sensitized solar cells using oriented TiO_2 nanotubes arrays," *Nano Letters*, vol. 7, no. 1, pp. 69–74, 2007.

[112] M. Paulose, K. Shankar, O. K. Varghese, G. K. Mor, B. Hardin, and C. A. Grimes, "Backside illuminated dye-sensitized solar cells based on titania nanotube array electrodes," *Nanotechnology*, vol. 17, no. 5, pp. 1446–1448, 2006.

[113] K. Zhu, T. B. Vinzant, N. R. Neale, and A. J. Frank, "Removing structural disorder from oriented TiO_2 nanotube arrays: reducing the dimensionality of transport and recombination in dye-sensitized solar cells," *Nano Letters*, vol. 7, no. 12, pp. 3739–3746, 2007.

[114] J. Wang and Z. Q. Lin, "Dye-Sensitized TiO_2 Nanotube Solar Cells: Rational Structural and Surface Engineering on TiO_2 Nanotubes," *Chemistry: An Asian Journal*, vol. 7, no. 12, pp. 2754–2762, 2012.

[115] Z. Liu and M. Misra, "Bifacial dye-sensitized solar cells based on vertically oriented TiO_2 nanotube arrays," *Nanotechnology*, vol. 21, no. 12, Article ID 125703, 2010.

[116] L. Sun, S. Zhang, X. Wang, X. W. Sun, D. Y. Ong, and A. K. Ko Kyaw, "A novel parallel configuration of dye-sensitized solar cells with double-sided anodic nanotube arrays," *Energy & Environmental Science*, vol. 4, no. 6, pp. 2240–2248, 2011.

[117] Q. Zheng, H. Kang, J. Yun, J. Lee, J. H. Park, and S. Baik, "Hierarchical construction of self-standing anodized titania nanotube arrays and nanoparticles for efficient and cost-effective front-illuminated dye-sensitized solar cells," *ACS Nano*, vol. 5, no. 6, pp. 5088–5093, 2011.

[118] A. Kongkanand, K. Tvrdy, K. Takechi, M. Kuno, and P. V. Kamat, "Quantum dot solar cells. Tuning photoresponse through size and shape control of CdSe-TiO_2 architecture," *Journal of the American Chemical Society*, vol. 130, no. 12, pp. 4007–4015, 2008.

[119] V. I. Klimov and D. W. McBranch, "Femtosecond 1P-to-1S electron relaxation in strongly confined semiconductor nanocrystals," *Physical Review Letters*, vol. 80, no. 18, pp. 4028–4031, 1998.

[120] P. Sudhagar, J. H. Jung, S. Park et al., "The performance of coupled (CdS:CdSe) quantum dot-sensitized TiO_2 nanofibrous solar cells," *Electrochemistry Communications*, vol. 11, no. 11, pp. 2220–2224, 2009.

[121] Q. Shen, A. Yamada, S. Tamura, and T. Toyoda, "CdSe quantum dot-sensitized solar cell employing TiO_2 nanotube working-electrode and Cu_2S counter-electrode," *Applied Physics Letters*, vol. 97, no. 12, Article ID 123107, 2010.

[122] W.-T. Sun, A. Yu, H.-Y. Pan, X.-F. Gao, Q. Chen, and L.-M. Peng, "CdS quantum dots sensitized TiO_2 nanotube-array photoelectrodes," *Journal of the American Chemical Society*, vol. 130, no. 4, pp. 1124–1125, 2008.

[123] Z. Yang, C.-Y. Chen, P. Roy, and H.-T. Chang, "Quantum dot-sensitized solar cells incorporating nanomaterials," *Chemical Communications*, vol. 47, no. 34, pp. 9561–9571, 2011.

[124] G. K. Mor, K. Shankar, M. Paulose, O. K. Varghese, and C. A. Grimes, "Enhanced photocleavage of water using titania nanotube arrays," *Nano Letters*, vol. 5, no. 1, pp. 191–195, 2005.

[125] J. Gong, C. Lin, M. Ye, and Y. Lai, "Enhanced photoelectrochemical activities of a nanocomposite film with a bamboo leaf-like structured TiO_2 layer on TiO_2 nanotube arrays," *Chemical Communications*, vol. 47, no. 9, pp. 2598–2600, 2011.

[126] F. Jia, Z. Yao, Z. Jiang, and C. Li, "Preparation of carbon coated TiO_2 nanotubes film and its catalytic application for H_2 generation," *Catalysis Communications*, vol. 12, no. 6, pp. 497–501, 2011.

[127] Y. Li, H. Yu, W. Song, G. Li, B. Yi, and Z. Shao, "A novel photoelectrochemical cell with self-organized TiO_2 nanotubes as photoanodes for hydrogen generation," *International Journal of Hydrogen Energy*, vol. 36, no. 22, pp. 14374–14380, 2011.

[128] L. X. Sang, Z. Y. Zhang, G. M. Bai, C. X. Du, and C. F. Ma, "A photoelectrochemical investigation of the hydrogen-evolving doped TiO_2 nanotube arrays electrode," *International Journal of Hydrogen Energy*, vol. 37, no. 1, pp. 854–859, 2012.

[129] Y. R. Smith, B. Sarma, S. K. Mohanty, and M. Misra, "Single-step anodization for synthesis of hierarchical TiO_2 nanotube arrays on foil and wire substrate for enhanced photoelectrochemical water splitting," *International Journal of Hydrogen Energy*, vol. 38, no. 5, pp. 2062–2069, 2013.

[130] P. Roy, C. Das, K. Lee et al., "Oxide nanotubes on Ti-Ru alloys: strongly enhanced and stable photoelectrochemical activity for water splitting," *Journal of the American Chemical Society*, vol. 133, no. 15, pp. 5629–5631, 2011.

[131] Y. Sun, G. Wang, and K. Yan, "TiO_2 nanotubes for hydrogen generation by photocatalytic water splitting in a two-compartment photoelectrochemical cell," *International Journal of Hydrogen Energy*, vol. 36, no. 24, pp. 15502–15508, 2011.

[132] S. Bae, E. Shim, J. Yoon, and H. Joo, "Photoanodic and cathodic role of anodized tubular titania in light-sensitized enzymatic hydrogen production," *Journal of Power Sources*, vol. 185, no. 1, pp. 439–444, 2008.

[133] J. Yoon, S. Bae, E. Shim, and H. Joo, "Pyrococcus furiosus-immobilized anodized tubular titania cathode in a hydrogen production system," *Journal of Power Sources*, vol. 189, no. 2, pp. 1296–1301, 2009.

[134] M. Park, A. Heo, E. Shim, J. Yoon, H. Kim, and H. Joo, "Effect of length of anodized TiO_2 tubes on photoreactivity: photocurrent, Cr(VI) reduction and H_2 evolution," *Journal of Power Sources*, vol. 195, no. 15, pp. 5144–5149, 2010.

[135] J. Gong, Y. Lai, and C. Lin, "Electrochemically multi-anodized TiO_2 nanotube arrays for enhancing hydrogen generation by photoelectrocatalytic water splitting," *Electrochimica Acta*, vol. 55, no. 16, pp. 4776–4782, 2010.

[136] G. F. Ortiz, I. Hanzu, P. Knauth, P. Lavela, J. L. Tirado, and T. Djenizian, "TiO_2 nanotubes manufactured by anodization of Ti thin films for on-chip Li-ion 2D microbatteries," *Electrochimica Acta*, vol. 54, no. 17, pp. 4262–4268, 2009.

[137] W.-H. Ryu, D.-H. Nam, Y.-S. Ko, R.-H. Kim, and H.-S. Kwon, "Electrochemical performance of a smooth and highly ordered TiO_2 nanotube electrode for Li-ion batteries," *Electrochimica Acta*, vol. 61, pp. 19–24, 2012.

[138] A. Ghicov, S. P. Albu, J. M. Macak, and P. Schmuki, "High-contrast electrochromic switching using transparent lift-off layers of self-organized TiO_2 nanotubes," *Small*, vol. 4, no. 8, pp. 1063–1066, 2008.

[139] A. Ghicov, M. Yamamoto, and P. Schmuki, "Lattice widening in niobium-doped TiO_2 nanotubes: efficient ion intercalation and swift electrochromic contrast," *Angewandte Chemie—International Edition*, vol. 47, no. 41, pp. 7934–7937, 2008.

[140] J.-H. Kim, K. Zhu, Y. Yan, C. L. Perkins, and A. J. Frank, "Microstructure and pseudocapacitive properties of electrodes constructed of oriented NiO-TiO_2 nanotube arrays," *Nano Letters*, vol. 10, no. 10, pp. 4099–4104, 2010.

[141] M. Salari, K. Konstantinov, and H. K. Liu, "Enhancement of the capacitance in TiO_2 nanotubes through controlled introduction of oxygen vacancies," *Journal of Materials Chemistry*, vol. 21, no. 13, pp. 5128–5133, 2011.

[142] I. Paramasivam, J. M. Macak, A. Ghicov, and P. Schmuki, "Enhanced photochromism of Ag loaded self-organized TiO_2 nanotube layers," *Chemical Physics Letters*, vol. 445, no. 4–6, pp. 233–237, 2007.

[143] J. M. Macak, P. J. Barczuk, H. Tsuchiya et al., "Self-organized nanotubular TiO_2 matrix as support for dispersed Pt/Ru nanoparticles: enhancement of the electrocatalytic oxidation of methanol," *Electrochemistry Communications*, vol. 7, no. 12, pp. 1417–1422, 2005.

[144] Y.-Y. Song, Z.-D. Gao, and P. Schmuki, "Highly uniform Pt nanoparticle decoration on TiO_2 nanotube arrays: a refreshable platform for methanol electrooxidation," *Electrochemistry Communications*, vol. 13, no. 3, pp. 290–293, 2011.

[145] O. K. Varghese, D. Gong, M. Paulose, K. G. Ong, E. C. Dickey, and C. A. Grimes, "Extreme changes in the electrical resistance of titania nanotubes with hydrogen exposure," *Advanced Materials*, vol. 15, no. 7-8, pp. 624–627, 2003.

[146] S. Mahshid, C. Li, S. S. Mahshid et al., "Sensitive determination of dopamine in the presence of uric acid and ascorbic acid using TiO_2 nanotubes modified with Pd, Pt and Au nanoparticles," *Analyst*, vol. 136, no. 11, pp. 2322–2329, 2011.

[147] Z.-Q. Lin, Y.-K. Lai, R.-G. Hu, J. Li, R.-G. Du, and C.-J. Lin, "A highly efficient ZnS/CdS@TiO_2 photoelectrode for photogenerated cathodic protection of metals," *Electrochimica Acta*, vol. 55, no. 28, pp. 8717–8723, 2010.

[148] Y. K. Lai, L. X. Lin, F. Pan et al., "Bioinspired patterning with extreme wettability contrast on TiO_2 nanotube array surface: a versatile platform for biomedical applications," *Small*, vol. 9, no. 17, pp. 2945–2953, 2013.

[149] Y. K. Lai, F. Pan, C. Xu, H. Fuchs, and L. F. Chi, "In situ surface-modification-induced superhydrophobic patterns with reversible wettability and adhesion," *Advanced Materials*, vol. 25, no. 12, pp. 1682–1686, 2013.

[150] J. M. Macak, C. Zollfrank, B. J. Rodriguez et al., "Ordered ferroelectric lead titanate nanocellular structure by conversion of anodic TiO_2 nanotubes," *Advanced Materials*, vol. 21, no. 30, pp. 3121–3125, 2009.

[151] Y. Xin, J. Jiang, K. Huo, T. Hu, and P. K. Chu, "Bioactive $SrTiO_3$ nanotube arrays: strontium delivery platform on Ti-based osteoporotic bone implants," *ACS Nano*, vol. 3, no. 10, pp. 3228–3234, 2009.

[152] K. Yasuda and P. Schmuki, "Formation of self-organized zirconium titanate nanotube layers by alloy anodization," *Advanced Materials*, vol. 19, no. 13, pp. 1757–1760, 2007.

[153] Y. Yang, X. Wang, C. Zhong, C. Sun, and L. Li, "Ferroelectric $PbTiO_3$ nanotube arrays synthesized by hydrothermal method," *Applied Physics Letters*, vol. 92, no. 12, Article ID 122907, 2008.

[154] J. Zhang, X. Tang, and D. Li, "One-step formation of crystalline TiO_2 nanotubular arrays with intrinsic p-n junctions," *Journal of Physical Chemistry C*, vol. 115, no. 44, pp. 21529–21534, 2011.

[155] R. Daghrir, P. Drogui, and D. Robert, "Modified TiO_2 for environmental photocatalytic applications: a review," *Industrial & Engineering Chemistry Research*, vol. 52, no. 10, pp. 3581–3599, 2013.

Hindawi Publishing Corporation
International Journal of Photoenergy
Volume 2013, Article ID 890240, 6 pages
http://dx.doi.org/10.1155/2013/890240

Research Article

Photocatalytic Oxidation of Gaseous Benzene under 185 nm UV Irradiation

Haibao Huang,[1,2] Xinguo Ye,[1] Huiling Huang,[1] Peng Hu,[1] Lu Zhang,[1] and Dennis Y. C. Leung[3]

[1] *School of Environmental Science and Engineering, Sun Yat-Sen University, Guangzhou 510275, China*
[2] *Guangdong Provincial Key Laboratory of Environmental Pollution Control and Remediation Technology, Guangzhou 510275, China*
[3] *Department of Mechanical Engineering, The University of Hong Kong, Pokfulam Road, Hong Kong*

Correspondence should be addressed to Haibao Huang; seabao8@gmail.com and Dennis Y. C. Leung; ycleung@hku.hk

Received 19 July 2013; Accepted 11 August 2013

Academic Editor: Guisheng Li

Benzene is a toxic air pollutant and causes great harm to human being. Photocatalytic oxidation (PCO) has been frequently studied for benzene removal, however, its PCO efficiency is still very low and the photocatalysts are easy to be deactivated. To improve the efficiency and stability of PCO, UV lamps with partial 185 nm UV irradiation were used to activate photocatalysts (denoted as 185-PCO). Cobalt modified TiO_2 (Co-TiO_2) was developed to improve the PCO activity and eliminate ozone generated from 185 nm UV irradiation. Results show that benzene removal efficiency of PCO with 254 nm UV irradiation (denoted as 254-PCO) is only 2.1% while it was greatly increased to 51.5% in 185-PCO. 185-PCO exhibited superior capacity for benzene oxidation. In the 185-PCO process, much ozone was left in case of TiO_2 as photocatalysts while it can be nearly eliminated by 1% Co-TiO_2.

1. Introduction

With the rapid development of economy and the increase in population, massive volatile organic compounds (VOCs) are discharged from both industry (such as chemical, petrochemical, painting, and coating factories) and human activities [1, 2]. VOCs not only do great harm to the health of human being but also cause serious damage to the atmospheric environment. They can lead to atmospheric compound pollution and haze. The haze weather, which lasted for a long time in many cities of China in early 2013, had caused much trouble to local people. It is of great significance to control VOCs pollution.

Benzene is a representative VOC. It is very toxic and carcinogenic. Benzene is hard to be destructed by conventional technology due to its benzene ring. The methods of benzene removal include conventional ways such as adsorption [3, 4], catalytic combustion [5], and biological degradation [6] and emerging ways such as nonthermal plasma [7] and photocatalysis [8–10]. However, the application of these methods is greatly limited due to their inherent drawbacks such as high cost, deactivation, and byproducts [11–14].

PCO is one of the fastest developed technologies for VOCs control. The most widely used UV sources in PCO are 254 nm and 365 nm UV lamp. However, the conventional PCO process has disadvantages such as photocatalyst deactivation, recombination of electron-hole pair, and low efficiency [15]. In order to improve the efficiency and stability of PCO, UV lamps with partial 185 nm UV irradiation (denoted as 185-PCO) were used to activate photocatalysts [16–18]. 185 nm UV lamps cannot only irradiate photocatalyst but also generate active oxidants such as •O, •OH, and ozone. They are also facile, cheap, and energy efficient. Previous study showed that the toluene removal of 185-PCO is 7 times higher than that of PCO under 254 nm UV irradiation (denoted as 254-PCO), and no obvious deactivation was observed in the former [19]. However, massive ozone was residual at the outlet of photocatalytic reactor since TiO_2 had poor activity towards ozone decomposition. Ozone is a byproduct and it is harmful to the environment and the health of human being; meanwhile it is a strong oxidant and can be used to enhance the oxidation of pollutants.

Cobalt is a commonly used metal not only for TiO_2 doping but also as an active component of ozone decomposition

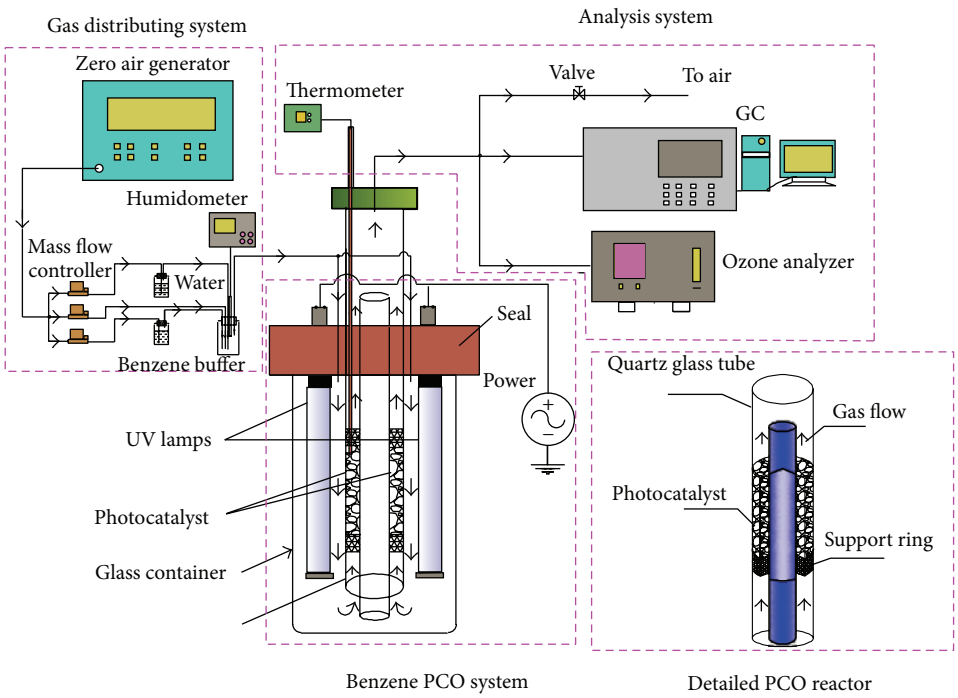

Figure 1: Schematic diagram of experimental setup.

agent. In this study, cobalt modified TiO_2 (Co-TiO_2) was developed to improve the PCO activity and eliminate ozone generated from 185 nm irradiation. Benzene was selected as representative VOC and its oxidation performance is compared between 185-PCO and 254-PCO. Results show that Co-TiO_2 can simultaneously increase benzene removal and ozone decomposition in 185-PCO. 185-PCO presents an efficient, economic, simple, and stable process for benzene removal.

2. Experimental Sections

2.1. Preparation of Photocatalysts. TiO_2 was prepared by sol-gel method using tetrabutyl titanate as the precursor, absolute alcohol as the solution, and HCl as the inhibitor, respectively. The preparation procedure is as follows: cobalt acetate was added into the mixture of 50 mL absolute alcohol and 17 mL tetrabutyl titanate and mixed for 30 min, forming solution A. Another mixture B containing 18 mL absolute alcohol, 1 mL HCl, and 3 mL deionized water was dropwise added into solution A under intensive stirring. The stirring was stopped till the gelatin was formed. The gelatin was aged for 12 h and then dried at 120°C for 6 h. The dry powder was followed by calcinations at 550°C for 4 h. Thus, cobalt doped TiO_2 was produced. Pure TiO_2 was fabricated by similar processes for the preparation of Co-TiO_2 except that no cobalt acetate was introduced during the synthesis. The catalysts were grinded into 40–60 mesh before use.

2.2. Catalytic Activity Test. The experimental setup and PCO reactor were shown in Figure 1. The catalytic activity test system was composed of 3 parts: gas distribution, benzene PCO, and gas analysis system. The gas from zero air generator is dry air free of CO, CO_2, and hydrocarbon. It was used for bubble water and benzene liquid to generate water and benzene vapor, respectively. The benzene concentration, humidity, and gas flow can be regulated by the mass flow controllers (S49, Horibametron). A 0.5 L/min gas flow of 50 ppm benzene concentration and 50% humidity was introduced into benzene PCO reactor. The reactor is a glass cylinder container with an effective volume of 0.5 L, in which a quartz glass tube was located in the centre and two UV lamps (4 W, Sungreen) were fixed in both sides of the tube with a distance of 8 mm. The detailed PCO reactor is shown in Figure 1. A solid rod of 8 mm diameter was placed in the center of the quartz glass tube with 1.3 cm i.d. and the photocatalysts was loaded in the space between the rod and glass tube. By this way, the photocatalysts have more chances to be irradiated by UV light. The UV lamps were turned on for 30 min for the warming-up of system before reaction and data recording. The gaseous benzene entered into the reactor from the bottom of glass tube and left from the top. The benzene and ozone concentrations of effluent were monitored by gas chromatography (GC) equipped with a FID (GC9790II, Fuli) and ozone analyzer (Model 202, 2B Technology) online, respectively.

2.3. Catalyst Characterization. BET surface areas of the samples were measured by N_2 adsorption-desorption isotherms at 77 K using Quadrasorb SI instrument. Prior to the measurement, the samples were degassed at 573 K for 2 h. The morphology of photocatalysts was obtained with scanning electron microscopy (SEM) (JSM-6330F, JEOL) operated at

Table 1: BET surface area of photocatalysts.

Samples	BET surface area, m^2/g	Particle size, nm
P25	55.4	29.0
TiO_2	96.6	10.5
Co-TiO_2	26.9	34.9

beam energy of 20.0 kV. XRD patterns were collected with a Panalytical Empyrean X-ray powder diffractometer operated at 35 kV and 25 mA, using Cu K α (λ = 1.5418 Å) radiation. The intensity data were collected in a 2θ range from 20° to 80°.

3. Results and Discussion

3.1. Characterization. Figure 2 shows the XRD spectra of the synthesized TiO_2 and Co-TiO_2 as well as the commercial TiO_2 (P25, Degussa). The nanocrystalline anatase structure was confirmed by (101), (004), (200), (105), and (204) diffraction peaks [20]. The XRD patterns of anatase have a main peak at $2\theta = 25.2°$ corresponding to the 101 plane (JCPDS 21-1272) while the main peaks of rutile and brookite phases are at $2\theta = 27.4°$ (110 plane) and $2\theta = 30.8°$ (121 plane), respectively. Therefore, rutile and brookite phases have not been detected on the synthesized TiO_2 and Co-TiO_2. They exhibit very similar shape of diffractive peaks of the crystal planes. The XRD patterns did not show any Co phase, indicating that Co ions uniformly dispersed among the anatase crystallites. Unlike the synthesized TiO_2, weak peaks of rutile phase can be observed on P25 (Figure 1). The average particle size of TiO_2 was estimated by applying the Scherrer equation ($D = K\lambda/\beta \cos\theta$) on the anatase and rutile diffraction peaks (the most intense peaks for each sample), where D is the crystal size of the catalyst, λ is the X-ray wavelength (1.54 Å), β is the full width at half maximum (FWHM) of the catalyst (radian), $K = 0.89$, and θ is the diffraction angle [21]. The average crystal sizes of TiO_2, 1% Co-TiO_2, and P25 were calculated to be around 10.5 nm, 34.9 nm, and 29.0 nm, respectively, as shown in Table 1. Compared with P25, the synthesized TiO_2 can greatly reduce the particle size; however, the doping of cobalt triggered the aggregation of particle during the synthesis process, leading to the increase in particle size.

This observation is consistent with the results of BET surface area and the observation of SEM images. The BET surface area of TiO_2, 1% Co-TiO_2 and P25 is 96.6, 26.9 and 55.4 m^2/g, respectively. TiO_2 with the smallest particle size has the largest BET surface area.

SEM micrograph of TiO_2, 1% Co-TiO_2, and P25 nanoparticles is shown in Figure 3. This image shows uniform small particles which are coherent together on the TiO_2 and P25; however, the particles of 1% Co-TiO_2 got aggregated. The results agree well with the results of XRD pattern and BET surface area.

3.2. Catalytic Activity Test. Figure 4 compared benzene removal efficiency in PCO processes with 185 nm and 254 nm UV irradiation. It can be found that it is very low in case

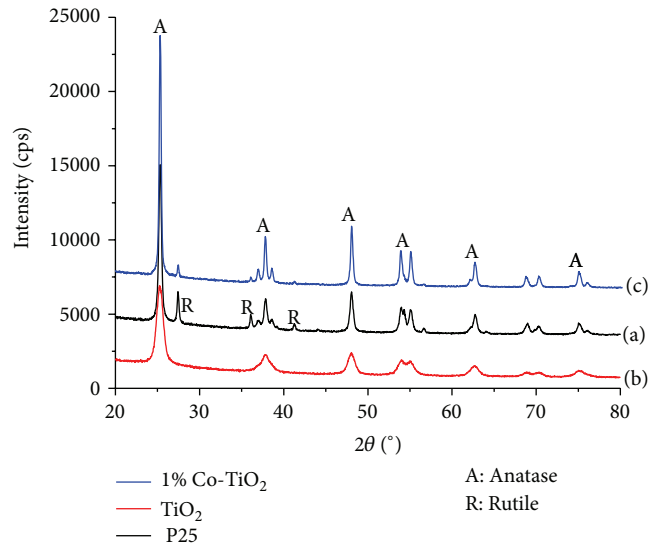

Figure 2: XRD spectra of photocatalysts: (a) P25, (b) TiO_2, and (c) 1% Co-TiO_2.

of 254-PCO process. Benzene removal efficiency is only about 2%. It is well known that benzene is very difficult to be destructed due to its stable π-bonding. Moreover, the intermediates from benzene PCO can lead to the serious deactivation of photocatalysts [22]. However, benzene conversion was greatly increased to about 50% under 185 nm UV irradiation and no obvious deactivation was observed after reaction for 3 h. Among 3 tested samples, Co-TiO_2 obtained the highest benzene removal efficiency of 51.5%, followed by P25 (50.2%) and TiO_2 (45.7%). Benzene removal efficiency of 185-PCO is over 20 times than that of 254-PCO. 185-PCO is a very complex process, in which 185 nm UV lamp not only acted as the irradiation light of photocatalysis but also generated reactive oxidants such as •O, •OH, and ozone. The reaction processes for the formation of reactive oxidants are as follows [23]:

$$\begin{aligned} H_2O + h\nu &\longrightarrow \bullet H + \bullet OH \\ O_2 + h\nu &\longrightarrow 2 \bullet O \\ \bullet O + H_2O &\longrightarrow 2 \bullet OH \\ \bullet O + O_2 &\longrightarrow O_3 \end{aligned} \quad (1)$$

In order to clarify the contribution of 185 nm irradiation, the photocatalysts were removed from the reactor. The new process is photolysis. It can be found that benzene removal efficiency reached 38% under 185 nm irradiation alone. 185 nm photolysis contributes much to benzene oxidation in the 185-PCO process. The sum of benzene removal efficiency due to PCO and 185 nm photolysis is about 40%, which is approximately 10% smaller than that of 185-PCO. This indicated that other factors were also involved in benzene oxidation in the 185-PCO process besides photolysis and PCO. As we know, ozone can be abundantly generated from 185 nm UV irradiation. The ozone concentration is 138 ppm in the absence of photocatalysts. Ozone is strong

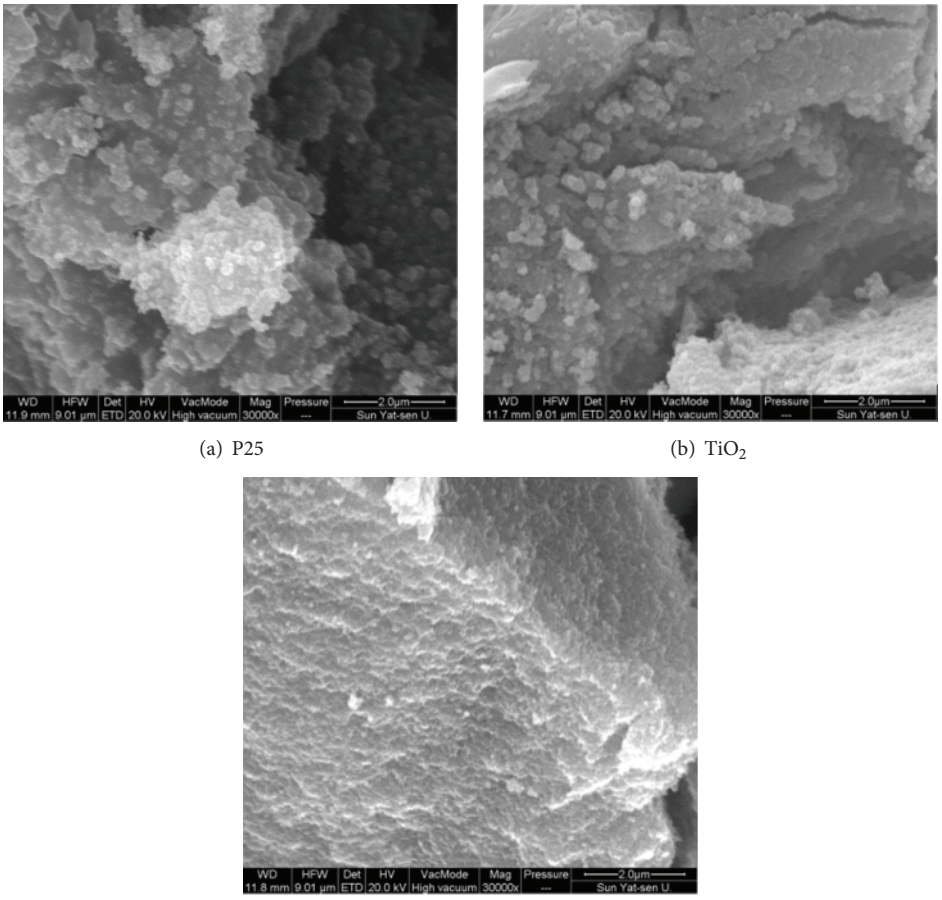

(a) P25 (b) TiO_2

(c) 1% Co-TiO_2

Figure 3: SEM images of photocatalysts: (a) P25, (b) TiO_2, and (c) 1% Co-TiO_2.

oxidant. Although it cannot directly oxidize benzene, it can be decomposed into more active oxygen species with the aid of catalysts [24]:

$$\begin{aligned} O_3 + {}^* &\longrightarrow O_2 + O^* \\ O^* + O_3 &\longrightarrow O_2 + O_2{}^* \\ O_2{}^* &\longrightarrow O_2 + {}^* \end{aligned} \tag{2}$$

* represents the catalytic active sites.

3.3. Ozone Decomposition. 185-PCO exhibited more superior capacity for benzene oxidation than 254-PCO. However, ozone is another important concern besides benzene removal since it is a toxic byproduct. Although 3 tested samples had similar benzene removal efficiency since 185 nm UV photolysis contributed to a large proportion of benzene removal, they had entirely different activity toward ozone decomposition. As shown in Figure 5, the ozone concentration at outlet of 185-PCO reactor after reaction for 2.5 h was 119 ppm in case of the synthesized TiO_2, and it was dropped to 58.4 ppm in case of P25. Although the synthesized TiO_2 had higher BET surface area than that of P25, its capacity for ozone decomposition is worse than that of the latter. It was reported

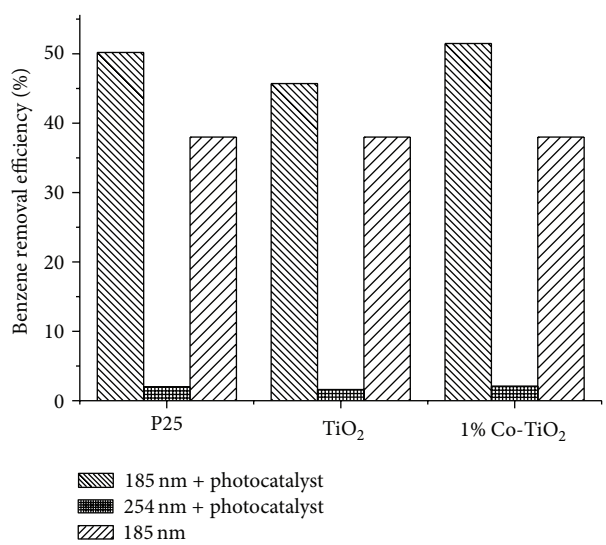

Figure 4: Benzene removal efficiency in different processes.

that higher BET surface area should be helpful for ozone decomposition [25]. The difference between synthesized TiO_2 and commercial P25 is that the former is pure anatase

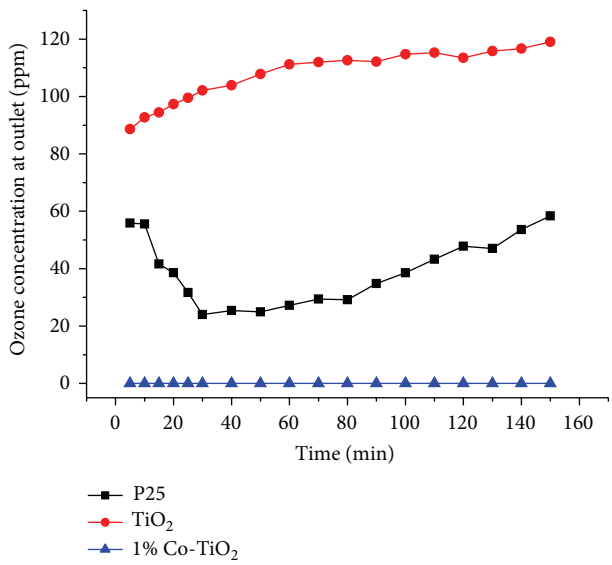

Figure 5: Ozone concentration at outlet of 185-PCO reactor with different photocatalysts.

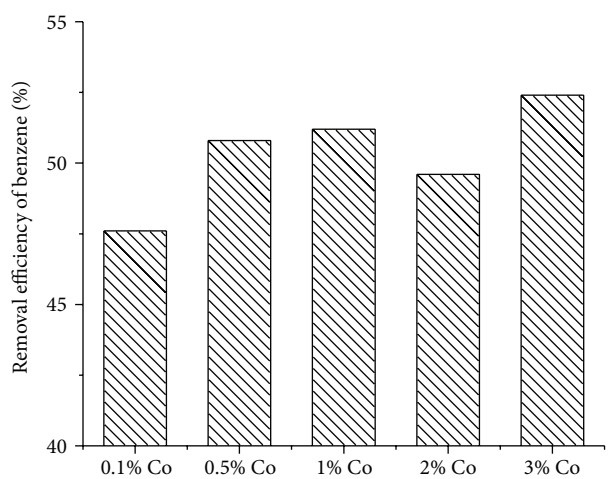

Figure 6: Effect of Co loading amount on benzene removal.

TiO_2 while P25 contained some rutile TiO_2 besides anatase one. A previous study showed that TiO_2 with partial rutile had better capacity for ozone decomposition than that of pure anatase TiO_2 [26]. As for Co-TiO_2, ozone can be completely eliminated. Cobalt is a very active component for ozone decomposition. Co doped TiO_2 exhibited superior activity toward ozone elimination. In comprehensive view of benzene removal and ozone decomposition, Co-TiO_2 exhibited the best performance among the 3 tested samples.

3.4. Effect of Co Doping. In order to study the effect of Co doping, 0.1%, 0.5%, 1%, 2%, and 3% Co-TiO_2 were prepared and tested in 185-PCO process. The results after reaction for 150 min are shown in Figure 6. Benzene removal efficiency is only 47.6% in case of 0.1% Co-TiO_2. As the increase in Co loading, benzene removal efficiency was increased to 51.5% in case of 1% Co-TiO_2 and 52.4% in case of 3% Co-TiO_2.

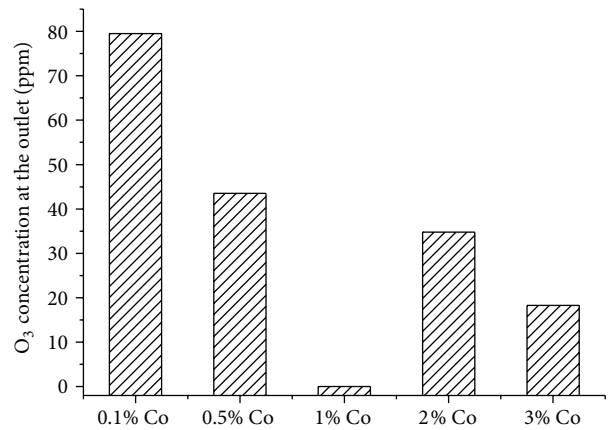

Figure 7: Effect of Co loading amount on ozone concentration at the outlet.

Figure 7 shows the effect of cobalt loading amount on ozone concentration at the outlet after reaction for 150 min. In case of Co doping amount lower than 1%, the ozone concentration at the outlet was dropped with the increase in Co loading. As for 0.1% Co doping, the ozone concentration is 79.5 ppm while it was decreased to nearly zero in case of 1% Co doping. The increase in Co doping can provide more catalytic active sites for ozone decomposition. However, the ozone concentration at the outlet was increased with further increase in Co doping. Too much Co doping is not beneficial to ozone decomposition since Co probably gets aggregated and blocks the micropore of TiO_2. This will reduce the catalytic active sites and BET surface area, leading to worse activities toward ozone decomposition.

4. Conclusion

To improve the efficiency and stability of PCO, 185-PCO was used to activate photocatalysts. Co-TiO_2 was developed to improve the PCO activity and eliminate the ozone generated from 185 nm UV irradiation. Results show that benzene removal efficiency of PCO with 254-PCO is only 2.1% while it was greatly increased to 51.5% in the 185-PCO process. 185 nm UV irradiation can generate much reactive oxygen species such as •O, •OH, and ozone, which can jointly enhance benzene oxidation together with PCO. In 185-PCO, much ozone is left in case of TiO_2 as photocatalysts while it can be completely eliminated by 1% Co-TiO_2. 185-PCO is an efficient and promising process for benzene removal.

Acknowledgments

The authors gratefully acknowledge the financial support from Research Fund for the Doctoral Program of Higher Education of China (no. 20120172120039), the National Nature Science Foundation of China (no. 51208207), the Research Fund Program of Guangdong Provincial Key Laboratory of Environmental Pollution Control and Remediation Technology (no. 2013K0001), and the Fundamental Research Funds for the Central Universities (no. 13lgzd03).

References

[1] R. Atkinson, "Atmospheric chemistry of VOCs and NO_x," *Atmospheric Environment*, vol. 34, no. 12–14, pp. 2063–2101, 2000.

[2] S. Zuo, F. Liu, J. Tong, and C. Qi, "Complete oxidation of benzene with cobalt oxide and ceria using the mesoporous support SBA-16," *Applied Catalysis A*, vol. 467, pp. 1–6, 2013.

[3] A. A. M. Daifullah and B. S. Girgis, "Impact of surface characteristics of activated carbon on adsorption of BTEX," *Colloids and Surfaces A*, vol. 214, no. 1–3, pp. 181–193, 2003.

[4] M. Farhadian, D. Duchez, C. Vachelard, and C. Larroche, "BTX femoval from polluted water through bioleaching processes," *Applied Biochemistry and Biotechnology*, vol. 151, no. 2-3, pp. 295–306, 2008.

[5] L. Wang, V. D. Vien, K. Suzuki, M. Sakurai, and H. Kameyama, "Preparation of anodised aluminium catalysts by an electrolysis supporting method for VOC catalytic combustion," *Journal of Chemical Engineering of Japan*, vol. 38, no. 2, pp. 106–112, 2005.

[6] G. Darracq, A. Couvert, C. Couriol, E. Dumont, A. Amrane, and P. Le Cloirec, "Activated sludge acclimation for hydrophobic VOC removal in a two-phase partitioning reactor," *Water, Air and Soil Pollution*, vol. 223, no. 6, pp. 3117–3124, 2012.

[7] M. Kang, B.-J. Kim, S. M. Cho et al., "Decomposition of toluene using an atmospheric pressure plasma/TiO_2 catalytic system," *Journal of Molecular Catalysis A*, vol. 180, no. 1-2, pp. 125–132, 2002.

[8] T.-C. Pan, H.-C. Chen, G.-T. Pan, and C.-M. Huang, "Photocatalytic oxidation of gaseous isopropanol using visible-light active silver vanadates/SBA-15 composite," *International Journal of Photoenergy*, vol. 2012, Article ID 314361, 8 pages, 2012.

[9] F.-L. Cao, J.-G. Wang, F.-J. Lv et al., "Photocatalytic oxidation of toluene to benzaldehyde over anatase TiO_2 hollow spheres with exposed 001 facets," *Catalysis Communications*, vol. 12, no. 11, pp. 946–950, 2011.

[10] A. Kachina, S. Preis, G. C. Lluellas, and J. Kallas, "Gas-phase and aqueous photocatalytic oxidation of methylamine: the reaction pathways," *International Journal of Photoenergy*, vol. 2007, Article ID 32524, 6 pages, 2007.

[11] S. K. Agarwal and J. J. Spivey, "Economic effects of catalyst deactivation during VOC oxidation," *Environmental Progress*, vol. 12, pp. 182–185, 1993.

[12] M. D. Driessen, T. M. Miller, and V. H. Grassian, "Photocatalytic oxidation of trichloroethylene on zinc oxide: characterization of surface-bound and gas-phase products and intermediates with FT-IR spectroscopy," *Journal of Molecular Catalysis A*, vol. 131, no. 1–3, pp. 149–156, 1998.

[13] M. Kosusko, "Catalytic oxidation of groundwater stripping emissions," *Environmental Progress*, vol. 7, no. 2, pp. 136–142, 1988.

[14] J. Jeong, K. Sekiguchi, W. Lee, and K. Sakamoto, "Photodegradation of gaseous volatile organic compounds (VOCs) using TiO_2 photoirradiated by an ozone-producing UV lamp: decomposition characteristics, identification of by-products and water-soluble organic intermediates," *Journal of Photochemistry and Photobiology A*, vol. 169, no. 3, pp. 279–287, 2005.

[15] H. B. Huang and D. Y. C. Leung, "Vacuum ultraviolet-irradiated photocatalysis: advanced process for toluene abatement," *Journal of Environmental Engineering*, vol. 137, no. 11, pp. 996–1001, 2011.

[16] J. Jeong, K. Sekiguchi, and K. Sakamoto, "Photochemical and photocatalytic degradation of gaseous toluene using short-wavelength UV irradiation with TiO_2 catalyst: comparison of three UV sources," *Chemosphere*, vol. 57, no. 7, pp. 663–671, 2004.

[17] L. Yang, Z. Liu, J. Shi, Y. Zhang, H. Hu, and W. Shangguan, "Degradation of indoor gaseous formaldehyde by hybrid VUV and TiO_2/UV processes," *Separation and Purification Technology*, vol. 54, no. 2, pp. 204–211, 2007.

[18] P. Zhang, J. Liu, and Z. Zhang, "VUV photocatalytic degradation of toluene in the gas phase," *Chemistry Letters*, vol. 33, no. 10, Article ID CL-040801, pp. 1242–1243, 2004.

[19] H. Huang, D. Y. C. Leung, G. Li, M. K. H. Leung, and X. Fu, "Photocatalytic destruction of air pollutants with vacuum ultraviolet (VUV) irradiation," *Catalysis Today*, vol. 175, no. 1, pp. 310–315, 2011.

[20] Y. Xie, S. H. Heo, S. H. Yoo, G. Ali, and S. O. Cho, "Synthesis and photocatalytic activity of anatase TiO_2 nanoparticles-coated carbon nanotubes," *Nanoscale Research Letters*, vol. 5, no. 3, pp. 603–607, 2010.

[21] M. Hamadanian, A. Reisi-Vanani, and A. Majedi, "Preparation and characterization of S-doped TiO_2 nanoparticles, effect of calcination temperature and evaluation of photocatalytic activity," *Materials Chemistry and Physics*, vol. 116, no. 2-3, pp. 376–382, 2009.

[22] H. Yuzawa, J. Kumagai, and H. Yoshida, "Reaction mechanism of aromatic ring amination of benzene and substituted benzenes by aqueous ammonia over platinum-loaded titanium oxide photocatalyst," *The Journal of Physical Chemistry C*, vol. 117, pp. 11047–11058, 2013.

[23] T. Alapi and A. Dombi, "Direct VUV photolysis of chlorinated methanes and their mixtures in an oxygen stream using an ozone producing low-pressure mercury vapour lamp," *Chemosphere*, vol. 67, no. 4, pp. 693–701, 2007.

[24] W. Li, G. V. Gibbs, and S. T. Oyama, "Mechanism of ozone decomposition on a manganese oxide catalyst—1. In situ Raman spectroscopy and Ab initio molecular orbital calculations," *Journal of the American Chemical Society*, vol. 120, no. 35, pp. 9041–9046, 1998.

[25] H. Huang, D. Ye, and X. Guan, "The simultaneous catalytic removal of VOCs and O_3 in a post-plasma," *Catalysis Today*, vol. 139, no. 1-2, pp. 43–48, 2008.

[26] H. Yin, J. Xie, Q. Yang, and C. Yin, "Mechanism of ozone decomposition on the surface of metal oxide," *Chemical Research and Application*, vol. 15, pp. 1–5, 2003.

Hindawi Publishing Corporation
International Journal of Photoenergy
Volume 2013, Article ID 158496, 7 pages
http://dx.doi.org/10.1155/2013/158496

Research Article

A Cost-Effective Solid-State Approach to Synthesize g-C_3N_4 Coated TiO_2 Nanocomposites with Enhanced Visible Light Photocatalytic Activity

Min Fu, Junmin Pi, Fan Dong, Qiuyan Duan, and Huan Guo

Chongqing Laboratory of Catalysis and Functional Organic Molecules, College of Environmental and Biological Engineering, Chongqing Technology and Business University, Chongqing 400067, China

Correspondence should be addressed to Min Fu; fumin1022@126.com and Fan Dong; dfctbu@126.com

Received 22 June 2013; Accepted 2 September 2013

Academic Editor: Guisheng Li

Novel graphitic carbon nitride (g-C_3N_4) coated TiO_2 nanocomposites were prepared by a facile and cost-effective solid-state method by thermal treatment of the mixture of urea and commercial TiO_2. Because the C_3N_4 was dispersed and coated on the TiO_2 nanoparticles, the as-prepared g-C_3N_4/TiO_2 nanocomposites showed enhanced absorption and photocatalytic properties in visible light region. The as-prepared g-C_3N_4 coated TiO_2 nanocomposites under 450°C exhibited efficient visible light photocatalytic activity for degradation of aqueous MB due to the increased visible light absorption and enhanced MB adsorption. The g-C_3N_4 coated TiO_2 nanocomposites would have wide applications in both environmental remediation and solar energy conversion.

1. Introduction

Visible light photocatalysis has attracted the worldwide attention due to its potential application in environmental remediation and solar energy conversion [1–7]. The photocatalyst TiO_2, however, can only utilize the ultraviolet light (about 5% of natural solar light) because of its wide band gap (ca. 3.2 eV for anatase TiO_2). During the past 40 years, many efforts have been devoted to enhance the visible light photocatalytic activity of TiO_2, including metal doping [8–10], nonmetal doping [11–14], surface modification [15], and heterojunction construction [16–19].

In recent years, polymeric g-C_3N_4 materials have attracted much attention because of their similarity to graphene. Zhang et al. reported that the polymeric g-C_3N_4 semiconductors exhibit high photocatalytic performance for water splitting under visible light irradiation [20]. Dong and coworkes reported that polymeric g-C_3N_4 layered materials as novel efficient visible light photocatalyst, which can be synthesized facilely by directly heating urea or thiourea [21, 22].

Very recently, Zhou et al. reported a g-C_3N_4/TiO_2 nanotube array heterojunction with excellent visible light photocatalytic activity [17]. Zhao et al. reported g-C_3N_4/TiO_2 hybrids with wide absorption wavelength and effective photogenerated charge separation [18]. However, the precursors for g-C_3N_4 (dicyandiamide and melamine) are poisonous and detrimental to the environment. The preparation processes were relatively tedious, which may prevent large-scale application [17, 18].

In the present work, g-C_3N_4/TiO_2 nanocomposites were prepared by a facile and cost-effective solid-state method using urea and commercial TiO_2 as precursors. It was interesting to find that g-C_3N_4 was *in situ* coated on the surface of TiO_2. The precursors (urea and commercial TiO_2) are low cost and easily available. The as-prepared g-C_3N_4 coated TiO_2 nanocomposites exhibited enhanced photocatalytic activity under visible light irradiation.

2. Experimental

2.1. Synthesis. The g-C_3N_4 coated TiO_2 nanocomposites were prepared by a facile and cost-effective solid-state method. In a typical synthesis, 2 g TiO_2 and 6 g urea were immersed in 10 mL H_2O and dried at 60°C to completely remove the water.

The mixtures were put into an alumina crucible with a cover, and then heated to a certain temperature in the range of 400 and 600°C in a muffle furnace for 1 h at a heating rate of 15°C min^{-1}. The final samples were collected for use without further treatment.

2.2. Characterization. The crystal phases of the sample were analyzed by X-ray diffraction with Cu Kα radiation (XRD: model D/max RA, Rigaku Co., Japan). The morphology and structure of the samples were examined by transmission electron microscopy (TEM: JEM-2010, Japan). The UV-vis diffuse reflection spectra were obtained for the dry-pressed disk samples using a Scan UV-Vis spectrophotometer (UV-Vis DRS: UV-2450, Shimadzu, Japan) equipped with an integrating sphere assembly, using $BaSO_4$ as reflectance sample. The spectra were recorded at room temperature in air range from 250 to 800 nm. X-ray photoelectron spectroscopy with Al Kα X-rays ($h\nu$ = 1486.6 eV) radiation operated at 150 W (XPS: Thermo ESCALAB 250, USA) was used to investigate the surface properties. The shift of the binding energy due to relative surface charging was corrected using the C1s level at 284.8 eV as an internal standard. FT-IR spectra were recorded on a Nicolet Nexus spectrometer on samples embedded in KBr pellets. The nitrogen adsorption-desorption isotherms were determined by the BET method (BET-BJH: ASAP 2020, USA), from which the surface area, pore volume, and average pore diameter were calculated by using the BJH method. All the samples were degassed at 200°C prior to measurements.

2.3. Evaluation of Photocatalytic Activity. Photocatalytic activity of g-C_3N_4/TiO_2 for MB photodegradation was evaluated in a quartz glass reactor. 0.05 g of N-TiO_2 was dispersed in MB aqueous solution (50 mL, 5 mg/L). The light irradiation system contains a 500 W Xe lamp with a jacket filled with flowing and thermostated aqueous $NaNO_2$ solution (1 M) between the lamp and the reaction chamber as a filter to block UV light (λ < 400 nm) and eliminate the temperature effect. The suspension was first allowed to reach adsorption-desorption equilibrium with continuous stirring for 60 min in the dark prior to irradiation. The degradation rate of MB was evaluated using the UV-Vis absorption spectra to measure the peak value of a maximum absorption of MB solution. During the irradiation, 5 mL of suspension was continually taken from the reaction cell at given time intervals for subsequent dye concentration analysis after centrifugation. The MB solution shows a similar pH value at 6.8, which does not affect the light absorption of MB. The maximum absorption of MB is at wavelength of 665 nm. The degradation rate η (%) can be calculated as

$$\eta\,(\%) = \frac{(C_0 - C)}{C_0} \times 100\%, \tag{1}$$

where C_0 is the initial concentration of MB considering MB adsorption on the catalyst and C is the revised concentration after irradiation.

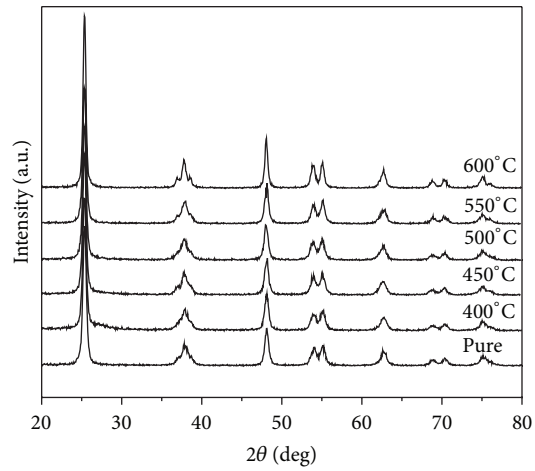

Figure 1: XRD patterns of the C_3N_4/TiO_2 nanocomposites obtained under different temperatures.

3. Results and Discussion

Figure 1 shows the XRD patterns of the as-prepared g-C_3N_4 coated TiO_2 nanocomposites at different temperatures. The peaks of all the samples can be indexed to the anatase phase of TiO_2 (JCPDS file No. 21-1272). It can be seen that the peak intensity increases gradually under higher treatment temperature, which indicates that the crystal sizes of TiO_2 nanocomposites increase under higher treatment temperature. No typical peaks of g-C_3N_4 can be found for all the samples due to the fact that g-C_3N_4 with layered structures on the surface of TiO_2 is ultrathin (Figure 2) and the crystallinity is low [22].

The morphology of pure TiO_2 and g-C_3N_4/TiO_2 nanocomposites were observed by TEM. As shown in Figure 2, both samples contain a number of monodispersed nanoparticles of TiO_2 with a size of about 11 nm. The intra-aggregation of particles could form the mesoporous structure [23]. It can be seen from Figure 2(b) that the ultrathin g-C_3N_4 with layered structures are dispersed and coated on the surface of TiO_2 particles, which is consistent with absence of the peaks of g-C_3N_4 in XRD (Figure 1).

The FT-IR spectra of pure TiO_2 and g-C_3N_4 coated TiO_2 nanocomposites are shown in Figure 3(a). The absorption band around 400–800 cm^{-1} is attributed to Ti–O bonds [23]. Several bands in the range of 1100–1650 cm^{-1} correspond to the typical stretching vibration of CN heterocycles in g-C_3N_4. The characteristic vibration mode of triazine units can also be found at 801 cm^{-1} [22]. The peak at 1630 cm^{-1} is associated with the stretching vibration of water molecules for both samples, including molecular water and hydroxyl groups [23]. The FT-IR spectra further confirm the existence of g-C_3N_4 on the surface of TiO_2.

The TG and DSC thermograms (Figure 3(b)) show that there are several phase transformations during heating. An endothermal peak at 135°C is the melting point of urea. The peak at 242°C indicates the reaction of urea into melamine. The weight loss during the two stages decreases rapidly by 36.1%. The sharp peak at 367°C implies that the thermal

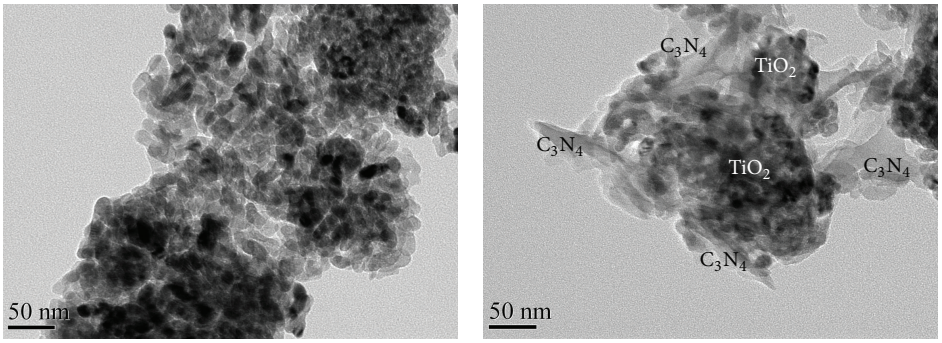

(a) (b)

Figure 2: TEM images of pure TiO_2 (a) and g-C_3N_4/TiO_2 nanocomposites sample obtained under 450°C (b).

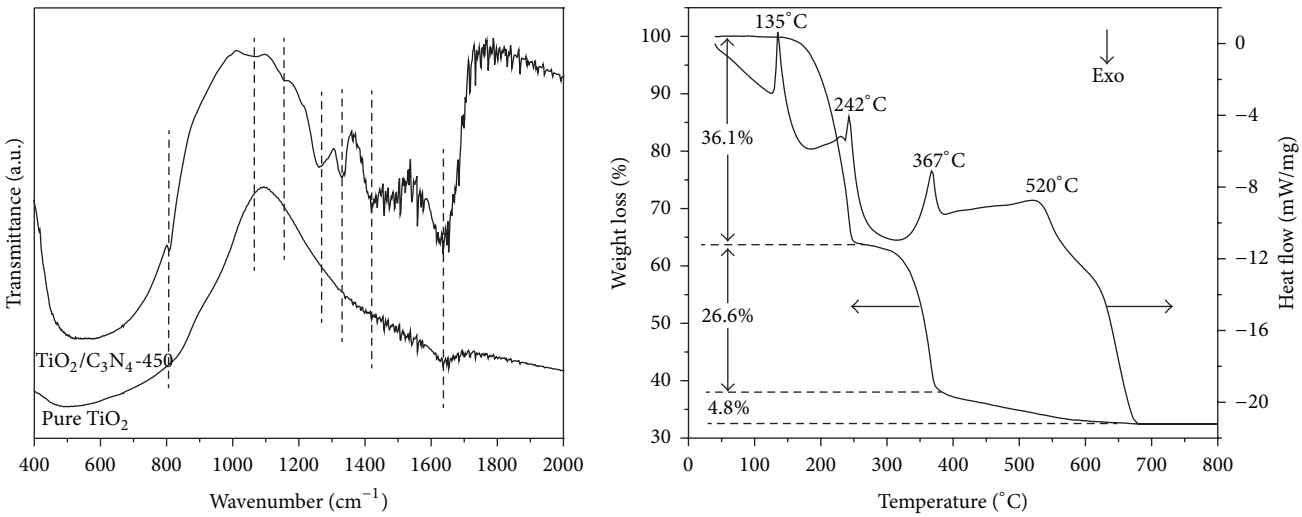

(a) (b)

Figure 3: FTIR spectra of pure TiO_2 and g-C_3N_4/TiO_2 nanocomposites (a) and TG-DSC for heating the mixture of TiO_2 and urea (b).

condensation of melamine into g-C_3N_4 occurred in this temperature range. The weight loss in this stage is about 26.6%. The further weight loss of 4.8% with endothermal peak at 520°C can be attributed to the decomposition of g-C_3N_4. The TG-DSC result implies that g-C_3N_4 can be *in situ* formed on the surface of TiO_2, which is consistent with Figure 2(b).

The C1s spectra in Figure 4(a) show that two main carbon species with binding energies of 284.9 and 288.1 eV, corresponding to C–C and C–N–C, respectively. Three binding energies in N1s region (Figure 4(b)) can be observed, which can be indexed to C–N–C (398.8 eV), N–$(C)_3$ (400.1 eV), and N–H groups (401.2 eV), respectively. The binding energy at 529.7 and 533.0 eV can be ascribed to Ti–O, surface hydroxyl groups, and adsorbed molecular water (Figures 4(c) and 4(d)) [22]. The XPS results are consistent with the FT-IR spectra. XPS results also indicate that no peak for Ti–C or Ti–N bond can be observed, which implies that there is no chemical bond connection between g-C_3N_4 and TiO_2.

The nitrogen adsorption-desorption isotherms of pure TiO_2 and g-C_3N_4/TiO_2 nanocomposites obtained under 450°C are shown in Figure 5(a). The two samples show a type IV adsorption isotherm with a H_2 hysteresis loop in the range (P/P_0) of 0.6–1.0, which indicates the presence of mesopores. The surface areas and pore volume of pure TiO_2 are 78 m^2/g and 0.281 cm^3/g, higher than those of g-C_3N_4/TiO_2 nanocomposites (48 m^2/g and 0.216 cm^3/g). The pore size distribution curve (Figure 5(b)) indicates that the large mesopores of pure TiO_2 and g-C_3N_4/TiO_2 nanocomposites are about 37 and 48 nm, respectively. The presence of large mesopores can be ascribed to the aggregation of TiO_2 particles. It can be observed that the g-C_3N_4/TiO_2 nanocomposites have small mesopores of around 13.6 nm (inset in Figure 5(b)), which originates from the presence of layered g-C_3N_4 on the TiO_2 surface. The small mesopore is advantageous for enhancing the adsorption for reactant.

Figure 6 shows the UV-Vis DRS spectra of pure TiO_2 and the as-prepared g-C_3N_4/TiO_2 nanocomposites. It is clear that the visible light absorption of g-C_3N_4/TiO_2 nanocomposites is enhanced with increased treatment temperatures until 450°C. Then the visible light absorption decreases when the temperature is higher than 450°C. This fact implies

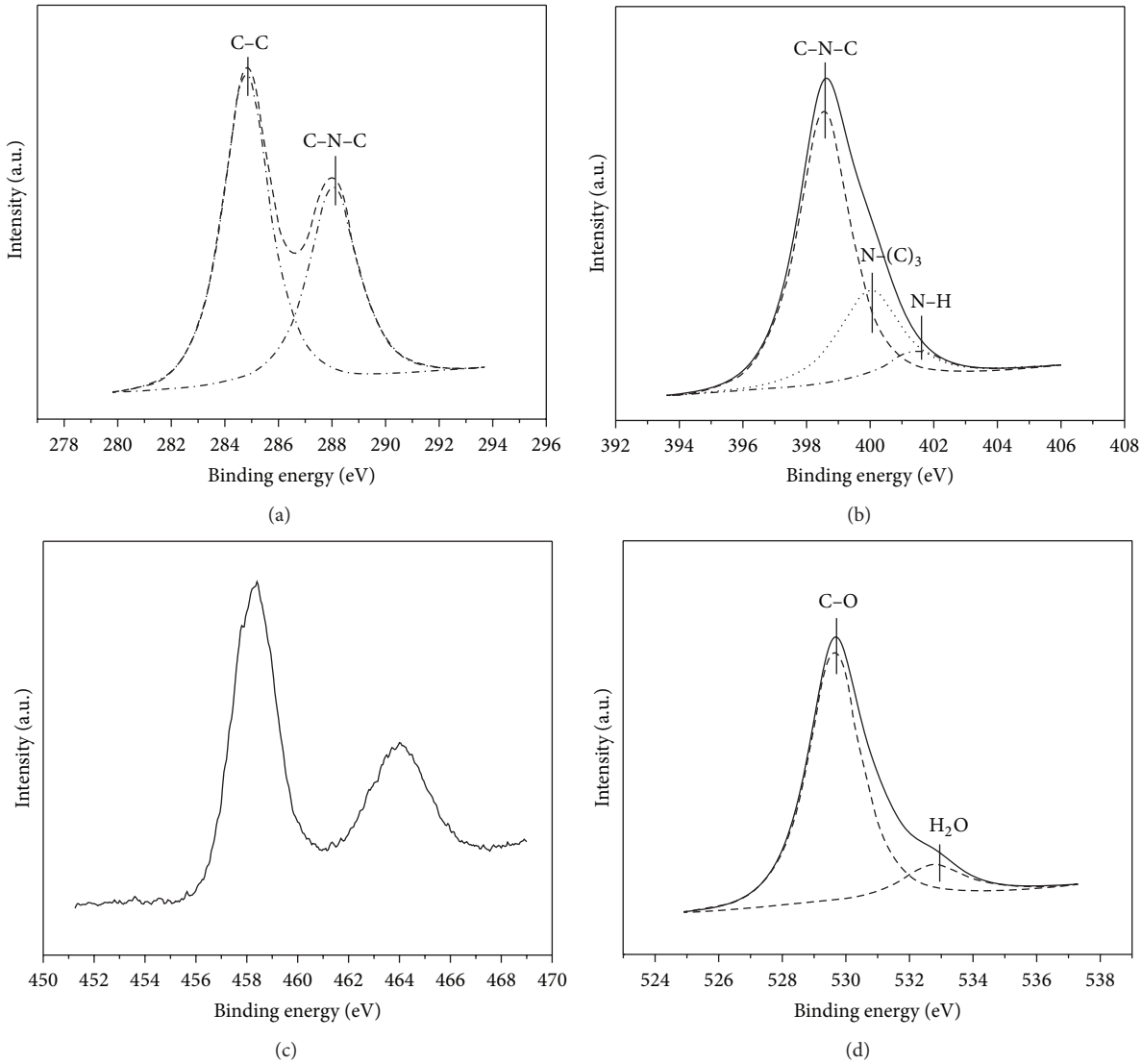

Figure 4: XPS spectra of the as-prepared C_3N_4 coated TiO_2 nanocomposite under 450°C.

that the as-prepared g-C_3N_4 coated TiO_2 nanocomposites under 450°C may exhibit excellent visible light photocatalytic activity. However, the decrease of visible light absorption intensity of coated TiO_2 nanocomposites under higher treatment temperature can be attributed to the decomposition of g-C_3N_4.

Figure 7 shows the adsorption and photocatalytic activity of pure TiO_2 and g-C_3N_4/TiO_2 nanocomposites for removal of MB. It can be seen that the g-C_3N_4/TiO_2 nanocomposites obtained under 450°C exhibit the highest adsorption capacity, which may be ascribed to presence of layered g-C_3N_4 and small mesopores of the nanocomposites sample. The photocatalytic activities of g-C_3N_4/TiO_2 nanocomposites first increase and then decrease with the increased treatment temperature. Pure TiO_2 shows low visible light activity due to its large band gap. The observed slight visible light activity for the pure TiO_2 sample can be ascribed to the photosensitization effect of the MB as MB can absorb visible light [18]. During the visible light irradiation, the part of MB was self-decomposed due to the photosensitization. When TiO_2 was coated by g-C_3N_4, all the nanocomposite samples show decent visible light activity. Under visible light irradiation, g-C_3N_4 with a band gap of 2.7 eV could be excited and the photogenerated electrons could transfer from the conduction band (CB) of g-C_3N_4 to the CB of TiO_2 [17, 18, 24]. The holes in the valence band (VB) of g-C_3N_4 and electrons on the CB of TiO_2 could initiate the following degradation reactions. The as-prepared g-C_3N_4/TiO_2 nanocomposites under 450°C exhibit the highest photocatalytic activity under visible light irradiation. Considering the fact that the surface area of g-C_3N_4/TiO_2 nanocomposites (48 m^2/g) is lower than that of pure TiO_2 (78 m^2/g), the surface area of g-C_3N_4/TiO_2 is not a positive factor. The enhanced visible light activity of g-C_3N_4/TiO_2 should be ascribed to the enhanced visible light adsorption because of the presence of g-C_3N_4 (Figures 2(b) and 6) and the improved MB adsorption

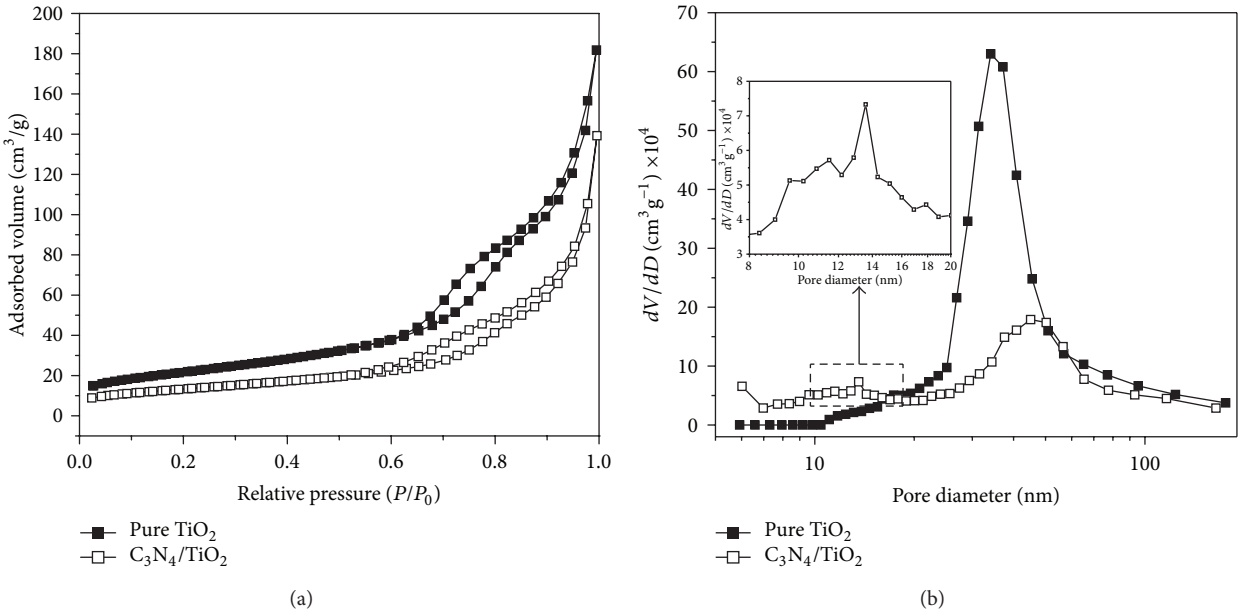

Figure 5: BET-BJH of the pure TiO_2 and C_3N_4 coated TiO_2 nanocomposite obtained under 450°C.

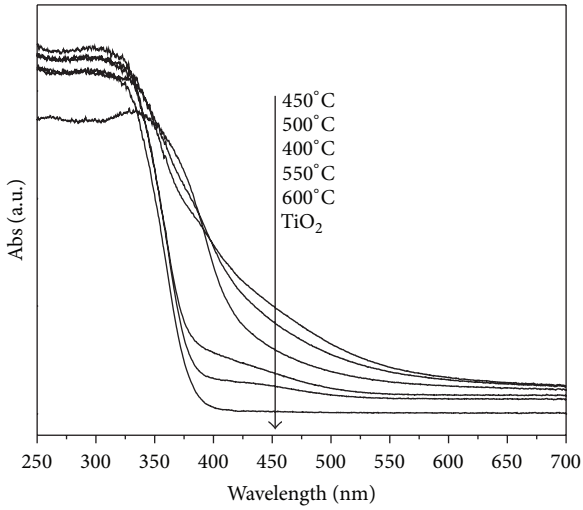

Figure 6: UV-Vis DRS of the pure TiO_2 and g-C_3N_4/TiO_2 samples obtained under different temperatures.

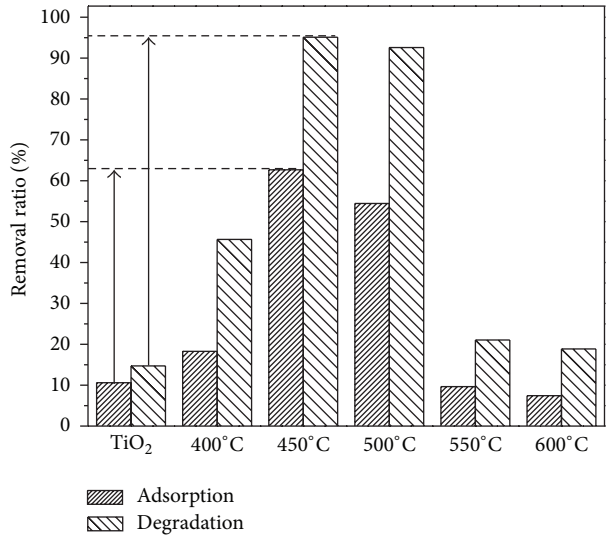

Figure 7: Adsorption and photocatalytic activity of the pure TiO_2 and g-C_3N_4/TiO_2 samples obtained under different temperatures for removal of MB.

because of the small mesopores of the nanocomposites sample (Figure 5(b)). As the precursors (urea and commercial TiO_2) are cheap and preparation method is very simple, the as-prepared g-C_3N_4 coated TiO_2 nanocomposites are ready for large-scale applications in environmental pollution control and solar energy conversion [25].

4. Conclusion

The g-C_3N_4/TiO_2 nanocomposites were synthesized by a cost-effective solid-state approach by thermal treatment of the mixture of urea and commercial TiO_2. It was found that the surface of TiO_2 particles was coated by the *in situ* formed thin layered g-C_3N_4 from urea. The adsorption capacity and visible light photocatalytic activity were significantly enhanced. Under the optimized treatment temperature of 450°C, the g-C_3N_4/TiO_2 nanocomposites exhibited highest adsorption capacity and visible light photocatalytic activity toward removal of MB. The enhanced adsorption capacity can be ascribed to the presence of g-C_3N_4 and small mesopores. The enhanced visible photocatalytic activity originated from the increased visible light adsorption and small mesopores of the nanocomposites sample. The novel

g-C_3N_4 coated TiO_2 nanocomposites prepared by the cost-effective solid-state approach would find wide application in environmental remediation.

Conflict of Interests

The authors declare no conflict of interests.

Acknowledgments

This research is financially supported by the Key Project from CQ CSTC (cstc2013yykfB50008), the Science and Technology Project from Chongqing Education Commission (KJZH11214, KJ120713, KJTD201314, KJTD201020, KJ130725, and KJ090727), the Key Discipline Development Project of CTBU (1252001), the National Natural Science Foundation of China (51108487), and the Natural Science Foundation Project of CQ CSTC (cstc2012jjA20014, CSTC2010BB0260).

References

[1] J. Zhang, J. Sun, K. Maeda et al., "Sulfur-mediated synthesis of carbon nitride: band-gap engineering and improved functions for photocatalysis," *Energy and Environmental Science*, vol. 4, no. 3, pp. 675–678, 2011.

[2] Y. J. Cui, Z. X. Ding, X. Z. Fu, and X. C. Wang, "Construction of conjugated carbon nitride nanoarchitectures in solution at low temperatures for photoredox catalysis," *Angewandte Chemie—International Edition*, vol. 51, no. 47, pp. 11814–11818, 2012.

[3] Z. Z. Lin and X. C. Wang, "Nanostructure engineering and doping of conjugated carbon nitride semiconductors for hydrogen photosynthesis," *Angewandte Chemie—International Edition*, vol. 52, no. 6, pp. 1735–1738, 2013.

[4] Q. Y. Chen and D. Ma, "Preparation of nanostructured Cu_2SnS_3 photocatalysts by solvothermal method," *International Journal of Photoenergy*, vol. 2013, Article ID 593420, 5 pages, 2013.

[5] N. Todorova, T. Giannakopoulou, G. Romanos, T. Vaimakis, J. Yu, and C. Trapalis, "Preparation of fluorine-doped TiO_2 photocatalysts with controlled crystalline structure," *International Journal of Photoenergy*, vol. 2008, Article ID 534038, 9 pages, 2008.

[6] Q. Xiang, J. Yu, and M. Jaroniec, "Graphene-based semiconductor photocatalysts," *Chemical Society Reviews*, vol. 41, no. 2, pp. 782–796, 2012.

[7] X. Li, P. Zhang, L. Jin, T. Shao, Z. Li, and J. Cao, "Efficient photocatalytic decomposition of perfluorooctanoic acid by indium oxide and its mechanism," *Environmental Science and Technology*, vol. 46, no. 10, pp. 5528–5534, 2012.

[8] Z. Wu, Z. Sheng, H. Wang, and Y. Liu, "Relationship between Pd oxidation states on TiO_2 and the photocatalytic oxidation behaviors of nitric oxide," *Chemosphere*, vol. 77, no. 2, pp. 264–268, 2009.

[9] M. Fu, Y. Li, S. Wu, P. Lu, J. Liu, and F. Dong, "Sol-gel preparation and enhanced photocatalytic performance of Cu-doped ZnO nanoparticles," *Applied Surface Science*, vol. 258, no. 4, pp. 1587–1591, 2011.

[10] X. W. Cheng, X. J. Yu, B. Y. Li, L. Yan, Z. P. Xing, and J. J. Li, "Enhanced visible light activity and mechanism of TiO_2 codoped with molybdenum and nitrogen," *Materials Science and Engineering B*, vol. 178, no. 7, pp. 425–430, 2013.

[11] Z. H. Ai, Z. T. Gao, K. Su, W. K. Ho, and L. Z. Zhang, "Aerosol flow synthesis of N, Si-codoped TiO_2 hollow microspheres with enhanced visible-light driven photocatalytic performance," *Catalysis Communications*, vol. 29, no. 5, pp. 189–193, 2012.

[12] F. Dong, W. Zhao, and Z. Wu, "Characterization and photocatalytic activities of C, N and S co-doped TiO_2 with 1D nanostructure prepared by the nano-confinement effect," *Nanotechnology*, vol. 19, no. 36, Article ID 365607, 2008.

[13] P. Periyat, D. E. McCormack, S. J. Hinder, and S. C. Pillai, "One-pot synthesis of anionic (nitrogen) and cationic (sulfur) codoped high-temperature stable, visible light active, anatase photocatalysts," *Journal of Physical Chemistry C*, vol. 113, no. 8, pp. 3246–3253, 2009.

[14] H. Wang, Z. B. Wu, and Y. Liu, "A simple two-step template approach for preparing carbon-doped mesoporous TiO_2 hollow microspheres," *Journal of Physical Chemistry C*, vol. 113, no. 30, pp. 13317–13324, 2009.

[15] F. Chen, W. Zou, W. Qu, and J. Zhang, "Photocatalytic performance of a visible light TiO_2 photocatalyst prepared by a surface chemical modification process," *Catalysis Communications*, vol. 10, no. 11, pp. 1510–1513, 2009.

[16] F. Dong, Y. J. Sun, and M. Fu, "Enhanced visible light photocatalytic activity of V_2O_5 cluster modified N-doped TiO_2 for degradation of toluene in air," *International Journal of Photoenergy*, vol. 2012, Article ID 569716, 10 pages, 2012.

[17] X. S. Zhou, B. Jin, L. D. Li et al., "A carbon nitride/TiO_2 nanotube array heterojunction visible-light photocatalyst: synthesis, characterization, and photoelectrochemical properties," *Journal of Materials Chemistry*, vol. 22, no. 34, pp. 17900–179055, 2012.

[18] S. S. Zhao, S. Chen, H. T. Yu, and X. Quan, "g-C_3N_4/TiO_2 hybrid photocatalyst with wide absorption wavelength range and effective photogenerated charge separation," *Separation and Purification Technology*, vol. 99, no. 8, pp. 50–54, 2012.

[19] J. G. Yu, S. H. Wang, B. Cheng, Z. Lin, and F. Huang, "Noble metal-free $Ni(OH)_2$-g-C_3N_4 composite photocatalyst with enhanced visible-light photocatalytic H_2-production activity," *Catalysis Science Technology*, vol. 3, no. 7, pp. 1782–1789, 2013.

[20] J. S. Zhang, M. W. Zhang, R. Q. Sun, and X. C. Wang, "A facile band alignment of polymeric carbon nitride semiconductors to construct isotype heterojunctions," *Angewandte Chemie—International Edition*, vol. 51, no. 40, pp. 10145–10149, 2012.

[21] F. Dong, L. Wu, Y. Sun, M. Fu, Z. Wu, and S. C. Lee, "Efficient synthesis of polymeric g-C_3N_4 layered materials as novel efficient visible light driven photocatalysts," *Journal of Materials Chemistry*, vol. 21, no. 39, pp. 15171–15174, 2011.

[22] F. Dong, Y. J. Sun, L. W. Wu, M. Fu, and Z. B. Wu, "Facile transformation of low cost thiourea into nitrogen-rich graphitic carbon nitride nanocatalyst with high visible light photocatalytic performance," *Catalysis Science and Technology*, vol. 2, no. 7, pp. 1332–1335, 2012.

[23] F. Dong, S. Guo, H. Wang, X. Li, and Z. Wu, "Enhancement of the visible light photocatalytic activity of C-doped TiO_2 nanomaterials prepared by a green synthetic approach," *Journal of Physical Chemistry C*, vol. 115, no. 27, pp. 13285–13292, 2011.

[24] S. K. Choi, S. Kim, S. K. Lim, and H. Park, "Photocatalytic comparison of TiO_2 nanoparticles and electrospun TiO_2 nanofibers: effects of mesoporosity and interparticle charge transfer," *Journal of Physical Chemistry C*, vol. 114, no. 39, pp. 16475–16480, 2010.

[25] W. D. Zhang, Q. Zhang, F. Dong, and Z. W. Zhao, "The multiple effects of precursors on the properties of polymeric carbon nitride," *International Journal of Photoenergy*, vol. 2013, Article ID 685038, 9 pages, 2013.

Hindawi Publishing Corporation
International Journal of Photoenergy
Volume 2013, Article ID 452542, 10 pages
http://dx.doi.org/10.1155/2013/452542

Research Article

Dynamic Hydrogen Production from Methanol/Water Photo-Splitting Using Core@Shell-Structured CuS@TiO_2 Catalyst Wrapped by High Concentrated TiO_2 Particles

Younghwan Im,[1] Sora Kang,[1] Kang Min Kim,[1] Taeil Ju,[1] Gi Bo Han,[2] No-Kuk Park,[3] Tae Jin Lee,[3] and Misook Kang[1]

[1] *Department of Chemistry, College of Science, Yeungnam University, Gyeongsan, Gyeongbuk 712-749, Republic of Korea*
[2] *Plant Engineering Division, Institute for Advanced Engineering, 633-2 Goan-ri, Baegam-myeon, Cheoin-gu, Yongin-si, Gyeonggi 449-863, Republic of Korea*
[3] *School of Chemical Engineering, Yeungnam University, Gyeongsan, Gyeongbuk 712-749, Republic of Korea*

Correspondence should be addressed to Misook Kang; mskang@ynu.ac.kr

Received 12 July 2013; Revised 1 August 2013; Accepted 1 August 2013

Academic Editor: Jiaguo Yu

This study focused on the dynamic hydrogen production ability of a core@shell-structured CuS@TiO_2 photocatalyst coated with a high concentration of TiO_2 particles. The rectangular-shaped CuS particles, 100 nm in length and 60 nm in width, were surrounded by a high concentration of anatase TiO_2 particles (>4~5 mol). The synthesized core@shell-structured CuS@TiO_2 particles absorbed a long wavelength (a short band gap) above 700 nm compared to that pure TiO_2, which at approximately 300 nm, leading to easier electronic transitions, even at low energy. Hydrogen evolution from methanol/water photo-splitting over the core@shell-structured CuS@TiO_2 photocatalyst increased approximately 10-fold compared to that over pure CuS. In particular, 1.9 mmol of hydrogen gas was produced after 10 hours when 0.5 g of 1CuS@4TiO_2 was used at pH = 7. This level of production was increased to more than 4-fold at higher pH. Cyclic voltammetry and UV-visible absorption spectroscopy confirmed that the CuS in CuS@TiO_2 strongly withdraws the excited electrons from the valence band in TiO_2 because of the higher reduction potential than TiO_2, resulting in a slower recombination rate between the electrons and holes and higher photoactivity.

1. Introduction

In recent years, hydrogen has been highlighted as a next-generation energy source because of its environmentally friendly nature and high-energy efficiency. Therefore, hydrogen production has recently become the most active research topic globally. In particular, the technology for generating hydrogen by the splitting of water using a photocatalyst has attracted considerable attention. In the early days, the photocatalytic formation of hydrogen and oxygen focused extensively on metal-loaded or incorporated-TiO_2 semiconductors due to the low band gap and high corrosion resistance of these materials [1–5]. On the other hand, hydrogen production from water photo-splitting using TiO_2-based photocatalysts is ineffective because the amount of hydrogen produced is limited by the rapid recombination of holes and electrons over TiO_2, resulting in the reformation of water [6]. In addition, more than 1.2 eV is needed to decompose water [7], which means that the photodecomposition of water should be performed at UV wavelengths of approximately 260 nm. Therefore, there is urgent need for the development of new and inexpensive photocatalysts that are both environmentally friendly and possess greater hydrogen-producing activity under visible light irradiation. Recently, studies of metal sulfide photocatalysts, such as ZnS- [8], CuS- [9, 10], FeS- [11], Bi_2S_3- [12], Sb_2S_3- [13], or CdS-loaded TiO_2 [14], have covered topics ranging from synthesis to applications in new photocatalytic reaction mechanisms. Narrow band gaps make it possible to absorb longer wavelengths compared to wide band gaps of conventional metal oxide semiconductor systems. A previous study reported high photocatalytic activity on the ZnS-loaded TiO_2 composite system for hydrogen

production [15]. In that study, the evolution of H_2 from methanol/water (1 : 1) photo-splitting over the ZnS/TiO_2 composite was enhanced dramatically compared to that over pure TiO_2 and ZnS. In particular, 1.2 mmol of H_2 gas was produced after 10 h when 0.5 g of a 5.0 wt% ZnS-loaded TiO_2 composite was used. Recently, many studies began to focus their attention on bimetallic sulfides photocatalysts, such as CdZnS [16], CuZnS [17], ZnInS [18], and AgZnS [19]. These studies have been extended to trimetallic sulfide photocatalysts, such as CuAgInS [20], ZnCuCdS [21], CuInZnS [22], and AgGaInS [23]. On the other hand, most papers are based on metal sulfides loaded on the surface of TiO_2 particles. Few studies have examined TiO_2 nanoparticles loaded on the surface of large-sized metal sulfide particles.

This study focused on the CuS core material with a shorter band-gap of 1.56 eV and a higher reduction potential [24] than those of pure TiO_2. Cu materials are widely used as catalysts for methanol steam reforming because of their excellent redox properties despite vulnerable to water. The potential ($Cu^{2+} + 2e^- = Cu^0$, $E^\circ = -0.224$ V) is slightly lower than the conduction band (−0.26 V) of anatase TiO_2 but is higher than the reduction potential of H^+ ($2H^+ + 2e^- = H_2$, $E^\circ = -0.000$ V), which favors electron transfer from the conduction band of TiO_2 to Cu^{2+}, and the reduction of H^+, thereby enhancing the photocatalytic H_2-production activity [25, 26]. In this study, CuS was synthesized by a hydrothermal method with sodium sulfate as the sulfur source. A Ti precursor at a high concentrated molar ratio was then coated on the surface of the CuS like a core-shell structure. The relationship between the spectroscopic properties and the catalytic performance for the hydrogen production over the core@shell-structured $CuS@TiO_2$ was examined by X-ray diffraction (XRD), transmission electron microscopy (TEM), UV-visible absorption spectroscopy, Brunauer, Emmett, and Teller (BET) surface areas, cyclic voltammetry (CV), and zeta potential measurements using an electrophoresis measurement apparatus.

2. Experimental

2.1. Synthesis of CuS and Core@Shell-Structured $CuS@TiO_2$. The TiO_2, CuS, and core@shell-structured $CuS@TiO_2$ photocatalysts were prepared using hydrothermal and impregnation methods, respectively. In the first step for TiO_2, titanium tetra-isopropoxide (TTIP, 99.99%, Junsei Chemical, Japan) as a titanium precursor was added dropwise to an aqueous solution and stirred homogeneously for 2 h. The pH of the final solution was set to pH = 3.0 using acetic acid to induce mild hydrolysis, and the resulting solution was transferred to an autoclave for thermal treatment. The thermal treatment at 200°C was kept for 12 h, and the resulting precipitates were obtained, washed with distilled water, and dried at 80°C for 24 h. In the second step of CuS synthesis, $CuSO_4{\cdot}5H_2O$ (99.99%, Junsei Chemical, Japan) and $Na_2S_2O_3{\cdot}5H_2O$ (99.99%, Junsei Chemical, Japan) were used as the Cu and S precursors to prepare the sol mixture, respectively. Copper sulfate and sodium sulfate were dissolved sequentially in distilled water and stirred to homogeneity for 2 h. The final solution was transferred to an autoclave for thermal treatment. Cu ions were sulfurized during the thermal treatment at 180°C for 12 h. The resulting precipitates were obtained, washed with distilled water, and dried at 80°C for 24 h. Finally the dried powders were treated at 400°C for 4 h to obtain crystallized CuS. Finally, 4.0 and 5.0 moles of TTIP (titanium tetraisopropoxide, 99.99%, Aldrich) for each 1.0 mole of CuS were added slowly to an ethanol solution containing the dispersed CuS particles during stirring to coat the CuS surface. The pH of the colloidal solution was kept at 4.0, and the solution was stirred homogeneously for 18 h. The final solution was evaporated at 80°C for 5 h and calcined at 400°C for 4 h to induce the anatase TiO_2. Finally, three types of materials, CuS and the core@shell-structured $1CuS@4TiO_2$ and $1CuS@5TiO_2$, were examined. Three samples of pure TiO_2 (by hydrothermal method), CuS, and physically mixed TiO_2/CuS were also prepared for comparison.

2.2. Characteristics of Synthesized CuS and Core@Shell-Structured $CuS@TiO_2$. The synthesized CuS and core@shell-structured $CuS@TiO_2$ photocatalysts were examined by XRD (X'Pert Pro *MPD PANalytical* 2-circle diffractometer) using nickel-filtered CuKα radiation (30 kV and 30 mA). The sizes and shapes of the CuS and core@shell-structured $CuS@TiO_2$ photocatalysts were examined by TEM (JEOL 2000EX). The BET surface areas of catalysts were measured using a Belsorp II instrument. All the catalysts were degassed under vacuum at 150°C for 30 min before the BET surface measurements. The catalysts were measured through the nitrogen gas adsorption using a continuous flow method with a mixture of nitrogen and helium as the carrier gas. The UV-visible absorption spectra of CuS and core@shell-structured $CuS@TiO_2$ powders were obtained using a Cary 500 spectrometer with a reflectance sphere. The CV measurements of the CuS and core@shell-structured $CuS@TiO_2$ pellets were obtained using a BAS 100B potentiostat at room temperature in 0.1 M KCl solution. A platinum wire as the counter electrode and Ag/AgCl as the reference electrode were used. The zeta potential of CuS and core@shell-structured $CuS@TiO_2$ particles was determined by the electrophoretic mobility using an electrophoresis measurement apparatus (ELS 8000, Otsuka Electronics, Japan) with a plate sample cell. Electrophoretic light scattering (ELS) was performed in reference beam mode using a laser light source of 670 nm, a modular frequency of 250 Hz, and a scattering angle of 15°. The standard error of the zeta potential, converted from the experimentally determined electrophoretic mobility, was typically <1.5%, and the percentage error was <5%. To measure the zeta potentials, 0.1 wt% of each sample was dispersed in deionized water, and the pH of the solution was adjusted with HCl or NaOH. The relative molecular diameter size distributions of the various solutions were also measured using this equipment.

2.3. Hydrogen Production from Photo-Splitting of Methanol/Water over CuS and Core@Shell-Structured $CuS@TiO_2$. Photo-splitting in methanol/water using CuS and core@shell-structured $CuS@TiO_2$ photocatalysts was carried out using a liquid photoreactor designed in house, as shown in Figure 1.

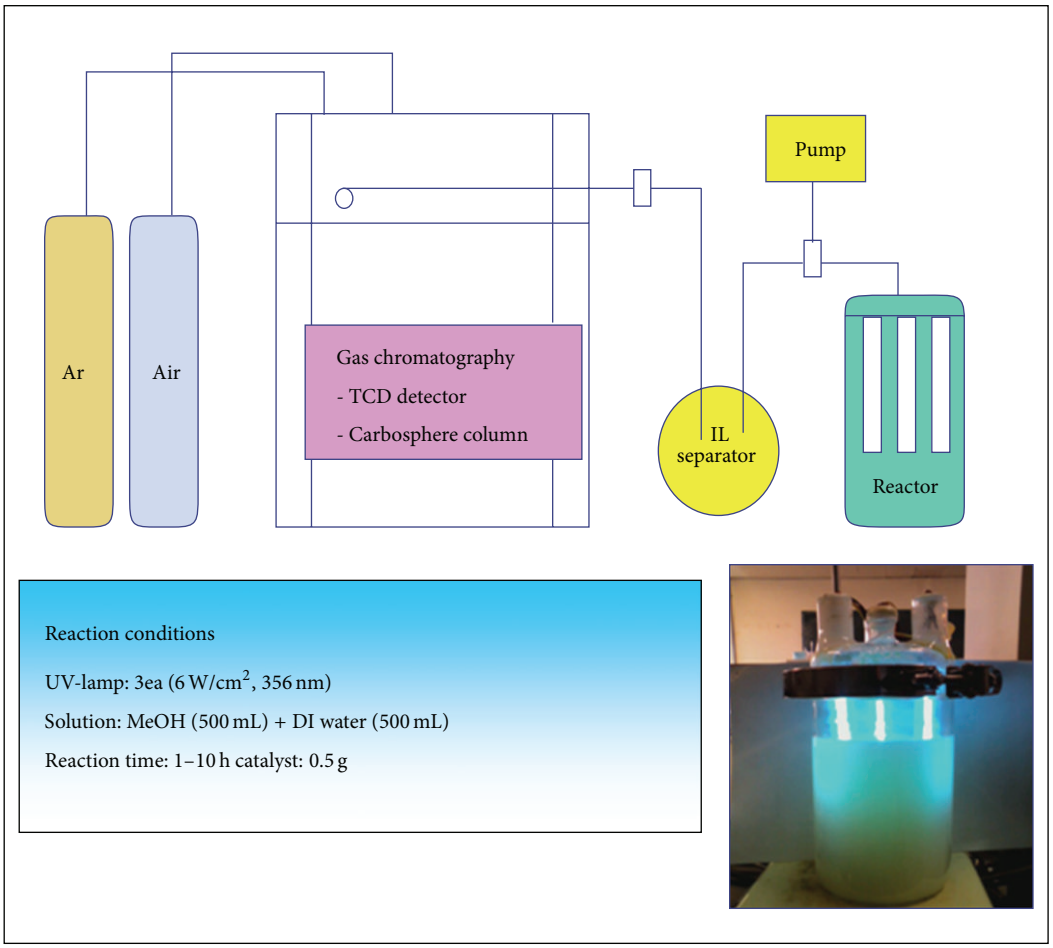

Figure 1: Apparatus of a liquid photoreactor for the methanol/water photo-splitting using CuS and core@shell-structured CuS@TiO_2 photocatalysts.

For methanol/water photo-splitting, 0.5 g of a photocatalyst was added to 1.0 L distilled water in a 2.0 L Pyrex reactor. UV-lamps (6×3 W cm^{-2} = 18 W cm^{-2}, 30 cm length × 2.0 cm diameter; Shinan Co.) emitting radiation with a wavelength of 365 nm were used. Methanol/water photo-splitting was carried out for 10 h with constant stirring, and the level of hydrogen evolution was measured at 1 h intervals. The hydrogen gas (H_2) produced during methanol/water photo-splitting was analyzed by TCD-type gas chromatography (GC, model DS 6200; Donam Instruments Inc., Republic of Korea). To determine the products and intermediates, the GC was connected directly to the methanol/water photo-splitting reactor. The following GC conditions were used: TCD detector; Carbosphere column (Alltech, Deerfield, IL, USA); and an injection, initial, final, and detector temperature of 413 K, 393 K, 393 K, and 423 K, respectively.

3. Results and Discussion

3.1. Properties of Synthesized CuS and Core@Shell-Structured CuS@TiO_2. Figure 2 shows XRD patterns of the TiO_2, CuS,

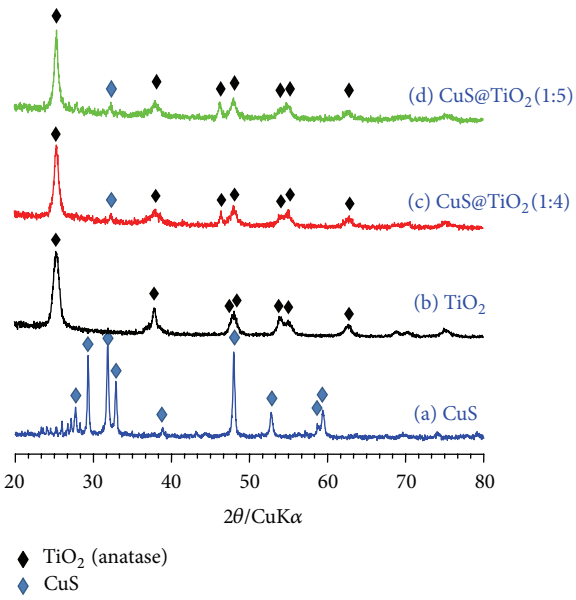

Figure 2: XRD patterns of the CuS and CuS@TiO_2 photocatalysts.

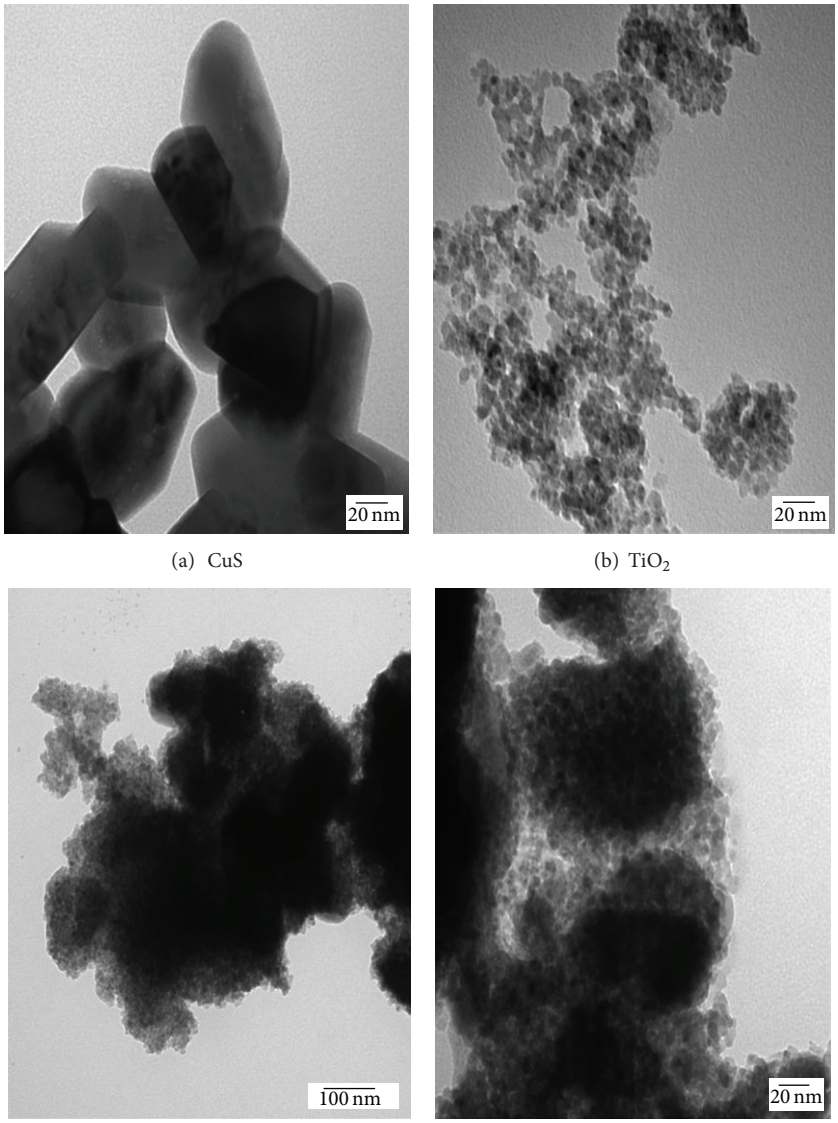

(a) CuS (b) TiO_2

(c) CuS@TiO_2 (1 : 4) (d) CuS@TiO_2 (1 : 5)

Figure 3: TEM images of the CuS and CuS@TiO_2 photocatalysts.

and CuS@TiO_2 photocatalysts. All the peaks in CuS were indexed to the hexagonal phase CuS (P63/mmc space, cell constants $a = 3.8$ Å, $b = 3.8$ Å, and $c = 16.43$ Å; JCPDS Card no. 02-0820). The XRD patterns showed the main peaks at 26.75, 27.51, 29.36, 31.82, 33.03, 38.96, 43.04, 44.60, 52.88, 59.18, 63.69, 67.86, 69.58, 74.00, and 79.08° 2θ, which were assigned to the (100), (101), (102), (103), (006), (105), (106), (008), (110), (114), (116), (1010), (0012), (207), (208), and (213) planes, respectively. In the case of CuS@TiO_2, the peaks for crystalline CuS almost disappeared except for a very small peak at 33.03° 2θ (006). This result coincides with the fact that in general if the core-shell structure formed completely in a core-shell material, the XRD peaks for the core do not appear; only the diffraction patterns for the shell are observed [27]. Otherwise, the XRD patterns for crystalline TiO_2 (anatase, tetragonal crystal system, I41/amd space, JCPDS Card no. 02-0387) in CuS@TiO_2 were observed at 25.35, 37.93, 48.10, 53.89, 55.30, 68.99, 70.18, and 75.37° 2θ, which were assigned to the (101), (004), (200), (105), (211), (116), (220), and (215) planes, respectively. The locations were the same as the hydrothermally prepared pure TiO_2 in (b). The peaks in CuS@TiO_2 were slightly larger according to the loaded Ti concentration. The XRD peak intensities that were assigned to anatase TiO_2 in 1CuS@5TiO_2 were slightly sharper than those of CuS@TiO_2 loaded with 4.0 mol-concentrated Ti. Generally, the line widths of the XRD peaks were broad, which indicated a smaller crystallite size. The Scherrer equation, $t = 0.9\lambda/\beta\cos\theta$, where λ is the wavelength of incident X-rays, β is the full width at half maximum (FWHM) in radians, and θ is the diffraction angle,

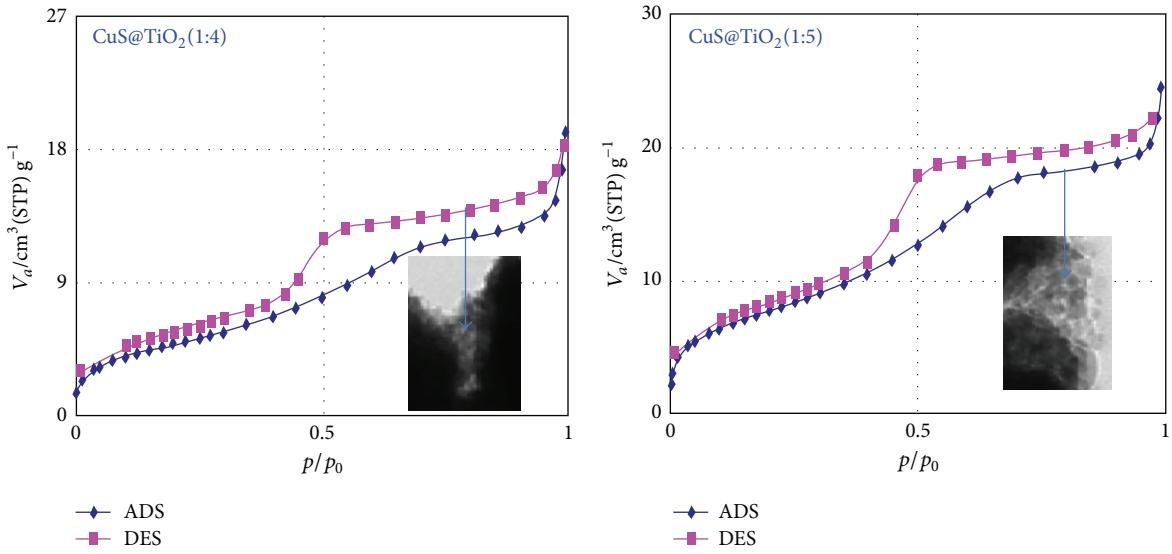

(a) (b)

	CuS@TiO_2(1:4)	CuS@TiO_2(1:5)
Surface area ($m^2\,g^{-1}$)	17.88	27.966
Total pore volume ($cm^3\,g^{-1}$)	0.02973	0.037988
Average pore diameter (nm)	6.651	5.4334

(c)

Figure 4: Adsorption-desorption isotherm curves of N_2 at 77 K for the core@shell-structured CuS@TiO_2.

was used to determine the crystallite size. The loaded TiO_2 crystallite sizes of 1CuS@4TiO_2 and 1CuS@5TiO_2 based on the 25.35° 2θ peak were 17.50 and 17.90 nm, respectively.

Figure 3 shows TEM images of the CuS and CuS@TiO_2 powders. Rectangular-shaped particles with 100 nm long and 60 nm wide sides were observed in the CuS sample, and 10 nm sized TiO_2 particles were also observed in TiO_2 samples. Here, the nanosized TiO_2 particles were synthesized hydrothermally for comparison. Interestingly, the huge CuS particles were surrounded by nanosized TiO_2 particles with high concentrations (4~5 moles compared to 1 mole of core CuS). This is in good agreement with the XRD patterns. This is a reliable result in that, when the loaded TiO_2 amounts increased, the shell composed of TiO_2 particles was thicker. TEM confirmed that the obtained CuS@TiO_2 sample had a core@shell structure.

Figure 4 shows the adsorption-desorption isotherm curves of N_2 at 77 K for the fresh powder samples and core@shell-structured CuS@TiO_2. The isotherms belonged to the IV type in the IUPAC classification [28]. Generally, this hysteresis slope has been observed in the presence of large mesopores. Here, the mesopores are considered to be bulk pores formed between TiO_2 particles in the shell. This suggests that the reaction of the catalyst with a high surface area facilitates adsorption, which can improve the catalytic activity. Therefore, it is expected that the methanol or water molecules are adsorbed more easily on the surfaces of the core@shell-structured CuS@TiO_2 than those of pure TiO_2 or CuS particles during methanol/water photo-splitting. The surface area increased from 17.88 to 27.97 $m^2\,g^{-1}$ according to the change in TiO_2 concentration from 4.0 to 5.0 mol. Generally, the specific surface area increases with decreasing particle size. Here, the loaded TiO_2 particle sizes in the two samples were similar. Therefore, the surface area in this study possibly depends on the bulk pores formed by aggregation between the TiO_2 particles in the shell. The total bulk-pore volumes increased from 0.029 (4 mol TiO_2 loading) to 0.038 (5 mol TiO_2 loading) $cm^3\,g^{-1}$. Eventually, the specific surface area increased with increasing pore volume.

Figure 5 shows the UV-visible absorption spectra of the CuS and core@shell-structured CuS@TiO_2 powders. The absorption edges of Ti^{4+} and Cu^{2+} with octahedral symmetries normally appear at a maximum of approximately 300 and 700 nm in pure TiO_2 and CuS, respectively [29, 30]. The band gap in a semiconductor material is closely related to the wavelength range absorbed, where the band gap decreases with increasing absorption wavelength. Consequently, a material with a narrow band gap can be extended readily to utilize visible light, whereas a narrow band gap can reduce photocatalytic activity by increasing the recombination rate

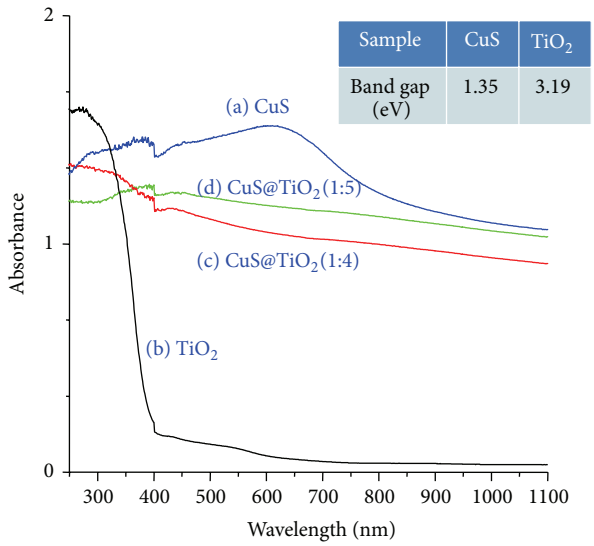

Figure 5: UV-visible absorption spectra of the CuS and core@shell-structured CuS@TiO_2 powders.

between the electrons and holes. Based on the Tauc equation [31], the band gaps obtained by extrapolation at the cross-section point of the two tangents were approximately 1.35 and 3.19 eV for pure CuS and TiO_2, respectively.

Figure 6 presents the CV measurements of CuS and the core@shell-structured CuS@TiO_2, indicating high dependence on the analytic conditions being studied, which must be redox active within the experimental potential window. A reversible wave that provides the following information is desirable: reversible reactions will show a ratio of the peak currents passed at reduction (E_{pc}) and oxidation (E_{pa}). When such reversible peaks are observed, thermodynamic information in the form of a half cell potential $E^{\circ}_{1/2}(E_{pc} + E_{pa}/2)$ can be determined. In particular, when the waves are semireversible, such as when $E_{pa}/E_{pc} \geq 1$, it can be possible to induce even more information, particularly in kinetic processes. Recently, some studies reported a useful equation that can determine the energy levels of the HOMO and LUMO using a CV method [32]. In the synthesized CuS, the Cu(II) $\rightarrow$ Cu(0) redox process appeared to be a reversible reaction, and the absolute potential in the reduction (E_{pc}) was observed at −0.732 V. The onset potentials in the core@shell-structured CuS@TiO_2 samples might be used to determine the thermodynamic $E^{\circ}_{1/2}$ as −1.255 and −2.59 V in 1CuS@4TiO_2 and 1CuS@5TiO_2, respectively. The CV curves were observed at two locations, and there might be two factors from TiO_2 (front) and CuS (back), −1.79 and −0.712 V, respectively. Therefore, the corresponding LUMO energy levels were calculated to be −3.65 (for CuS), −3.12 (for 1CuS@4TiO_2), and −3.668 (for 1CuS@5TiO_2) eV, respectively.

Figure 7 summarizes the hydrogen evolution from methanol/water photo-splitting over the CuS, TiO_2, and two types of core@shell-structured CuS@TiO_2 photocatalysts in a batch-type liquid photosystem, and the catalytic performance of a physically mixed CuS+TiO_2 sample was also evaluated for comparison. The catalytic activities of the core@shell-structured CuS@TiO_2 photocatalysts were enhanced considerably compared to the pure CuS or TiO_2. In Figure 7(a), a very small amount of hydrogen was collected over CuS (0.2 mmol) and TiO_2 (0.09 mmol) after methanol/water photo-splitting for 10 h. A significant amount of hydrogen gas was collected over CuS@TiO_2, and the amount of hydrogen produced reached 1.9 mmol over 0.5 g 1CuS@4TiO_2. On the other hand, the amount produced was significantly lower on the core@shell-structured 1CuS@5TiO_2 catalyst with higher Ti incorporation. Here, CuS absorbs longer wavelengths easily, but recombination between the excited electrons and the holes also causes rapid catalytic deactivation. In contrast, the core@shell-structured CuS@TiO_2 has stronger oxidation-reduction ability than pure CuS. Here, the CuS core acts as a good electron collector excited from TiO_2 and transporter, resulting in the retardation of electron-hole recombination, leading to an increase in photocatalytic performance. On the other hand, the collected hydrogen did not increase significantly over the physically mixed CuS+TiO_2 sample. The catalytic performance of methanol/water destruction over the core@shell-structured 1CuS@4TiO_2 was enhanced more under the alkali electrolytes solution, as shown in Figure 7(b). When OH^- ions are present in the alkali solution, the subsequent reaction occurs: $OH^- + \text{hole} \rightarrow {}^{\bullet}OH$ in the valence band. Therefore, a large number of OH radicals are generated in the alkali solution, resulting in an increase in hydrogen evolution. Hydrogen production was increased dramatically in the alkali solution by generating more OH ions, reaching up to 8.0 mmol after 10 h in a KOH (pH = 11) solution. In an acidic solution, however, the level of production was decreased due to SO_4^{2-} ions formed after the reaction. The S ions inside the CuS catalyst appear to dissolve in the acidic solution, followed by a reaction with O ions in water to form SO_4^{2-} ions. Eventually, the sulfate ions combine with the hydrogen ions generated during the methanol/water photo-splitting process, which occurs during the formation of H_2SO_4.

Figure 8 shows the influence of pH on the zeta potential distribution in the CuS, TiO_2, and two types of core@shell-structured CuS@TiO_2. The adjacent table summarizes the aggregated particle sizes in the aqueous solution. The zeta potential of the 1CuS@4TiO_2 suspensions decreased significantly with increasing pH. The surface charges in all samples changed from a positive value in an acidic solution to a larger negative value in an alkali solution. The isoelectric points, meaning the large aggregation of particles, were different: 5.8, 7.9, 7.0, and 7.7 for CuS, TiO_2, 1CuS@4TiO_2, and 1CuS@5TiO_2, respectively. At pH = 11.0, the surface charges in all samples showed the highest absolute value. This suggests that the colloidal samples were stable [33] with high mobility, which is closely related to the reaction sites over the photocatalyst surface. This result matches the results in Figure 6 well.

The CV curves, UV-visible absorption spectra, and their photocatalytic performance suggest a photocatalysis model over the core@shell-structured CuS@TiO_2, as shown in Scheme 1. The TiO_2 shells covered the core CuS completely, which means that the electrons on the valence band of

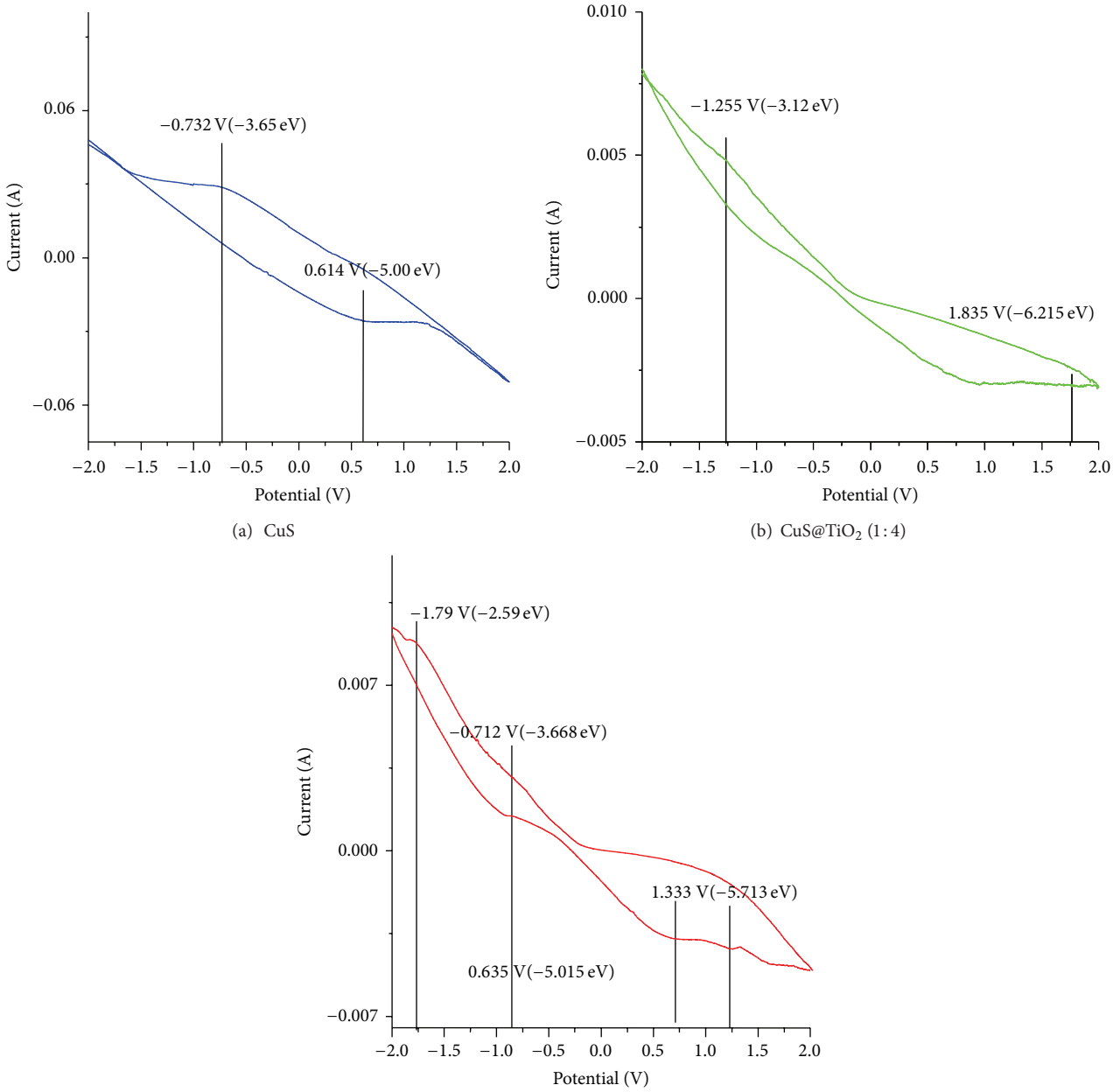

(a) CuS

(b) CuS@TiO_2 (1 : 4)

(c) CuS@TiO_2 (1 : 5)

Figure 6: Cyclic voltammetry for the CuS and core@shell-structured CuS@TiO_2.

TiO_2 will be transferred to the conduction band. The excited electrons are moved to the valence band in CuS because of its higher reduction potential than TiO_2. In this study the core CuS acted as a good electron collector and transporter, similar to reduced graphene oxide reported in another paper [34]. Therefore, the recombination of electrons and holes was reduced, and finally more OH radicals were generated easily at the holes in the valence band of TiO_2. Radicals with strong oxidative power attack CH_3OH molecules, and CO_2, H_2, and H_2O are produced by the complete oxidation of methanol. In addition, if the core CuS also absorbs the radiation (if it does not have a complete core@shell structure), the electrons would be excited more easily from the valence band of CuS. Overall, the catalytic activity of CuS@TiO_2 is performed more effectively in the methanol/water photosplitting reaction. This also means that the electrons excited from the valence band over CuS@TiO_2 recombine slowly with the holes during photocatalysis. Therefore, the hole effect at the valence band continues for a longer time than those in pure CuS or TiO_2. In addition, according to the UV-visible spectra, the CuS@TiO_2 samples exhibited enhanced absorbance over the entire visible-light region. Therefore, the CuS core can also absorb visible radiation compared to the TiO_2 shell, which can only absorb UV light. Consequently,

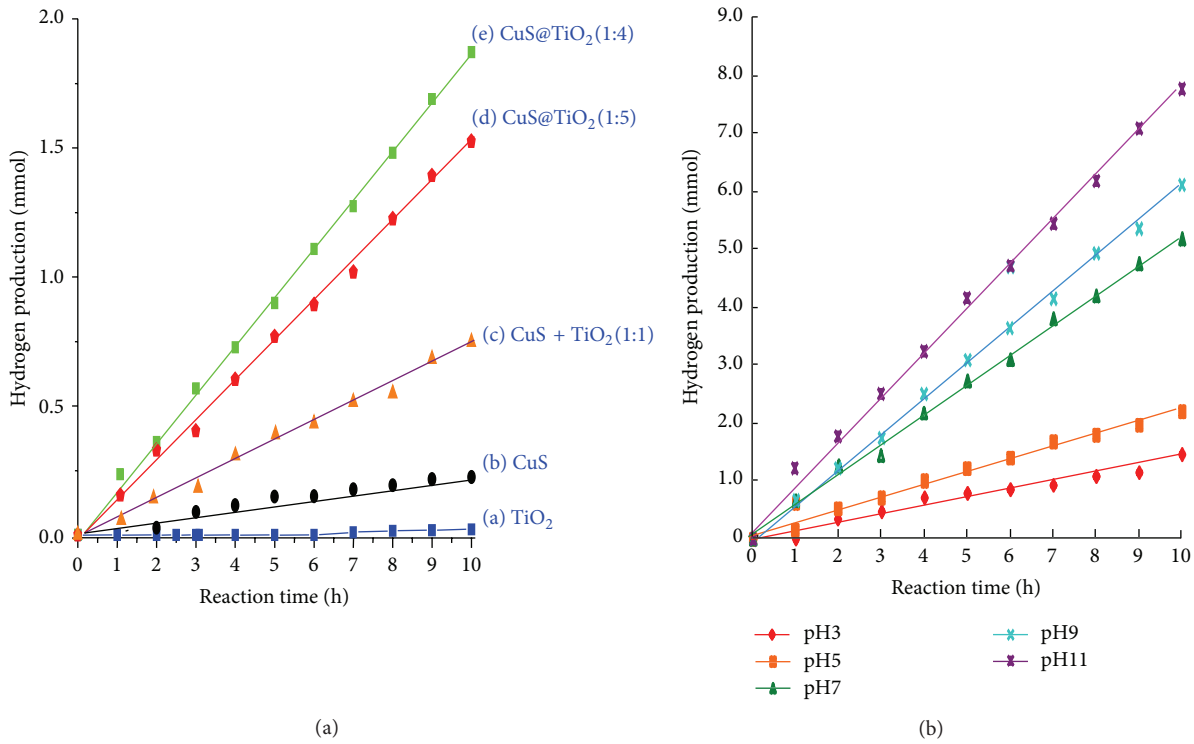

Figure 7: Evolution of H_2 from methanol/water photo-splitting over the CuS, TiO_2, and two types of core@shell-structured CuS@TiO_2 photocatalysts in a batch-type liquid photosystem. (a) Hydrogen production according to the catalysts and (b) hydrogen production according to the pH for 1CuS@4TiO_2.

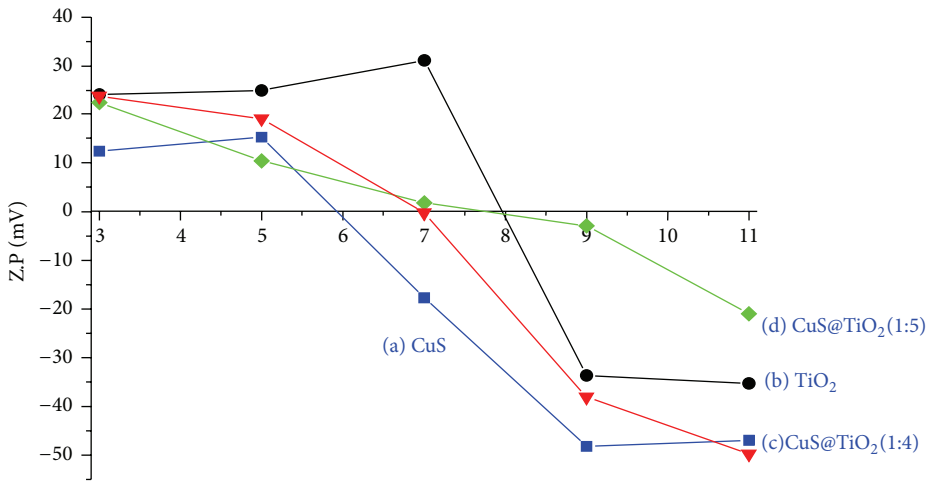

	(a) CuS		(b) TiO_2		(c)CuS@TiO_2(1:4)		(d) CuS@TiO_2(1:5)	
pH	Zeta potential (mV)	Mobility (cm^2/Vs)	Zeta potential (mV)	Mobility (cm^2/Vs)	Zeta potential (mV)	Mobility (cm^2/Vs)	Zeta potential (mV)	Mobility (cm^2/Vs)
3	12.47	9.739e(−4)	24.06	1.944e(−4)	23.76	1.853e(−4)	22.42	1.749e(−4)
5	15.34	1.199e(−5)	24.89	1.944e(−4)	19.13	1.492e(−4)	10.5	8.189e(−5)
7	−17.65	−1.377e(−4)	31.13	4.478e(−4)	−0.23	−1.802e(−6)	1.84	1.435e(−5)
9	−48.24	−3.775e(−4)	−33.61	−2.752e(−4)	−38.08	−2.970e(−4)	−2.88	−2.246e(−4)
11	−47.01	−3.673e(−4)	−35.29	−2.752e(−4)	−49.78	−3.887e(−4)	−20.94	−1.636e(−4)

Figure 8: Zeta potential distributions of the CuS, TiO_2, and two types of core@shell-structured CuS@TiO_2 according to the pH.

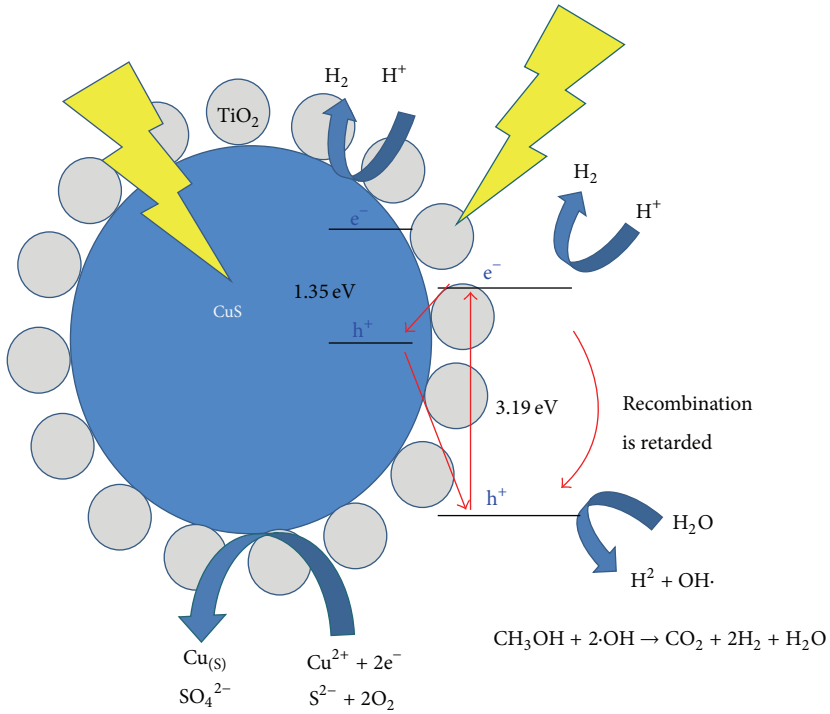

Scheme 1: Supposed photocatalysis model over the core@shell-structured CuS@TiO_2.

the photocatalytic activity is enhanced over the core@shell-structured CuS@TiO_2 photocatalysts.

4. Conclusions

Core@shell-structured CuS@TiO_2 was synthesized using hydrothermal/impregnation methods. Based on the UV-visible absorption and CV results, the band gap of the pure CuS was estimated to be approximately 1.35 eV, respectively, and the corresponding LUMO energy level was −3.65 eV. ELS showed that the core@shell-structured 1CuS@4TiO_2 particles were stable in an alkali solution. A significant amount of hydrogen gas was collected over 0.5 g of the core@shell-structured 1CuS@4TiO_2 photocatalyst, and the amount reached 1.9 mmol with a maximum yield of 8.0 mmol after 10 h in a KOH solution. This was due most likely to the slower recombination between the electrons and a hole, which enables higher catalytic performance over the core@shell-structured 1CuS@4TiO_2. These results are expected to play a significant role in the development of new photocatalysts with a core@shell structure for dramatic hydrogen production.

Acknowledgment

This work was supported by the New & Renewable Energy of the Korea Institute of Energy Technology Evaluation and Planning (KETEP) Grant funded by the Korea government Ministry of Knowledge Economy (no. 20103020050040).

References

[1] S. Xu, A. J. Du, J. Liu, J. Ng, and D. D. Sun, "Highly efficient CuO incorporated TiO_2 nanotube photocatalyst for hydrogen production from water," *International Journal of Hydrogen Energy*, vol. 36, no. 11, pp. 6560–6568, 2011.

[2] S. Xu, J. Ng, X. Zhang, H. Bai, and D. D. Sun, "Fabrication and comparison of highly efficient Cu incorporated TiO_2 photocatalyst for hydrogen generation from water," *International Journal of Hydrogen Energy*, vol. 35, no. 11, pp. 5254–5261, 2010.

[3] S. Onsuratoom, T. Puangpetch, and S. Chavadej, "Comparative investigation of hydrogen production over Ag-, Ni-, and Cu-loaded mesoporous-assembled TiO_2-ZrO_2 mixed oxide nanocrystal photocatalysts," *Chemical Engineering Journal*, vol. 173, no. 2, pp. 667–675, 2011.

[4] Q. Wang, N. An, Y. Bai et al., "High photocatalytic hydrogen production from methanol aqueous solution using the photocatalysts CuS/TiO_2 ," *International Journal of Hydrogen Energy*, vol. 38, no. 25, pp. 10739–10745, 2013.

[5] T. Miwa, S. Kaneco, H. Katsumata et al., "Photocatalytic hydrogen production from aqueous methanol solution with CuO/Al_2O_3/TiO_2 nanocomposite," *International Journal of Hydrogen Energy*, vol. 35, no. 13, pp. 6554–6560, 2010.

[6] M. Zhong, J. Shi, W. Zhang, H. Han, and C. Li, "Charge recombination reduction in dye-sensitized solar cells by depositing ultrapure TiO_2 nanoparticles on "inert" $BaTiO_3$ films," *Materials Science and Engineering B*, vol. 176, no. 14, pp. 1115–1122, 2011.

[7] L. S. Yoong, F. K. Chong, and B. K. Dutta, "Development of copper-doped TiO_2 photocatalyst for hydrogen production under visible light," *Energy*, vol. 34, no. 10, pp. 1652–1661, 2009.

[8] A. H. Gordillo, F. Tzompantzi, and R. Gómez, "An efficient ZnS-UV photocatalysts generated in situ from $ZnS(en)_{0.5}$ hybrid

during the H_2 production in methanol-water solution," *International Journal of Hydrogen*, vol. 37, no. 22, pp. 17002–17008, 2012.

[9] P. Gomathisankar, K. Hachisuka, H. Katsumata, T. Suzuki, K. Funasaka, and S. Kaneco, "Photocatalytic hydrogen production with CuS/ZnO from aqueous $Na_2S + Na_2SO_3$ solution," *International Journal of Hydrogen Energy*, vol. 38, no. 21, pp. 8625–8630, 2013.

[10] L. Qi, J. Yu, and M. Jaroniec, "Preparation and enhanced visible-light photocatalytic H_2-production activity of CdS-sensitized Pt/TiO_2 nanosheets with exposed (001) facets," *Physical Chemistry Chemical Physics*, vol. 13, no. 19, pp. 8915–8923, 2011.

[11] G. Lee and M. Kang, "Physicochemical properties of core/shell structured pyrite FeS_2/anatase TiO_2 composites and their photocatalytic hydrogen production performances," *Current Applied Physics*, vol. 13, no. 7, pp. 1482–1489, 2013.

[12] J. Kim and M. Kang, "High photocatalytic hydrogen production over the band gap-tuned urchin-like Bi_2S_3-loaded TiO_2 composites system," *International Journal of Hydrogen Energy*, vol. 37, no. 10, pp. 8249–8256, 2012.

[13] J. Kim, Y. Sohn, and M. Kang, "New fan blade-like core-shell $Sb_2Ti_xS_y$ photocatalytic nanorod for hydrogen production from methanol/water photolysis," *International Journal of Hydrogen Energy*, vol. 38, no. 10, pp. 2136–2143, 2013.

[14] P. Gao, J. Liu, T. Zhang, D. D. Sun, and W. Ng, "Hierarchical TiO_2/CdS "spindle-like" composite with high photodegradation and antibacterial capability under visible light irradiation," *Journal of Hazardous Materials*, vol. 229-230, pp. 209–216, 2012.

[15] H. Lee, Y. Park, and M. Kang, "Synthesis of characterization of Zn_xTi_yS and its photocatalytic activity for hydrogen production from methanol/water photo-splitting," *Journal of Industrial and Engineering Chemistry*, vol. 19, no. 4, pp. 1162–1168, 2013.

[16] C. Xing, Y. Zhang, W. Yan, and L. Guo, "Band structure-controlled solid solution of $Cd_{1-x}Zn_xS$ photocatalyst for hydrogen production by water splitting," *International Journal of Hydrogen Energy*, vol. 31, no. 14, pp. 2018–2024, 2006.

[17] T. T. ThanhThuy, P. Sheng, C. Huang et al., "Synthesis and photocatalytic application of ternary Cu-Zn-S nanoparticle-sensitized TiO_2 nanotube arrays," *Chemical Engineering Journal*, vol. 210, pp. 425–431, 2012.

[18] K. W. Cheng and C. J. Liang, "Preparation of Zn-In-S film electrodes using chemical bath deposition for photoelectrochemical applications," *Solar Energy Materials and Solar Cells*, vol. 94, no. 6, pp. 1137–1145, 2010.

[19] S. Sahai, M. Husain, V. Shanker, N. Singh, and D. Haranath, "Facile synthesis and step by step enhancement of blue photoluminescence from Ag-doped ZnS quantum dots," *Journal of Colloid and Interface Science*, vol. 357, no. 2, pp. 379–383, 2011.

[20] F. Jia, Z. Yao, and Z. Jiang, "Solvothermal synthesis ZnS-In_2S_3-Ag_2S solid solution coupled with $TiO_{2-x}S_x$ nanotubes film for photocatalytic hydrogen production," *International Journal of Hydrogen Energy*, vol. 37, no. 4, pp. 3048–3055, 2012.

[21] J. U. Kim, Y. K. Kim, and H. Yang, "Reverse micelle-derived Cu-doped $Zn_{1-x}Cd_xS$ quantum dots and their core/shell structure," *Journal of Colloid and Interface Science*, vol. 341, no. 1, pp. 59–63, 2010.

[22] K. W. Cheng, C. M. Huang, Y. C. Yu, C. T. Li, C. K. Shu, and W. L. Liu, "Photoelectrochemical performance of Cu-doped $ZnIn_2S_4$ electrodes created using chemical bath deposition," *Solar Energy Materials and Solar Cells*, vol. 95, no. 7, pp. 1940–1948, 2011.

[23] J. Sun, G. Chen, G. Xiong, J. Pei, and H. Dong, "Hierarchical microarchitectures of $AgGa_{1-x}In_xS_2$: long chain alcohol assisted synthesis, band gap tailoring and photocatalytic activities of hydrogen generation," *International Journal of Hydrogen Energy*, vol. 38, no. 25, pp. 10731–10738, 2013.

[24] H. Qi, J. Huang, L. Cao, J. Wu, and J. Li, "Controlled synthesis and optical properties of doughnut-aggregated hollow sphere-like CuS," *Ceramics International*, vol. 38, no. 8, pp. 6659–6664, 2012.

[25] J. Zhang, J. Yu, Y. Zhang, Q. Li, and J. R. Gong, "Visible light photocatalytic H_2-production activity of CuS/ZnS porous nanosheets based on photoinduced interfacial charge transfer," *Nano Letters*, vol. 11, no. 11, pp. 4774–4779, 2011.

[26] J. Yu and J. Ran, "Facile preparation and enhanced photocatalytic H_2-production activity of $Cu(OH)_2$ cluster modified TiO_2," *Energy and Environmental Science*, vol. 4, no. 4, pp. 1364–1371, 2011.

[27] J. Zhang, Z. Liu, B. Han et al., "Preparation of silica and TiO_2-SiO_2 core-shell nanoparticles in water-in-oil microemulsion using compressed CO_2 as reactant and antisolvent," *Journal of Supercritical Fluids*, vol. 36, no. 3, pp. 194–201, 2006.

[28] J. Du, G. Zhao, H. Pang, Y. Qian, H. Liu, and D. J. Kang, "A template method for synthesis of porous Sn-doped TiO_2 monolith and its enhanced photocatalytic activity," *Materials Letters*, vol. 93, pp. 419–422, 2013.

[29] F. Deng, Y. Li, X. Luo, L. Yang, and X. Tu, "Preparation of conductive polypyrrole/TiO_2 nanocomposite via surface molecular imprinting technique and its photocatalytic activity under simulated solar light irradiation," *Colloids and Surfaces A*, vol. 395, pp. 183–189, 2012.

[30] F. Li, T. Kong, W. Bi, D. Li, Z. Li, and X. Huang, "Synthesis and optical properties of CuS nanoplate-based architectures by a solvothermal method," *Applied Surface Science*, vol. 255, no. 12, pp. 6285–6289, 2009.

[31] G. P. Joshi, N. S. Saxena, R. Mangal, A. Mishra, and T. P. Sharma, "Band gap determination of Ni-Zn ferrites," *Bulletin of Materials Science*, vol. 26, no. 4, pp. 387–389, 2003.

[32] Y. Kim, J. H. Jeong, and M. Kang, "Rapid synthesis of bis (2,2′-bipyridine) nitratocopper(II) nitrate using a hydrothermal method and its application to dye-sensitized solar cells," *Inorganica Chimica Acta*, vol. 365, no. 1, pp. 400–407, 2011.

[33] S. Giraud, G. Loupias, H. Maskrot et al., "Dip-coating on TiO_2 foams using a suspension of Pt-TiO_2 nanopowder synthesized by laser pyrolysis-preliminary evaluation of the catalytic performances of the resulting composites in deVOC reactions," *Journal of the European Ceramic Society*, vol. 27, no. 2-3, pp. 931–936, 2007.

[34] J. Zhang, J. Yu, M. Jaroniec, and J. R. Gong, "Noble metal-free reduced graphene oxide-$ZnxCd_{1-x}S$ nanocomposite with enhanced solar photocatalytic H_2 production performance," *Nano Letters*, vol. 12, pp. 4584–4589, 2012.

Hindawi Publishing Corporation
International Journal of Photoenergy
Volume 2013, Article ID 419182, 5 pages
http://dx.doi.org/10.1155/2013/419182

Research Article

H_2 Fuels from Photocatalytic Splitting of Seawater Affected by Nano-TiO_2 Promoted with CuO and NiO

A.-J. Simamora,[1] Fang-Chih Chang,[1] H. Paul Wang,[1,2,3] T.-C. Yang,[1] Y.-L. Wei,[4] and W.-K. Lin[5]

[1] *Department of Environmental Engineering, National Cheng Kung University, Tainan 70101, Taiwan*
[2] *Sustainable Environment Research Center, National Cheng Kung University, Tainan 70101, Taiwan*
[3] *Center for Micro/Nano Science and Technology, National Cheng Kung University, Tainan 70101, Taiwan*
[4] *Department of Environmental Science and Engineering, Tunghai University, Taichung 40704, Taiwan*
[5] *Department of Engineering and System Science, National Tsing Hua University, Hsinchu 30013, Taiwan*

Correspondence should be addressed to Fang-Chih Chang; d90541003@ntu.edu.tw and H. Paul Wang; wanghp@mail.ncku.edu.tw

Received 30 May 2013; Revised 24 July 2013; Accepted 24 July 2013

Academic Editor: Jiaguo Yu

To enhance H_2 yields from the photocatalytic splitting of seawater, better photocatalysts such as nanostructured TiO_2 promoted with NiO (2.5%) and CuO (2.5%) have been studied in the present work. The accumulated H_2 yielded from the photocatalytic splitting of seawater containing oxalic acid (50 mM) as the sacrificial reagents on CuO/nano-TiO_2 is 8.53 μmol/g_{cat} after the 5 h radiation. On the NiO/nano-TiO_2 photocatalyst, the H_2 yield is relatively low (i.e., 1.46 μmol/g_{cat}). Note that the hole scavenging with chlorides in seawater may be associated with the less H_2 yielded from the seawater photocatalysis (on CuO/nano-TiO_2) if compared with that from water (42.4 μmol/g_{cat}).

1. Introduction

Utilization of fossil energy which may cause air pollution or global warming has negative impacts on the human health and environment. Today's world is also facing an urgency need in developing alternative fuels. Renewable hydrogen energy (H_2) is becoming one of the better alternatives. Combustion of H_2 for energy does not emit pollutant gases such as CO, NO_x, or SO_x. H_2 has also been widely used in many sectors such as food, metallurgical, electronic, chemical, petroleum, and refinery industries. H_2 has been technically demonstrated for transportation, heating, and power generation [1].

H_2 yielded from the photocatalytic splitting of water has extensively received attention recently [2–4]. Since the H_2 generation by the water electrochemical method was demonstrated, splitting of water photocatalyzed by TiO_2 for the H_2 fuel has been considered to be one of the alternates [5]. The TiO_2-based photocatalysts for H_2 generation could be promoted by codoping of antimony and chromium [6], nickel and either tantalum or niobium [7], cobalt [8], Pt [9], and nitrogen [10]. During photocatalysis, photo-excited holes can irreversibly oxidize electron donor compounds, and thus facilitate water reduction by conduction band electrons if the bottom of the conduction band of the photocatalyst is located at a more negative redox potential than the reduction potential of water [11]. Inorganic reagents such as Na_2S and Na_2SO_3 are generally used as the sacrificial compounds [12, 13].

In the present work, CuO and NiO were used as the promoters on the nanosize TiO_2 to enhance catalytic splitting of water and seawater. Oxalic acid which may be formed from the photocatalytic reduction of CO_2 in H_2O was used as the sacrificial reagent during photocatalysis.

2. Materials and Methods

The CuO (2.5%) and NiO (2.5%) supported on nanosize TiO_2 (P25) (UR, ITIT001) were prepared by the impregnation method. The samples were dried and calcined at 673 K for two

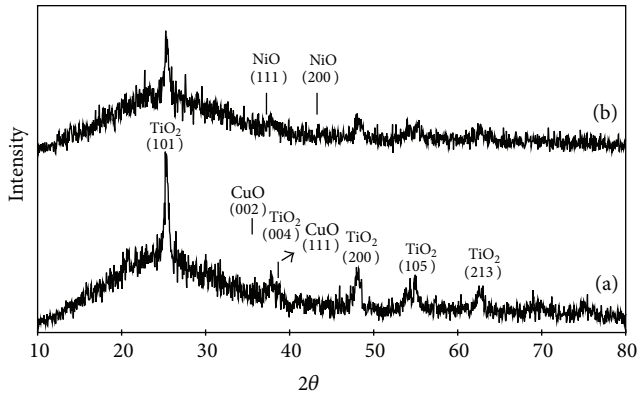

Figure 1: XRD patterns of (a) CuO and (b) NiO promoted nano-TiO_2.

hours to form CuO and NiO dispersed on TiO_2 (CuO/nano-TiO_2 and NiO/nano-TiO_2), respectively. The X-ray diffraction (XRD) patterns of the photocatalysts were recorded on a XRD spectrometer using Cu Kα radiation (λ = 1.5418 Å) ranged from 10° to 80° (2θ) at the scanning speed of 5°/min.

The XANES spectra of the TiO_2 photocatalysts were also recorded on the Wigler 17C beam line at the Taiwan National Synchrotron Radiation Research Center (NSRRC). The electron storage ring was operated at the energy of 1.5 GeV (ring current = 120–200 mA). A Si(111) double crystal monochromator was used for selection of energy at an energy resolution ($\Delta E/E$ (eV/eV)) of 1.9×10^{-4}. The absorption spectra were collected in ion chambers that were filled with helium and nitrogen mixed gases. Beam energy was calibrated by the adsorption edges of nickel and copper foils at the energy of 8335 and 8979 eV, respectively.

The photocatalytic splitting of water and seawater experiments was carried out in a quartz reactor (45 mL) having a total reflection mirror system. About 100 mg of the catalyst samples were dispersed in the simulated seawater (about 35 g of NaCl in the 1 L of pure water) under magnetic stirring for five hours. A 300 W Xenon arc lamp (Oriel Instruments, Model 6259) equipped with a water filter was used as the photocatalytic light source. The H_2 gas generated from the photocatalytic splitting of water and seawater was analyzed by a gas chromatography (Varian 430-GC) equipped with a thermal conductivity detector. The apparent quantum efficiency (QE) of the photocatalysts was obtained by the equation QE (%) = (number of reacted electrons)/(number of incident photons) × 100 = (number of evolved H_2 molecules × 2)/(number of incident photons) × 100.

3. Results and Discussion

The XRD patterns of the CuO/nano-TiO_2 and NiO/nano-TiO_2 photocatalysts are shown in Figure 1. The main diffraction peaks of the photocatalysts at (101), (200), (004), and (105) are observed, suggesting that the photocatalysts have mainly anatase crystallites. The XRD peaks of CuO and NiO are barely observed in the CuO/nano-TiO_2 and NiO/nano-TiO_2, which may be due to the existence of subnanosize CuO and NiO crystallites that are well dispersed on the nano-TiO_2.

The XANES spectra of nickel and copper in the photocatalysts are shown in Figure 2. Metallic nickel (Ni) and copper (Cu) are not found. The absorption features observed at 8335 and 8979 eV suggest that NiO and CuO are the main nickel and copper species on the TiO_2, respectively.

Figure 3 presents the photocatalytic splitting of water and seawater containing 0.05 M oxalic acid as the sacrificial reagent. On the nano-TiO_2 photocatalyst, a very small amount of H_2 is formed from the photocatalytic splitting of water and seawater. Notably, the accumulated H_2 yielded from the photocatalytic splitting of water on CuO/nano-TiO_2 and NiO/nano-TiO_2 is about 32.4 and 3.07 μmol/g_{cat} after the 5 h radiation, respectively. Compared to the photocatalytic splitting of seawater on CuO/nano-TiO_2 and NiO/nano-TiO_2, the accumulated H_2 yields are less than those from water by 3.8 and 2.1 times, respectively. Hole scavenging with chlorides may occur during photocatalysis [14, 15]. Many hydroxyl groups such as $TiOH_2$, TiOH on TiO_2 may absorb Cl^- to form TiCl, which may decrease the H_2 yield in the photocatalysis [16, 17]. Generally, CuO on TiO_2 can be reduced to Cu^+ (E_0 = 0.16 V) or Cu^0 (E_0 = 0.34 V) by attracting the excited electrons from the valence band of TiO_2 during photooxidizing [18–21]. The reduction potential of NiO (E_0 = −0.25 V) is slightly less than the TiO_2 conduction band gap (E_0 = −0.26 V) [22, 23]. Additionally, the reduction potential of H^+/H_2 (E_0 = −0.00 V) is less than that of CuO or NiO. CuO and NiO can thus promote TiO_2 in the photocatalytic H_2 formation.

In the separate experiments, oxalic acid was formed from simultaneously photocatalytic reduction of H_2O and CO_2. It is of great interest to study the behavior of acetic acid as the sacrificial compound for photocatalytic splitting of water and seawater for the H_2 fuel. Note that addition of sacrificial reagents in water or seawater may cause water pollution.

Effects of the oxalic acid sacrificial reagent concentrations on the photocatalytic splitting of water and seawater on CuO/nano-TiO_2 are shown in Figure 4. Without oxalic acid, H_2 may not be formed in the photocatalysis. A small amount of oxalic acid can enhance the H_2 generation. Note that

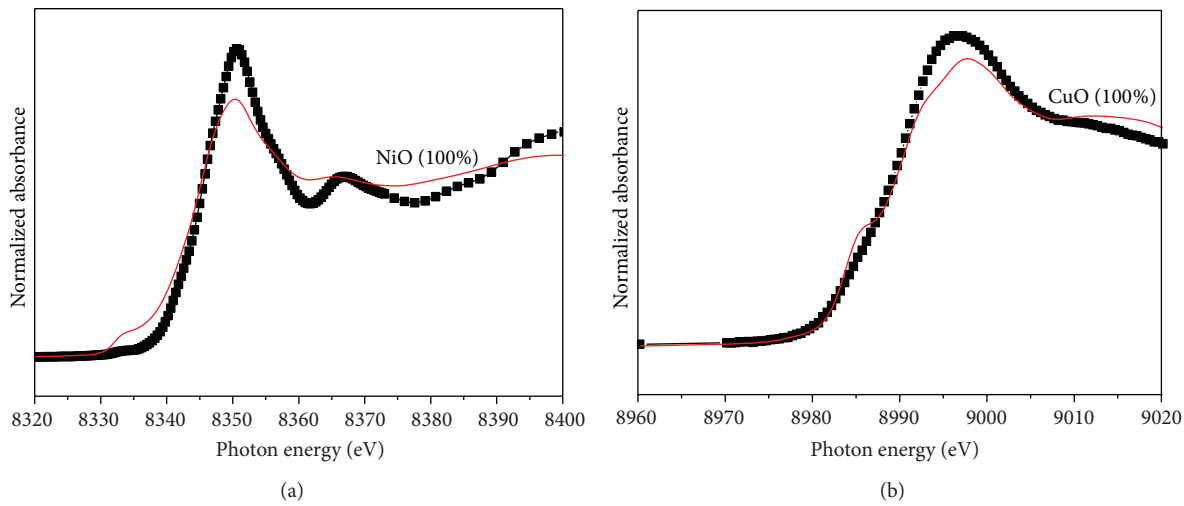

Figure 2: Component-fitted XANES spectra of (a) nickel and (b) copper in the NiO/nano-TiO_2 and CuO/nano-TiO_2 photocatalysts, respectively.

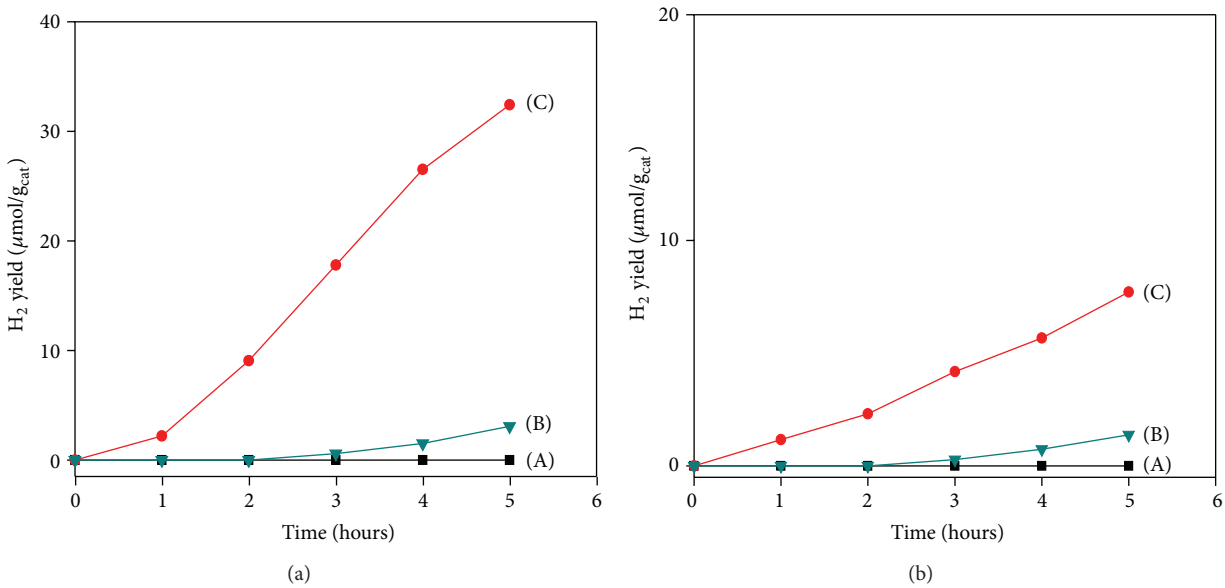

Figure 3: Photocatalytic splitting of (a) water and (b) seawater with 50 mM oxalic acid sacrificial reagent affected by (A) nano-TiO_2, (B) NiO/nano-TiO_2, and (C) CuO/nano-TiO_2.

oxalic acid is a strong reductive reagent which may consume the photogenerated holes. After a 5 h UV-Vis irradiation, a better H_2 yield from the photocatalytic splitting of water is about 42.4 μmol/g_{cat} when the initial concentration of oxalic acid is 12.5 mM. However, the photocatalytic H_2 formation from water and seawater affected by CuO and NiO promoted TiO_2 was less than that of related studies, mainly due to the fact of the much less amount of the sacrificial reagents used in the photocatalysis. With an increase of the initial oxalic acid concentration by two times, the photocatalytic H_2 generation is slightly decreased. As the initial concentration of oxalic acid is increased by four times, the H_2 yields from the photocatalytic splitting of water are decreased by 24%. It seems that excessive oxalic acid sacrificial reagent may not have a positive effect on the photocatalytic splitting of water.

4. Conclusions

Photocatalytic splitting of seawater for H_2 formation on CuO/nano-TiO_2 and NiO/nano-TiO_2 is feasible experimentally. The sacrificial reagent (oxalic acid) can enhance the H_2 yields in the photocatalytic splitting of seawater. However, the excessive sacrificial reagent may not favor the photocatalysis. It is worth noting that a better H_2 can be yielded from the photocatalytic splitting of seawater affected by CuO/nano-TiO_2 (8.53 μmol/g_{cat}) than that by NiO/nano-TiO_2 (1.46 μmol/g_{cat}). In particular, the hole scavenging with

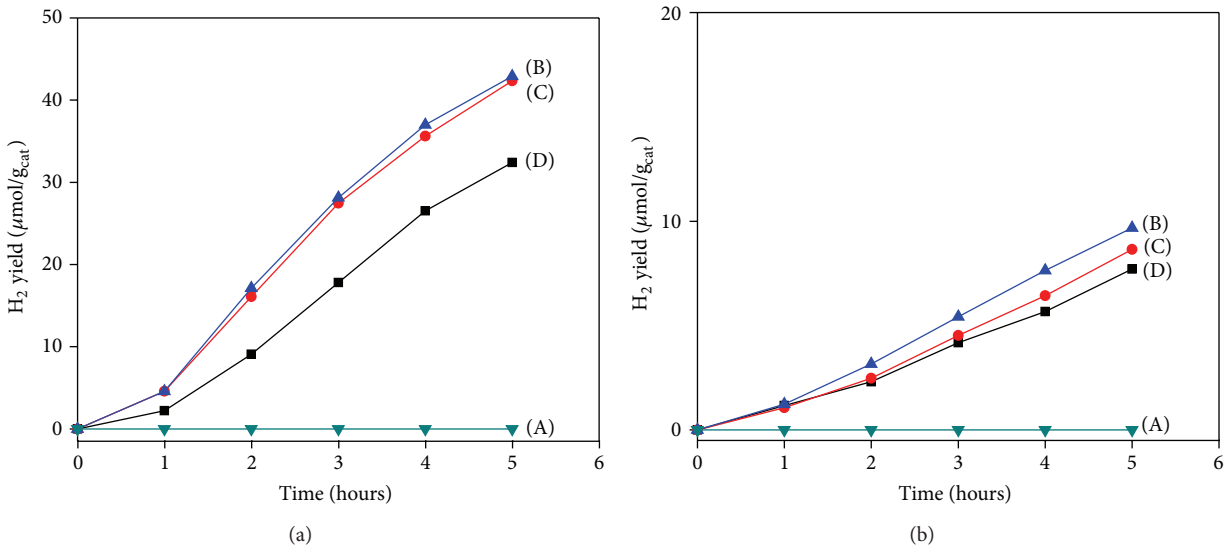

Figure 4: Photocatalytic splitting of (a) water and (b) seawater affected by CuO/nano-TiO_2 with (A) 0, (B) 12.5, (C) 25, and (D) 50 mM of the oxalic acid sacrificial reagent.

chlorides in seawater may be associated with the less H_2 yielded from the seawater photocatalysis (on CuO/nano-TiO_2) if compared with that from water (42.4 μmol/g_{cat}).

Acknowledgment

The financial supports of the Taiwan National Science Council and Bureau of Energy are gratefully acknowledged.

References

[1] M. M. Hussain, I. Dincer, and X. Li, "A preliminary life cycle assessment of PEM fuel cell powered automobiles," *Applied Thermal Engineering*, vol. 27, no. 13, pp. 2294–2299, 2007.

[2] S. J. Choung, J. Kim, and H. R. Kim, "The characterization and hydrogen production from water decomposition with methanol in a semi-batch type reactor using In, P-TiO_2s," *International Journal of Photoenergy*, vol. 2011, Article ID 359161, 7 pages, 2011.

[3] A. Y. Kim and M. Kang, "Effect of Al-Cu bimetallic components in a TiO_2 framework for high hydrogen production on methanol/water photo-splitting," *International Journal of Photoenergy*, vol. 2012, Article ID 618642, 9 pages, 2012.

[4] G. Lee, M. K. Yeo, M. H. Um, and M. Kang, "High-efficiently photoelectrochemical hydrogen production over Zn-incorporated TiO_2 nanotubes," *International Journal of Photoenergy*, vol. 2012, Article ID 843042, 10 pages, 2012.

[5] A. Fujishima and K. Honda, "Electrochemical photolysis of water at a semiconductor electrode," *Nature*, vol. 238, no. 5358, pp. 37–38, 1972.

[6] H. Kato and A. Kudo, "Visible-light-response and photocatalytic activities of TiO_2 and $SrTiO_3$ photocatalysts codoped with antimony and chromium," *Journal of Physical Chemistry B*, vol. 106, no. 19, pp. 5029–5034, 2002.

[7] R. Niishiro, H. Kato, and A. Kudo, "Nickel and either tantalum or niobium-codoped TiO_2 and $SrTiO_3$ photocatalysts with visible-light response for H_2 or O_2 evolution from aqueous solutions," *Physical Chemistry Chemical Physics*, vol. 7, no. 10, pp. 2241–2245, 2005.

[8] Y. Wu, G. Lu, and S. Li, "The long-term photocatalytic stability of Co^{2+}-modified P25-TiO_2 powders for the H_2 production from aqueous ethanol solution," *Journal of Photochemistry and Photobiology A*, vol. 181, no. 2-3, pp. 263–267, 2006.

[9] M. Kitano, M. Takeuchi, M. Matsuoka, J. M. Thomas, and M. Anpo, "Photocatalytic water splitting using Pt-loaded visible light-responsive TiO_2 thin film photocatalysts," *Catalysis Today*, vol. 120, no. 2, pp. 133–138, 2007.

[10] T. Sreethawong, S. Laehsalee, and S. Chauadej, "Comparative investigation of mesoporous- and non-mesoporous-assembled TiO_2 nanocrystals for photocatalytic H_2 production over N-doped TiO_2 under visible light irradiation," *International Journal of Hydrogen Energy*, vol. 33, no. 21, pp. 5947–5957, 2008.

[11] K. Maeda and K. Domen, "New non-oxide photocatalysts designed for overall water splitting under visible light," *Journal of Physical Chemistry C*, vol. 111, no. 22, pp. 7851–7861, 2007.

[12] S. Xu and D. D. Sun, "Significant improvement of photocatalytic hydrogen generation rate over TiO_2 with deposited CuO," *International Journal of Hydrogen Energy*, vol. 34, no. 15, pp. 6096–6104, 2009.

[13] H. Yan, J. Yang, G. Ma et al., "Visible-light-driven hydrogen production with extremely high quantum efficiency on Pt-PdS/CdS photocatalyst," *Journal of Catalysis*, vol. 266, no. 2, pp. 165–168, 2009.

[14] A. Lair, C. Ferronato, J. M. Chovelon, and J. M. Herrmann, "Naphthalene degradation in water by heterogeneous photocatalysis: an investigation of the influence of inorganic anions," *Journal of Photochemistry and Photobiology A*, vol. 193, no. 2-3, pp. 193–203, 2008.

[15] Y. Li, D. Gao, S. Peng, G. Lu, and S. Li, "Photocatalytic hydrogen evolution over Pt/Cd0.5Zn0.5S from saltwater using glucose as electron donor: an investigation of the influence of electrolyte NaCl," *International Journal of Hydrogen Energy*, vol. 36, no. 7, pp. 4291–4297, 2011.

[16] M. R. Hoffmann, S. T. Martin, W. Choi, and D. W. Bahnemann, "Environmental applications of semiconductor photocatalysis," *Chemical Reviews*, vol. 95, no. 1, pp. 69–96, 1995.

[17] Y. Li, F. He, S. Peng, D. Gao, G. Lu, and S. Li, "Effects of electrolyte NaCl on photocatalytic hydrogen evolution in the presence of electron donors over Pt/TiO_2 ," *Journal of Molecular Catalysis A*, vol. 341, no. 1-2, pp. 71–76, 2011.

[18] J. Yu, Y. Hai, and M. Jaroniec, "Photocatalytic hydrogen production over CuO-modified titania," *Journal of Colloid and Interface Science*, vol. 357, no. 1, pp. 223–228, 2011.

[19] J. Yu and J. Ran, "Facile preparation and enhanced photocatalytic H_2-production activity of $Cu(OH)_2$ cluster modified TiO_2," *Energy and Environmental Science*, vol. 4, no. 4, pp. 1364–1371, 2011.

[20] H. J. Choi and M. Kang, "Hydrogen production from methanol/water decomposition in a liquid photosystem using the anatase structure of Cu loaded TiO_2 ," *International Journal of Hydrogen Energy*, vol. 32, no. 16, pp. 3841–3848, 2007.

[21] T. Sreethawong and S. Yoshikawa, "Comparative investigation on photocatalytic hydrogen evolution over Cu-, Pd-, and Au-loaded mesoporous TiO_2 photocatalysts," *Catalysis Communications*, vol. 6, no. 10, pp. 661–668, 2005.

[22] J. Yu, Y. Hai, and B. Cheng, "Enhanced photocatalytic H_2-production activity of TiO_2 by $Ni(OH)_2$ cluster modification," *Journal of Physical Chemistry C*, vol. 115, no. 11, pp. 4953–4958, 2011.

[23] W. Wang, S. Liu, L. Nie, B. Cheng, and J. Yu, "Enhanced photocatalytic H_2-production activity of TiO_2 using $Ni(NO_3)_2$ as an additive," *Physical Chemistry Chemical Physics*, vol. 15, no. 29, pp. 12033–12039, 2013.

Hindawi Publishing Corporation
International Journal of Photoenergy
Volume 2013, Article ID 350570, 6 pages
http://dx.doi.org/10.1155/2013/350570

Research Article

Removal of Formaldehyde Using Highly Active Pt/TiO_2 Catalysts without Irradiation

Haibao Huang,[1,2] Huiling Huang,[1] Peng Hu,[1] Xinguo Ye,[1] and Dennis Y. C. Leung[3]

[1] *School of Environmental Science and Engineering, Sun Yat-Sen University, Guangzhou 510275, China*
[2] *Guangdong Provincial Key Laboratory of Environmental Pollution Control and Remediation Technology, Guangzhou 510275, China*
[3] *Department of Mechanical Engineering, The University of Hong Kong, Pokfulam Road, Hong Kong*

Correspondence should be addressed to Haibao Huang; seabao8@gmail.com and Dennis Y. C. Leung; ycleung@hku.hk

Received 19 July 2013; Accepted 29 July 2013

Academic Editor: Jiaguo Yu

Formaldehyde (HCHO) is one of the major indoor air pollutants. TiO_2 supported Pt catalysts were prepared by sol-gel method and used to eliminate HCHO at room temperature without irradiation. The reduced Pt/TiO_2 catalyst (denoted as Pt/TiO_2-H_2) showed much higher activity than that calcined in air (denoted as Pt/TiO_2-air). More than 96% of the conversion of HCHO was obtained over 0.5 wt% Pt/TiO_2-H_2, on which highly dispersed metallic Pt nanoparticles with very small size (~2 nm) were identified. Metallic Pt rather than cationic Pt nanoparticles provide the active sites for HCHO oxidation. Negatively charged metallic Pt nanoparticles facilitate the transfer of charge and oxygen species and the activation of oxygen.

1. Introduction

Gaseous formaldehyde (HCHO) may cause adverse effects on both air quality and human health [1–3]. Great efforts have been made to eliminate indoor HCHO to satisfy the stringent environmental regulations and improve air quality. Physical adsorption with porous materials or the combined physical adsorption and chemical reaction by impregnating the chemical reagents (such as potassium permanganate and organic amine) on the adsorption materials was found to be effective for eliminating HCHO emission but only for a short period before saturation. The overall efficiency of these adsorbent materials is not so promising due to their limited removal capacities [4, 5]. Catalytic oxidation is recognized as the most promising HCHO removal technology [6–8]. Nevertheless, HCHO oxidation can only occur under irradiation (UV or visible light) or at high temperature over most of the reported catalysts [9–11]. In these cases, an extra irradiation or heating apparatus is needed, causing higher operating cost and more severe reaction conditions, which is not suitable for the control of indoor air pollution [10]. For air cleaning, low energy demand and low concentration of HCHO strongly require a catalyst to exhibit high activity for complete oxidation of HCHO. HCHO purification at room temperature is highly desirable due to its environment-friendly reaction conditions and energy saving consideration [6, 7, 12]. Moreover, indoor air is often enriched with water vapor, which frequently leads to severe catalytic deactivation through the strong adsorption of water on the active sites, especially at low temperatures [10]. The development of effective catalysts for complete oxidation of low-concentration HCHO at ambient temperature is a challenging subject for scientists [4, 7].

Recently, several studies related to HCHO removal at low temperature have been carried out using supported noble metal (Pt, Rh, Au, and Pd) [6, 7, 13, 14] and nonnoble metal catalysts [15, 16]. Among them, Pt/TiO_2 is the most active [6, 14]. Peng and Wang [5] found that HCHO conversion for 1 wt% Pt/TiO_2 is only 14.3% at 20°C and it increased to 97% at 120°C. However, the oxidation state of active component may be changed due to HCHO reduction at high temperature, which may cause confusion to mechanistic study although supported Pt catalysts have been proved to be effective for HCHO oxidation at low temperature, even at room temperature in some cases. However, high loading of Pt is generally needed for effective oxidation of HCHO, which greatly limits its widespread application due to the expensive cost [10]. One

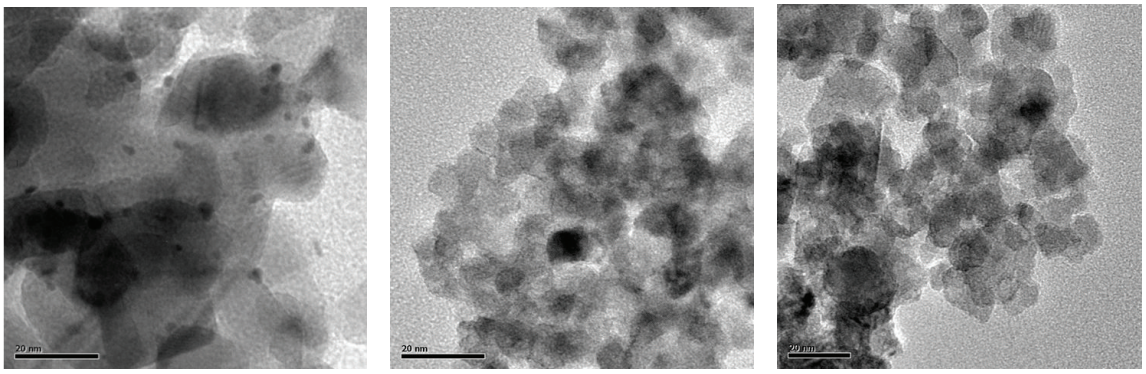

(a) (b) (c)

Figure 1: TEM micrographs for (a) Pt/TiO_2-H_2, (b) Pt/TiO_2-air, and (c) TiO_2.

alternative is to improve the catalytic activity by optimizing catalysts with lower Pt loading. In addition, several hundred ppm of HCHO concentration used for the performance test is much higher than the normal HCHO concentration in indoor environments, which generally ranges from dozens of ppb to ppm. Furthermore, the Pt catalysts were generally pretreated in air at high temperature [4, 6, 7, 14], which result in the formation of PtOx. As known, oxidation state of Pt is one of the most important factors controlling the catalytic activity [17]. The effect of metallic Pt on catalytic activity and the mechanism leading to high activity for HCHO oxidation at room temperature has not well demonstrated yet.

Herein, we present an effective catalyst with low Pt loading for the purification of indoor HCHO at room temperature without any irradiation. Efficient elimination of low-concentration HCHO was obtained over a reduced 0.5 wt% Pt/TiO_2 catalyst prepared by sol-gel method. Structural analysis of the catalysts used was performed and subsequently correlated with their catalytic performances to investigate the mechanism leading to the high activity over the reduced Pt nanoparticles.

2. Experimental Sections

2.1. Preparation and Characterization of Pt/TiO_2 Catalysts. The Pt-doped TiO_2 catalysts were prepared by the sol-gel method. A mixture solution containing 34 mL of ethanol, 1.7 mL of water, and 1.7 mL of hydrochloric acid was added dropwise under vigorous stirring to another mixture solution containing 17 mL of tetrabutyl titanate, 5.1 mL of 0.02 mol/L chloroplatinic acid ($H_2PtCl_6 \cdot 6H_2O$), and 45 mL of absolute ethanol. The resulting transparent colloidal suspension was stirred for 5 h and aged until the formation of gel. The gel was dried at 353 K for 12 h and then calcined at 673 K for 4 h in air and hydrogen flow, obtaining the oxidized and reduced Pt catalysts, respectively. They were referred to as Pt/TiO_2-air and Pt/TiO_2-H_2, respectively. The Pt loading is 0.5 wt% on both catalysts. The catalysts were crushed and then sieved through 40–60 meshes.

Transmission electron microscopy (TEM) images were recorded by a Tecnai G2 20 microscope operated at 200 kV. BET surface areas of the samples were measured by N_2 adsorption-desorption isotherms at 77 K using a Micromeritics ASAP 2020 instrument. Prior to the measurement, the samples were degassed at 573 K for 2 h. X-ray powder diffraction (XRD) patterns were collected with a Bruker D8 Advance X-ray powder diffractometer, using Cu Kα (λ = 1.5418 Å) radiation. The working voltage of the instrument was 40 kV, and the current was 40 mA. The intensity data were collected in a 2θ range from 20° to 90°. The average crystal size was determined from the anatase peak broadening (101) crystal plane for anatase with Scherrer's formula. X-ray photoelectron spectroscopy (XPS) measurements of the catalysts were performed with a PHI 5000 VersaProbe system using a monochromatic Al Kα source. The binding energies (BEs) were determined by utilizing C1s line as a reference with energy of 284.8 eV.

2.2. Measurement of Catalytic Activity. The oxidation of HCHO was performed in a quartz tubular (i.d. = 6 mm) fixed-bed reactor in a dark environment at ambient temperature (25 ± 1°C). Also, 0.5 g of the catalyst in 40–60 mesh was loaded in the reactor. Gaseous HCHO was generated by zero air flowing through an HCHO solution in an incubator. An air mixture containing 10 ppm HCHO and water vapor (50% relative humidity) was introduced as the reactants. The total flow rate was 1 L/min, corresponding to a gas hourly space velocity (GHSV) of 120,000 mL/g_{cat}·h. The HCHO and CO_2 in the air stream were analyzed by an HCHO monitor (Formaldemeter 400, PPM Technology) and a CO_2 monitor (HAL-$HCO_2$01, Chinaway), respectively.

3. Results and Discussion

3.1. Catalyst Characterization

3.1.1. TEM. Representative TEM micrographs of the TiO_2 and Pt/TiO_2 are presented in Figure 1. The TEM micrograph for the Pt/TiO_2-air catalyst was similar to that of TiO_2. No distinguishable Pt particles are observed over the Pt/TiO_2-air catalyst, indicating that their sizes were probably very small and could not be detected by TEM. Pt nanoparticles prepared

Table 1: BET surface area of Pt/TiO_2 and TiO_2.

Sample	Pt/TiO_2-H_2	Pt/TiO_2-air	TiO_2	P-25
BET surface area (m^2/g)	74.1	84.5	74.9	50 [18]

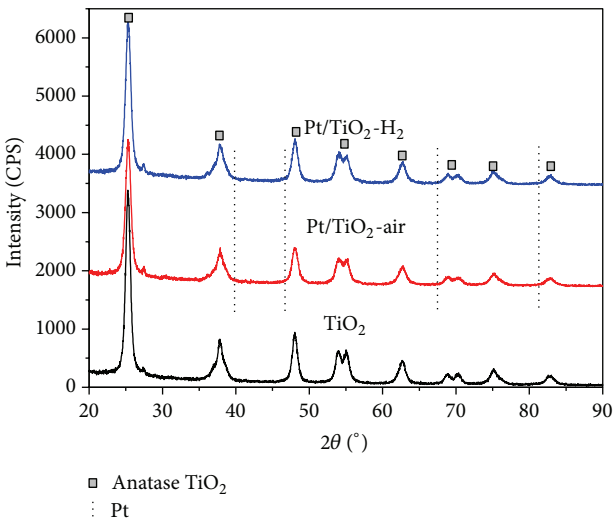

Figure 2: XRD patterns of the Pt/TiO_2 and TiO_2 catalysts.

by different methods existed with different crystal structure. Pt nanoparticles with very small and homogeneous size (~2 nm) present uniformly on the surface of the Pt/TiO_2-H_2 catalyst. Hence, the H_2 reduction promoted the formation of Pt clusters.

3.1.2. BET Surface Areas. Table 1 shows the BET surface area of the tested catalysts. TiO_2 prepared by sol-gel method obtained a BET surface area of 74.9 m^2/g, which is much larger than that of commercially available P-25 TiO_2 (Degussa, Germany) with a BET surface area of 50 m^2/g [18]. It is worth noting that the BET surface area of Pt/TiO_2-air is increased to 84.5 m^2/g, which is larger than that of Pt/TiO_2-H_2 (74.1 m^2/g). This is probably because Pt nanoparticles on Pt/TiO_2-H_2 cover the surface of TiO_2 and block its pores. As observed in TEM, small Pt nanoparticles were highly dispersed on the support, which may cause the loss of surface area. Pt/TiO_2 prepared by sol-gel method possesses much higher surface area, which can provide more absorption sites for HCHO.

3.1.3. XRD. As shown in Figure 2, XRD patterns for pure TiO_2 exhibited strong diffraction peaks at 25.2° and 48.1° indicating TiO_2 in the anatase phase. The peaks of the Pt/TiO_2-H_2 and Pt/TiO_2-air catalyst are essentially the same as pure TiO_2, and no significant Pt peaks are observed, suggesting that Pt particles are very small, as observed by the TEM (Figure 1). The average particle sizes as calculated with the Scherrer formula were 14.1, 12.8, and 12.9 nm for the samples of TiO_2, Pt/TiO_2-H_2, and Pt/TiO_2-air, respectively. They are much smaller than P-25 with an average crystal sizes of about 30 nm [18]. The particle sizes for the Pt/TiO_2-H_2 and

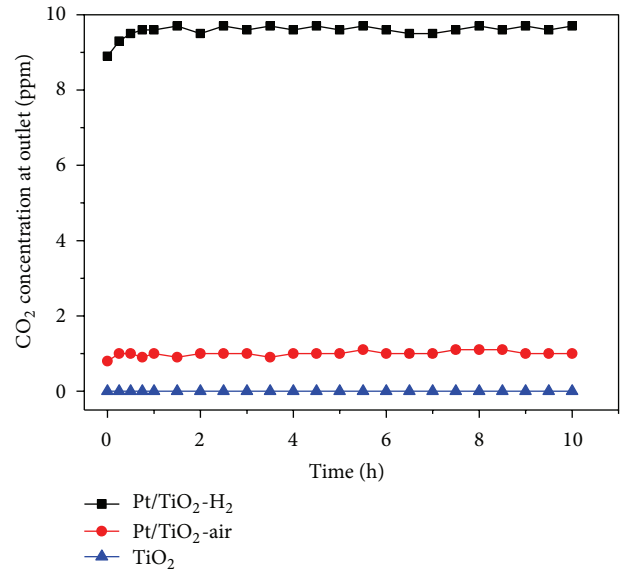

Figure 3: CO_2 concentration at the outlet of reactor.

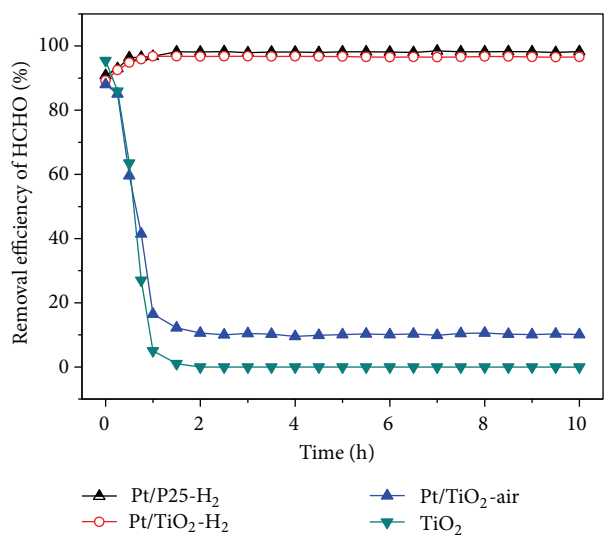

Figure 4: HCHO removal efficiency over the Pt/TiO_2 and TiO_2 catalysts.

Pt/TiO_2-air are smaller than TiO_2, indicating that the deposition of Pt can inhibit the growth of TiO_2 crystal. The doping of Pt probably changed the surface character of TiO_2 and avoided the sintering and conglobation during thermal treatment hence inhibiting its growth. It can be found that the average particle size of the Pt/TiO_2-H_2 catalyst is almost the same as that of the Pt/TiO_2-air catalyst. The small TiO_2 crystal accounts for the high BET surface area of the Pt/TiO_2, as shown in Table 1.

3.2. Catalytic Activity Test. HCHO oxidation by pure TiO_2 can be excluded from the discussion since no CO_2 was identified during the reaction, as shown in Figure 3. However, CO_2 concentration was increased to about 1 ppm and 9.6 ppm over Pt/TiO_2-air and Pt/TiO_2-H_2, respectively. Figure 4 shows

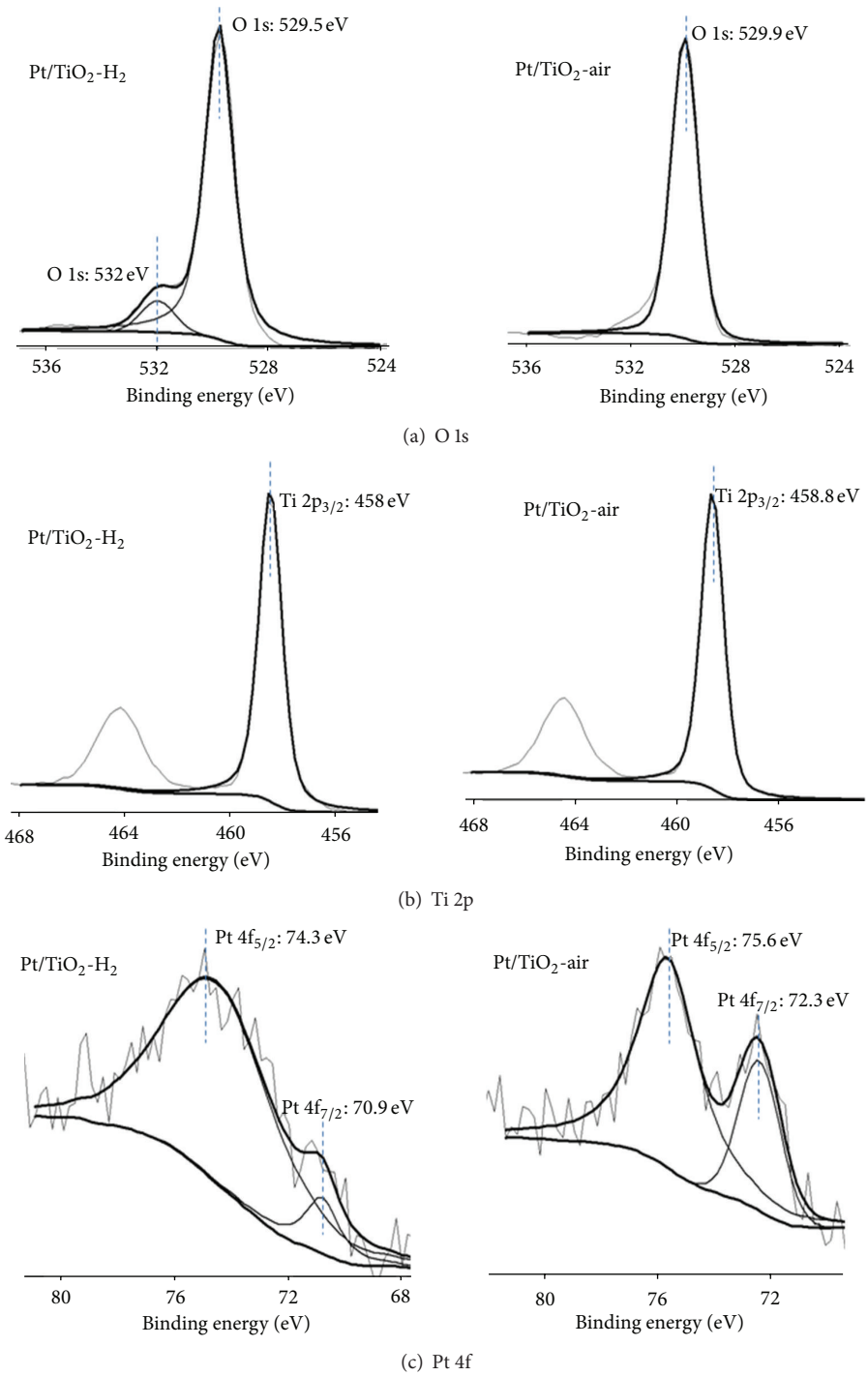

Figure 5: XPS spectra of the Pt/TiO_2-H_2 and Pt/TiO_2-air catalyst.

the time dependence of HCHO removal efficiency for Pt/TiO_2 together with TiO_2 at ambient temperature. The removal of HCHO at initial stage over pure TiO_2 and Pt/TiO_2-air was mainly ascribed to the adsorption by TiO_2. Only about 10% HCHO conversion was obtained over the Pt/TiO_2-air catalyst at the stable stage, whereas it was notably increased to 96.6% over the Pt/TiO_2-H_2 catalyst. HCHO removal efficiency was significantly improved over the Pt/TiO_2-H_2 catalyst. The results showed that the catalytic activities were greatly influenced by the catalyst's preparation methods.

The most important factors controlling the catalytic activity of nanoscale noble metal catalysts appear to be the particle size, nature of support, and noble metal oxidation state [19]. The smaller the size of nanoparticles is, the more active centers are formed, leading to better catalytic activity [20]. As described previously, the unreduced catalyst possesses higher

surface area and smaller Pt particles than the reduced one, which can provide more active sites for the adsorption and oxidation of HCHO. Therefore, the Pt/TiO_2-air catalyst is expected to be more active for HCHO oxidation than the Pt/TiO_2-H_2 catalyst. On the contrary, the former showed much poorer activity for HCHO oxidation than the latter, as shown in Figure 4. Therefore, Pt oxidation state should be the most important factors controlling the catalytic activity in this reaction. Reduced Pt supported on commercial TiO_2 (P25, Degussa) (Pt/P25-H_2) also confirmed this. HCHO removal efficiency reached 98% over 0.5% Pt/P25-H_2. Pt oxidation state was analyzed by XPS, as shown in Figure 5(a). The binding energy of Pt $4f_{7/2}$ is 72.3 and 70.9 eV on the Pt/TiO_2-air and Pt/TiO_2-H_2 catalyst, corresponding to Pt^{2+} and Pt^0 [21], respectively. Pt was reduced into metallic state on the Pt/TiO_2-H_2 catalyst. Figure 4 clearly showed that the reduced Pt/TiO_2 with metallic Pt achieved much higher HCHO removal efficiency than the oxidized one with Pt^{2+}, suggesting that metallic Pt is the active site for HCHO oxidation. Similar conclusions were made for active centers of Pd [22–25] and Au [26–28] in oxidation reaction. It is worth noting that Pt $4f_{7/2}$ of Pt/TiO_2-H_2 was shifted to lower BE by approximately 0.3 eV compared with bulk metallic Pt with typical Pt $4f_{7/2}$ BE around 71.2 eV, indicating that nanoparticles are negatively charged on the Pt/TiO_2-H_2 catalyst. The electron transfer was proposed to be responsible for this negative shift [21]. It can be observed from Figure 5(b) that Ti $2p_{3/2}$ on the Pt/TiO_2-air catalyst is located at 458.8 eV, corresponding to Ti^{4+} of TiO_2. However, it was slightly shifted to 458.4 eV on the Pt/TiO_2-H_2 catalyst, suggesting that Ti^{4+} is partially reduced. The electron transfer can be expected from the reduced TiO_2 to Pt nanoparticles [29]. Oxygen vacancies on the reduced TiO_2 and the negative charged Pt showed enhanced capacity of O_2 adsorption. The charge was further transferred from negative charged Pt to the adsorbed O_2, leading to negative charge of adsorbed O_2. This was confirmed by the change of O 1s BE after reduction, as shown in Figure 5(c). The O 1s core level peak on the Pt/TiO_2-air catalyst appears at 529.9 eV, which is ascribed to the lattice oxygen in TiO_2 [30]. However, it was negatively shifted to 529.5 eV on the Pt/TiO_2-H_2 catalyst. Charge transfer from Pt particles to oxygen in the meanwhile activates the oxygen. Activated oxygen may exist in the form of Pt-O complex. It was confirmed by a significant shoulder peak of O 1s at 532.0 eV on the Pt/TiO_2-H_2 catalyst, as shown in Figure 5(c). This shoulder peak of O 1s should belong to O of OH groups on the surface of the catalyst [31]. It is probably highly active and responsible for the HCHO oxidation. Thus, the transfer of charge and oxygen species and the activation of oxygen can efficiently occur at room temperature, which may account for the high activity of the Pt/TiO_2-H_2 catalyst for HCHO oxidation.

HCHO in indoor air is often enriched with water vapor, which frequently leads to severe catalytic deactivation through the strong adsorption on the active sites, especially at low temperatures [10]. The Pt/TiO_2-H_2 catalyst can keep active in moist air (50% relative humidity) at room temperature, and no deactivation was observed after reaction for 10 h. Thus, the activity of Pt/TiO_2 is stable and resistant to water.

4. Conclusions

Purification of indoor HCHO at room temperature was investigated using TiO_2 supported Pt catalysts without irradiation. The H_2 reduced Pt/TiO_2 catalysts showed much higher removal efficiency than the unreduced one. More than 96% HCHO conversion was obtained over the reduced 0.5 wt% Pt/TiO_2 catalyst, on which highly dispersed metallic Pt nanoparticles with very small size (~2 nm) were identified. Oxidation state of Pt is the most important factor controlling the catalytic activity. Metallic Pt rather than cationic Pt nanoparticles provide the active sites for HCHO oxidation. Efficient purification of indoor HCHO was successfully achieved over a low Pt-loading catalyst at room temperature without any heating or illumination. It is a very efficient and promising technology for the removal of indoor HCHO.

Conflict of Interests

The authors declare that there is no conflict of interests regarding the publication of this paper.

Acknowledgments

The authors gratefully acknowledge the financial supports from Research Fund for the Doctoral Program of Higher Education of China (no. 20120172120039), National Nature Science Foundation of China (no. 51208207), Research Fund Program of Guangdong Provincial Key Laboratory of Environmental Pollution Control and Remediation Technology (no. 2013K0001) and Guangdong Provincial Key Laboratory of Atmospheric Environment and Pollution Control, and the Fundamental Research Funds for the Central Universities (no. 13lgzd03).

References

[1] F. Chen, X. Yang, and Q. Wu, "Photocatalytic oxidation of *Escherischia coli*, *Aspergillus niger*, and formaldehyde under different ultraviolet irradiation conditions," *Environmental Science and Technology*, vol. 43, no. 12, pp. 4606–4611, 2009.

[2] X. Tang, J. Chen, Y. Li, Y. Li, Y. Xu, and W. Shen, "Complete oxidation of formaldehyde over Ag/MnO_x-CeO_2 catalysts," *Chemical Engineering Journal*, vol. 118, no. 1-2, pp. 119–125, 2006.

[3] Y. Sekine, "Oxidative decomposition of formaldehyde by metal oxides at room temperature," *Atmospheric Environment*, vol. 36, no. 35, pp. 5543–5547, 2002.

[4] C. Zhang, H. He, and K.-I. Tanaka, "Perfect catalytic oxidation of formaldehyde over a Pt/TiO_2 catalyst at room temperature," *Catalysis Communications*, vol. 6, no. 3, pp. 211–214, 2005.

[5] J. Peng and S. Wang, "Performance and characterization of supported metal catalysts for complete oxidation of formaldehyde at low temperatures," *Applied Catalysis B*, vol. 73, no. 3, pp. 282–291, 2007.

[6] C. Zhang, H. He, and K.-I. Tanaka, "Catalytic performance and mechanism of a Pt/TiO_2 catalyst for the oxidation of formaldehyde at room temperature," *Applied Catalysis B*, vol. 65, no. 1-2, pp. 37–43, 2006.

[7] X. Tang, J. Chen, X. Huang, Y. Xu, and W. Shen, "Pt/MnO_x-CeO_2 catalysts for the complete oxidation of formaldehyde at

ambient temperature," *Applied Catalysis B*, vol. 81, no. 1-2, pp. 115–121, 2008.

[8] J. Peng and S. Wang, "Correlation between microstructure and performance of Pt/TiO_2 catalysts for formaldehyde catalytic oxidation at ambient temperature: effects of hydrogen pretreatment," *Journal of Physical Chemistry C*, vol. 111, no. 27, pp. 9897–9904, 2007.

[9] Y. Wen, X. Tang, J. Li, J. Hao, L. Wei, and X. Tang, "Impact of synthesis method on catalytic performance of MnO_x-SnO_2 for controlling formaldehyde emission," *Catalysis Communications*, vol. 10, no. 8, pp. 1157–1160, 2009.

[10] X. Tang, Y. Li, X. Huang et al., "MnO_x-CeO_2 mixed oxide catalysts for complete oxidation of formaldehyde: effect of preparation method and calcination temperature," *Applied Catalysis B*, vol. 62, no. 3-4, pp. 265–273, 2006.

[11] J. Yu, M. Jaroniec, and G. Lu, "TiO_2 Photocatalytic Materials," *International Journal of Photoenergy*, vol. 2012, Article ID 206183, 5 pages, 2012.

[12] L. Wang, Q. Zhang, M. Sakurai, and H. Kameyama, "Development of a Pt/TiO_2 catalyst on an anodic alumite film for catalytic decomposition of formaldehyde at room temperature," *Catalysis Communications*, vol. 8, no. 12, pp. 2171–2175, 2007.

[13] L. Wang, M. Sakurai, and H. Kameyama, "Study of catalytic decomposition of formaldehyde on Pt/TiO_2 alumite catalyst at ambient temperature," *Journal of Hazardous Materials*, vol. 167, no. 1–3, pp. 399–405, 2009.

[14] C. Zhang and H. He, "A comparative study of TiO_2 supported noble metal catalysts for the oxidation of formaldehyde at room temperature," *Catalysis Today*, vol. 126, no. 3-4, pp. 345–350, 2007.

[15] Z. Xu, J. Yu, and W. Xiao, "Microemulsion-assisted preparation of a mesoporous ferrihydrite/SiO_2 composite for the efficient removal of formaldehyde from air," *Chemistry*, vol. 19, pp. 9592–9598, 2013.

[16] Z. Xu, J. Yu, G. Liu, B. Cheng, P. Zhou, and X. Li, "Microemulsion-assisted synthesis of hierarchical porous $Ni(OH)_2$/SiO_2 composites toward efficient removal of formaldehyde in air," *Dalton Transactions*, vol. 42, pp. 10190–10197, 2013.

[17] H. Yoshida, Y. Yazawa, and T. Hattori, "Effects of support and additive on oxidation state and activity of Pt catalyst in propane combustion," *Catalysis Today*, vol. 87, no. 1–4, pp. 19–28, 2003.

[18] K. Vinodgopal, U. Stafford, K. A. Gray, and P. V. Kamat, "Electrochemically assisted photocatalysis. 2. The role of oxygen and reaction intermediates in the degradation of 4-Chlorophenol on immobilized TiO_2 particulate films," *Journal of Physical Chemistry*, vol. 98, no. 27, pp. 6797–6803, 1994.

[19] M. C. Kung, R. J. Davis, and H. H. Kung, "Understanding au-catalyzed low-temperature CO oxidation," *Journal of Physical Chemistry C*, vol. 111, no. 32, pp. 11767–11775, 2007.

[20] Y. Shen, X. Yang, Y. Wang et al., "The states of gold species in CeO_2 supported gold catalyst for formaldehyde oxidation," *Applied Catalysis B*, vol. 79, no. 2, pp. 142–148, 2008.

[21] M. A. Aramendía, J. C. Colmenares, A. Marinas et al., "Effect of the redox treatment of Pt/TiO_2 system on its photocatalytic behaviour in the gas phase selective photooxidation of propan-2-ol," *Catalysis Today*, vol. 128, no. 3-4, pp. 235–244, 2007.

[22] S. Huang, C. Zhang, and H. He, "Complete oxidation of o-xylene over Pd/Al_2O_3 catalyst at low temperature," *Catalysis Today*, vol. 139, no. 1-2, pp. 15–23, 2008.

[23] S.-K. Ihm, Y.-D. Jun, D.-C. Kim, and K.-E. Jeong, "Low-temperature deactivation and oxidation state of Pd/γ-Al_2O_3 catalysts for total oxidation of n-hexane," *Catalysis Today*, vol. 93-95, pp. 149–154, 2004.

[24] W. G. Shim, J. W. Lee, and S. C. Kim, "Analysis of catalytic oxidation of aromatic hydrocarbons over supported palladium catalyst with different pretreatments based on heterogeneous adsorption properties," *Applied Catalysis B*, vol. 84, no. 1-2, pp. 133–141, 2008.

[25] E. M. Cordi and J. L. Falconer, "Oxidation of volatile organic compounds on Al_2O_3, Pd/Al_2O_3, and PdO/Al_2O_3 catalysts," *Journal of Catalysis*, vol. 162, no. 1, pp. 104–117, 1996.

[26] M. Haruta, N. Yamada, T. Kobayashi, and S. Iijima, "Gold catalysts prepared by coprecipitation for low-temperature oxidation of hydrogen and of carbon monoxide," *Journal of Catalysis*, vol. 115, no. 2, pp. 301–309, 1989.

[27] S. Arrii, F. Morfin, A. J. Renouprez, and J. L. Rousset, "Oxidation of CO on gold supported catalysts prepared by laser vaporization: direct evidence of support contribution," *Journal of the American Chemical Society*, vol. 126, no. 4, pp. 1199–1205, 2004.

[28] N. Weiher, A. M. Beesley, N. Tsapatsaris et al., "Activation of oxygen by metallic gold in Au/TiO_2 catalysts," *Journal of the American Chemical Society*, vol. 129, no. 8, pp. 2240–2241, 2007.

[29] O. S. Alexeev, S. Y. Chin, M. H. Engelhard, L. Ortiz-Soto, and M. D. Amiridis, "Effects of reduction temperature and metal-support interactions on the catalytic activity of Pt/γ-Al_2O_3 and Pt/TiO_2 for the oxidation of CO in the presence and absence of H_2," *Journal of Physical Chemistry B*, vol. 109, no. 49, pp. 23430–23443, 2005.

[30] Y. Liu, X. Wang, F. Yang, and X. Yang, "Excellent antimicrobial properties of mesoporous anatase TiO_2 and Ag/TiO_2 composite films," *Microporous and Mesoporous Materials*, vol. 114, no. 1–3, pp. 431–439, 2008.

[31] L. Nie, J. Yu, X. Li, B. Cheng, G. Liu, and M. Jaroniec, "Enhanced performance of NaOH-Modified Pt/TiO_2 toward room temperature selective oxidation of formaldehyde," *Environmental Science & Technology*, vol. 47, pp. 2777–2783, 2013.

Hindawi Publishing Corporation
International Journal of Photoenergy
Volume 2013, Article ID 812376, 7 pages
http://dx.doi.org/10.1155/2013/812376

Research Article

Photocatalytic Degradation of Organic Dyes by $H_4SiW_6Mo_6O_{40}/SiO_2$ Sensitized by H_2O_2

Li Yu, Yongkui Huang, Yun Yang, Yulin Xu, Guohong Wang, and Shuijin Yang

Hubei Key Laboratory of Pollutant Analysis & Reuse Technology, College of Chemistry and Chemical Engineering, Hubei Normal University, Huangshi 435002, China

Correspondence should be addressed to Shuijin Yang; yangshuijin@163.com

Received 28 June 2013; Accepted 22 July 2013

Academic Editor: Huogen Yu

$H_4SiW_6Mo_6O_{40}/SiO_2$ was sensitized by H_2O_2 solution that significantly improved its catalytic activity under simulated natural light. Degradation of basic fuchsin was used as a probe reaction to explore the influencing factors on the photodegradation reaction. The results showed that the optimal conditions were as follows: initial concentration of basic fuchsin 8 mg/L, pH 2.5, catalyst dosage 4 g/L, and light irradiation time 4 h. Under these conditions, the degradation rate of basic fuchsin is 98%. The reaction of photocatalysis for basic fuchsin can be expressed as the first-order kinetic model. After being used continuously for four times, the catalyst kept the inherent photocatalytic activity for degradation of dyes. The photodegradation of malachite green, methyl orange, methylene blue, and rhodamine B were also tested, and the degradation rate of dyes can reach 90%–98%.

1. Introduction

In the past few years, a great deal of attention has been paid to water-treatment technology [1]. A lot of water treatment techniques including condensation, ultrafiltration, membrane separation, and adsorption have been adopted to remove persistent organic compounds and microorganisms in water [2, 3]. Especially, advanced oxidation processes (AOPs), which have the potential to completely mineralize organic compounds to CO_2 and H_2O, have shown a great potential as a low-cost and high efficiency water treatment technology [4]. Semiconductor photocatalytic process have played an important role in many advanced oxidation processes. Semiconductor materials including Ag_2O [5], Ag-loaded Bi_2WO_6 [6], TiO_2 [7, 8], bismuth tungstate [9], ZnO [10], and TiO_2-rGO [11] have been found to exhibit high photocatalytic activity. Although TiO_2 has been investigated widely in photocatalytic degradation of organic chemicals in water under ultraviolet (UV) light, constituting only 4% of the solar light, it cannot be effectively activated under solar light irradiation due to its wide intrinsic band gap. Because the light wavelength of light sources is one of the few parameters that affects the overall photocatalytic rate, it is essential to use solar light efficiently to achieve a high photocatalytic reaction rate. Visible-light responsive photocatalysts have been investigated quite intensively in recent years, including modified TiO_2 [12–15].

Heteropoly acid (HPA) has been extensively studied as acid or oxidation catalyst for a wide range of reactions [16, 17]. In recent years, HPA has also attracted much attention as photocatalysts owing to its photophysics and photochemical properties, analogous to these of semiconductors [18, 19]. Upon absorbing UV-near visible light irradiation, HPA will be excited to generate electron-hole pairs. The electron and hole will initiate reductive and oxidative reactions to decomposition of organic pollutants. However, several reports related to the photocatalysis of HPAs are concentrated on UV irradiation. In order to overcome their disadvantages, such as low surface area (1–10 m^2/g), highly soluble in polar media, and difficulty in separation, HPAs should be immobilized on a support like montmorillonite clay [20], MCM-41 [21], and TiO_2 [22] to obtain insoluble catalysts. Moreover, some support materials seem to improve the catalytic performance of the combined catalysts because of a synergistic catalytic effect [23].

In this paper, it was attempted to improve photocatalytic activity of $H_4SiW_6Mo_6O_{40}/SiO_2$ according to sensitization by H_2O_2 solution. The photocatalytic degradation of some dyes having different chemical structures with the catalyst under simulated natural light irradiation was investigated.

2. Experimental

2.1. Preparation of Samples. $H_4SiW_6Mo_6O_{40}/SiO_2$ was synthesized according to reference [24, 25] by a sol-gel technique. An amount of $H_4SiW_6Mo_6O_{40}$ was dissolved in 26 mL of H_2O, and a stoichiometric amount of TEOS was mixed with 1-BuOH. The latter was added dropwise to the aqueous solution. The resultant was allowed to be stirred at room temperature for 1 h, at 45°C for 1 h, and then at 80°C until a uniform gel was formed. The hydrogel obtained was dehydrated slowly at 45°C for 16 h in vacuum and then at 90°C for 3.5 h. Thus, the silica network was fastened, and the removal of the $H_4SiW_6Mo_6O_{40}$ molecules from it was avoided. The particulate gel was washed with hot water for several times until the filtrate was neutral, and then the products were calcined for the required duration.

$H_4SiW_6Mo_6O_{40}/SiO_2$ was treated by H_2O_2 as follows [26]: 1 g $H_4SiW_6Mo_6O_{40}/SiO_2$ was added into 15 mL 30% H_2O_2 solution and sonicated the mixture for 20 min. The slurry mixture was filtrated and dried at room temperature. This catalyst is denoted by $H_4SiW_6Mo_6O_{40}/SiO_2(x)$.

2.2. Characterization. The FT-IR spectra of the samples in KBr matrix were recorded on a Nicolet 5700 FT-IR spectrometer in the range 400~4000 cm^{-1}. The X-ray powder diffraction pattern of the samples was measured by a Bruker AXS D8-Advanced diffractometer (Bruker, Germany) employing Cu K_α radiation. Scanning electron micrographs (SEM) were obtained on a Hitachi S-3400N scanning electron microscope.

2.3. Photocatalytic Activity Measurement. The photocatalytic activities of the samples were determined by measuring the degradation of dyes in an aqueous solution under simulated sunlight irradiation. Simulated sunlight irradiation was provided by a 500 W xenon lamp (Nanjing Xujiang Electromechanical Factory), and the intensity of the lamp was 1200 $\mu mol \cdot m^{-2} \cdot s^{-1}$. Solution pH was adjusted with dilute aqueous HCl and NaOH solutions. The system was cooled by circulating water and maintained at room temperature. Before irradiation, the suspension was vigorously stirred in the dark for 30 min to reach the adsorption-desorption equilibrium of dyes on the catalyst surface. At given time intervals, about 3 mL suspension was continually taken out from the photoreactor and centrifuged. The change of the basic fuchsin concentrations was analyzed by the UV-vis spectrophotometer (Hitachi U-3010).

3. Results and Discussion

3.1. Characterization of the $H_4SiW_6Mo_6O_{40}/SiO_2$ Catalyst. The IR spectra of $H_4SiW_6Mo_6O_{40}$ and $H_4SiW_6Mo_6O_{40}/SiO_2$ are shown in Figure 1. As shown in Figure 1, the characteristic bands of $H_4SiW_6Mo_6O_{40}$ Keggin anion at 972.9, 918.2, 774.6, and 538.6 cm^{-1} are observed for pure $H_4SiW_6Mo_6O_{40}$. In addition, the band at 1618.3 cm^{-1}, which is the bending mode of the water, indicates the presence of the water. When $H_4SiW_6Mo_6O_{40}$ is bonded to the Si-OH group of SiO_2, these bands have changed. However, the characteristic bands for the Keggin anion could be observed for $H_4SiW_6Mo_6O_{40}/SiO_2$. The shifts indicate that a strong chemical interaction, not simple physical adsorption, exists between the $H_4SiW_6Mo_6O_{40}$ and the support.

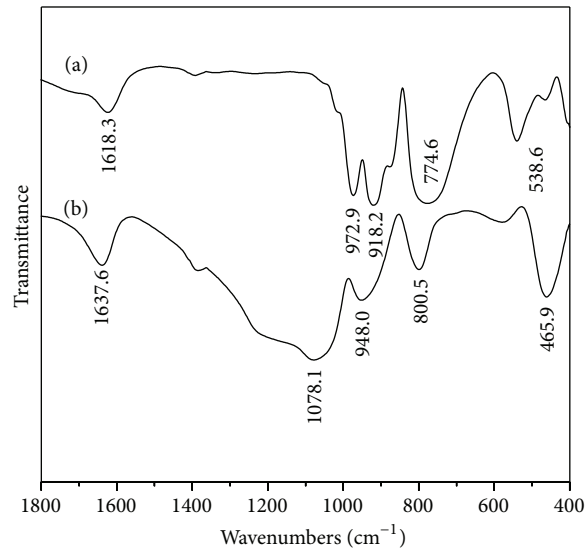

Figure 1: FT-IR spectra of $H_4SiW_6Mo_6O_{40}$ (a) and $H_4SiW_6Mo_6O_{40}/SiO_2$ (b).

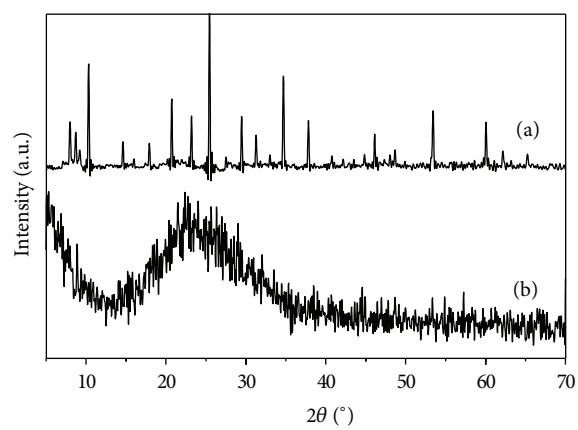

Figure 2: The XRD patterns of $H_4SiW_6Mo_6O_{40}$ (a) and $H_4SiW_6Mo_6O_{40}/SiO_2$ (b).

Figure 2 shows the XRD patterns of $H_4SiW_6Mo_6O_{40}$ and $H_4SiW_6Mo_6O_{40}/SiO_2$. The characteristic diffraction peaks of $H_4SiW_6Mo_6O_{40}$ that were explored at 8.0, 10.4, 20.7, 25.5, 29.2, 34.5, and 37.8° can be assigned to the diffraction characteristic peaks of crystalline $H_4SiW_6Mo_6O_{40}$ Keggin structure. For $H_4SiW_6Mo_6O_{40}/SiO_2$, only a broad band at $2\theta = 22.4°$ that can be assigned to the diffraction peaks of

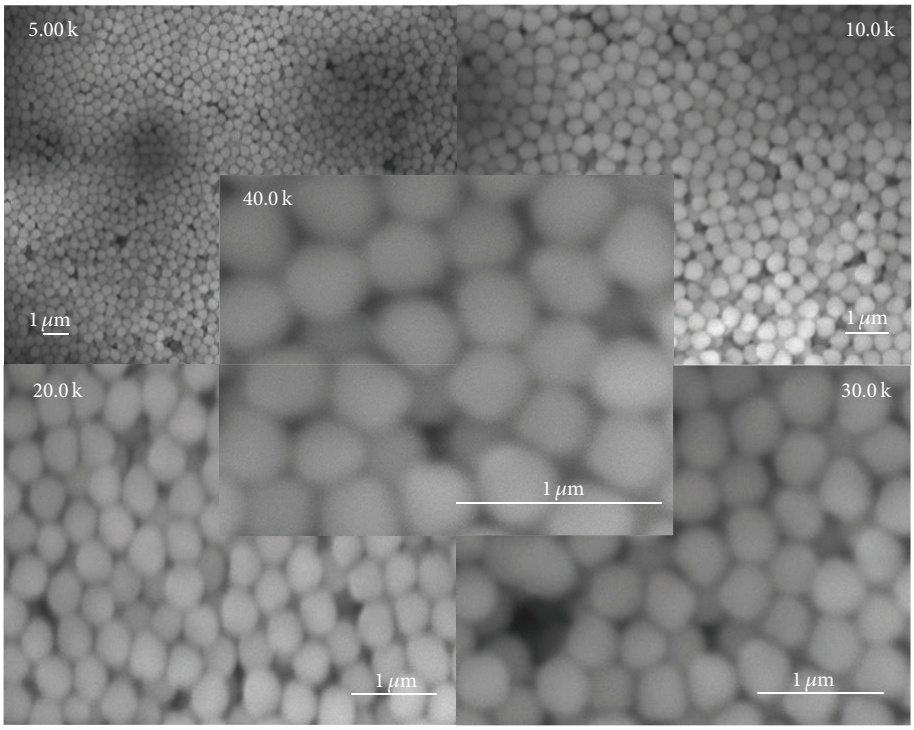

Figure 3: SEM images of SiO_2 particles at different multiples.

amorphous silica appears, but no signals of $H_4SiW_6Mo_6O_{40}$ are displayed. Thus, it can be proposed that $H_4SiW_6Mo_6O_{40}$ is well dispersed on the surface of silica support.

Figure 3 shows the SEM images of SiO_2 particles at different multiples. As can be seen from the figure, surface morphology of SiO_2 is spherical and massive. Silicon sphere is dispersed evenly in the whole system, and its diameter is about 4.5 μm.

Figure 4 shows the SEM patterns of SiO_2, $H_4SiW_6Mo_6O_{40}$, and $H_4SiW_6Mo_6O_{40}/SiO_2$ at 5000 times. Surface morphology of SiO_2 is massive, dispersed evenly in the whole system. Surface morphology of $H_4SiW_6Mo_6O_{40}$ is net-like, and its specific surface area is relatively small. The results show that the catalyst not only uniformly dispersed in the system, but also the specific surface area is bigger than before.

3.2. Investigation of Photocatalytic Activity of Catalysts

3.2.1. Comparison of Photocatalytic Activity of Catalysts. In order to detect the catalytic activity of catalysts, the degradation of model basic fuchsin aqueous over the samples was carried out at the basic fuchsin concentration of 16 mg/L, pH 2.5 and 4 g/L of catalyst, and the results are shown in Figure 5.

As shown in Figure 5, direct photolysis of an aqueous basic fuchsin under simulated natural light irradiation for 3.5 h did not cause any changes of its concentration. In addition, the degradation rate of basic fuchsin over $H_4SiW_6Mo_6O_{40}/SiO_2$ is only 31.0%, while the degradation rate over $H_4SiW_6Mo_6O_{40}/SiO_2(x)$ is as high as 98%. The photocatalytic performance of $H_4SiW_6Mo_6O_{40}/SiO_2(x)$ is much higher than that of $H_4SiW_6Mo_6O_{40}/SiO_2$. So, the peroxo complexes formed from the decomposition of $H_4SiW_6Mo_6O_{40}$ in hydrogen peroxide have played an important role in the photodegradation of dyes. Therefore, it is concluded that the sensitizing effect has a remarkable influence on the photocatalytic activity of catalyst.

3.2.2. Effect of the Initial Concentration of Dye. To investigate the effects of initial concentration on the photocatalytic degradation of basic fuchsin, this was varied from 8 mg/L to 40 mg/L, and the results are presented in Figure 6.

From Figure 6, it can be seen that the photocatalytic degradation rate of basic fuchsin decreases with an increase in the initial concentration of basic fuchsin. This phenomenon could be attributed to the excessive absorption of the basic fuchsin molecules on the surface of catalyst and a diminishing of light penetration through the solution at high initial concentration of basic fuchsin, which inhibits the process of activated catalyst. Then, the optimum of the initial concentration is 8 mg/L.

3.2.3. Effect of Catalyst Dosage. We have also investigated the effects of catalyst dosage on the degradation rate of basic fuchsin, and the results were shown in Figure 7.

It was found that the degradation rate of basic fuchsin increases with an increase in the amount of catalyst from 1 g/L to 4 g/L, then decreases when the catalyst dosage is higher

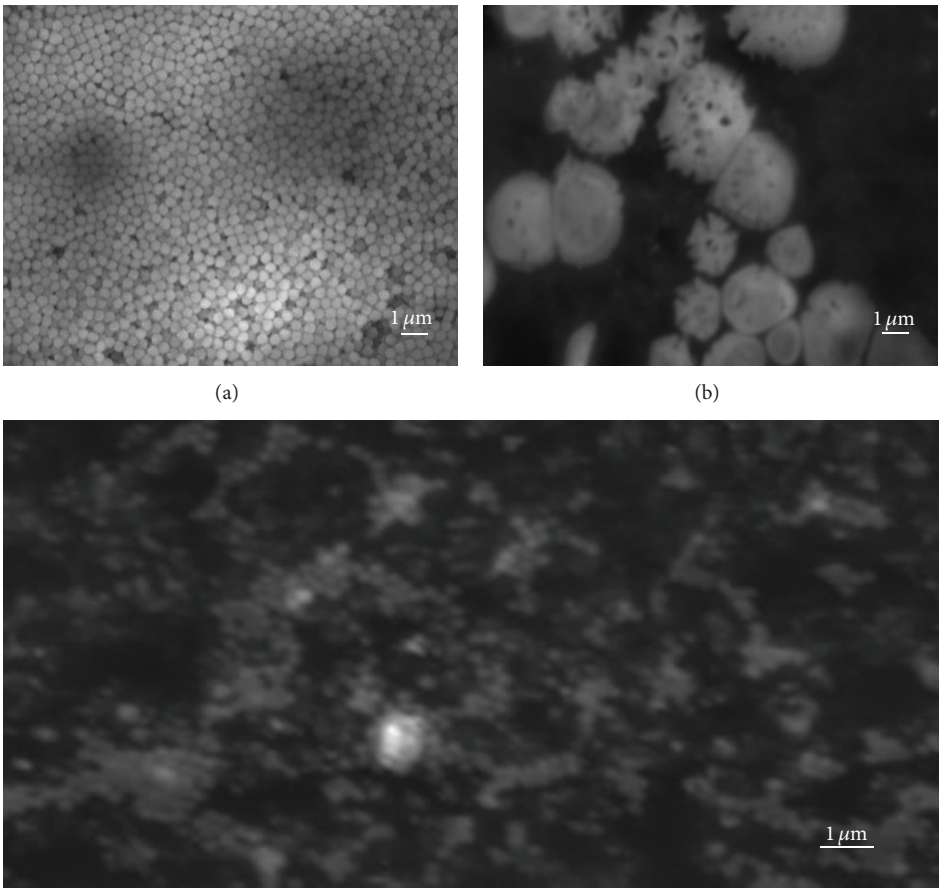

Figure 4: SEM images of SiO_2 (a), $H_4SiW_6Mo_6O_{40}$ (b), and $H_4SiW_6Mo_6O_{40}/SiO_2$ (c).

than 4 g/L. This may be attributed to the scattering effect. The high turbidity of catalyst decreased the penetration depth of solar radiation [22]. So, the optimum amount of catalyst is 4 g/L.

3.2.4. Effect of pH. The pH value is one of the most important parameters in the photodegradation of organic compounds. The effect of pH on the photodegradation rate of basic fuchsin was also investigated at different pH. The results are shown in Figure 8.

From Figure 8, it can be seen that the degradation rate increased with decreasing pH of the solution, then decreases when pH of the solution is lower than 2.5. This is mainly ascribed to the variations of surface charge properties of the photocatalyst.

3.2.5. Effect of HPA. The effect of the kind of HPA on photocatalytic degradation of organic compounds was examined, and the results were shown in Figure 9.

From Figure 9, it can be seen that the kind of HPA plays an important role in the photocatalytic reaction. After 3.5 h irradiation under simulated natural light irradiation, the degradation rate of basic fuchsin over $H_4SiW_6Mo_6O_{40}/SiO_2(x)$, $H_3PW_{12}O_{40}/SiO_2(x)$, $H_4SiW_{12}O_{40}/SiO_2(x)$, $H_3PW_6Mo_6O_{40}/SiO_2(x)$, and $H_4SiW_6Mo_6O_{40}$ is 98%, 96%, 68%, 82%, and 68%, respectively. The activity of various HPA in the reaction follows the order $H_4SiW_6Mo_6O_{40}/SiO_2(x) > H_3PW_{12}O_{40}/SiO_2(x) > H_3PW_6Mo_6O_{40}/SiO_2(x) > H_4SiW_{12}O_{40}/SiO_2(x) > H_4SiW_6Mo_6O_{40}$.

3.3. Photocatalytic Degradation of Various Dyes. In order to determine the feasibility of the catalyst in treatment of some dyes having different chemical structures, we attempted to choose other dyes such as methyl orange, rhodamine B, malachite green, and methylene blue as reactants. The results are shown in Figure 10. The degradation rate of dyes can reach 90%~98% at the optimized conditions. Therefore, the catalysts have good prospects of application in treatment of organic pollutants.

3.4. Reuse of the Catalyst. Reusability of the catalyst was also studied under the optimized conditions. After the reaction finished, the catalyst was recovered and washed with distilled

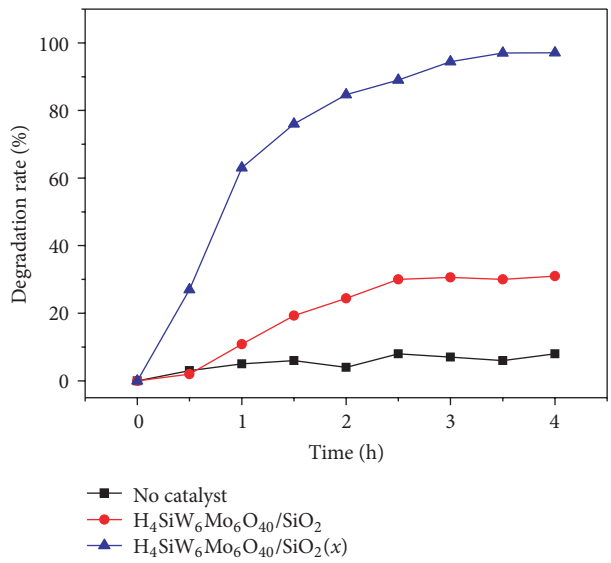

Figure 5: Comparison of photocatalytic activity of catalysts.

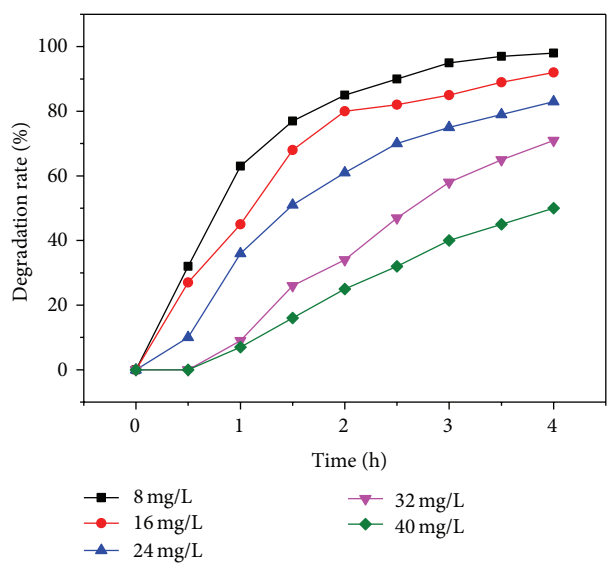

Figure 6: Effects of initial dye concentration on photocatalytic activity of catalyst.

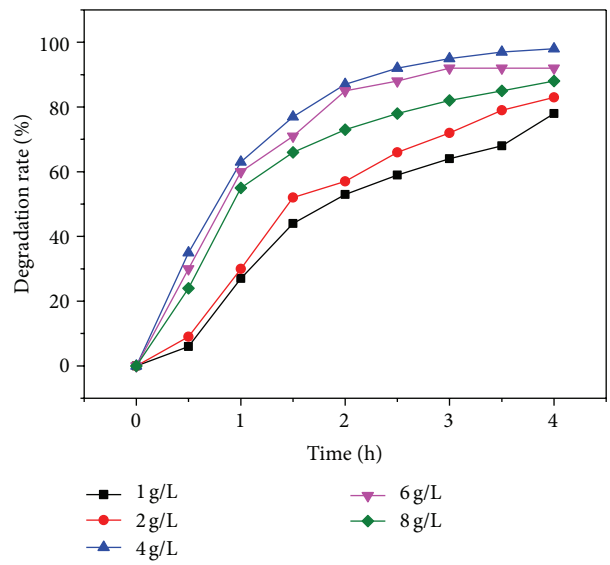

Figure 7: Effect of catalyst dosage on photocatalytic activity of catalyst.

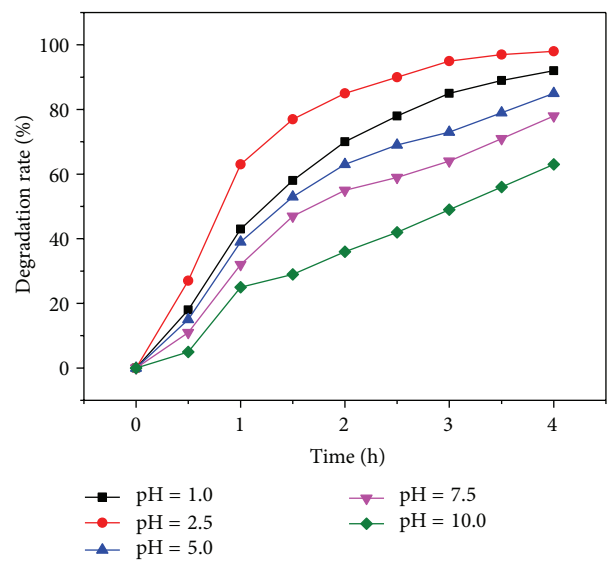

Figure 8: Effects of the solution pH on photocatalytic activity of catalyst.

water and ethyl alcohol. The recovered catalyst was treated again by H_2O_2 for the next degradation run.

The results are shown in Figure 11. It was observed that a decrease in catalytic activity is observed with its subsequent reuse. However, the degradation rate of basic fuchsin can reach 87% in the fifth run. So, it can be concluded that the high catalytic activity is retained in a next run.

3.5. Kinetic Analysis. The kinetics of photocatalytic degradation of basic fuchsin by $H_4SiW_6Mo_6O_{40}/SiO_2(x)$, $H_3PW_{12}O_{40}/SiO_2(x)$, $H_4SiW_{12}O_{40}/SiO_2(x)$, and $H_3PW_6Mo_6O_{40}/SiO_2(x)$ was studied under optimized conditions. The results are shown in Figure 12.

The results show that a plot of $\ln(C_0/C_t)$ versus "time" exhibits a nearly straight line, and the linear correlation coefficients (R) are ca. 0.985, 0.991, 0.994, 0.986, and 0.997, respectively. It can be concluded that the photodegradation reactions follow the first-order kinetics, which follow Langmuir-Hinshelwood kinetics. The rate constants were calculated to be 0.85, 0.45, 0.29, 0.15, and 0.99 h^{-1}.

4. Conclusion

$H_4SiW_6Mo_6O_{40}/SiO_2$ was prepared by a sol-gel method and sensitized by H_2O_2 solution. Degradation of basic fuchsin was used as a probe reaction to explore the influencing factors

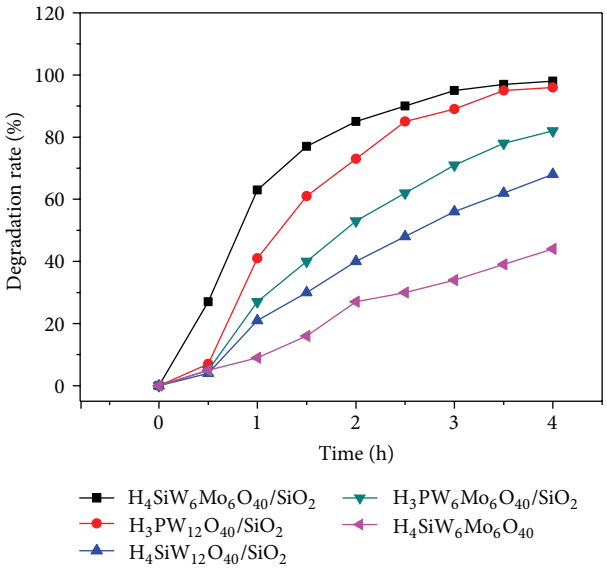

Figure 9: Effect of HPA on photocatalytic activity of catalyst.

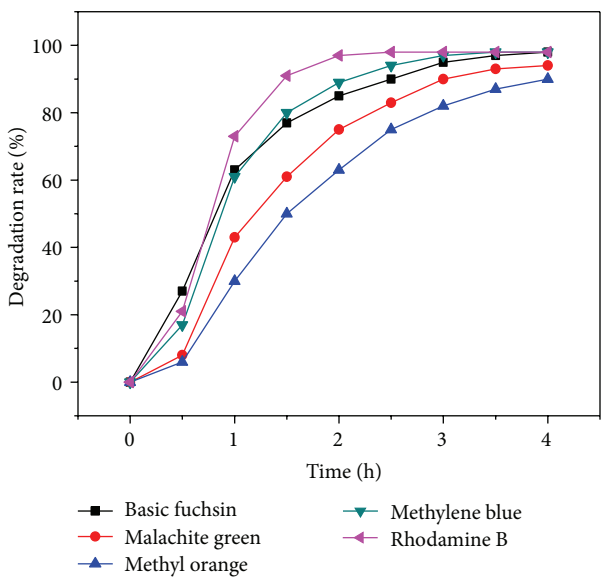

Figure 10: Photocatalytic degradation of various dyes using $H_4SiW_6Mo_6O_{40}/SiO_2(x)$ as a catalyst.

on the photodegradation reaction. The results showed the optimal conditions were as follows: initial concentration of basic fuchsin 8 mg/L, pH 2.5, catalyst dosage 4 g/L, and light irradiation time 4 h. Under these conditions, the degradation rate of basic fuchsin is 98%. The photodegradation of other dyes such as malachite green, methyl orange, methylene blue, and rhodamine B were also tested, and the degradation rate of dyes can reach 90%–98%. The high activity and stability of the catalyst is well retained after 5 runs. The reaction of photocatalysis for basic fuchsin can be expressed as the first-order kinetic model.

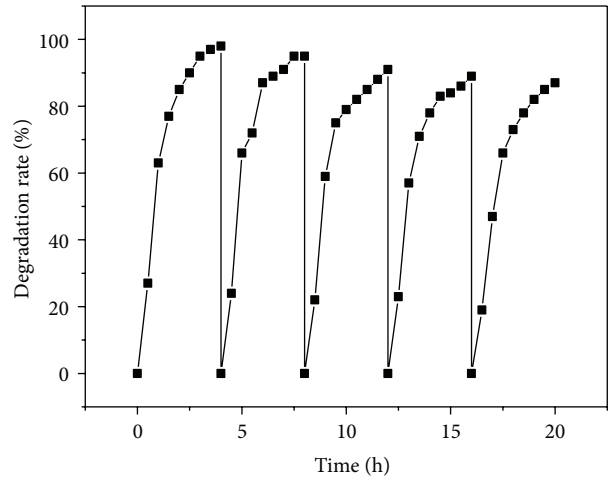

Figure 11: Recycling of the catalyst.

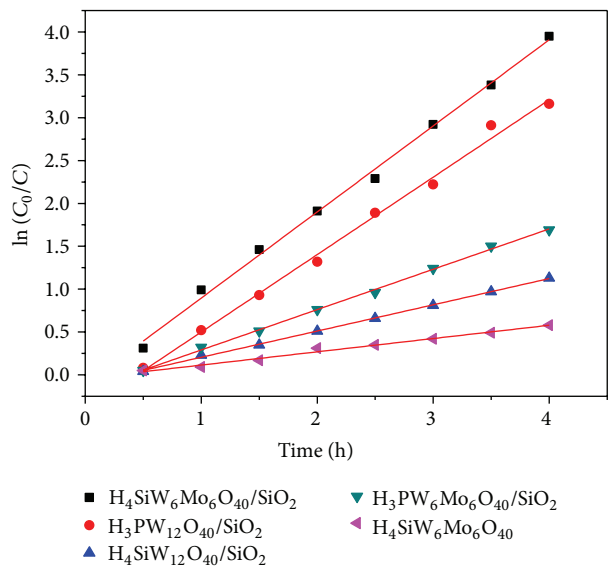

Figure 12: Relation curve of $\ln(C_0/C)$ and time (t).

Acknowledgment

This work was financially supported by the Hubei Key Laboratory of Pollutant Analysis & Reuse Technology (no. KL2013G01).

References

[1] M. N. Chong, B. Jin, C. W. K. Chow, and C. Saint, "Recent developments in photocatalytic water treatment technology: a review," *Water Research*, vol. 44, no. 10, pp. 2997–3027, 2010.

[2] E. Sahinkaya, N. Uzal, U. Yetis, and F. B. Dilek, "Biological treatment and nanofiltration of denim textile wastewater for reuse," *Journal of Hazardous Materials*, vol. 153, no. 3, pp. 1142–1148, 2008.

[3] R. Abe, "Recent progress on photocatalytic and photoelectrochemical water splitting under visible light irradiation," *Journal*

of Photochemistry and Photobiology C, vol. 11, no. 4, pp. 179–209, 2010.

[4] S. H. S. Chan, T. Yeong Wu, J. C. Juan, and C. Y. Teh, "Recent developments of metal oxide semiconductors as photocatalysts in advanced oxidation processes (AOPs) for treatment of dye waste-water," *Journal of Chemical Technology and Biotechnology*, vol. 86, no. 9, pp. 1130–1158, 2011.

[5] X. Wang, S. Li, H. Yu, J. Yu, and S. Liu, "Ag_2O as a new visible-light photocatalyst: self-stability and high photocatalytic activity," *Chemistry*, vol. 17, no. 28, pp. 7777–7780, 2011.

[6] Z. Zhang, W. Wang, E. Gao, S. Sun, and L. Zhang, "Photocatalysis coupled with thermal effect induced by SPR on Ag-loaded Bi_2WO_6 with enhanced photocatalytic activity," *The Journal of Physical Chemistry C*, vol. 116, pp. 25898–25903, 2012.

[7] X. Zhang, T. Zhang, J. Ng, J. H. Pan, and D. D. Sun, "Transformation of bromine species in TiO_2 photocatalytic system," *Environmental Science and Technology*, vol. 44, no. 1, pp. 439–444, 2010.

[8] J. Liao, S. Lin, L. Zhang, N. Pan, X. Cao, and J. Li, "Photocatalytic degradation of methyl orange using a TiO_2/Ti mesh electrode with 3D nanotube arrays," *ACS Applied Materials and Interfaces*, vol. 4, no. 1, pp. 171–177, 2011.

[9] H. Yu, R. Liu, X. Wang, P. Wang, and J. Yu, "Enhanced visible-light photocatalytic activity of Bi_2WO_6 nanoparticles by Ag_2O cocatalyst," *Applied Catalysis B*, vol. 111-112, pp. 326–333, 2012.

[10] J. Yu and X. Yu, "Hydrothermal synthesis and photocatalytic activity of zinc oxide hollow spheres," *Environmental Science and Technology*, vol. 42, no. 13, pp. 4902–4907, 2008.

[11] P. Wang, J. Wang, X. Wang et al., "One-step synthesis of easy-recycling TiO_2-rGO nanocomposite photocatalysts with enhanced photocatalytic activity," *Applied Catalysis B*, vol. 132-133, pp. 452–459, 2013.

[12] Q. Xiang, J. Yu, W. Wang, and M. Jaroniec, "Nitrogen self-doped nanosized TiO_2 sheets with exposed 001 facets for enhanced visible-light photocatalytic activity," *Chemical Communications*, vol. 47, no. 24, pp. 6906–6908, 2011.

[13] C. Chen, W. Ma, and J. Zhao, "Semiconductor-mediated photodegradation of pollutants under visible-light irradiation," *Chemical Society Reviews*, vol. 39, no. 11, pp. 4206–4219, 2010.

[14] H. Fu, S. Zhang, T. Xu, Y. Zhu, and J. Chen, "Photocatalytic degradation of RhB by fluorinated Bi_2WO_6 and distributions of the intermediate products," *Environmental Science and Technology*, vol. 42, no. 6, pp. 2085–2091, 2008.

[15] R. Liu, P. Wang, X. Wang, H. Yu, and J. Yu, "UV- and visible-light photocatalytic activity of simultaneously deposited and doped Ag/Ag(I)-TiO_2 photocatalyst," *The Journal of Physical Chemistry C*, vol. 116, pp. 17721–17728, 2012.

[16] I. V. Kozhevnikov, "Catalysis by heteropoly acids and multicomponent polyoxometalates in liquid-phase reactions," *Chemical Reviews*, vol. 98, no. 1, pp. 171–198, 1998.

[17] M. N. Timofeeva, "Acid catalysis by heteropoly acids," *Applied Catalysis A*, vol. 256, no. 1-2, pp. 19–35, 2003.

[18] H. Salavati, N. Tavakkoli, and M. Hosseinpoor, "Preparation and characterization of polyphosphotungstate/ZrO_2 nanocomposite and their sonocatalytic and photocatalytic activity under UV light illumination," *Ultrasonics Sonochemistry*, vol. 19, no. 3, pp. 546–553, 2012.

[19] C. Sui, C. Li, X. Guo et al., "Facile synthesis of silver nanoparticles-modified PVA/$H_4SiW_{12}O_{40}$ nanofibers-based electrospinning to enhance photocatalytic activity," *Applied Surface Science*, vol. 258, pp. 7105–7111, 2012.

[20] S. K. Bhorodwaj and D. K. Dutta, "Heteropoly acid supported modified montmorillonite clay: an effective catalyst for the esterification of acetic acid with sec-butanol," *Applied Catalysis A*, vol. 378, no. 2, pp. 221–226, 2010.

[21] B. Rabindran Jermy and A. Pandurangan, "Synthesis of geminal diacetates (acylals) using heterogeneous $H_3PW_{12}O_{40}$ supported MCM-41 molecular sieves," *Catalysis Communications*, vol. 9, no. 5, pp. 577–583, 2008.

[22] S. Yang, Y. Xu, Y. Huang et al., "Photocatalytic degradation of Methyl Violet with $TiSiW_{12}O_{40}/TiO_2$," *International Journal of Photoenergy*, vol. 2013, Article ID 191340, 5 pages, 2013.

[23] G. Zhang, A. Dong, Y. Liu, B. Hu, S. Ouyang, and H. Liu, "Research and application of photocatalysts," *Rare Metal Materials and Engineering*, vol. 34, no. 3, pp. 341–345, 2005.

[24] Y. Izumi, K. Hisano, and T. Hida, "Acid catalysis of silica-included heteropolyacid in polar reaction media," *Applied Catalysis A*, vol. 181, no. 2, pp. 277–282, 1999.

[25] S. Yang, Y. Huang, Y. Wang, Y. Yang, M. Xu, and G. Wang, "Photocatalytic degradation of rhodamine B with $H_3PW_{12}O_{40}/SiO_2$ sensitized by H_2O_2," *International Journal of Photoenergy*, vol. 2012, Article ID 927132, 6 pages, 2012.

[26] J. Zou, J. Gao, and Y. Wang, "Synthesis of highly active H_2O_2-sensitized sulfated titania nanoparticles with a response to visible light," *Journal of Photochemistry and Photobiology A*, vol. 202, no. 2-3, pp. 128–135, 2009.

Hindawi Publishing Corporation
International Journal of Photoenergy
Volume 2013, Article ID 954914, 7 pages
http://dx.doi.org/10.1155/2013/954914

Research Article

Bactericidal Activity of TiO_2 on Cells of *Pseudomonas aeruginosa* ATCC 27853

J. L. Aguilar Salinas,[1] J. R. Pacheco Aguilar,[2] S. A. Mayén Hernández,[2] and J. Santos Cruz[2]

[1] *Facultad de Ingeniería, Universidad Autónoma de Querétaro, 76010 QRO, Mexico*
[2] *Facultad de Química, Materiales, Universidad Autónoma de Querétaro, 76010 QRO, Mexico*

Correspondence should be addressed to J. Santos Cruz; jsantos@uaq.edu.mx

Received 25 May 2013; Revised 21 July 2013; Accepted 21 July 2013

Academic Editor: Guisheng Li

The photocatalytic activity of semiconductors is increasingly being used to disinfect water, air, soils, and surfaces. Titanium dioxide (TiO_2) is widely used as a photocatalyst in thin films, powder, and in mixtures with other semiconductors or metals. This work presents the antibacterial effects of TiO_2 and light exposure (at 365 nm) on *Pseudomonas aeruginosa* ATCC 27853. TiO_2 powder was prepared from a mixture of titanium isopropoxide, ethanol, and nitric acid using a green and short time sol-gel technique. The obtained gel annealed at 450°C was characterized by X-ray diffraction, Raman spectroscopy, ultraviolet-visible spectroscopy, diffuse reflectance, scanning electron microscopy, and transmission electron microscopy. The nanocomposite effectively catalyzed the inactivation of *Pseudomonas aeruginosa*. Following 90 minutes exposure to TiO_2 and UV light, logarithm of cell density was reduced from 6 to 3. These results were confirmed by a factorial design incorporating two experimental replicates and two independent factors.

1. Introduction

The gram-negative bacterium *Pseudomonas aeruginosa* (PA) is considered an opportunistic pathogen because it requires minimal nutrients to survive, can tolerate a wide variety of physicochemical conditions, and possesses one of the largest and most complex known prokaryotic genomes (conferring strong resistance to antibiotics). In addition, a high proportion of its proteins is involved in regulation, virulence functions, and transport. PA is a major cause of nosocomial infections, cystic fibrosis, ulcer-like keratitis, lung infections, and fatal diseases in immunocompromised individuals. Self-produced antibiotic-inactivating enzymes cause high antibiotic resistance, low outer membrane permeability, and the expression of genes encoding various efflux pumps [1–3]. One area of continuing study is the type of surfaces likely to harbor pathogens, as reservoirs of contamination present a significant health hazard. Common sources of infection are hospitals, food, both consumption and production centers, and public places.

In 1972, Fujishima and Honda demonstrated that titanium dioxide TiO_2 (TD) exhibits strong bactericidal activity in the presence of light ($\lambda \leq 385$ nm) [4]. To date, there have been several reports which tested the antibacterial activity of both powder in solution and surfaces coated with TD on clinically relevant microorganisms such as *Escherichia coli*, *Staphylococcus aureus*, *Listeria monocytogenes,* and *Pseudomonas aeruginosa* [5, 6].

At the cellular level, some researchers have found different modes of action of bactericidal activity on TD, between which there are two commonly accepted mechanisms that have been proposed for the bactericidal action of TD (i) direct oxidation of intracellular coenzyme A, leading to respiratory inhibition [7], and (ii) loss of potassium ions and the slow release of pathogenic proteins and RNA, resulting in death by intracellular disorder and cell wall decomposition [8]. Conversely, photocatalysis has been shown to promote destruction of the cell membrane [9]. Some studies have identified the most resistant pathogens as those with both complex gene expression systems and thickened cell walls [9–11]. The bactericidal activity of PA has been reported. Others researchers have found variable results, 100% inhibition in 25 minutes using TD solutions (1 mg/mL) [6] until reports

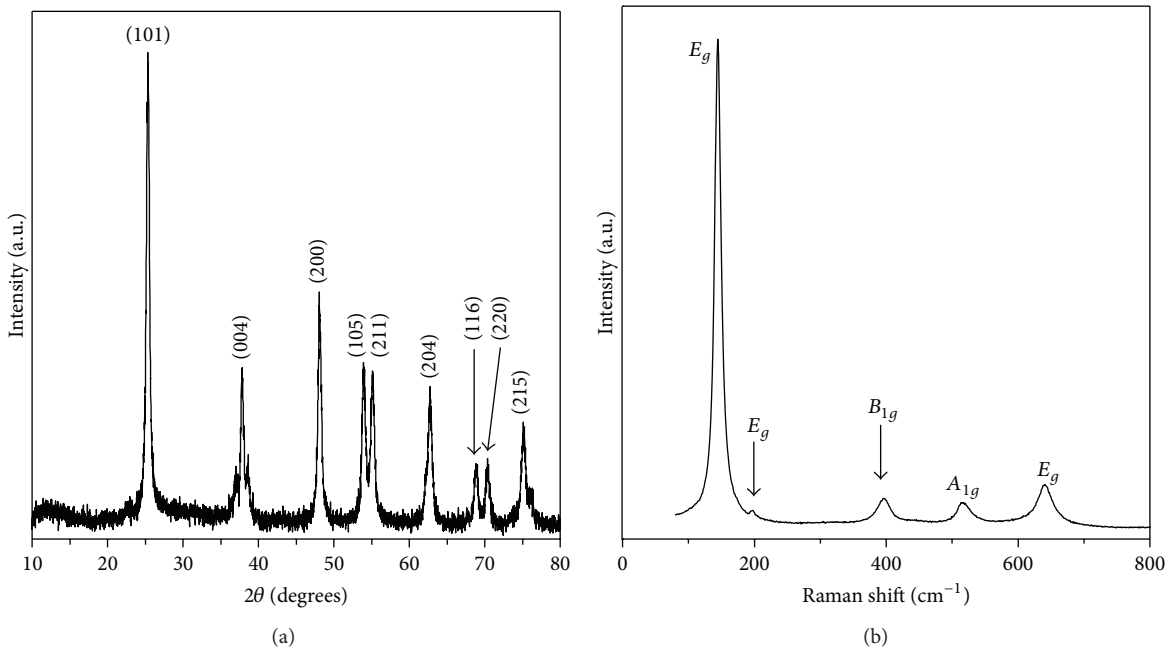

Figure 1: (a) Powder XRD of TiO_2 synthesized by sol-gel at 450°C. (b) Raman spectrum of TiO_2 powder obtained at 450°C.

indicate that the use of concentrations of 10 mg/mL of Ag doped TD with similar inhibition values reached in 120 minutes [12] and tests on films of TD. The nature of the materials used due to the synthesis and thermal treatment are some of the factors that have an influence on the antibacterial ability. Our group has obtained the synthesis of TD in thin film by the sol-gel method, according to the method reported in [13], obtaining good results in the degradation of methylene blue; however, antimicrobial activity was unknown in TD powder. So in this research paper we carried out the characterization and evaluated the antimicrobial effect of the TD powder on *Pseudomonas aeruginosa* ATCC 27853.

2. Experimental Methods

2.1. Powder of Titanium Dioxide. The titanium dioxide TiO_2 powder was prepared by the sol-gel technique from a precursor solution containing titanium isopropoxide, ethanol, deionized water, and nitric acid (molar ratio 2 : 72 : 6 : 1 [13]). The preparation of this solution requires an inert atmosphere. The precursor solution, thus prepared, was removed from the inert atmosphere and dried at 80°C until all solvents had evaporated. The powder obtained was annealed at 100°C for 1 hour and 450°C for another hour in an open atmosphere, after which, pure titanium dioxide powder was obtained. The characterization of the TD powders was carried out by XRD patterns and was registered using a Rigaku Miniflex$^+$ Diffractometer (CuKα_1 radiation, 1.54 Å). For the Raman measurements a Dilor Labram II microRaman was employed. The diffuse reflectance of the samples was measured using an Ocean Optic Spectrometer. The SEM and TEM images were obtained by a JEOL JSM-6060LV and JEOL JEM1010 microscopies, respectively.

2.2. Bactericidal Activity. Pseudomonas aeruginosa ATCC 27853 was grown in a 30 mL nutrient broth at 37°C for 16 h. The bacterial suspension was then centrifuged at 3,000 rpm for 10 min. and washed twice with saline solution (NaCl 0.85%). The resulting cell pellet was resuspended in 1 mL of saline solution, and cell density was determined using a Neubauer counting chamber. Prior to testing the antimicrobial properties of TiO_2, the cell count was adjusted to 10^6 cells mL^{-1}. The test itself was performed in glass vessels in which 10^6 cells were mixed with 0.5 and 1 mg (final volume 1 mL). A vessel without TiO_2 was prepared as a control.

The mixed solutions were irradiated with UVA (365 nm) from a black-light bulb (9 W). Exposure times were 30, 60, 90, and 120 min. Following exposure, the solution was sampled to determine the cell viable counts using the most probable number method (MPN). Decimal dilutions of samples were inoculated in quintuplicate in tubes containing nutrient broth and incubated at 37°C for 24 h. Tubes in which the solution had become turbid during incubation were considered positive for bacterial growth. Data from these tubes were used to calculate cell numbers and cell viability (as a percentage of all cells). The Degussa P25 (P25) was used in order to compare the TD synthesized for our experimental method. The characteristics of the P25 are nanopowder with 21 nm particle size (TEM), >99.5%.

3. Results and Discussion

X-ray diffraction (XRD) was performed on the TD powders to determine their phase and crystallinity. Figure 1(a) shows the XRD patterns with peaks at 2θ = 25.32, 37.82, 48.12, 53.94, 55.11, 62.76, 68.8, 70.38, and 75.14°, corresponding to the planes (101), (004), (200), (105), (211), (204), (116), (220), and (215), respectively. These planes closely match

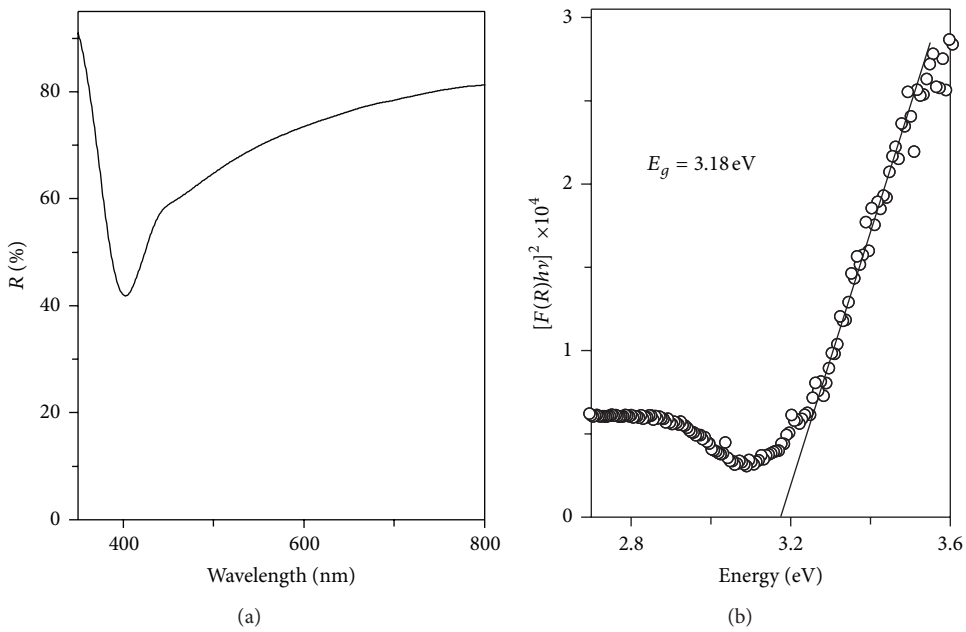

Figure 2: (a) Uv-Vis diffuse reflectance spectra of TiO_2 obtained at 450°C. (b) Band gap of the TiO_2 computed by Kubelka-Munk function, where E_g is the band gap energy, R is the reflectance of the TD, h is Planck's constants, and ν is the frequency of the radiation.

those of PDF number 78-2486, corresponding to the pure tetragonal anatase TD phase. The grain size, calculated from the XRD pattern using the Scherer formula, is 25.27±0.11 nm. The anatase phase in TD is one of the most important metal oxides in terms of potential applications to photonic crystals, sensors, smart surfaces coatings, photovoltaic cells, photocatalysis, and bactericidal agents and as such has been extensively studied [9, 14–17]. The phase of bactericidal TD powder was determined by Raman spectroscopy. The TD displays six Raman active modes of anatase phase, with symmetries of 3 vibrating modes for E_g, and 2 for B_{1g} and A_{1g}, corresponding to 144, 197, 399, 515, 519, and 639 cm^{-1} [18–20]. Figure 1(b) displays the Raman spectra of TD obtained at 450°C in an open atmosphere, in which the vibrating modes occur at 144, 196, 396, 516, and 638 cm^{-1}, consistent with those reported previously for the anatase phase [18–20].

Figure 2 shows the Uv-Vis diffuse reflectance spectra of TD powder annealed in an open atmosphere at 450°C. The maximum of the reflection edge can be estimated as 390 nm. From the plot of the Kubelka-Munk function versus the energy of the incoming radiation and supposing that the anatase phase of TD is an indirect band gap semiconductor, a band gap of 3.18 eV was obtained (Figure 2(b)).

The superficial structure of the TD annealing at 450°C was characterized by scanning electron microscopy (SEM) imaging (Figures 3(a) and 3(b)). The sample contains a range of particle sizes (diameter 30 to 1 micron). The larger particles comprise aggregates of smaller particles. Under transmission electron microscopy (TEM), the nanocrystalline form of the TD powder is revealed (Figures 3(c) to 3(e)). The TEM images display tetragonal nanocrystals with facets (001) and (101) of anatase phase. The space group is I4(1)/amd. Recently, it has been revealed that the reactivity of TD depends not only on its superficial separation properties but also on low recombination of bulk charge carriers and/or the ability of TD to tune its reaction preferences during reaction [21, 22]. Conversely, materials with structures such as (001) facets of anatase exhibited enhanced photocatalytic activity, because they efficiently generate $OH^{\bullet}$ radicals that promote the chemical destruction. In the context of our study, such radicals can penetrate the bacterial cell wall, leading to death of the bacterium.

The predominance of the facet is {001}, {101}, and {010} [23–25]. Figures 3(d) and 3(e) show the different morphologies obtained in the anatase TD nanocrystals. Similar results of the TEM images were found by Hao et al. [22] and Jiao et al. [24]. To control the crystal morphology, the exposed (001) and (101) facets (see insets) were synthesized via a green and short time sol-gel method in the absence of fluorine compounds, which are hazardous to both environment and health. Being the most electronegative element in the periodic table, fluorine is extremely reactive (corrosive and poisonous) and requires care in handling.

Figure 4 displays photocatalytic activity of the TD and commercial P25 (exposed to light at 365 nm) versus time, for concentrations 0.5 mg mL^{-1} (Figure 4(a)) and 1 mg mL^{-1} (Figure 4(b)). The black squares in both plots represent the effect of the light source only (control without TD and P25).

As revealed in Figure 4(a) the viability of cells exposed to 0.5 mg mL^{-1} TD was affected significantly at 60, 90, and 120 minutes after which 99, 99.92, and 100% and for P25 99.38, 99.996, and 100% of the microorganism, respectively, were killed. Similar results were obtained at 1 mg mL^{-1}, where cell viability was reduced by 99.7, 99.99, and 100% after 60, 90, and 120 min exposure, respectively, and the P25 99.997 and 100% for 60 and 90 min. With commercial P25 exposure

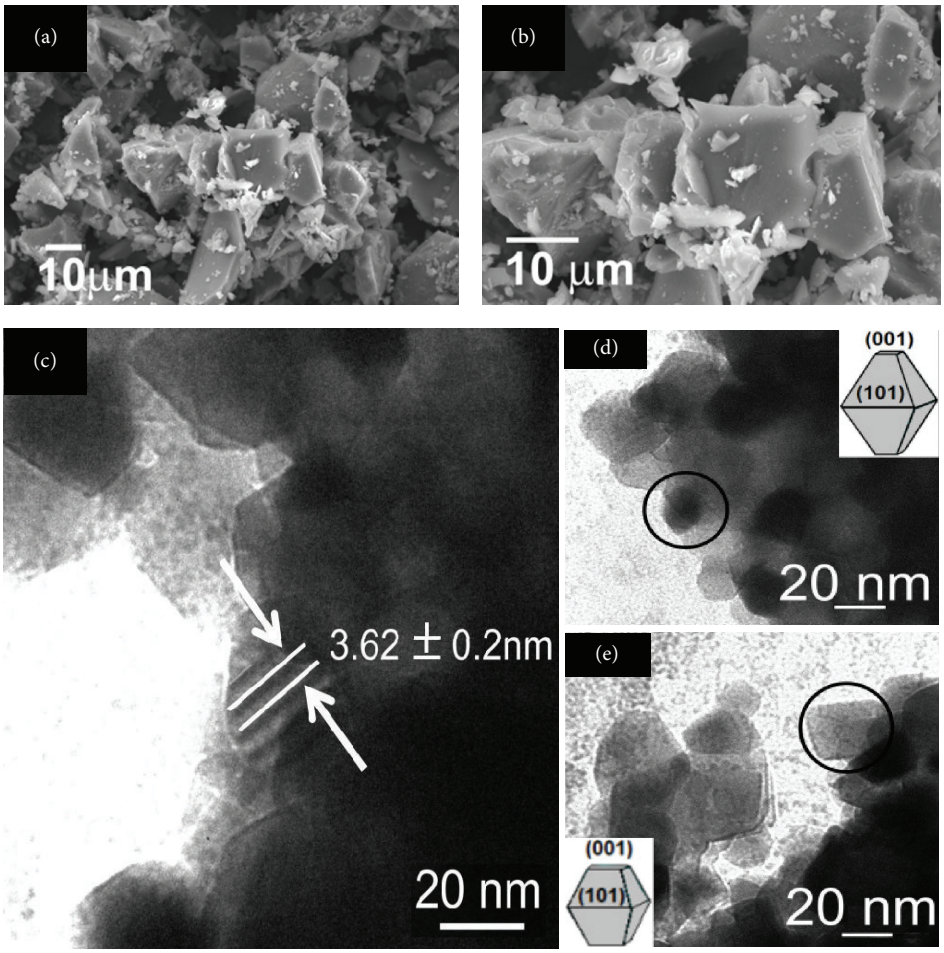

Figure 3: SEM and TEM images of the TiO_2 powder, magnified by (a) 1000x and (b) 2000x. (c) Morphology of the anatase (distance between marks is 3.8 nm). (d) 2D tetragons showing highly absorbing (001) facets and (e) images of TD synthetized in the absence of fluorine compounds. Insets of Figures (d) and (e) are representative sketches of the faceted nanoparticles.

to the same times, we can observe better results with 1% (times ≥ 60 minutes), see Figures 4(a) and 4(b). As a control, a solution with 1.7×10^6 and 9×10^5 cells mL^{-1} for 0.5 and 1 mg mL^{-1}, respectively, was utilized. They were exposed to UV light (365 nm), showing no change in the density population; this was maintained in the order of 10^6, so it discarded any inhibitory effect of UV light. The main difference between our TD and P25 is the crystal size. Currently in our laboratory, is underway additional work in order to find a new synthesis to obtain crystal size of the order of 21 nm, we probably get comparable results (closer) since it is well known that nanoparticles significantly increase the surface area. Ibáñez et al., 2003 [26], using Degussa P25 in a concentration of 0.1 mg mL^{-1} on PA ATCC, starting with a cell density of 10^6 to 10^7, after 40 min it observed that there is a decrease of 3 log. This is very comparable to the present study. Amézaga et al. 2003 [27] conducted a similar test on TiO_2 thin films (anatase phase) prepared on glass slides by the sol-gel process, in which it was found that *Pseudomonas aeruginosa* ATTC 27853 was inhibited by 32 to 72%, over a range of irradiation times (40 to 120 min). Under TEM they observed abnormal cell division after 40 min exposure to TiO_2/UV. At 240 min, wavy structures and bubble-like protuberances appeared, and intracellular material was expelled [22]. Some biochemical mechanisms have been proposed for the powerful bactericidal action of photocatalytic anatase TD powder in the presence of an illumination source. Illumination encourages the generation of highly reactive chemical oxidative species ($OH^{\bullet}$) that promote the peroxidation of phospholipid components in the lipid membrane and the oxidation of intracellular coenzymes, resulting in the inhibition of respiratory activity and subsequent cell death [7, 8, 26]. The intensity of the radiation used during the tests could have an effect on microbial inhibition. Robertson et al., 2005 [28], using Degussa P25 material at a concentration of 1 mg mL^{-1}, obtained a 3 log reduction of PA in a time of 2 h, which is comparable to the test performed in this study; however, it was found that they used a 480 W lamp with a 330 to 450 nm wavelength range, which had a bactericidal activity confirmed in the controls when the test was performed in the absence of Degussa P25, obtained for exposing the cells to UV light; higher percentages of inhibition were reached. In the present research work no inhibition was observed by UV light lamp in the controls.

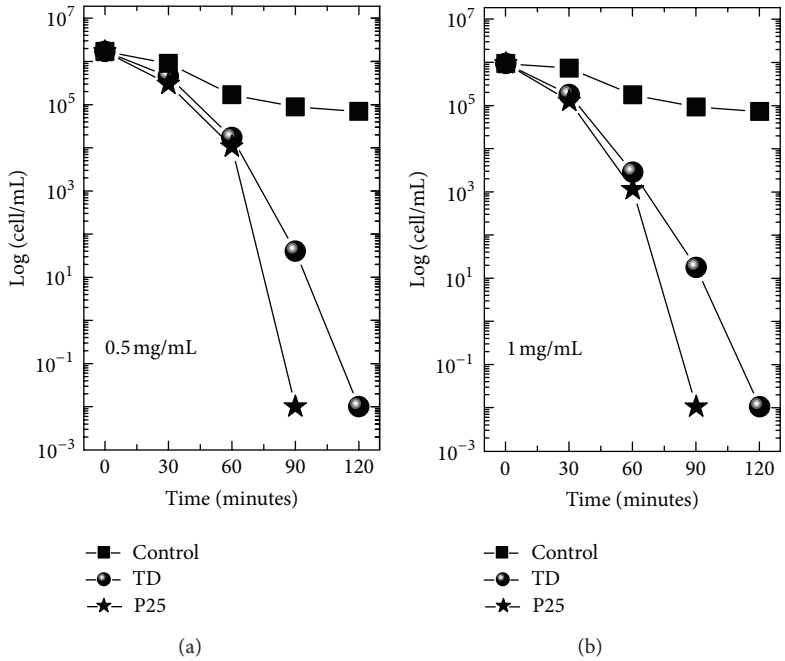

Figure 4: Effect of light and TiO_2 concentration on viability of the *Pseudomonas aeruginosa* ATCC 27853 exposed to (a) 0.5 mg mL^{-1} TD and P25 and (b) 1 mg mL^{-1} TD and P25. In both plots, the control data (light exposure without TD and P25) are displayed as black squares.

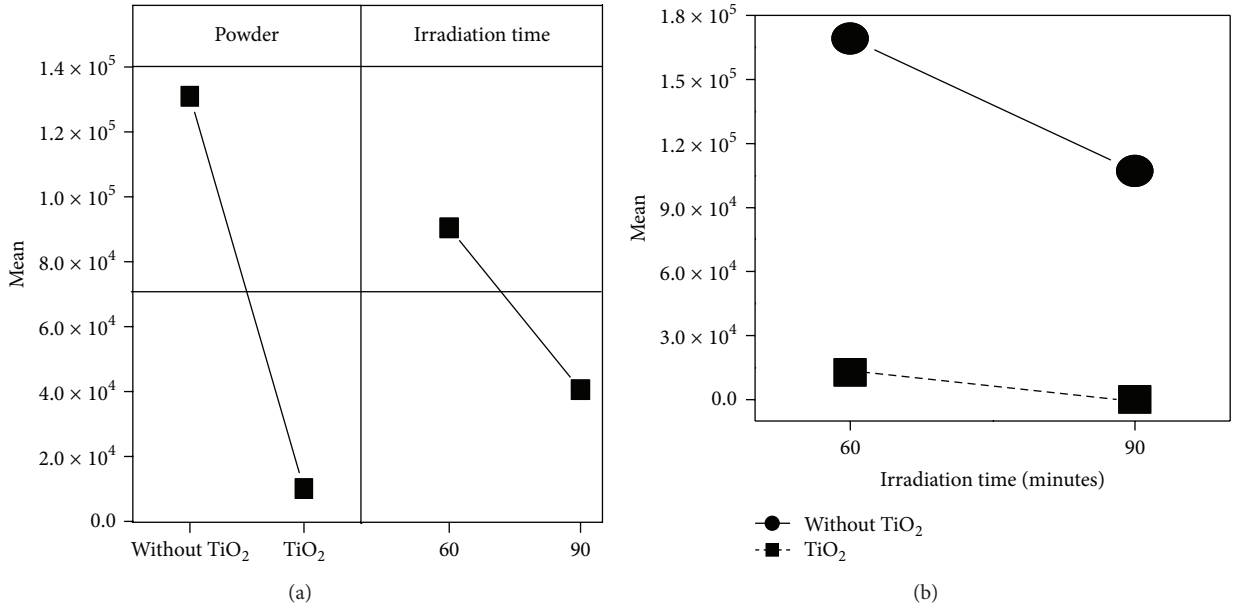

Figure 5: Principal effects and interaction between light and TD on the *Pseudomonas aeruginosa* survival at TD concentration 0.5 mg mL^{-1}.

The grain size could also be related to bactericidal activity due to the increase in the reaction surface. Ubonchonlakate et al. conducted a test in 2012 [29] with porous film with grain size of 15 to 25 nm, and they obtained close to 100% at 60 minutes for a cell density of PA 1×10^3 cells/mL. They also found that the use of porous materials and Ag particles reached almost 100% inhibition for 45 and 10 min, respectively. Similar results were obtained by Hitkova et al. 2012 [6] with thin films of TD, and they found efficiencies of 100% inhibition (10^5 cells/mL) in a 25 min. The particle size employed was 20 nm, the preparation time of the material was 340 h, and the thermal treatment was 500°C. In addition to particle size, the presence of Ag could influence the rapid reduction of cell viability, since it has been reported that this metal has bactericidal activity.

To assess the bactericidal effect of the anatase TD on *Pseudomonas aeruginosa*, the results were input to the Minitab program as an experimental design with two factors and two levels (results were analyzed at 60 and 90 minutes only). The computation was performed using full factorial design

Table 1: Experimental data entered for the experimental design run.

StdOrder	RunOrder	CenterPt	Blocks	Powder	t/min	Y_1 (0.5 mg/mL)	Y_2 (1 mg/mL)
5	1	1	1	WTD	60	1.690×10^5	1.69×10^5
4	2	1	1	TD	90	4.700×10^1	1.30×10^1
1	3	1	1	WTD	60	1.690×10^5	1.69×10^5
7	4	1	1	WTD	90	6.915×10^4	6.91×10^4
2	5	1	1	TD	60	1.275×10^4	2.16×10^3
6	6	1	1	TD	60	2.159×10^4	3.28×10^3
3	7	1	1	WTD	90	1.070×10^5	1.07×10^5
8	8	1	1	TD	90	3.300×10^1	2.10×10^1

Table 2: ANOVA factorial fit: Y_1 (0.5 mg mL^{-1}) versus TD powder and irradiation time.

Estimated effects and coefficients for Y_1 (0.5 mg/mL) (coded units)					
Term	Effect	Coeff	SE Coeff	T	P
Constant		68581	4861	14.11	**0.000**
TD	−119951	−59976	4861	−12.34	**0.000**
Irradiation time	−9037	−24518	4861	−5.04	**0.007**
TD × Irrad time	31906	15953	4861	3.28	**0.030**
S = 13750.1		PRESS = 3025065282			
R^2 = 97.92%		R^2 = 91.68%		**R^2 (adj) = 96.36%**	

with TD and WTD as the two factors and two replicates (see Table 1, where WTD is without TiO_2). To analyze the significance of factors, TD concentrations of 0.5 mg mL^{-1} and 1 mg mL^{-1} were considered separately, for two separate observations of the cell viability (Y_1 and Y_2), representing independent experiments.

The results of the factorial fit for 0.5 mg mL^{-1} powdered TD are presented in Table 2. We observe that the selected factors are significant at the 95% confidence level, because all of the P values are less than 0.05. The presence of TD powder, the exposure time, and the interaction between these two variables are similarly significant. The model further shows that the factorial design can account for 96.36% of the data behavior, confirming the bactericidal activity of the TD. At 1 mg mL^{-1} TD (data not shown) similar P values are obtained and the model fits 96.86% of the data.

Figure 5 presents the principal effects of light irradiation (at 365 nm), TD presence, and irradiation time, as well as their combined effects, on *Pseudomonas aeruginosa*. The presence of TD and exposure to light independently decrease the estimated bacterial population significantly. The interaction between exposure time and the presence of TD powder is also significant, and their combined impact is greater than that of either factor alone.

4. Conclusions

Powdered titanium dioxide in anatase phase with possible facets (001) and (010) was synthesized by the sol-gel technique from a simple, green, and short time route. The bactericidal properties of the synthesized compound were confirmed in aqueous solution. Titanium dioxide combined with illumination (at 365 nm) exerted significant antibactericidal activity. The efficacy of this activity was confirmed by factorial design, which demonstrated that the mortality of *Pseudomonas aeruginosa* ATCC 27853 exposed for 90 minutes to 0.5 and 1 mg mL^{-1} TD was 99.92 and 99.99%, respectively. The results consolidate previous reports of the unique physical and chemical properties of synthesized TiO_2 powder (namely, strong oxidizing and photocatalytic activity) that render it an effective bactericidal material.

Acknowledgment

Authors are grateful for technical assistance provided by IBQ Ma. Lourdes Palma Tirado, Neurobiology Institute of UNAM Juriquilla Qro., on the TEM measurements.

References

[1] R. E. W. Hancock, "Resistance mechanisms in *Pseudomonas aeruginosa* and other nonfermentative gram-negative bacteria," *Clinical Infectious Diseases*, vol. 27, no. 1, pp. S93–S99, 1998.

[2] N. Mesaros, P. Nordmann, P. Plésiat et al., "*Pseudomonas aeruginosa*: resistance and therapeutic options at the turn of the new millennium," *Clinical Microbiology and Infection*, vol. 13, no. 6, pp. 560–578, 2007.

[3] R. Vaisvila, R. D. Morgan, J. Posfai, and E. A. Raleigh, "Discovery and distribution of super-integrons among pseudomonads," *Molecular Microbiology*, vol. 42, no. 3, pp. 587–601, 2001.

[4] A. Fujishima and K. Honda, "Electrochemical photolysis of water at a semiconductor electrode," *Nature*, vol. 238, no. 5358, pp. 37–38, 1972.

[5] N. G. Chorianopoulos, D. S. Tsoukleris, E. Z. Panagou, P. Falaras, and G.-J. E. Nychas, "Use of titanium dioxide (TiO_2) photocatalysts as alternative means for *Listeria monocytogenes*

biofilm disinfection in food processing," *Food Microbiology*, vol. 28, no. 1, pp. 164–170, 2011.

[6] H. Hitkova, A. Stoyanova, N. Ivanova et al., "Study of antibacterial activity of nonhydrolytic synthesized TiO_2 againts *E. Collo*, *P. Aeruginosa* and *S. Aureus*," *Journal of Optoelectronics and Biomedical Materials*, vol. 4, no. 1, pp. 9–17, 2012.

[7] T. Matsunaga, R. Tomoda, T. Nakajima, and H. Wake, "Photoelectrochemical sterilization of microbial cells by semiconductor powders," *FEMS Microbiology Letters*, vol. 29, no. 1-2, pp. 211–214, 1985.

[8] T. Saito, T. Iwase, J. Horie, and T. Morioka, "Mode of photocatalytic bactericidal action of powdered semiconductor TiO_2 on mutans streptococci," *Journal of Photochemistry and Photobiology B*, vol. 14, no. 4, pp. 369–379, 1992.

[9] P. K. J. Robertson, J. M. C. Robertson, and D. W. Bahnemann, "Removal of microorganisms and their chemical metabolites from water using semiconductor photocatalysis," *Journal of Hazardous Materials*, vol. 211-212, pp. 161–171, 2012.

[10] N. Lydakis-Simantiris, D. Riga, E. Katsivela, D. Mantzavinos, and N. P. Xekoukoulotakis, "Disinfection of spring water and secondary treated municipal wastewater by TiO_2 photocatalysis," *Desalination*, vol. 250, no. 1, pp. 351–355, 2010.

[11] S. Malato, P. Fernández-Ibáñez, M. I. Maldonado, J. Blanco, and W. Gernjak, "Decontamination and disinfection of water by solar photocatalysis: recent overview and trends," *Catalysis Today*, vol. 147, no. 1, pp. 1–59, 2009.

[12] S. Khan, I. A. Qazi, Hasmi, M. A. Awan, and N. S. Zaidi, "Synthesis of silver-doped titanium TiO_2 powder-coated surfaces and its ability to inactive *Pseudomona aeruginosa* and bacillus subtilis," *Journal of Nanomaterials*, vol. 2013, Article ID 531010, 8 pages, 2013.

[13] J. G. Mendoza-Alvarez, A. Cruz-Orea, O. Zelaya-Angel et al., "Characterization of TiO_2 thin films for photocatalysis applications using photoacoustic spectroscopy," *Journal De Physique IV France*, vol. 125, pp. 407–409, 2005.

[14] X. Chen and S. S. Mao, "Titanium dioxide nanomaterials: synthesis, properties, modifications and applications," *Chemical Reviews*, vol. 107, no. 7, pp. 2891–2959, 2007.

[15] X. Chen, S. Shen, L. Guo, and S. S. Mao, "Semiconductor-based photocatalytic hydrogen generation," *Chemical Reviews*, vol. 110, no. 11, pp. 6503–6570, 2010.

[16] M. Grätzel, "Materials science: ultrafast colour displays," *Nature*, vol. 414, pp. 575–576, 2001.

[17] H. J. Snaith and L. Schmidt-Mende, "Advances in liquid-electrolyte and solid-state dye-sensitized solar cells," *Advanced Materials*, vol. 19, no. 20, pp. 3187–3200, 2007.

[18] T. Ohsaka, F. Izumi, and Y. Fujiki, "Raman spectrum of anatase, TiO_2," *Journal of Raman Spectroscopy*, vol. 7, no. 6, pp. 321–324, 1978.

[19] G. Liu, H. G. Yang, X. Wang et al., "Enhanced photoactivity of oxygen-deficient anatase TiO_2 sheets with dominant 001 facets," *Journal of Physical Chemistry C*, vol. 113, no. 52, pp. 21784–21788, 2009.

[20] J. Zhang, M. Li, Z. Feng, J. Chen, and C. Li, "UV raman spectroscopic study on TiO_2- I. phase transformation at the surface and in the bulk," *Journal of Physical Chemistry B*, vol. 110, no. 2, pp. 927–935, 2006.

[21] H. G. Yang, C. H. Sun, S. Z. Qiao et al., "Anatase TiO_2 single crystals with a large percentage of reactive facets," *Nature*, vol. 453, no. 7195, pp. 638–641, 2008.

[22] F. Hao, X. Wang, C. Zhou et al., "Efficient ligth harvesting and change collection of dye-sensitized solar cells with (001) faceted single crystalline anatase nanoparticles," *The Journal of Physical Chemistry C*, vol. 116, no. 36, pp. 19164–19172, 2012.

[23] F. Tian, Y. Zhang, J. Zhang, and C. Pan, "Raman spectroscopy: a new approach to measure the percentage of anatase TiO_2 exposed (001) facets," *Journal of Physical Chemistry C*, vol. 116, no. 13, pp. 7515–7519, 2012.

[24] W. Jiao, L. Wang, G. Liu, G. Q. Lu, and H. M. Cheng, "Hollow anatase TiO_2 single crystals and mesocrystals with dominant 101 facets for improved photocatalysis activity and preference," *ACS Catalysis*, vol. 2, pp. 1854–1859, 2012.

[25] Z. Zhao, Z. Li, and Z. Zou, "A Theoretical study of water adsorption and decomposition on the low-index stoichiometric anatase TiO_2 surfaces," *Journal of Physical Chemistry C*, vol. 116, no. 13, pp. 7430–7441, 2012.

[26] J. A. Ibáñez, M. I. Litter, and R. A. Pizarro, "Photocatalytic bactericidal effect of TiO_2 on Enterobacter cloacae. Comparative study with other Gram (−) bacteria," *Journal of Photochemistry and Photobiology A*, vol. 157, no. 1, pp. 81–85, 2003.

[27] M. P. Amézaga, M. R. Silveyra, F. L. Córdoba et al., "TEM evidence ultrastructural alteration on *Pseudomonas aeruginosa* by photocatalytic TiO_2 thin films," *Journal of Photochemistry and Photobiology*, vol. 70, pp. 45–50, 2003.

[28] J. M. C. Robertson, P. K. J. Robertson, and L. A. Lawton, "A comparison of the effectiveness of TiO_2 photocatalysis and UVA photolysis for the destruction of three pathogenic microorganisms," *Journal of Photochemistry and Photobiology A*, vol. 175, no. 1, pp. 51–56, 2005.

[29] K. Ubonchonlakate, L. Sikong, and F. Saito, "Photocatlytic disinfection of *P. aeruginosa* bacterial Ag-doped TiO_2 film," *Procedia Engineering*, vol. 32, pp. 656–662, 2012.

Hindawi Publishing Corporation
International Journal of Photoenergy
Volume 2013, Article ID 685038, 9 pages
http://dx.doi.org/10.1155/2013/685038

Research Article

The Multiple Effects of Precursors on the Properties of Polymeric Carbon Nitride

Wendong Zhang,[1] Qin Zhang,[1] Fan Dong,[2] and Zaiwang Zhao[2]

[1] *College of Urban Construction and Environmental Engineering, Chongqing University, Chongqing 400045, China*
[2] *Chongqing Key Laboratory of Catalysis and Functional Organic Molecules, College of Environmental and Biological Engineering, Chongqing Technology and Business University, Chongqing 400067, China*

Correspondence should be addressed to Fan Dong; dfctbu@126.com

Received 21 May 2013; Accepted 18 July 2013

Academic Editor: Pengyi Zhang

Polymeric graphitic carbon nitride (g-C_3N_4) materials were prepared by direct pyrolysis of thiourea, dicyandiamide, melamine, and urea under the same conditions, respectively. In order to investigate the effects of precursors on the intrinsic physicochemical properties of g-C_3N_4, a variety of characterization tools were employed to analyze the samples. The photocatalytic activity of the samples was evaluated by the removal of NO in gas phase under visible light irradiation. The results showed that the as-prepared CN-T (from thiourea), CN-D (from dicyandiamide), CN-M (from melamine), and CN-U (from urea) exhibited significantly different morphologies and microstructures. The band gaps of CN-T, CN-D, CN-M, and CN-U were 2.51, 2.58, 2.56, and 2.88 eV, respectively. Both thermal stability and yield are in the following order: CN-M > CN-D > CN-T > CN-U. The photoactivity of CN-U (31.9%) is higher than that of CN-T (29.6%), CN-D (22.2%), and CN-M (26.8%). Considering the cost, toxicity, and yield of the precursors and the properties of g-C_3N_4, the best precursor for preparation of g-C_3N_4 was melamine. The present work could provide new insights into the selection of suitable precursor for g-C_3N_4 synthesis and in-depth understanding of the microstructure-dependent photocatalytic activity of g-C_3N_4.

1. Introduction

Visible-light-active photocatalysts are attracting increasing interests for their potential application in the areas of environmental protection, material science, and solar energy conversion by directly utilizing nature sunlight and artificial indoor illumination [1–3]. During the past few decades, many efforts have been devoted to develop novel and efficient visible light photocatalytic systems, including inorganic photocataylsts (e.g., Fe_2O_3, $(BiO)_2CO_3$, Cu_2SnS_3, $SrTiO_3$, and WO_3/BiOCl) [4–7], organic photocataylsts (e.g., graphitic carbon nitride, g-C_3N_4), and elemental photocataylsts (e.g., Si, P, S, and Se) [8–10].

In particular, g-C_3N_4 material as a novel mental-free organic photocatalyst has triggered great attention in the fundamental and applied scientific researches due to its suitable electronic band structure, nontoxic nature, biocompatibility, high thermal and chemical stability, easily available at low cost, and amenability to chemical modification [11–16]. Properties mentioned previously make it a promising organic photocatalyst for solar energy converting, organic photosynthesis, drug delivery, and environment remediation under visible light irradiation [17–19].

g-C_3N_4 can be prepared by the direct pyrolysis of various organic precursors. Dong et al. prepared g-C_3N_4 from thiourea and urea at 550°C for 2 h [20, 21], respectively. Yan et al. obtained g-C_3N_4 from melamine at 550°C for 4 h [22]. Xu et al. prepared g-C_3N_4 by directly heating dicyandiamide first at 350°C for 2 h and then 550°C for another 2 h [23], respectively. The different pyrolysis conditions for g-C_3N_4 synthesis made the comparison of the precursors difficult. Until now, little information is known about the effects of precursors on intrinsic physicochemical properties of g-C_3N_4 under the same pyrolysis conditions, including morphology, band gap,

Table 1: The cost, acute toxicity, and melting point of thiourea, dicyandiamide, melamine, and urea [16].

Precursors	Cost ($/t)	Acute toxicity LD_{50} (oral, rat)	Melting point (°C)
Thiourea	3906	125 mg/kg	182
Dicyandiamide	1538	4000 mg/kg	209
Melamine	2025	3248 mg/kg	345
Urea	450	8500 mg/kg	133

thermal stability, surface area, pore volume, and yield and visible light photocatalytic activity. It is thus highly desirable to solve this issue in order to screen the most suitable precursors for synthesis of g-C_3N_4.

In this paper, g-C_3N_4 materials were prepared by directly treating thiourea, dicyandiamide, melamine, and urea under the same condition (550°C for 3 h in air), respectively. The precursors are easily available in the chemical industry at low cost (see Table 1). Various characterization tools were utilized to analyze the effects of precursors on the intrinsic physicochemical properties and photocatalytic activity of g-C_3N_4. The results showed that the precursors had significant effect on the properties of g-C_3N_4. Considering the cost, toxicity, and yield of the precursors and the properties of g-C_3N_4, the best precursor was confirmed.

2. Experimental

2.1. Synthesis of g-C_3N_4. In a typical synthesis, 12 g of thiourea was put into a semiclosed alumina crucible with a cover and then heated to 550°C in a muffle furnace for 3 h at a heating rate of 10°C min^{-1}. Following the same procedure, g-C_3N_4 samples were prepared by directly treating dicyandiamide, melamine, and urea, respectively. After the reaction, the alumina crucible was cooled to room temperature. The resultant g-C_3N_4 were collected and ground into powder, respectively. The different g-C_3N_4 prepared from thiourea, dicyandiamide, melamine, and urea were labeled as CN-T, CN-D, CN-M, and CN-U, respectively.

2.2. Characterization. The crystal phases of the samples were analyzed by X-ray diffraction with Cu Kα radiation (XRD: model D/max RA, Rigaku Co., Japan). FT-IR spectra were recorded on a Nicolet Nexus spectrometer on samples embedded in KBr pellets. The morphology and structure of the samples were further examined by transmission electron microscopy (TEM: JEM-2010, Japan). The UV-vis diffuse reflection spectra were obtained for the dry-pressed disk samples using a Scan UV-vis spectrophotometer (UV-vis DRS: UV-2450, Shimadzu, Japan) equipped with an integrating sphere assembly, using $BaSO_4$ as the reflectance sample. Nitrogen adsorption-desorption was conducted on a nitrogen adsorption apparatus (ASAP 2020, USA). The thermal stability was detected by using thermogravimetry analysis (TG-DSC, Netsch STA 449F3) under N_2 gas atmosphere. All the samples were degassed at 150°C prior to measurements.

2.3. Visible Light Photocatalytic Performance. The photocatalytic activity was investigated by removal of NO at ppb levels in a continuous flow reactor at ambient temperature. The volume of the rectangular reactor, which was made of polymethyl methacrylate plastics and covered with quartz-glass, was 4.5 L (30 cm × 15 cm × 10 cm). A 100 W commercial tungsten halogen lamp (General Electric) was vertically placed outside and above the reactor. Four minifans were used to cool the flow system. Adequate distance was also kept from the lamp to the reactor for the same purpose to keep the temperature at a constant level. For the visible light photocatalytic activity test experiment, a UV cut-off filter (420 nm) was adopted to remove UV light in the light beam.

For each photocatalytic activity test, two sample dishes (with a diameter of 12.0 cm) containing photocatalyst powder were placed in the center of the reactor. The weight of the photocatalyst used for each dish was kept at 0.1 g. g-C_3N_4 sample was added into 30 mL of H_2O and sonicated for 10 min, and then photocatalyst samples were prepared by coating aqueous suspension of the samples onto the glass dishes. The coated dish was pretreated at 60°C to remove water in the suspension and then cooled to room temperature before photocatalytic testing.

The NO gas was acquired from a compressed gas cylinder at a concentration of 100 ppm of NO (N_2 balance, BOC gas) with the National Institute of Standards and Technology (NIST) standard. The initial concentration of NO was diluted to about 600 ppb by the air stream supplied by a zero air generator (Thermo Environmental Inc., model 111). The relative humidity at indoor environmental condition is 40%–80%. The desired relative humidity in the present system is controlled at 50% in the gas flow which could simulate the indoor environmental conditions. The desired relative humidity (RH) level of the NO flow was controlled at 50% by passing the zero air streams through a humidification chamber. The gas streams were premixed completely by a gas blender, and the flow rate was controlled at 2.4 L min^{-1} by a mass flow controller. After the adsorption-desorption equilibrium was achieved, the lamp was turned on. The concentration of NO was continuously measured by a chemiluminescence NO analyzer (Thermo Environmental Instruments Inc., model 42c), which monitors NO, NO_2, and NOx (NOx represents NO + NO_2) with a sampling rate of 0.7 L min^{-1}. The removal ratio (η) of NO was calculated as $\eta\,(\%) = (1 - C/C_0) \times 100\%$, where C and C_0 are concentrations of NO in the outlet steam and the feeding stream, respectively. The kinetics of photocatalytic NO removal reaction is a pseudofirst order reaction at low NO concentration as $\ln(C_0/C) = kt$, where k is the apparent rate constant.

3. Result and Discussion

The XRD patterns (Figure 1(a)) of the samples prepared from thiourea, dicyandiamide, melamine, and urea can be indexed to g-C_3N_4 [24–26]. The strongest interplanar stacking peaks of the conjugated aromatic systems at around 27.6° are indexed to graphitic materials as the (002) peak. The small angle peaks at around 13.0° can be indexed to (100) peak

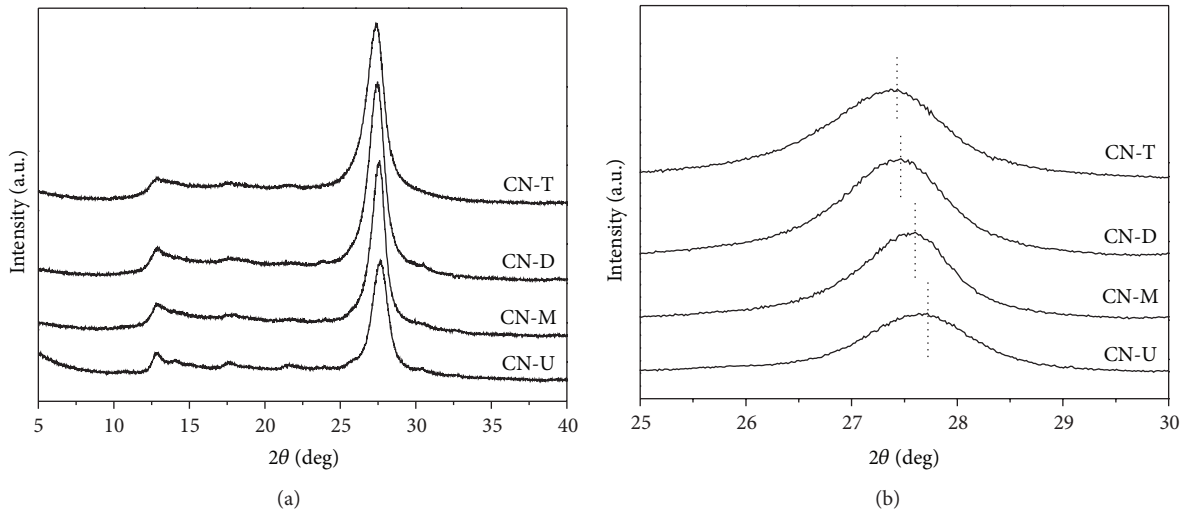

Figure 1: XRD patterns of the CN-T, CN-D, CN-M, and CN-U (a) and enlarged view of the (002) peak (b).

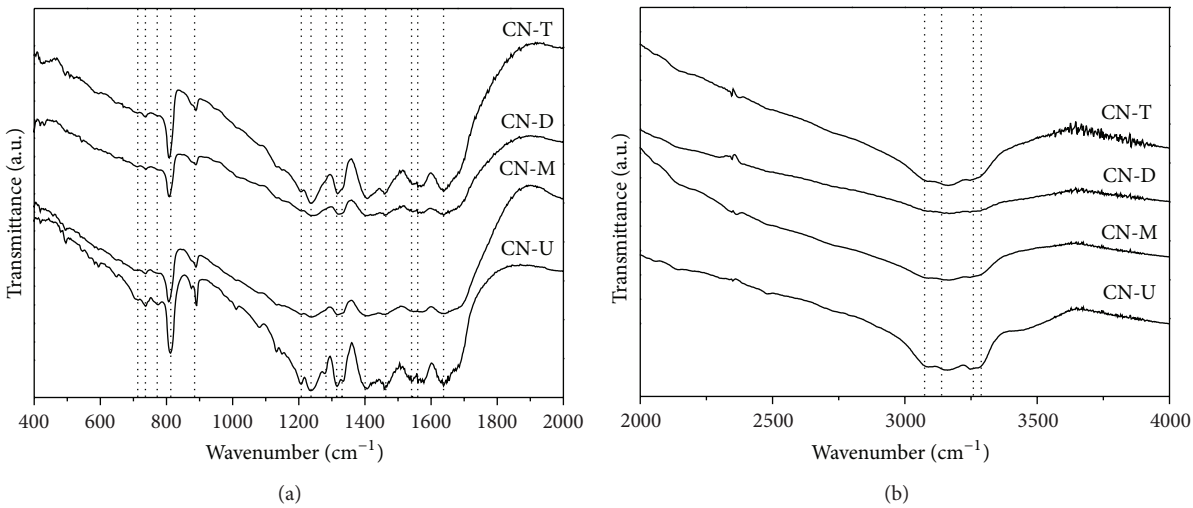

Figure 2: FT-IR spectra for CN-T, CN-D, CN-M, and CN-U.

of graphitic materials, corresponding to the in-plane tri-s-triazine units which formed one-dimensional (1D) melon strands. Further observation implies (Figure 1(b)) that the typical (002) peak is 27.43° for CN-T, 27.47° for CN-D, 27.60° for CN-M, and 27.72° for CN-U, respectively, indicating that the interplanar distance tends to decrease and g-C_3N_4 structure becomes more compact. The dense structure can be ascribed to the localization of the electrons and stronger binding between the layers [27, 28]. The dominant (002) diffraction peaks shifted toward higher diffraction angles for CN-U compared with CN-T, indicating that O-containing precursors (urea) could improve the polycondensation of g-C_3N_4. In addition, the intensity and breadth of the XRD patterns (Figure 1) are different, due to the presence of different nanostructures and morphologies of the as-prepared g-C_3N_4 [29].

The chemical structures of dicyandiamide and melamine containa C=N bond which plays a key role in the formation of g-C_3N_4. However, both the S-containing thiourea and O-containing urea do not containa C=N bond. The fact indicates that the formation mechanisms and condensation degrees of thiourea and urea are different from that of dicyandiamide and melamine [20–22, 30].

Figure 2(a) shows that the weak absorption at the 700–800 cm^{-1} region is assigned to the bending vibration mode of CN heterocycles and the characteristic out of plane bending vibration mode of the triazine units at 810 cm^{-1} for all the samples [31]. All the samples reveal several bands in the 1200–1650 cm^{-1} region, which corresponds to the typical stretching vibration modes of the heptazine heterocyclic ring (C_6N_7) units [32].

The stretching vibration modes of N–H and O–H at 3000–3500 cm^{-1} are also observed (Figure 2(b)), indicating the existence of uncondensed amino groups and absorbed H_2O molecules in all the samples [33]. It can be seen that the peak intensity of CN-U at 400–4000 cm^{-1} is stronger than that of CN-T, CN-D, and CN-M, indicating that O-containing

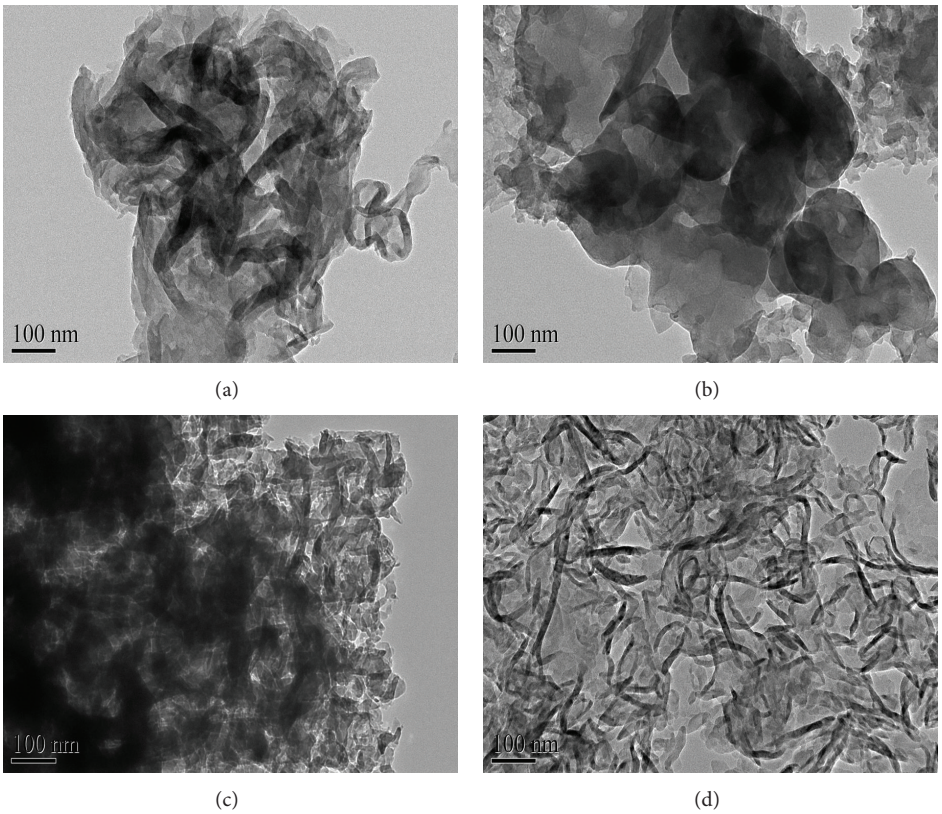

(a) (b) (c) (d)

Figure 3: TEM images of CN-T (a), CN-D (b), CN-M (c), and CN-U (d).

precursors could improve the polycondensation of g-C_3N_4 [34].

The morphologies and microstructures of CN-T, CN-D, CN-M, and CN-U were observed by TEM. As shown in Figure 3, all the samples consist of large amounts of packing layers with different sizes of nanosheets and nanoparticles, which exhibit obviously wrinkles and irregular shapes. Figure 3(a) shows that CN-T is composed of smooth and flat layers. Numerous large buckle nanosheets with aggregated structures which formed smooth layers in the CN-D sample can be seen in Figure 3(b). By observing carefully for CN-M (Figure 3(c)), the layers consist of dense and thick nanosheets with irregular shape. Figure 3(d) shows that CN-U is composed of smooth and thin layers with typical porous morphology and loose structure. The result clearly shows that CN-U prepared from urea favors the formation of typical porous structure. The fact indicates that the morphologies and microstructures of the resultant g-C_3N_4 strongly depend on the different heteroatom-containing precursors.

As shown in Figure 4(a), all the samples exhibit excellent visible light absorption, and the absorption edges of the samples shift apparently to longer wavelengths from CN-U to CN-T. The band energies (E_g) which can be estimated from the intercept of the tangents to the plots of $(Ah\nu)^{1/2}$ versus photo energy (Figure 4(b)) are 2.51, 2.58, 2.56, and 2.88 eV for CN-T, CN-D, CN-M, and CN-U, respectively. The fact indicates that the precursors could affect the band gap and absorption edge of g-C_3N_4, which may be caused by the different local structures, defects, and degrees of condensation during the pyrolysis [8, 11].

Figure 5 shows the nitrogen adsorption-desorption isotherms and corresponding curves of the pore size distribution for CN-T, CN-D, CN-M, and CN-U. The isotherms of CN-T (Figure 5(a)), CN-D (Figure 5(c)), and CN-M (Figure 5(e)) can be classified to type IV, which indicates the presence of mesopores. The CN-U exhibits type III behavior (Figure 5(g)), which can be ascribed to the weak adsorbent-adsorbent interaction [35]. The specific surface areas and pore volumes of CN-T (23 m^2/g and 0.14 cm^3/g) and CN-U (153 m^2/g and 0.40 cm^3/g) are significantly higher than that of CN-D (18 m^2/g and 0.09 cm^3/g) and CN-M (14 m^2/g and 0.06 cm^3/g). The data illustrates that the heteroatoms of sulfur and oxygen play a key role in increasing the specific surface area and enlarging the pore volume during the condensation. The formation of H_2S and CO_2, release of NH_3, and generation of additional H_2O vapor during the pyrolysis of thiourea and urea favor the expansion of the packing layers and porous structure [32, 35]. Further observation implies that all the samples have micropores and mesopores. The interconnected porous network could mainly contribute to the formation of micropores and mesopores of CN-T (Figure 5(b)) and CN-U (Figure 5(h)), the aggregation of nanosheets and nanoparticles could result in the formation of the micropores and mesopores of CN-D (Figure 5(d)) and CN-M (Figure 5(f)) [19, 20].

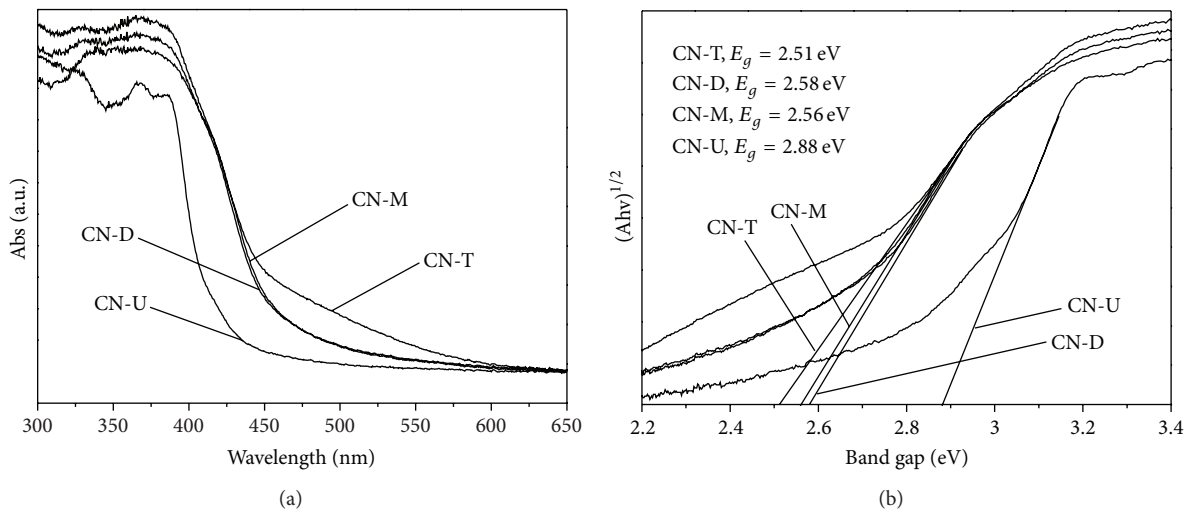

Figure 4: UV-vis DRS (a) and plots of $(Ah\nu)^{1/2}$ versus photo energy (b) of CN-T, CN-D, CN-M, and CN-U.

Table 2: The S_{BET}, pore volume, band gap, removal ration, initial rate constant k, yield, and thermal stability of CN-T, CN-D, CN-M, and CN-U.

Samples	S_{BET} (m^2/g)	Pore volume (cm^3/g)	Band gap (eV)	Removal ratio η (%)	k (min^{-1})	Yield (g)	Thermal stability (°C)
CN-T	23	0.14	2.51	29.6	0.310	1.46	<550°C
CN-D	18	0.09	2.58	22.2	0.079	3.73	<563°C
CN-M	14	0.06	2.56	26.8	0.298	5.32	<575°C
CN-U	153	0.40	2.88	31.9	0.384	0.12	<530°C

In order to understand the thermal stability of CN-T, CN-D, CN-M, and CN-U, the thermal analysis was carried out by using TG-DSC and the heating rate of 20°C/min under N_2 gas atmosphere. It can be found that the CN-T (Figure 6(a)), CN-D (Figure 6(b)), and CN-M (Figure 6(c)) became unstable when the heating temperature was above 550, 563, and 575°C, respectively. The exothermic peaks can be seen at 672.4 for CN-T, 683.1 for CN-D, and 649.5°C for CN-U, which should be attributed to the decomposition for the samples. Figure 6(d) shows that no significant weight loss of CN-U is recorded when the temperature is below 530°C, and complete decomposition of CN-U occurred at 750°C. Further observation reveals that there are two strong exothermic peaks at 550.1 and 682.4°C of CN-U, which can be ascribed to the sublimation and thermal decomposition [36], respectively. It should be noted that the thermal stability of the samples is different, due to the different degrees of condensation and the packing between the layers during the polymerization [37, 38].

The photocatalytic performance of the as-prepared samples was further evaluated by removal of NO in gas phase in order to demonstrate their potential ability for indoor air purification under visible light irradiation at room temperature (Figure 7). There are four reactions of the photocatalytic materials, which involved that NO reacted with the photo-generated reactive radicals and produced HNO_2 and HNO_3 displayed in the following [39]:

$$\begin{gathered} NO + 2^{\bullet}OH \longrightarrow NO_2 + H_2O \\ NO_2 + {}^{\bullet}OH \longrightarrow NO_3^- + H^+ \\ NO + NO_2 + H_2O \longrightarrow 2HNO_2 \\ NO + {}^{\bullet}O_2^- \longrightarrow NO_3^- \end{gathered} \tag{1}$$

Figure 7(a) shows the variation of NO concentration (C/C_0%) with irradiation time over the samples under visible light irradiation ($\lambda > 420$ nm). Here, C_0 is the initial concentration of NO, and C is the concentration of NO after photocatalytic reaction for time t.

As shown in Figure 7(a), the concentration of NO for all samples decreased rapidly due to the photocatalytic degradation in 5 min. However, the reaction intermediates, and final products generated during irradiation may occupy the active sites of photocatalyst, which result in the decrease in activity. After 40 min irradiation, the removal rates and apparent rate constants of CN-T (29.2% and 0.310 min^{-1}) and CN-U (32.2% and 0.384 min^{-1}) are higher than that of CN-D (22.2% and 0.079 min^{-1}) and CN-M (26.2% and

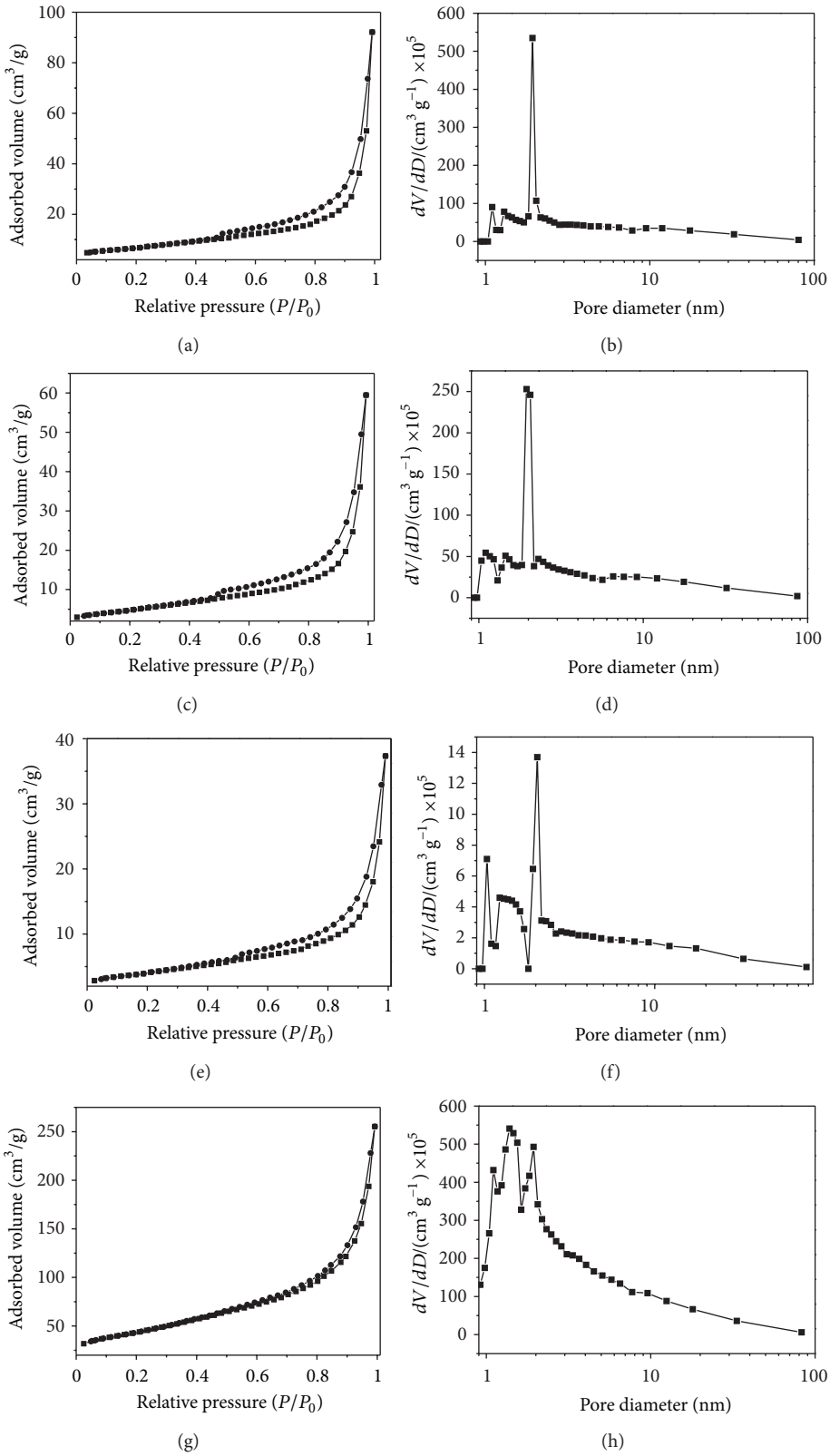

Figure 5: N_2 adsorption-desorption isotherms of CN-T (a), CN-D (c), CN-M (e), and CN-U (g) and the corresponding pore size distribution curves of CN-T (b), CN-D (d), CN-M (f), and CN-U (h).

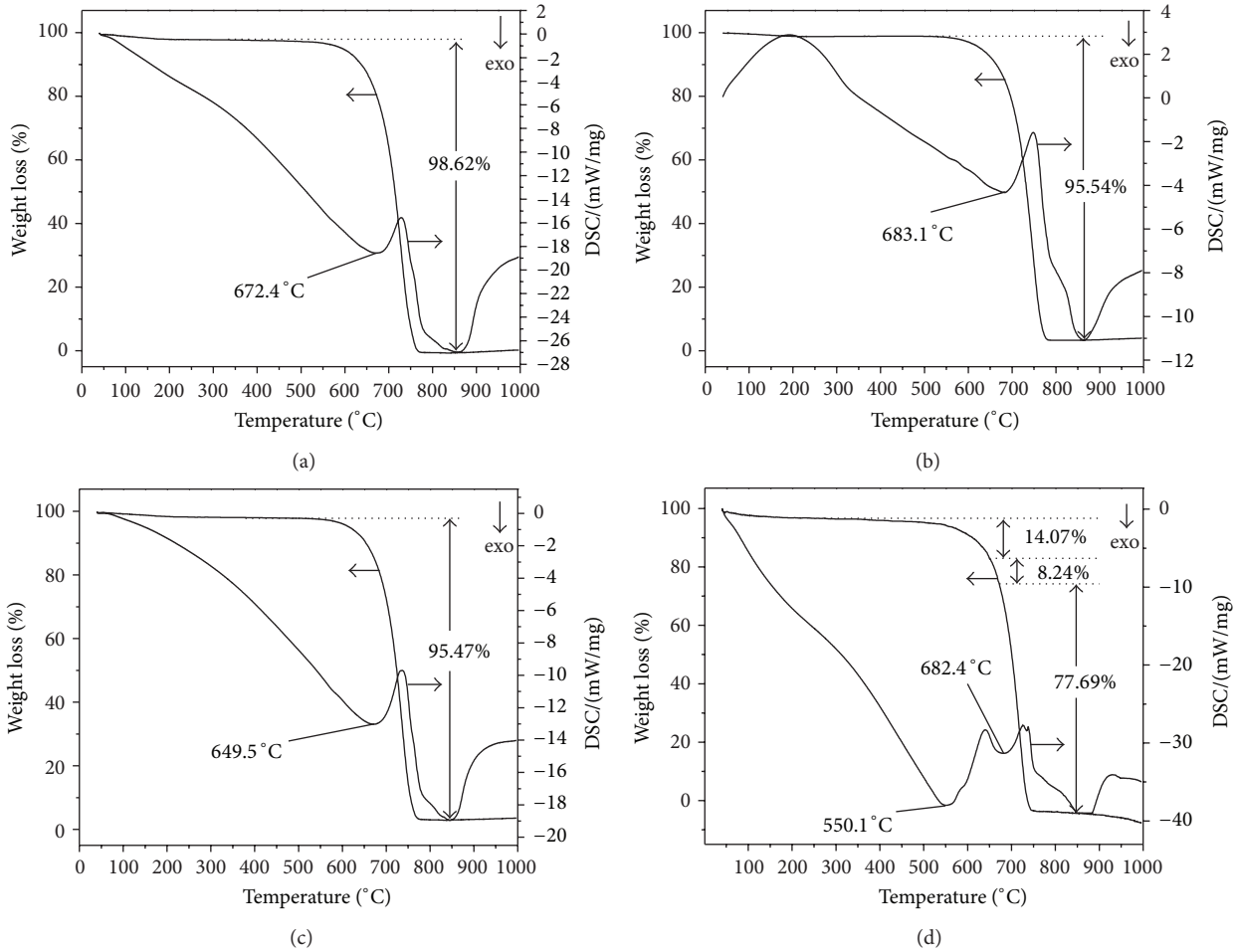

Figure 6: TG-DSC thermalgrams for CN-T (a), CN-D (b), CN-M (c), and CN-U (d).

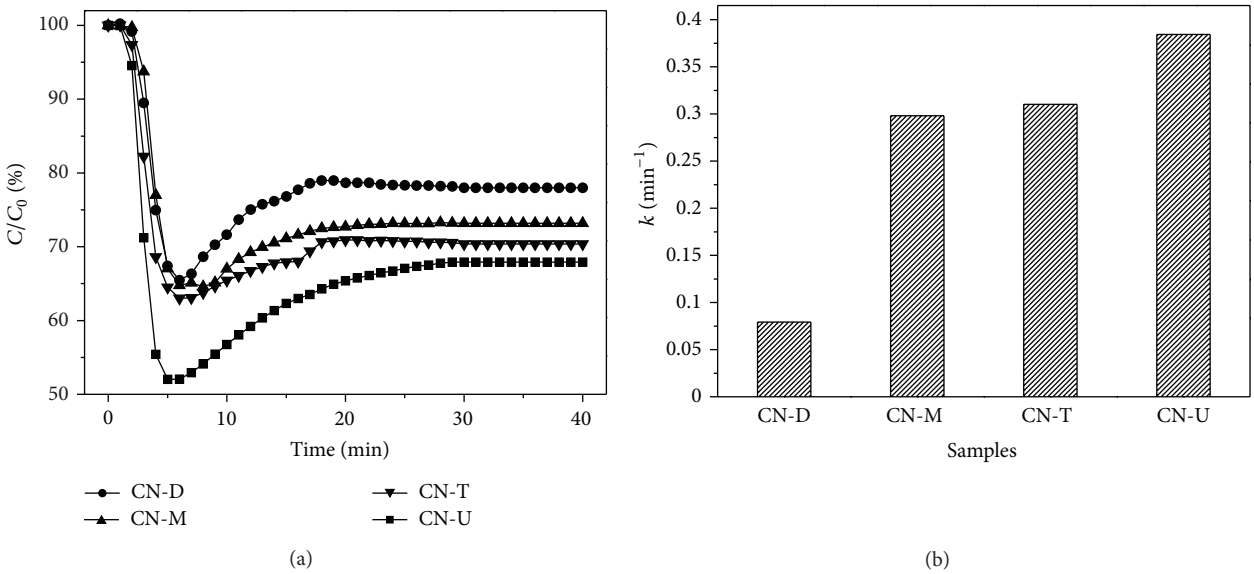

Figure 7: Photocatalytic activity (a) and initial rate constants (b) of CN-T, CN-D, CN-M, and CN-U for removal of NO under visible light irradiation ($\lambda > 420$ nm) at room temperature.

0.298 min^{-1}), respectively. Generally, CN-T, CN-D, and CN-M with narrower band gaps than CN-U (see Table 2) are favorable for photocatalytic reaction, due to the enhanced visible light absorption with more available photogenerated electron hole. In fact, the high surface areas and large pore volumes can enhance the adsorption of reactants and diffusion of the reaction products and provide more efficient active sites for photochemical reaction [40, 41]. Thus, the surface area and pore volume of CN-U play a more significant role in NO degradation than the electronic properties. However, it is interesting to find that the CN-M exhibits higher photocatalytic activity than that of CN-D. Figure 4(b) shows that the band energy of CN-M is narrower than that of CN-D, which can enhance visible light absorption in CN-M sample. On the other hand, the enhanced condensation of CN-M can effectively reduce the number of structure defects (e.g., uncondensation groups of $-NH_2$ and –NH) which always capture the electrons or holes to prevent the following photoredox reaction [8]. The fact indicates that the photocatalytic efficiency strongly depends on the surface area, pore volume, band energy, and the degree of condensation of g-C_3N_4.

To ensure the large-scale application, four evaluation indicators were proposed for screening the most suitable precursors, including the cost, toxicity, and yield of the precursors and the removal rate for the contaminant. As shown in Tables 1 and 2, melamine exhibits the middle cost, toxicity, and removal ratio for the degradation of NO. However, it possesses the highest yield among the four precursors. Based on the advantages analysis previously mentioned, the best precursor is melamine.

4. Conclusions

In summary, g-C_3N_4 samples were prepared by a simple pyrolysis of thiourea, dicyandiamide, melamine, and urea under the same procedures, respectively. The systematic research results confirmed that the precursors have significant effect on the morphology, band gap, surface area, pore volume, thermal stability, and visible light photocatalytic activity of g-C_3N_4. Considering the cost, toxicity, and yield of the precursors and the properties of g-C_3N_4, the best precursor for preparation of g-C_3N_4 is melamine. The present work could provide new insights into appropriate selection of precursors for g-C_3N_4 synthesis as visible light photocatalyst in environmental protection.

Conflict of Interests

The authors declare that they have no conflict of interests.

Acknowledgments

This research is financially supported by the National Natural Science Foundation of China (51108487), the National High Technology Research and Development Program (863 Program) of China (2010AA064905), the Natural Science Foundation Project of CQ CSTC (cstc2012jjA20014), and the Critical Patented Projects in the Control and Management of the National Polluted Water Bodies (2012ZX07102-001-003).

References

[1] J. S. Zhang, J. H. Sun, K. Maeda et al., "Sulfur-mediated synthesis of carbon nitride: band-gap engineering and improved functions for photocatalysis," *Energy & Environmental Science*, vol. 4, no. 3, pp. 675–678, 2011.

[2] H. Tong, S. X. Ouyang, Y. P. Bi, N. T. Umezawa, M. Oshikiri, and J. H. Ye, "Nano-photocatalytic materials: possibilities and challenges," *Advanced Materials*, vol. 24, no. 2, pp. 229–251, 2012.

[3] J. G. Yu, M. Jaroniec, and G. X. Lu, "TiO_2 photocatalytic materials," *International Journal of Photoenergy*, vol. 2012, Article ID 206183, 5 pages, 2012.

[4] N. Todorova, T. Giannakopoulou, G. Romanos, T. Vaimakis, J. G. Yu, and C. Trapalis, "Preparation of fluorine-doped TiO_2 photocatalysts with controlled crystalline structure," *International Journal of Photoenergy*, vol. 2008, Article ID 534038, 9 pages, 2008.

[5] F. Dong, W. K. Ho, S. C. Lee et al., "Template-free fabrication and growth mechanism of uniform $(BiO)_2CO_3$ hierarchical hollow microspheres with outstanding photocatalytic activities under both UV and visible light irradiation," *Journal of Materials Chemistry*, vol. 21, no. 33, pp. 12428–12436, 2011.

[6] J. G. Yu, P. Y. Zhang, H. G. Yu, and C. Trapalis, "Environmental photocatalysis," *International Journal of Photoenergy*, vol. 2012, Article ID 594214, 4 pages, 2012.

[7] Q. Y. Chen and D. Ma, "Preparation of nanostructured Cu_2SnS_3 photocatalysts by solvothermal method," *International Journal of Photoenergy*, vol. 2013, Article ID 593420, 5 pages, 2013.

[8] X. C. Wang, S. Blechert, and M. Antonietti, "Polymeric graphitic carbon nitride for heterogeneous photocatalysis," *ACS Catalysis*, vol. 2, no. 8, pp. 1596–1606, 2012.

[9] Y. J. Cui, Z. X. Ding, X. Z. Fu, and X. C. Wang, "Construction of conjugated carbon nitride nanoarchitectures in solution at low temperatures for photoredox catalysis," *Angewandte Chemie*, vol. 51, no. 47, pp. 11814–11818, 2012.

[10] G. Liu, P. Niu, and H. M. Cheng, "Visible-light-active elemental photocatalysts," *ChemPhysChem*, vol. 14, no. 5, pp. 885–892, 2013.

[11] Y. Wang, X. C. Wang, and M. Antonietti, "Polymeric graphitic carbon nitride as a heterogeneous organocatalyst: from photochemistry to multipurpose catalysis to sustainable chemistry," *Angewandte Chemie*, vol. 51, no. 1, pp. 68–89, 2012.

[12] Z. Z. Lin and X. C. Wang, "Nanostructure engineering and doping of conjugated carbon nitride semiconductors for hydrogen photosynthesis," *Angewandte Chemie*, vol. 52, no. 6, pp. 1735–1738, 2013.

[13] G. Xin and Y. L. Meng, "Pyrolysis synthesized g-C_3N_4 for photocatalytic degradation of methylene blue," *Journal of Chemistry*, vol. 2013, Article ID 187912, 5 pages, 2013.

[14] J. D. Hong, X. Y. Xia, Y. S. Wang, and R. Xu, "Mesoporous carbon nitride with *in situ* sulfur doping for enhanced photocatalytic hydrogen evolution from water under visible light," *Journal of Materials Chemistry*, vol. 22, no. 30, pp. 15006–15012, 2012.

[15] G. P. Mane, D. S. Dhawale, C. Anand et al., "Selective sensing performance of mesoporous carbon nitride with a highly ordered porous structure prepared from 3-amino-1,2,4-triazine," *Journal of Materials Chemistry A*, vol. 1, no. 8, pp. 2913–2920, 2013.

[16] http://en.wikipedia.org/wiki/MainPage.

[17] X. H. Li, X. C. Wang, and M. Antonietti, "Mesoporous g-C_3N_4 nanorods as multifunctional supports of ultrafine metal nanoparticles: hydrogen generation from water and reduction of nitrophenol with tandem catalysis in one step," *Chemical Science*, vol. 3, no. 6, pp. 2170–2174, 2012.

[18] B. Kiskan, J. S. Zhang, X. C. Wang, M. Antonietti, and Y. Yagci, "Mesoporous graphitic carbon nitride as a heterogeneous visible light photoinitiator for radical polymerization," *ACS Macro Letters*, vol. 1, no. 5, pp. 546–549, 2012.

[19] M. Shalom, S. Inal, C. Fettkenhauer, D. Neher, and M. Antonietti, "Improving carbon nitride photocatalysis by supramolecular preorganization of monomers," *Journal of the American Chemical Society*, vol. 135, no. 19, pp. 7118–7121, 2013.

[20] F. Dong, L. W. Wu, Y. J. Sun, M. Fu, Z. B. Wu, and S. C. Lee, "Efficient synthesis of polymeric g-C_3N_4 layered materials as novel efficient visible light driven photocatalysts," *Journal of Materials Chemistry*, vol. 21, no. 39, pp. 15171–15174, 2011.

[21] F. Dong, Y. J. Sun, L. W. Wu, M. Fu, and Z. B. Wu, "Facile transformation of low cost thiourea into nitrogen-rich graphitic carbon nitride nanocatalyst with high visible light photocatalytic performance," *Catalysis Science & Technology*, vol. 2, no. 7, pp. 1332–1335, 2012.

[22] S. C. Yan, Z. S. Li, and Z. G. Zou, "Photodegradation performance of g-C_3N_4 fabricated by directly heating melamine," *Langmuir*, vol. 25, no. 17, pp. 10397–10401, 2009.

[23] H. Xu, J. Yan, Y. G. Xu et al., "Novel visible-light-driven AgX/graphite-like C_3N_4 (X = Br, I) hybrid materials with synergistic photocatalytic activity," *Applied Catalysis B*, vol. 129, pp. 182–193, 2013.

[24] A. Vinu, "Two-dimensional hexagonally-ordered mesoporous carbon nitrides with tunable pore diameter, surface area and nitrogen content," *Advanced Functional Materials*, vol. 18, no. 5, pp. 816–827, 2008.

[25] A. Vinu, K. Ariga, T. Mori et al., "Preparation and characterization of well-ordered hexagonal mesoporous carbon nitride," *Advanced Materials*, vol. 17, no. 13, pp. 1648–1652, 2005.

[26] A. Vinu, P. Srinivasu, D. P. Sawant et al., "Three-dimensional cage type mesoporous CN-based hybrid material with very high surface area and pore volume," *Chemistry of Materials*, vol. 19, no. 17, pp. 4367–4372, 2007.

[27] X. G. Ma, Y. H. Lv, J. Xu, Y. F. Liu, R. Q. Zhang, and Y. F. Zhu, "A strategy of enhancing the photoactivity of g-C_3N_4 via doping of nonmetal elements: a first-principles study," *The Journal of Physical Chemistry C*, vol. 116, no. 44, pp. 23485–23493, 2012.

[28] J. Gracia and P. Kroll, "First principles study of C_3N_4 carbon nitride nanotubes," *Journal of Materials Chemistry*, vol. 19, no. 19, pp. 3020–3026, 2009.

[29] F. Goettmann, A. Fischer, M. Antonietti, and A. Thomas, "Chemical synthesis of mesoporous carbon nitrides using hard templates and their use as a metal-free catalyst for Friedel-Crafts reaction of benzene," *Angewandte Chemie*, vol. 45, no. 27, pp. 4467–4471, 2006.

[30] Y. Zhang, Z. M. Pan, and X. C. Wang, "Advances in photocatalysis in China," *Chinese Journal of Catalysis*, vol. 34, no. 3, pp. 524–535, 2013.

[31] V. N. Khabashesku, J. L. Zimmerman, and J. L. Margrave, "Powder synthesis and characterization of amorphous carbon nitride," *Chemistry of Materials*, vol. 12, no. 11, pp. 3264–3270, 2000.

[32] G. G. Zhang, J. S. Zhang, M. W. Zhang, and X. C. Wang, "Polycondensation of thiourea into carbon nitride semiconductors as visible light photocatalysts," *Journal of Materials Chemistry*, vol. 22, no. 16, pp. 8083–8091, 2012.

[33] Y. Ham, K. Maeda, D. Cha, K. Takanabe, and K. Domen, "Synthesis and photocatalytic activity of poly (triazine imide)," *Chemistry*, vol. 8, no. 1, pp. 218–224, 2013.

[34] Y. J. Cui, J. S. Zhang, G. G. Zhang et al., "Synthesis of bulk and nanoporous carbon nitride polymers from ammonium thiocyanate for photocatalytic hydrogen evolution," *Journal of Materials Chemistry*, vol. 21, no. 34, pp. 13032–13039, 2011.

[35] Y. W. Zhang, J. H. Liu, G. Wu, and W. Chen, "Porous graphitic carbon nitride synthesized via direct polymerization of urea for efficient sunlight-driven photocatalytic hydrogen production," *Nanoscale*, vol. 4, no. 17, pp. 5300–5303, 2012.

[36] S. Wang, Q. Y. Gao, and J. C. Wang, "Thermodynamic analysis of decomposition of thiourea and thiourea oxides," *The Journal of Physical Chemistry B*, vol. 109, no. 36, pp. 17281–17289, 2005.

[37] J. Xu, H. T. Wu, X. Wang, B. Xue, Y. X. Li, and Y. Cao, "A new and environmentally benign precursor for the synthesis of mesoporous g-C_3N_4 with tunable surface area," *Physical Chemistry Chemical Physics*, vol. 15, no. 13, pp. 4510–4517, 2013.

[38] M. Sadhukhan and S. Barman, "Bottom-up fabrication of two-dimensional carbon nitride and highly sensitive electrochemical sensors for mercuric ions," *Journal of Materials Chemistry A*, vol. 1, no. 8, pp. 2752–2756, 2013.

[39] H. T. Tian, J. W. Li, M. Ge, Y. P. Zhao, and L. Liu, "Removal of bisphenol a by mesoporous BiOBr under simulated solar light irradiation," *Catalysis Science & Technology*, vol. 2, no. 11, pp. 2351–2355, 2012.

[40] J. S. Zhang, X. F. Chen, K. Takanabe et al., "Synthesis of a carbon nitride structure for visible-light catalysis by copolymerization," *Angewandte Chemie*, vol. 49, no. 2, pp. 441–444, 2010.

[41] J. H. Li, B. Shen, Z. H. Hong, B. Z. Lin, B. F. Gao, and Y. L. Chen, "A facile approach to synthesize novel oxygen-doped g-C_3N_4 with superior visible-light photoreactivity," *Chemical Communications*, vol. 48, no. 98, pp. 12017–12019, 2012.

Hindawi Publishing Corporation
International Journal of Photoenergy
Volume 2013, Article ID 471674, 8 pages
http://dx.doi.org/10.1155/2013/471674

Research Article

Enhanced Visible Light Photocatalytic Activity for TiO_2 Nanotube Array Films by Codoping with Tungsten and Nitrogen

Min Zhang, Juan Wu, DanDan Lu, and Jianjun Yang

Key Laboratory of Ministry of Education for Special Functional Materials, Henan University, Kaifeng 475004, China

Correspondence should be addressed to Min Zhang; zm1012@henu.edu.cn and Jianjun Yang; yangjianjun@henu.edu.cn

Received 10 May 2013; Revised 15 July 2013; Accepted 15 July 2013

Academic Editor: Jiaguo Yu

A series of W, N codoped TiO_2 nanotube arrays with different dopant contents were fabricated by anodizing in association with hydrothermal treatment. The samples were characterized by scanning electron microscopy, X-ray diffraction, X-ray photoelectron spectroscopy, and ultraviolet-visible light diffuse reflection spectroscopy. Moreover, the photocatalytic activity of W and N codoped TiO_2 nanotube arrays was evaluated by degradation of methylene blue under visible light irradiation. It was found that N in codoped TNAs exists in the forms of Ti-N-O, while W exists as W^{6+} by substituting Ti in the lattice of TiO_2. In the meantime, W and N codoping successfully extends the absorption of TNAs into the whole visible light region and results in remarkably enhanced photocatalytic activity under visible light irradiation. The mechanism of the enhanced photocatalytic activity could be attributed to (i) increasing number of hydroxyl groups on the surface of TNAs after the hydrothermal treatment, (ii) a strong W-N synergistic interaction leads to produce new states, narrow the band gap which decrease the recombination effectively, and then greatly increase the visible light absorption and photocatalytic activity; (iii) W ions with changing valences in all codoped samples which are considered to act as trapping sites, effectively decrease the recombination rate of electrons and holes, and improve the photocatalytic activity.

1. Introduction

Nowadays, photocatalysis has attracted lively interest due to its potential applications in environmental remediation and clean energy production. Among various photocatalysts, TiO_2 is most frequently employed owing to the advantages of earth abundance, low toxicity, and thermal and chemical stability. However, because of the wide band gap of titanium dioxide, only a small UV fraction of solar light (3–5%) can be utilized [1–3]. Many investigations have been conducted to extend optical absorption of TiO_2-based materials to the visible light region and to improve visible light photocatalytic activity by nonmetal doping using N [4], C [5, 6], S [7] or multielemental-doped materials [8–11]. In particular, TiO_2 photocatalysts codoped with N and another metal had attracted many attentions in recent years [12, 13]. For example, Yang et al. prepared C- and V-doped TiO_2 photocatalysts by a sol-gel method with high photocatalytic activity for the degradation of acetaldehyde both under visible light irradiation (>420 nm) and in the dark [14]. Liu et al. prepared a series of $Ti_{1-x}Mo_xO_{2-y}N_y$ samples using sol-gel method and found that Mo + N codoping can increase the up-limit of dopant concentration and create more impurity bands in the band gap of TiO_2 by first-principles band structure calculations [15]. It reveals that Mo + N codoped TiO_2 material is a promising photocatalyst with high photocatalytic activity under visible light.

Recently, many reports have focused on the W, N codoped TiO_2 nanoparticles to increase photocatalytic activity under visible light irradiation. Shen et al. fabricated the W, N codoped TiO_2 nanopowders using sol-gel and mechanical alloying methods. The samples exhibited strong absorbance in the visible range and enhanced photocatalytic activities under visible light irradiation from the results of photodegradation experiments and chemical oxygen demand analysis [16]. Li et al. prepared W, N codoped TiO_2 nanophotocatalysts with twist-like helix structure by a facile and template-free one-pot method, which showed higher visible light

response compared with pure TiO_2 and P25 [17]. Kubacka et al. synthesized W- and N-doped TiO_2 anatase-based materials with both unprecedented high activity and selectivity in the gas-phase partial oxidation of aromatic hydrocarbons using sunlight as excitation energy and molecular oxygen as oxidant [18–20]. The doped tungsten and nitrogen species plays a key role in narrowing the band gap and then in expanding the photoactivity to visible light region and also in decreasing the recombination rate of excited electron and holes. However, most of the reported W- and N-doped TiO_2 photocatalysts were typically present in powders which usually display low surface area due to the closed packing and limit their industrial applications as photocatalysts.

Highly ordered TiO_2 nanotube arrays (TNAs) fabricated via electrochemical anodization of high purity Ti foils have attracted extensive interests in recent years. Owing to the presence of unique structural features such as large surface area, high porosity, and ordered pore channels facilitating reactant diffusion and adsorption, TiO_2 nanotube arrays are more attractive for use in the applications of photocatalysis [21], gas sensing [22], solar cells [23], photoelectrochemistry [24], and so on. However, full technological applications of TiO_2 nanotube arrays are hampered by the wide band gap of TiO_2 and the activation only under ultraviolet light irradiation. Although nonmetal doping of TiO_2 nanotube arrays has been confirmed as an effective method to enhance the photocatalytic activity under visible light irradiation [22, 23]; to our knowledge, there is little work about the fabrication and visible light photocatalytic activity of the W and N codoped TiO_2 nanotube arrays. In this work, we successfully prepared W, N codoped TiO_2 nanotube arrays by anodization and hydrothermal synthesis. The photocatalytic activity of as-prepared samples was studied based on methylene blue dye degradation under visible light irradiation. The results demonstrated that the W and N codoped TiO_2 nanotube arrays exhibited a higher photocatalytic activity than the single N-doped sample under visible light irradiation. The mechanism of visible light photocatalytic activity enhancement was also discussed.

2. Experimental Sections

2.1. Synthesis of W and N Codoped TiO_2 Nanotube Arrays. Self-organized and well-aligned TNAs were fabricated by two-step electrochemical anodization process [25]. Briefly, commercial titanium sheets (20 mm × 40 mm, purity > 99.6%) with a thickness of 0.25 mm were sequentially sonicated in acetone, isopropanol, and methanol for 10 min, followed by etching in the mixture of $HF/HNO_3/H_2O$ for 20 s, rinsing with deionized water, and drying under a N_2 stream. Resultant rectangular Ti sheet was used as an anode to couple with Pt meshwork as a cathode in the anodic oxidation test setup. A direct current power supply and a mixed electrolyte solution of ethylene glycol containing 0.25 wt% NH_4F and 2 vol% deionized water were used in the electrochemical processes. The first oxidation step was conducted at 60 V for 1 h, with which the oxidized surface films were removed by sonication in distilled water before the oxidized samples were dried under high purity N_2 stream at room temperature. As-dried Ti substrates were subsequently oxidized in the original electrolyte at 60 V for 2 h, followed by sonication in ethanol for 7 min to remove the surface cover and drying under high purity N_2 stream to afford as-prepared TNAs. Magnetic stirring was adopted throughout the oxidation processes, while a circulation pump was performed at a low temperature of about 20°C. After electrochemical anodization, as-prepared TNAs were calcinated at 500°C for 3 h in a furnace. Interstitial nitrogen species were formed in the TNAs due to the electrolyte containing NH_4F [26]. We denoted these single N-doped TiO_2 nanotube arrays samples fabricated by two-step oxidization as N-TiO_2.

W and N codoped TNAs with different dopant concentration (0.01%, 0.05%, 0.5%, 1.00%, and 3.00%, referring to different concentration of W and N source) were then prepared by hydrothermally treating the anodized N-TiO_2 in a teflon-lined autoclave (120 mL, Parr Instrument) containing approximately 60 mL of ammonium tungstate ($(NH_4)_{10}H_2(W_2O_7)_6$) as the source of both W and N. The hydrothermal synthesis was conducted at 180°C for 5 h in a box oven, and then the autoclave was naturally cooled down to room temperature affording target products denoted as W-N-TiO_2-water, W-N-TiO_2-0.01, W-N-TiO_2-0.05, W-N-TiO_2-0.5, W-N-TiO_2-1, and W-N-TiO_2-3 (numeral suffixes water, 0.01, 0.05, 0.5, 1 and 3 refer to pure water and ammonium tungstate solution concentration of 0.01%, 0.05%, 0.50%, 1.00%, and 3.00%). All samples were rinsed with distilled water and dried under high purity N_2 stream at room temperature.

2.2. Characterization. Surface morphologies of TNAs were observed using a field emission scanning electron microscopy (FESEM, Nova NanoSEM 230). A Philips X'Pert Pro PW3040/60 X-ray diffractometer (XRD, Philips Corporation, Holland) was used to determine the crystal structure of as-prepared samples. Chemical state analysis was conducted with an Axis Ultra X-ray photoelectron spectroscopy (XPS, Kratos, UK; a monochromatic Al source operating at 36 W with a pass energy of 40 eV and a step of 0.1 eV was used). All XPS spectra were corrected using the C 1*s* line at 284.8 eV. A Cary-5000 scanning ultraviolet-visible light diffuse reflection spectrophotometer (denoted as UV-vis DRS; Varian, USA) equipped with a labsphere diffuse reflectance accessory was performed to collect the UV-vis diffuse reflectance spectra. The adsorption spectra of N-TiO_2 and W + N codoped TNAs in the range of 300~800 nm were recorded with the UV-vis DRS facility at a scan rate of 600 nm min^{-1}.

2.3. Photocatalytic Activity Measurements. Photocatalytic activity of all samples was evaluated by monitoring the photocatalytic degradation of methylene blue (denoted as MB) in aqueous solution under visible light with vertical irradiation as light source. Briefly, to-be-tested N-TiO_2 and W-N-TiO_2-X (X = water, 0.01, 0.05, 0.5, 1, and 3) samples were dipped into 25 mL of MB solution with an initial concentration of 10 mg L^{-1}. The effective photocatalytic reaction area of all samples was 4 cm^2. A 300 W Xenon lamp (PLS-SEX300, Beijing Changtuo) was used as the light source. A cut-off filter was used to remove any radiation below 420 nm to ensure

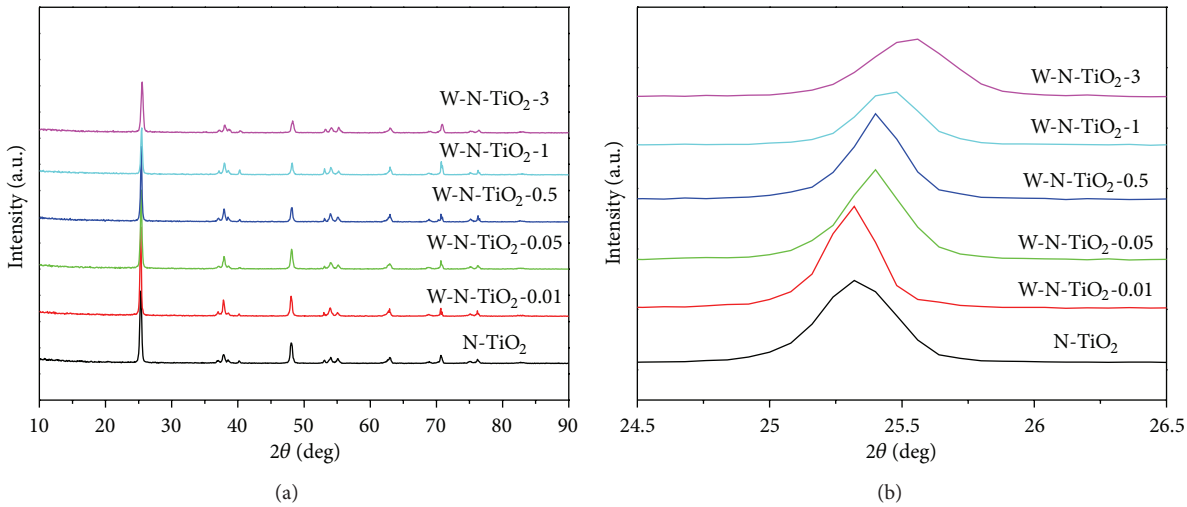

Figure 1: XRD patterns of N-TiO_2 and W-N-TiO_2-X (a), the enlarged XRD peaks of crystal plane (101) (b).

visible light irradiation only. The light intensity was measured by a photodetector, and the value is about 30 mW/cm^2 at 420 nm. Prior to irradiation, the MB solution containing to-be-tested sample was magnetically stirred in the dark for 30 min to establish adsorption-desorption equilibrium. During the photocatalytic reaction, the absorbance of MB solution at 664 nm was measured using an SP-2000 spectrophotometer at a time interval of 30 min. The decoloration rate of MB solution is calculated as $(C_0 - C)/C_0 \times 100\%$, where C_0 is the concentration of MB at adsorption–desorption equilibrium in the dark and C is the concentration of MB upon completion of the photocatalytic reaction under visible light irradiation. In this way, the influence of adsorption amount of MB on its solution decoloration rate is excluded (different photocatalyst samples adsorb different amount of MB).

3. Results and Discussion

The phase structure, crystallite size, and crystallinity of TiO_2 play important roles in photocatalytic activity and photochemical properties. Many studies have confirmed that the anatase phase of TiO_2 exhibits higher photocatalytic activity than brookite or rutile phases [27]. Herein, XRD measurements were performed to investigate the changes of phase structure of TiO_2 nanotube arrays codoped with different ammonium tungstate addition. XRD patterns of various samples are shown in Figure 1. It can be seen that all the diffraction peaks of N-TiO_2 and W-N-TiO_2-X can be ascribed to anatase TiO_2, which indicates that W and N codoping has no effect on the crystal structure and phase composition of TNAs. It is worth noting that no WO_3 phase could be observed in all the XRD patterns, even in that of the sample with the W doping amount reaching 3%. Accordingly, we propose that tungsten ions may be incorporated into the titania lattice and replaced titanium ions to form W–O–Ti bonds.

From the enlarged image in Figure 1(b), it is interesting to note that W and N codoping causes the diffraction peak of anatase TiO_2 along (101) plane to shift towards higher values of 2θ. Moreover, slight enhancement of crystallinity properties can be observed when comparing the (101) peak intensities of the TNAs samples before and after the hydrothermal treatments. The XRD results imply that the Ti atoms in the anatase lattice of codoped TNAs samples may be substituted by W atoms, since W^{6+} ions with a radius close to that of Ti^{4+} are easy to enter into the lattices of TiO_2 and displace Ti^{4+} ions, while nitrogen and tungsten have a synergistic doping effect [17, 21].

Figure 2 presents typical FESEM top view images of the N-TiO_2 and W-N-TiO_2-1 photocatalysts. Both images show the similar morphology of highly ordered nanotube arrays grown on the Ti substrate. SEM observation indicates that there is no apparent structural transformation of the TNAs samples after hydrothermal codoping process. The nanotubes of N-TiO_2 samples are open at the top end with an average diameter of 70 nm (Figure 2(a)). However, the diameter of nanotube in W-N-TiO_2-1 sample is found to be slightly increased to 80 nm. This difference of pore size is due to the enhanced crystallinity of the anatase nanotube walls after hydrothermal treatments in agreement with the XRD results. Yu et al. had reported that the nanotube array structures were completely destroyed after 180°C hydrothermal treatments with as-prepared TNAs samples due to the strongly enhanced anatase crystallinity and phase transformation from amorphous to anatase [28]. In our work, the as-prepared TNAs samples were calcinated at 500°C to realize the phase transformation from amorphous to anatase before subsequently hydrothermal process. The reported hydrothermally induced collapse was prevented with the simple calcination method. The calcined TNAs samples show better crystallinity with no apparent morphology change after hydrothermal codoping process.

XPS measurements are used to investigate the chemical states of W, N, Ti, and O in N-TiO_2 and W-N-TiO_2-1 samples. Figure 3(a) shows the high resolution XPS spectra for the N 1*s* region of N-TiO_2 and W-N-TiO_2-1. The N 1*s* binding energy peaks are broad, extending from 396 to 403 eV. The centre

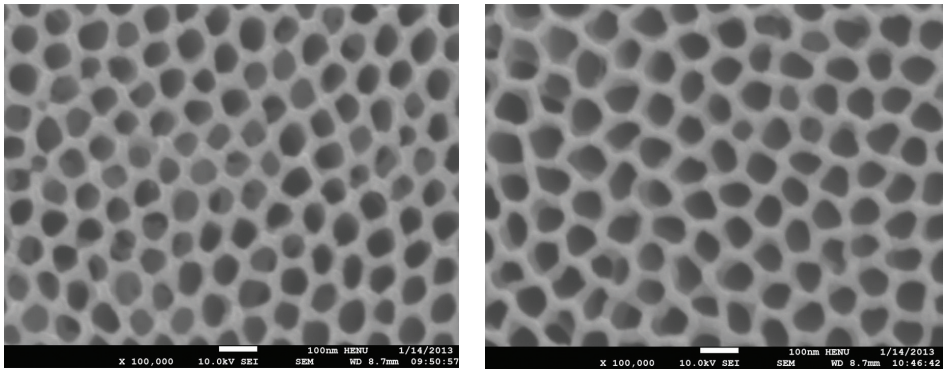

(a) (b)

Figure 2: FESEM cross-sectional views of W and N codoped TiO_2 nanotube arrays: (a) N-TiO_2, (b) W-N-TiO_2-1.

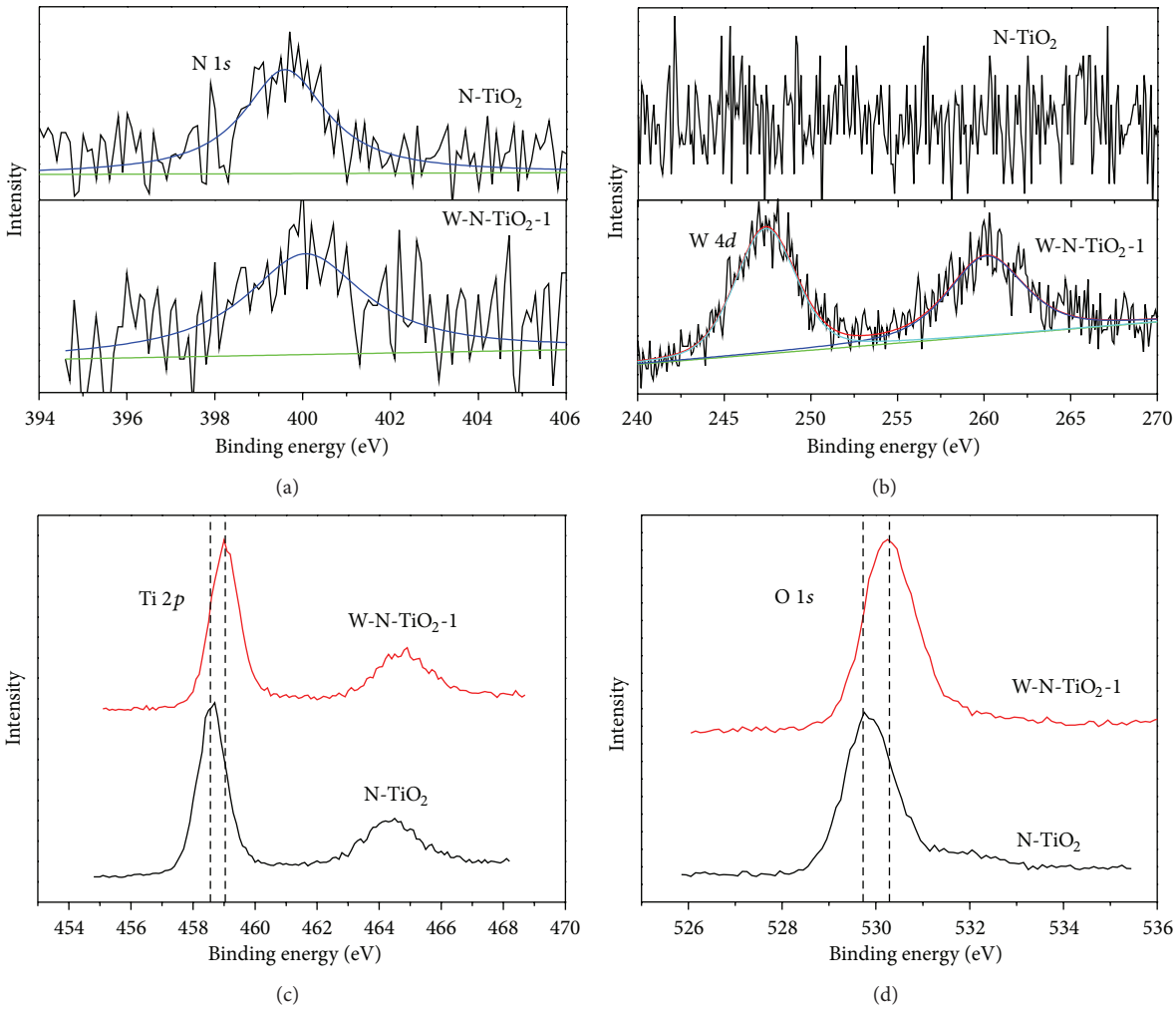

Figure 3: High resolution XPS spectra of (a) N 1*s*, (b) W 4*d*, (c) Ti 2*p*, and (d) O 1*s* for N-TiO_2 and W-N-TiO_2-1 samples.

of the N 1*s* peak locates at ca. 399.8 eV and 400.1 eV for N-TiO_2 and W-N-TiO_2-1 sample, respectively. These two peaks are much higher than that of typical binding energy of N 1*s* (396.9 eV) in TiN [29], indicating that the N atoms in N-TiO_2 and W-N-TiO_2-1 interact strongly with O atoms [30]. The binding energy of 399.8 eV and 400.1 eV here is attributed to the oxidized nitrogen similar to NO_x species, meaning Ti-N-O linkage possibly formed on the surface of N-TiO_2 and W-N-TiO_2-1 [13, 31, 32]. The N 1*s* peak of N-TiO_2 at 399.8 eV is assigned to interstitial nitrogen species

according to the previous report of Varghese et al. [26]. They suggested that the nitrogen incorporated within TiO_2 nanotubes during anodization is primarily supplied by NH_4F or low extent of atmospheric nitrogen dissolved into the electrolyte. Furthermore, it is highly possible that some N-O species coordinate with W to form the W-N-O linkage on the surface of W-N-TiO_2-1. For the latter case, the electron density of N atoms in W-N-O is lower than that in Ti-N-O since the electronegativity of W is larger than that of Ti [13, 33]. It may explain why the binding energy of nitrogen surface species for W-N-TiO_2-1 (400.1 eV) is higher than that for N-TiO_2 (399.8 eV). High resolution W 4*d* spectra of N-TiO_2 and W-N-TiO_2-1 are presented in Figure 3(b). The W 4*d* peaks of W-N-TiO_2-1 at about 247.5 eV and 260.2 eV are assigned to $4d_{5/2}$ and $4d_{3/2}$ electronic states of W^{6+}, respectively [19, 20].

Figures 3(c) and 3(d) show high-resolution spectra of Ti 2*p*, O 1*s* of N-TiO_2, and W-N-TiO_2-1. For N-TiO_2 sample, two peaks at 458.6 and 464.3 eV correspond to the Ti $2p_{3/2}$ and Ti2 $p_{1/2}$ states, indicating that Ti is 4+ valence. A strong peak centered at 529.8 eV is observed in the O 1*s* XPS spectra of N-TiO_2, attributing to bulk oxygen bonded to titanium. For the W and N codoped TiO_2 sample, both the Ti 2*p* and O 1*s* peaks are slightly shifted toward higher binding energy due to the doping of W in the TiO_2 lattice, which is in agreement with the result reported by Gong et al. [34]. All XPS results indicate that the W^{6+} ions were doped into the bulk TiO_2 lattice by displacing Ti^{4+} ions and forming the W–O–Ti bonding, which is in accordance with relevant XRD analytical results. According to the previous XPS and XRD results, it indicates that nitrogen is present as interstitial nitrogen in codoped TNAs samples, and W incorporates into TiO_2 lattice in substitutional mode.

The exact amounts of surface elements in all doped samples were studied by XPS analysis. The surface N/Ti and W/Ti ratio of all samples are calculated and listed in Table 1. It is found that the surfaces N/Ti and W/Ti ratio increased with the concentration of ammonium tungsten solution. Then, both the surfaces N/Ti and W/Ti ratio reaches their maximum value with the concentration of ammonium tungsten solution to 1% (theoretical doping concentration). However, the N/Ti and W/Ti ratio decreased clearly with further increasing the ammonium tungsten concentration to 3%. It indicates that the dopant concentration has an optimal value of about 1%. Above this optimal concentration, excess W and N ions cannot be doped in TiO_2 and show no contribution to the visible light absorption and subsequent photocatalytic activity. Moreover, the concentration of doped N increases with the codoping of W, which demonstrates that W and N codoping is in favor of enhancing the dopant solubility.

Figure 4 presents the UV-vis diffuse reflectance spectra of all samples. A relatively weak visible light absorption can be observed for the oxidized N-TiO_2 sample, which corresponds to a typical reported absorption feature of nitrogen-doped TiO_2 arising from the electron transition from surface state of NO_x species to the conduction band of TiO_2 [13, 35]. Compared with that of N-TiO_2 sample, UV-vis spectra of all W and N codoped TNAs samples present red-shifted absorption edge and a strong absorption in the visible light region with typical extended absorption tail of about 600 nm. Moreover, for W and N codoped TNAs samples, the intensity of visible light absorption is enhanced with the increase of W and N concentration (the ammonium tungsten solution concentration from 0.01% to 1%). We consider that this absorption enhancement is due to the contribution of both interstitially doped N and substitutionally doped W. W and N incorporated in the lattice of TNAs show synergistic doping effect which favors to increase the solubility limits of W and N thereby greatly enhancing the visible light absorption along with the increase of the up-limits of W and N concentration [15, 36]. For the W-N-TiO_2-3 sample, the absorption edge is decreased because the superfluous W and N atoms cannot be doped into the lattice of TiO_2. Overall, the UV-vis DRS results indicate that nitrogen and tungsten codoped TiO_2 nanotube arrays are more sensitive to the visible light than N-TiO_2 samples.

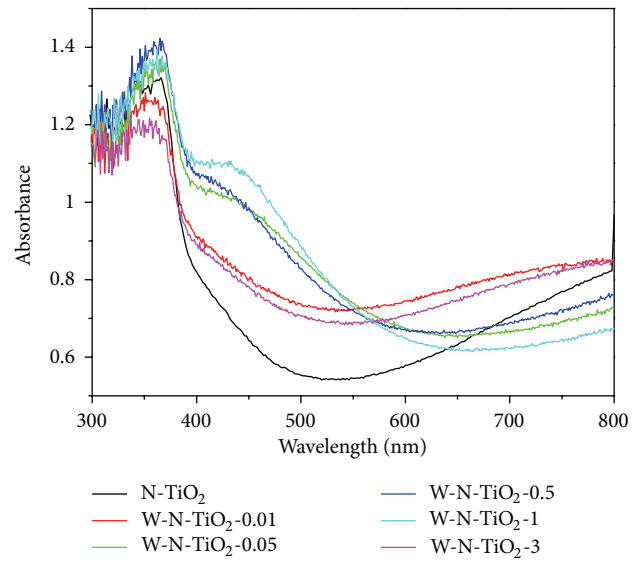

Figure 4: UV-vis diffuse reflectance spectra of N-TiO_2 and W-N-TiO_2-X samples.

The photocatalytic activities of N-TiO_2 and hydrothermal treated W-N-TiO_2-X samples were evaluated by monitoring the degradation of MB under visible light irradiation. To investigate the effect of hydrothermal treatment on the photocatalytic activity, the oxidized N-TiO_2 was firstly hydrothermally treated in pure water, and the obtained sample was denoted as W-N-TiO_2 water. An obviously enhanced photocatalytic activity was found for the W-N-TiO_2 water sample after hydrothermal treatment as shown in Figure 5. Many reports have shown that the photocatalytic activity of TiO_2 samples strongly depends on the preparing methods and posttreatments [36, 37]. Yu et al. had demonstrated an obvious increase of photocatalytic activity after thermal treatment of TiO_2 (P25) in pure water [36]. Recently, Dai et al. reported the enhanced photoelectrocatalytic activity of the TiO_2 nanotube arrays by hydrothermal modification [37]. They suggested that the enhanced photocatalytic activity was attributed to the formation of increasing number of hydroxyl groups on the surface of TiO_2 nanotube arrays

Table 1: W/Ti and N/Ti ratio of W-N-TiO_2-X samples determined by XPS analysis.

Sample	N-TiO_2	W-N-TiO_2-0.01	W-N-TiO_2-0.05	W-N-TiO_2-0.5	W-N-TiO_2-1	W-N-TiO_2-3
W/Ti	0	0.11	0.11	0.12	0.16	0.12
N/Ti	0.02	0.13	0.16	0.19	0.22	0.14

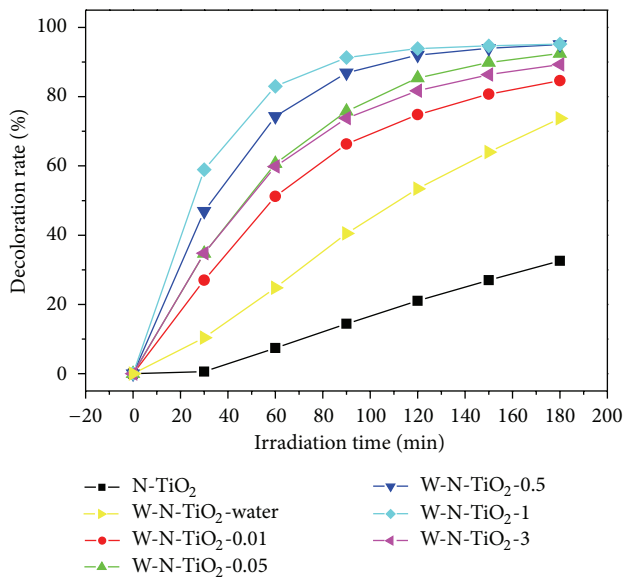

Figure 5: Photocatalytic degradation rate of MB in the presence of N-TiO_2 and W-N-TiO_2-X photocatalysts under visible light irradiation.

after hydrothermal treatment. The increased hydroxyl groups would react with photoexcited holes on the surface of TiO_2 and produce hydroxyl radicals, which in turn are powerful oxidants in the photocatalytic reaction. In our work, before codoping, the number of hydroxyl groups on the surface of N-TiO_2 decreases due to the dehydration reaction during the higher temperature calcination process of oxidized TiO_2 nanotube arrays. When N-TiO_2 was codoped with W and N by hydrothermal treatment, Ti-OH leading to an enhanced photocatalytic activity can be regenerated on the surface of W-N-TiO_2-X samples due to the rupture of Ti–O–Ti bond.

W and N codoping of N-TiO_2 samples was performed by the hydrothermal treatment in a series of concentrations of ammonium tungstate solution (concentration from 0.01% to 3%). As shown in Figure 5, W and N codoped TNAs possess much higher photocatalytic activity under visible light irradiation than N-TiO_2 sample and the W-N-TiO_2-water sample hydrothermal treated in pure water. Besides, the decoloration rate of MB for W and N codoped TNAs increases under visible light irradiation with the increase of dopant concentration. The decoloration rate reaches a maximum value for W-N-TiO_2-1, and it allows nearly complete elimination of MB within 3 h. Then, the photocatalytic activity for W-N-TiO_2-3 shows clear decrease due to its visible light absorption as discussed before.

The origin of the visible light photocatalytic activity of W and N codoped TNAs can be attributed to the interactions between N doping and W doping in the preparation processes. For the single N-doped sample (N-TiO_2) prepared by electrochemical anodization, isolated N 2*p* states above the top of valence band are responsible for the red shifts in the optical absorption edge. After hydrothermal codoping with W and N, a hybridized state (composed of N 2*p* orbitals and W 5*d* states) is formed; in particular, the hybridized states are located mainly at the edge of the valence band, whereas other W 5*d* states are at the edge of the conduction band. W 5*d* states may contribute to the lowering of the energy levels of the N 2*p* states, bringing the N states closer to the valence band and therefore enhancing mixing of N 2*p* and O 2*p* states in the valence band. Therefore, the addition of W to N-TiO_2 changes the character of N 2*p* orbitals from isolated midgap states to N 2*p* states mixed with O 2*p* states [38]. At the same time, W 5*d* states were located at the conduction band edge. Moreover, as electrons move from occupied W 5*d* states to empty lower energy N 2*p* states, a strong N–W bond forms in N and W codoped TNAs. This synergistic effect is beneficial for the increased doping amount of W and N in TiO_2 nanotube arrays. Consequently, the band gap energy of TiO_2 is significantly reduced, and its absorption in the visible light region is considerably increased due to modified conduction and valence band edges simultaneously. The band gap narrowing effect makes it feasible for W and N codoped TNAs to be activated by visible light with more electrons and holes being generated to participate in the photocatalytic reactions.

Moreover, W ions with changing valences in all codoped samples are considered to act as a temporary photogenerated electron or hole-trapping site thereby inhibiting the recombination of photogenerated charge carriers, prolonging their lifetime and improving the photocatalytic activity [17]. The detailed reaction steps are as follows:

$$\begin{gathered} TiO_2 + h\nu \longrightarrow e^- + h^+, \\ W^{6+} + e^- \longrightarrow W^{5+}, \\ W^{5+} + O_2 \longrightarrow W^{6+} + O_2^{-\bullet}, \\ W^{6+} + h^+ \longrightarrow W^{7+}, \\ W^{7+} + OH^- \longrightarrow W^{6+} + OH^{\bullet}. \end{gathered} \tag{1}$$

When W^{6+} (d^5) trap an electron, its electronic configuration is transferred to d^6, and if it traps a hole, its electronic configuration will be transferred to d^4 which is highly unstable. Therefore, to restore the stable electronic configuration, the trapped charge carrier tends to be transferred from W^{5+} or W^{7+} to the adsorbed O_2 or surface hydroxyl (OH^-) thereby regenerating W^{6+}. These newly produced active species (such

as $OH^{\bullet}$ and $O_2^{-\bullet}$) are able to initiate the photocatalytic reactions.

4. Conclusions

W and N codoped TiO_2 nanotube arrays have been successfully synthesized by combining anodizing technique with hydrothermal method. W and N codoped TNAs samples show better crystallinity with no apparent morphology change after hydrothermal codoping process. XPS data reveal that, in as-prepared W and N codoped TNAs, nitrogen is present in the forms of Ti-N-O and W incorporates into TiO_2 lattice in substitutional mode. UV-vis DRS data show that W and N codoping was found to successfully extend the absorption of TiO_2 nanotube arrays into the whole visible light region. Increased number of hydroxyl groups produced by hydrothermal treatment shows an important role for the enhancement of photocatalytic activity. The synergetic doping effect between W and N plays a key role in producing new states, narrowing the band gap, and reducing the recombination effectively thereby greatly improving the visible light absorption and photocatalytic activity of TNAs. Besides, W ions with multiple valences in W-N-TiO_2-X samples can act as trapping sites to effectively decrease the recombination rate of electrons and holes, also resulting in improved photocatalytic activity of TNAs. Therefore, W and N codoped TiO_2 nanotube arrays with higher visible light absorption and photocatalytic activity are promising materials for visible light photocatalysts.

Conflict of Interests

The authors declare that they do not have any commercial or associative interests that represents a conflict of interest in connection with the work submitted.

Acknowledgments

The authors thank the National Natural Science Foundation of China (Grant no. 21203054) and the Science and Technology Department of Henan Province (Natural Science Project Grant no. 112300410171) for financial support.

References

[1] A. Fujishima, X. T. Zhang, and D. A. Tryk, "TiO_2 photocatalysis and related surface phenomena," *Surface Science Reports*, vol. 63, no. 12, pp. 515–582, 2008.

[2] H. Tong, S. X. Ouyang, Y. P. Bi, N. Umezawa, M. Oshikiri, and J. H. Ye, "Nano-photocatalytic materials: possibilities and challenges," *Advanced Materials*, vol. 24, no. 2, pp. 229–251, 2012.

[3] X. B. Chen and S. S. Mao, "Titanium dioxide nanomaterials: synthesis, properties, modifications and applications," *Chemical Reviews*, vol. 107, no. 7, pp. 2891–2959, 2007.

[4] R. Asahi, T. Morikawa, T. Ohwaki, K. Aoki, and Y. Taga, "Visible-light photocatalysis in nitrogen-doped titanium oxides," *Science*, vol. 293, no. 5528, pp. 269–271, 2001.

[5] S. U. M. Khan, M. Al-Shahry, and W. B. Ingler Jr., "Efficient photochemical water splitting by a chemically modified n-TiO_2," *Science*, vol. 297, no. 5590, pp. 2243–2245, 2002.

[6] J. G. Yu, G. P. Dai, Q. J. Xiang, and M. Jaroniec, "Fabrication and enhanced visible-light photocatalytic activity of carbon self-doped TiO_2 sheets with exposed 001 facets," *Journal of Materials Chemistry*, vol. 21, no. 4, pp. 1049–1057, 2011.

[7] X. H. Tang and D. Y. Li, "Sulfur-doped highly ordered TiO_2 nanotubular arrays with visible light response," *Journal of Physical Chemistry C*, vol. 112, no. 14, pp. 5405–5409, 2008.

[8] M. H. Zhou and J. G. Yu, "Preparation and enhanced daylight-induced photocatalytic activity of C,N,S-tridoped titanium dioxide powders," *Journal of Hazardous Materials*, vol. 152, no. 3, pp. 1229–1236, 2008.

[9] Y.-C. Nah, I. Paramasivam, and P. Schmuki, "Doped TiO_2 and TiO_2 nanotubes: synthesis and applications," *ChemPhysChem*, vol. 11, no. 13, pp. 2698–2713, 2010.

[10] U. G. Akpan and B. H. Hameed, "The advancements in sol-gel method of doped-TiO_2 photocatalysts," *Applied Catalysis A*, vol. 375, no. 1, pp. 1–11, 2010.

[11] Y.-F. Li, D. H. Xu, J. I. Oh, W. Z. Shen, X. Li, and Y. Yu, "Mechanistic study of codoped titania with nonmetal and metal ions: a case of C + Mo Codoped TiO_2," *ACS Catalysis*, vol. 2, no. 3, pp. 391–398, 2012.

[12] J. L. Zhang, Y. M. Wu, M. Y. Xing, S. A. K. Leghari, and S. Sajjad, "Development of modified N doped TiO_2 photocatalyst with metals, nonmetals and metal oxides," *Energy and Environmental Science*, vol. 3, no. 6, pp. 715–726, 2010.

[13] E. J. Wang, T. He, L. S. Zhao, Y. M. Chen, and Y. A. Cao, "Improved visible light photocatalytic activity of titania doped with tin and nitrogen," *Journal of Materials Chemistry*, vol. 21, no. 1, pp. 144–150, 2011.

[14] X. X. Yang, C. D. Cao, K. Hohn et al., "Highly visible-light active C- and V-doped TiO_2 for degradation of acetaldehyde," *Journal of Catalysis*, vol. 252, no. 2, pp. 296–302, 2007.

[15] H. L. Liu, Z. H. Lu, L. Yue et al., "(Mo + N) codoped TiO_2 for enhanced visible-light photoactivity," *Applied Surface Science*, vol. 257, no. 22, pp. 9355–9361, 2011.

[16] Y. F. Shen, T. Y. Xiong, T. F. Li, and K. Yang, "Tungsten and nitrogen co-doped TiO_2 nano-powders with strong visible light response," *Applied Catalysis B*, vol. 83, no. 3-4, pp. 177–185, 2008.

[17] J. X. Li, J. H. Xu, W.-L. Dai, H. Li, and K. Fan, "One-pot synthesis of twist-like helix tungsten-nitrogen-codoped titania photocatalysts with highly improved visible light activity in the abatement of phenol," *Applied Catalysis B*, vol. 82, no. 3-4, pp. 233–243, 2008.

[18] A. Kubacka, B. Bachiller-Baeza, G. Colón, and M. Fernández-García, "W, N-codoped TiO_2-anatase: a sunlight-operated catalyst for efficient and selective aromatic hydrocarbons photo-oxidation," *Journal of Physical Chemistry C*, vol. 113, no. 20, pp. 8553–8555, 2009.

[19] A. Kubacka, B. Bachiller-Baeza, G. Colón, and M. Fernández-García, "Doping level effect on sunlight-driven W,N-co-doped TiO_2-anatase photo-catalysts for aromatic hydrocarbon partial oxidation," *Applied Catalysis B*, vol. 93, no. 3-4, pp. 274–281, 2010.

[20] A. Kubacka, G. Colón, and M. Fernández-García, "N- and/or W-(co)doped TiO_2-anatase catalysts: effect of the calcination treatment on photoactivity," *Applied Catalysis B*, vol. 95, no. 3-4, pp. 238–244, 2010.

[21] C. W. Lai and S. Sreekantan, "Study of WO_3 incorporated C-TiO_2 nanotubes for efficient visible light driven water splitting performance," *Journal of Alloys and Compounds*, vol. 547, pp. 43–50, 2013.

[22] P. Roy, S. Berger, and P. Schmuki, "TiO_2 nanotubes: synthesis and applications," *Angewandte Chemie*, vol. 50, no. 13, pp. 2904–2939, 2011.

[23] G. K. Mor, O. K. Varghese, M. Paulose, K. Shankar, and C. A. Grimes, "A review on highly ordered, vertically oriented TiO_2 nanotube arrays: fabrication, material properties, and solar energy applications," *Solar Energy Materials and Solar Cells*, vol. 90, no. 14, pp. 2011–2075, 2006.

[24] G. P. Dai, J. G. Yu, and G. Liu, "Synthesis and enhanced visible-light photoelectrocatalytic activity of p-N junction BiOI/TiO_2 nanotube arrays," *Journal of Physical Chemistry C*, vol. 115, no. 15, pp. 7339–7346, 2011.

[25] G. T. Yan, M. Zhang, J. Hou, and J. J. Yang, "Photoelectrochemical and photocatalytic properties of N + S co-doped TiO_2 nanotube array films under visible light irradiation," *Materials Chemistry and Physics*, vol. 129, no. 1-2, pp. 553–557, 2011.

[26] O. K. Varghese, M. Paulose, T. J. LaTempa, and C. A. Grimes, "High-rate solar photocatalytic conversion of CO_2 and water vapor to hydrocarbon fuels," *Nano Letters*, vol. 9, no. 2, pp. 731–737, 2009.

[27] J. G. Yu and B. Wang, "Effect of calcination temperature on morphology and photoelectrochemical properties of anodized titanium dioxide nanotube arrays," *Applied Catalysis B*, vol. 94, no. 3-4, pp. 295–302, 2010.

[28] J. G. Yu, G. P. Dai, and B. Cheng, "Effect of crystallization methods on morphology and photocatalytic activity of anodized TiO_2 nanotube array films," *Journal of Physical Chemistry C*, vol. 114, no. 45, pp. 19378–19385, 2010.

[29] N. C. Saha and H. G. Tompkins, "Titanium nitride oxidation chemistry: an x-ray photoelectron spectroscopy study," *Journal of Applied Physics*, vol. 72, no. 7, pp. 3072–3079, 1992.

[30] M. Sathish, B. Viswanathan, R. P. Viswanath, and C. S. Gopinath, "Synthesis, characterization, electronic structure, and photocatalytic activity of nitrogen-doped TiO_2 nanocatalyst," *Chemistry of Materials*, vol. 17, no. 25, pp. 6349–6353, 2005.

[31] Q. C. Xu, D. V. Wellia, R. Amal, D. W. Liao, S. C. J. Loo, and T. T. Y. Tan, "Superhydrophilicity-assisted preparation of transparent and visible light activated N-doped titania film," *Nanoscale*, vol. 2, no. 7, pp. 1122–1127, 2010.

[32] X. B. Chen, Y. B. Lou, A. C. S. Samia, C. Burda, and J. L. Gole, "Formation of oxynitride as the photocatalytic enhancing site in nitrogen-doped titania nanocatalysts: comparison to a commercial nanopowder," *Advanced Functional Materials*, vol. 15, no. 1, pp. 41–49, 2005.

[33] M. X. Sun and X. L. Cui, "Anodically grown Si-W codoped TiO_2 nanotubes and its enhanced visible light photoelectrochemical response," *Electrochemistry Communications*, vol. 20, pp. 133–136, 2012.

[34] J. Y. Gong, W. H. Pu, C. Z. Yang, and J. L. Zhang, "Novel one-step preparation of tungsten loaded TiO_2 nanotube arrays with enhanced photoelectrocatalytic activity for pollutant degradation and hydrogen production," *Catalysis Communications*, vol. 36, pp. 89–93, 2013.

[35] H. Q. Sun, Y. Bai, W. Q. Jin, and N. P. Xu, "Visible-light-driven TiO_2 catalysts doped with low-concentration nitrogen species," *Solar Energy Materials and Solar Cells*, vol. 92, no. 1, pp. 76–83, 2008.

[36] J. G. Yu, H. G. Yu, B. Cheng, M. Zhou, and X. Zhao, "Enhanced photocatalytic activity of TiO_2 powder (P25) by hydrothermal treatment," *Journal of Molecular Catalysis A*, vol. 253, no. 1-2, pp. 112–118, 2006.

[37] G. P. Dai, S. Q. Liu, T. X. Luo, S. Wang, and A. Z. Hu, "Hydrothermal treatment and enhanced photoelectrocatalytic activity of anatase TiO_2 nanotube arrays," *Chinese Journal of Inorganic Chemistry*, vol. 28, pp. 1617–1622, 2012.

[38] R. Long and N. J. English, "First-principles calculation of nitrogen-tungsten codoping effects on the band structure of anatase-titania," *Applied Physics Letters*, vol. 94, no. 13, Article ID 132102, 2009.

Hindawi Publishing Corporation
International Journal of Photoenergy
Volume 2013, Article ID 234806, 9 pages
http://dx.doi.org/10.1155/2013/234806

Research Article

Synthesis and Characterization of Pyrochlore $Bi_2Sn_2O_7$ Doping with Praseodymium by Hydrothermal Method and Its Photocatalytic Activity Study

Weicheng Xu,[1] Guangyin Zhou,[1] Jianzhang Fang,[1] Zhang Liu,[1] YunFang Chen,[1] and Chaoping Cen[2]

[1] *College of Chemistry and Environment, South China Normal University, Guangzhou 510631, China*
[2] *The Key Laboratory of Water and Air Pollution Control of Guangdong Province, South China Institute of Environmental Sciences, Guangzhou 510655, China*

Correspondence should be addressed to Jianzhang Fang; fangjzh@scnu.edu.cn

Received 30 May 2013; Revised 15 July 2013; Accepted 15 July 2013

Academic Editor: Jiaguo Yu

Praseodymium doped $Bi_2Sn_2O_7$ (BSO), as a visible-light responsive photocatalyst, was prepared by a hydrothermal method with different dopant contents. The as-prepared photocatalysts were investigated by X-ray diffraction (XRD), scanning electron microscope (SEM), transmission electron microscope (TEM), N_2 adsorption-desorption isotherm, X-ray photoelectron spectroscopy analysis (XPS), and UV-Vis diffuse reflectance spectroscopy (DRS). The photocatalytic activity of prepared catalysts was evaluated by the degradation of Rhodamine Bextra (RhB) and 2,4-dichlorophenol (2,4-DCP) in aqueous solution under visible light irradiation. It was found that Pr doping inhibited the growth of crystalline size and the as-prepared materials were small in size (10–20 nm). In our experiments, Pr-doped BSO samples exhibited enhanced visible-light photocatalytic activity compared to the undoped BSO, and the optimal dopant amount of Pr was 1.0 mol% for the best photocatalytic activity. On the basis of the calculated PL spectra, the mechanism of enhanced photocatalytic activity has been discussed.

1. Introduction

Semiconductor photocatalysis has been a very attractive research topic since its potential in the treatment of biorecalcitrant components in wastewaters [1, 2]. Among the semiconductors, TiO_2 has been widely discussed as a photocatalyst to purify air and water polluted with various hazardous chemicals due to its high photocatalytic activity, low cost, nontoxicity, and good stability [3, 4]. However, low quantum yields and the lack of visible-light utilization blocked its practical application. Therefore, much effort has been done in order to enhance the photocatalytic efficiency and visible-light utilization of TiO_2, such as metal ion doping [5–7], nonmetal doping [8, 9], and coupling with other semiconductors [10]. In addition, the development of novel visible-light respond photocatalysts has been put forward and drawn great attention, such as $Bi_2Ti_2O_7$ [11, 12], $La_2Zr_2O_7$ [13], and $Bi_{1.5}MgNb_{1.5}O_7$ [14].

As a kind of pyrochlore-type composite oxides, bismuth pyrostannate ($Bi_2Sn_2O_7$) has received considerable attention by a number of groups due mainly to its demonstrated applications in catalysis and gas sensing [15–18]. Moens et al. [19] used $Bi_2Sn_2O_7$ (BSO) mechanically mixed with MoO_3 to evidence a cooperation catalytic effect between BSO and $Bi_2Mo_3O_{12}$. Kim et al. [20] utilized a novel method to prepare SnO_2 nanowires with BSO nanoparticles and investigated its oxygen sensing properties. Wu et al. [21] explored band engineering to improve visible light photocatalysis of nano-BSO. All previous research studies showed that it was necessary to take steps to promote the photocatalytic efficiency of pure BSO. Doping with rare earth ions also could reduce the recombination rate of electron-hole pairs and enhance the interfacial charge transfer efficiency [22], such as La-TiO_2 [23], Nd-TiO_2 [24], and Ce-Bi_2O_3 [25]. However, rare-earth doped BSO and its corresponding photocatalytic activity have been rarely investigated.

In the present work, in order to expand its absorption in visible light, the Pr-doping within the BSO photocatalyst was carried out by hydrothermal method. Furthermore, the effects of different Pr-doping amounts and the reasons accounting for the photocatalytic results were discussed. Meanwhile, the model pollutants of RhB and 2,4-CP were chosen to evaluate the photocatalytic activity of as-prepared photocatalysts under visible light irradiation.

2. Experimental

2.1. Synthesis. All chemicals were obtained commercially and used without further purification. $Bi(NO_3)_3{\cdot}5H_2O$ and $K_2SnO_3{\cdot}3H_2O$ were used as the starting materials for the syntheses. Pr-doped BSO was synthesized by hydrothermal method, and in every aqueous phase, dosage of 1.46 g of $Bi(NO_3)_3{\cdot}5H_2O$ (3 mmol) and 0.9 g of $K_2SnO_3{\cdot}3H_2O$ (3 mmol) was added to 80.0 mL of deionized water and then mixed with $Pr(NO_3)_3{\cdot}6H_2O$ according to the doping ratio of Pr/BSO of 0, 0.5, 1.0, 2.0, and 3.0 mol%, respectively. Under vigorous stirring, the pH value of the mixture was adjusted to 12 by using 2 mol/L KOH. After the solids were completely dissolved in the solution at room temperature, the autoclave was sealed, heated under autogenerous pressure at 180°C for 24 h, and then cooled down to room temperature naturally. The resultant precipitates were filtered, washed with deionized water and anhydrous ethanol, and then dried in a vacuum oven at 60°C for 12 h. The final products were milled using an agate mortar before characterization. The samples were labeled as x%-Pr-BSO, where x% was the molar ratio of Pr to BSO.

2.2. Characterization. The as-prepared samples were characterized by powder X-ray diffraction (XRD) instrument (Bruker D8 ADVANCE). The scanning electron microscopy (SEM) images were obtained on a JEOL JSM 6700F instrument with an accelerating voltage of 20 kV. Transmission electron micrographs (TEM) images were recorded using a JEM-2100HR (JEOL, Japan) microscope at an accelerating voltage of 200 kV. X-ray photoelectron spectroscopy (XPS) analysis was performed on an ESCALAB 250 photoelectron spectroscopy (Thermo-VG Scientific) at 2.0×10^{-10} mbar using Al Kα X-ray beam (1486.6 eV). UV-Vis diffuse reflectance spectrum (DRS) was determined on a Hitachi U-3010 UV-Vis spectrophotometer with $BaSO_4$ as the background between 250 and 800 nm. The BET surface area and pore volume of samples were measured by a Micromeritics ASAP 2010 nitrogen adsorption apparatus. The photoluminescence (PL) spectra of photocatalysts were recorded by a fluorescence spectrophotometer (Shimadzu Rf-540, Japan) using a 150 W xenon lamp as light source.

2.3. Photocatalytic Activity Measurement. RhB and 2,4-DCP were adopted as a representative organic pollutant to evaluate the photocatalytic activity of as-prepared samples under visible light irradiation. All photocatalytic experiments were conducted at room temperature. The catalyst (0.1 g) was immersed in a 250 mL Pyrex beaker with 100 mL of RhB solution (5 mg/L) or 2,4-DCP solution (20 mg/L). The suspensions were magnetically stirred in the dark for 40 min prior to irradiation to achieve adsorption-desorption equilibrium on the catalysts surface at room temperature. As for the photocatalytic reactions, a 300 W Xe arc lamp (LTIC 300BF, BoYi Ltd., China), with a 420 nm cut-off filter, was provided about 10 cm from the top surface of the suspensions, and the concentration of pollutants during photocatalysis was monitored by pulling out about 5.0 mL suspension periodically from the reactor and centrifuging for analysis. A UV-vis 8500 spectrophotometer (Shanghai Tianmei Science Apparatus Ltd., Co., China) was used to analyse the RhB and the high performance liquid chromatography (HPLC, Shimadzu) was assisted to determine the degradation of 2,4-DCP.

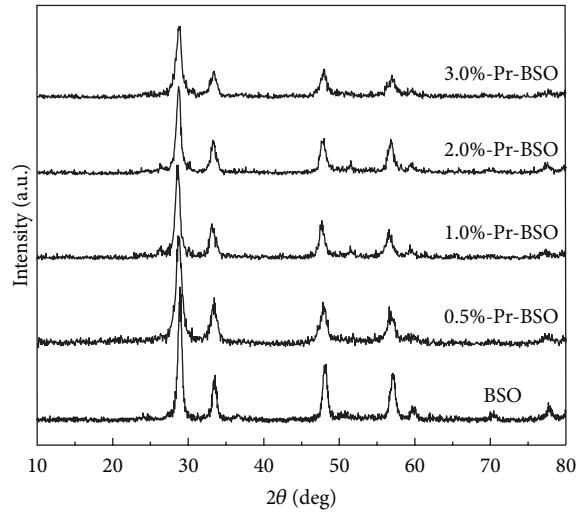

Figure 1: XRD analysis of different Pr-doped photocatalysts.

3. Results and Discussion

3.1. Phase Structure and Morphology of the As-Prepared Samples. BSO has three polymorphs (monoclinic α, face-centered cubic β, and cubic pyrochlore γ) [17], and the thermodynamically stable phase is α-BSO. In this paper, γ-BSO is obtained by a hydrothermal method. The powder XRD patterns of different Pr-doped BSO photocatalysts are presented in Figure 1. The XRD of samples shows several strong peaks at $2\theta = 28.8°$, 33.4°, 47.9°, and 56.9°, which represent the formation of pyrochlore structure. The diffraction peaks of pure BSO and the doped samples are similar and are found to be in a good agreement with the standard XRD patterns of cubic pyrochlore (JCPDS no. 87-0284). In terms of Pr-doped BSO, the peak at 28.8° corresponding to characteristic peak of the crystal plane (222) becomes broader and the relative intensity decreases with increasing Pr ion dosage. On the basis of the Scherrer equation, the average size of crystallite is calculated from the (222) peak of pyrochlore BSO. The results are summarized in Table 1, and the crystallite size decreased with increasing the amount of praseodymium. It can be attributed to the segregation of the praseodymium cations at the grain boundary, which inhibited the grain growth by restricting direct contact of grains [26].

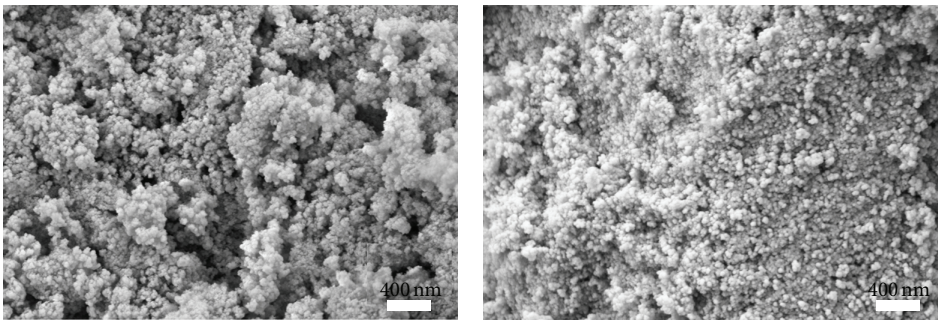

(a) (b)

Figure 2: SEM images of as-prepared samples: (a) BSO sample and (b) 1%-Pr-BSO sample.

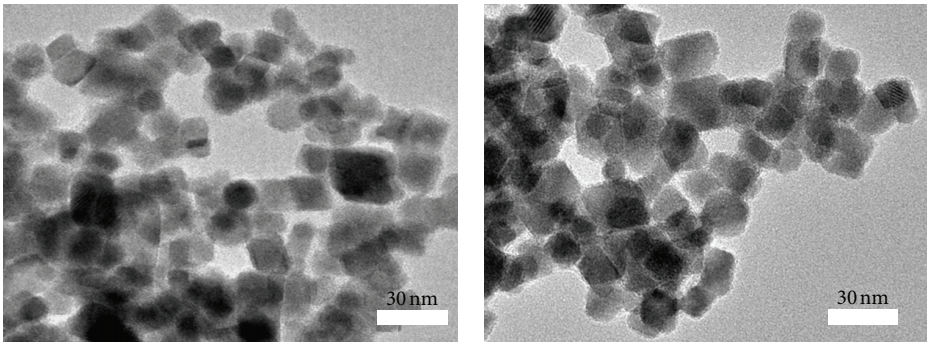

(a) (b)

Figure 3: TEM images of (a) BSO sample and (b) 1%-Pr-BSO sample.

Table 1: Crystallite size, BET surface areas, and pore size of different photocatalysts.

Sample	Crystallite size $D(222)/(\text{nm})$	S_{BET} (m^2/g)	Pore size (nm)
Pure BSO	13.5	45.3	9.4
0.5%-Pr-BSO	12.5	52.4	9.1
1.0%-Pr-BSO	11.3	61.6	8.1
2.0%-Pr-BSO	10.6	59.3	8.5
3.0%-Pr-BSO	9.8	54.7	8.8

Figure 2 shows the typical SEM images of pure BSO and 1.0%-Pr-BSO. As seen from the SEM micrograph, a large number of small particles are presented in Figure 2(a) (BSO) and Figure 2(b) (1.0%-Pr-BSO), demonstrating that high yield of products can be readily achieved through this approach. The diameters of particles that consisted of spherical clusters are around 8–20 nm.

Figures 3(a) and 3(b) show the TEM photograph of BSO and 1.0%-Pr-BSO, respectively. From Figure 3(a), it can be seen that BSO nanoparticles have irregular lump-like and spherical-like morphology, and the diameter is about 8–20 nm. However, 1.0%-Pr-BSO with a thin layer of about 2 nm in thickness has smaller grain size than BSO, which is consistent well with that calculated from the XRD data (Table 1).

3.2. N_2 Adsorption/Desorption Isotherm Analysis. The specific surface areas and pore size distributions of the BSO and 1.0%-Pr-BSO are measured using nitrogen gas sorption. The nitrogen adsorption-desorption isotherms of BSO (Figure 4(a)) and 1.0%-Pr-BSO (Figure 4(b)) exhibit stepwise adsorption and desorption (type-IV isotherm), indicating that the samples have mesoporous structure [26]. The specific surface area of BSO is 45.3 m^2/g, but after Pr coating, the BET surface area of 1.0%-Pr-BSO is increased to 61.6 m^2/g. High specific surface area of 1.0%-Pr-BSO will provide more active site for the photocatalytic reaction and enhance the interfacial reaction process. The pore size distribution plots of as-prepared samples calculated using the BJH equation from the absorption branch of the isotherm are shown in the inset of Figure 4. The result suggests that the spherical BSO sample has pronounced mesoporosity of narrow pore size distribution with average pore diameter around 12 nm. The specific surface area and pore diameter are calculated and also listed in Table 1.

3.3. X-Ray Photoelectron Spectroscopy Analysis. 1.0%-Pr-BSO is analyzed by XPS to discuss the elemental composition and chemical state on the BSO surface. The XPS survey spectrum is shown in Figure 5(a). It can be seen that 1.0%-Pr-BSO contains only five elements, namely, Bi, Sn, O, Pr, and C. Carbon probably originates from the calcinations residue of the precursor and adventitious hydrocarbon from the XPS instrument itself. In Bi 4f XPS spectrum (Figure 5(b)), two symmetric peaks at 164.3 eV and 159.1 eV, assigned to Bi4 $f_{5/2}$ and Bi4 $f_{7/2}$, correspond to Bi^{4+} and Bi^{3+}, respectively [27].

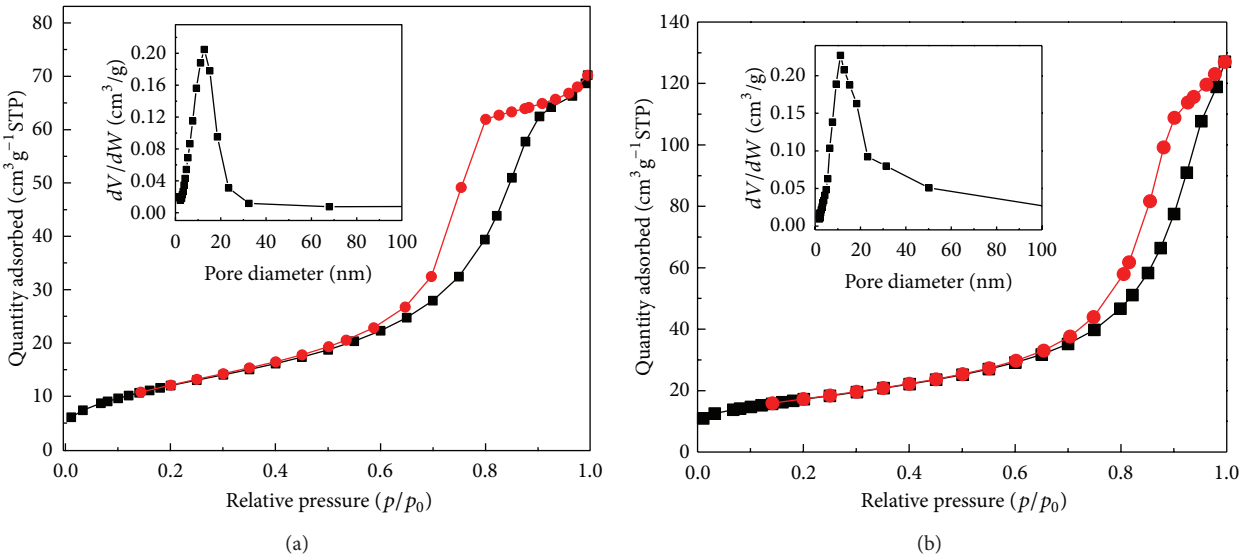

Figure 4: The N_2 sorption isotherms and pore size distribution of (a) BSO and (b) 1%-Pr-BSO.

Table 2: Maximum absorption and band gap of as-prepared samples.

Sample	Maximum absorption (nm)	Band gap (eV)
BSO	450	2.76
0.5%-Pr-BSO	436	2.84
1.0%-Pr-BSO	460	2.70
2.0%-Pr-BSO	422	2.94
3.0%-Pr-BSO	436	2.84

From the high resolution XPS spectra, it can be observed that the binding energies of Sn $3d_{5/2}$ and O 1s are 486.8 eV and 530.4 eV, respectively. Moreover, the binding energies of Sn $3d_{5/2}$ and O 1s are consistent with the literature values for Sn^{4+} and O^- in BSO [28, 29]. Figure 5(e) shows that the peaks of Pr $3d_{5/2}$ and Pr $3d_{3/2}$ are located at 933.7 eV and 953.5 eV. The results mean that the Pr oxidation state shows the presence of Pr^{3+} [21].

3.4. UV-Vis Diffuse Reflectance Spectra. Figure 6 displays UV-Vis diffuse reflection spectrum (DRS) of BSO precursors and Pr-BSO samples with different Pr contents. Figure 6(a) shows a phenomenon that the maximum absorptions of Pr-BSO photocatalysts, except the 1.0%-Pr-BSO sample, are slightly shifted to a shorter wavelength compared to those of pure BSO. The red shift of the absorption edge in 1.0%-Pr-BSO has been attributed to the charge-transfer transition between Pr ion f electrons and the BSO conduction or valence band [24]. As it is shown in Figure 6(b), the band gap achieved by extrapolation in 1.0%-Pr-BSO (460 nm) at the meeting point of the two tangents is about 2.70 eV. The maximum absorption wavelength and band gap of other photocatalysts are displayed in Table 2.

3.5. Photocatalytic Activity. To evaluate the photocatalytic activity of BSO and Pr-BSO with different molar ratios, the photodegradation of RhB and 2,4-DCP is carried out in aqueous dispersions under visible light illumination (Figure 7). In order to ensure adsorption/desorption equilibrium, adsorption experiments are carried out on all samples in the dark for 40 min. From Figure 7, it can be observed that the doped samples have a higher absorbtion rate compared with that of the undoped BSO. So it is obvious that Pr ions benefit the adsorption processes. When the BSO nanoparticles are modified by Pr ions, the Pr-BSO photocatalysts show an obvious enhanced photocatalytic activity and model pollutants (RhB and 2,4-DCP) are quickly decomposed with increasing irradiation time. After visible-light irradiation for 4 h, the degradation of RhB and 2,4-DCP over pure BSO reaches 52.0% and 50.2%, respectively. However, 90.8% of RhB and 87.6% of 2,4-DCP are degraded in 4 h irradiation over 1.0%-Pr-BSO. In this experiment, 1.0 mol% praseodymium is the optimal dopant content. It is found that the photocatalytic activity increased with increasing Pr loading to the optimum value and then decreased with further increase of Pr content. This result can be attributed to the influence of the space charge layer thickness [30]. As the doped contents are low, the surface barrier becomes higher and the space charge region becomes narrower, and at last the electron-hole pairs are efficiently separated before recombination. However, when the doped content is above its optimum, the space charge region becomes very narrow and the penetration depth of light into photocatalysts greatly exceeds the space charge layer, so that the electron and hole pairs recombine easily. Consequently, there is an optimum concentration of Pr ions.

3.6. Visible Light Photodegradation Mechanism. According to many previous investigations on the mechanism of photocatalytic degradation, it is widely confirmed that hydroxyl radicals ($^{\bullet}OH$) are a key active species in the photocatalytic process [31, 32]. It can attack the adsorbed toxic organic molecules to produce oxidized species and/or

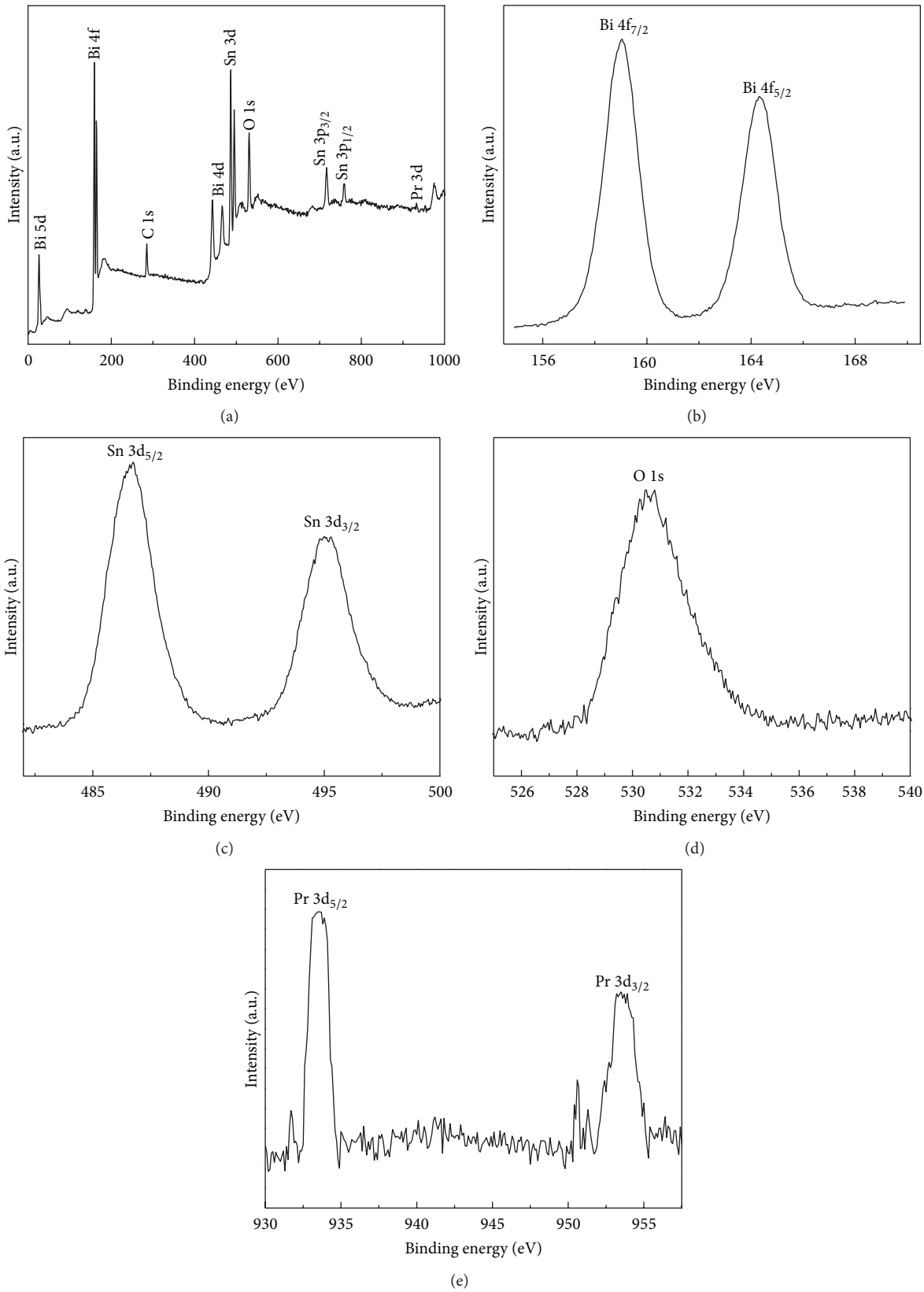

Figure 5: XPS spectra of 1%-Pr-BSO sample: (a) survey spectrum, (b) Bi 4f, (c) Sn 3d, (d) O 1s, and (e) Pr 3d.

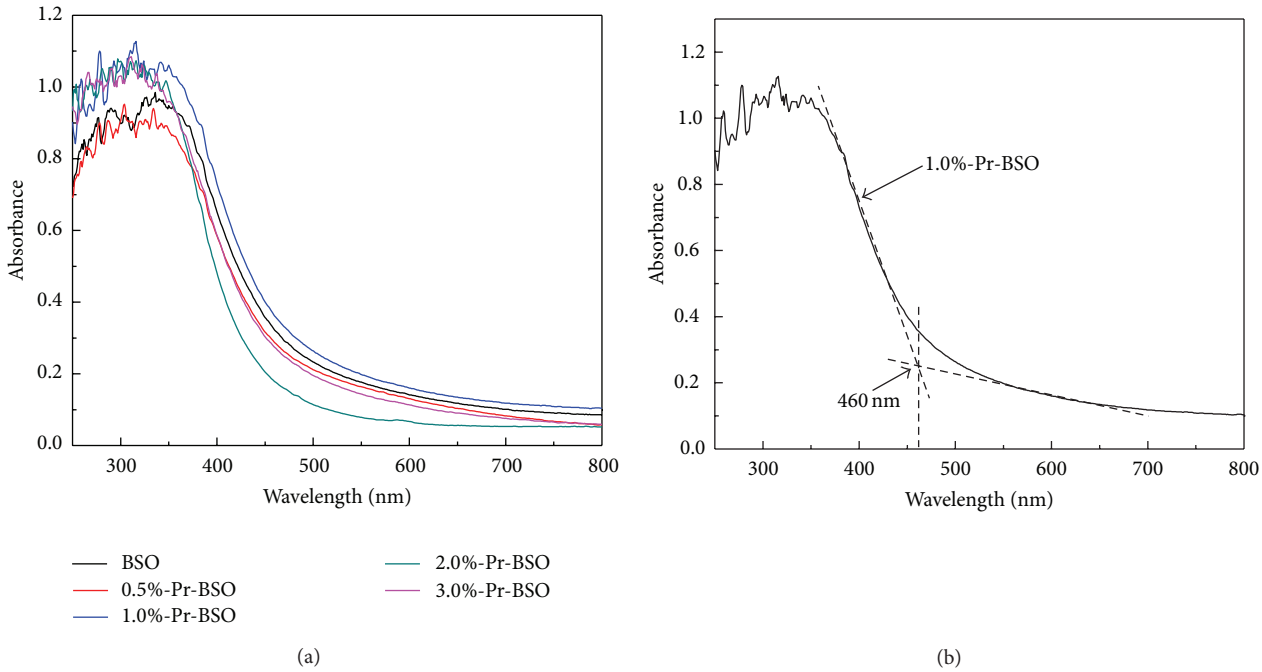

Figure 6: UV-Vis diffuse reflectance spectra of (a) different Pr-doped BSOs and (b) 1%-Pr-BSO.

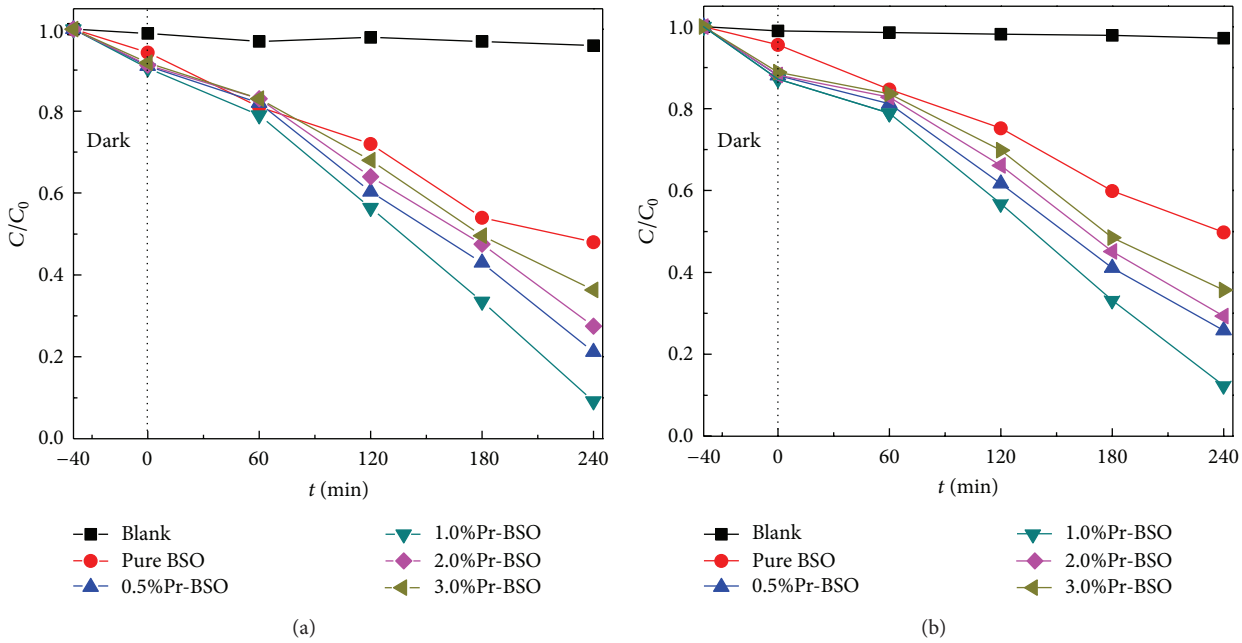

Figure 7: Degradation curves of (a) RhB and (b) 2,4-DCP.

decomposed products [33]. The analysis of $^{\bullet}$OH radical is performed by fluorescence technique using terephthalic acid, which can react with $^{\bullet}$OH radical in basic solution and generate 2-hydroxy terephthalic acid (TAOH) [34]. TAOH emits a strong fluorescence signal at around 426 nm on the excitation of its own 312 nm absorption band. Therefore, the formation of $^{\bullet}$OH radicals at the photocatalytic system was detected by PL technique using terephthalic acid as a probe molecule. Figure 8(a) shows the fluorescence spectra of 1%-Pr-BSO catalyst recorded at the same interval of irradiation time. It was obvious that the photoluminescence emission peak at about 426 nm was continuously enhanced. However, no fluorescence emission was observed in the absence of visible light. Figure 8(b) shows the plot of increase in fluorescence intensity against illumination time at 426 nm. The fluorescence intensity by visible light illumination in terephthalic acid solutions increased linearly against time. Based on the results, we could conclude that the large amount

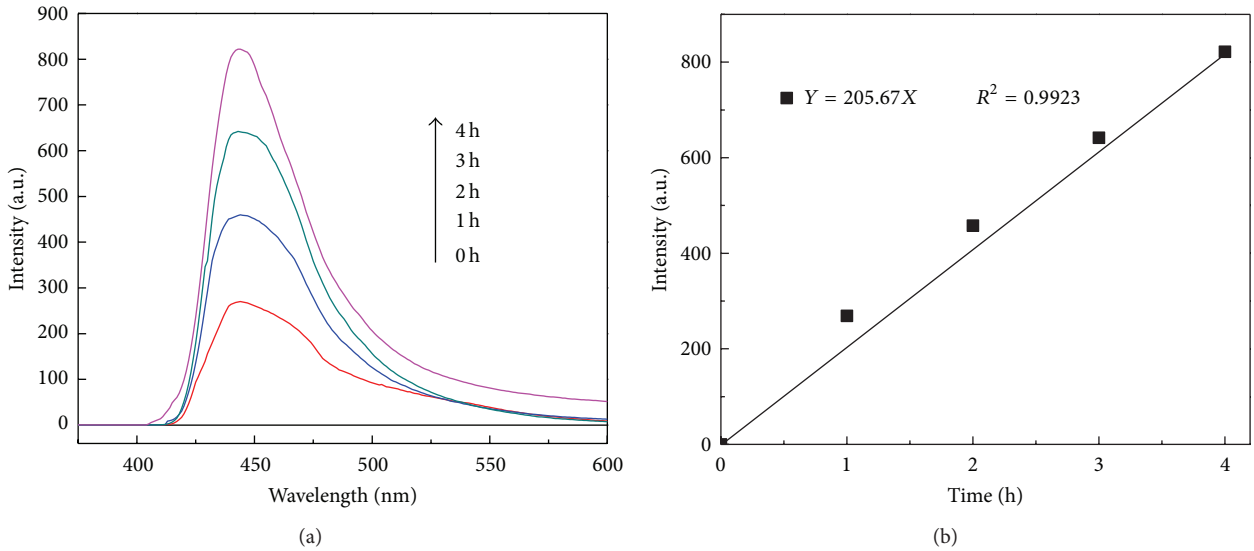

Figure 8: (a) •OH-trapping photoluminescence spectra of 1%-Pr-BSO in solution of terephthalic acid at room temperature (ex, 312 nm; em, 426 nm) and (b) plots of the induced PL intensities of 1%-Pr-BSO at 426 nm on the irradiation time.

of •OH was generated in the 1%-Pr-BSO photocatalytic system under visible light irradiation. The generation of •OH radicals was the main active specials in the photocatalytic system.

3.7. Discussion on Photocatalysis Process of Pr-BSO. Generally, the photoexcited state of Pr cations is generated by the absorption of light, corresponding to the transition of the electrons situated in the inner 4f orbital to the 4s orbital [35]. The excited state ions have the capability of transferring their excited energy to other adsorbed molecules (f-f transition) [36]. The transitions of 4f electrons can lead to the enforcement of the optical adsorption of catalysts [24]. Reddy et al. [37] reported that rare earth elements could be used as good electron acceptors, and it could capture excited electron and facilitate the separation of electron-hole pairs. As we all know, photons from visible irradiation are used to generate electrons and holes. The holes react with H_2O or OH^- to form hydroxyl radicals (•OH) and the electron-hole separation process is improved because BSO sample transfers photoelectrons to Pr when praseodymium appears on BSO surface [22, 30]. Subsequently, the electrons migrate from Pr to the adsorbed O_2 to form $O_2^{\bullet-}$. •OH and $O_2^{\bullet-}$ are important species which posses strong capability of oxidizing and breaking RhB and 2,4-DCP in aqueous solution [25]. The photocatalytic procedure is presented in Figure 9.

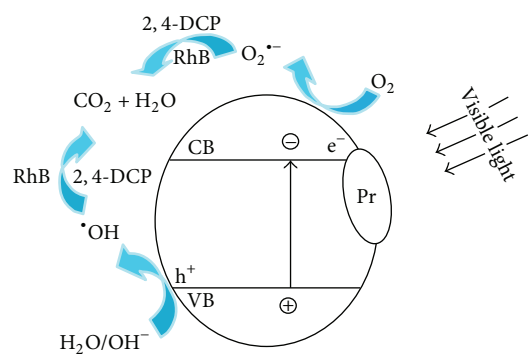

Figure 9: Photocatalysis process of Pr-doped BSO photocatalyst under visible light irradiation.

4. Conclusions

Pr-doped BSO materials prepared by a facile hydrothermal method were successfully used in the photocatalytic conversion of RhB and 2,4-DCP under visible light. The nanostructured Pr-BSO samples possessed high photocatalytic activity, fine-grained distribution and large surface area. The praseodymium doping effectively shifted the BSO absorption edge and retarded the growth of crystallite. The as-prepared Pr-BSO photocatalysts displayed approximately the spherical shape and owned the mesoporous surface. An optimal Pr doping concentration existed and was 1.0 mol%, and superfluous Pr would make negative influence on photodegradation efficiency.

Acknowledgment

This work was supported by Guangdong Water and Air Pollution Control Key Laboratory (2011 A060901002) open funded project.

References

[1] A. M. Ali, E. A. C. Emanuelsson, and D. A. Patterson, "Photocatalysis with nanostructured zinc oxide thin films: the relationship between morphology and photocatalytic activity under oxygen limited and oxygen rich conditions and evidence

for a Mars Van Krevelen mechanism," *Applied Catalysis B: Environmental*, vol. 97, no. 1-2, pp. 168–181, 2010.

[2] I. Bouzaida, C. Ferronato, J. M. Chovelon, M. E. Rammah, and J. M. Herrmann, "Heterogeneous photocatalytic degradation of the anthraquinonic dye, Acid Blue 25 (AB25): a kinetic approach," *Journal of Photochemistry and Photobiology A: Chemistry*, vol. 168, no. 1-2, pp. 23–30, 2004.

[3] Z. Liu, Z. Jian, J. Fang, X. Xu, X. Zhu, and S. Wu, "Low-temperature reverse microemulsion synthesis, characterization, and photocatalytic performance of nanocrystalline titanium dioxide," *International Journal of Photoenergy*, vol. 2012, Article ID 702503, 8 pages, 2012.

[4] J. Choi, H. Park, and M. R. Hoffmann, "Effects of single metal-ion doping on the visible-light photoreactivity of TiO_2," *Journal of Physical Chemistry C*, vol. 114, no. 2, pp. 783–792, 2010.

[5] M. Zhou, J. Zhang, B. Cheng, and H. Yu, "Enhancement of visible-light photocatalytic activity of mesoporous Au-TiO_2 nanocomposites by surface plasmon resonance," *International Journal of Photoenergy*, vol. 2012, Article ID 532843, 10 pages, 2012.

[6] H. Znad, M. H. Ang, and M. O. Tade, "Ta/TiO_2-and Nb/TiO_2-mixed oxides as efficient solar photocatalysts: preparation, characterization, and photocatalytic activity," *International Journal of Photoenergy*, vol. 2012, Article ID 548158, 9 pages, 2012.

[7] J. Yu, Q. Xiang, and M. Zhou, "Preparation, characterization and visible-light-driven photocatalytic activity of Fe-doped titania nanorods and first-principles study for electronic structures," *Applied Catalysis B: Environmental*, vol. 90, no. 3-4, pp. 595–602, 2009.

[8] N. Lu, X. Quan, J. Li, S. Chen, H. Yu, and G. Chen, "Fabrication of boron-doped TiO_2 nanotube array electrode and investigation of its photoelectrochemical capability," *Journal of Physical Chemistry C*, vol. 111, no. 32, pp. 11836–11842, 2007.

[9] J. Qian, G. Cui, M. Jing, Y. Wang, M. Zhang, and J. Yang, "Hydrothermal synthesis of nitrogen-doped titanium dioxide and evaluation of its visible light photocatalytic activity," *International Journal of Photoenergy*, vol. 2012, Article ID 198497, 6 pages, 2012.

[10] M. Sun, G. Chen, Y. Zhang, Q. Wei, Z. Ma, and B. Du, "Efficient degradation of azo dyes over Sb_2S_3/TiO_2 heterojunction under visible light irradiation," *Industrial and Engineering Chemistry Research*, vol. 51, no. 7, pp. 2897–2903, 2012.

[11] J. Ren, G. Liu, Y. Wang, and Q. Shi, "A novel method for the preparation of $Bi_2Ti_2O_7$ pyrochlore," *Materials Letters*, vol. 76, pp. 184–186, 2012.

[12] X. Lin, P. Lv, Q. Guan, H. Li, H. Zhai, and C. Liu, "Bismuth titanate microspheres: directed synthesis and their visible light photocatalytic activity," *Applied Surface Science*, vol. 258, no. 18, pp. 7146–7153, 2012.

[13] V. Cloet, P. Lommens, R. Hühne, K. de Buysser, S. Hoste, and I. van Driessche, "A study of the parameters influencing the microstructure of thick $La_2Zr_2O_7$ films," *Journal of Crystal Growth*, vol. 325, no. 1, pp. 68–75, 2011.

[14] L. Li, X. Zhang, L. Ji, P. Ning, and Q. Liao, "Dielectric properties and electrical behaviors of tunable $Bi_{1.5}MgNb_{1.5}O_7$ thin films," *Ceramics International*, vol. 38, no. 5, pp. 3541–3545, 2012.

[15] C. S. Rastomjee, R. S. Dale, R. J. Schaffer et al., "An investigation of doping of SnO_2 by ion implantation and application of ion-implanted films as gas sensors," *Thin Solid Films*, vol. 279, no. 1-2, pp. 98–105, 1996.

[16] C. A. Mims, A. J. Jacobson, R. B. Hall, and J. T. Lewandowski, "Methane oxidative coupling over nonstoichiometric bismuth-tin pyrochlore catalysts," *Journal of Catalysis*, vol. 153, no. 2, pp. 197–207, 1995.

[17] A. Ratna Phani, S. Manorama, and V. J. Rao, "Effect of additives on the response of sensors utilizing semiconducting oxide on carbon monoxide sensitivity," *Applied Physics Letters*, vol. 66, no. 25, pp. 3489–3491, 1995.

[18] Q. Tian, J. Zhuang, J. Wang, L. Xie, and P. Liu, "Novel photocatalyst, $Bi_2Sn_2O_7$, for photooxidation of As(III) under visible-light irradiation," *Applied Catalysis A: General*, vol. 425-426, pp. 74–78, 2012.

[19] L. Moens, P. Ruiz, B. Delmon, and M. Devillers, "Evaluation of the role played by bismuth molybdates in $Bi_2Sn_2O_7$-MoO_3 catalysts used for partial oxidation of isobutene to methacrolein," *Applied Catalysis A: General*, vol. 180, no. 1-2, pp. 299–315, 1999.

[20] H. W. Kim, S. H. Shim, J. W. Lee et al., "$Bi_2Sn_2O_7$ nanoparticles attached to SnO_2 nanowires and used as catalysts," *Chemical Physics Letters*, vol. 456, no. 4–6, pp. 193–197, 2008.

[21] J. Wu, F. Huang, X. Lü, P. Chen, D. Wan, and F. Xu, "Improved visible-light photocatalysis of nano-$Bi_2Sn_2O_7$ with dispersed s-bands," *Journal of Materials Chemistry*, vol. 21, no. 11, pp. 3872–3876, 2011.

[22] J. Yang, J. Dai, and J. Li, "Synthesis, characterization and degradation of Bisphenol A using Pr, N co-doped TiO_2 with highly visible light activity," *Applied Surface Science*, vol. 257, no. 21, pp. 8965–8973, 2011.

[23] H. X. Shi, T. Y. Zhang, T. C. An et al., "Enhancement of photocatalytic activity of nano-scale TiO_2 particles co-doped by rare earth elements and heteropolyacids," *Journal of Colloid and Interface Science*, vol. 380, no. 1, pp. 121–127, 2012.

[24] V. Stengl, S. Bakardjieva, and N. Murafa, "Preparation and photocatalytic activity of rare earth doped TiO_2 nanoparticles," *Materials Chemistry and Physics*, vol. 114, no. 1, pp. 217–226, 2009.

[25] S. X. Wu, J. Z. Fang, X. X. Xu et al., "Microemulsion synthesis, characterization of highly visible light responsive rare earth doped Bi_2O_3," *Photochemistry and Photobiology*, vol. 88, no. 5, pp. 1205–1210, 2012.

[26] X. Z. Ding and X. H. Liu, "Correlation between anatase-to-rutile transformation and grain growth in nanocrystalline titania powders," *Journal of Materials Research*, vol. 13, no. 9, pp. 2556–2559, 1998.

[27] M. Ge, Y. F. Li, L. Liu et al., "Bi_2O_3—Bi_2WO_6 composite microspheres: hydrothermal synthesis and photocatalytic performances," *The Journal of Physical Chemistry*, vol. 115, no. 13, pp. 5220–5225, 2011.

[28] Y. C. Zhang, Z. N. Du, K. W. Li, and M. Zhang, "Size-controlled hydrothermal synthesis of SnS_2 nanoparticles with high performance in visible light-driven photocatalytic degradation of aqueous methyl orange," *Separation and Purification Technology*, vol. 81, no. 1, pp. 101–107, 2011.

[29] M. Takeuchi, Y. Shimizu, H. Yamagawa, T. Nakamuro, and M. Anpo, "Preparation of the visible light responsive N^3—doped WO_3 photocatalyst by a thermal decomposition of ammonium paratungstate," *Applied Catalysis B: Environmental*, vol. 110, no. 2, pp. 1–5, 2011.

[30] A.-W. Xu, Y. Gao, and H.-Q. Liu, "The preparation, characterization, and their photocatalytic activities of rare-earth-doped TiO_2 nanoparticles," *Journal of Catalysis*, vol. 207, no. 2, pp. 151–157, 2002.

[31] K.-I. Ishibashi, A. Fujishima, T. Watanabe, and K. Hashimoto, "Detection of active oxidative species in TiO_2 photocatalysis using the fluorescence technique," *Electrochemistry Communications*, vol. 2, no. 3, pp. 207–210, 2000.

[32] S. X. Wu, J. Z. Fang, W. C. Xu et al., "Hydrothermal synthesis, characterization of visible-light-driven α-Bi_2O_2 enhanced by Pr^{3+} doping," *Journal of Chemical Technology and Biotechnology*, vol. 2013, 8 pages, 2013.

[33] Q. Xiang, J. Yu, and P. K. Wong, "Quantitative characterization of hydroxyl radicals produced by various photocatalysts," *Journal of Colloid and Interface Science*, vol. 357, no. 1, pp. 163–167, 2011.

[34] Y. Yang, G. Zhang, and W. Xu, "Facile synthesis and photocatalytic properties of $AgAgClTiO_2$/rectorite composite," *Journal of Colloid and Interface Science*, vol. 376, no. 1, pp. 217–223, 2012.

[35] K. Ebitani, Y. Hirano, and A. Morikawa, "Rare earth Ions as heterogeneous photocatalysts for the decomposition of dinitrogen monoxide (N_2O)," *Journal of Catalysis*, vol. 157, no. 1, pp. 262–265, 1995.

[36] X. Yan, J. He, D. G. Evans, X. Duan, and Y. Zhu, "Preparation, characterization and photocatalytic activity of Si-doped and rare earth-doped TiO_2 from mesoporous precursors," *Applied Catalysis B: Environmental*, vol. 55, no. 4, pp. 243–252, 2005.

[37] J. K. Reddy, B. Srinivas, V. D. Kumari et al., "Sm^{3+}-doped Bi_2O_3 photocatalyst prepared by hydrothermal synthesis," *ChemCatChem*, vol. 3, no. 2, pp. 360–364, 2009.

Hindawi Publishing Corporation
International Journal of Photoenergy
Volume 2013, Article ID 570587, 9 pages
http://dx.doi.org/10.1155/2013/570587

Research Article

Solar Photocatalytic Degradation of Bisphenol A on Immobilized ZnO or TiO_2

Andreas Zacharakis,[1] Efthalia Chatzisymeon,[1] Vassilios Binas,[2] Zacharias Frontistis,[1] Danae Venieri,[1] and Dionissios Mantzavinos[1,3]

[1] *Department of Environmental Engineering, Technical University of Crete, Polytechneioupolis, 73100 Chania, Greece*
[2] *Institute of Electronic Structure and Laser (IESL), FORTH, P.O. Box 1527, Vassilika Vouton, 71110 Heraklion, Greece*
[3] *Department of Chemical Engineering, University of Patras, Caratheodory 1, University Campus, 26504 Patras, Greece*

Correspondence should be addressed to Dionissios Mantzavinos; mantzavinos@chemeng.upatras.gr

Received 30 May 2013; Accepted 14 July 2013

Academic Editor: Christos Trapalis

The removal of bisphenol A (BPA) under simulated solar irradiation and in the presence of either TiO_2 or ZnO catalysts immobilized onto glass plates was investigated. The effect of various operating conditions on degradation was assessed including the amount of the immobilized catalyst (36.1–150.7 mg/cm^2 for TiO_2 and 0.5–6.8 mg/cm^2 for ZnO), initial BPA concentration (50–200 μg/L), treatment time (up to 90 min), water matrix (wastewater, drinking water, and pure water), the addition of H_2O_2 (25–100 mg/L), and the presence of other endocrine disruptors in the reaction mixture. Specifically, it was observed that increasing the amount of immobilized catalyst increases BPA conversion and so does the addition of H_2O_2 up to 100 mg/L. Moreover, BPA degradation follows first-order reaction kinetics indicating that the final removal is not practically affected by the initial BPA concentration. Degradation in wastewater is slower than that in pure water up to five times, implying the scavenging behavior of effluent's constituents against hydroxyl radicals. Finally, the presence of other endocrine disruptors, such as 17α-ethynylestradiol, spiked in the reaction mixture at low concentrations usually found in environmental samples (i.e., 100 μg/L), neither affects BPA degradation nor alters its kinetics to a considerable extent.

1. Introduction

Endocrine disrupting compounds (EDCs) constitute an important class of emerging environmental contaminants, which pose an increasing threat to aquatic organisms, as well as to human health [1]. In particular, the exposure to EDCs has been linked with altering functions of the endocrine system in male fish such as vitellogenin induction and feminized reproductive organs [2]. Moreover, the increasing incidence of cancer and the hypothesis of a decreasing reproductive fitness of men are thought to be attributed to endocrine disruptors. Among various EDCs, bisphenol A (BPA) is well-known for its interference with the endocrine system of living beings [3, 4]. BPA is widely used in the manufacturing of numerous chemical products, such as CDs, DVDs, drink containers, electrical and electronic equipment, and protective coatings [1, 5]. These substances enter municipal wastewater treatment plants (WWTPs) through either human excretion or their direct disposal in the sewage system. Currently, when EDCs enter conventional biological WWTP, only a small amount of these chemicals are removed via biodegradation processes because most of them are xenobiotics and thus non-biodegradable [6]. Therefore, the majority of EDCs remain soluble in the effluent, and they are discharged to aquatic bodies. In the last decade, several studies have confirmed the occurrence of EDCs at the level of ng/L–μg/L in inland waters (rivers and streams) and wastewaters (outlets of municipal and industrial WWTPs) worldwide [7–11]. Not only this, but it has been found that these compounds can pose a potential danger to fish and other aquatic organisms, even at low concentrations of 0.1–10 ng/L [12]. Thus, it is necessary to look further on the removal mechanisms, in order to improve

the efficiency of the existing treatment systems and to develop new and reliable treatment strategies to remove EDCs from wastewaters.

Semiconductor photocatalysis using solar radiation as the source of photons for the activation of the catalyst has received considerable attention over the past several years. Several heterogeneous photocatalysts have been investigated, and, amongst them, the use of TiO_2 under ultraviolet and/or visible light has extensively been researched. Another photocatalyst that absorbs over a large fraction of the solar spectrum is ZnO with a gap energy of 3.2 eV. The photocatalytic mechanism of ZnO is similar to that of TiO_2 [13]. Moreover, solar photocatalysis is considered as a cost-effective and sustainable treatment technique due to the utilization of solar energy (an abundant source of energy). However, the biggest problem with slurry photocatalysis has been recognized to be the need for a posttreatment recovery step [14, 15]. Therefore, research has been conducted to produce catalysts on supports that would keep the catalyst powder out of the treated water and sufficiently reduce even more the cost of the photocatalytic process, since there will be no need for catalyst aftertreatment. So far, few studies have dealt with the treatment of EDCs by means of TiO_2 or ZnO catalysts immobilized onto supports, such as glass [4, 16], PTFE mesh sheets [17], titanium substrates [18, 19], and polyurethane foam cubes [20].

Hence, in this work, the efficacy of solar photocatalytic process to remove BPA from aqueous environmental samples was investigated. For this purpose, two different photocatalytic materials, namely, ZnO and TiO_2, were immobilized onto appropriate glass substrate by means of a heat attachment technique. The effect of various operating parameters, such as the immobilized catalyst amount, the initial BPA concentration, the treatment time, the water matrix, the addition of H_2O_2, and the presence of other organic substances, on process efficiency, was investigated.

2. Materials and Methods

2.1. Materials. BPA and 17α-ethynylestradiol (EE2) were purchased from Sigma-Aldrich, while ZnO (≥99%, particle size < 100 nm, 15–25 m^2/g BET surface area) and TiO_2-P25 (anatase : rutile 75 : 25, 21 nm primary crystallite particle size, 50 m^2/g BET surface area) were purchased from Fluka and Degussa-Evonik Corp., respectively. The water matrix was either of the following three: (i) wastewater (WW) collected from the outlet of the secondary treatment of the municipal WWTP of Chania, W. Crete, Greece; (ii) commercially available bottled water, which will be referred to in the text as drinking water (DW); and (iii) ultrapure water (UPW) at pH = 6.1 taken from a water purification system (EASYpureRF-Barnstead/Thermolyne, USA). The main properties of WW and DW are given in Table 1.

2.2. Catalyst Preparation. The ZnO or TiO_2 catalyst powders were immobilized on glass plates (1.5 cm × 1.5 cm) by a heat attachment method. Analytically, the glass plates were first treated with a 38% HF solution and then washed with 0.01 M NaOH in order to increase the number of OH groups and achieve better contact of the catalyst on glass plates [14]. Moreover, a suspension of 8 g/L catalyst in distilled water was prepared. This suspension was sonicated at 80 kHz for 120 min in order to improve the dispersion of the solid catalyst in water. Afterwards, the sonicated catalyst solution was poured on the glass plates at various volumes, ranging from some μL to about 10 mL and then placed in an oven at 120°C for 60 min. After drying, the glass plates were calcined at 500°C for 180 min. Finally, the glass plates were washed with distilled water to remove the loosely attached catalytic particles.

Table 1: Properties of wastewater and drinking water matrices used in this study.

Parameter	Wastewater	Drinking water
pH	8	7.7
TOC (mg/L)	7.8	0.3
COD (mg/L)	24	ND
Conductivity (μs/cm)	820	329
HCO_3^- (mg/L)	190	188
Cl^- (mg/L)	220	<5
NO_2^- (mg/L)	57	<0.09
NO_3^- (mg/L)	26	<5

ND: not determined.

2.3. Catalyst Characterization Techniques. The crystal structure, particle size, and morphology were examined with a powder X-ray diffraction (XRD) system and scanning electron microscopy (SEM), respectively. XRD patterns were collected on a Rigaku D/MAX-2000H rotating anode diffractometer (Cukα radiation) equipped with a secondary pyrolytic graphite monochromator operating at 40 kV and 80 mA over the 2θ collection range of 10–80°. The scan rate was 0.05/min with a step size of 0.01. Surface morphology of the catalytic plates was carried out on a JEOL JSM-6400V SEM instrument.

2.4. Photocatalytic Experiments. Photocatalytic experiments were performed using a solar simulator (Newport, model 96000) equipped with a 150 W xenon ozone-free lamp and an Air Mass 1.5 Global Filter (Newport, model 81094), simulating solar radiation reaching the surface of the earth at a zenith angle of 48.2°.

The incident radiation intensity on the photochemical reactor in the UV region of the electromagnetic spectrum was measured actinometrically using 2-nitrobenzaldehyde (purchased from Sigma-Aldrich) as the chemical actinometer [21], and it was found to be 16.5 10^{-5} einstein/m^2. In a typical photocatalytic run, 64 mL of the water matrix spiked with the appropriate amount of the organic substance was fed in a cylindrical pyrex cell and the ZnO or TiO_2 catalytic plate was added, while the cell was open to the atmosphere. The solar simulator was placed on top of the liquid surface, while the catalytic glass plate was held by a Ti support dipped into

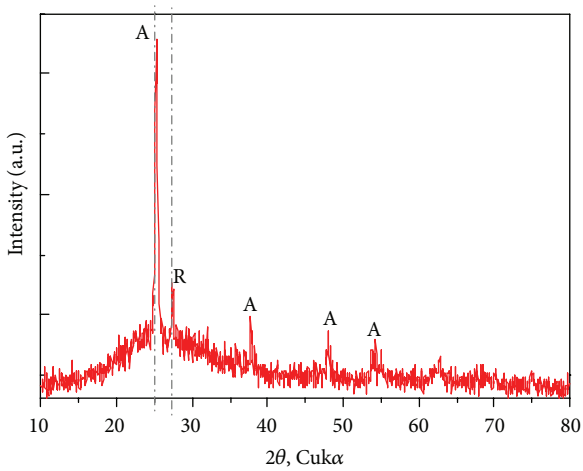

Figure 1: XRD pattern of the TiO_2 immobilized particles on glass plate (A: anatase; R: rutile).

the reaction mixture. Samples of about 1 mL were periodically taken from the cell and analyzed as follows.

2.5. Analytical Techniques. High-performance liquid chromatography (Alliance 2690, Waters) was employed to monitor the concentrations of BPA and EE2. Separation was achieved on a Luna C-18(2) column (5 μm, 250 mm × 4.6 mm) and a security guard column (4 mm × 3 mm), both purchased from Phenomenex. The mobile phase consists of 35 : 65 UPW : acetonitrile eluted isocratically at 1 mL/min and 30°C, while the injection volume was 100 μL. Detection was achieved through a fluorescence detector (Waters 474), in which the excitation wavelength was 280 nm and the emission wavelength was 305 nm. Under these conditions, the retention time for BPA was 4.3 min, the limit of detection was 0.68 μg/L, and the limit of quantitation was 2.32 μg/L; the respective values for EE2 were 5.1 min, 0.63 μg/L, and 2.11 μg/L. Residual H_2O_2 concentration was monitored using Merck peroxide test strips in the range 0–100 mg/L. Changes in effluent pH during photocatalytic treatment were checked using a Toledo 225 pH meter.

3. Results and Discussion

3.1. TiO_2 Catalyst Plates. Figure 1 shows XRD pattern of the TiO_2 immobilized particles on glass plate subjected to heat treatment at 500°C for 3 h. Peaks at 2θ values of 25° and 27° correspond to the anatase (101) and rutile (110) planes, respectively. The crystalline size (D) was calculated at 17 nm using the Scherrer equation:

$$D = \frac{k\lambda}{\beta \cos\theta}, \tag{1}$$

where k is a constant equal to 0.9, λ is the wavelength of characteristics X-ray applied (0.15418 nm), β is the full width at half maximum of the anatase (101) peak obtained by XRD, and θ is the Bragg angle.

The phase content of TiO_2 particles can be calculated as follows:

$$f_A = \frac{1}{1 + I_R/0.79 I_A}, \tag{2}$$

where f_A is the content of anatase, and I_A and I_R are the integrated intensities of the anatase (101) and rutile (110) peaks, respectively. The TiO_2 catalytic plate mainly consists of the anatase phase with mirror rutile phase (70 : 30).

Figure 2 shows SEM images of the immobilized catalytic particles on glass plates with different amounts of TiO_2 in the range 81.3–339.2 mg (36.1–150.7 mg/cm^2). The TiO_2 layer is homogeneous with a porous surface, while the morphology of TiO_2 particles is amorphous. As the amount of TiO_2 increases the homogeneity increases and so does the film thickness in the range 2–6 μm.

The effect of increasing the amount of immobilized TiO_2 on BPA removal is shown in Figure 3; the 90 min conversion increases from 60% to 80% as TiO_2 increases from 36.1 to 150.7 mg/cm^2, and this is expected since more catalyst surface sites are available for reaction at higher catalyst loadings. An additional run was performed in the absence of catalyst yielding only 15% photolytic removal after 90 min. Since TiO_2 in slurry has extensively been used for photocatalytic purposes, an extra run was carried out to compare the efficiencies of slurry and immobilized catalysts. Hence, 0.65 mg TiO_2 powder was added to the reaction mixture, and complete removal of 100 μg/L BPA could be achieved after 35 min of reaction (data not shown). This shows that slurry catalysts, even at extremely low concentrations, yield higher reaction rates than the immobilized systems, presumably due to lower mass transfer limitations.

3.2. ZnO Catalyst Plates. Figure 4 shows XRD pattern of the ZnO immobilized particles on glass plate subjected to heat treatment at 500°C for 3 h. The sharp intense peaks of ZnO confirm the good crystalline nature of ZnO and form (100), (002), (101), (102), (110), (103), (200), and (112) reflections of hexagonal ZnO. The size of the particles was calculated at 47 nm using (1).

Figure 5 shows SEM images of the immobilized catalytic particles for the fresh and used ZnO. Moreover, the initial glass plate, as well as the HF-treated surface, is shown. It is evident that the glass surface becomes rough after acid treatment (Figure 5(b)), thus facilitating catalyst attachment. Figure 5(c) shows the dispersion of fresh ZnO onto the glass surface, where agglomeration of the particles takes place to some extent. Conversely, Figure 5(d) shows the SEM image of a plate that has been employed for more than 30 h of photocatalytic experiments under various conditions (including runs with wastewater). It is observed that particles dispersion is more homogeneous than that of the fresh plate and this is probably due to the presence of several organic and/or inorganic impurities accumulated onto the surface during its photocatalytic use. The film thickness is in the range 2–4 μm.

The effect of increasing ZnO loading in the range 1.2–15.3 mg (0.5–6.8 mg/cm^2) on BPA removal is shown in

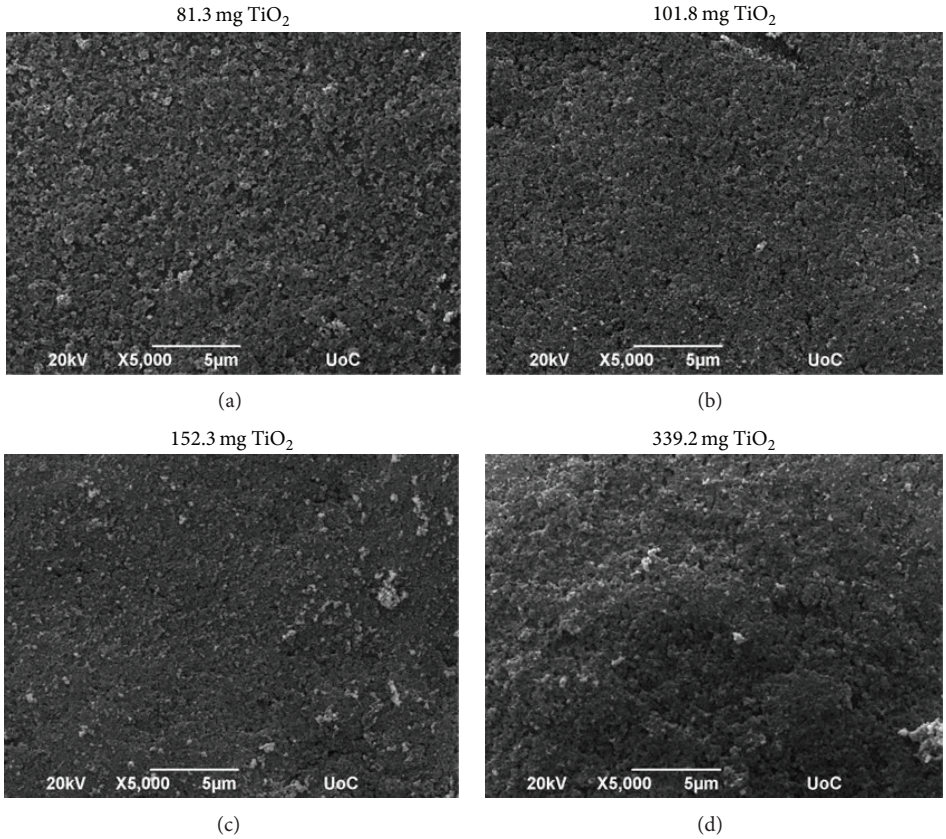

Figure 2: SEM images of TiO_2 immobilized particles on glass plate with increasing amount of catalyst from 81.3 to 339.2 mg (36.1 to 150.7 mg/cm^2).

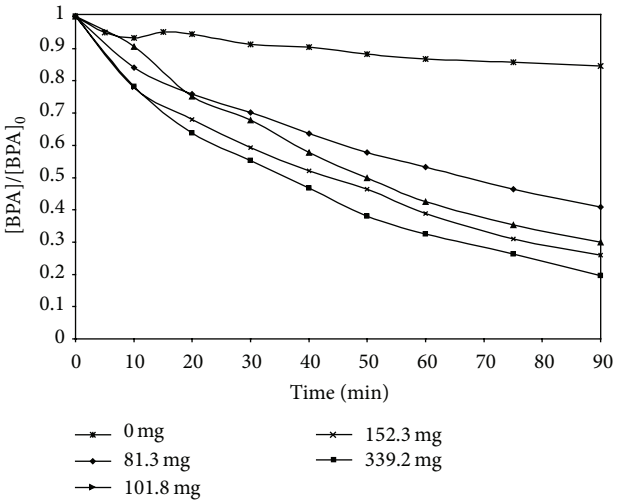

Figure 3: Effect of TiO_2 loading on the conversion of 100 μg/L BPA in UPW.

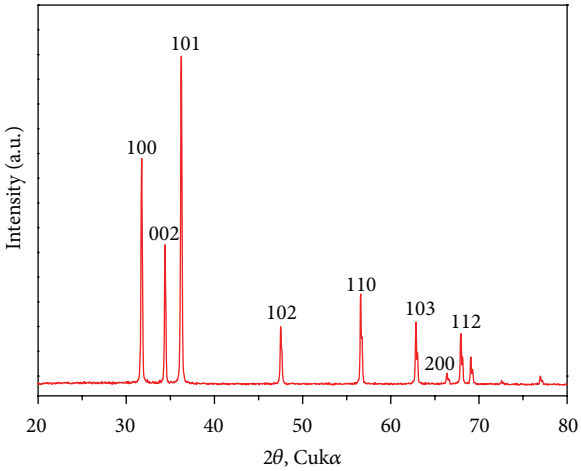

Figure 4: XRD pattern of the ZnO immobilized particles on glass plate.

Figure 6, where the 90 min conversion is enhanced from 52% to 90%. Notably, for ZnO loadings between 1.6 and 2.5 mg/cm^2, BPA degradation remains practically unchanged at about 65%.

Another interesting finding is that for the same volume of the catalyst aqueous suspension (i.e., from 200 μL to 10 mL), the quantity of ZnO attached onto the glass support is 1-2 orders of magnitude lower than that of TiO_2. This is due to the fact that TiO_2 is known to have more hydroxyl anions on its surface than ZnO, thus enhancing the adhesion of

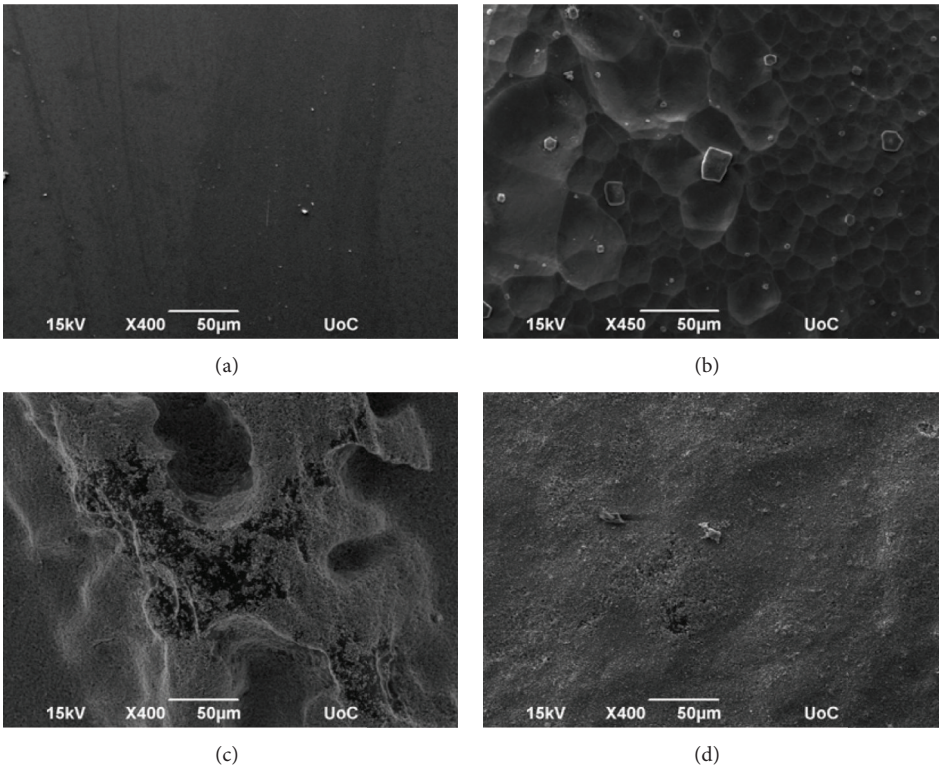

Figure 5: SEM images of (a) glass plates; (b) glass plates treated with HF solution; (c) 3.7 mg fresh ZnO (1.6 mg/cm^2) immobilized onto the plate; and (d) 3.7 mg used ZnO (1.6 mg/cm^2) immobilized onto the plate.

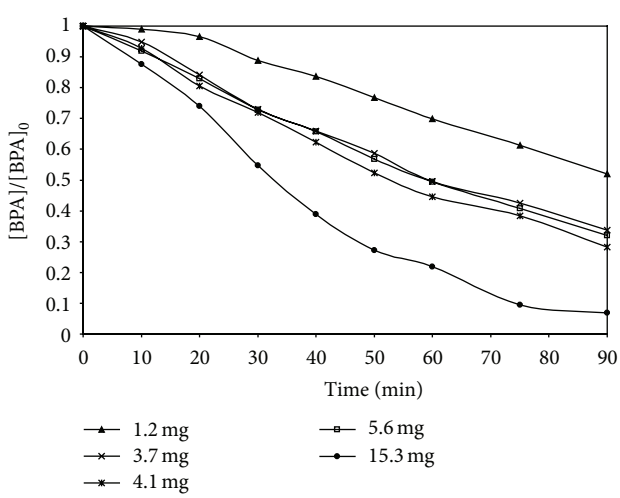

Figure 6: Effect of ZnO loading on the conversion of 100 μg/L BPA in UPW.

powder onto the appropriate substrate. Nevertheless, this does not seem to affect the catalytic activity of ZnO which, on a catalyst-loading basis, is more efficient than TiO_2; for example, a common BPA conversion can be achieved after 90 min at 1.8 mg/cm^2 ZnO or 45.2 mg/cm^2 TiO_2, as can be observed from Figures 3 and 6.

3.3. Effect of Initial BPA Concentration. The effect of initial BPA concentration (50, 100, and 200 μg/L) on its degradation over 150.7 mg/ cm^2 TiO_2 was investigated and concentration-time profiles were followed (data not shown). The 90 min BPA removal was 77 ± 3% irrespective of the initial BPA concentration, thus implying first-order kinetics, that is,

$$-\frac{d\,[\mathrm{BPA}]}{dt} = k_{\mathrm{app}}\,[\mathrm{BPA}] \Longleftrightarrow \ln\frac{[\mathrm{BPA}]_o}{[\mathrm{BPA}]} = k_{\mathrm{app}}t \Longleftrightarrow \ln(1-X) = -k_{\mathrm{app}}t, \quad (3)$$

where k_{app} is an apparent reaction rate constant and X is BPA conversion independent of its initial concentration $[\mathrm{BPA}]_o$.

Figure 7(a) confirms that the reaction approaches, indeed, first-order kinetics. Plotting the logarithm of normalized BPA concentration against time results in straight lines (the coefficient of linear regression of data fitting, r^2, is between 99.3% and 99.6%) with a nearly common slope, which corresponds to the apparent reaction rate constant; this is 15 ± 1 10^{-3} min^{-1}.

The effect of initial BPA concentration was also studied at 1.6 mg/cm^2 ZnO; the 90 min removal was 64±2% irrespective of the initial concentration. Figure 7(b) shows the respective first-order degradation kinetics, from which the apparent rate constant is computed at 11 ± 1 10^{-3} min^{-1} (the coefficient of linear regression of data fitting, r^2, is between 99.4% and 99.6%).

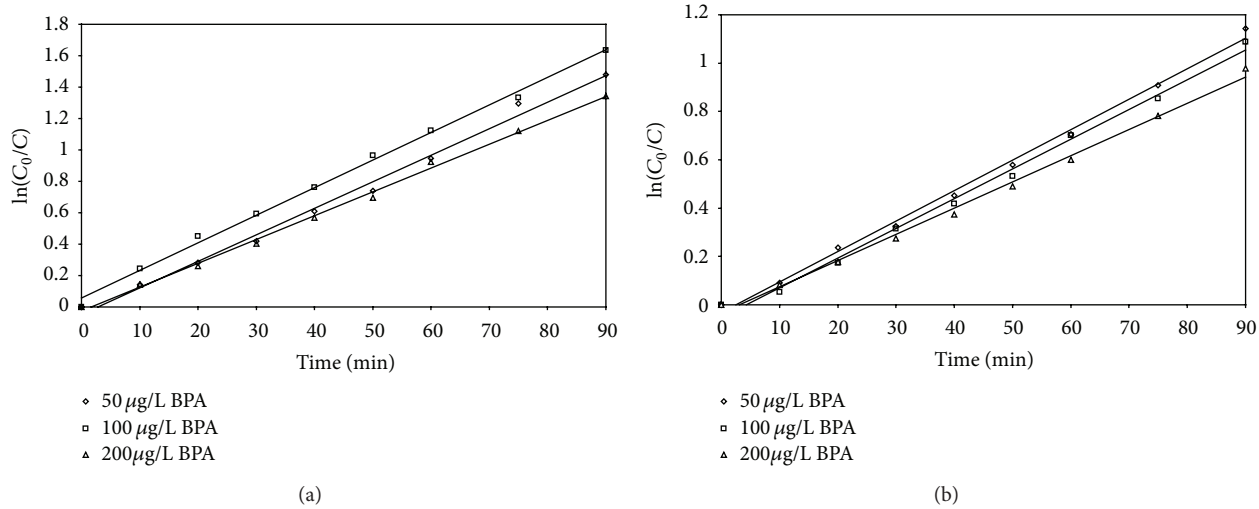

Figure 7: Effect of initial BPA concentration on its degradation in UPW at (a) 150.7 mg/cm^2 TiO_2 and (b) 1.6 mg/cm^2 ZnO. Plot of (3).

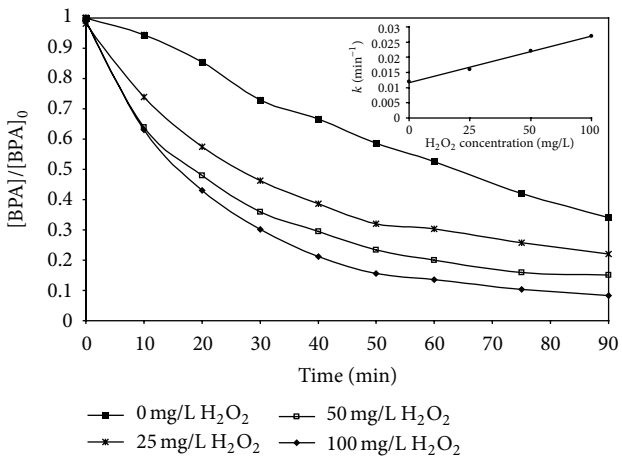

Figure 8: Effect of H_2O_2 on the conversion of 100 μg/L BPA in UPW at 1.6 mg/cm^2 ZnO. Inset graph: change of k_{app} with H_2O_2 concentration.

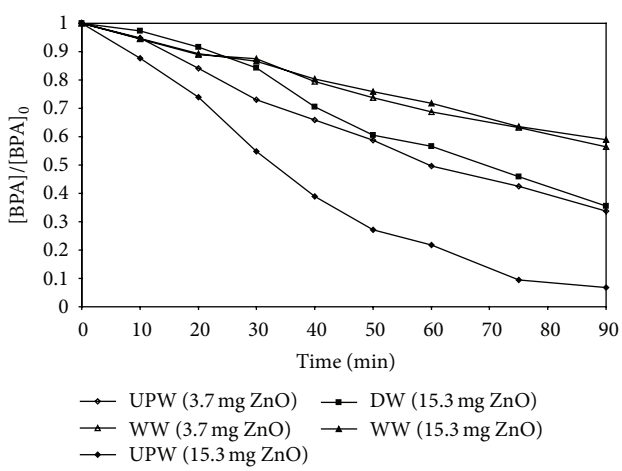

Figure 9: Effect of water matrix on the conversion of 100 μg/L BPA at two ZnO loadings.

From the results presented so far, it is evident that both catalysts exhibit a similar performance for BPA degradation through first-order kinetics. We decided to expand experimentation with ZnO since (a) TiO_2 has extensively been studied in the literature for several environmental applications and (b) ZnO has the potential to achieve improved photocatalytic performance as it absorbs over a wide region of the UV-A spectrum [22]. It should be mentioned here that ZnO is generally more susceptible to photo corrosion and/or chemical corrosion (i.e., leaching) than TiO_2 and this is a point of concern; nonetheless, our previous studies [13] showed that ZnO was remarkably stable during the photocatalytic oxidation of slightly alkaline, wastewater matrices.

3.4. Effect of Hydrogen Peroxide. The addition of oxidizing species increases the efficiency of the photocatalytic process because H_2O_2 is an electron acceptor and reacts with the electrons of the photo-activated surface of the catalyst:

$$H_2O_2 + e^- \longrightarrow {}^{\bullet}OH + OH^- \quad (4)$$

Thus, the addition of peroxide constitutes an extra source of hydroxyl radicals and increases the photoreactivity of ZnO during the photocatalytic degradation [23].

According to our findings (Figure 8), increasing hydrogen peroxide concentration from 0 to 100 mg/L results in increased removal; for example, the 90 min conversion is 66%, 78%, 85%, and 92% at 0, 25, 50, and 100 mg/L H_2O_2, respectively. The inset of Figure 8 shows that the respective apparent rate constants increase almost linearly with the amount of H_2O_2 added up to 100 mg/L.

It should be noted here that H_2O_2 was only partly consumed during the previous photocatalytic runs as confirmed with the peroxide test strips; unfortunately, precise determination of residual peroxide was not possible with this method.

3.5. Effect of Water Matrix. Figure 9 clearly shows that BPA degradation is impeded in complex water matrices

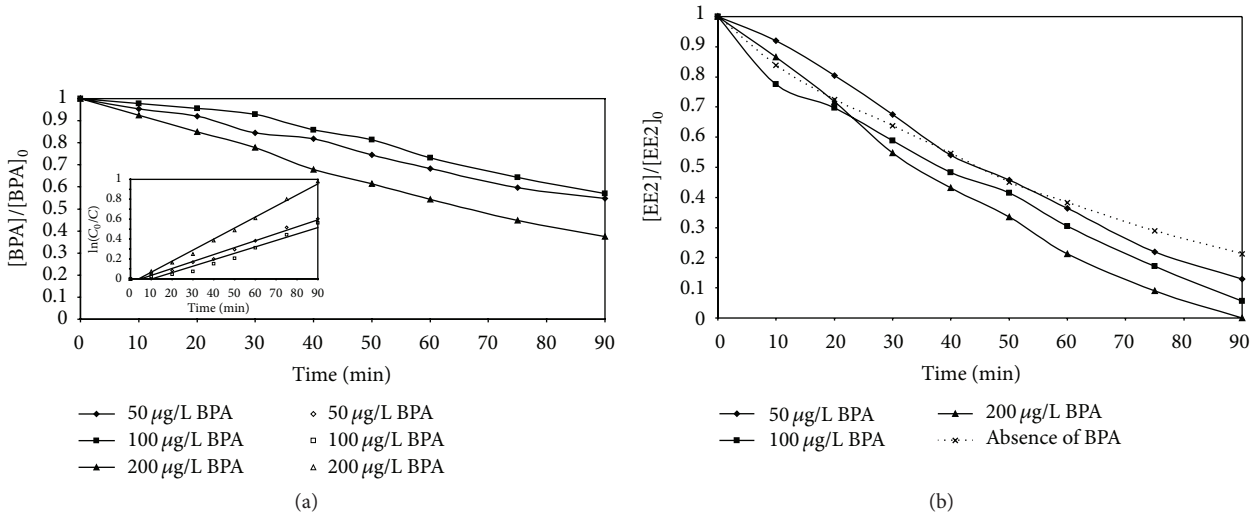

Figure 10: Degradation of a mixture of BPA and EE2 in UPW at 1.6 mg/cm^2 ZnO. Effect of (a) 100 μg/L EE2 on 50, 100 and 200 μg/L BPA; (b) 50, 100 and 200 μg/L BPA on 100 μg/L EE2. Inset graph: plot of (3).

containing organic and inorganic constituents; for instance the 90 min conversion is 93%, 65%, and 41% in UPW, DW, and WW, respectively, at 15.3 mg (6.8 mg/cm^2) ZnO. The respective apparent kinetic constants are computed equal to 0.342 (r^2 = 0.955), 0.128 (r^2 = 0.95), and 0.064 min^{-1} (r^2 = 0.979). The discrepancy by an order of magnitude between kinetics in UPW and WW can be explained taking into account that (a) the oxidizing agents are competitively consumed in reactions involving the residual organic fraction present in treated WW (i.e., COD = 24 mg/L) but not in UPW. Since this is known to be refractory to biological or chemical oxidation [24] and constitutes most of the matrix's total organic content, nonselective oxidizing agents will partly be wasted attacking this fraction; (b) hydroxyl radicals may be scavenged by bicarbonates and chlorides present in WW and/or DW to form the respective radicals, whose oxidation potential is lower than that of hydroxyl radicals [25, 26].

The experiments were repeated at a reduced ZnO loading of 3.7 mg (1.6 mg/cm^2). In this case, the 90 min BPA conversion is 60% in UPW and decreases to 44% in WW with the respective rate constants being 12 10^{-3} min^{-1} (r^2 = 0.994) and 6 10^{-3} min^{-1} (r^2 = 0.992); the ratio $k_{\mathrm{UPW}}/k_{\mathrm{ww}}$ is 5.3 and 2 at 6.8 and 1.6 mg/cm^2 ZnO, respectively. These results clearly indicate that the degree of deceleration of the photocatalytic process due to the complexity of the water matrix strongly depends on the catalyst-loading.

3.6. Degradation of EDCs Mixture. Experiments were carried out to investigate the possible interactions of BPA with EE2, a synthetic hormone typically found in the contraceptive pill and well-known for its interference with the endocrine system of living beings [27].

Figure 10(a) shows BPA concentration-time profiles (50–200 μg/L initial concentration) in UPW and in the presence of 100 μg/L EE2, while Figure 10(b) shows EE2 concentration-time profiles (100 μg/L initial concentration) in UPW and in the presence of different BPA concentrations in the range 0–200 μg/L. Comparing Figures 7(b) and 10(a) (inset graph), it is deduced that BPA degradation is slightly impeded by the presence of EE2, especially at 50 and 100 μg/L BPA initial concentrations. On the other hand, Figure 10(b) shows an enhancement of EE2 degradation from 79% in the absence of BPA to 87%, 94.5%, and 99% in the presence of 50, 100, and 200 μg/L BPA, respectively. These results are consistent with our previous work [16], where the photocatalytic EE2 degradation was studied in the presence of BPA. Possible explanations of this observation would involve the following (a) differences in BPA and EE2 chemical structures; EE2 has a longer molecular chain with more complicated structure than BPA and this could render it more readily susceptible to oxidative attack; (b) the simultaneous BPA-EE2 degradation may create active radicals that would also attack firstly EE2, facilitating thus its degradation; and (c) EE2, due to its longer and more complex molecule chain, may act as a shield to BPA molecule preventing its diffusion to the catalyst surface, thus decreasing its degradability.

The experiments were then performed in WW and the results are shown in Figure 11. The previous phenomenon is far less pronounced in this case, and this is possibly due to the fact that the WW matrix has already had a strong adverse impact (see Section 3.5), thus masking any interactions between BPA and EE2.

A kinetic simulation of BPA degradation in the presence of EE2 was performed for both UPW and WW matrices. Based on the experimental data shown in Figures 10(a) and 11(a), BPA degradation seems to follow near first-order kinetics as its degradation rate does not depend strongly on its initial concentration. The apparent rate constant for degradation in UPW is 9 ± 2 10^{-3} min^{-1} (computed from the

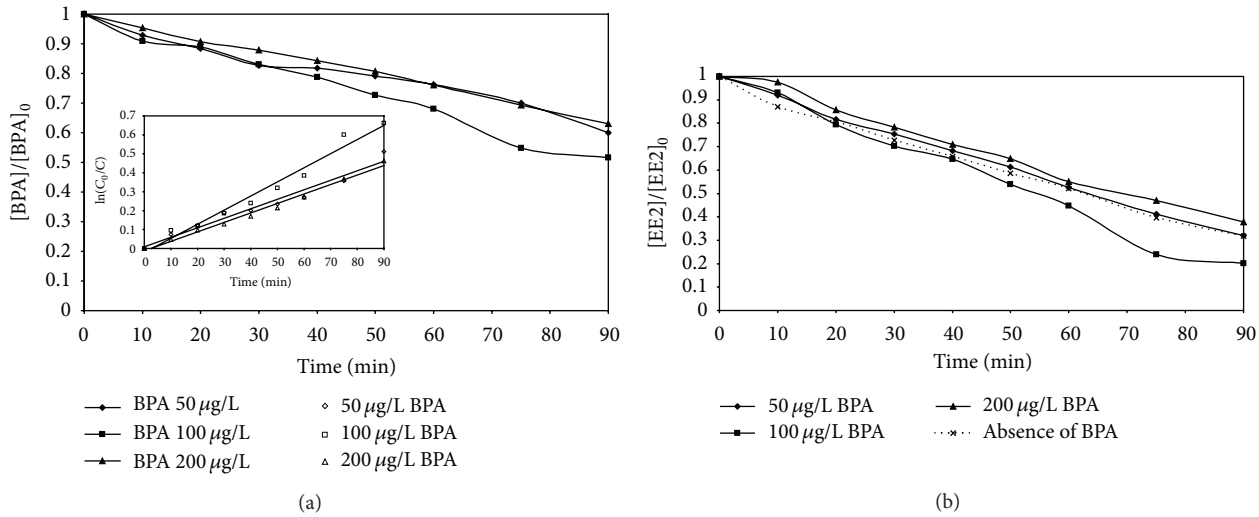

Figure 11: Degradation of a mixture of BPA and EE2 in WW at 1.6 mg/cm^2 ZnO. Effect of (a) 100 μg/L EE2 on 50, 100, and 200 μg/L BPA and (b) 50, 100 and 200 μg/L BPA on 100 μg/L EE2. Inset graph: plot of (3).

slope of the straight lines shown in inset Figure 10(a)) and decreases to $6 \pm 1\ 10^{-3}$ min^{-1} in WW (inset Figure 11(a)).

4. Conclusions

Overall, the removal of BPA under simulated solar irradiation and in the presence of either TiO_2 or ZnO catalysts immobilized onto glass plates was investigated. It was observed that the amount of catalyst attached onto the glass plate can affect process efficiency, which generally increases at increased catalyst loadings under the conditions tested. BPA removal follows a first-order reaction rate indicating that the removal is not practically affected by the initial BPA concentration, in the presence of either TiO_2 or ZnO catalyst. At the conditions employed in this study, apparent reaction rates increase with (a) increasing H_2O_2 concentration in a proportional fashion and (b) decreasing complexity of the water matrix (i.e., from wastewater to drinking water to ultrapure water). The presence of other EDCs, such as EE2, spiked in the reaction mixture does not seem to obstruct BPA degradation.

Hence, solar photocatalytic treatment using immobilized TiO_2 or ZnO photocatalysts can be a promising, with low energy requirements and efficient process to remove endocrine disrupting compounds, found at low concentrations, from aqueous matrices. The key advantage of the proposed setup is that there is no need for catalyst aftertreatment and separation in train with the photocatalytic process, thus decreasing the overall cost of a large-scale treatment plant.

References

[1] P. K. Jjemba, *Pharma-Ecology: The Occurrence and Fate of Pharmaceuticals and Personal Care Products in the Environment*, John Wiley & Sons, Hoboken, NJ, USA, 2008.

[2] V. Belgiorno, L. Rizzo, D. Fatta et al., "Review on endocrine disrupting-emerging compounds in urban wastewater: occurrence and removal by photocatalysis and ultrasonic irradiation for wastewater reuse," *Desalination*, vol. 215, no. 1–3, pp. 166–176, 2007.

[3] C. Lindholst, S. N. Pedersen, and P. Bjerregaard, "Uptake, metabolism and excretion of bisphenol A in the rainbow trout (*Oncorhynchus mykiss*)," *Aquatic Toxicology*, vol. 55, no. 1-2, pp. 75–84, 2001.

[4] H. Barndõk, M. Peláez, C. Han et al., "Photocatalytic degradation of contaminants of concern with composite NF-TiO_2 films under visible and solar light," *Environmental Science and Pollution Research*, vol. 20, no. 6, pp. 3582–3591, 2013.

[5] V. M. Daskalaki, I. Fulgione, Z. Frontistis, L. Rizzo, and D. Mantzavinos, "Solar light-induced photoelectrocatalytic degradation of bisphenol-A on TiO_2/ITO film anode and BDD cathode," *Catalysis Today*, vol. 209, pp. 74–78, 2013.

[6] S. D. Richardson, "Water analysis: emerging contaminants and current issues," *Analytical Chemistry*, vol. 81, no. 12, pp. 4645–4677, 2009.

[7] C. I. Kosma, D. A. Lambropoulou, and T. A. Albanis, "Occurrence and removal of PPCPs in municipal and hospital wastewaters in Greece," *Journal of Hazardous Materials*, vol. 179, no. 1–3, pp. 804–817, 2010.

[8] J. L. Rodríguez-Gil, M. Catalá, S. G. Alonso et al., "Heterogeneous photo-Fenton treatment for the reduction of pharmaceutical contamination in Madrid rivers and ecotoxicological evaluation by a miniaturized fern spores bioassay," *Chemosphere*, vol. 80, no. 4, pp. 381–388, 2010.

[9] G. Gatidou, E. Vassalou, and N. S. Thomaidis, "Bioconcentration of selected endocrine disrupting compounds in the Mediterranean mussel, *Mytilus galloprovincialis*," *Marine Pollution Bulletin*, vol. 60, no. 11, pp. 2111–2116, 2010.

[10] M. Gros, M. Petrović, and D. Barceló, "Tracing pharmaceutical residues of different therapeutic classes in environmental waters by using liquid chromatography/quadrupole-linear ion trap mass spectrometry and automated library searching," *Analytical Chemistry*, vol. 81, no. 3, pp. 898–912, 2009.

[11] A. S. Stasinakis, G. Gatidou, D. Mamais, N. S. Thomaidis, and T. D. Lekkas, "Occurrence and fate of endocrine disrupters in Greek sewage treatment plants," *Water Research*, vol. 42, no. 6-7, pp. 1796–1804, 2008.

[12] M. Auriol, Y. Filali-Meknassi, R. D. Tyagi, C. D. Adams, and R. Y. Surampalli, "Endocrine disrupting compounds removal from wastewater, a new challenge," *Process Biochemistry*, vol. 41, no. 3, pp. 525–539, 2006.

[13] Z. Frontistis, D. Fatta-Kassinos, D. Mantzavinos, and N. P. Xekoukoulotakis, "Photocatalytic degradation of 17α-ethynylestradiol in environmental samples by ZnO under simulated solar radiation," *Journal of Chemical Technology and Biotechnology*, vol. 87, no. 8, pp. 1051–1058, 2012.

[14] M. A. Behnajady, N. Modirshahla, N. Daneshvar, and M. Rabbani, "Photocatalytic degradation of C.I. Acid Red 27 by immobilized ZnO on glass plates in continuous-mode," *Journal of Hazardous Materials*, vol. 140, no. 1-2, pp. 257–263, 2007.

[15] A. R. Khataee, "Photocatalytic removal of C.I. Basic Red 46 on immobilized TiO_2 nanoparticles: artificial neural network modelling," *Environmental Technology*, vol. 30, no. 11, pp. 1155–1168, 2009.

[16] V. Koutantou, M. Kostadima, E. Chatzisymeon et al., "Solar photocatalytic decomposition of estrogens over immobilized zinc oxide," *Catalysis Today*, vol. 209, pp. 66–73, 2013.

[17] T. Nakashima, Y. Ohko, D. A. Tryk, and A. Fujishima, "Decomposition of endocrine-disrupting chemicals in water by use of TiO_2 photocatalysts immobilized on polytetrafluoroethylene mesh sheets," *Journal of Photochemistry and Photobiology A*, vol. 151, no. 1–3, pp. 207–212, 2002.

[18] V. M. Daskalaki, Z. Frontistis, D. Mantzavinos, and A. Katsaounis, "Solar light-induced degradation of bisphenol-A with TiO_2 immobilized on Ti," *Catalysis Today*, vol. 161, no. 1, pp. 110–114, 2011.

[19] J. Gunlazuardi and W. A. Lindu, "Photocatalytic degradation of pentachlorophenol in aqueous solution employing immobilized TiO_2 supported on titanium metal," *Journal of Photochemistry and Photobiology A*, vol. 173, no. 1, pp. 51–55, 2005.

[20] R. Wang, D. Ren, S. Xia, Y. Zhang, and J. Zhao, "Photocatalytic degradation of Bisphenol A (BPA) using immobilized TiO_2 and UV illumination in a horizontal circulating bed photocatalytic reactor (HCBPR)," *Journal of Hazardous Materials*, vol. 169, no. 1–3, pp. 926–932, 2009.

[21] E. S. Galbavy, K. Ram, and C. Anastasio, "2-Nitrobenzaldehyde as a chemical actinometer for solution and ice photochemistry," *Journal of Photochemistry and Photobiology A*, vol. 209, no. 2-3, pp. 186–192, 2010.

[22] M. A. Behnajady, N. Modirshahla, and R. Hamzavi, "Kinetic study on photocatalytic degradation of C.I. Acid Yellow 23 by ZnO photocatalyst," *Journal of Hazardous Materials*, vol. 133, no. 1–3, pp. 226–232, 2006.

[23] F. Méndez-Arriaga, M. I. Maldonado, J. Gimenez, S. Esplugas, and S. Malato, "Abatement of ibuprofen by solar photocatalysis process: enhancement and scale up," *Catalysis Today*, vol. 144, no. 1-2, pp. 112–116, 2009.

[24] Z. Frontistis and D. Mantzavinos, "Sonodegradation of 17α-ethynylestradiol in environmentally relevant matrices: laboratory-scale kinetic studies," *Ultrasonics Sonochemistry*, vol. 19, no. 1, pp. 77–84, 2012.

[25] L. A. T. Espinoza, M. Neamţu, and F. H. Frimmel, "The effect of nitrate, Fe(III) and bicarbonate on the degradation of bisphenol A by simulated solar UV-irradiation," *Water Research*, vol. 41, no. 19, pp. 4479–4487, 2007.

[26] C. Sirtori, A. Agüera, W. Gernjak, and S. Malato, "Effect of water-matrix composition on trimethoprim solar photodegradation kinetics and pathways," *Water Research*, vol. 44, no. 9, pp. 2735–2744, 2010.

[27] Z. Frontistis, C. Drosou, K. Tyrovola et al., "Experimental and modeling studies of the degradation of estrogen hormones in aqueous TiO_2 suspensions under simulated solar radiation," *Industrial and Engineering Chemistry Research*, vol. 51, no. 51, pp. 16552–16563, 2012.

Hindawi Publishing Corporation
International Journal of Photoenergy
Volume 2013, Article ID 394079, 7 pages
http://dx.doi.org/10.1155/2013/394079

Research Article

CTAB-Assisted Hydrothermal Synthesis of $Bi_2Sn_2O_7$ Photocatalyst and Its Highly Efficient Degradation of Organic Dye under Visible-Light Irradiation

Weicheng Xu,[1] Zhang Liu,[1] Jianzhang Fang,[1] Guangyin Zhou,[1] Xiaoting Hong,[1] Shuxing Wu,[1] Ximiao Zhu,[1] YunFang Chen,[1] and Chaoping Cen[2]

[1] *College of Chemistry and Environment, South China Normal University, Guangzhou 510631, China*
[2] *The Key Laboratory of Water and Air Pollution Control of Guangdong Province, South China Institute of Environmental Sciences, Guangzhou 510655, China*

Correspondence should be addressed to Jianzhang Fang; fangjzh@scnu.edu.cn

Received 24 May 2013; Accepted 3 July 2013

Academic Editor: Jiaguo Yu

Pyrochlore-type $Bi_2Sn_2O_7$ (BSO) nanoparticles have been prepared by a hydrothermal method assisted with a cationic surfactant cetyltrimethylammonium bromide (CTAB). These BSO products were characterized by powder X-ray diffraction (XRD), infrared spectroscopy (IR), scanning electron microscopy (SEM), transmission electron microscopy (TEM), Brunauer-Emmett-Teller (BET), and UV-visible diffuse reflectance spectroscopy (DRS). The results indicated that CTAB alters the surface parameters and the morphology and enhances the photoinduced charge separation rate of BSO. The photocatalytic degradation test using rhodamine B as a model pollutant showed that the photocatalytic activity of the BSO assisted with CTAB was two times that of the reference BSO. Close investigation revealed that the size, the band gap, the structure, and the existence of impurity level played an important role in the photocatalytic activities.

1. Introduction

Synthetic textile dyes and other industrial dyestuffs are important organic pollutants and produced all over the world. Their release as wastewater in the ecosystem will cause serious consequences, such as esthetic pollution, eutrophication, and perturbations in aquatic life [1, 2]. Many treatments have been developed and photocatalytic oxidation is regarded as a "green" technology for the decomposition of the soluble dyes in wastewater [3]. Nanosized TiO_2 semiconductor has been considered as one of the most promising photocatalysts in practical applications due to its high photocatalytic activity, chemical stability, low cost, and nontoxicity [4, 5]. However, the TiO_2 photocatalyst has no visible-light response due to its large band gap of 3.2 eV [6]. As a result, there are two strategies to develop the visible-light-driven photocatalysts: modification of TiO_2 [7–11] and exploitation of novel semiconductor materials [12–15]. Recently, many investigations have been undertaken on the latter strategy. A great deal of effort has been devoted to developing photocatalysts containing bismuth with high activities for environmental applications and/or water splitting, such as α-Bi_2O_3 [14], Bi_2WO_6 [15], $BiVO_4$ [12], $CaBi_2O_4$ [16] and $Bi_2O_2CO_3$ [17]. Zhou et al. [7] have synthesized mesoporous Au-TiO2 nanocomposite with high visible-light photocatalytic activity. Chen et al. [6] reported that some dyes could be degraded under visible-light irradiation over TiO2 by a self-photosensitized process. However, its photoefficiency was rather low due to the much slower interfacial electron transfer to the oxidize sensitizer. Therefore, the development of efficient visible-light-induced bismuth-based oxides photocatalysts through new synthetic routes has been an urgent issue.

$Bi_2Sn_2O_7$, a novel important semiconducting material with a typical pyrochlore structure and a band gap of 2.88 eV [18], has received considerable attention in catalysis and gas sensors [19–23]. However, the photocatalytic performance of bismuth stannate should be further improved for practical use. In order to overcome the defect, some researches have

shown that properties of the matter were limited by its size, shape, and specific surface area. Therefore, recently, in order to explore some photocatalysts with specific morphologies and unique properties, surfactant containing system has been employed to the preparation of nanosized photocatalysts. Liu et al. achieved nanocrystalline TiO_2 in microemulsions by using CTAB as surfactant [24]. Yin et al. have synthetized highly efficient monoclinic $BiVO_4$ with the assistance of CTAB [25]. Shen et al. found that the photocatalytic activities of $ZnIn_2S_4$ photocatalysts improved with the amounts of CTAB increasing [26]. CTAB can make the surface of photocatalysts hydrophobic, which is beneficial to the adsorption of nonionic organic compounds onto the photocatalyst and will improve the photocatalytic efficiency. Moreover, synthetic method also played an important role in preparing samples. Solid-state reaction technique had been a common method for the synthesis of pyrochlore BSO [12, 16, 17]. Compared with solid-state reaction, hydrothermal route [18] provided a milder environment for the pyrochlore BSO and the reaction parameters could be easily tuned. However, to the best of our knowledge, the synthesis of BSO by hydrothermal method with surfactant CTAB as the template has not been reported.

In this paper, we developed a facile surfactant (CTAB)-assisted hydrothermal method to prepare BSO photocatalyst at 180°C and the sample was labeled as C-BSO. A model dye of rhodamine B (RhB) was used to evaluate its photocatalytic efficiency under visible-light irradiation. Furthermore, the effects of CTAB on the crystal structure, morphology, and photocatalytic activity were discussed in detail.

2. Experimental

2.1. Synthesis. All the reagents were of analytical purity and used without further purification. In a typical reaction, $K_2SnO_3{\cdot}3H_2O$ (3 mmol) and $Bi(NO_3)_3{\cdot}5H_2O$ (3 mmol) were added by stoichiometric ratio, and 0.3 mmol CTAB was dissolved in a Teflon liner with 100 mL capacity containing 80 mL of deionized water. Under vigorous stirring, the pH value of the mixture was adjusted to 12 by using 2 mol/L KOH, and then the Teflon liner was sealed in the stainless steel autoclave and maintained at 180°C for 24 h. The as-prepared products were obtained by filtration and washed with deionized water and absolute ethanol several times. Finally, the products were dried in hot air oven at 80°C for 12 h. BSO was also prepared by the same procedure mentioned previously without the presence of CTAB.

2.2. Characterization. Samples were characterized by using X-ray diffraction (XRD) with a Bruker D8 Advance diffractometer using Cu KR (λ = 1.5406 nm) and operating at 40 kV and 40 mA. FT-IR spectra were taken in a Shimadzu IR Prestige-21 Fourier transform spectrometer. A scanning electron microscopy (SEM) images were obtained on a JEOL JSM-6700F instrument. Transmission electron microscopy (TEM) images were obtained with a JEOL JEM-2100HR field-emission electron microscope. The Brunauer-Emmett-Teller (BET) specific surface areas of the materials were detected by Micromeritics ASAP 2010 nitrogen adsorption apparatus. UV-visible absorption spectra of the samples were determined on a Hitachi U-3010 UV-Vis spectrophotometer with $BaSO_4$ as the reference.

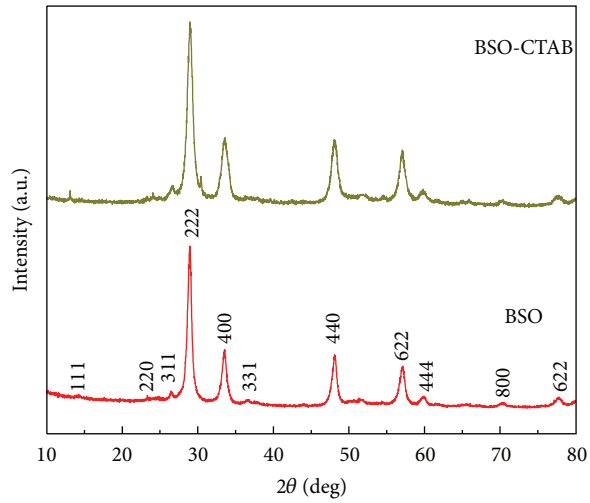

Figure 1: XRD patterns of BSO and C-BSO photocatalysts.

2.3. Photocatalytic Test. The photocatalytic efficiencies of BSO were evaluated by the degradation of RhB under visible-light irradiation. A 300 W Xe arc lamp (LTIC 300BF, Boyi Ltd, China) was used as the light source with a 420 nm cutoff filter. In every experiment, 0.1 g of catalyst was immersed in a 250 mL Pyrex beaker with 100 mL of RhB solution (5 mg/L). In order to ensure adsorption/desorption equilibrium between RhB and the photocatalyst, the suspension was stirred in the dark for 1 h. As for the photocatalytic reactions, 3 mL of the suspensions was taken out at given time intervals and centrifuged to remove the photocatalyst particles. The concentrations of the centrifuged RhB solutions were monitored using a UV-Vis 8500 spectrophoto-meter (Shanghai Tianmei Science Apparatus Ltd. Co. China).

3. Results and Discussion

3.1. Structural and Morphological Characterization. The XRD patterns of as-prepared samples are shown in Figure 1. All strong peaks can be indexed to a pure cubic phase of BSO (JCPDS no. 87-0284). No other peaks can be observed, indicating high purity of the final products. The average sizes of the crystallite estimated using the Scherrer equation from (222) crystal plane of pyrochlore phase at $2\theta = 28.8^\circ$ are 13.5 and 10.2 nm for BSO and C-BSO, respectively. Compared with the BSO sample, the diffraction peak intensity of the C-BSO nanoparticles is weak and broad. This implies that the crystallite size of C-BSO catalyst is smaller than that of the BSO catalyst.

The IR spectrum of the BSO and C-BSO samples, recorded in the range 400–4000 cm^{-1}, is shown in Figure 2. Subramanian et al. have reported the infrared spectra of the pyrochlore oxides and demonstrated that the band at about 600 cm^{-1} was from the B-O stretching vibration in the BO_6

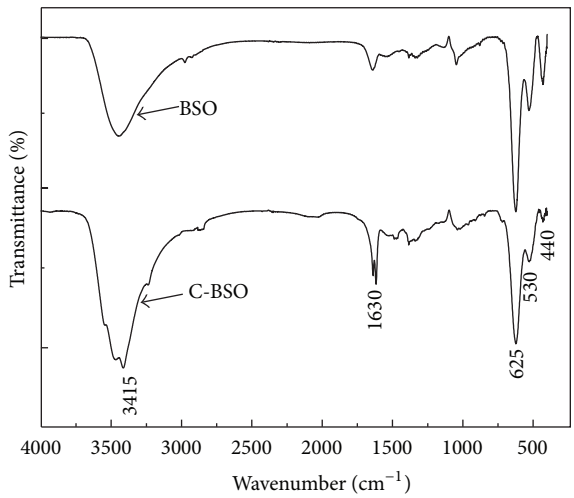

Figure 2: IR spectrum of the as-prepared BSO and C-BSO samples.

octahedron and the A-O stretching vibration of pyrochlore $A_2B_2O_7$ centered at about 500 cm^{-1} [27]. Similar results are obtained by the previous present work. It can be seen clearly that the main band at about 625 cm^{-1} is assigned to the Sn-O stretching vibration while the weak bands of 440 cm^{-1} and 530 cm^{-1} are ascribed to Bi-O-Bi bonds vibrations [28]. The bands centered at about 3415 cm^{-1} and 1630 cm^{-1} are assigned to O-H stretching and bending modes of water, respectively [29].

The morphology of BSO and C-BSO is characterized by SEM as shown in Figure 3. Figure 3(a) shows the BSO samples which consist of a large number of microspheres, indicating that highyield of products can be readily achieved through this approach. Figure 3(b) shows the SEM image of the C-BSO photocatalyst; it can be seen that the irregular lumps and particles are relatively dispersed. The size of the as-prepared BSO nanoparticles is in the range of 8–20 nm (Figure 3(a)). After modification by CTAB, the size of the C-BSO sample has slightly changed. The mean mesopore size is about 10–15 nm, which is consistent with the pore size calculated from N2 isotherms.

The high-magnification TEM images of the BSO and C-BSO samples are shown in Figure 4. Figure 4(a) displays various specifications block-like morphology with sizes of 8–20 nm. Figure 4(b) shows irregular spherical-like morphology of C-BSO, and the sizes of C-BSO are only slightly smaller than BSO sample. Clearly, the size of the as-synthesized C-BSO is smaller than BSO. This phenomenon is consistent with the typical crystallite sizes calculated from XRD results.

3.2. N_2 Adsorption/Desorption Isotherm Analysis. The N_2 adsorption-desorption isotherms and pore size distributions of BSO and C-BSO are determined by BET and BJH methods (shown in Figure 5). The isotherms of all the two samples are of classical type IV, characteristic of mesoporous materials according to the IUPAC. The result indicates that the BET surface area of nanosized BSO samples increased, from 45.3 to 71.9 m^2/g, accompanied with the increase of pore volumes from 0.11 to 0.18 m^2/g. The pore size distribution curves of BSO and C-BSO determined by BJH method from the absorption branch of the isotherms exhibit one single narrow peak centered at 12.7 nm, indicating the good homogeneity of the pores.

3.3. UV-Vis Diffuse Reflectance Spectra. Figure 6 shows the diffuse reflectance spectra of the BSO and C-BSO samples. It is clearly visible from the spectra that the absorption edge of C-BSO gets further shifted to the visible region comparing to the BSO sample. The band gap absorption edges of the BSO and C-BSO are measured to be 450 nm (2.76 eV) and 464 nm (2.67 eV), respectively. Such differences may be ascribed to the changes of crystallite phase and the size of coupled oxides, defects, and so on [30]. In this work, we believe that C-BSO photocatalyst, with its long wavelength absorption band, is an attractive photocatalyst for pollutant. The narrower band gap of C-BSO photocatalyst not only benefits the absorption of more photons in sunlight, but also promotes the excitation of photogenerated electrons from the valence band (VB) to the conduction band (CB), which may make the photocatalyst with high photocatalytic activity.

3.4. Photocatalytic Activity of BSO and C-BSO Nanocomposites under Visible Conditions. The photocatalytic performance of BSO and C-BSO is compared and presented in Figure 7, where C and C_0 represent the time-dependent concentration and the initial concentration of pollutants solution, respectively. The blank test exhibits extremely low photodegradation efficiency in the absence of a photocatalyst under visible-light irradiation. The decrease of RhB concentration in the presence of BSO under visible light is about 51.0% after six hours of illumination. It can be found that the photodegradation efficiency of BSO assisted with CTAB decreases with the increase of CTAB amounts. However, their photocatalytic efficiency can be significantly improved compared with the sample without CTAB. 0.3 mmol C-BSO product exhibits better photodegradation activity than 1.5 mmol C-BSO photocatalyst, with the RhB concentration reduced as much as 97.8% under the same condition.

3.5. Effect of CTAB Assistance. As an efficient sorbent material, supramolecular assemblies (hemimicelles/admicelles) are formed from adsorption of surfactants on the surface of metal oxides. Attractive electrostatic interactions between the head group of ionic surfactants and oppositely charged groups on the oxide lead to the formation of monolayers of adsorbed surfactant termed hemimicelles. After saturation of the oxide surface, hydrophobic interactions between hydrocarbon chains of surfactant molecules lead to the formation of admicelles [31]. In term of hemimicelles, the hydrophobic tails are exposed to aqueous solution, so that the surfactant-coated oxide surface will become hydrophobic, which contributes to the adsorption of nonionic organic compounds onto the adsorbents [32]. Owing to the possession of higher special areas and more ion-exchangeable OH groups on surface, BSO materials have obvious advantage for the sorption

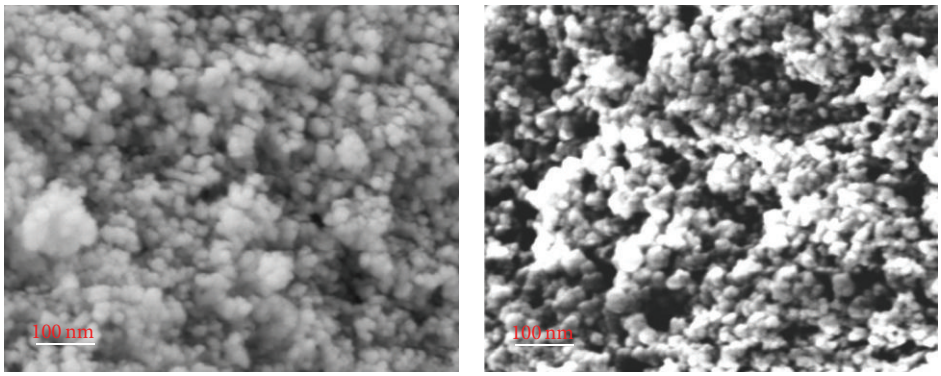

(a) (b)

Figure 3: SEM images of as-prepared samples, (a) BSO sample and (b) C-BSO sample.

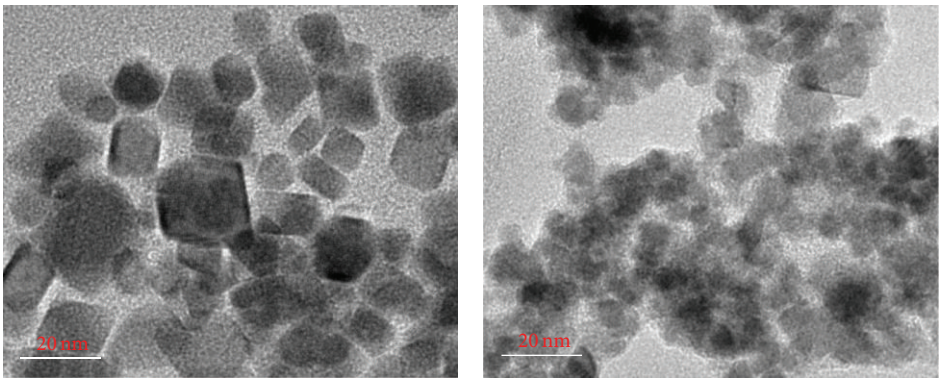

(a) (b)

Figure 4: TEM images of (a) BSO sample and (b) C-BSO sample.

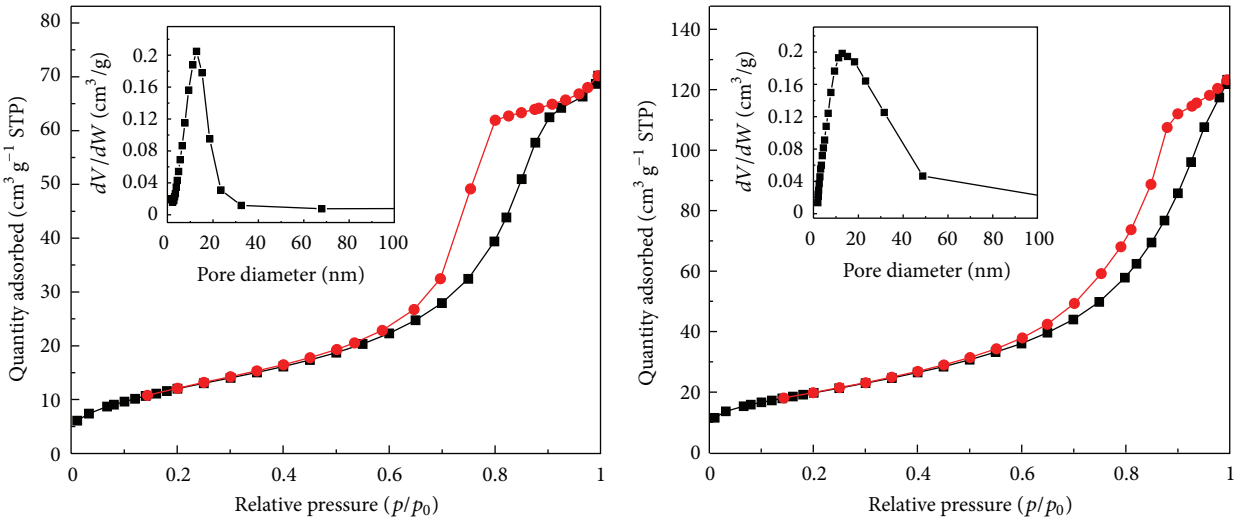

(a) (b)

Figure 5: The N_2 sorption isotherms and pore width distribution of as-synthesized samples and (a) BSO, (b) C-BSO sample.

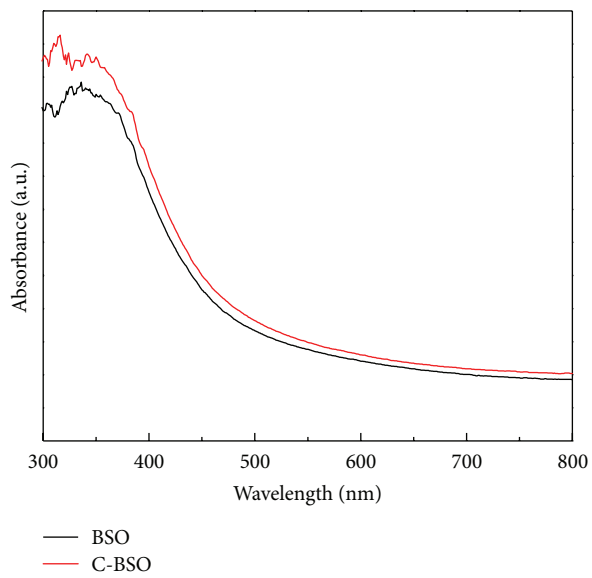

Figure 6: UV-Vis diffuse reflectance spectra of BSO and C-BSO samples.

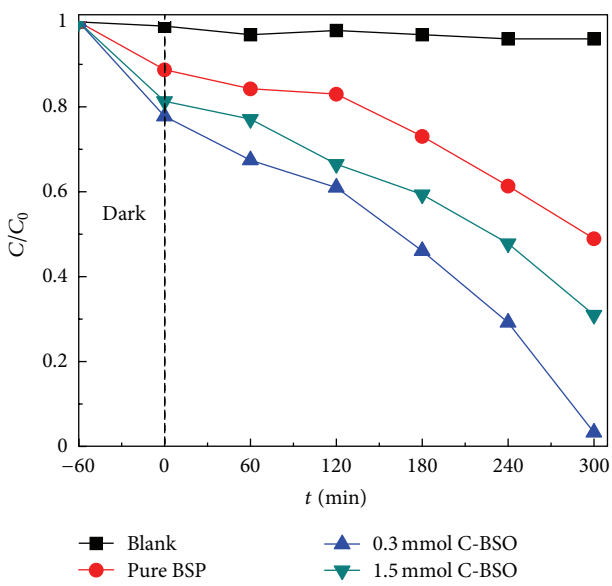

Figure 7: Degradation curves of RhB over as-prepared nanoparticles.

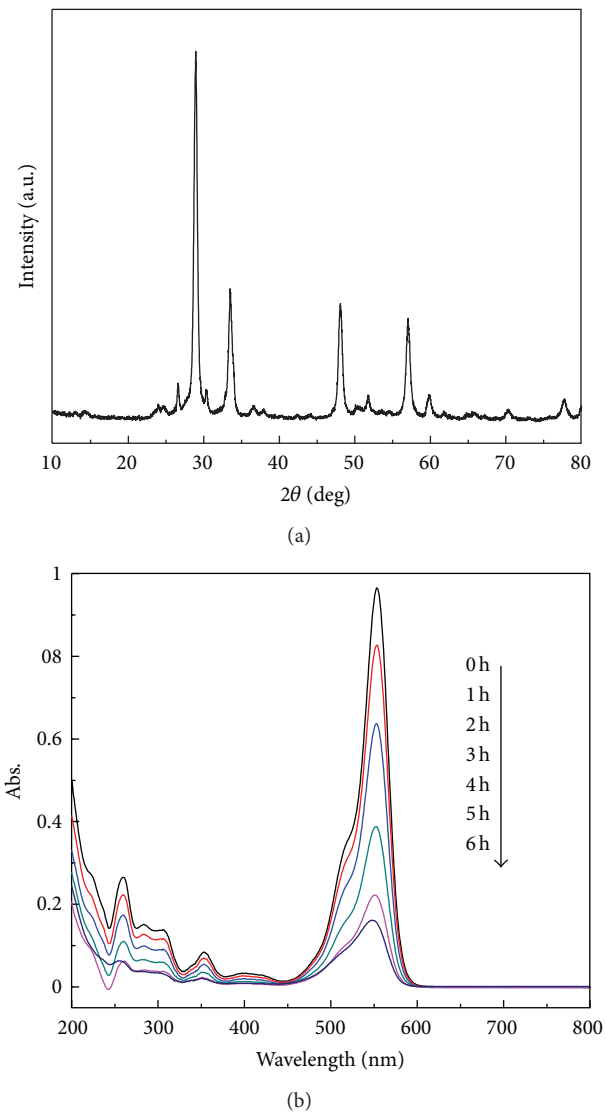

Figure 8: (a) XRD patterns of C-BSO-cal; (b) photocatalytic activities of RhB of C-BSO-cal product.

of ionic surfactant and have remarkable adsorption capability to organic compounds correspondingly [33]. Therefore, as shown in Figure 7, the nanomaterials BSO prepared by using CTAB are advantageous in photocatalytic reaction.

3.6. Reasons for Enhanced Efficiency of Photocatalysts. The photocatalytic activity of pyrochlore BSO is strongly influenced by its phase structure, crystallite size, and specific surface area [25]. From the XRD results, the phase structure of BSO did not change before and after using CTAB and retained the good crystallization. The crystallite size of BSO decreased from 13.5 nm to 10.2 nm after using CTAB, which may be good for the enhancement of their photocatalytic performance. Moreover, the sample prepared with CTAB exhibited larger surface area (71.9 m^2/g) than the reference BSO (45.3 m^2/g). As the specific surface area and pore volume increased, it could result in the transition of band electron indirectly and the enhancement of the generation rate of photogenerated carriers [34]. Therefore, it also can be concluded that the surface area and pore structure of this sample played an important role in its degradation efficiency for wastewater. Moreover, another factor may be the existence of impurity level which could give rise to the shift of absorption edge to the long wavelength side and thus improves photocatalytic efficiency.

In order to test the previous assertion, the C-BSO is calcined at 600°C for 2 h to remove the impurity level (labelled as C-BSO-cal). The XRD pattern of C-BSO-cal (Figure 8(a)) reveals that the C-BSO-cal has the same phase as the C-BSO. The BET surface area of the C-BSO-cal is much smaller

than that of the C-BSO, which can respond for the decline of photocatalytic efficiency of the C-BSO-cal. The photocatalytic efficiency of the C-BSO-cal is presented in Figure 8(b). Obviously, only about 85.1% of RhB is degraded after 6 h of irradiation. It can be attributed to the elimination of impurity level by calcination that affects the removal efficiency of RhB.

4. Conclusions

In conclusion, nanoscale BSO could be conveniently synthesized by a CTAB assisted hydrothermal process at the temperature 180°C for 24 h. The experimental results show that adding CTAB into the synthesis system resulted in excellent dispersivity of lumps blocks and particles spheres with irregular shapes. BET surface area and pore volume of C-BSO are higher than those of BSO sample. Moreover, the photocatalytic activity of C-BSO is two times that of the reference BSO. The results demonstrate that the excellent photocatalytic activity of C-BSO stems from the efficiency of electron-hole pairs separation rate and the existence of impurity levels in C-BSO crystals.

Acknowledgment

This work was supported by Guangdong Water and Air Pollution Control Key Laboratory (2011 A060901002) open funded project.

References

[1] M. A. Brown and S. C. deVito, "Predicting azo dye toxicity," *Critical Reviews in Environmental Science and Technology*, vol. 23, no. 3, pp. 249–324, 1993.

[2] N. Z. Bao, X. Feng, Z. H. Yang, L. Shen, and X. Lu, "Highly efficient liquid-phase photooxidation of an azo dye methyl orange over novel nanostructured porous titanate-based fiber of self-supported radially aligned $H_2Ti_8O_{17}\cdot 1.5H_2O$ nanorods," *Environmental Science and Technology*, vol. 38, no. 9, pp. 2729–2736, 2004.

[3] J. Bi, L. Wu, J. Li, Z. Li, X. Wang, and X. Fu, "Simple solvothermal routes to synthesize nanocrystalline Bi_2MoO_6 photocatalysts with different morphologies," *Acta Materialia*, vol. 55, no. 14, pp. 4699–4705, 2007.

[4] L. Zhao, J. R. Ran, Z. Shu, G. Dai, P. Zhai, and S. Wang, "Effects of calcination temperatures on photocatalytic activity of ordered titanate nanoribbon/SnO_2 films fabricated during an EPD process," *International Journal of Photoenergy*, vol. 2012, Article ID 472958, 7 pages, 2012.

[5] G. F. Shang, H. B. Fu, S. Yang, and T. Xu, "Mechanistic study of visible-light-induced photodegradation of 4-chlorophenol by $TiO_{2-x}N_x$ with low nitrogen concentration," *International Journal of Photoenergy*, vol. 2012, Article ID 759306, 9 pages, 2012.

[6] C. C. Chen, W. Zhao, J. Y. Li, J. Zhao, H. Hidaka, and N. Serpone, "Formation and identification of intermediates in the visible-light-assisted photodegradation of sulforhodamine-B dye in aqueous TiO_2 dispersion," *Environmental Science and Technology*, vol. 36, no. 16, pp. 3604–3611, 2002.

[7] P. Zhou, J. G. Yu, and Y. X. Wang, "The new understanding on photocatalytic mechanism of visible-light response N-S codoped anatase TiO_2 by first-principles," *Applied Catalysis B*, vol. 142-143, pp. 45–53, 2013.

[8] R. Asahi, T. Morikawa, T. Ohwaki, K. Aoki, and Y. Taga, "Visible-light photocatalysis in nitrogen-doped titanium oxides," *Science*, vol. 293, no. 5528, pp. 269–271, 2001.

[9] J. G. Yu, G. P. Dai, Q. Xiang, and M. Jaroniec, "Fabrication and enhanced visible-light photocatalytic activity of carbon self-doped TiO_2 sheets with exposed 001 facets," *Journal of Materials Chemistry*, vol. 21, no. 4, pp. 1049–1057, 2011.

[10] M. H. Zhou, J. Zhang, B. Cheng, and H. G. Yu, "Enhancement of visible-light photocatalytic activity of mesoporous Au-TiO_2 nanocomposites by surface plasmon resonance," *International Journal of Photoenergy*, vol. 2012, Article ID 532843, 10 pages, 2012.

[11] R. Liu,, P. Wang, X. Wang, H. Yu, and J. Yu, "UV-and visible-light photocatalytic activity of simultaneously deposited and doped Ag/Ag(I)-TiO_2 photocatalyst," *Journal of Physical Chemistry C*, vol. 116, no. 33, pp. 17721–17728, 2012.

[12] M. Long, W. Cai, J. Cai, B. Zhou, X. Chai, and Y. Wu, "Efficient photocatalytic degradation of phenol over Co_3O_4/$BiVO_4$ composite under visible light irradiation," *Journal of Physical Chemistry B*, vol. 110, no. 41, pp. 20211–20216, 2006.

[13] Q. Li, H. Meng, P. Zhou et al., "$Zn_{1-x}Cd_xS$ solid solutions with controlled bandgap and enhanced visible-light photocatalytic H_2-production activity," *ACS Catalysis*, vol. 3, no. 5, pp. 882–889, 2013.

[14] S. X. Wu, J. Z. Fang, W. C. Xu, and C. Cen, "Hydrothermal synthesis, characterization of visible-light-driven α-Bi_2O_3 enhanced by Pr^{3+} doping," *Journal of Chemical Technology and Biotechnology*, 2013.

[15] H. Yu, R. Liu, X. Wang, P. Wang, and J. Yu, "Enhanced visible-light photocatalytic activity of Bi_2WO_6 nanoparticles by Ag_2O cocatalyst," *Applied Catalysis B*, vol. 111-112, pp. 326–333, 2012.

[16] J. Tang, Z. Zou, and J. Ye, "Efficient photocatalytic decomposition of organic contaminants over $CaBi_2O_4$ under visible-light irradiation," *Angewandte Chemie International Edition*, vol. 43, no. 34, pp. 4463–4466, 2004.

[17] P. Madhusudan, J.G. Yu, W. G. Wang, B. Cheng, and G. Liu, "Facile synthesis of novel hierarchical grapheme-$Bi_2O_2CO_3$ composites with enhanced photocatalytic performance under visible light," *Dalton Transactions*, vol. 41, no. 47, pp. 14345–14353, 2012.

[18] Q. Tian, J. Zhuang, J. Wang, L. Xie, and P. Liu, "Novel photocatalyst, $Bi_2Sn_2O_7$, for photooxidation of As(III) under visible-light irradiation," *Applied Catalysis A*, vol. 425-426, no. 28, pp. 74–78, 2012.

[19] L. Moens, P. Ruiz, B. Delmon, and M. Devillers, "Evaluation of the role played by bismuth molybdates in $Bi_2Sn_2O_7\pm MoO_3$ catalysts used for partial oxidation of isobutene to methacrolein," *Applied Catalysis A*, vol. 180, no. 1-2, pp. 299–315, 1999.

[20] H. Du, X. Yao, and L. Zhang, "Structure, IR spectra and dielectric properties of Bi_2O_3-ZnO-SnO_2-Nb_2O_5 quarternary pyrochlore," *Ceramics International*, vol. 28, no. 3, pp. 231–234, 2002.

[21] A. Walsh, G. W. Watson, D. J. Payne, G. Atkinson, and R. G. Egdell, "A theoretical and experimental study of the distorted pyrochlore $Bi_2Sn_2O_7$," *Journal of Materials Chemistry*, vol. 16, no. 34, pp. 3452–3458, 2006.

[22] C. A. Mims, A. J. Jacobson, R. B. Hall, and J. T. Lewandowski, "Methane oxidative coupling over nonstoichiometric bismuth-tin pyrochlore catalysts," *Journal of Catalysis*, vol. 153, no. 2, pp. 197–207, 1995.

[23] J. Wu, F. Huang, X. Lu, P. Chen, D. Wan, and F. Xu, "Improved visible-light photocatalysis of nano-$Bi_2Sn_2O_7$ with dispersed s-bands," *Journal of Materials Chemistry*, vol. 21, no. 11, pp. 3872–3876, 2011.

[24] Z. Liu, Z. Jian, J. Fang, X. Xu, X. Zhu, and S. Wu, "Low-temperature reverse microemulsion synthesis, characterization, and photocatalytic performance of nanocrystalline titanium dioxide," *International Journal of Photoenergy*, vol. 2012, Article ID 702503, 8 pages, 2012.

[25] W. Yin, W. Wang, L. Zhou, S. Sun, and L. Zhang, "CTAB-assisted synthesis of monoclinic $BiVO_4$ photocatalyst and its highly efficient degradation of organic dye under visible-light irradiation," *Journal of Hazardous Materials*, vol. 173, no. 1–3, pp. 194–199, 2010.

[26] S. Shen, L. Zhao, and L. Guo, "Cetyltrimethylammonium-bromide (CTAB)-assisted hydrothermal synthesis of $ZnIn_2S_4$ as an efficient visible-light-driven photocatalyst for hydrogen production," *International Journal of Hydrogen Energy*, vol. 33, no. 17, pp. 4501–4510, 2008.

[27] M. A. Subramanian, G. Aravamudan, and G. V. Subba Rao, "Oxide pyrochlores—a review," *Indian Academy of Sciences*, vol. 15, no. 2, pp. 55–143, 1983.

[28] P. Pascuta and E. Culea, "FTIR spectroscopic study of some bismuth germanate glasses containing gadolinium ions," *Materials Letters*, vol. 62, no. 25, pp. 4127–4129, 2008.

[29] Y. Wang, J. C. Shi, J. L. Cao, G. Sun, and Z. Y. Zhang, "Synthesis of Co_3O_4 nanoparticles via the CTAB-assisted method," *Materials Letters*, vol. 65, no. 2, pp. 222–224, 2011.

[30] M. Zhang, T. An, X. Hu, C. Wang, G. Sheng, and J. Fu, "Preparation and photocatalytic properties of a nanometer ZnO-SnO_2 coupled oxide," *Applied Catalysis A*, vol. 260, no. 2, pp. 215–222, 2004.

[31] A. Moral, M. D. Sicilia, S. Rubio, and D. Pérez-Bendito, "Determination of bisphenols in sewage based on supramolecular solid-phase extraction/liquid chromatography/fluorimetry," *Journal of Chromatography A*, vol. 1100, no. 1, pp. 8–14, 2005.

[32] Y. Huang, Q. Zhou, and G. Xie, "Development of micro-solid phase extraction with titanate nanotube array modified by cetyltrimethylammonium bromide for sensitive determination of polycyclic aromatic hydrocarbons from environmental water samples," *Journal of Hazardous Materials*, vol. 193, pp. 82–89, 2011.

[33] H. Niu, Y. Cai, Y. Shi, F. Wei, S. Mou, and G. Jiang, "Cetyltrimethylammonium bromide-coated titanate nanotubes for solid-phase extraction of phthalate esters from natural waters prior to high-performance liquid chromatography analysis," *Journal of Chromatography A*, vol. 1172, no. 2, pp. 113–120, 2007.

[34] S. I. Shah, W. Li, C. P. Huang, O. Jung, and C. Ni, "Study of Nd^{3+}, Pd^{2+}, Pt^{4+}, and Fe^{3+} dopant effect on photoreactivity of TiO_2 nanoparticles," *Proceedings of the National Academy of Sciences of the United States of America*, vol. 99, no. 2, pp. 6482–6486, 2002.

Hindawi Publishing Corporation
International Journal of Photoenergy
Volume 2013, Article ID 824130, 7 pages
http://dx.doi.org/10.1155/2013/824130

Research Article

Enhancement of Photocatalytic Activity on TiO_2-Nitrogen-Doped Carbon Nanotubes Nanocomposites

Lingling Wang,[1] Long Shen,[2] Yihuai Li,[1] Luping Zhu,[1] Jiaowen Shen,[1] and Lijun Wang[1]

[1] *School of Urban Development and Environment Engineering, Shanghai Second Polytechnic University, 2360 Jinhai Road, Shanghai 201209, China*
[2] *Shanghai Shanshan Technology Co., Ltd., 3158 Jinhai Road, Shanghai 201209, China*

Correspondence should be addressed to Lijun Wang; wang_lijun@yahoo.cn

Received 20 May 2013; Revised 21 June 2013; Accepted 21 June 2013

Academic Editor: Jiaguo Yu

TiO_2-nitrogen-doped carbon nanotubes (TiO_2-CNx) nanocomposites are successfully synthesized via a facile hydrothermal method. The prepared photocatalysts were systematically characterized by X-ray diffraction (XRD), scanning electron microscopy (SEM), transmission electron microscopy (TEM), and thermogravimetric and differential scanning calorimetry analyses (TGA-DSC). The results show that the TiO_2 nanoparticles with a narrow size of 7 nm are uniformly deposited on CNx. The photocatalytic activity of the nanocomposite was studied using methyl orange (MO) as a model organic pollutant. The experimental results revealed that the strong linkage between the CNx and TiO_2 played a significant role in improving photocatalytic activity. However, the mechanical process for CNx and TiO_2 mixtures showed lower activity than neat TiO_2. Moreover, TiO_2-CNx nanocomposites exhibit much higher photocatalytic activity than that of neat TiO_2 and TiO_2-CNTs nanocomposites. The improved photodegradation performances are attributed to the suppressed recombination of electrons and holes caused by the effective transfer of photogenerated electrons from TiO_2 to CNx.

1. Introduction

Photocatalysis has been widely applied as a technique of destruction of organic pollutants due to its high performance, low cost, nontoxicity, stability, and availability [1, 2]. Titanium dioxide (TiO_2), a semiconductor with direct bandgap of 3.2 eV, has excellent photocatalytic properties and chemical stability, and it is an environmentally friendly and abundant substance [3, 4]. However, a major limitation to achieve high photocatalytic efficiency is the quick recombination of photogenerated charge carries [5]. Recombination has faster kinetics than surface redox reactions and greatly reduces the quantum efficiency of photocatalysis. Therefore, currently a particularly attractive option is to design and develop hybrid materials based on TiO_2 to solve this problem.

Recently, carbon-based nanomaterials, such as carbon nanotubes (CNTs) and graphene, have been reported as the hybrid component to be incorporated into TiO_2 due to their unique electrical properties, superior chemical stability, and good conductivity. The common approaches to synthesize TiO_2-CNTs composites include sol-gel method [6, 7], chemical vapor deposition (CVD) [8, 9], and electrospinning [10]. Various structural forms of titania-carbon nanotubes photocatalysts have been prepared, such as TiO_2 nanoparticles on CNTs [11], TiO_2 layer coating on aligned CNTs arrays [12], CNTs incorporating into the TiO_2 film [13], TiO_2 layer coating on CNTs [14], and low loading amounts of CNTs embedded inside mesoporous TiO_2 aggregates [15]. Cong et al. [16] have prepared uniform and fine well-dispersed carbon-doped TiO_2 coating on multiwalled carbon nanotubes by oxidation of titanium-carbide-(TiC-) coated CNTs, and the prepared carbon-doped TiO_2 coating on CNTs shows a higher visible light photocatalytic activity.

However, to fabricate the TiO_2-CNTs composites, the CNTs required a pretreatment process to modify their inert surface nature via harsh processes for activation by refluxing in concentrated acids, which destroys the π conjugation and reduces the conductance of the CNTs base [17]. Unfavorably,

the harsh process would risk CNTs to some damages in their inherent properties. To bypass the drawbacks suffered by CNTs, employing CNx without requiring any pretreatment to composite with the functional materials directly is a promising method because the nitrogen atoms on the surface of the CNTs modify the adsorption strength of the nanotubes towards foreign elements. Moreover, nitrogen atoms in the framework of CNx will form chemically active points which are available for metal or metallic oxide nanoparticles anchoring. Ghosh and coworkers [17] prepared ZnO/CNx composites via a simple wet-chemical method and studied their field emission performance. CNx decorated with CeO_2 and SnO_2 nanoparticles showed greater activity and sensitivity than the conventional CNT-based composites for NO electrooxidation [18].

In this work, according to the unique properties of CNx, we have synthesized TiO_2-CNx nanocomposites with different weight ratios via a facile hydrothermal method. The resulting materials were well characterized for their physicochemical properties, structural features, as well as potential applications to the photodegradation of MO.

2. Experimental

2.1. Synthesis of TiO_2-CNx. Following the procedures reported previously [19], CNx was synthesized using diethylamine as the carbon and nitrogen source. The purification process for CNx was as follows: CNx was firstly washed three times by 20% HF solution, then soaked in 20% HF solution overnight, gathered by filtration, and finally dried at 80°C for 2 h.

TiO_2-CNx nanocomposites were prepared using a hydrothermal synthesis method. CNx was added to provide a weight ratio of TiO_2 over CNx in the range from 5% to 20%, indicated with X wt% TiO_2-CNx. CNx was initially dispersed into a 30 mL solution containing 2.7 mL water and 27.3 mL isopropanol, and the suspension was treated by sonication overnight. Then the titanium precursor solution, 3.41 mL titanium isopropoxide in 18 mL isopropanol was added dropwise into the CNx suspension under vigorous stirring. The mixture was left at room temperature under stirring for 2 h to complete the hydrolysis reaction. The mixed solution was then transferred into a teflon-lined stainless-steel autoclave (50 mL capacity). The autoclave was maintained at 140°C for 24 h and then cooled down to room temperature. The resulting solid was washed with ethanol and deionized water, gathered by filtration, and subsequently dried at 80°C overnight. The TiO_2-CNx solids were ground into powder and stored in a dessicator for further usage. For comparison, TiO_2-CNTs composites were synthesized using the similar procedures besides CNTs pretreated in concentrated HNO_3 at 140°C for 14 h, and neat TiO_2 sample was synthesized without adding CNTs.

2.2. Characterization. The bare CNx and the composites were characterized by a wide range of analytical techniques. The degree of crystallinity of the TiO_2-CNx composites was characterized by powder X-ray diffraction (XRD). The XRD patterns with diffraction intensity versus 2θ were recorded in a Bruker D8 ADVANCE instrument with Cu-Ka radiation (λ = 1.5418 Å) from 20° to 70° at a scanning speed of 2°/min. X-ray tube voltage and current were set at 40 kV and 40 mA, respectively. Thermogravimetric and differential scanning calorimetry analyses (TGA-DSC) were performed by a Netzsch STA-449C analyzer with a heating rate of 10°C/min and an air flow rate of 100 mL/min. Scanning electron microscopy (SEM) was carried out on Hitachi S-4800 with an acceleration voltage of 5 kV. Transmission electron microscopy (TEM) was carried out on JEOL-JEM-1005 at 200 kV. The specimens for SEM and TEM imaging were prepared by suspending solid samples in ethanol with 15 min ultrasonication and placing a drop of this mixture on a 3.05 mm diameter copper mesh, which was then dried in air.

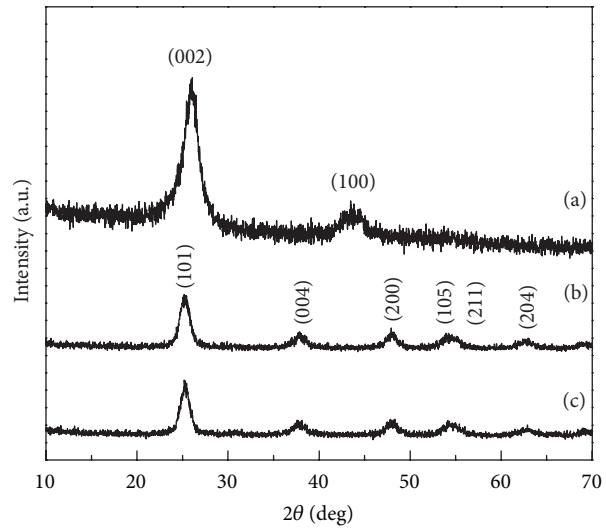

Figure 1: XRD patterns of bare CNx (a) and TiO_2-CNx composites with different weight ratio of TiO_2 over CNx 5% (b) and 20% (c).

2.3. Photodegradation of MO. The photoreactor was designed with a cylindrical quartz cell configuration and an internal light source surrounded by a quartz jacket, where MO aqueous solution completely surrounded the light source. An external cycled cooling flow of water was used to maintain the reaction temperature constant.

Photocatalytic experiments were carried out by adding 0.01 g TiO_2 or TiO_2-CNTs composites or TiO_2-CNx composites into photoreactor containing 30 mL MO solution with an initial concentration of 15 mg/L. The mixture was stirred for 30 min in the dark to favor the adsorption equilibration, and then the stirred suspensions were illuminated with a 300 W high-pressure mercury lamp 10 cm high over the solution. The solution was stirred continuously during the photocatalytic reaction. The concentration of MO was analyzed by recording the absorption band maximum at 464 nm in the absorption spectra, using Shimadzu UV-2550 spectrophotometer.

3. Results and Discussion

The XRD patterns of the bare CNx and TiO_2-CNx nanocomposites are shown in Figure 1. The main peaks at 26.1° and

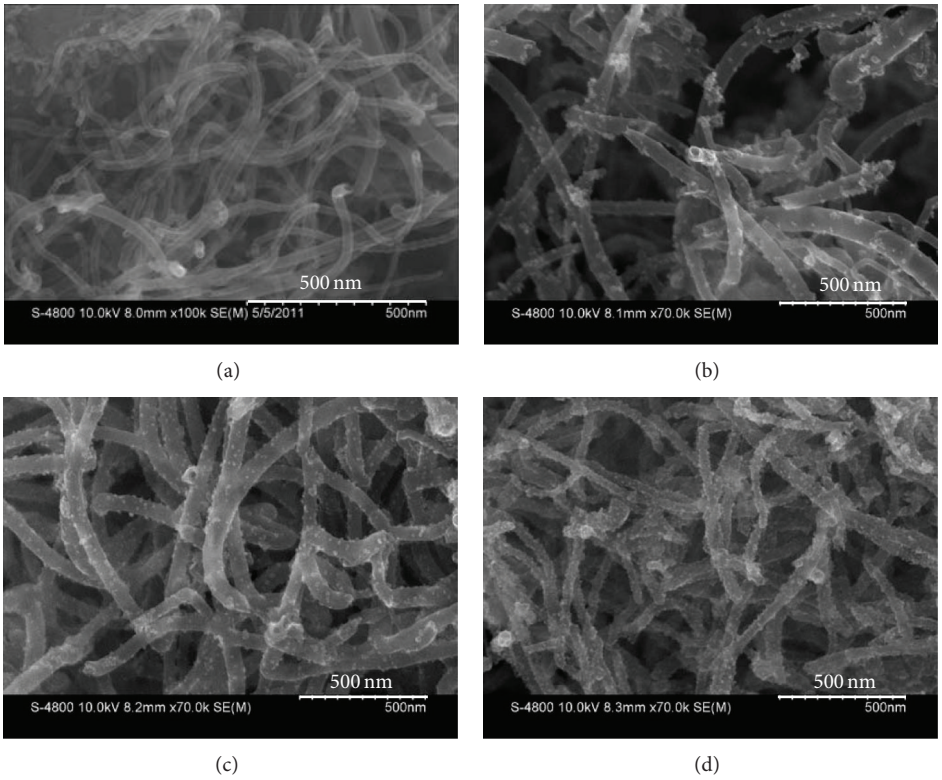

Figure 2: SEM images of bare CNx (a), TiO_2-CNx composites with different weight ratio of TiO_2 over CNx 5% (b), 10% (c), and 20% (d).

42.6° corresponded to the (002) and (100) reflections of CNx, respectively, (JCPDS 41-1487), which indicated that the employed CNx was highly graphitized (Figure 1(a)). It is obvious that the TiO_2-CNx nanocomposites show the same characteristic diffraction peaks referred to as anatase TiO_2 (JCPDS number 21-1272). The characteristic peaks at 2θ of 25.3, 37.8, 48.0, 53.9, 55.1, and 62.7° can be indexed to (101), (004), (200), (105), (211), and (204) crystal planes of anatase TiO_2, respectively. Notably, no typical diffraction peaks belonging to the separate CNx are observed in the TiO_2-CNx nanocomposites. The reason can be ascribed to the fact that the main characteristic peak of CNx at 26.1° might be shielded by the main peak of anatase TiO_2 at 25.3°.

Figures 2 and 3 show the SEM and TEM images of bare CNx and TiO_2-CNx composites. CNx with relatively outer diameter (30~60 nm) was obtained, and the nanomaterial has a bamboo-like morphology with a clear, smooth surface. It is clearly seen that, for TiO_2-CNx nanocomposites, the TiO_2 nanoparticles are almost uniformly deposited on the surface of CNx. The more weight ratio of TiO_2 over CNx, the more visible nanoparticles observed (Figures 2(b), 2(c), and 2(d)). Figure 3(b) is TEM image of an individual CNx fully coated with TiO_2 nanoparticles. The bamboo-like morphology of CNx can be also clearly observed, and its surface is entirely and homogeneously covered by TiO_2 nanoparticles. There are no clear boundary and vacant space between the TiO_2 coating and CNx substrate. The nanoparticles covered on the CNx show clear crystal lattice fringes (Figure 3(c)). The intimate contact between CNx and TiO_2 favors the formation of junctions between the two materials, as a result, being helpful for improving the charge separation and thus the photocatalytic activity. As estimated from the TEM images, the size of TiO_2 nanoparticles is about 7 nm. EDX spectrum presented in Figure 3(d) further determined the existence of Ti and O atoms.

TGA-DSC analysis was carried out to estimate the carbon nanotube content of the nanocomposite. The results of weight loss and heat flow as a function of temperature for TiO_2-CNx nanocomposites are shown in Figure 4. For the 5 wt% and 15 wt% TiO_2-CNx nanocomposites, the weight loss due to the combustion of the CNx was 93.5% and 83.8%, respectively, indicating that TiO_2/CNx ratios estimated from the synthesis precursors of the nanocomposites were in close agreement with the results obtained from TGA-DSC analyses. Therefore, negligible losses of CNx occurred during the composite preparation procedure. The combustion point of CNx in the 15 wt% TiO_2-CNx composite was found to be 544.3°C, whereas CNx in 5 wt% TiO_2-CNx composite could not be combusted until approximately 647.6°C. The combustion temperature shift between different TiO_2/CNx ratios may be ascribed to the following two reasons: (i) more amount of TiO_2 grafted on the sidewall of CNx may provide more oxygen required by the combustion of CNx and (ii) more amount of TiO_2 restrains the heat transfer creating localized hot spots, facilitating the oxidation of carbon.

Figure 5 shows the results of the decomposition of MO under irradiation, in the presence of neat TiO_2, TiO_2-CNTs, and TiO_2-CNx nanocomposites with different weight

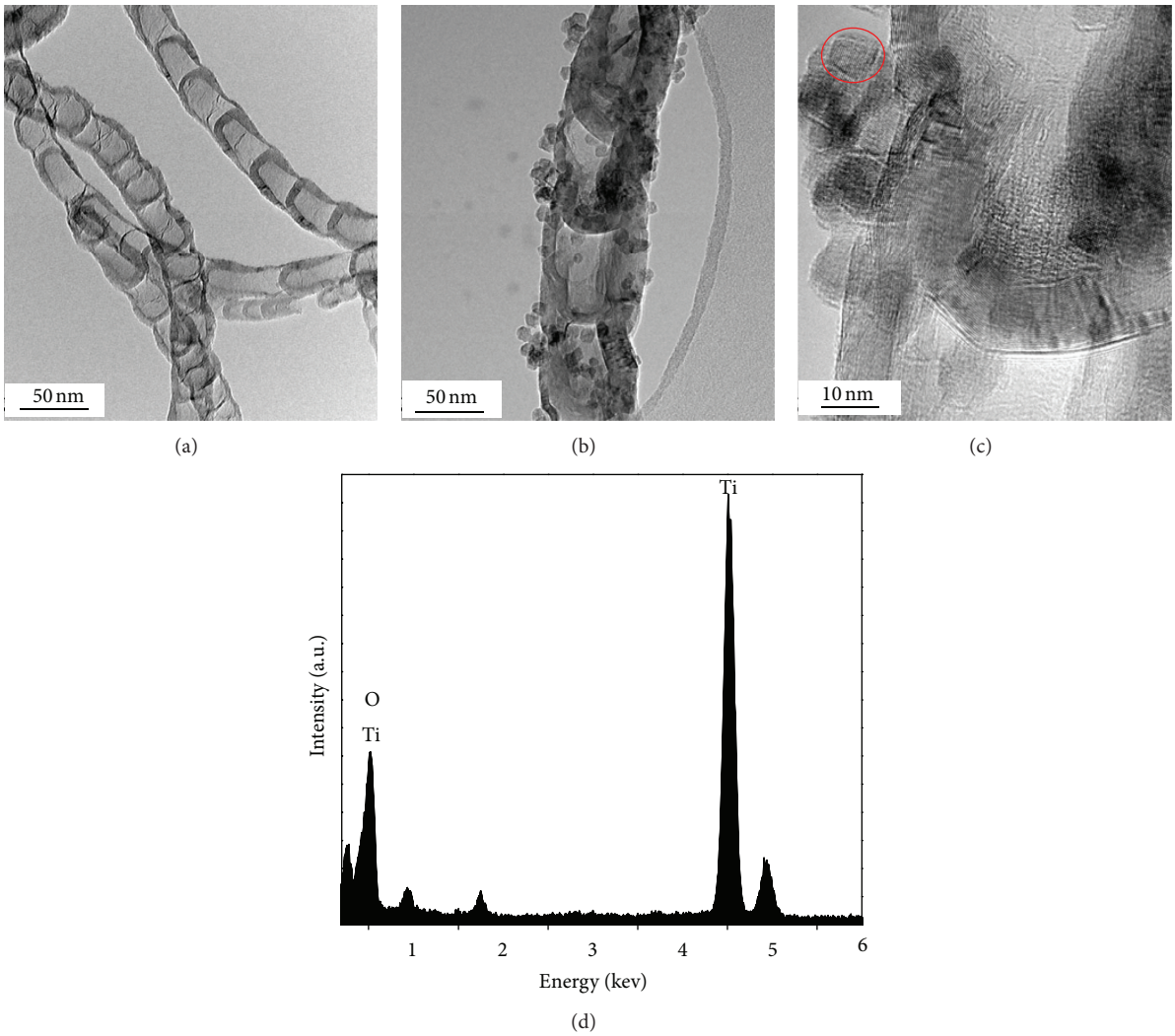

Figure 3: TEM images of bare CNx (a), low-magnification TEM image (b), high-magnification TEM image (c), and EDS spectrum of 10 wt% TiO_2-CNx composites (d).

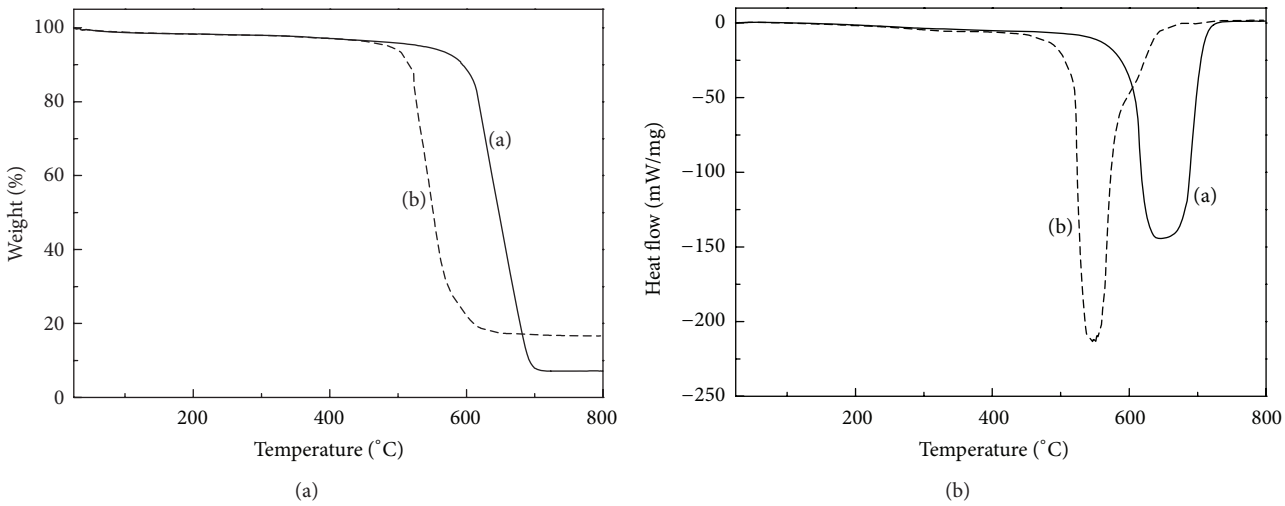

Figure 4: TG and DSC curves of TiO_2-CNx composites with different weight ratio of TiO_2 over CNx 5% (a) and 15% (b).

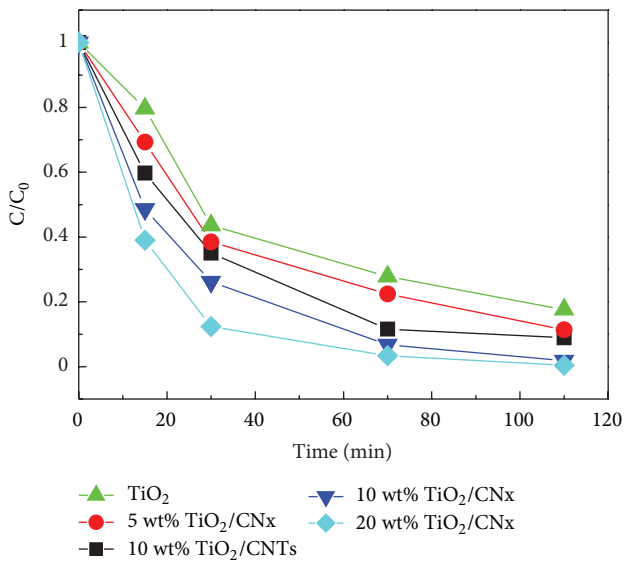

Figure 5: Comparison of photocatalytic activity between different photocatalysts.

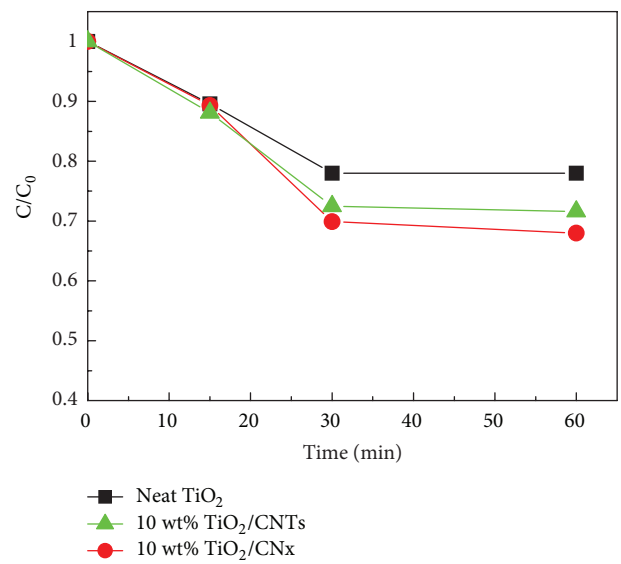

Figure 6: Influence of adsorption time on the remaining fraction of MO (C/C_0) by neat TiO_2, 10 wt% TiO_2-CNTs composites, and 10 wt% TiO_2-CNx composites.

ratios. Control experiments showed that UV irradiation with no catalyst and catalyst (composite or bare CNx) without irradiation could not degrade MO dye solutions. When TiO_2 photocatalyst is used, the degradation efficiency is calculated to be 82.4% at 110 min. When CNTs is introduced, the degradation efficiency is increased to 91.1% for 10 wt% TiO_2-CNTs composites and reaches the maximum value of 99.6% for 20 wt% TiO_2-CNx composites at 110 min. It is noteworthy that TiO_2-CNx composites show superior activity to TiO_2-CNTs composites with the same TiO_2 weight ratio. With the reaction time at 110 min, the MO degradation efficiency of 10 wt% TiO_2-CNTs catalysts is about 91.1%. However, the

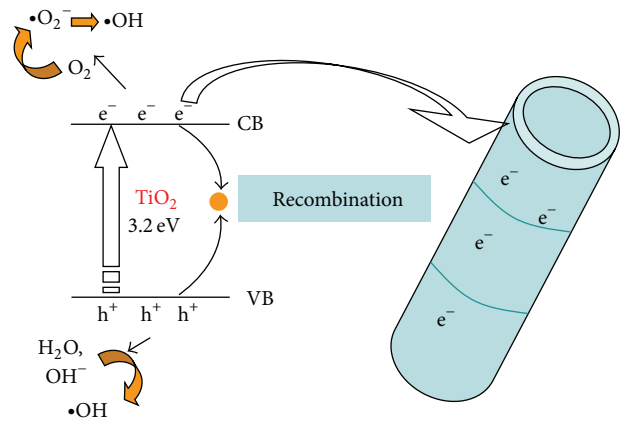

Figure 7: Schematic diagram showing band configuration and electron-hole separation at interface of TiO_2-CNx nanocomposites under UV irradiation (CB: the bottom of conduction band, VB: the top of valence band).

value of 10 wt% TiO_2-CNx is 98.2%. Hence, TiO_2-CNx is an excellent photocatalyst in our experiment.

It has been reported that high adsorption capacities of photocatalysts can lead to the rapid diffusion of MO molecules from solution to the surface of photocatalysts and thus improve photocatalytic performances [20]. Figure 6 shows the remaining fraction of MO (C/C_0) in solution during adsorption for 60 min in dark by neat TiO_2, TiO_2-CNTs composites and TiO_2-CNx composites. It is obvious that three photocatalysts exhibited adsorption capacities for MO molecules in the following order: 10 wt% TiO_2-CNx > 10 wt% TiO_2-CNTs > TiO_2. The improved adsorption capacity of 10 wt% TiO_2-CNx is attributed to its larger specific surface area of 150.25 m^2/g than these of 10 wt% TiO_2-CNTs (128.26 m^2/g) and neat TiO_2 (85.49 m^2/g). It is noteworthy that the concentration of MO molecules shows negligible change after 30 min, indicating the adsorption equilibration. So the adsorption is not the main reason for the improvement of photocatalytic activity in our experiment because the mixture was stirred for 30 min in advance. The enhancement of the photocatalytic performance should be mainly ascribed to the promotion of separation rate of photogenerated electron and hole by the formation of heterostructure, as shown in Figure 7.

Under UV irradiation, the valence band electrons of TiO_2 can be excited to its conduction bands, giving rise to high-energy electron-hole pairs. Compared with CNTs, CNx has a high degree of defects introduced by nitrogen doping [21]. When the electrons generated by TiO_2 transfer into CNx, it could be used as a larger capacity container of electron in comparison with the usual CNTs. So the separation efficiency of electron-hole pairs improved, leading to the dramatically enhanced photoactivity. Moreover, compared to carbon, nitrogen has an extra electron, and from an electronic point of view it is natural to expect an excess of donors in the N-rich areas of the CNTs upon doping [22, 23]. That is to say, impurities significantly enhanced the CNx metallic/conductive character [24]. Hence, the rapid transferring of

electron enhanced separation rate of photogenerated electron and hole.

In order to further explore the effect of the interphase linkage, a mechanical mixture of CNx and TiO_2 was prepared. The composition of the mixture was prepared with the same ratio as that in 10 wt% TiO_2-CNx nanocomposites. The photocatalytic activity of the mixture photocatalyst was 76.4% at 110 min, much lower than that of 10 wt% TiO_2-CNx nanocomposites (98.2%). The low activity is ascribed to CNx in the photocatalyst not being effective in trapping electrons. This lack of effectiveness prevents a decrease in recombination rate. In the mechanical mixture, it is possible that the mechanical mixture process cannot form a strong interphase between the TiO_2 and the CNx. In contrast, a strong interphase was formed in TiO_2-CNx composites, as evidenced by the previous analysis. Therefore, TiO_2-CNx composites showed high activity. Moreover, CNx was almost inactive during MO degradation by UV light irradiation. Once CNx became incapable of bonding strongly with TiO_2, they simply occupied the active sites and scattered the incident light. Therefore, the hydrothermal synthesis procedure is a critical factor in forming high-activity TiO_2-CNx nanocomposites photocatalysts.

4. Conclusions

In this work, we have synthesized uniformly dispersed TiO_2 on the surface of CNx via a hydrothermal synthesis method. The nanocomposites showed excellent photocatalytic activity compared with neat TiO_2 and TiO_2-CNTs. The rapid transferring of electron and high separation efficiency of electron-hole pairs lead to the dramatically enhanced photocatalytic activity. According to the activity and characterization results, the interphase linkage of TiO_2 and CNx is a critical factor for promoting photocatalysis. A mechanical mixture cannot provide strong binding between TiO_2 and CNx, thus showing decreased activity.

Acknowledgments

This work is supported by Leading Academic Discipline Project of Shanghai Municipal Education Commission (J51803), the National Science Foundation of China (NSFC, nos. 21101105 and 51174274), Innovation Program supported by Shanghai Municipal Education Commission (12ZZ195 and 13YZ134), Shanghai Educational Development Foundation and the Shanghai Municipal Education Commission (12CG66), "Shu Guang" Project supported by Shanghai Municipal Education Commission (09SG54), and Teachers in Shanghai Colleges and Universities (egd11008 and ZZegd12003).

References

[1] Y. Wang and C. Hong, "TiO_2-mediated photomineralization of 2-chlorobiphenyl: the role of O_2" *Water Research*, vol. 34, no. 10, pp. 2791–2797, 2000.

[2] K. Tanaka, K. Padermpole, and T. Hisanaga, "Photocatalytic degradation of commercial azo dyes," *Water Research*, vol. 34, no. 1, pp. 327–333, 2000.

[3] A. Fujishima, T. N. Rao, and D. A. Tryk, "Titanium dioxide photocatalysis," *Journal of Photochemistry and Photobiology C*, vol. 1, no. 1, pp. 1–21, 2000.

[4] Q. Xiang, J. Yu, W. Wang, and M. Jaroniec, "Nitrogen self-doped nanosized TiO_2 sheets with exposed 001 facets for enhanced visible-light photocatalytic activity," *Chemical Communications*, vol. 47, no. 24, pp. 6906–6908, 2011.

[5] C. Minero and D. Vione, "A quantitative evalution of the photocatalytic performance of TiO_2 slurries," *Applied Catalysis B*, vol. 67, no. 3-4, pp. 257–269, 2006.

[6] S. Wang, L. Ji, B. Wu, Q. Gong, Y. Zhu, and J. Liang, "Influence of surface treatment on preparing nanosized TiO_2 supported on carbon nanotubes," *Applied Surface Science*, vol. 255, no. 5, pp. 3263–3266, 2008.

[7] W. Wang, P. Serp, P. Kalck, and J. L. Faria, "Photocatalytic degradation of phenol on MWNT and titania composite catalysts prepared by a modified sol-gel method," *Applied Catalysis B*, vol. 56, no. 4, pp. 305–312, 2005.

[8] H. Yu, X. Quan, S. Chen, H. Zhao, and Y. Zhang, "TiO_2-carbon nanotube heterojunction arrays with a controllable thickness of TiO_2 layer and their first application in photocatalysis," *Journal of Photochemistry and Photobiology A*, vol. 200, no. 2-3, pp. 301–306, 2008.

[9] H. Yu, X. Quan, S. Chen, and H. Zhao, "TiO_2-multiwalled carbon nanotube heterojunction arrays and their charge separation capability," *Journal of Physical Chemistry C*, vol. 111, no. 35, pp. 12987–12991, 2007.

[10] S. Aryal, C. K. Kim, K. Kim, M. S. Khil, and H. Y. Kim, "Multi-walled carbon nanotubes/TiO_2 composite nanofiber by electrospinning," *Materials Science and Engineering C*, vol. 28, no. 1, pp. 75–79, 2008.

[11] Y. Yao, G. Li, S. Ciston, R. M. Lueptow, and K. A. Gray, "Photoreactive TiO_2/carbon nanotube composites: synthesis and reactivity," *Environmental Science and Technology*, vol. 42, no. 13, pp. 4952–4957, 2008.

[12] O. Akhavan, M. Abdolahad, Y. Abdi, and S. Mohajerzadeh, "Synthesis of titania/carbon nanotube heterojunction arrays for photoinactivation of *E. coli* in visible light irradiation," *Carbon*, vol. 47, no. 14, pp. 3280–3287, 2009.

[13] G. Jiang, Z. Lin, L. Zhu, Y. Ding, and H. Tang, "Preparation and photoelectrocatalytic properties of titania/carbon nanotube composite films," *Carbon*, vol. 48, no. 12, pp. 3369–3375, 2010.

[14] A. Jitianu, T. Cacciaguerra, R. Benoit, S. Delpeux, F. Béguin, and S. Bonnamy, "Synthesis and characterization of carbon nanotubes-TiO_2 nanocomposites," *Carbon*, vol. 42, no. 5-6, pp. 1147–1151, 2004.

[15] J. Yu, T. Ma, and S. Liu, "Enhanced photocatalytic activity of mesoporous TiO_2 aggregates by embedding carbon nanotubes as electron-transfer channel," *Physical Chemistry Chemical Physics*, vol. 13, no. 8, pp. 3491–3501, 2011.

[16] Y. Cong, X. Li, Y. Qin et al., "Carbon-doped TiO_2 coating on multiwalled carbon nanotubes with higher visible light photocatalytic activity," *Applied Catalysis B*, vol. 107, no. 1-2, pp. 128–134, 2011.

[17] K. Ghosh, M. Kumar, H. Wang, T. Maruyama, and Y. Ando, "Nitrogen-mediated wet-chemical formation of carbon nitride/ZnO heterojunctions for enhanced field emission," *Langmuir*, vol. 26, no. 8, pp. 5527–5533, 2010.

[18] R. Zhang, L. Li, L. Chen, G. Zhang, and K. Shi, "N-doped carbon nanotubes synthesized in high yield and decorated with CeO_2 and SnO_2 nanoparticles," *Journal of Alloys and Compounds*, vol. 509, no. 35, pp. 8620–8624, 2011.

[19] L. Wang, L. Wang, H. Jin, and N. Bing, "Nitrogen-doped carbon nanotubes with variable basicity: preparation and catalytic properties," *Catalysis Communications*, vol. 15, no. 1, pp. 78–81, 2011.

[20] R. Leary and A. Westwood, "Carbonaceous nanomaterials for the enhancement of TiO_2 photocatalysis," *Carbon*, vol. 49, no. 3, pp. 741–772, 2011.

[21] Y. T. Lee, N. S. Kim, S. Y. Bae et al., "Growth of vertically aligned nitrogen-doped carbon nanotubes: control of the nitrogen content over the temperature range 900–1100°C," *Journal of Physical Chemistry B*, vol. 107, no. 47, pp. 12958–12963, 2003.

[22] S. K. Hong and S. Jeong, "Nitrogen doping and chirality of carbon nanotubes," *Physical Review B*, vol. 70, no. 23, Article ID 233411, 4 pages, 2004.

[23] A. H. Nevidomskyy, G. Csányi, and M. C. Payne, "Chemically active substitutional nitrogen impurity in carbon nanotubes," *Physical Review Letters*, vol. 91, no. 10, Article ID 105502, 4 pages, 2003.

[24] M. Terrones, P. M. Ajayan, F. Banhart et al., "N-doping and coalescence of carbon nanotubes: synthesis and electronic properties," *Applied Physics A*, vol. 74, no. 3, pp. 355–361, 2002.

Hindawi Publishing Corporation
International Journal of Photoenergy
Volume 2013, Article ID 875456, 10 pages
http://dx.doi.org/10.1155/2013/875456

Research Article

Effect of Different Calcination Temperatures on the Structural and Photocatalytic Performance of Bi-TiO_2/SBA-15

Jing Ma,[1] Jia Chu,[2] Liangsheng Qiang,[3] and Juanqin Xue[1]

[1] *College of Metallurgical Engineering, Xi'an University of Architecture and Technology, Xi'an 710055, China*
[2] *College of Chemistry and Chemical Engineering, Xi'an University of Science and Technology, Xi'an 710054, China*
[3] *Department of Chemistry, Harbin Institute of Technology, Harbin 150001, China*

Correspondence should be addressed to Jing Ma; mjhit@yahoo.cn and Jia Chu; chujiahit@yahoo.cn

Received 17 May 2013; Revised 27 June 2013; Accepted 28 June 2013

Academic Editor: Huogen Yu

The new novel material Bi-TiO_2/SBA-15 was synthesized by an easy wet impregnation method. A combination of XRD, XPS, Raman, N_2 adsorption-desorption isotherm measurement, TEM, and solid state UV-Vis spectroscopy has been used to characterize the Bi-TiO_2/SBA-15 material. It was found that SBA-15 retained the ordered hexagonal mesostructure after incorporation of TiO_2 and Bi. The photodecomposition of rhodamine B (RhB) in aqueous medium was selected to evaluate the photocatalytic performance of Bi-TiO_2/SBA-15 under visible light irradiation ($\lambda \geq 420$ nm). The experiment results indicated that Bi-TiO_2/SBA-15 exhibited higher photocatalytic activities than pure TiO_2 and Bi_2O_3. The influences of calcination temperature were studied. It strongly influenced the activity of the samples. The sample calcined at 550°C shows the highest photocatalytic activity in the decomposition of RhB under visible light. The catalyst preserved almost its initial photocatalytic activity after six reuses.

1. Introduction

The photocatalytic properties of TiO_2 have been exploited in various applications since Fujishima and Honda reported a TiO_2 photochemical electrode for splitting water in 1972 [1]. TiO_2 is regarded as the most promising one for its high photocatalytic activity, chemical/photocorrosion stability, low cost, and environmental friendiness. However, the large band gap of TiO_2 (3.20 eV) and low quantum efficiency restricts its wide application [2]. This factor can be minimized by doping of semiconductors such as WO_3, Bi_2O_3, and CdS, which could change the electronic properties of TiO_2 [3–5]. Among them, Bi-based photocatalysts (Bi_2O_3 or its related compounds) have attracted much attention. Bi_2O_3 (2.8 eV) exhibits good charge carrier mobility, in which species with lone electron pair forming Bi-O polyhedra can act as electron trapping centers and hinder electron-hole pair recombination to improve the photoabsorptivity and photocatalytic activity [6, 7].

Recently, there are several works on the photocatalytic properties of Bi-doped TiO_2 materials under visible light irradiation [8–10]. Hou et al. used Bi_2O_3 quantum dots to enhance the photoactivity of TiO_2 nanosheets with exposed (001) facets [11]. Di Camillo et al. reported that Bi-doped TiO_2 NFs have been deposited by electrospinning and showed very interesting photocatalytic properties [12]. Su et al. synthesized a new TiO_2-based photocatalyst with both B doping and Bi_2O_3 coupling ($Bi_2O_3/TiO_{2-x}B_x$). The catalyst was used in degrading pentachlorophenol under visible light ($\lambda > 420$ nm) irradiation [13]. Li et al. reported the preparation of highly monodisperse spherical Bi-doped TiO_2. Their hybrid showed enhanced photocatalytic activity under visible light [14]. Shamaila et al. demonstrated an approach for the preparation of a mesoporous nanocrystalline TiO_2 based on EISA method [15]. The catalyst showed the superior activity as compared to M-TiO_2 (M refers to metal ion), Degussa P25, and impregnated Degussa P25 for the photodegradation of Methyl Orange (MO) and 2,4-dichlorophenol (2,4-DCP). Rengaraj and coworkers synthesized a Bi^{3+}-doped TiO_2 nanocatalyst. According to their results, the presence of Bi species in TiO_2 catalysts substantially enhanced the photocatalytic degradation of methyl parathion under UV irradiation [16].

Generally, the present Bi_2O_3-TiO_2 composite photocatalysts were limited by the low adsorption ability. To address this issue, much effort has been focused on enhancing the adsorption ability of the catalysts to improve their photocatalytic performance. Well-ordered mesoporous silica materials such as MCM-41 and SBA-15 have been widely used for adsorption, separation and catalysis [17–20]. SBA-15 is a type of uniform hexagonal pores and high surface area mesoporous material. Such type of highly interconnected mesostructured porous material is expected to allow the guest species to access the opened porous host easily. Design of photocatalysts modified by SBA-15 is a promising way to enhance high photocatalytic activity. However, no studies have attempted to establish a system consisting of a Bi_2O_3-TiO_2 hybrid incorporated into mesoporous silica.

Herein, the aim of the present paper is to investigate the synthesis of size controlled Bi_2O_3 and TiO_2 supported on mesostructured SBA-15. The photodegradation of RhB was employed to evaluate the photocatalytic activities of the Bi-TiO_2/SBA-15, with a 300 W Xe lamp ($\lambda \geq 420$ nm) as the light source.

Rhodamine B (RhB, N,N,N′,N′-tetraethylrhodamine) has moderate wash and light fastness properties. It is a useful analytical reagent for the detection and determination of metals. However, the use of RhB as a food color has been discontinued for a number of years on account of its suspected carcinogenic nature. Therefore, the removal of these dyes from wastewater is of great concern. Based on these considerations, the photodecomposition of RhB in aqueous medium was selected to evaluate the photocatalysis performance of Bi-TiO_2/SBA-15.

Considering the different calcination temperatures having an influence on the photocatalytic performance, the activities on different calcination temperatures were tested and discussed. Moreover, the recycle ability of Bi-TiO_2/SBA-15 was also evaluated.

2. Experimental

2.1. Catalyst Preparations. The SBA-15 was prepared according to the previous procedure by reaction from a solution of triblock copolymer P123 ($EO_{20}PO_{70}EO_{20}$, Aldrich) and tetraethoxysilane (TEOS) [21, 22]. P123 was used as a structure directing agent. In a typical process, 2 g of P123 was added to 75 mL of aqueous HCl under stirring at 40°C for 2 h. 4.17 mL of TEOS was then added to the solution which was stirred for another 24 h. The suspension was transferred into a steel autoclave and kept at 100°C for 72 h. After cooling to room temperature, the precipitate in the bottom of Teflon vessel was collected, filtered, thoroughly washed with water to remove any unreacted chemicals, and dried at room temperature. Calcinations were performed by heating in air at 550°C for 6 h to remove the template.

TiO_2/SBA-15 material was first prepared by internal hydrolysis method with little modification [23]. In this case, the calculated amount of tetrabutyl titanate (TBT) was dissolved in ethanol in a volume ratio of 1 : 5 (the amount of TBT is 0.92 mL). 0.5 g SBA-15 was then added to the solution containing TBT and stirred for 1 h to make the TBT adsorb completely on the SBA-15. The condensation reaction was started by dropwise addition of water and then the stirring was continued for 2 h to hydrolyze TBT completely. The solid product was recovered by filtration, washed with ethanol to remove any unanchored titanium species, dried at 80°C overnight, and calcined in air at 550°C for 3 h. The calcined samples were designated as TiO_2/SBA-15.

For Bi-doping TiO_2/SBA-15 supports, samples containing Bi were prepared by an easy wet impregnation method. TiO_2/SBA-15 and $Bi(NO_3)_3{\cdot}5H_2O$ were mixed in an ethanol solution with a drop of HNO_3 and stirred for 5 h, where the Bi/Ti molar ratio is 2.0%. The suspension was dried and calcined in air at different temperatures. The samples were designated as Bi-TiO_2/SBA-15(x), where x refers to the calcination temperatures, which are 400°C, 550°C, 700°C, and 850°C, respectively.

2.2. Characterization Techniques. Small-angle X-ray diffraction (SAXRD) measurements were performed on a Siemens D5005 instrument with CuKα ($\lambda = 0.154$ nm) radiation. The diffractograms were recorded in the 2ϑ range of 0.5–5° with a 2ϑ step size of 0.01°. Wide-angle X-ray diffraction (WAXRD) measurements were carried out on an XRD-6000 X-ray diffractometer (Shimadzu) CuKα ($\lambda = 0.154$ nm) radiation. The diffractograms were recorded in the 2ϑ range of 10–80° with a 2ϑ step size of 0.2°. Raman spectra were measured with JOBIN YVON HR800 Raman spectrophotometer (France) in the range of 100–1400 cm^{-1}, using an Ar ion laser. N_2 adsorption-desorption isotherms were measured at 77 K in a Quantachrome Autosorb-1 sorption analyzer. Samples were outgassed at 300°C for 10 h before the measurement. TEM was performed by an FEI Tecnai G2 S-Twin electron microscope with an acceleration voltage of 200 kV. XPS was obtained using a physical electronics model PHI5700 X-ray photoelectron spectrometer with MgKα X-rays as the excitation source. The binding energies were calibrated with reference to C1s at 285 eV. UV-V is absorption spectra scans were performed on a Shimadzu UV-2550 spectrometer in the range from 300 to 600 nm. $BaSO_4$ was used as a reflectance standard material during the experiment. Photoluminescence (PL) spectra were performed on JASCO FP-6500 fluorescence spectrometer.

2.3. Photocatalytic Activity Measurement. The photocatalytic activities were investigated for the photodegradation of RhB in aqueous solution under visible light in a photolysis glass reactor. The pH of solution was 7 during the reaction. The visible light source was a 300 W Xe lamp ($\lambda \geq 420$ nm to provide visible light irradiation) with a double wall jacket in which water was circulated to prevent overheating of the reaction mixture. 50 mg of Bi-TiO_2/SBA-15(x) was added to rhodamine B (RhB) (100 mL, 1×10^{-5} M) and stirred for 30 min without visible light irradiation in order to establish an adsorption-desorption equilibrium between RhB and the catalyst. Next, the solution was illuminated by visible light. At a given time interval, 4 mL of the suspension was withdrawn. After centrifugation at 5000 rpm for 5 min, the filtrate was monitored by UV-Vis spectrophotometer (UV-5200).

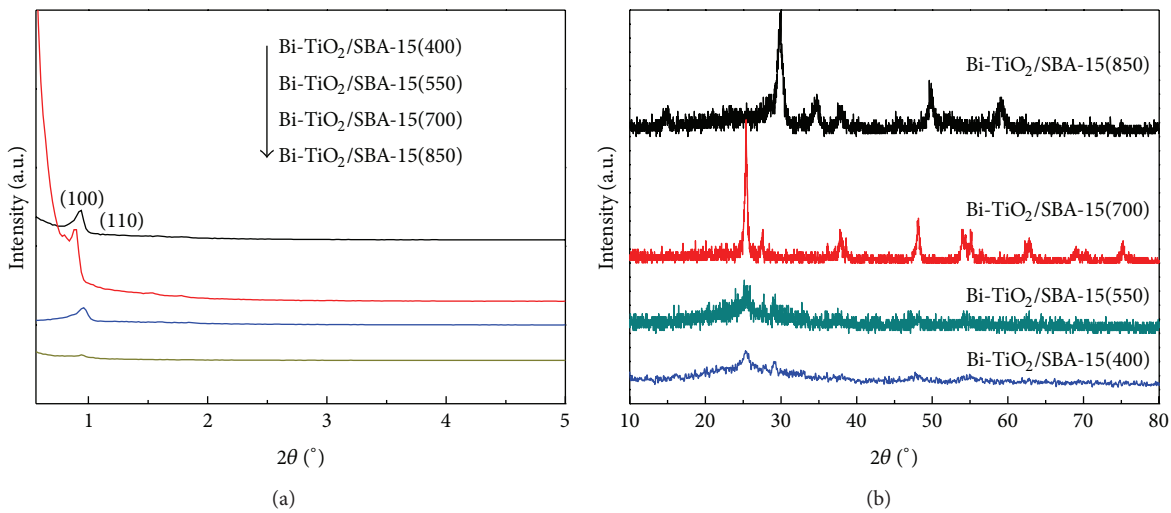

Figure 1: Small-angle (a) and wide-angle (b) XRD patterns of Bi-TiO_2/SBA-15(x).

Table 1: Textural properties of Bi-TiO_2/SBA-15(x).

Samples	Bi/Ti[a]	BET area ($m^2 \cdot g^{-1}$)	V_{tot}[b] ($cm^3 \cdot g^{-1}$)	D[c] (nm)
SBA-15	0	590.3	0.961	7.224
Bi-TiO_2/SBA-15(400)	2.01%	540.1	0.544	5.936
Bi-TiO_2/SBA-15(550)	1.95%	527.7	0.518	5.882
Bi-TiO_2/SBA-15(700)	1.89%	299.5	0.307	5.767
Bi-TiO_2/SBA-15(850)	1.62%	182.7	0.221	4.061
TiO_2/SBA-15(550)	0	568.3	0.924	6.818

[a]Bi/Ti was measured by ICP, [b]V_{tot}: the total pore volume, [c]D: average pore diameter.

3. Results and Discussions

3.1. Textural Properties and Characterization Typical. Small-angle XRD patterns of calcined Bi-TiO_2/SBA-15(x) samples in the range of 0.5–5° were shown in Figure 1(a). All samples exhibit well-resolved diffraction peak at $2\vartheta = 0.8$-$0.9°$ corresponding to the (100) diffraction peak of the hexagonal features of the SBA-15, indicating that their ordered pore structure is maintained well. The position of the diffraction peak shifted to a higher angle indicating a small decrease of the pore size and unit cell. It is seen that SBA-15 has a good thermal stability. The diffraction intensity gradually decreased with increasing the calcination temperature.

Figure 1(b) shows the wide-angle XRD pattern of the Bi-TiO_2/SBA-15(x) calcined at different calcination temperatures. The XRD patterns of the samples evidenced that when the temperature is 400 and 550°C, a typical broad diffraction peak centered at 2ϑ of 25°, which is typical characteristic of amorphous silica. No clear characteristic peaks of crystalline TiO_2 and Bi_2O_3 were observed in XRD patterns of sample, which indicated that the small nanoparticle sizes of TiO_2 and Bi_2O_3 were successfully incorporated into the silica framework. However, sample calcined at 700°C shows the appearance of anatase phase. It is observed that, with increase of calcination temperature, TiO_2 grain size increases. With further increase of calcination temperature to 850°C, a new diffraction peak at $2\vartheta = 30°$ was observed in the XRD pattern, which might be due to the formation a new phase of $Bi_4Ti_3O_{12}$ at 850°C. It is indicated that the new phase gradually dominates the composition of the samples. So it is feasible to control the ratio of the anatase phases by varying the calcination temperatures. In addition, no significant diffraction peak of Bi species was observed regardless of the calcination temperature because of the higher dispersion of Bi and the low content of Bi.

The adsorption-desorption isotherms for Bi-TiO_2/SBA-15 are shown in Figure 2(a). The samples exhibit isotherms of typical type IV with a H2 hysteresis loop due to the capillary condensation steps at relative pressure of $0.5 < p/p_0 < 0.8$, which is characteristic of a mesopores material [24, 25]. It can be clearly observed that the amount of N_2 adsorption decreases upon Bi_2O_3 and TiO_2 addition. Such a decrease of N_2 adsorption for samples is reasonable, considering the formation of Bi_2O_3 and TiO_2 nanoparticles inside the mesopores of SBA-15. When the calcination temperature increases to 850°C, the isotherm changes to H1 hysteresis loop. The hysteresis loop in the isotherms is obviously shifted to the high relative pressure, indicating that pore sizes of the samples decrease with the calcination temperature.

The BET specific area and the pore size of TiO_2/SBA-15 and Bi-TiO_2/SBA-15(x) were summarized in Table 1. The specific surface area, pore size, and volume decrease

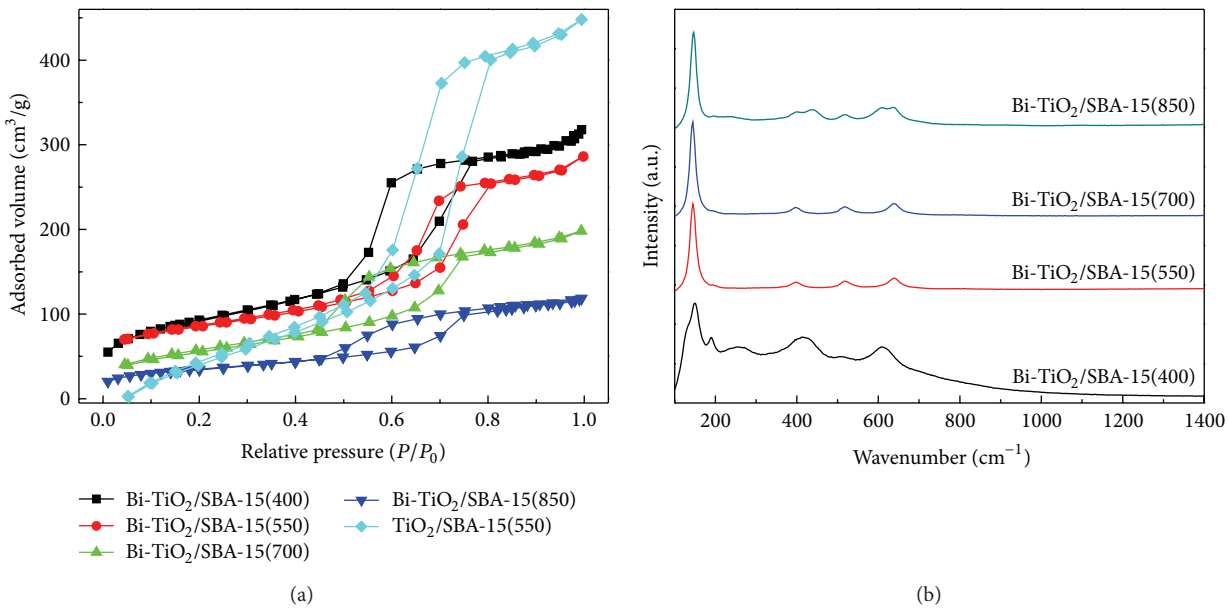

Figure 2: (a) N_2 adsorption-desorption isotherms of Bi-TiO_2/SBA-15(x). (b) Raman spectra of Bi-TiO_2/SBA-15(x).

with the calcination temperature increasing. Based on the observations, with the calcination temperature increasing, total pore volume and BET surface area were decreased 16.0% and 5.9% at least, respectively. It is clear that the increasing calcination temperature leads to decrease pore volume, specific surface area, and the porosity of the samples. Meanwhile, the increasing calcination temperature helps to increase the TiO_2 nanoparticles crystallization degree. We also noted that, when the temperature increased to 850°C, there was a mutation of the specific surface area, which was attributed to the new phase, obstructing the pores of the SBA-15.

Raman spectroscopy further verified the TiO_2 transformation for Bi-TiO_2/SBA-15(x), as shown in Figure 2(b). The Raman bands appear at 147, 400, 520, and 641 cm^{-1} and can be assigned to the E_g, B_{1g}, A_{1g}, and B_{1g} vibration modes of anatase TiO_2 [26]. The results indicate that the doping of Bi has not influenced the anatase type of TiO_2. A new peak appears at 200 cm^{-1} when the calcination temperature was 400°C, which is attributed to the brookite phase. When the temperature is higher, the TiO_2 in brookite phase has been full conversion to anatase with improving the crystalline. When the calcination temperature is up to 850°C, TiO_2 is still in anatase phase in the samples with partial conversion to a new phase of $Bi_4Ti_3O_{12}$. It is indicated that the introduction of Bi can inhibit the transformation of TiO_2 phase in the high temperature.

Figure 3 shows that it retains a regular hexagonal array of uniform channels characteristic of SBA-15 with Bi and TiO_2. It displays highly ordered hexagonal regularity mesopores, where nanoparticles are embedded in the pore walls with random orientation. When the calcination temperature is up to 850°C, the nanocrystals structures do not change and slightly increased the nanoparticles size derived from XRD data. After the same treatment (up to 850°C), the crystal domain size of TiO_2 increased with partial conversion to $Bi_4Ti_3O_{12}$ and that of Bi_2O_3 crystals increased with partial conversion to monoclinic modification.

HRTEM image (Figure 3(e)) reveals that the materials were well crystallized, as evidenced by well-defined lattice fringes. The lattice fringes of 0.35 nm match the (101) plane of anatase TiO_2, while that of 0.325 nm match the (120) plane of Bi_2O_3 nanoparticles, respectively. The HRTEM analysis confirmed that Bi_2O_3 and TiO_2 coexisted in the resulting samples.

In order to analyze the chemical composition and purity of the prepared particles, the XPS survey spectrum of Bi-TiO_2/SBA-15 is shown in Figure 4. Figure 4(a) shows that Bi-TiO_2/SBA-15 contains only Ti, O, Bi, Si, and C elements. The C element can be ascribed to the residual carbon from our characterization. The high-resolution XPS spectra of Bi4f are shown in Figure 4(b). The peaks of Bi 4f7/2 and Bi 4f5/2 are centered at 159.3 and 164.5 eV, which is in agreement with Bi_2O_3 values of other observations [27, 28]. After calcinations at higher temperature, these two peaks move a little to lower energies, hinting that bismuth element brings more effective positive charge and tends to convert to its stable oxidation state from +3 to 0. The Bi species would segregate from the shallow surface and move onto the photocatalyst surface, and some Bi^0 species are oxidized into Bi^{3+} species. This means that calcination may lead to more Bi_2O_3 species formed and to segregation on photocatalyst surface. A weak signal centred at 157.2 eV indicated the existence of Bi^0 [29].

The XPS spectra of O 1s are shown in Figure 4(c). The O 1s peak is broad and complicated due to the nonequivalence of oxygen ions. The peak shape suggests that it is composed of multiple peaks that arise due to the overlapping contributions of oxide ions. The strong peak at 529.8 eV is ascribed to Ti–O bond in TiO_2, the peak at 531.4 eV, which is assigned to the oxygen attached to bismuth (Bi–O bond), and

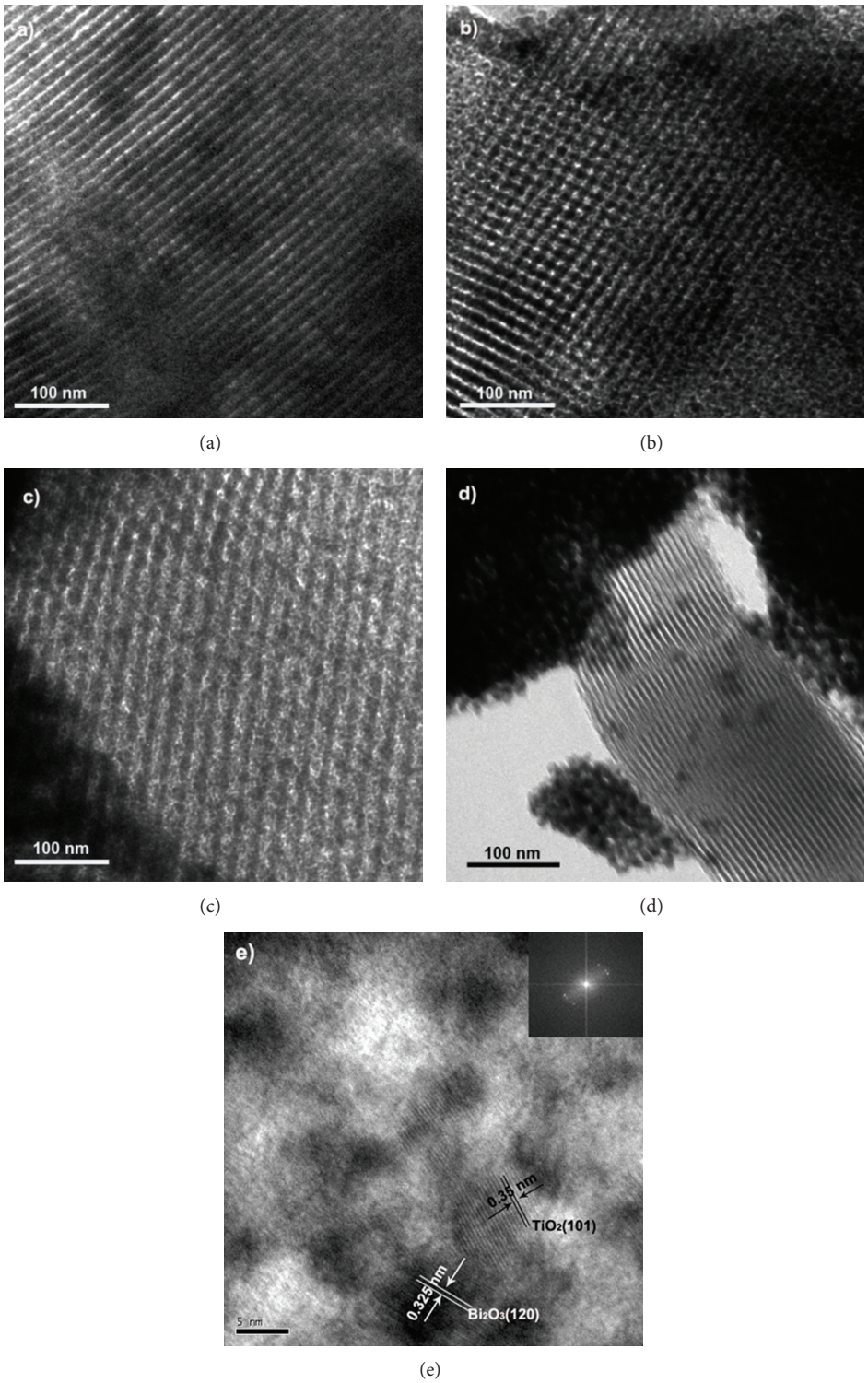

Figure 3: TEM images of Bi-TiO_2/SBA-15: (a) Bi-TiO_2/SBA-15(400), (b) Bi-TiO_2/SBA-15(550), (c) Bi-TiO_2/SBA-15(700), (d) Bi-TiO_2/SBA-15(850), and (e) HRTEM image of Bi-TiO_2/SBA-15(550) (inset is the corresponding FFT pattern).

the shoulder at 533.6 eV is attributed to the OH^- group absorbed on the surface. The Ti 2p of Bi-TiO_2/SBA-15 is shown in Figure 4(d). The peaks of Ti2p3/2 and Ti2p1/2 were centered at 458.2 and 464.7 eV, which showed that the main valence of Ti in the prepared catalysts is +4 and Ti^{4+} is in tetrahedral coordination with oxygen in the catalysts. Meanwhile, there was no significant influence on the spectra in either Ti 2p or O 1s in the presence of Bi_2O_3.

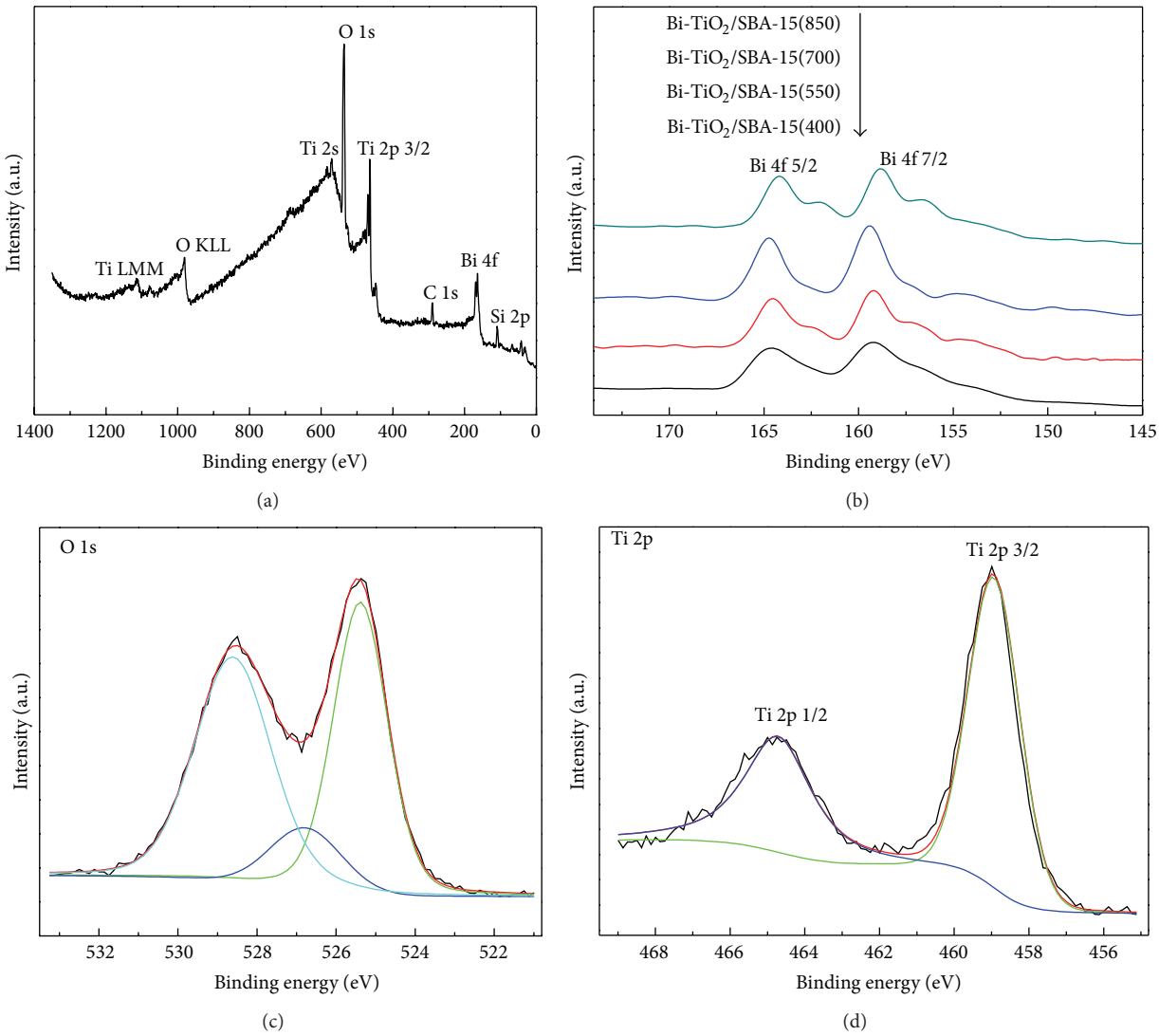

FIGURE 4: XPS survey spectrum of Bi-TiO_2/SBA-15 (a), the high-resolution XPS spectra of Bi 4f region (b), O 1s (c), and Ti 2p (d).

The UV-Vis absorption spectra of the Bi-TiO_2/SBA-15 were presented in Figure 5(a). There a red shift for Bi-TiO_2/SBA-15 in the visible region. The results show that the doping of Bi can increase the absorbance of visible light and extend the absorption edge to longer wavelengths. It can be seen that the Bi-TiO_2/SBA-15 calcined at 400–700°C displayed similar absorbance for visible lights, suggesting that, in the composite, Bi_2O_3 mainly resulted in the spectral response in the visible region. However, with the increase of calcination temperature to 850°C, the Bi-TiO_2/SBA-15 showed an obviously stronger absorption in the visible light region than that of calcined at other temperatures, which might be due to the formation of a new phase of $Bi_4Ti_3O_{12}$ at 850°C. Moreover, the plot of $(\alpha h\nu)^{1/2}$ versus the energy of light afforded band gap energy of 2.81 eV for Bi-TiO_2/SBA-15 (see the inset in Figure 5(a)), which could be easily induced photoelectrons and holes by visible lights.

PL emission spectra have been used to investigate the efficiency of charge carrier trapping, immigration, transfer and to understand the fate of electron-hole pairs in semiconductor particles [30]. Figure 5(b) showed the PL spectra of TiO_2 and Bi-TiO_2/SBA-15 in the range of 400–525 nm. The PL intensity of the samples decreases as follows: TiO_2 > Bi-TiO_2/SBA-15(400) > Bi-TiO_2/SBA-15(700) > Bi-TiO_2/SBA-15(850) > Bi-TiO_2/SBA-15(550). It indicated that, when increasing the calcination temperature, the decrease in trap states on samples surface may slow the recombination process of photogenerated electrons and holes in TiO_2, which benefit the photocatalytic reaction.

3.2. The Photocatalytic Activity of Bi-TiO_2/SBA-15. The UV-Vis absorption spectra clearly reveal that the visible light absorption of Bi-TiO_2/SBA-15 is higher than that of TiO_2. Therefore, it is reasonable to expect higher photocatalytic activity when the Bi species and TiO_2 deposited on the SBA-15 mesostructure. We evaluated the Bi-TiO_2/SBA-15(x) samples for degradation of RhB under visible light irradiation and compared the catalytic efficiency of Bi-TiO_2/SBA-15(x) with

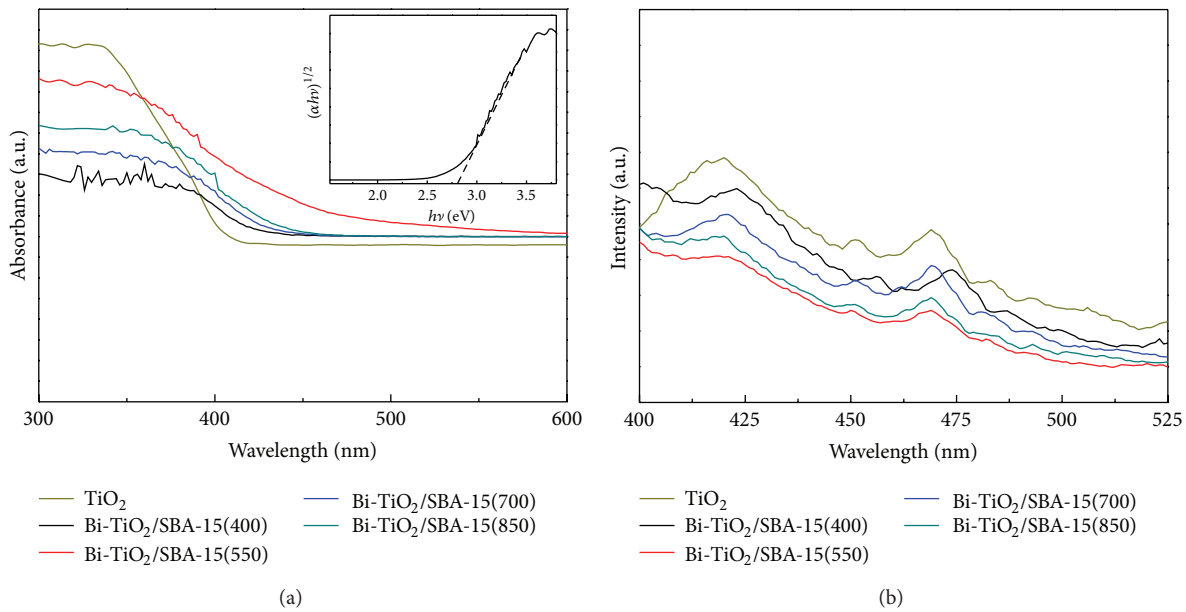

Figure 5: UV-Vis absorption spectra (a) and PL spectra of Bi-TiO_2/SBA-15 (b).

that of TiO_2. The photoactivities for RhB in dark in the presence of the photocatalyst under visible light irradiation in the absence of the photocatalyst are evaluated. It is found that there was no degradation for the RhB in the dark and in the presence of the photocatalyst. There is no degradation observed for RhB when the solution is placed under visible light radiation without the addition of photocatalysts.

Figure 6(a) displayed the effect of the calcination temperature on the photocatalytic activity. The activities decrease showed in the following order: Bi-TiO_2/SBA-15 (550) > Bi-TiO_2/SBA-15(850) > Bi-TiO_2/SBA-15(700) > Bi-TiO_2/SBA-15(400) > Bi_2O_3/SBA-15 > TiO_2/SBA-15(550) > Bi_2O_3 >TiO_2.

It is well known that pure TiO_2 and TiO_2/SBA-15 have no photocatalytic activity under visible light irradiation. However, in Figure 6(a), the experiment results show a little decomposition ability of RhB, which is due to the small size of TiO_2 nanoparticles improving the photocatalytic activity. The degradation efficiency by Bi_2O_3/SBA-15 and Bi_2O_3 is also low.

The Bi-TiO_2/SBA-15(x) almost decomposed the RhB solution within 90 min, compared to the TiO_2 sample, which implies that the doped Bi is essential as a cocatalyst for the efficient degradation. That is to say, the Bi doping on TiO_2/SBA-15 is accorded to the higher photodegradation, which resulted from the formation of Bi species enhancing the electron and hole separation by capturing the photoinduced charges efficiently. There are two reasons for the superior photocatalytic performance. Firstly, valence band (VB) composed of hybridized Bi 6s, Ti 3d, and O 2p orbitals has a strong oxidizing ability and can effectively degrade organic pollutants. And the hybridization of the Bi 6s, Ti 3d, and O 2p levels makes the VB largely dispersed, which favors the mobility of photoholes in the VB and is beneficial for the oxidation reaction. Secondly, the assembled Bi_2O_3 increases the mobility of the photogenerated carriers, and good crystallization may lead to the enhancement of photocatalytic activity for the decomposition of the organic compounds. It is allowing more opportunities for electrons to participate in the reduction reaction to form active oxygen species. The transfer of the photoexcited electrons from the surface of Bi_2O_3 to TiO_2 occurs due to the small Bi_2O_3 band gap and its higher conduction band potential compared to that of TiO_2.

It is known that photodegradation kinetics follow Langmuir-Hinshelwood kinetics model [31]. The reaction can be represented as follows (1):

$$\ln \frac{C_0}{C} = k_{\text{app}} t, \tag{1}$$

where k_{app} is the apparent first-order reaction constant and C_0 is the initial concentration of the RhB solution. A kinetic linear simulation curve of RhB photocatalytic degradation using Bi-TiO_2/SBA-15(x) is shown in Figure 6(b). The fact that the curve showed good linearity indicating that the photocatalytic degradation of RhB using Bi-TiO_2/SBA-15(x) as catalyst fits well with the first-order reaction kinetics. The rate constant of Bi-TiO_2/SBA-15(x) for RhB photodegradation is shown in Table 2. k_{app} value of the Bi-TiO_2/SBA-15(550) is $0.0212\,\text{min}^{-1}$, which is higher than that of TiO_2 and other samples of Bi-TiO_2/SBA-15. It suggested that k_{app} improved by Bi doping. It is widely accepted that the high calcination temperature usually results in smaller specific surface area and particle size, as illustrated in Table 1. The calcination temperature strongly influenced the activity of the samples. Though the sample calcined at 400°C has the largest BET surface area and particle size, its crystalline is worse than that of the calcined at higher temperature, leading to lower photoactivity. Meanwhile, the effect of the photocatalytic activity is decreased when the calcination temperature is up to 700–850°C. It can be explained that the high calcination

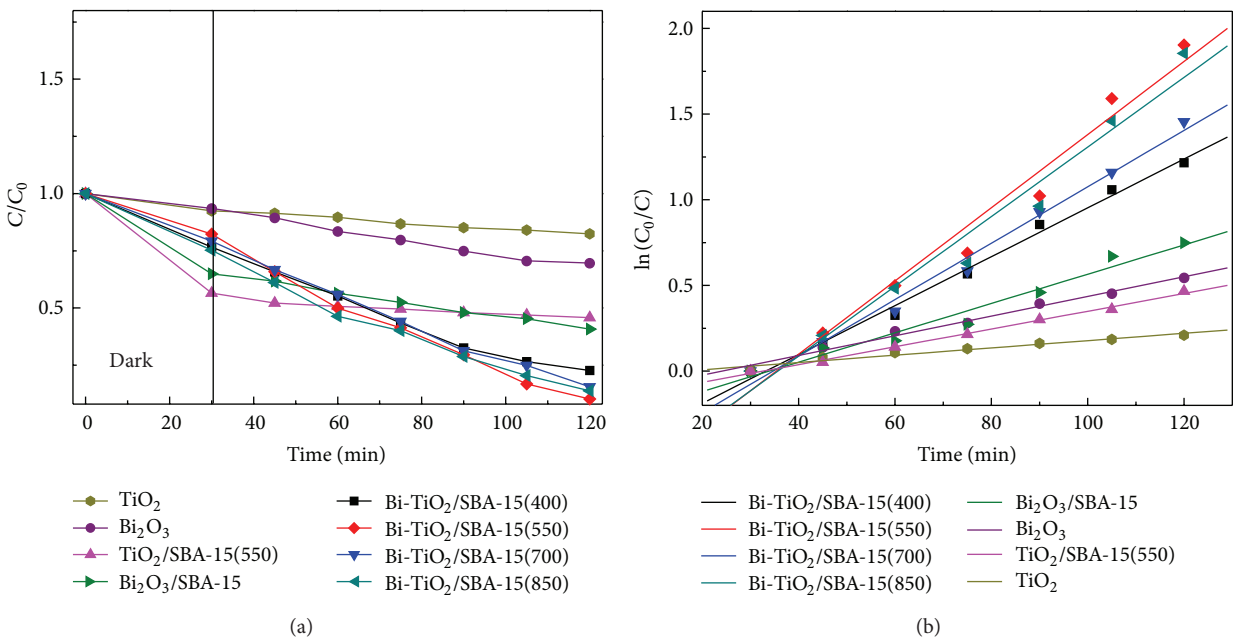

Figure 6: Photocatalytic activity (a) and kinetic linear simulation curve (b) of photocatalytic degradation by Bi-TiO_2/SBA-15(x) under visible light.

Table 2: The rate constant of Bi-TiO_2/SBA-15(x) for RhB photodegradation.

Samples	k_{app} (min^{-1})
Bi-TiO_2/SBA-15(400)	0.0135
Bi-TiO_2/SBA-15(550)	0.0212
Bi-TiO_2/SBA-15(700)	0.0162
Bi-TiO_2/SBA-15(850)	0.0206
Bi_2O_3/SBA-15	0.00818
TiO_2/SBA-15(550)	0.00553
Bi_2O_3	0.00755
TiO_2	0.00540

temperature destructed pore structure and caused loss in surface area to some extent, reducing the oxygen vacancies. The samples at 850°C show better photocatalytic activity than samples at 700°C, which might be due to the formation of a new phase of $Bi_4Ti_3O_{12}$ having higher photocatalytic activity. The sample calcined at 550°C shows the highest photocatalytic activity in the decomposition of RhB under visible light. Furthermore, the doping of Bi could effectively limit the phase transformation, preventing the overgrowth of crystallites and enhancing the visible light absorption in comparison with TiO_2 and TiO_2/SBA-15.

In addition, the Bi-TiO_2/SBA-15 obtained at 550°C presents the highest photocatalytic activity. However, as an excellent catalyst, it should not only show higher activity but also present stability in recycle process. As shown in Figure 7, Bi-TiO_2/SBA-15 can preserve most of its catalytic activity after six cycles and this confirms that the as-prepared Bi-TiO_2/SBA-15 is stable under irradiation for photocatalytic decomposition of organic pollutants.

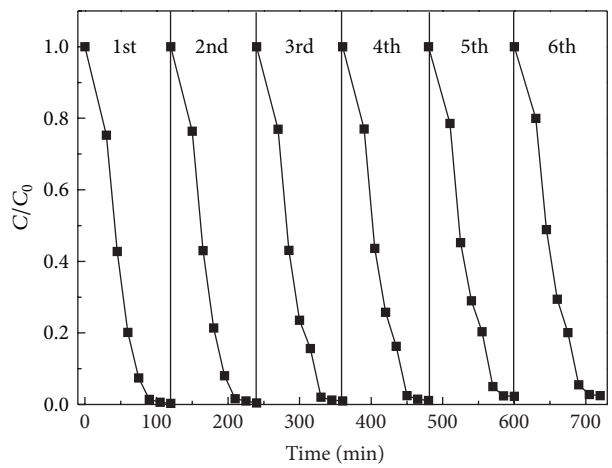

Figure 7: Recycling photocatalytic test of Bi-TiO_2/SBA-15 calcined at 550°C.

4. Conclusions

In conclusion, we have fabricated a visible photocatalyst Bi-TiO_2/SBA-15 material. The photocatalytic activity of the prepared photocatalysts was investigated by the photodegradation of RhB. A combination of XRD, XPS, Raman, nitrogen adsorption-desorption isotherm measurement, TEM, and UV-Vis absorption spectra has been used to characterize the Bi-TiO_2/SBA-15 material. The experiment results indicated that the Bi doping could enhance the photocatalytic activities than TiO_2. The calcination temperature strongly influenced the activity of the samples. The sample calcined at 550°C shows the highest photocatalytic activity in the decomposition of RhB under visible light. This work provides a new

pathway to design and fabricate novel photoactive materials for practical application in environmental cleaning.

Conflict of Interests

The authors declare that they do not have any commercial or associative interests that represents a conflict of interest directly or indirectly in connection with our work.

Acknowledgments

The authors are grateful for the financial support from the National Natural Science Foundation of China (no. 50978212), the State Key Program of Shaanxi Province Natural Science Foundation Project (no. 2012JZ7003), the Shaanxi Province Science and Technology and Innovation Project Foundation (no. 2011KTDZ01-05-05), and the Science Foundation from Education Department of Shaanxi Provincial Government (no. 2013JK0885 and no. 2013JK0650).

References

[1] A. Fujishima and K. Honda, "Electrochemical photolysis of water at a semiconductor electrode," *Nature*, vol. 238, no. 5358, pp. 37–38, 1972.

[2] J. Zhang, Z. Xiong, and X. S. Zhao, "Graphene-metal-oxide composites for the degradation of dyes under visible light irradiation," *Journal of Materials Chemistry*, vol. 21, no. 11, pp. 3634–3640, 2011.

[3] Y. Wang, R. Shi, J. Lin, and Y. Zhu, "Enhancement of photocurrent and photocatalytic activity of ZnO hybridized with graphite-like C_3N_4," *Energy and Environmental Science*, vol. 4, no. 8, pp. 2922–2929, 2011.

[4] Q. Y. Li, T. Kako, and J. H. Ye, "WO_3 modified titanate network film: highly efficient photo-mineralization of 2-propanol under visible light irradiation," *Chemical Communications*, vol. 46, no. 29, pp. 5352–5354, 2010.

[5] R. Li, W. Chen, H. Kobayashi, and C. Ma, "Platinum-nanoparticle-loaded bismuth oxide: an efficient plasmonic photocatalyst active under visible light," *Green Chemistry*, vol. 12, no. 2, pp. 212–215, 2010.

[6] J. Wang, Q. Cai, H. Li, Y. Cui, and H. Wang, "A review on TiO_2 nanotube film photocatalysts prepared by liquid-phase deposition," *International Journal of Photoenergy*, vol. 2012, Article ID 702940, 11 pages, 2012.

[7] H. Chen, J. Li, Q. Chen, D. Li, and B. Zhou, "Photoelectrocatalytic performance of benzoic acid on TiO_2 nanotube array electrodes," *International Journal of Photoenergy*, vol. 2013, Article ID 567426, 7 pages, 2013.

[8] Y. Wang, Y. Wang, Y. Meng et al., "A highly efficient visible-light-activated photocatalyst based on bismuth- and sulfur-codoped TiO_2," *Journal of Physical Chemistry C*, vol. 112, no. 17, pp. 6620–6626, 2008.

[9] L. Q. Jing, J. Wang, Y. C. Qu, and Y. B. Luan, "Effects of surface-modification with Bi_2O_3 on the thermal stability and photoinduced charge property of nanocrystalline anatase TiO_2 and its enhanced photocatalytic activity," *Applied Surface Science*, vol. 256, no. 3, pp. 657–663, 2009.

[10] Y. Q. Wu, G. X. Lu, and S. B. Li, "The doping effect of Bi on TiO_2 for photocatalytic hydrogen generation and photodecolorization of rhodamine B," *Journal of Physical Chemistry C*, vol. 113, no. 22, pp. 9950–9955, 2009.

[11] J. Hou, C. Yang, Z. Wang, S. Jiao, and H. Zhu, "Bi_2O_3 quantum dots decorated anatase TiO_2 nanocrystals with exposed (001) facets on graphene sheets for enhanced visible-light photocatalytic performance," *Applied Catalysis B*, vol. 129, pp. 333–341, 2013.

[12] D. Di Camillo, F. Ruggieri, S. Santucci, and L. Lozzi, "N-doped TiO_2 nanofibers deposited by electrospinning," *Journal of Physical Chemistry C*, vol. 116, pp. 18427–18431, 2012.

[13] K. Su, Z. Ai, and L. Zhang, "Efficient visible light-driven photocatalytic degradation of pentachlorophenol with Bi_2O_3/TiO_2-xBx," *Journal of Physical Chemistry C*, vol. 116, pp. 17118–17123, 2012.

[14] H. Y. Li, D. J. Wang, P. Wang, H. Fan, and T. Xie, "Synthesis and studies of the visible-light photocatalytic properties of near-monodisperse Bi-doped TiO_2 nanospheres," *Chemistry*, vol. 15, no. 45, pp. 12521–12527, 2009.

[15] S. Shamaila, A. K. L. Sajjad, F. Chen, and J. L. Zhang, "Study on highly visible light active Bi_2O_3 loaded ordered mesoporous titania," *Applied Catalysis B*, vol. 94, no. 3-4, pp. 272–280, 2010.

[16] S. Rengaraj, X. Z. Li, P. A. Tanner, Z. F. Pan, and G. K. H. Pang, "Photocatalytic degradation of methylparathion—an endocrine disruptor by Bi^{3+}-doped TiO_2," *Journal of Molecular Catalysis A*, vol. 247, no. 1-2, pp. 36–43, 2006.

[17] W. J. J. Stevens, K. Lebeau, M. Mertens, G. Van Tendeloo, P. Cool, and E. F. Vansant, "Investigation of the morphology of the mesoporous SBA-16 and SBA-15 materials," *Journal of Physical Chemistry B*, vol. 110, no. 18, pp. 9183–9187, 2006.

[18] C.-C. Yang, J. Vernimmen, V. Meynen, P. Cool, and G. Mul, "Mechanistic study of hydrocarbon formation in photocatalytic CO_2 reduction over Ti-SBA-15," *Journal of Catalysis*, vol. 284, no. 1, pp. 1–8, 2011.

[19] S. C. Zhang, D. Jiang, T. Tang et al., "TiO_2/SBA-15 photocatalysts synthesized through the surface acidolysis of $Ti(OnBu)_4$ on carboxyl-modified SBA-15," *Catalysis Today*, vol. 158, no. 3-4, pp. 329–335, 2010.

[20] V. Tajer-Kajinebaf, H. Sarpoolaky, and T. Mohammadi, "Synthesis of nanostructured anatase mesoporous membranes with photocatalytic and separation capabilities for water ultrafiltration process," *International Journal of Photoenergy*, vol. 2013, Article ID 509023, 11 pages, 2013.

[21] D. Zhao, J. Feng, Q. Huo et al., "Triblock copolymer syntheses of mesoporous silica with periodic 50 to 300 angstrom pores," *Science*, vol. 279, no. 5350, pp. 548–552, 1998.

[22] D. Zhao, Q. Huo, J. Feng, G. H. Fredrickson, and G. D. Stucky, "Nonionic triblock and star diblock copolymer and oligomeric sufactant syntheses of highly ordered, hydrothermally stable, mesoporous silica structures," *Journal of the American Chemical Society*, vol. 120, no. 24, pp. 6024–6036, 1998.

[23] J. Ma, J. Chu, L. S. Qiang, and J. Xue, "Synthesis and structural characterization of novel visible photocatalyst Bi-TiO_2/SBA-15 and its photocatalytic performance," *RSC Advances*, vol. 2, pp. 3753–3758, 2012.

[24] S. Y. Chai, Y. J. Kim, M. H. Jung, A. K. Chakraborty, D. Jung, and W. I. Lee, "Heterojunctioned BiOCl/Bi_2O_3, a new visible light photocatalyst," *Journal of Catalysis*, vol. 262, no. 1, pp. 144–149, 2009.

[25] Q. S. Huo, R. Leon, P. M. Petroff, and G. D. Stucky, "Mesostructure design with gemini surfactants: supercage formation in

a three-dimensional hexagonal array," *Science*, vol. 268, no. 5215, pp. 1324–1327, 1995.

[26] Y. J. Acosta-Silva, R. Nava, V. Hernández-Morales, S. A. Macías-Sánchez, M. L. Gómez-Herrera, and B. Pawelec, "Methylene blue photodegradation over titania-decorated SBA-15," *Applied Catalysis B*, vol. 110, pp. 108–117, 2011.

[27] S. Perathoner, P. Lanzafame, R. Passalacqua, G. Centi, R. Schlögl, and D. S. Su, "Use of mesoporous SBA-15 for nanostructuring titania for photocatalytic applications," *Microporous and Mesoporous Materials*, vol. 90, no. 1–3, pp. 347–361, 2006.

[28] J. J. Xu, Y. H. Ao, D. G. Fu, and C. Yuan, "Synthesis of Bi_2O_3-TiO_2 composite film with high-photocatalytic activity under sunlight irradiation," *Applied Surface Science*, vol. 255, no. 5, pp. 2365–2369, 2008.

[29] M.-W. Chu, M. Ganne, M. T. Caldes, and L. Brohan, "X-ray photoelectron spectroscopy and high resolution electron microscopy studies of Aurivillius compounds: $Bi_{4-x}La_XTi_3O_{12}$($x = 0$, 0.5, 0.75, 1.0, 1.5, and 2.0)," *Journal of Applied Physics*, vol. 91, no. 5, pp. 3178–3187, 2002.

[30] Y. Z. Li and S.-J. Kim, "Synthesis and characterization of nano titania particles embedded in mesoporous silica with both high photocatalytic activity and adsorption capability," *Journal of Physical Chemistry B*, vol. 109, no. 25, pp. 12309–12315, 2005.

[31] S. Zheng, Y. Cai, and K. E. O'Shea, "TiO_2 photocatalytic degradation of phenylarsonic acid," *Journal of Photochemistry and Photobiology A*, vol. 210, no. 1, pp. 61–68, 2010.